SEISMIC STRENGTHENING OF LOW-RISE UNREINFORCED MASONRY STRUCTURES WITH FLEXIBLE DIAPHRAGMS

A Thesis
Presented to
The Academic Faculty

by

Franklin L. Moon

In Partial Fulfillment
of the Requirements for the Degree
Doctor of Philosophy in
Civil and Environmental Engineering

Georgia Institute of Technology
May 2004

SEISMIC STRENGTHENING OF LOW-RISE UNREINFORCED MASONRY STRUCTURES WITH FLEXIBLE DIAPHRAGMS

Approved:

Roberto T. Leon, Advisor

Lawrence F. Kahn, Co-Advisor

Reginald DesRoches

Russell T. Gentry

Date Approved: December 9, 2004

ACKNOWLEDGMENTS

The author would like to express his sincere gratitude to his advisor Dr. Roberto T. Leon and his co-advisor Dr. Lawrence F. Kahn for their guidance, technical expertise, and continuous support throughout this research. The author is indebted to them for the education, direction, and example they have provided, and looks forward to a continued relationship with them in the future. The assistance provided by the dissertation advisory committee is also gratefully acknowledged. Thank you Dr. Reginald DesRoches, and Dr. Russell T. Gentry.

The author would like to extend his sincere appreciation to his good friend and colleague, Tianyi Yi, for his invaluable contribution throughout all phases of this research. The laboratory assistance of Justin Ocel, Thomas Pfeifer, Brandon Buchberg, Michael Delemont, Adam Slapkus, Jason McCormick, Scott Canfield, Malcolm Foss, and Jason Frost is gratefully acknowledged. The author would also like to acknowledge Dr. Daniel P. Abrams (University of Illinois), Steven C. Sweeney and Orange S. Marshall (Construction Engineering Research Laboratory), Bill Kjorlein and Bryan Light (Southern Brick Institute), Gordon Brown (Clark Schwebel Tech-Fab), and Fred Isley (Hexcel Composites) for their contributions to this research.

This research was primarily supported by the National Science Foundation through the Mid-America Earthquake Center (award number EEC-9701785). Financial support was also provided by the US Army Corps of Engineers Construction Engineering Research Laboratory and the Market Development Alliance of the FRP Composites Industry. Material donations by Cherokee Brick and Tile, Lafarge (Blue Circle) Cement,

A&P Technology, Clark Schwebel Tech-Fab, Hexcel Composites, Hughes Brothers, Saint-Gobain, Sika Corporation, Dur-O-Wal Inc., and Simpson Strong-Tie, are also gratefully acknowledged. The findings and conclusions reported herein are those of the author and do not necessarily represent the opinions, conclusions, or recommendations of the National Science Foundation or any other sponsoring or cooperating organization.

The author would like to thank his parents, Helen S. Moon and Joseph M. Moon for their loving support and encouragement. Finally, to my wife, Erica C. Moon, thank you for your patience, love, and encouragement.

TABLE OF CONTENTS

LIST OF TABLES

LIST OF FIGURES

NOTATION

α	factor accounting for different boundary conditions, 0.5 for a cantilever pier and 1.0 for a fixed-fixed pier
Δ_{cf}	pier displacement at compression failure after retrofit with flexural FRP
Δ_{db2}	pier displacement at compression failure after debonding of flexural FRP
Δ_{dtdb}	pier displacement at debonding of diagonal FRP
Δ_{tc}	pier displacement at compression failure
$\Delta_{elastic}$	maximum elastic displacement of pier
Δ_{tf}	displacement at tension failure of flexural FRP
$d\varepsilon_{c,j}$	incremental change in the centroid strain of the cross-section at step j
$d\varepsilon_{i,j}$	incremental change in the axial strain of fiber i at step j
$d\phi_j$	incremental increase in the curvature of the cross-section at step j
ε_{db}	debonding strain of FRP
ε_{fu}	ultimate tensile strain of FRP
ϕ_{tc}	pier curvature at compression failure
γH	height of pier inflection point above the base
λ	indicator of boundary condition, 12 for a fixed-fixed pier and 3 for a cantilever pier
$\sigma_{i,j}$	stress in fiber i at step j
θ	angle of diagonal tension FRP
θ_j	rotation at the top of the first story

τ_f	shear strength of flexural FRP in the transverse direction
a_{cf}	depth of compressive stress block at compression failure of masonry following the application of flexural FRP
a_{db}	depth of compressive stress block at compression failure of masonry following the debonding of flexural FRP
a_{tc}	depth of compressive stress block at compression failure of masonry
A_i	area of fiber i
A_n	net area of pier
A_v	shear area of pier
c	distance from extreme compressive fiber to the neutral axis
c_{db}	distance from extreme compressive fiber to the neutral axis at debonding of flexural FRP
d	distance from extreme compression fiber to the centroid of reinforcement
d_i	distance between the centroid of the cross-section and fiber i
dM_j	incremental change in the moment applied to the cross-section at step j
dP_j	incremental change in the axial force applied to the cross-section at step j
E_f	FRP elastic modulus
$E_{i,j}$	tangent elastic modulus of fiber i at step j
f_{ctm}	surface tensile strength of substrate
f_{db}	tensile stress in FRP at debonding
f_{dt}'	diagonal tension strength of masonry
f_f	stress in FRP

f_{flange}	initial vertical stress in flange
f_m'	compression strength of masonry
G_m	shear modulus of masonry (taken as $0.4E_m$)
H	pier effective height
H_1	the height of the first story.
I_g	pier gross moment of inertia
k_m	fraction of ultimate strain attainable prior to debonding
k_p	factor to account for the influence of FRP width relative to substrate width
$K_{elastic}$	pier elastic stiffness
L	pier length
L_d	required bond length of FRP to maximize bond strength
L_f	bond length of FRP
L_{gf}	effective length of global tension flange
m	number of plies
M_{cf}	moment at compressive failure of masonry following the application of flexural FRP
M_{db}	moment at debonding of flexural FRP
M_{db2}	moment at compressive failure of masonry following the debonding of flexural FRP
M_{tf}	moment at tension failure of flexural FRP
n	ratio of FRP elastic modulus to masonry elastic modulus
P	vertical compressive force on the pier

t_{dt}	thickness of diagonal FRP
t_f	thickness of flexural FRP
t_{gf}	thickness of out-of-plane wall
t_m	pier thickness
T_u	tension force in FRP at bond failure
v_{te}	bed-joint shear strength
v_{me}	expected bed-joint shear strength including frictional resistance
V_{bjs1}	initial bed-joint sliding strength of pier
V_{bjs2}	bed-joint sliding of pier after cracking
V_{cf}	pier strength associated with compressive failure of masonry after the application of flexural FRP
V_{db1}	pier strength associated at debonding of flexural FRP
V_{db2}	pier strength associated with compressive failure of masonry after debonding of flexural FRP
V_{dt}	diagonal tension strength of pier
V_{dtdb1}	pier strength at debonding of diagonal FRP
V_{dtdb2}	pier strength provided by diagonal FRP after debonding
V_{dttf}	pier strength at tension failure of diagonal FRP
V_r	rocking strength of pier
V_{sf}	pier strength at shear failure of flexural FRP
V_{tc}	toe crushing strength of pier
V_{tf}	shear force at tension failure of flexural FRP
w_{dt}	width of diagonal FRP

w_f	width of flexural FRP
W_{gf}	weight of the global tension flange

SUMMARY

As a capstone to several Mid-America Earthquake Center (MAE Center) projects, a full-scale two story unreinforced masonry (URM) building was tested following the application of several retrofit techniques, which included the use of fiber reinforced polymer (FRP) overlays, near surface mounted (NSM) rods, vertical unbonded post-tensioning, and joist anchors. The test structure was composed of four URM walls, flexible timber diaphragms and interior stud walls, and was designed and built following construction practices consistent with those used in Mid-America prior to 1950. Initial testing subjected both the roof diaphragm and in-plane walls to slowly applied lateral load reversals in an unreinforced sate. Following this series of tests, each in-plane wall was retrofit and retested.

Experimental results indicated that global issues such as flange participation and the effects of overturning moment substantially impacted the response of primary components both before and after retrofit. FRP retrofit techniques resulted in strength increases up to 32% and displayed a pseudo-ductile response caused by progressive debonding. For cases where such retrofits forced sliding failures, large increases in energy dissipation resulted. The use of vertical unbonded post-tensioning resulted in strength increases between 40%-60%; however, piers displayed a tendency to switch from a ductile rocking/sliding mode to a more brittle diagonal tension mode. In addition, results highlighted the need for retrofit schemes to employ both horizontal and vertical reinforcement to prevent progressive crack opening that can decrease wall displacement capacity.

Based on the experimental results, the model implied by the "Prestandard for the Rehabilitation of Existing Structures", FEMA 356, for the analysis of in-plane URM walls was modified and extended to (1) include the effect of FRP pier retrofits and (2) consider the global effects of URM structures. The resulting model displayed reasonable estimates of measured response both before and after retrofit, with an average error of 14%. In addition, the proposed model displayed improvements over the current model from 14% to 66%. Based on the results of sensitivity analyses this improved accuracy was primarily attributed to the consideration of global effects.

CHAPTER 1

INTRODUCTION

1.1 Problem Statement

Past earthquakes, including the 1886 Charleston, 1906 San Francisco, 1925 Santa Barbara, and the 1933 Long Beach earthquakes, have illustrated the seismic vulnerability of unreinforced masonry (URM) structures in the United States. These events prompted the 1933 passage of the California Field Act, which banned the use of URM for public buildings in California. This ban was subsequently adopted by other western states; thus, URM construction was effectively halted west of the Rocky Mountains. Until recently however, URM structures continued to be constructed in other areas, including areas erroneously classified as low seismic regions, such as the Mid-Western United States (Mid-America region). As a result, a large population of URM structures, which present a risk to life safety, are currently in service in seismic regions as commercial, residential and essential facilities.

1.2 URM Construction in Mid-America

The construction of URM buildings in the Mid-America region dates back to the 1770s (ATC, 1997). Typically these structures were built with exterior masonry bearing walls, interior cross walls (either masonry or timber), and flexible timber diaphragms (see Figure 1.1). The masonry walls were commonly composed of sand-lime mortar and solid clay bricks laid in standard American bond with brick headers supplied every sixth or seventh course to connect the wythes. The joints were unreinforced, which results in

brittle material behavior that contributes to the seismic vulnerability of these structures. In addition, this lack of steel reinforcement also makes these structures extremely durable, and enables them to remain in service for hundreds of years, thus creating a large inventory of these hazardous structures. Diaphragms in these structures were commonly constructed of timber and employ either straight or diagonal sheathing boards. Typical connections consisted of joists supported in pockets in the masonry wall, commonly one wythe deep. In many structures no additional connections exist between the diaphragm and the masonry walls.

Figure 1.1. St. Louis Firehouse #11 (circa 1950)

1.3 Overview of MAE Center Research

To address the seismic vulnerability of the built inventory in the Mid-Western United States, the Mid-America Earthquake Center (MAE Center) was formed in 1997. This center was charged with the formidable task of reducing earthquake losses

throughout Mid-America. As a first step, an investigation focused on providing information on the age and structural characteristics of the building stock in Mid-America was undertaken. The study focused primarily on essential facilities, which were defined as facilities that support functions related to post-earthquake emergency response and disaster recovery, and included hospitals, schools, fire stations, and police stations (French and Olshansky, 2000). Through this project, approximately 5,500 essential facilities were identified in 93 counties throughout the New Madrid Seismic Zone (see Figure 1.2). Of these facilities, a sample of 1,300 were chosen to gain insight into the overall inventory. The findings were sobering; nearly one third of all essential facilities were composed of URM, including over 15% of the essential facilities constructed between 1980 and 2000. In addition, it was found that only 6% of these facilities have been retrofit to reduce their vulnerability.

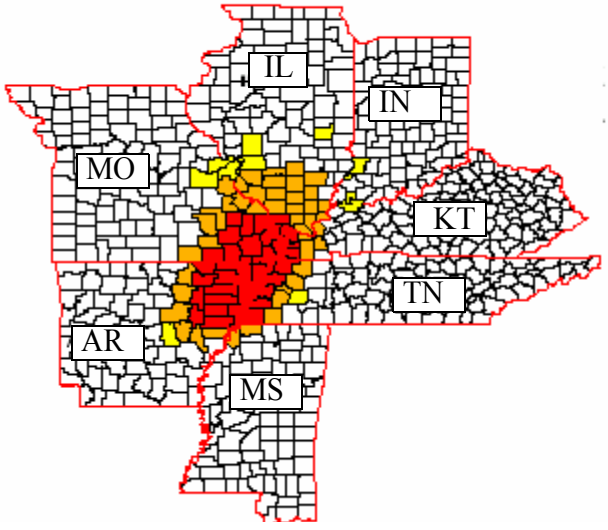

Figure 1.2. Map illustrating the 93 counties included in MAE Center Project SE-1 (taken from French and Olshansky, 2000)

Due to the large population of URM structures throughout the Mid-America region (and their poor performance in past earthquakes), reducing the vulnerability posed by these structures became a major focus of the MAE Center. The resulting research program was aimed at (1) investigating the behavior of URM structures and (2) the development of effective rehabilitation strategies. A list of these project numbers and titles is given in Table 1.1.

Table 1.1. Summary of supporting MAE Center projects

MAE Center Project #	Project Title
SE-1 (Georgia Tech)	Inventories of Essential Facilities in Mid-America
ST-4 (Georgia Tech)	Response Modification Applications for Essential Facilities
ST-5 (Georgia Tech)	MDOF Response of Low-Rise Buildings
ST-6 (University of Illinois)	Performance of Rehabilitated URM Components
ST-8 (Texas A&M)	Performance of Rehabilitated Floor and Roof Diagrams
ST-9 (Georgia Tech)	Performance Objectives for Essential Facilities
ST-10 (University of Illinois)	Dynamic Tests of Low-Rise Building Systems
ST-11 (Georgia Tech)	Large-Scale Tests of Low-Rise Building Systems
ST-22 (CERL)	Performance of Rehabilitated Unreinforced Masonry Building Systems
ST-45 (CERL)	Seismic Rehabilitation of Unreinforced Masonry Walls

The first stage of this program investigated the behavior of each major component found in typical URM essential facilities in the Mid-America region. Specifically, projects ST-6 and ST-45 investigated the behavior of in-plane URM piers and several retrofit

techniques including the application of FRP overlays, reinforced cores, shotcrete, and ferrocement. The dynamic stability of out-of-plane URM walls was the focus of project ST-10, which involved several dynamic tests on an idealized URM structure. Project ST-8 assessed the behavior of flexible timber diaphragms as well as the effectiveness of plywood overlays, steel trusses, and joist anchors as retrofit techniques.

As a capstone to these investigations, two URM structures were tested to (1) identify the extent to which component data could be extrapolated to predict overall structure response; (2) validate the effectiveness of several component retrofit techniques to improve overall structure performance; and (3) compare the response of URM structures to quasi-static and dynamic loadings. The first of these capstone projects (Project ST-11) centered on the quasi-static testing of a full-scale two story URM structure (the research described in this thesis is part of Project ST-11). In parallel with this investigation, a similar half-scale structure was tested dynamically at the Construction Engineering Research Laboratory (CERL) in Champaign, IL (Project ST-22). These projects examined the behavior of the test structures in an unreinforced state as well as after retrofit. Retrofit techniques focused primarily on in-plane components and included the use of FRP overlays, near surface mounted (NSM) rods, and vertical unbonded post-tensioning.

1.4 Motivation for Research

Current guidelines and prestandards (ATC, 1997 and ATC, 2000) available for the analysis and subsequent rehabilitation of URM structures, are based almost entirely on past research that has focused on component behavior. As a result, these documents

provide guidance for the determination of component response; however, little insight is offered into the interaction between components or the impact of global effects on component response.

To fill this void, a full-scale test of a URM structure before and after retrofit was conducted. Specifically, the purpose of this test is to make contributions in three primary areas. First, such a test allows the relevance of the large amount of work conducted on component behavior to be identified. While it is common practice to extrapolate out component behavior to predict overall structure response, the simplifying assumptions required to make such a step must be experimentally validated. Second, this test provides a means to validate analytical models and current code provisions, thus increasing the accuracy of tools available to practicing engineers. Third, this test determines the effectiveness of modern retrofit techniques on overall structure performance. Knowing how the retrofit techniques contribute to overall building response permits their safe and effective application for seismic upgrading of URM facilities.

1.5 Research Plan and Objectives

The research described in this thesis, which was part of Project ST-11, centers on the seismic rehabilitation of low-rise URM structures in the Mid-America region. Table 1.2 gives a summary of the research plan and objectives.

Table 1.2. Summary of research plan and objectives

Research Plan	Research Objectives
Review the available literature on strengthening techniques for URM structures	Gain insight into past research in order to maximize the impact of this investigation
Test a full-scale two story URM structure before and after the application of several seismic retrofit techniques	Investigate the behavior of each retrofit technique in terms of damage progression and failure modes
	Assess the effect of each retrofit technique on overall structure performance in terms of strength, stiffness, energy dissipation, damage progression, and failure modes
	Identify global effects of URM structures that impact the behavior of primary components
Modify and extend the model presented in FEMA 356 (ATC, 2000) to consider (1) the effect of retrofit techniques and (2) the global effects of URM structures	Investigate the ability of simplified models based on component behavior to predict overall structure response
	Investigate the influence of global effects on the response of low-rise URM walls
	Investigate the influence of material properties on the response of low-rise URM walls
Summarize principal findings	Propose recommendations for the evaluation and subsequent rehabilitation of URM structures

1.6 Outline

Chapter 2 presents a brief review of the literature available on the behavior of URM structures as well as retrofit techniques. In Chapter 3 the experimental program is detailed including descriptions of the test structure, retrofit measures, test sequence, loading protocol, and instrumentation. Chapter 4 presents the experimental results of the testing of the structure before and after retrofit. The proposed modifications to the existing

FEMA 356 (ATC, 2000) model are presented in Chapter 5. In addition, a comparison between the proposed model and the experimental results is also presented. Chapter 6 provides a summary of the findings of this research.

This dissertation is divided into two volumes. Volume I contains the main body as described in the previous paragraph. Volume II contains appendices that provide detailed drawings of the test setup and instrumentation plan (Appendix A), descriptions of the reduction and manipulation of test data (Appendix B), detailed descriptions of the behavior of each wall of the test structure after retrofit (Appendix C through F), and a numerical analysis example (Appendix G).

CHAPTER 2

LITERATURE REVIEW

2.1 Behavior of URM Structures

The response of URM structures to earthquake excitation differs substantially from the response of more modern structural systems, such as reinforced concrete or steel frame structures. This unique behavior is primarily caused by the high stiffness and brittle material behavior exhibited by masonry, coupled with the presence of flexible floor diaphragms. As a result, a special procedure, known as the ABK method, was developed in the early 1980's to analyze and subsequently rehabilitate these structures. This methodology was the result of a joint venture by three Los Angeles engineering consulting firms (Agbabian & Associates, S. B. Barnes & Associates, and Kariotis & Associates), and was based on several analytical, experimental, and post-earthquake investigations. Although this procedure was developed for use in California, it has become the foundation of nearly all standard and prestandards aimed at mitigating the seismic hazard posed by URM structures, such as UCBC (ICBO, 1991), ATC-14 (1987), ATC-22 (1989), and ATC (1992). It is interesting to note, that although the ABK method has enjoyed wide acceptance, many of its key principles remain controversial (Bruneau, 1994). Whatever controversy remains, the foundation of the ABK method provides a great deal of insight into the seismic behavior of URM structures and the subsequent need for strengthening.

To illustrate the response of URM structures, as defined by the ABK method, consider a typical URM building under earthquake excitation shown in Figure 2.1. For

simplicity, the direction of the ground motion is assumed to be parallel to one pair of walls. Based on this assumption, three principal components of URM structures are defined: in-plane walls (walls parallel to the direction of ground motion), out-of-plane walls (walls perpendicular to the direction of ground motion), and flexible floor diaphragms. Due to their high stiffness, ground accelerations are assumed to be exclusively transmitted into the structure through the in-plane walls. Essentially, this assumption recognizes that the low strength exhibited by out-of-plane URM walls severely limits their capacity to transfer forces. The vibration of the in-plane walls then excites the diaphragms at their ends. Since the diaphragms in these structures are typically flexible, large acceleration amplifications along the diaphragms can result. Finally, the response of the diaphragms load the out-of-plane walls. Based on this idealized behavior, a load path capable of transferring forces from the out-of-plane walls through the diaphragms to the in-plane walls is required to avoid failure. This non-redundant load path, coupled with brittle material behavior and poor connections, renders URM structures extremely vulnerable to ground accelerations.

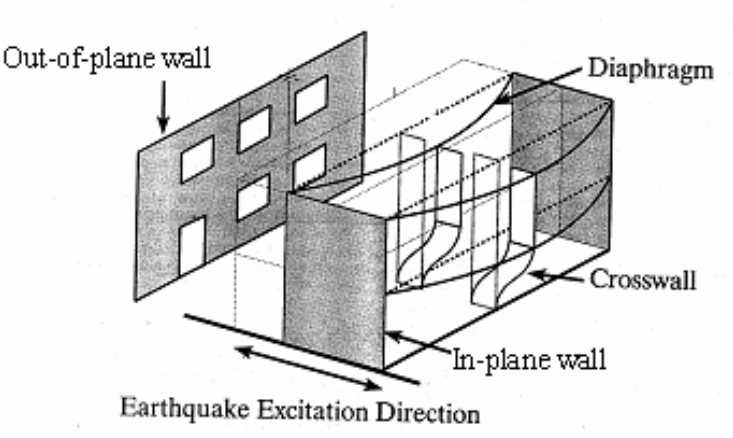

Figure 2.1. Schematic of typical URM building under earthquake excitation (taken from Bruneau, 1994)

2.2 Common URM Failures

The poor performance of URM structures during earthquakes has been well documented. Post-earthquake investigations and experimental research have shown that failures of URM structures can be grouped into the following categories (Deppe, 1988; Boussabah and Bruneau, 1992; Bruneau, 1994; Tomazevic, 1999; ST-8, 2000):

- Lack of connections, or connection failure
- Out-of-plane failures
- In-plane failures
- Diaphragm related failures
- Combined in-plane and out-of-plane failures, including cracks at wall intersections

2.2.1 Connection Failures

One of the most common failures observed is associated with insufficient connections between major components of URM structures. The more common type of these failures is due to poor anchorage between the diaphragm and the out-of-plane wall (i.e. either lack of anchorage or anchorage failure). Based on past studies, the stability of the out-of-plane walls during an earthquake has been shown to be directly related to the effective height to thickness ratio (ABK, 1984; ATC, 2000). Without sufficient anchorage, out-of-plane URM walls effectively act as cantilevers spanning from the foundation to the roof, and as a result can become unstable even during relatively minor ground motions (Bruneau 1994). The result is the complete or partial collapse of the out-of-plane wall (see Figure 2.2). If the out-of-plane walls are supporting the floor systems, the failure of the out-of-plane walls can result in the collapse of the diaphragms.

The other common type of connection failure is due to a poor shear connection between the in-plane walls and the diaphragms. In these cases the diaphragm relies primarily on the more vulnerable out-of-plane walls for lateral support. The result is damage to the corners between the out-of-plane walls and in-plane walls, and in some cases the complete collapse of the out-of-plane walls and diaphragm.

Figure 2.2. Typical out-of-plane wall collapse due to insufficient anchorages (taken from www.nisee.org).

2.2.2 Out-of-Plane Failures

If sufficient anchorage is provided to transmit forces from the out-of-plane wall to the diaphragm, failures of out-of-plane URM walls are rare (Bruneau, 1994). The sufficient anchorage allows the out-of-plane walls to span between floors thus reducing their slenderness and improving their stability. However even with sufficient anchorage, URM walls may fail out-of-plane if the wythes are not properly tied together. That is, if header courses are not sufficient, cracks can develop in the collar joint thus causing each

wythe of the wall to behave independently. Other common out-of-plane failures include the collapse of parapets or gables that cantilever above the roof level (see Figure 2.3).

Figure 2.3. Typical parapet failure (taken from www.nisee.org).

2.2.3 In-Plane Failures

In-plane failures are a result of excessive shear or flexural forces placed on the components of URM in-plane walls. Perforated masonry walls are composed of two main elements: piers (shear walls between openings) and spandrels (deep beams above and below openings). Typically, in-plane failures occur in only one of these elements. In most cases, the resulting damage alters the behavior of the walls and precludes the failure of the other component. However, past research has almost exclusively focused on the behavior of pier elements, since the final collapse of URM structures is almost always a result of pier failure (Calvi et al., 1996). The four principal failure modes for URM piers have been studied extensively and are identified in Figure 2.4 and as follows (ATC, 2000):

- Rocking - failure initiates with large flexural cracks developing at the bottom and the top of the pier. As the displacement increases the pier deforms as a rigid body rotating about the compressive toe.
- Bed-joint sliding - failure initiates by the formation of horizontal shear cracks in the bed-joint. The pier deforms by sliding along the bed-joint with resistance offered by friction alone.
- Diagonal tension - identified by diagonal shear cracking caused by the maximum principle tension stress exceeding the tension strength of masonry. The cracks may propagate in a stair-stepped manner through the bed-joints and head-joints of the masonry or may pass directly through the bricks, depending on the relative strength of the mortar joints, brick-mortar interface, and bricks.
- Toe crushing - defined as a compressive failure of masonry occurring at the toe of the pier. Toe crushing is typically observed after rocking deformations.

Several researchers have noted that the behavior of URM piers is highly dependant on the level of vertical stress (ATC, 1999b). Typically for piers with low levels of vertical stress, rocking or sliding govern the response. These failure mode have been observed to exhibit large displacement capacities. At higher levels of vertical stress, diagonal tension and toe-crushing failures are far more common. These failures are typically assumed to be brittle; however, if a diagonal crack forms in a stair stepped manner (i.e. around the units) large displacement capacities have been observed due to the sliding deformation that results.

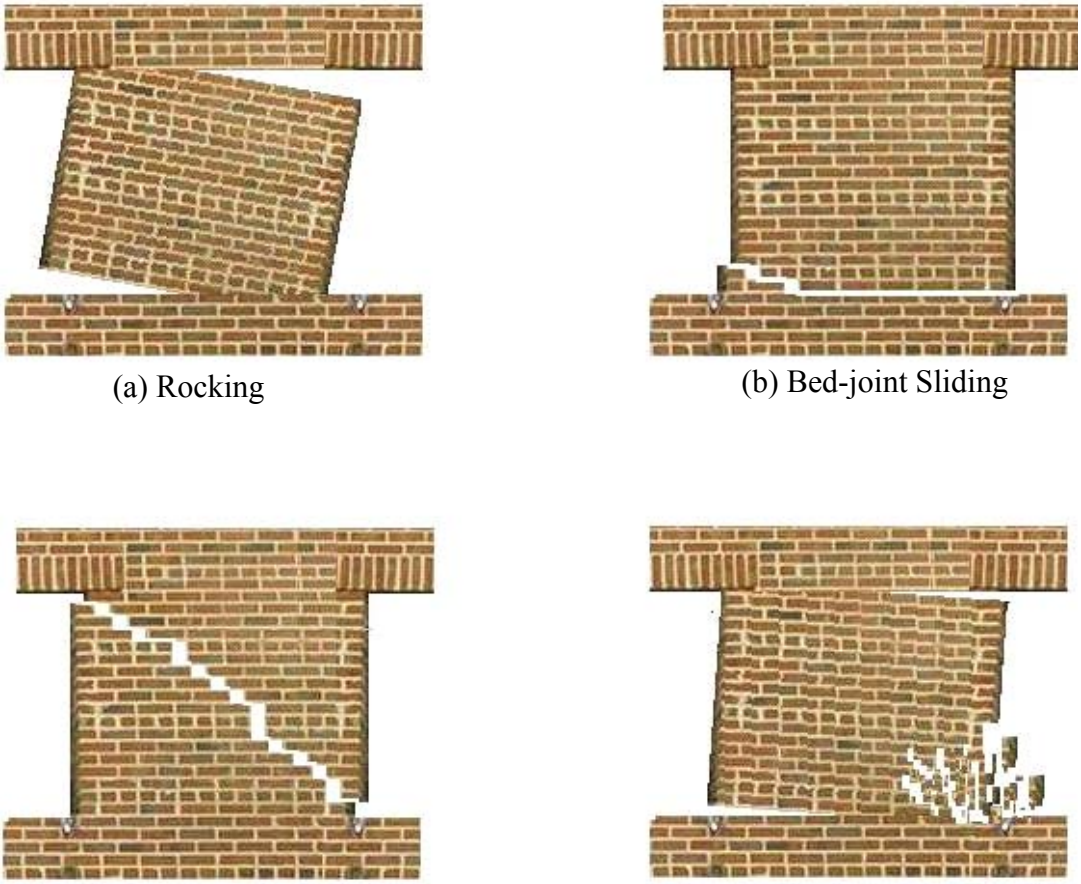

(a) Rocking (b) Bed-joint Sliding

(c) Diagonal Tension (d) Toe Crushing

Figure 2.4. In-plane URM pier failure modes

2.2.4 Diaphragm Failures

Diaphragm failures in URM structures are rarely seen during earthquake reconnaissance. This is likely due to the relatively large displacement capacity associated with typical diaphragms. However, diaphragms can cause damage to other portions of URM structures. Diaphragms in URM structures behave as deep beams simply supported at either end. Under lateral load, the ends of the diaphragms rotate which can cause damage to the corners of URM structures.

2.3 Retrofit Techniques

In an attempt to mitigate the observed failures discussed in the previous section, several investigations have been conducted to develop effective retrofit techniques (ATC, 1999c). As outlined in Chapter 1, the primary focus of this research (in terms of retrofit) was on in-plane techniques. As a result, the review of literature on URM retrofit focused primarily on in-plane methods. A brief discussion of connection retrofit techniques is also presented as this is a secondary focus of this investigation.

2.3.1 Connection Retrofit

As apparent from the idealized behavior adopted by the ABK methodology and commonly observed failures, sufficient connections between the diaphragms and URM walls are essential to ensure acceptable behavior. However, the majority of URM structures currently in service throughout Mid-America do not contain such a connection. Typical construction details consist of supporting the joists of the diaphragm in pockets of the URM walls. Although these pockets are typically grouted, little, if any resistance to tensile forces can be developed in such a connection. Furthermore, in most cases no connections between the diaphragm and URM walls parallel to the joists exist.

To mitigate these potentially hazardous details, a connection retrofit technique, known as joist anchors or wall anchors, has been developed. Joist anchors commonly consist of a steel strap, developed into the diaphragm, which is connected to a 5/8 in. to 3/4 in. threaded rod that runs through the URM wall and is anchored on the outside of the structure by a bearing plate. According to FEMA 178 (ATC, 1992), the bearing plate should have an area of at least 30 in^2 to avoid a pullout failure of the anchor. Furthermore,

a minimum connection spacing of 4 ft. is recommended to avoid collapses in between connections. The effectiveness of joist anchors has been investigated through several reduced-scale dynamic tests of URM structures (see Section 2.4.1).

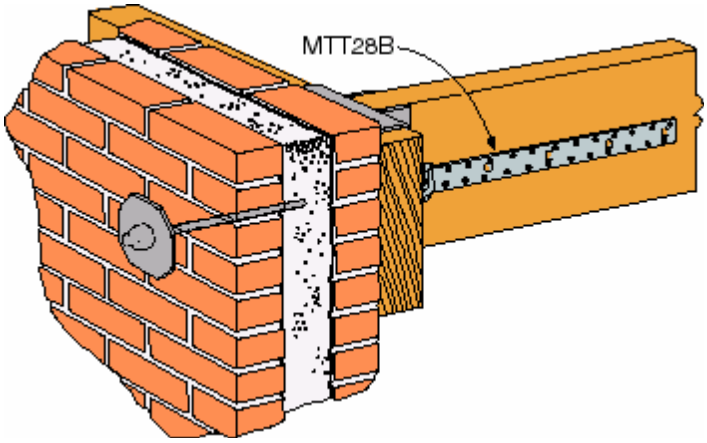

Figure 2.5. Schematic of installed joist anchor retrofit (taken from www.strong-tie.com).

2.3.2 Traditional In-Plane Wall Retrofit Techniques

Two methods have traditionally been used for seismic strengthening of URM walls. The first method involves the removal of one or more wythes of brick and subsequently filling the void with pneumatically applied concrete (shotcrete). Kahn (1984) showed that this method is very effective in increasing both the strength and the ductility of URM walls. However, the use of shotcrete is costly, due both to the large amount of formwork and surface preparation it requires. In addition, this method typically adds considerable weight to the structure, which results in larger inertia forces during an earthquake and may require foundation adjustments.

The second strengthening method that has been traditionally used involves the application of thin surface coatings to one or both sides of a URM wall. Typical surface

coatings include glass-reinforced cement, ferrocement, and wire mesh reinforced cement, Prawel et al. (1986). Several studies conducted on the use of mesh-reinforced mortar coatings showed that such coatings were able to double the in-plane strength of the URM walls (Jabarov et al., 1980; Sheppard and Terceli, 1980). Lee and Prawel (1991), focused on experimental tests of URM walls retrofit with a ferrocement coating. Results showed that in-plane strength, out-of-plane strength, ductility, and energy dissipation increased. While several of these surface coating techniques have been shown to be effective in improving the behavior of URM walls, they are typically labor intensive and create a great deal of disturbance to the occupants of the structure during retrofit.

In addition to strengthening methods, two methods have been developed and used for repair of damaged URM walls. One method, known as crack injection, consists of pumping a structural adhesive into existing cracks in order to bond the damage substrate together. Typically epoxy is used; however, for the cases of partially filled collar joints, epoxy can escape into the voids and thus is not an effective adhesive. The second type of repair technique is called repointing. This involves the removal of damaged bed-joints and the replacement with new mortar. For more information on these traditional methods as well as others, the reader is directed to FEMA 307 (ATC, 1999b).

2.3.3 In-Plane Wall Retrofit with FRP

The introduction of advanced composite materials into the field of structural engineering has prompted the re-examination of several issues previously investigated with traditional materials. This is particularly true for the case of URM structures where traditional retrofit techniques typically are extremely intrusive to building occupants,

expensive, and in some cases add considerable mass to the structure requiring foundation adjustments. In contrast, FRP techniques are non-intrusive, inexpensive, and add little mass. Although these techniques are relatively new, several applications to existing URM structures have been reported (Ehsani and Saadatmanesh, 1996; Ehsani, 1995; Velazquesz et al., 2000b; Tumialan et al., 2001). In one case, the FRP solution was approximately 15% the cost of the shotcrete alternative, hightlighting the enormous economical advantage of FRP systems (Ehsani, 1995). In general, two types of FRP systems have received attention. The first system is commonly referred to as FRP overlays and consists of FRP sheets or strips bonded to one or both sides of a URM wall. The second system requires that bed-joints of a URM wall be raked out and FRP bars bonded in with a high strength epoxy. This system is commonly referred to as near surface mounted (NSM) bars or structural re-pointing.

Several investigations on the use of FRP materials to improve the in-plane behavior of URM walls have been conducted in recent years. At the material level, a three-brick assemblage has been used to assess the impact of FRP overlays on bed-joint shear strength (Marshall at al., 2000; Ehsani and Saadatmanesh, 1996; Ehsani, 1995; and Ehsani et al., 1997). Figure 2.6 shows a schematic of a typical test setup. Results have shown increases in bed-joint shear strength of over ten times the strength of control specimens. It has been noted that the increase in strength is directly proportional to the strength and size of the fabric used (Marshall et al., 2000). Force-displacement responses were found to be highly dependent on fiber orientation, although the ultimate strengths associated with the different fiber orientations did not vary much (Ehsani, 1995; and Ehsani et al., 1997). Fibers oriented at +/-45^{o} from the direction of the load displayed

behavior classified as linear to failure, while specimens strengthened with fibers oriented at 0^o-90^o to the direction of the load displayed a nonlinear response. This behavior is consistent with the findings of earlier research that reported the stress-strain relation of composites is linear in tension and compression and nonlinear is shear (Vinson, 1998).

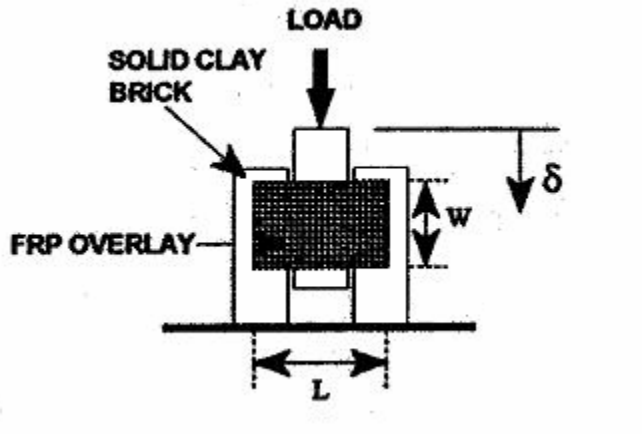

Figure 2.6. Schematic of 3-brick test setup (taken from Ehsani et al., 1997)

The second type of experiment that has been employed, subjected 4 ft. by 4 ft. sections of URM walls to diagonal compression in accordance with ASTM 518-80 (Marshall et al., 2000). Results showed little strength increase. However, the walls strengthened with FRP overlays displayed a pseudo-ductile response as opposed to the brittle failures observed for unstrengthened walls. In addition, it was noted that the composite overlays held together the fragments of the failed walls. This suggests that a reduction in falling hazards may be achieved, which would mitigate a common source of injury during earthquakes. Although this test is standardized, the authors concluded that it did not accurately represent the forces on URM piers and recommended that racking shear tests be performed in the future.

Racking shear tests have been conducted by several researchers. Such tests subject

an individual pier to in-plane shear loads. Typically, these piers are supported with idealized boundary conditions (i.e. either cantilever or fixed-fixed) and subjected to cyclic displacements under a constant vertical stress. A typical test setup is shown in Figure 2.7. In general, the following three patterns of reinforcement have been investigated:

- Bi-directional full coverage sheets
- Unidirectional vertical strips designed to strengthen rocking
- Unidirectional diagonal strips designed to strengthen diagonal tension

While all of these patterns have been shown to be effective, Triantafillou (1998) concluded that for both economy and mechanical response, systems that employ unidirectional strips are superior. In addition, several researchers have found that these systems can be effective even if only applied to one surface of the wall (Al-Chaar and Hasan, 1998; Marshall et al., 2000, Schwegler, 1994, Elgwady et al., 2002). As a result, the appearance of the structure is not altered, a particularly important issue for historic structures. In addition, both glass (GFRP) and carbon (CFRP) systems have received attention and have shown potential. However, several researchers have noted the economic advantage of glass systems over carbon system (Hamilton and Dolan, 2001; Ehsani and Saadatmanesh, 1996).

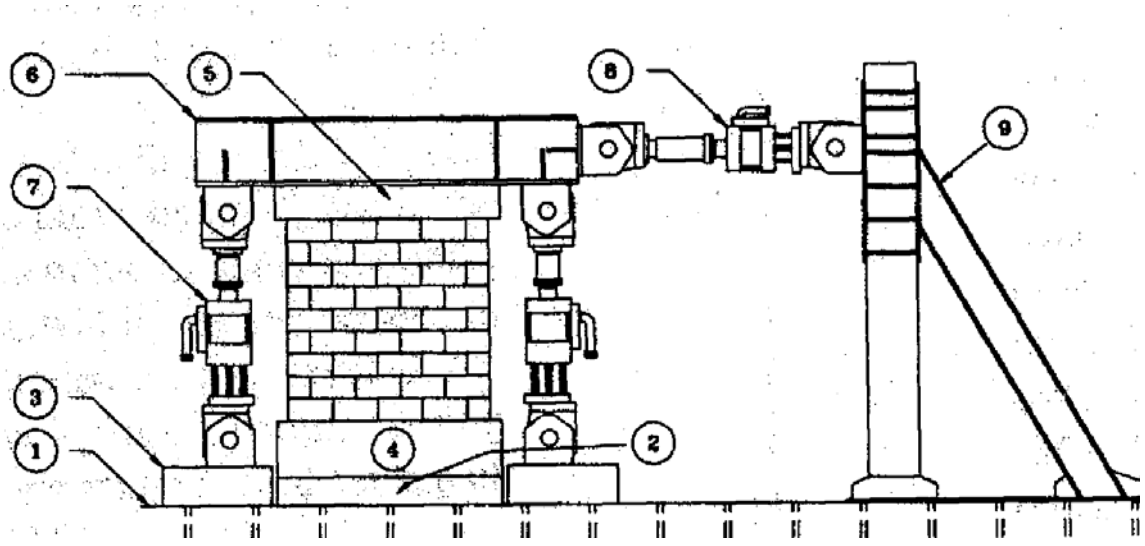

Figure 2.7. Schematic of typical racking test setup (taken from Laursen et al., 1995)

The results of pier racking tests have shown that the application of FRP overlays can greatly increase shear capacity. In several cases, the shear capacity has reportedly been doubled (Holberg and Hamilton, 2002; Franklin et al. 2001, Elgwady et al., 2002). Laursen et al. (1995) highlighted one of the most desirable characteristics of FRP retrofit, that is, the fact that the engineer can force a specific failure mode. In the case of this research, a wall that exhibited a brittle shear failure mode was retrofit with FRP overlays and a much more desirable rocking failure was forced. On the other hand, if a pier is expected to behave in a ductile manner (i.e. rocking or sliding), retrofitting with FRP overlays can alter the behavior resulting in a decreased displacement capacity (Franklin et al., 2001).

The most common type of failure observed for FRP overlays is a debonding between the overlay and the substrate. In general, this type of failure has been observed to occur in two locations: (1) at the end of the FRP overlay where peeling stresses exists (Triantafillou, 1998) and (2) directly adjacent to cracks were local strain concentrations

are presents (Hamilton and Dolan, 2001). This failure is typically characterized by a cohesive failure of the substrate. Several researchers have observed that a progressive stable debonding failure results in highly pseudo-ductile response (Kiss et al., 2002; Franklin et al. 2001). However, in most cases a debonding failure leads to a brittle fracture of the FRP overlay. A likely cause of this brittle fracture is the out-of-plane displacement that results from slip along the rough crack surface. This out-of-plane displacement has been observed to cause a Mode I fracture of FRP overlays bonded to concrete (Neubauer and Rostasy, 1997).

Although this failure has been widely observed, limited work has been conducted to develop a reliable model for predicting the stress at which debonding will occur (Tumialan et al., 2001). Triantafillou (1998) developed a method for approximating the bond strength of the end of FRP strips that considered peeling stresses. Errors associated with the method have been shown to be approximately 30%; although, limited experimental data were used to validate this model. Kiss et al. (2002) proposed a debonding model based on an energy balance approach; however, the experimental validation of this model is still forthcoming.

In contrast, a large amount of attention has been focused on the development of debonding models for FRP strengthened reinforced concrete. While these models may provide a reasonable starting point, issues specific to URM applications still need to be addressed such as:

- the differential stiffness between bed-joints and units (Roko et al., 2001)
- geometric discontinuities caused by tooled bed-joints and/or the misalignment of masonry courses

• surface texture and absorption capacity (Roko et al., 2001)

As a result, future research is required to investigate the applicability of FRP debonding models developed for concrete and masonry. A comprehensive review of the work conducted on FRP to concrete debonding models can be found elsewhere (Teng et al., 2001; Chen and Teng, 2001).

To alleviate FRP debonding and promote ductile behavior, two approaches have been investigated. The first involves the use of ductile steel anchors designed to yield prior to the fracture of the FRP (Holberg and Hamilton, 2002, Hall et al., 2002). Results obtained from several pier racking tests have shown that providing ductile steel anchors can result in increased energy dissipation and nearly double the strength as compared with the control specimen. However, while the initial failure was ductile, in some cases brittle fracture of the composite was observed directly adjacent to the steel connection due to stress concentrations. Based on this experimental investigation a design methodology was proposed; however, it was noted that more work was required to verify the concept (Holberg and Hamilton, 2002).

The second method involves designing the strengthening scheme to force a bed-joint sliding failure. This method attempts to exploit the desirable energy dissipation capability and displacement capacity associated with a bed-joint sliding failure. Recently, researchers at CERL have investigated this technique through the testing of three URM walls. Preliminary results suggest that the retrofit was successful in forcing a bed-joint sliding failure. This method is extremely economical because it does not require any special anchorage. However, one potential downside is that large residual displacements typically result from bed-joint sliding failures.

Several researchers have proposed analysis procedures based on the equivalent stress block analogy for the determination of flexural strength of retrofitted piers (Triantafillou 1998, Holdberg and Hamilton, 2002). For cases where the tension failure of the FRP governs, these methods have provide good strength estimates; however, when debonding governs, the lack of an accurate method to predict debonding stress causes large errors. For the determination of shear strength, several researchers have proposed analytical models based on the truss analogy (Jai et al. 2000, Triantafillou 1998, and Zhao et al. 2000). However, little experimental validation has been done.

Experimental investigations centered on the specific FRP systems that were investigated in this research are outlined in the following sections.

2.3.3.1 27oz/yd^2 Unidirectional Glass Fibers with an Epoxy Matrix

This system utilizes reinforcement extensively employed by the California Department of Transportation to wrap concrete columns. As a result, it is one of the most commonly manufactured composite materials for structural applications. This availability makes this system extremely attractive, and, as a result, it has received extensive attention (Franklin et al., 2001; Marshall et al., 2002). Typically this system is composed of unidirectional glass fabric strips (either stitched or braided) and a low viscosity two part epoxy, and is typically applied using a wet lay-up technique. While this type of application is very efficient, it does require special attention to quality control issues since the material is effectively being created out in the field.

The effectiveness of this system as a retrofitting method for URM in-plane piers has been widely studied; for the sake of brevity only MAE Center project ST-6 will be

summarized in detail. Franklin et al. (2001) evaluated this system on a slender 49.6 in. tall URM pier with an aspect ratio (H/L) of 1.77. The pier was subjected to a constant vertical stress of 42 psi and tested as a cantilever (i.e. rotation at the top of the pier was not restrained). In order to obtain hysteretic response, the pier was subjected to increasing cyclic displacements until failure. A schematic of the test specimen showing the location of the FRP reinforcement is given in Figure 2.8.

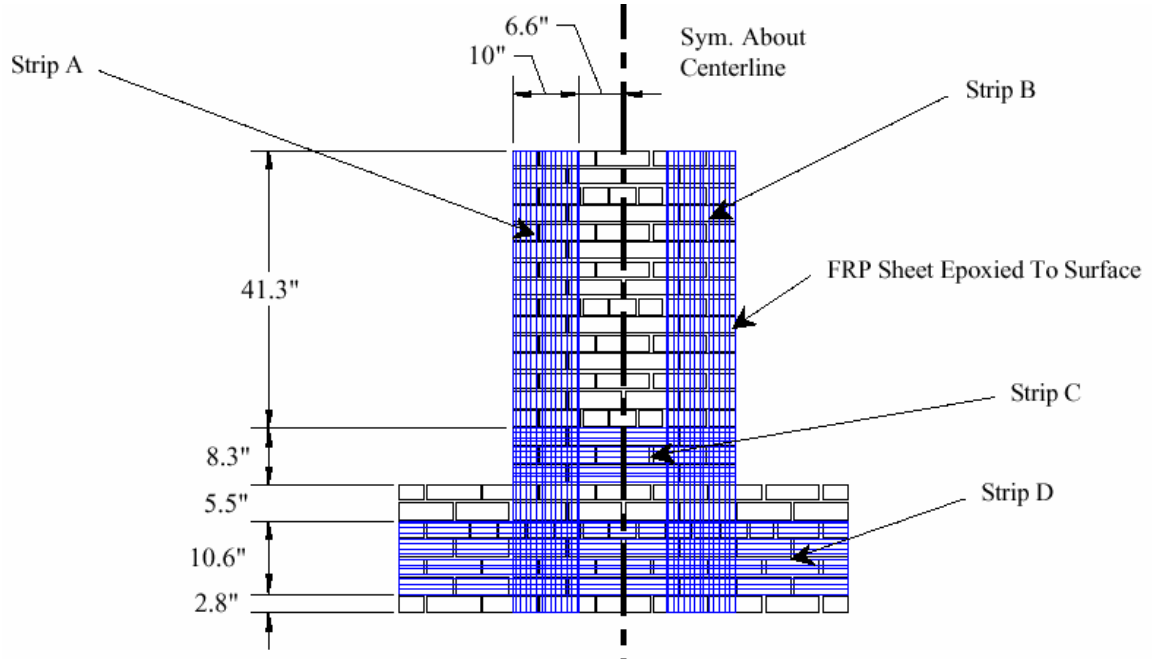

Figure 2.8. Schematic of in-plane test specimen 3F showing the location of FRP reinforcement (taken from Franklin et al., 2001).

Experimental results showed that the FRP retrofitted pier displayed over twice the strength of the control specimen (see Figure 2.9). However, a decrease in displacement capacity compared with the control specimen was observed (note that the governing failure mode of the control specimen was rocking). While the displacement capacity did decrease, a large ultimate drift of 1.9% was reported. The failure mode consisted of

gradual debonding of the composite at low displacement levels followed by diagonal cracking through the center of the pier. This gradual debonding resulted in the pseudo-ductile response shown in Figure 2.9. Finally, the test was concluded when a vertical FRP strip completely fractured causing a sharp drop in load carrying capacity. Based on the loss of ductility, the authors suggest that this type of retrofit should be avoided if the pier is expected to exhibit ductile type behavior (i.e. rocking or bed-joint sliding).

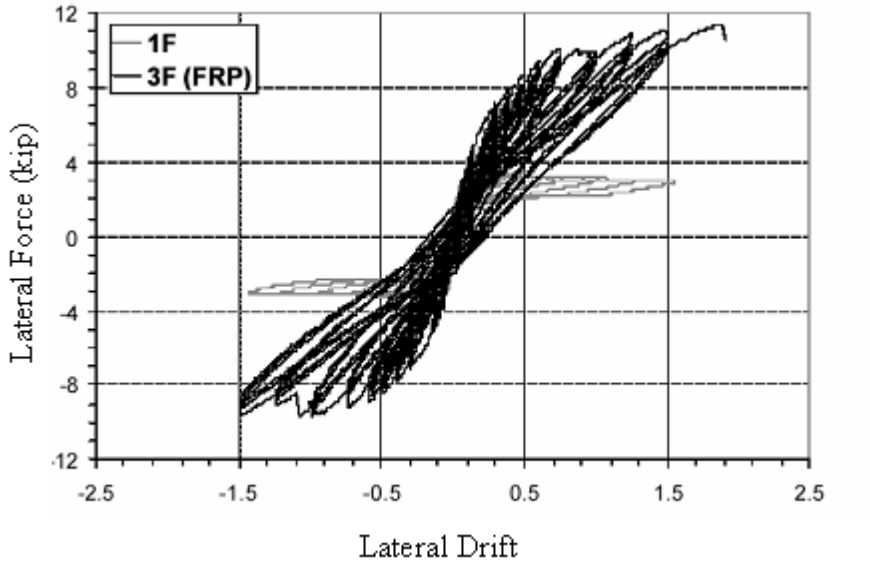

Figure 2.9. Comparison of the lateral force-drift behavior between specimen 1F (URM) and specimen 3F (retrofitted with FRP overlays) (taken from Franklin et al., 2001).

2.3.3.2 Bi-Directional Glass Grid with a Cementitous Matrix

This system is proprietary and consists of an alkali resistant bi-directional glass grid in a fiber reinforced cementitous matrix. The system is typically applied as a series of mortar and grid layers. This allows for the engineer to specify the principal angles of reinforcement in any layer (e.g. 0^o-90^o or $\pm 45^o$). Due to the breathable matrix, this system has the ability to be applied as a full coverage retrofit. Possibly the most attractive aspect of this material is its aesthetic qualities. Specifically, if applied to the exterior of a

structure it can be colored to resemble a plaster coat, which is consistent with typical architecture in the Mid-America region during the early 1900's. As a result, this system can potentially be applied to the outer surface of a URM structure without the addition of a costly architectural finish.

The effectiveness of the Saint-Gobain system was assessed through components tests conducted at CERL (Marshall, 2002). This project applied in-plane shear to three walls retrofitted with this system. All of the walls were constructed of a single wythe of lightly reinforced CMU and measured 48 in. in length and 48 in. in height. The walls were tested with a fixed-fixed boundary condition and a vertical force of 54 kip in order to assess shear behavior (i.e. diagonal tension failure). The angles of the grid reinforcement were varied in an attempt to assess which lay-up was most effective. Walls 1 and 2 contained two layers of reinforcement oriented at 0^o-90^o and $\pm 45^o$, respectively. Wall 3 contained three layers of reinforcement with one oriented at 0^o-90^o and two at $\pm 45^o$. The reinforcement was only applied to one side of the test piers. A schematic of a typical test specimen is shown in Figure 2.10.

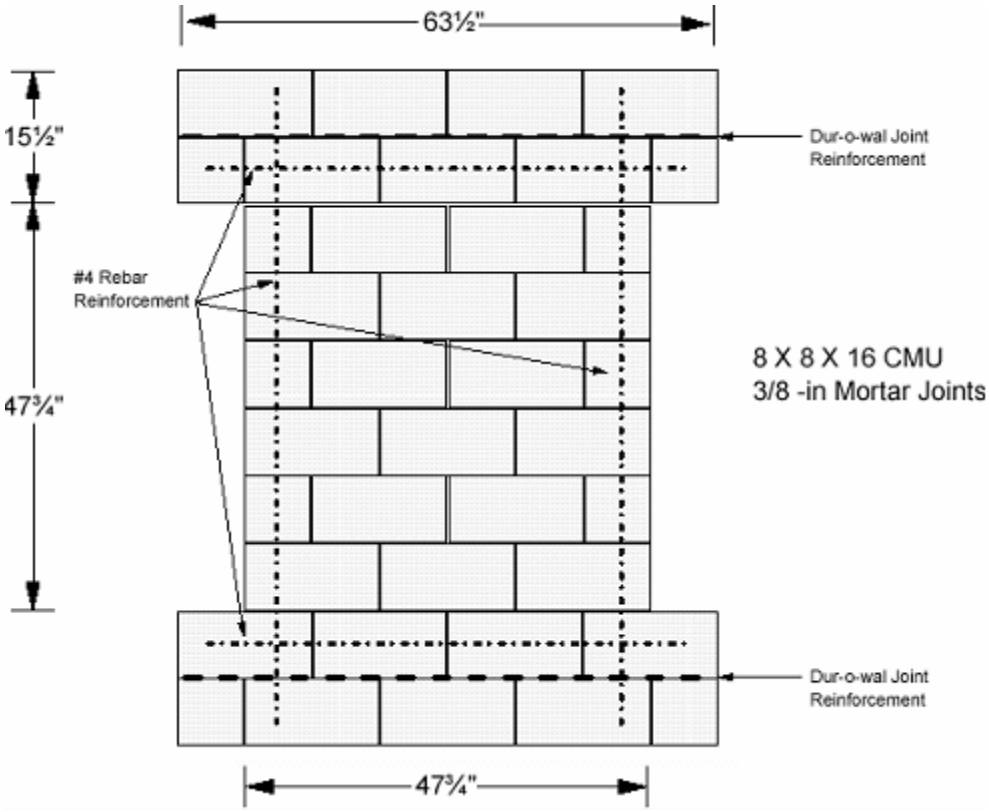

Figure 2.10. Schematic of in-plane test specimen showing the location of reinforcement.(taken from Marshall, 2002).

The failure of each wall tested was due to a shear failure of the CMU at the intersection between the web and face. While this can be considered a brittle failure, it occurred only after large increases in both strength and displacement capacity as compared with the control specimen. While all orientations showed an improvement in both strength and displacement capacity, the 0^o-90^o orientation (tested on Wall 1) resulted in the best performance. The backbone curve of Wall 1 is shown in Figure 2.11 along with the backbone curve of the control specimen. From the figure it is apparent that the 0^o-90^o orientation resulted in approximately a 60% increase in strength and over a 200% increase in displacement capacity as compared to the control specimen.

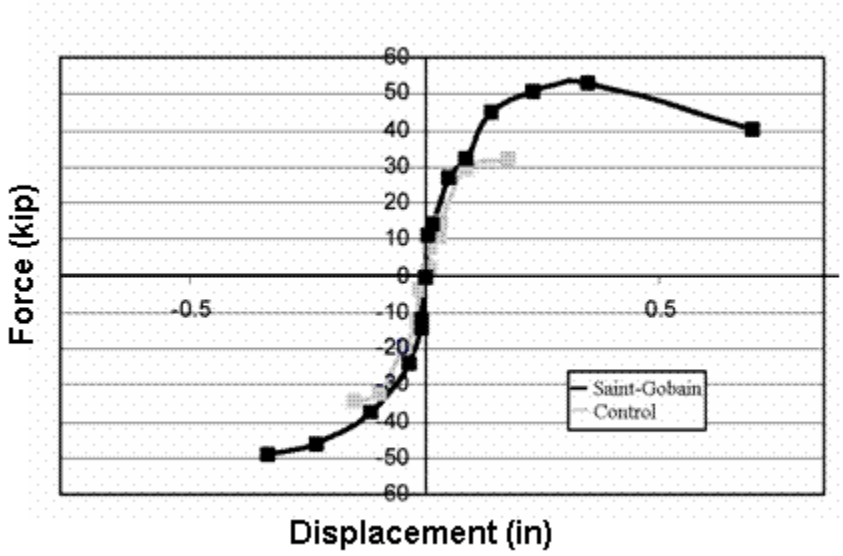

Figure 2.11. Comparison of the lateral force-displacement behavior between Wall 1 (Saint-Gobain system) and the control specimen (Marshall, 2002).

2.3.3.3 Pre-cured 18oz/yd^2 Unidirectional Glass Grid with an Epoxy Matrix

This system consists of a pre-manufactured unidirectional glass grid that is applied with a low-modulus adhesive. Since the grid is pre-manufactured, some of the quality control issues present with wet lay-up systems, such as straightness of fibers, are alleviated. However, quality control remains important in relation to issues such as the glass transition temperature of the adhesive. The main motivation behind this system was to allow for more displacement capacity by the use of a ductile, low-modulus adhesive. This can potentially alleviate some of the issues with debonding since the shear transfer between the substrate and the reinforcement is spread out over a larger area.

The effectiveness of this system for the retrofit of in-plane URM piers was investigated at CERL through the testing of a single in-plane pier (Marshall, 2001). The test specimen was constructed of 10-hole clay bricks laid in standard america bond and was approximately 48in. in length, 48in. in height, and 8 in. in width (i.e. two wythes).

The wall was tested with idealized fixed-fixed boundary conditions and a vertical load of 54 kip in order to investigate shear behavior. The reinforcement was applied in 8 in. strips to only one side of the URM pier. The pattern consisted of two vertical strips and two diagonal strips as show in Figure 2.12.

Figure 2.12. Photograph of the in-plane test specimen showing the location of the GFRP reinforcement (taken from Marshall, 2001).

During the testing of the retrofit pier, no signs of debonding were observed. The failure of the specimen occurred due to diagonal cracking of the unreinforced wythe that eventually resulted in the fracture of the diagonal GFRP strips. The backbone curve of the specimen is shown in Figure 2.13 along with the backbone curve of the control specimen. From this figure it is apparent that the strength of the specimen was increased slightly (approximately 16%). In addition, the authors report that the retrofit resulted in a 60% increase in displacement capacity prior to failure. From the figure it is apparent that the increase in displacement capacity was only achieved following a substantial decrease in

strength (approximately 60%). As a result, it should be concluded that the increase in displacement capacity was minimal.

On the other hand, the figure does suggest that while the strength was decreasing, the failure was not brittle. In contrast, the failure of the control specimen was sudden and resulted in the complete collapse of the wall. This highlights the ability of the system to maintain the stability of the wall following failure (as defined by some percentage drop in strength). In addition, the authors point out that this system remained bonded to the wall throughout testing and kept the wall intact. During an earthquake this would alleviate any debris from falling off of the wall, which is a primary cause of injury associated with URM structures.

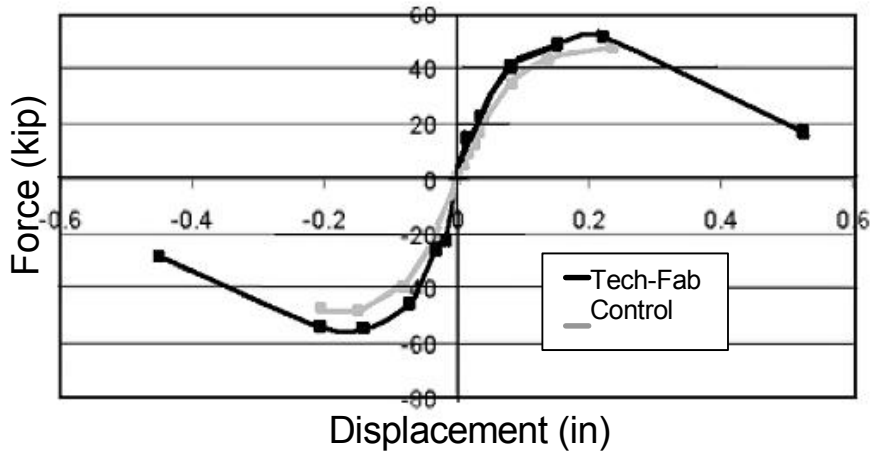

Figure 2.13. Comparison of the lateral force-displacement behavior between the MeC-Grid retrofitted pier and the control specimen (Marshall, 2001).

2.3.3.4 Near Surface Mounted Rods

As mentioned previously, a NSM rod retrofit consists of FRP bars that are bonded into grooves cut into the face of URM walls. If horizontal reinforcement is desired, the grooves are typically created by raking out bed-joints. In this case the technique is commonly referred to as structural re-pointing. One of the major advantages of structural

re-pointing in reference to URM structures is the aesthetic characteristics. That is, the appearance of a URM wall is not substantially changed if the NSM rods are bonded into existing bed-joints. This system has been investigated with respect to both flexural and shear strengthening of URM walls; however, for the sake of brevity only the shear strengthening of in-plane URM walls will be discussed.

Tumialam et. al (2002), subjected five URM piers to in-plane shear in order to assess the effectiveness of structural re-pointing. All five specimens were constructed of a single wythe of 6x8x16 CMU in running bond. The specimens measured 64 in. in length and 64 in. in height. Load was applied to the walls diagonally by a single jack through loading shoes attached to opposite corners of the pier. A photograph of the test setup is shown in Figure 2.14. Table 2.1 gives the type and pattern of reinforcement for each of the specimens tested.

Figure 2.14. Photograph of the in-plane test setup (taken from Tumialam et al., 2002).

Table 2.1. Reinforcement type and location for each test specimen (Tumialam et al., 2002).

Specimen	Type and Pattern of Reinforcement
Wall 1	Control, no reinforcement
Wall 2	#2 GFRP bars placed in every bed-joint on one side of the wall.
Wall 3	#2 GFRP bars placed in every bed-joint on alternating sides of the wall.
Wall 4	#2 GFRP bars placed in every other bed-joint on one side of the wall
Wall 2S	Four horizontal 4in wide GFRP strips applied to one side of the wall (equivalent material to Wall 2 in terms of axial stiffness)

Results of the experimental program are summarized in Table 2.2. Due to the test setup, the shear strain, γ, was used to assess displacement capacity. Ductility, μ, was defined as the ultimate shear strain, γ_{ult}, divided by the yield shear strain, γ_y. Table 2.2 shows that the NSM rods were effective in increasing both the strength and ductility of the URM walls. The largest ductility increase was observed from Wall 3 while the largest strength increase was observed from Wall 2 (approximately 80%). The relatively low strength increase displayed by Wall 4 was due to a premature sliding failure which occurred in a non-reinforced bed-joint. Comparing Wall 2 and Wall 2S, it is apparent that while the effectiveness of the two systems were similar from a strengthening standpoint, the ductility associated with Wall 2 was superior.

Table 2.2. Summary of NSM shear test results (taken from Tumialan et. al, 2002).

Specimen	In-Plane Strength	γ_{ult} ($x10^{-3}$)	γ_y ($x10^{-3}$)	m
Wall 1	24.3 kip	0.09	0.09	1.0
Wall 2	44.4 kip	1.75	0.13	13.5
Wall 3	43.8 kip	1.82	0.09	20.2
Wall 4	31.3 kip	1.38	0.11	12.5
Wall 2S	42.1 kip	0.95	0.12	7.9

2.3.4 In-Plane Wall Retrofit with Vertical Post-Tensioning

Although not common in the United States, post-tensioned masonry has been used extensively throughout Europe and Australia. According to Lissel et al. (1999), the lack of reliable design procedures has fueled the resistance to post-tensioned masonry in North America. In areas where post-tensioned masonry has enjoyed acceptance, the majority of the applications have been for new construction. However, several applications of post-tensioning as a retrofit measure have been reported. Schultz and Scolforo (1991), report that retrofit of church steeples and historic buildings have been carried out in Europe and Mexico. In these cases, tendons were installed on the interior of the structure. More recently, VSL International has used post-tensioning as a means to strengthen two-story URM structures in both Australia and California. For these retrofits, holes were drilled into the existing masonry walls, and unbonded tendons were installed to vertically post-tension the walls to the foundation. Typical tendons are constructed of high strength steel, although some work on the use of carbon fiber tendons has been conducted (Lissel et al., 1998, Sayed-Ahmed et al, 1998). While a post-tensioning retrofit is somewhat costly, it has advantages in that it does not alter the appearance of the structure (especially important for historical structures) and that the occupants of the structure need not be disturbed during the retrofit process.

Similar to FRP retrofit techniques, the in-plane behavior of post-tensioned masonry has mainly been investigated through pier racking test (see Figure 2.7). Results of these tests suggest large increases in strength and displacement capacity are possible. Post-tensioned masonry walls have been reported to display capacities 3.5 to 7 times greater than equivalent URM walls (Hinkley, 1996). In addition, Page and Huizer (1988)

compared the response of a post-tensioned masonry pier with that of a reinforced masonry pier. Results showed that the post-tensioned pier displayed more strength and an equivalent displacement capacity as the pier with unstressed reinforcement. However, several researchers have noted that diagonal tension failures are common (Laursen and Ingham, 2001, and Page and Huizer, 1988). Although this type of failure is typically considered brittle, large post-peak displacements have been reported with ultimate drifts greater than 1% in some cases (Page and Huizer, 1988). In addition, compressive failures have also been reported (Huizer and Shrive, 1986).

This increased likelihood of diagonal tension or toe crushing failures at higher levels of vertical stress has been well documented for the case of URM piers. This relationship between unbonded post-tensioned masonry and URM has been recognized by FEMA 356 (ATC, 2000), which recommends that unbonded post-tensioned masonry walls be treated as URM wall with an increased level of vertical stress. Following this recommendation, Moon et al. (2001) plotted the strength expressions given by FEMA 356 versus the level of post-tensioning stress (see Figure 2.15). This figure shows that these strength expressions provide the observed trend in failure modes. However, it is important to mention that FEMA 356 utilizes a Mohr-Coulomb envelope to model bed-joint shear strength. Such a model has been shown to be effective for low levels of vertical stress; however, for higher levels of vertical stress this model does not provide accurate predictions (Meli, 1973; ABK, 1981; Costley and Abrams, 1996; Hegemier et al., 1978; Atkinson et al, 1989; Xiao, 1995; Hamid, 1980). In addition, Hamid and Drysdale (1979) observed that the coefficient of friction of bed-joints is not constant for higher levels of vertical stress. As a result, care should be taken when employing such a model to predict

the shear behavior of masonry bed-joints subjected to high levels of prestressing force.

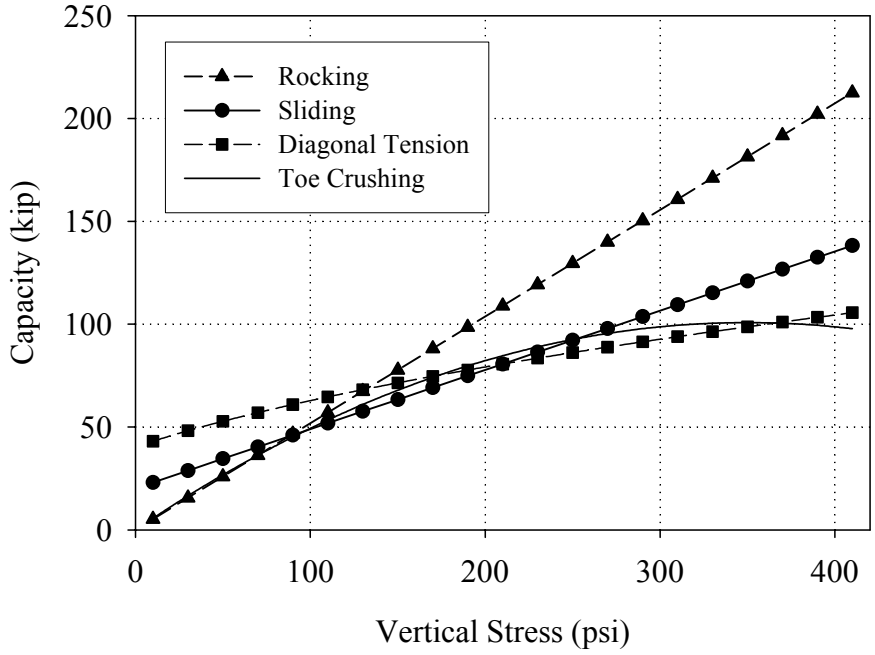

Figure 2.15. Capacity of the four principal URM failure modes versus post-tensioning stress.

The behavior of grouted versus ungrouted post-tensioned walls has also been investigated. Results have shown that grouted post-tensioned walls displayed an elastic-plastic behavior while ungrouted walls displayed a nonlinear elastic behavior (Laursen and Ingham, 2001). Several researchers observed substantial changes in tendon stress during loading (Page and Huizer, 1988; Huizer and Shrive, 1986). This change was attributed to rocking of the wall which produced vertical displacements. In some cases this phenomenon was so pronounced that it caused yielding of unbonded tendons, which resulted in a progressive decrease in prestressing force. In order to avoid tendon yielding, it was recommended that the tendons be tensioned between 25% and 50% of the yield stress and that they remain unbonded over two to three stories (Laursen and Ingham,

2001).

A complete review of research conducted on in-plane and out-of-plane post-tensioned masonry walls has been previously reported (Lissel et al., 1999, Shultz and Scolforo, 1991).

2.4 Global Characteristics of URM Structures

The discussion thus far has almost exclusively focused on the behavior of components found within a URM structure. While it is common to segment a structure into components in engineering practice, such an approach may neglect important global effects which can result in large errors. This issue was recognized by several researchers who responded by conducting experimental investigations on complete URM structures. In general these tests fall into two categories: (1) reduced-scale dynamic tests; and (2) full-scale quasi-static tests (including those which impose pseudo-dynamic loading). The following sections outline several of these experiments. The specific investigations highlighted were chosen due to the thorough documentation available.

2.4.1 Reduced-Scale Dynamic Experiments

The first experimental investigation to subject a URM structure to dynamic loads was conducted by Clough et al. (1979). The motivation for this research was the seismic re-zoning of Phoenix, AZ in the mid-1970s, which resulted in a requirement that masonry houses be partially reinforced (prior to this re-zoning, no reinforcement was required in masonry housing). The primary objectives of this study were to (1) determine the maximum earthquake intensity that could be resisted by a typical URM house, and (2)

evaluate the additional resistance supplied by partial reinforcement. The testing program subjected four masonry one-story houses (representative of the construction found in Phoenix, AZ) to ground accelerations on the shake table at the University of California.

The test structures employed full-size masonry units, wall components, and diaphragm-to-wall connections; however, the length of the walls were 1/3 the length of the prototype structure. To account for the decrease in vertical load resulting from the smaller plan area, and assuming a 20 psf load, concrete blocks were added to the roof diaphragm. House 1 was constructed with continuous corner piers and interior piers along each of the four walls (see Figure 2.16). The other three specimens (Houses 1 through 3) were constructed with four perforated walls and no direct connections between the wall panels (See Figure 2.17). For each specimen, standard two-hole clay bricks or concrete blocks were used with a type S mortar. Typical timber trusses with plywood sheathing were used for the floor systems of each structure.

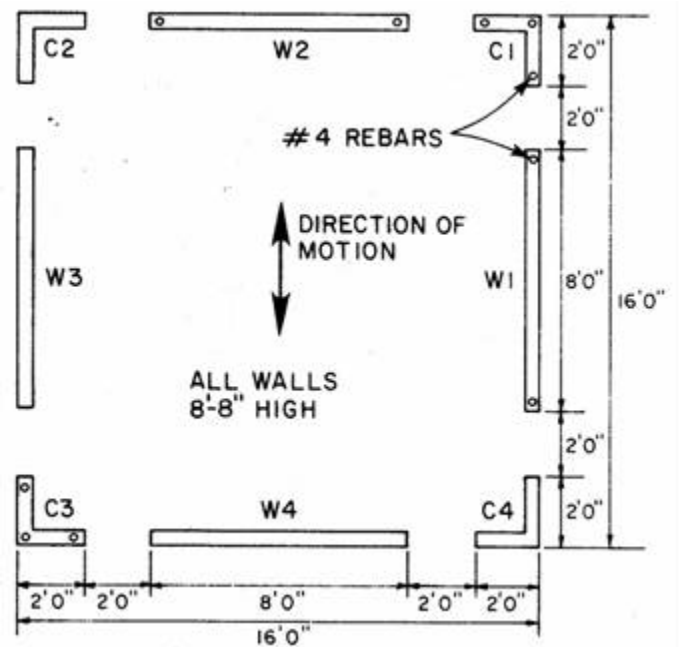

Figure 2.16. Plan view of House 1 (taken from Clough et al., 1979).

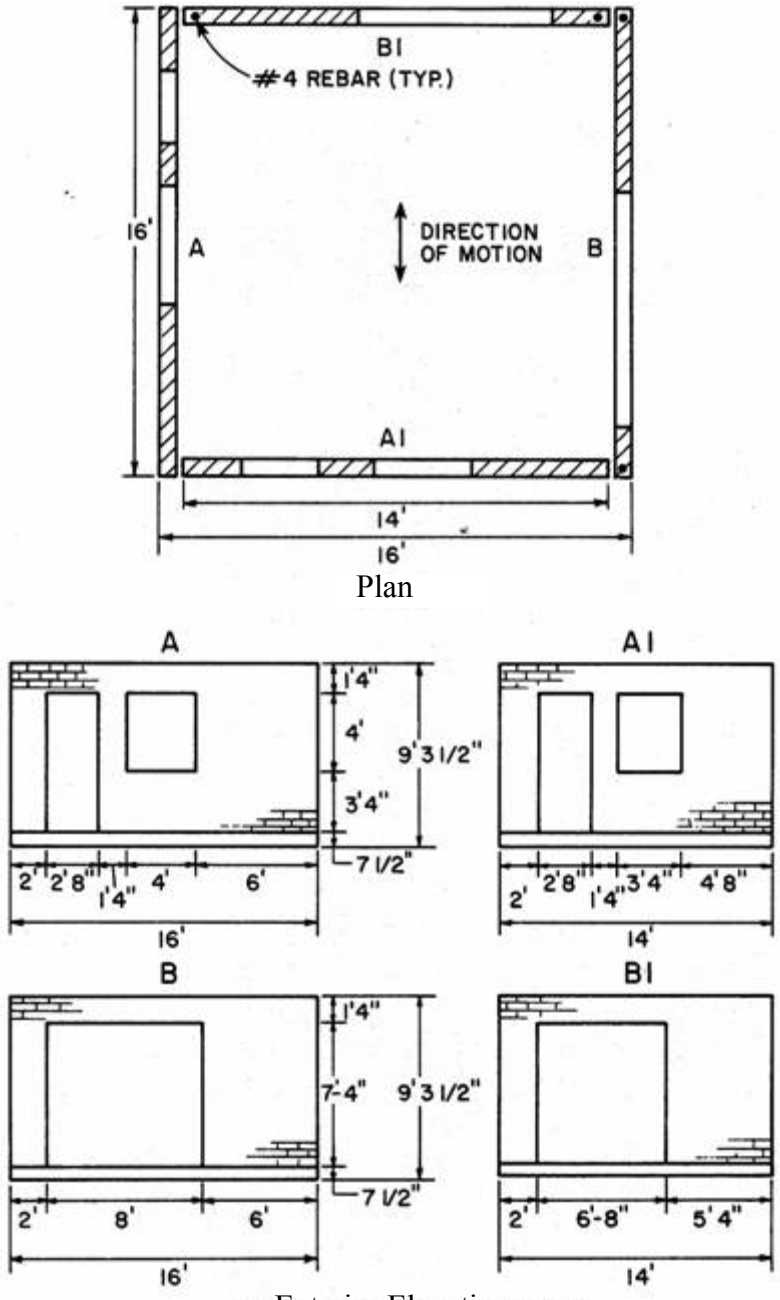

Figure 2.17. Plan and elevation views of Houses 2 through 4 (taken from Clough et al., 1979).

Results of the experimental testing showed that since the stiffness of the in-plane walls was much larger than that of the out-of-plane walls, the majority of the seismic forces were resisted by the in-plane walls. Furthermore, due to the high stiffnesses

displayed by the in-plane walls, the structures followed the motion of the shake table very closely. In general the deformation of the structures were in phase and proportional to the base accelerations. As a result, the authors concluded that the peak acceleration, instead of the frequency characteristics, was a major factor to be considered when assessing the damage of URM buildings. However, extension of this conclusion to the Mid-America region is questionable, since the earthquake records used in this investigation were all typical of the Western United States (1940 El Centro, 1952 Taft, and 1971 Pacoima Dam).

Results also indicated that the torsional response of URM structures with flexible diaphragms was negligible. Although the differential stiffnesses of the parallel in-plane walls did result in differential displacements of the in-plane walls, and a tendency for the structure to rotate, negligible rotation was observed since the the in-plane stiffness of the out-of-plane walls was sufficient to force this displacement to be accommodated through in-plane racking of the flexible timber diaphragms.

Tomazevic et al. (1993) tested four, 1:4 scale simplified two-story URM models dynamically. These models were based on the prototypes of old urban masonry residential houses in the earthquake-prone areas of central Europe and the Mediterranean. Each of the four models tested employed solid load bearing in-plane walls and perforated out-of-plane walls constructed of unreinforced stone masonry (see Figure 2.18). A principal goal of this research was to investigate the influence of diaphragms on the behavior of URM structures. As a result, each model was built with a different diaphragm. Model A contained wooden floors made of freely supported wood joists without any additional connection to the URM walls. Model B contained reinforced concrete slab diaphragms connected to the URM walls with bond-beams. Model C contained diaphragms identical

to Model A; however, in Model C steel ties where supplied between the diaphragm and out-of-plane walls. These ties were intended to represent a joist anchor retrofit as discussed in Section 2.3.1. The diaphragms of Model D were similar to those of Model C, except that a brick vault was used instead of the timber roof.

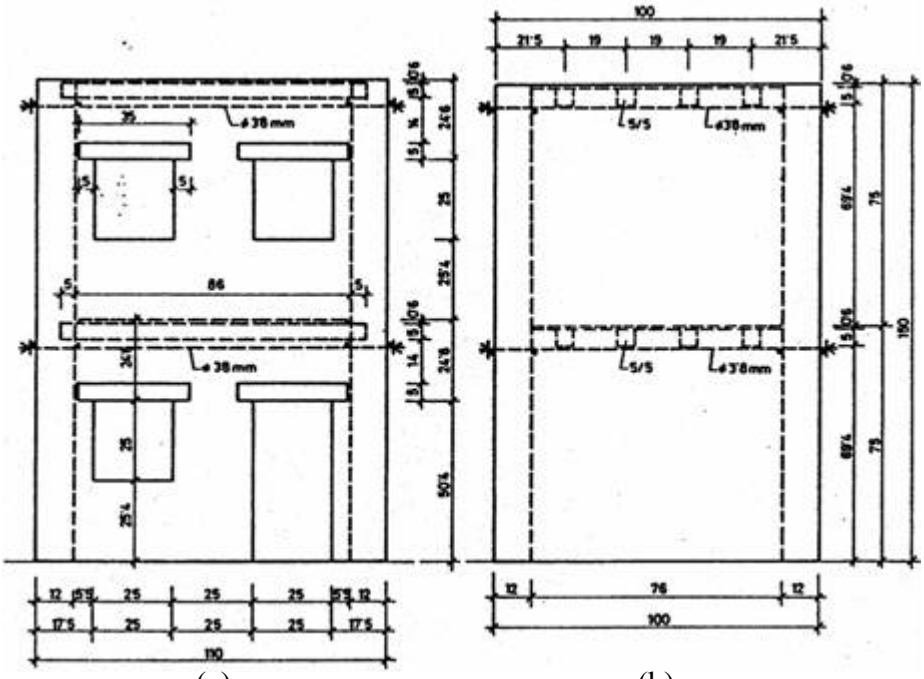

Figure 2.18. Elevation of (a) out-of-plane walls and (b) in-plane walls (taken from Tomazevic et. al., 1993 (dimensions are in cm)).

The primary damage observed in Model A was the collapse of the second story of the out-of-plane wall, whereas the damage in Models B, C, and D was focused on the first story of the in-plane walls. Based on this observed damage, the authors concluded that for a URM structure without joist anchors to prevent the separation of the walls, the out-of-plane walls are prone to collapse before severe damage develops in other parts of the structure. In addition, for rigid diaphragms (i.e. Models B and D) or flexible diaphragms that are properly tied to the out-of-plane walls (i.e. Model C), the critical element is the

first story of the in-plane wall. As a result it was concluded that the structural characteristics of the diaphragms and the connection between the diaphragms and URM walls represent decisive parameters for the seismic resistance of masonry walls.

Costley and Abrams (1996) tested two reduced-scale URM buildings dynamically at the University of Illinois. Both structures were identical and contained two solid out-of-plane walls and two perforated in-plane walls denoted Window Wall and Door Wall (see Figure 2.19). The masonry walls were composed of clay masonry units and a Type O mortar. The Window Wall of each structure was built continuous with the out-of-plane walls creating a C-shaped channel section in plan. In contrast, the Door Wall was built independent of the out-of-plane walls by suppling an expansion joint extending vertically from the foundation to the roof at the wall intersections. A diaphragm consisting of a series of steel bars spanning between the Window and Door Walls was employed in the structures to represent a typical timber diaphragm. The floor system was loaded with steel weights to achieve realistic gravity stresses in the URM piers ranging from 33 psi to 48 psi. The floor system was also tied to the out-of-plane walls to simulate a joist anchor retrofit.

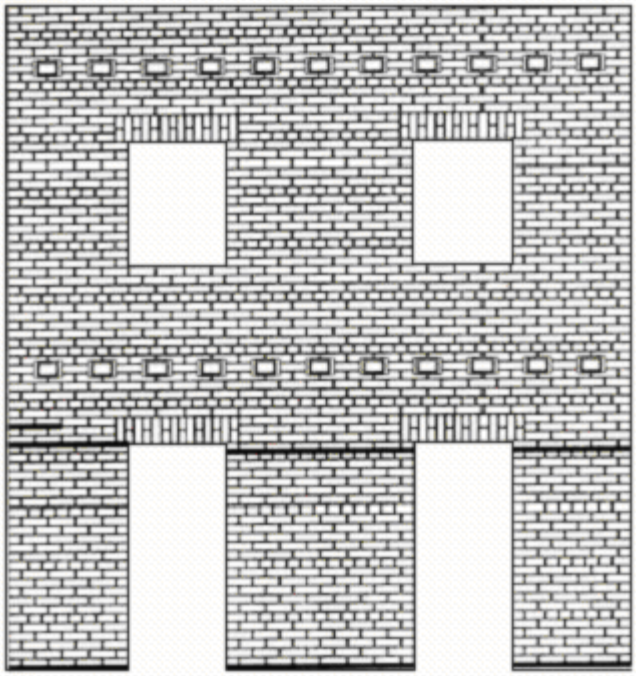

(a)

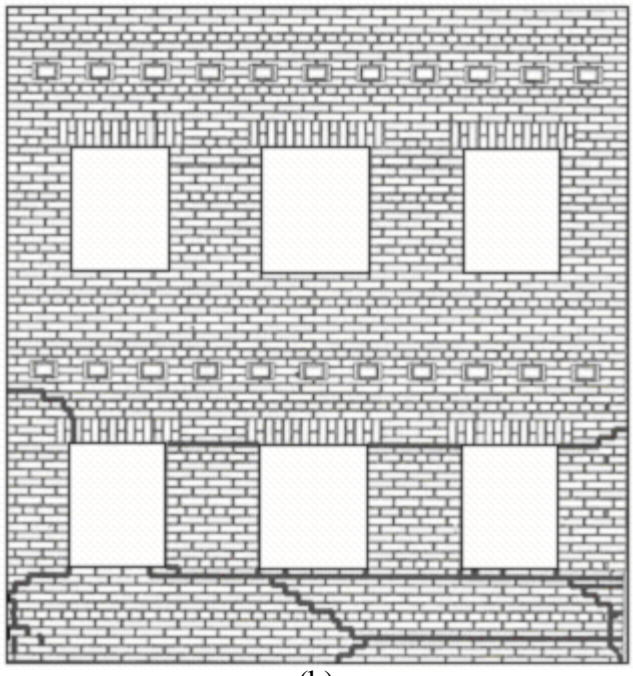

(b)

Figure 2.19. Configuration of perforated in-plane walls (a) Door Wall (b) Window Wall (taken from Costley 1996)

The majority of the damage in the test structures focused on the first story of the in-plane walls (see Figure 2.19). The first story piers displayed primarily rocking deformation which effectively isolated the second story of the structure. As the testing progressed the second story appeared to be fixed in space as the first story walls moved with the base excitation. Measured deflections also supported this observation by indicating that after cracking the relative displacements of the second story and diaphragms decreased with respect to the first story deflection. In addition, the results showed that the flexible diaphragm system provided negligible coupling between the in-plane walls. Although the in-plane walls vibrated independently (in some cases the displacement of the Door Wall was twice the displacement of the Window Wall), the differential displacement between in-plane walls was accommodated by shear deformation of the diaphragm. The authors also noted that flange participation seemed to have a minimal effect on pier rocking behavior; however, future work on this subject was recommended.

Benedetti et al. (1998) subjected 14 half-scale models of two-story URM structures to three-component dynamic excitation on shake tables. Each structure consisted of four perforated URM walls constructed of either brick or stone masonry (see Figure 2.20). Several of the stone masonry buildings were intentionally built with poor connections between orthogonal walls. During the first test, these poor connections resulted in the separation of walls and the complete collapse during a moderate ground motion. As a result, all other buildings employing poor connections between walls were retrofit prior to testing to avoid such a failure. The structures built with sound connections between orthogonal walls (i.e. interlocking units) were first tested in an unreinforced state

and then retrofit and retested. In all 24 dynamic tests were conducted (10 on URM buildings and 14 on URM buildings after retrofit). The retrofit measured included three types: (1) joist anchors; (2) sealing cracks with several types of adhesives; and (3) strengthening the spandrels with either a continuous reinforced concrete band around the structure or different types of horizontal post-tensioning systems. Flexible diaphragms consisting of timber joists and sheathing were employed in each structure at the second floor and roof levels.

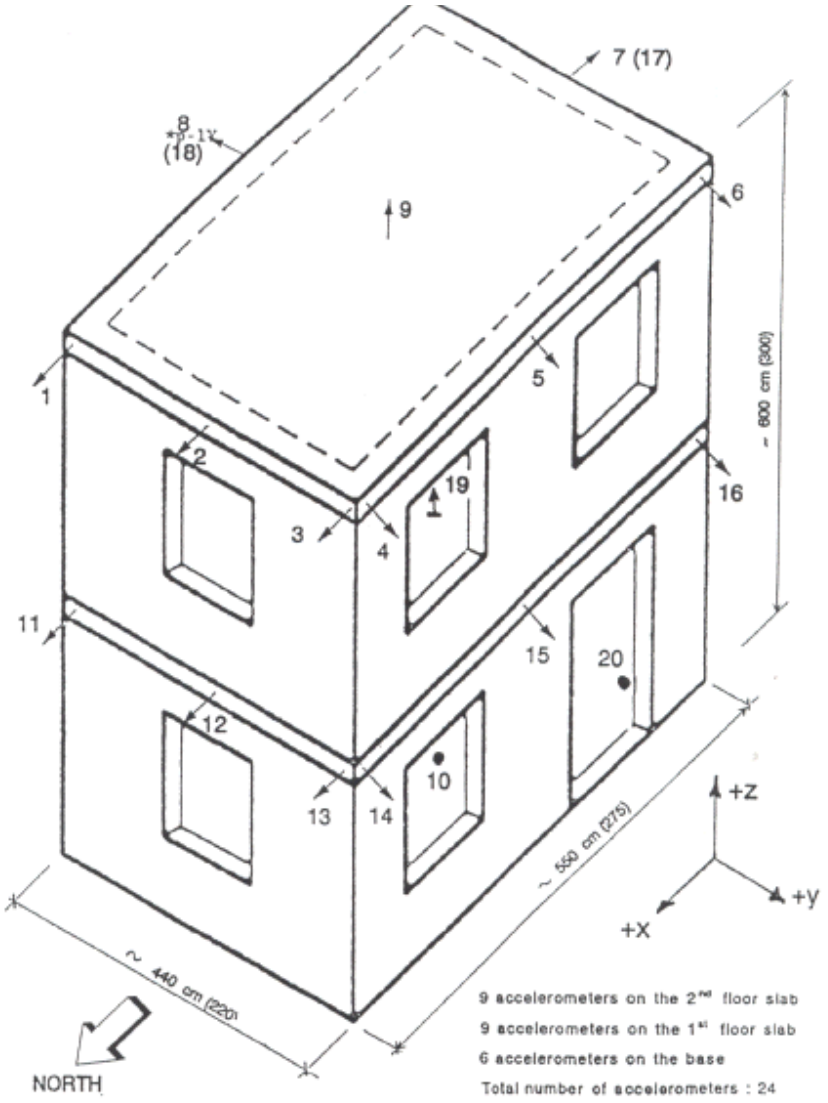

Figure 2.20. Basic configuration of test models (taken from Benedetti et al., 1998)

In all of the structures tested prior to retrofit, the damage focused primarily on the spandrels, thus resulting in the retrofit measures focused primarily on spandrels. In addition, several first story piers exhibited diagonal cracking. Although not pointed out by the authors, these failure modes are consistent with larger levels of vertical stress. The only observed wall separation occurred in the first stone masonry building tested, which was deliberately constructed with poor connections between orthogonal walls. Note that following this test, all other stone masonry buildings were retrofit prior to testing.

In general, the retrofit methods investigated performed well. The joist anchor retrofit along with the horizontal reinforcement of the spandrels forced opposite walls to respond in phase. In addition, the horizontal reinforcement of the spandrels successfully eliminated the separation of orthogonal walls (in the stone masonry buildings) and was successful in recovering, and in some cases increasing, the initial fundamental frequency of the structure. The sealing of cracks did improve the response of the structure; however, the initial response of the structure was not recovered. In addition, cracks tended to form in the same locations as the original ones.

In all structures, during relatively minor ground motions, torsional response was observed; however, as the ground motions increased in magnitude the torsion response became negligible. As a result, the authors concluded that the connections between the walls, although intact, did not have sufficient moment capacity to transfer horizontal moments between orthogonal walls. This caused the structure to loose its box-type behavior. Although not mentioned by the authors, this behavior is also consisted with the negligible coupling supplied by flexible timber diaphragms.

The ductility, μ, was estimated for each wall before and after retrofit. For walls in a

URM state, μ values ranged from 1.5 to 1.8 exceeding the values given in most seismic codes for URM structures. Following retrofit, the estimated μ increased slightly and ranged from 1.8 to 2.7. Furthermore, the ultimate base shear coefficients estimated for the brick masonry structures prior to retrofit ranged from 0.22 to 0.3. Following retrofit, nearly all techniques resulted in an ultimate base shear coefficient of approximately 0.3.

2.4.2 Full-Scale Experiments

Magenes et al. (1995) conducted a quasi-static test on a full-scale version of the test structures used in the dynamic test conducted by Costley and Abrams (1996). While the geometry of the full-scale structure was nearly identical to the reduced-scale model (see Figure 2.19), the mortar and gravity stresses differed. Specifically, the full-scale structure employed a sand-lime mortar and gravity stresses between 60-70 psi, whereas the reduced scale model used a Type O mortar and had gravity stresses between 33-48 psi. The structure was loaded cyclically by actuators located at the roof and second floor levels. The relative magnitude of the roof and second floor displacements was updated throughout loading to achieve a constant force distribution at each floor level. This was done to approximate the force distribution observed during the reduced-scale dynamic test (Costley and Abrams, 1996).

Observations made during testing indicated that the behavior of each in-plane wall was very different. The Door Wall responded as a coupled shear wall displaying significant vertical deformations of the roof due to an overall rotation. In contrast, the response of the Window Wall was characterized by local deformations of individual piers, with only small vertical displacements measured at the roof. This difference was attributed

to the connection between the out-of-plane walls and the Window Wall, as well as the different aspect ratios of the piers in each wall.

The final crack pattern of the test structure is shown in Figure 2.21. Initially, cracking in both in-plane walls was limited to the spandrels above the first floor openings. As the displacements increased however, substantial shear cracks occurred within the interior piers of both walls. In the case of the Door Wall, diagonal cracks formed in all piers; however, the outside piers only displayed diagonal cracks in one direction. Specifically, the diagonal cracks in the outside piers formed when the effects of overturning moment acted to increase the vertical compressive stress in these piers. Rocking deformation was observed for the outside piers in the Window Wall in both loading directions. The authors point out that this rocking deformation did not occur between horizontal cracks defined by the adjacent openings, but over a larger distance.

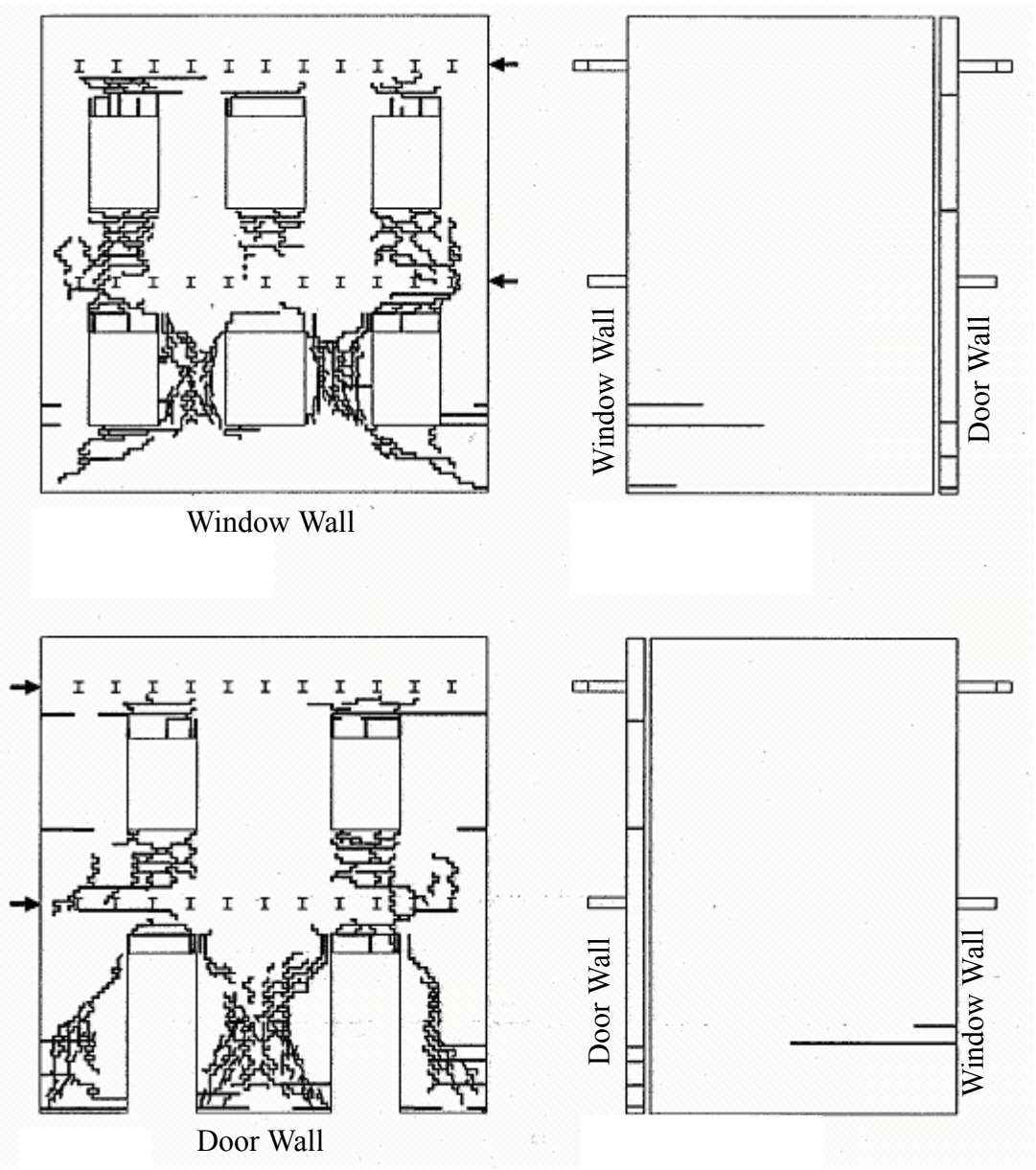

Figure 2.21. Final crack pattern of the Window and Door Walls (taken from Magenes et al. (1995).

Based on the similarity between the full-scale (FS) test structure utilized by Magenes et al. (1995) and the reduced-scale (RS) test structure employed by Costley and Abrams (1996), a comparison between the responses is appropriate. The primary differences in the observed response of structures were: (1) substantial cracking of the

spandrels were observed in the FS structure, whereas the spandrels of the RS structure remain free of cracks, and (2) pier behavior was dominated by diagonal cracking in the FS structure, while the piers of the RS structure displayed primarily rocking behavior. Both of these differences were likely due to the different vertical stresses employed by each structure as well as the different mortars used. The larger vertical stress in the FS structure acted to increase the strengths of the piers in relation to the spandrels, since the strength of a spandrel is not dependent on vertical stress. Furthermore, the increased level of vertical stress also made the first floor piers more prone to diagonal tension failures. The poor quality of mortar used in the FS structure also contributed to this tendency for the first floor piers to display diagonal cracking.

Paquette and Bruneau (2003) loaded a one-story URM structure pseudo-dynamically in order to investigate the interaction between flexible diaphragms and rigid walls. The test structure was composed of two identical perforated in-plane URM walls (denoted East and West walls, see Figure 2.22) and two solid out-of-plane walls. The East wall and out-of-plane walls were continuous, whereas an expansion joint was left between the West wall and the out-of-plane walls (similar to Costley and Abrams, 1996). A flexible diaphragm composed of timber joists and diagonal sheathing overlaid with straight sheathing was used. The diaphragm was connected to the out-of-plane walls via joist anchors designed according to UCBC (ICBO, 1997). The building was loaded pseudo-dynamically through a single actuator attached to the structure at the center of the diaphragm.

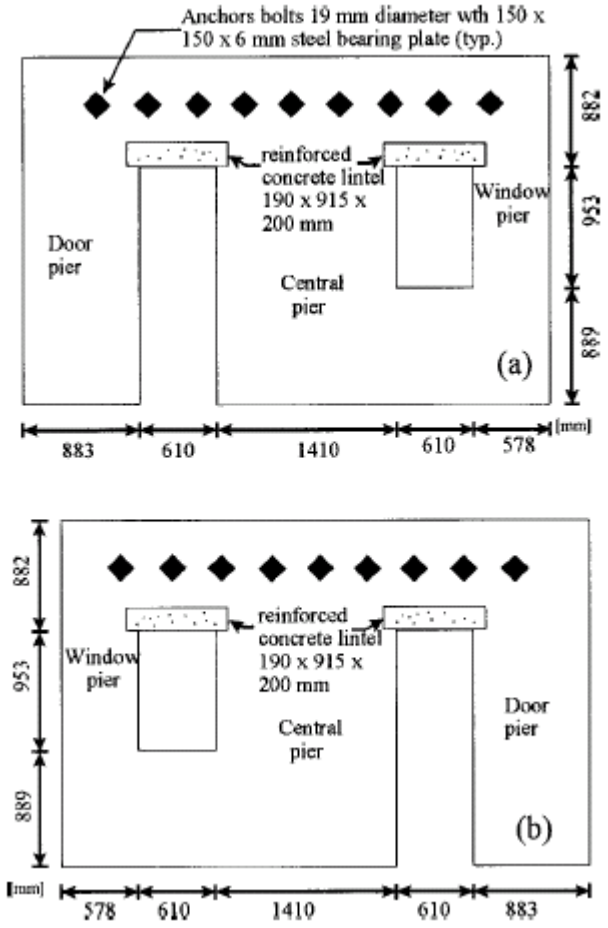

Figure 2.22. Elevation of (a) East wall and (b) West wall (taken from Paquette and Bruneau, 2003).

During all cycles the timber diaphragm remained elastic and all of the in-plane piers displayed rocking behavior or a combination of rocking and sliding behavior. Although not mentioned by the authors, this suggests that the rocking/sliding response of the in-plane piers limited the force developed in the diaphragms thus enabling them to remain elastic throughout loading. During low-intensity ground motions the East wall displayed a larger stiffness than the West wall; however, as the intensity of the imposed ground motion increased the difference in stiffness became negligible. As a result, the authors concluded that the effect of continuous corners becomes negligible for high

intensity ground motions.

2.5 Summary

Several past studies have been conducted to assess the effectiveness of retrofitting URM piers with FRP overlays, NSM rods, and vertical post-tensioning. Results have indicated that these techniques have the potential to greatly improve in-plane behavior of individual URM piers. In addition, several applications of these retrofit techniques have shown that they are practical and economical alternatives to more traditional methods. However, the research to date has almost exclusively focused on component behavior.

Several structure tests have been conducted to assess the behavior of URM buildings; however, these tests have primarily focused on the response of the structures in an as-built state. As a result, the effectiveness of FRP overlays, NSM rods, and vertical post-tensioning retrofits on overall structure response has yet to be determined. This points to the need for a full-scale test of a URM structure (following the application of these retrofit techniques), to enhance the significance of past component research and to validate these methods for future use.

CHAPTER 3

EXPERIMENTAL PROGRAM

As outlined in the previous chapter, past studies conducted on the retrofit of URM structures have primarily focused on the behavior of components with little attention paid to more global issues. To fill this void, a full-scale test of a URM structure before and after retrofit was conducted. As outlined in Chapter 1, the principal goals of this study were to:

- Investigate the behavior of each retrofit technique in terms of damage progression and failure modes.
- Assess the effect of each retrofit technique on overall structure performance in terms of strength, stiffness, energy dissipation, damage progression, and failure modes
- Identify global effects of URM structures that impact the behavior of primary components.

The remainder of this chapter provides a detailed description of the experimental program. The design of the test structure including descriptions of the URM walls, timber diaphragms, construction details, and material properties are presented in Section 3.1. Section 3.2 describes the design of each retrofit technique employed in the test structure. Section 3.3 provides an overview of the test setup, loading protocol, and instrumentation plan.

3.1 Test Structure

The test structure consisted of four URM bearing walls with timber diaphragms at both the floor and roof levels (see Figure 3.1). The dimensions of the building were 24 ft by 24 ft in plan with story heights of 12 ft for the first story and 10 ft for the second story. The aim of the design was not to replicate a specific structure but rather to create a structure that was representative of common URM construction in Mid-America. This section outlines the key global features, details, and material properties of the test structure.

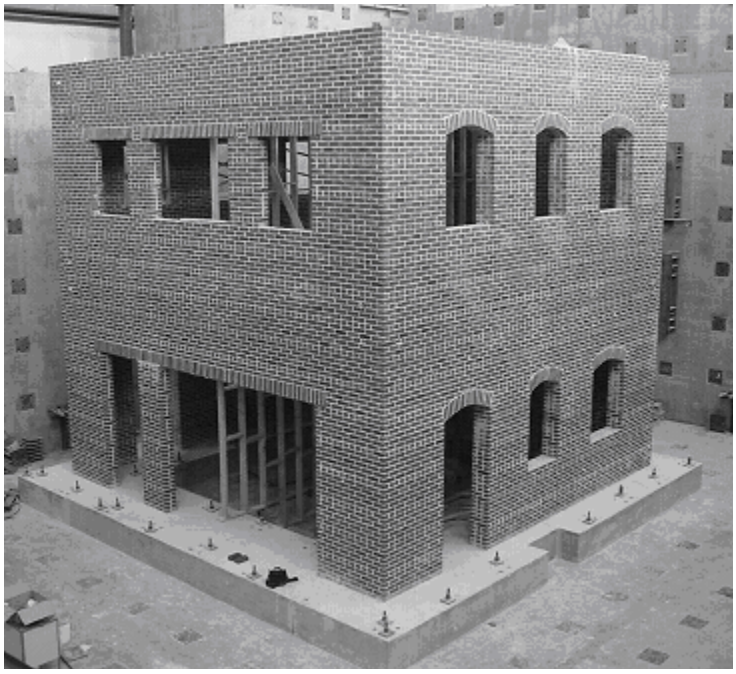

Figure 3.1. Photograph of the test structure

3.1.1 URM Walls

A plan view of the entire structure as well as elevation views of each URM wall are shown in Figures 3.2 through 3.5. The building was composed of four walls constructed of URM laid in standard American bond with headers every sixth course.

Walls A and B supported the floor and roof diaphragms and were composed of three wythes of masonry giving a nominal thickness of 12 in. Walls 1 and 2 were composed of two wythes of masonry giving a nominal thickness of 8 in.

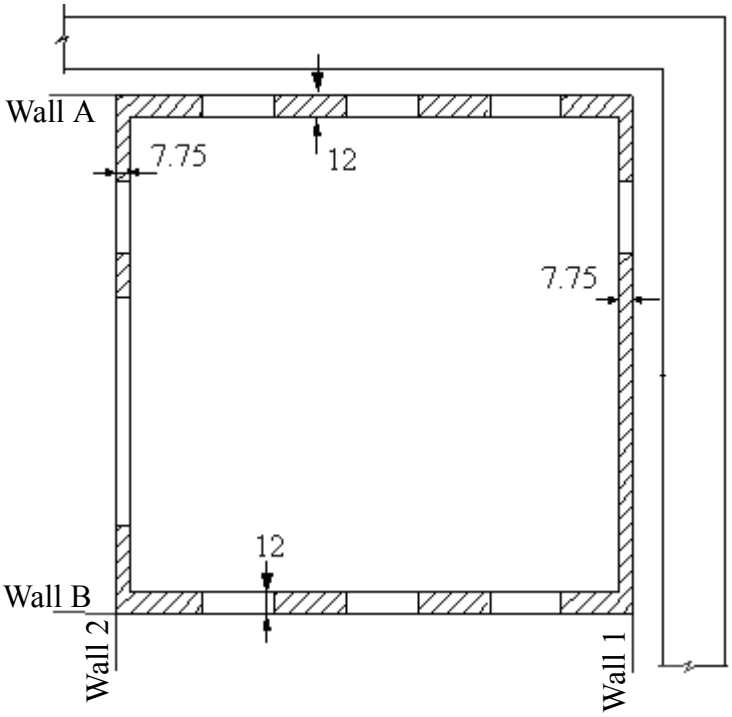

Figure 3.2. Plan view of the test structure (dimensions are in inches).

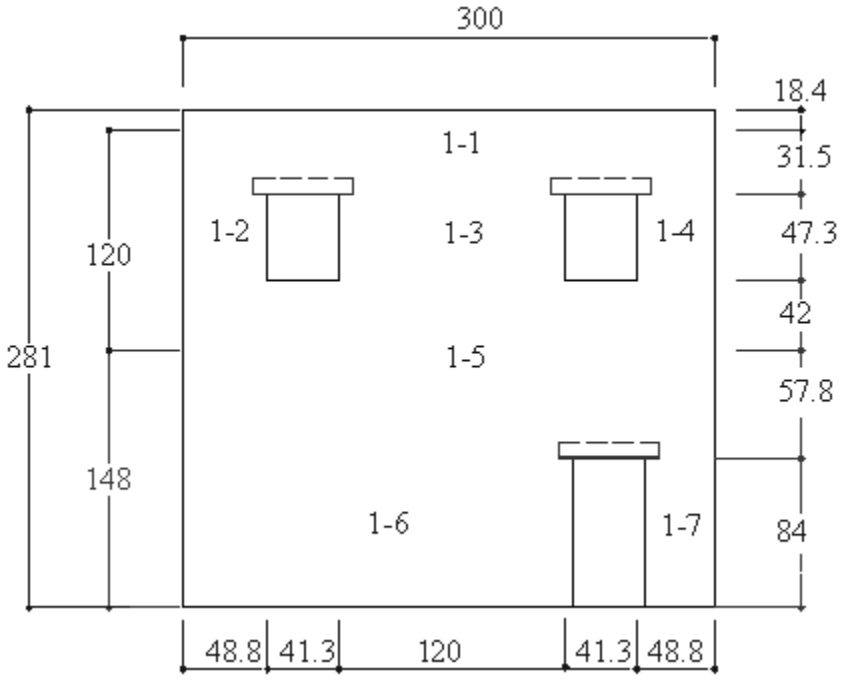

Figure 3.3. Elevation view of Wall 1 (dimensions are in inches).

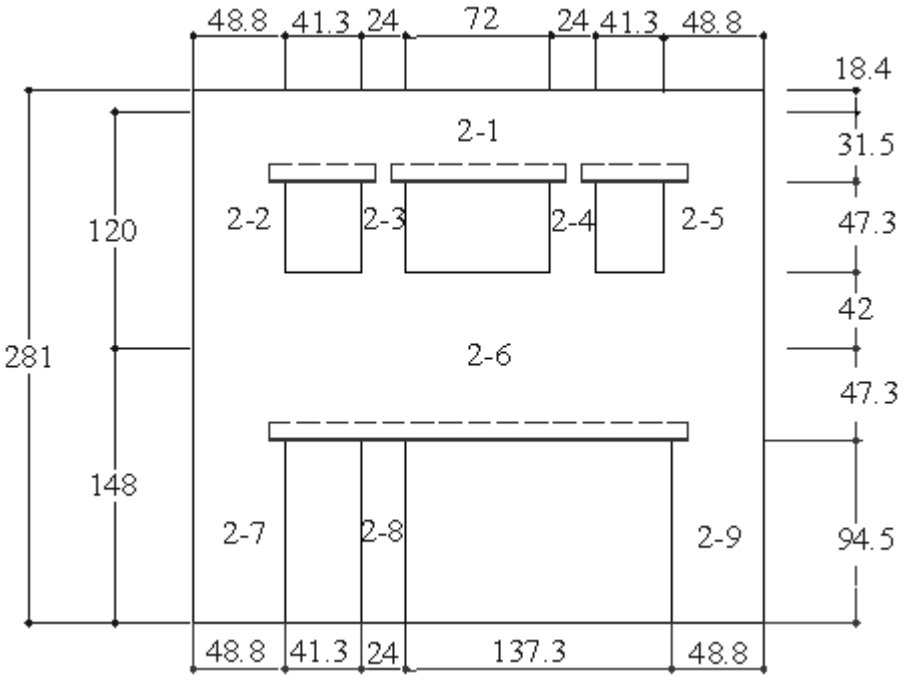

Figure 3.4. Elevation view of Wall 2 (dimensions are in inches).

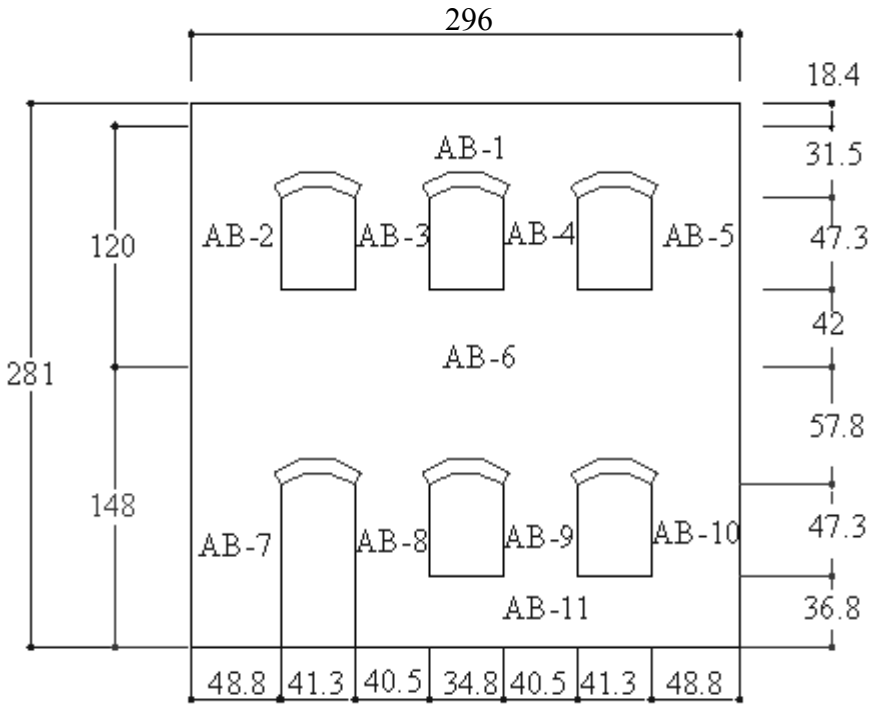

Figure 3.5. Elevation view of Walls A and B (dimensions are in inches).

3.1.1.1 URM Piers

Based on past experimental studies it has been established that the behavior of URM piers is strongly dependent on the height-to-length ratio (Epperson and Abrams, 1989; Abrams and Shah, 1992; Anthoine et al., 1995; Magenes and Calvi, 1992; Manzouri et al., 1995). In order to allow a variety of pier behaviors to be investigated, the URM walls of the test structure were composed of piers with a large range of aspect ratios (i.e. 0.4 to 4.0). The pier sizes and H/L ratios of each pier are listed in Table 3.1.

Table 3.1. Pier dimensions and aspect ratios

Pier	Length (in)	Height (in)	H/L	Pier	Length (in)	Height (in)	H/L
AB-2	48.4	47.3	1.0	1-4	48.4	47.3	1.0
AB-3	40.3	47.3	1.2	1-6	48.4	84	1.7
AB-4	40.3	47.3	1.2	1-7	210.6	84	0.4
AB-5	48.4	47.3	1.0	2-2	48.4	47.3	1.0
AB-7	48.4	84	1.7	2-3	24	47.3	2.0
AB-8	40.3	47.3	1.2	2-4	24	47.3	2.0
AB-9	40.3	47.3	1.2	2-5	48.4	47.3	1.0
AB-10	48.4	47.3	1.0	2-7	48.4	94.5	2.0
1-2	48.4	47.3	1.0	2-8	24	94.5	4.0
1-3	121.3	47.3	0.4	2-9	48.4	94.5	2.0

In addition, aspect ratios investigated in several past component tests were employed in the test structure to facilitate comparison. The primary supporting component data for this investigation was provided by MAE Center Projects ST-6 and ST-45. As a result, similar pier aspect ratios and dimensions were chosen for the test structure. The focus of Project ST-6 was on the behavior of two types of wall piers: (1) cantilever flexural member with an H/L ratio of 1.77; and (2) cantilever shear member with an H/L ratio of 0.5 (Franklin, 2001). For design, the piers in the first floor were assumed to act as "fixed-fixed" columns or walls, and the piers in the second floor were assumed to act as cantilever columns or walls. Following this assumption, the piers with H/L ratios between 3.0 and 4.0 employed in the first floor, and H/L ratios between 1.5 and 2.0 employed in the second floor of the test structure are equivalent to the flexure piers tested in ST-6. Similarly, piers with H/L ratios of 1.0 employed in the first floor, and H/L ratios of 0.5 employed in the second floor are representative of the shear piers tested in ST-6.

3.1.1.2 Wall Configuration

Due to the large variety of existing wall configurations found throughout the Mid-America region, the approach taken was to design the test structure in order to allow three general wall types to be investigated. The opening ratios of each wall are listed in Table 3.2. As apparent from the elevation view shown in Figure 3.4, Wall 2 contains a large door opening and relatively large opening ratio (see Table 3.2). This type of wall configuration is commonly found in firehouses and was designed to represent a lower bound on both strength and stiffness. In contrast, Wall 1 has relatively small openings and was designed to represent an upper bound on both strength and stiffness. Walls A and B were designed to represent an intermediate-type wall and contained several piers in series, which is also a common characteristic of URM structures in the Mid-America region.

Table 3.2. Opening ratios for each wall of the test structure

	Story	Total Area (in^2)	Opening Area (in^2)	Opening Ratio
Wall 1	First Second	44,400 41,500	3,400 3,900	8% 9%
Wall 2	First Second	44,400 41,500	17,000 7,300	38% 18%
Wall AB	First Second	43,800 40,900	7,100 5,600	14% 16%

3.1.1.3 Structural Configuration

Many structures in Mid-America, specifically firehouses, contain parallel walls with large differences in stiffness. This imbalance in stiffness can cause torsion of the structure under lateral loads, which can lead to undesirable behavior. As a result, the torsional response of URM structures subjected to ground accelerations is of interest. The

test structure allowed this type of behavior to be investigated since Walls 1 and 2 (i.e. the upper and lower bound walls in terms of stiffness) where placed in parallel (see Figure 3.2). In addition to parallel walls with differing stiffnesses, the torsional response of a structure is greatly affected by the degree of coupling between in-plane walls. Due to the relatively small stiffness of the out-of-plane wall and diaphragm, little coupling is expected. Figure 3.2 also shows that the structure contained two identical walls (i.e. Walls A and B). While this feature is not necessarily common, it did provide the opportunity for different retrofit methods to be investigated and directly compared.

3.1.2 Diaphragms

Based on the building inventory created through MAE Center Project SE-1, URM buildings constructed in Mid-America prior to 1950 typically contain timber diaphragms (Peralta, 2000). In general, these diaphragms are composed of framing and sheathing. Framing refers to the main gravity load carrying members which typically consist of joists and blocking. The flooring placed on top of the framing system is referred to as sheathing and typically is composed of boards placed either perpendicular to the joists (straight sheathing), boards placed at a 45 degree angle to the joists (diagonal sheathing), or plywood. In general, timber diaphragms may also employ chords, which are elements placed at the boundary of the diaphragm to increase in-plane strength and stiffness. However, the use of chords was not common in Mid-America prior to 1950 (Peralta, 2000).

To investigate the behavior of typical timber diaphragms, a comprehensive experimental study was conducted through MAE Center Project ST-8. The goals of this

project were to experimentally determine the behavior of common diaphragms as well as to investigate the effectiveness of several rehabilitation techniques such as joist anchors, plywood blocking, and the addition of steel truss elements. The framing for each of the diaphragms tested was composed of 2x10 spaced at 16 in. on center and were approximately 12 ft by 24 ft in plan. Various types of sheathing were investigated such as plywood, straight sheathing, and diagonal sheathing. All of the diaphragms tested were unchorded.

Based on the results of this investigation, a blocked plywood diaphragm was chosen for the second floor of the test structure and a straight sheathing diaphragm was chosen for the roof level of the test structure. These diaphragms represent an upper and lower bound on both strength and stiffness for all of the diaphragms tested. Figure 3.6 shows a plan view of the framing system used for the these diaphragms. This framing system was composed of 2x10 joists spaced at 16 in. on center with full depth blocking supplied every 4 ft.

To facilitate the use of this framing system, stud walls were built along the centerline of the structure parallel to Walls A and B. This was required in order to reduce the span from 24 ft to 12 ft. These stud walls remained unsheathed throughout the entire experimental program to ensure that they did not supply either lateral stiffness or strength to the structure.

The straight sheathing for the roof diaphragm was provided by 1x6 square edge boards. These boards were staggered symmetrically with respect to the diaphragm mid-span. For the second floor diaphragm, sheathing was provided by fully blocked 3/4 in. plywood. Both diaphragms used 8d nails to connect the sheathing to the framing and 16d

nails to attached the blocking to the joists. For the straight sheathing diaphragm, two nails were provided at every interior joist and three nails were used at the end of each board. The plywood diaphragm was connected by nails at 1.5 in. on center at the end of each plywood sheet and 3 in. on center for all other joists. All timber members were southern yellow pine.

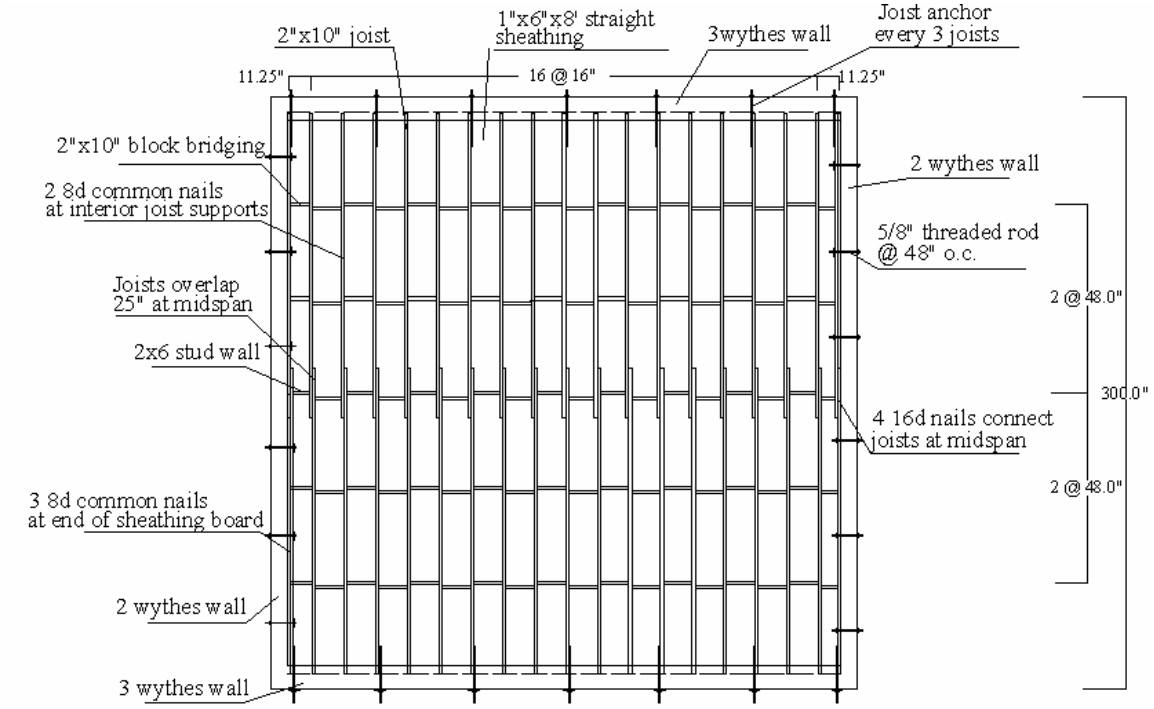

Figure 3.6. Schematic of diaphragm framing employed in the test structure

3.1.3 Construction Details

The test structure was built following techniques typical of pre-1950 construction in Mid-America. The masonry walls were composed of clay masonry bricks in a standard American bond (see Figure 3.7). Header courses were supplied every sixth course to tie the wythes together. In addition, both shallow arch lintels (Walls A and B) and steel lintels (Walls 1 and 2) were used in the test structure (see Figure 3.8). Both of these lintels are

representative of typical lintels used in URM construction throughout Mid-America.

The test structure was constructed with two types of shear connections between the diaphragms and URM walls. The first type was formed by placing the joist in a one wythe deep pocket in Walls A and B (see Figure 3.9). This connection detail is commonly found in existing URM structures and transfers shear by the joists bearing against the inside of the pocket. The second type of shear connection consisted of 5/8 in. diameter threaded rods cast into Walls 1 and 2 with nonshrink grout. These rods were then bolted to the joists directly adjacent to the wall (see Figure 3.10). In many cases this connection is considered a retrofit measure; however, the structure was constructed with these connections to facilitate the testing of the diaphragm. These connections were spaced 48 in. on center and 24 in. from the edges of Walls 1 and 2. This spacing represents a maximum allowable spacing as given by FEMA 178 (ATC, 1997).

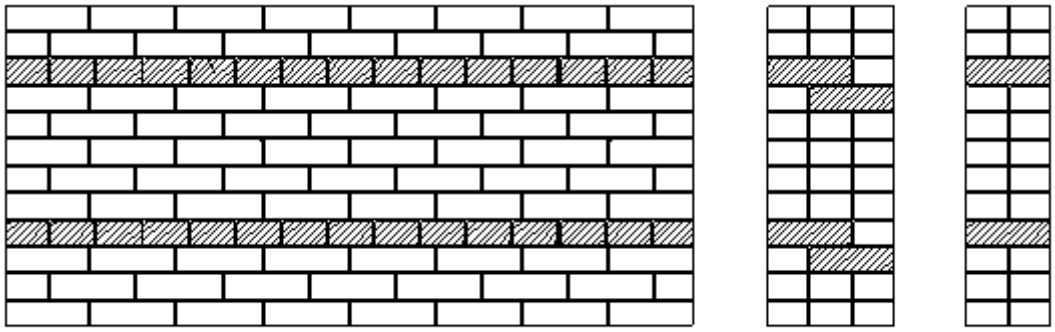

Figure 3.7. Detail of standard american bond (a) face of URM wall, (b) end of three-wythe URM wall, (c) end of two-wythe URM wall.

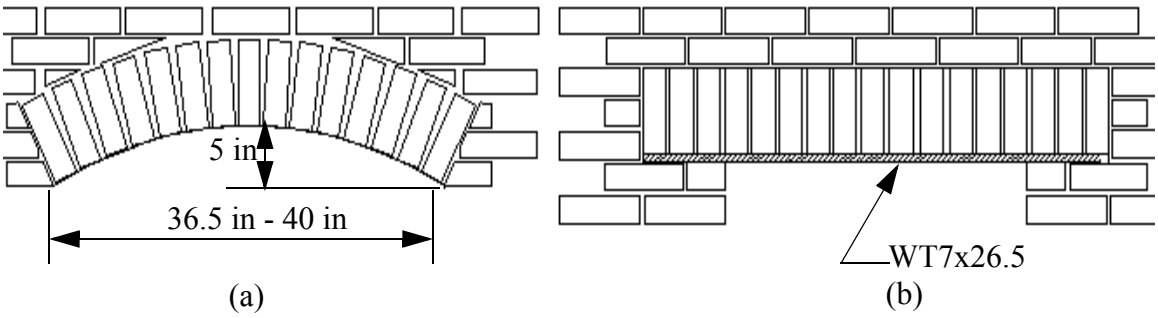

Figure 3.8. Details of (a) arch lintel and (b) steel lintel.

Figure 3.9. Photograph showing the construction of the pocket connection between the floor/roof 2x10 joists and Walls A and B.

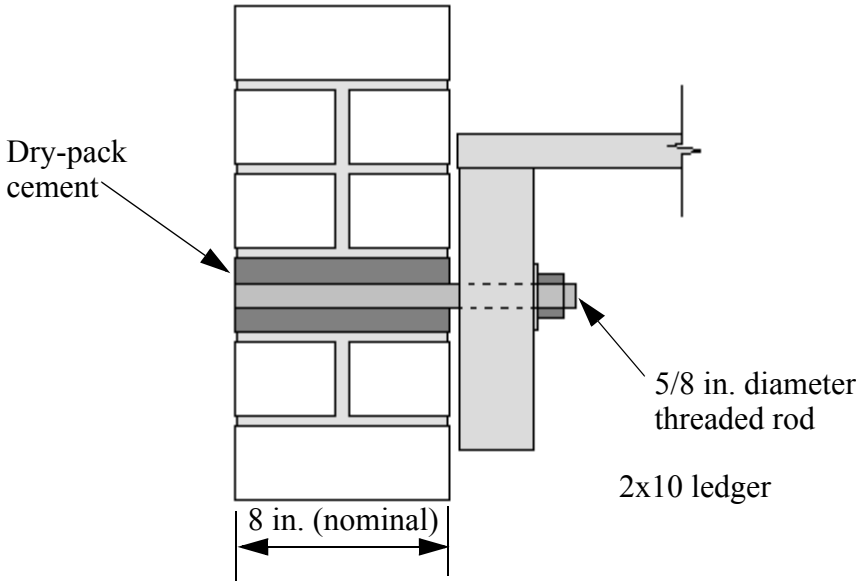

Figure 3.10. Schematic of threaded rod shear connection (Walls 1 and 2).

Neither of the shear connections supplied in the test structure can be relied upon to transfer tension from the URM walls to the diaphragm. The pocket connection can only transfer tension through friction, which is typically very low. For the case of the threaded rod connection, the connection between the joist and the sheathing typically fails at low loads thus limiting the amount of tension that can be transferred. Furthermore, under this loading condition the joist adjacent to the URM wall is placed into cross-grain tension, which causes the joist to crack longitudinally at relatively low loads.

3.1.4 Materials

The test structure was constructed by experienced masons and was composed of clay bricks and a type K mortar. Mortar mix proportions were 0.5: 2: 9 by volume of Type I Portland cement, hydrated lime, and masonry sand, respectively. This proportion is not standard and was derived based on material tests (Yi, 2004). The aim was to create a

mortar that displayed properties consistent with those obtained from common construction practices prior to 1950. This was required since materials available today are of considerably higher quality than those used in the first half of the 20th century. As a result, mortars made from current materials cannot be based on past standards if similar properties are desired. Field studies conducted in Mid-America showed that the majority of URM structures contained mortars with low levels of Portland cement, which is consistent with either a sand-lime or a Type K mortar. During construction no attempt was made to control the amount of water in the mortar. The masons were permitted to add water until the desired consistency was achieved.

The building employed solid bricks as well as bricks that contained a longitudinal hole through the center. Nominal dimensions of both types of bricks were 7.75 in length, 3.5 in width, and 2.25 in thickness. The results of preliminary material tests indicated that, while the bed-joint shear strength associated with each type of brick was similar, the masonry compressive strengths had large variations. In an attempt to isolate this anomaly, the solid bricks were used for the lower 54 courses (12 ft) and the cored bricks were used for the remainder of the structure. However, all header courses were composed of solid bricks for aesthetic reasons. The results of the preliminary material tests are given in Table 3.3 (Yi, 2004).

Table 3.3. Result of preliminary material tests

Property	Test	Type of Brick	Number of tests	Mean	COV
Prism (5 brick) Compressive Strength	ASTM C1314-00	Solid	3	1460 psi	0.25
		Cored	3	590 psi	0.09
Bed-joint Shear Strength	4-brick assemblage	-	11	58 psi	0.4
Brick Compressive Strength	ASTM C67-00	Solid	5	6,030 psi	0.23
		Cored	5	5,290 psi	0.31

3.2 Retrofit Techniques

Several different retrofit techniques were investigated to assess their effectiveness in improving the behavior of URM structures during seismic events. In general, the methods can be classified as two types: (1) connection retrofit and (2) in-plane wall retrofit. The following sections describes each of retrofit techniques investigated during this research.

3.2.1 Connection Retrofit

As discussed in Section 3.1.3, the test structure was constructed without tension connections between the URM walls and diaphragms. This lack of connection is common in existing URM structures throughout Mid-America and renders masonry walls vulnerable to failure from out-of-plane excitation (see Chapter 2). Past studies have shown that the installation of joist anchors can effectively reduce the vulnerability of URM walls in the out-of-plane (Clough et al., 1979 and Tomazevic et al., 1993).

To investigate this retrofit, joists anchors supplied by Simpson Strong-Tie^{TM} were employed in the test structure. These anchors consist of a steel strap that is developed into the diaphragm either through 16d nails or 1/2 in. diameter bolts. This steel strap is then bolted to a bearing plate located on the outside of the URM wall via a 5/8 in. diameter threaded rod (see Figure 3.11). Table 3.4 gives the properties of the these anchors as provided by the manufacturer.

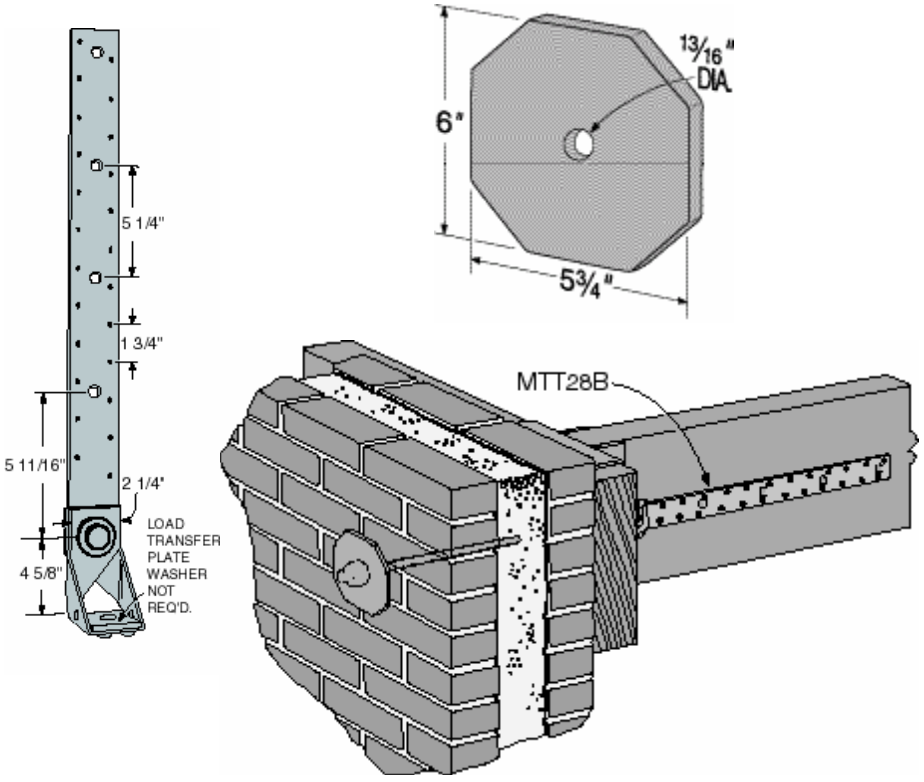

Figure 3.11. Schematic of joist anchors (taken from www.strong-tie.com)

Table 3.4. Properties of joist anchors (taken from www.strong-tie.com)

Fastener type	Allowable tension capacity (kips)
18-16d nails	4.5
4- 1/2in diameter bolts	2.7

For loading in the direction parallel to the joists, anchors were supplied at every third joist and were attached via four 1/2 in. bolts. For loading in the perpendicular direction, the anchors were place every 48 in. and where attached to the diaphragm with 18 16d nails through the sheathing and into the blocking between joists. These spacings roughly correspond to the maximum allowable spacing as given by FEMA 178 (ATC, 1992).

3.2.2 In-Plane Retrofit

3.2.2.1 FRP Overlays

The general philosophy adopted for the retrofit of the test structure with FRP overlays was to promote bed-joint sliding to exploit the resulting pseudo-ductile behavior and relatively large amount of energy dissipation. The specific design of each retrofit was done empirically since currently no reliable method exists for predicting the behavior of URM components after retrofit with FRP overlays. In addition, to facilitate future comparisons with component test results, retrofits similar to those examined in past component tests were used. In particular, the following systems were chosen:

- Precured unidirectional glass grid (18 oz/yd^2) with an epoxy matrix.
- Bidirectional alkali-resistant glass grid with a cementitous matrix.
- Unidirectional glass (27 oz/yd^2) with an epoxy matrix.

Detailed accounts of component research conducted on each of these systems can be found in Chapter 2.

Schematics illustrating the configuration of each FRP overlay retrofit are given in Figure 3.12 through Figure 3.14. The systems employed on Walls 1 and B consisted of

unidirectional composite strips, whereas the system applied to Wall 2 contained bi-directional full coverage composite sheets. Due to the difficulties involved with anchoring the composite overlays onto the foundation, the base of the structure was designated as the desired sliding plane. That is, the vertical FRP strips were simply stopped at the top of the bed-joint adjacent to the foundation to allow for sliding to occur. In addition, these systems were only applied to the inside of the structure. This was done in an attempt to eliminate the adverse effects of these retrofit techniques on building aesthetics.

The configuration of the partial coverage systems consisted of both vertical and diagonal strips of unidirectional glass-epoxy composite to strengthen the piers. This was done to suppress both diagonal tension failure and rocking, thus promoting sliding behavior. Successfully increasing the compression strength of a pier with the use of FRP overlays is difficult, and since the low levels of vertical stress present in the test structure rendered toe crushing unlikely, no suppression of this failure mode was deemed necessary. In addition to these pier retrofit schemes, the configuration of reinforcement applied to Wall 1 also contained horizontal strips. The horizontal strips at the base of pier P1-6 were used to force a smooth horizontal crack at the base. This was required since during the initial testing of Wall 1, a stair-stepped flexural crack was formed which impeded sliding. The horizontal strips at the top of the wall were used to provide continuity between individual piers by resisting the lateral opening of diagonal cracks in the spandrels. The horizontal reinforcement for Wall B consisted of NSM rods and is discussed in Section 3.2.2.2. To facilitate comparisons between MAE Center Projects ST-6 and ST-45, all FRP strips were applied in 8 in. widths.

The retrofit system applied to Wall 2, shown in Figure 3.13, consisted of full

coverage bi-directional composite sheets. The bi-directional nature of this composite provided both horizontal reinforcement for continuity and local pier reinforcement to suppress diagonal tension and rocking failures. The reinforcement consisted of two layers of a bi-directional alkali-resistance glass grid in a fiber reinforced cementitous matrix. The choice of two layers of grid was based on component test results that suggested this was an optimum configuration (see Chapter 2).

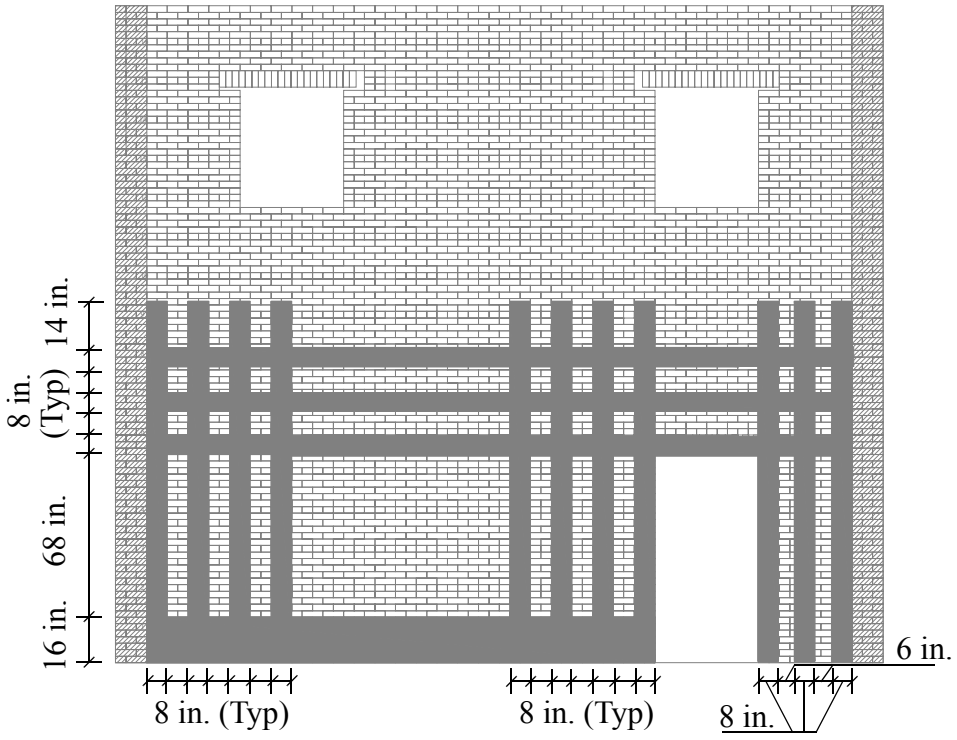

Figure 3.12. Schematic of the FRP overlay retrofit scheme applied to Wall 1.

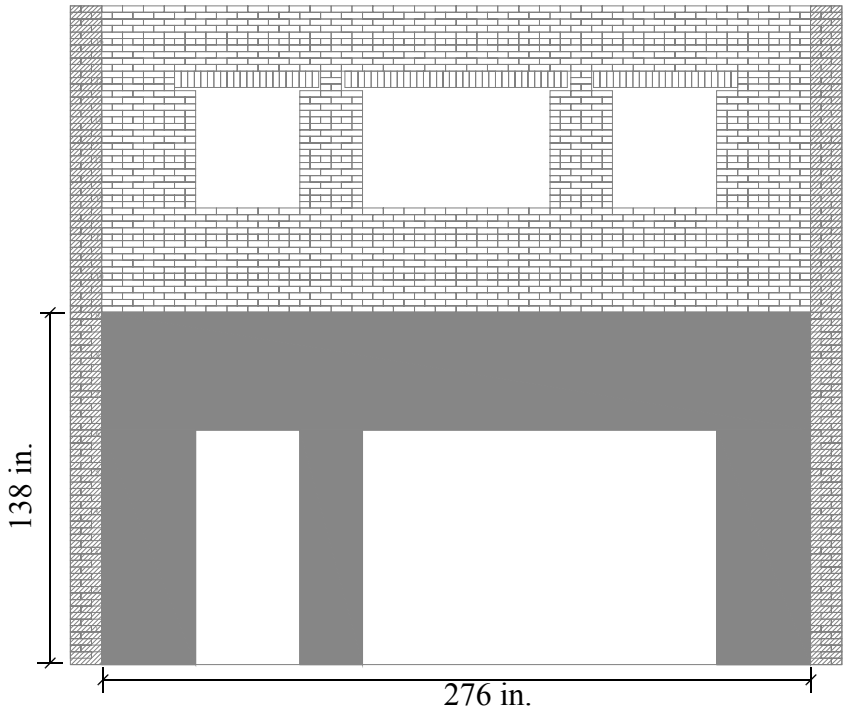

Figure 3.13. Schematic of the FRC overlay retrofit scheme applied to Wall 2.

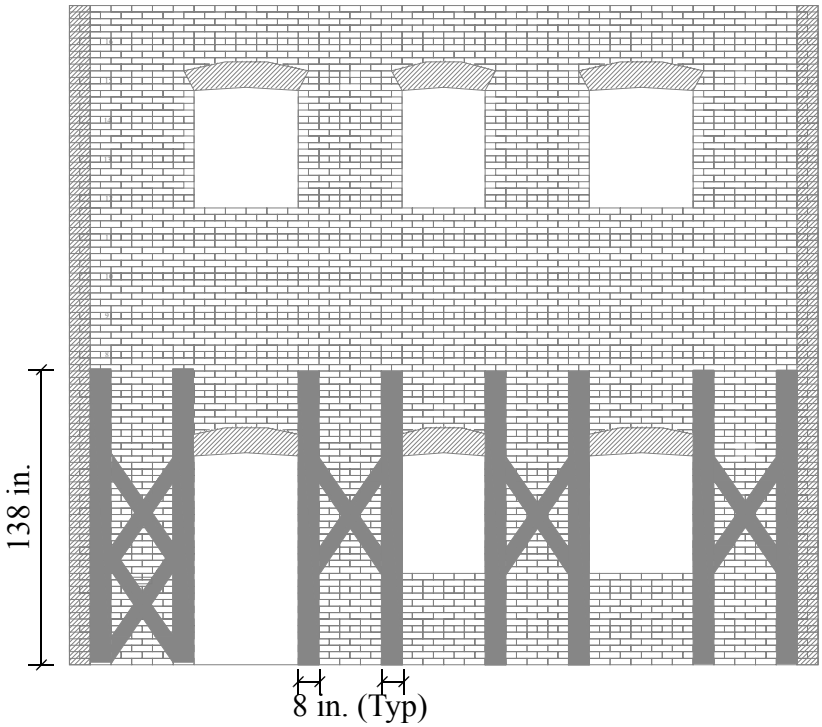

Figure 3.14. Schematic of the FRP overlay retrofit scheme applied to the inside of Wall B.

3.2.2.2 Near Surface Mounted Rods

To supply horizontal reinforcement in Wall B, near surface mounted (NSM) rods were employed. A schematic showing the location of these rods is given in Figure 3.15. These rods were placed in every third bed-joint (approximately 8 in. apart). The rods used were composed of a unidirectional glass-epoxy composite. Number 2 rods were chosen (diameter of 0.25 in.) to facilitate placement in the existing bed-joints which were approximately 3/8 in. to 1/2 in. thick. To increase the bond characteristics, sand particles were bonded to the outside of the rods. The description of a component investigation focused on the behavior of URM piers strengthened with NSM rods can be found in Chapter 2.

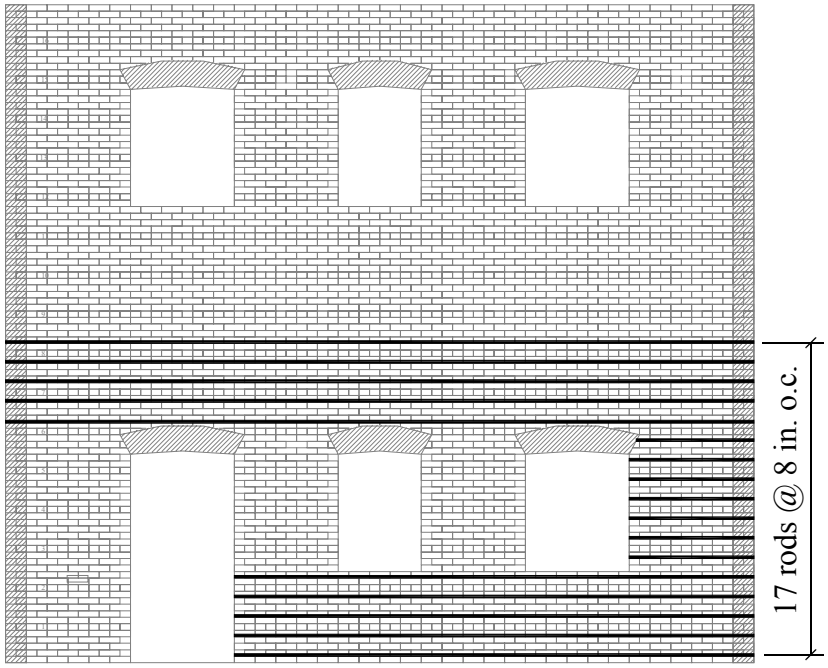

Figure 3.15. Schematic of the NSM retrofit scheme applied to the outside of Wall B

3.2.2.3 Vertical Post-tensioning

Wall A was constructed with four vertical unbonded post-tensioning tendons throughout the height of the structure for two reasons: (1) to facilitate the investigation of vertical post-tensioning as a retrofit measure and (2) to investigate the behavior of Wall A under higher levels of vertical stress (note: FEMA 356 (ATC, 2000) states that vertical unbonded post-tensioning is equivalent to an increased level of vertical stress). In order to gain insight into the effect of different levels of post-tensioning force, Wall A was tested with both an additional 25 kips of vertical load and 50 kips of vertical load. Since the wall itself weighed roughly 50 kips, these post-tensioning levels corresponded to an increase in vertical stress of approximately 50% and 100% for the first floor piers.

Post-tensioning tendons were placed in the center of each of the piers from the base of the structure to the roof, as shown in Figure 3.16. The Sure-Stress^{TM} post-tensioning system manufactured by DUR-O-WAL was selected to investigate this retrofit. The system was composed of 7/16 in. diameter tendons (100 ksi yield strength), foundation anchors, direct tension indicating (DTI) washers, bearing plates, couplers, and nuts, as shown in Figure 3.17. This system was installed by bonding the SureStress^{TM} anchors into the foundation with Sikadur^{TM} 35 Hi-Mod LV (low viscosity) epoxy. During construction of the walls, PVC tubes were place with the URM wall to allow for the insertion of the post-tensioning tendons in the center wythe of the wall.

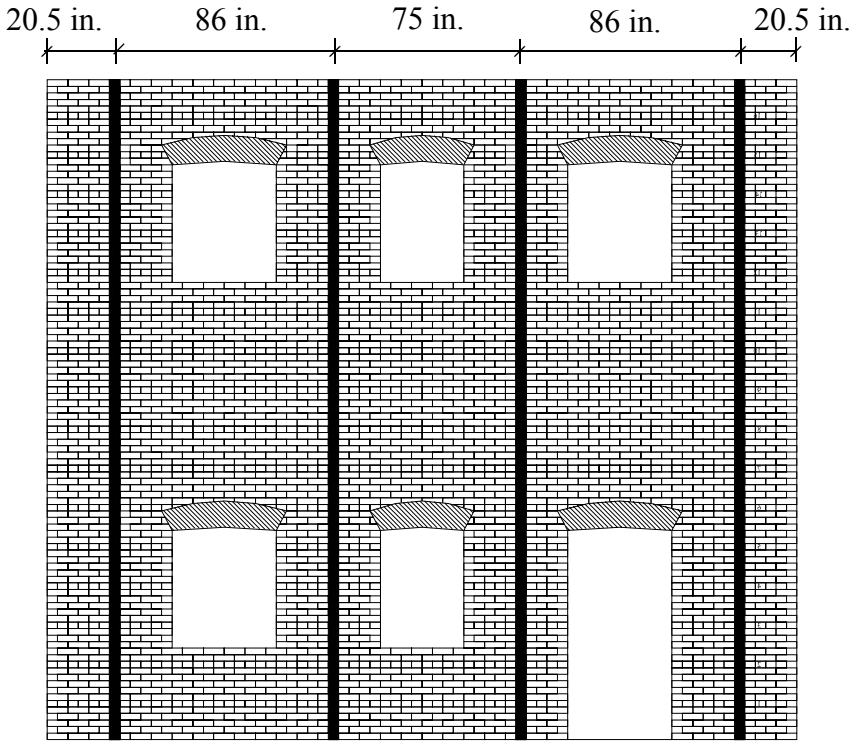

Figure 3.16. Schematic showing the location of the post-tensioning tendon in Wall A

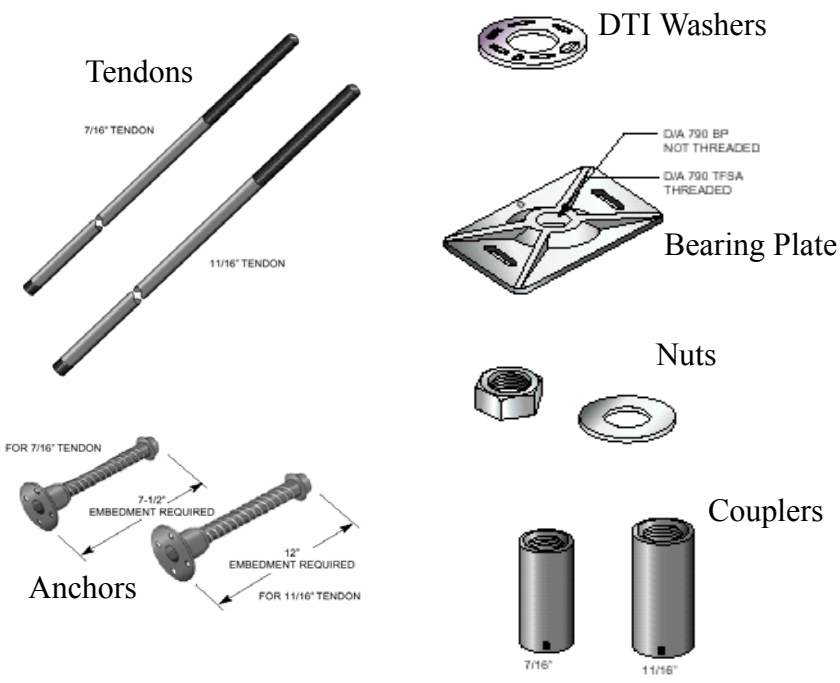

Figure 3.17. Sure-Stress^{TM} post-tensioning system (taken from www.dur-o-wal.com)

3.3 Test Overview

To accomplish the overall objectives of this project, tests were conducted on the structure both before and after retrofit. In general, the experimental program was composed of two main sections: (1) the testing of the diaphragm and out-of-plane walls and (2) the testing of the in-plane walls. All of these tests were carried out without any additional weight added to the test structure. This was done due to the low levels of vertical stress common in typical URM structures throughout Mid-America.

3.3.1 Diaphragm and Out-of-Plane Wall Testing

The initial tests conducted subjected the roof diaphragm to low-level cyclic displacements. These tests were first carried out with the existing diaphragm-to-wall connections as described in Section 3.1.3. The goals of these cycles were to (1) determine the elastic stiffness of the diaphragm and out-of-plane wall and (2) provide insight into the behavior of the existing connections at low displacement levels. Following this loading, the joist anchor retrofit described in Section 3.2.1 was installed and the diaphragm was retested. This series of tests were aimed at assessing the effectiveness of the joists anchor retrofit under small displacements. To investigate the behavior of the structure in both directions, the diaphragms were first loaded parallel to the joists and then loaded perpendicular to the joists.

Loading of the diaphragm was accomplished by attaching a single servo hydraulic actuator directly to the diaphragm. During construction portions of the parapets on Walls 1 and A were not constructed to facilitate access to the roof diaphragm. A photograph of the test setup showing the loading fixture used to transfer the load from the actuator to the

diaphragm is shown in Figure 3.18. To avoid local damage at load introduction, four 2x10 boards were employed to reinforce the center portion of the diaphragm (see Figure 3.18). To allow for cyclic loading, the actuator was bolted to four Simpson Strong-Tie^{TM} joist anchors that were developed into the reinforced portion of the diaphragm. In addition, the center of the diaphragm was reinforced with a timber diamond constructed from 2x10 boards (see Figure 3.18). Detailed drawings of the diaphragm test setup can be found in Appendix A.

Each cycle conducted on the roof diaphragm imposed a +/- 0.2 in. displacement at mid-span. This small displacement was chosen to limit the amount of damage induced in the masonry walls due to out-of-plane loading. No cracking of the masonry walls were observed during this test.

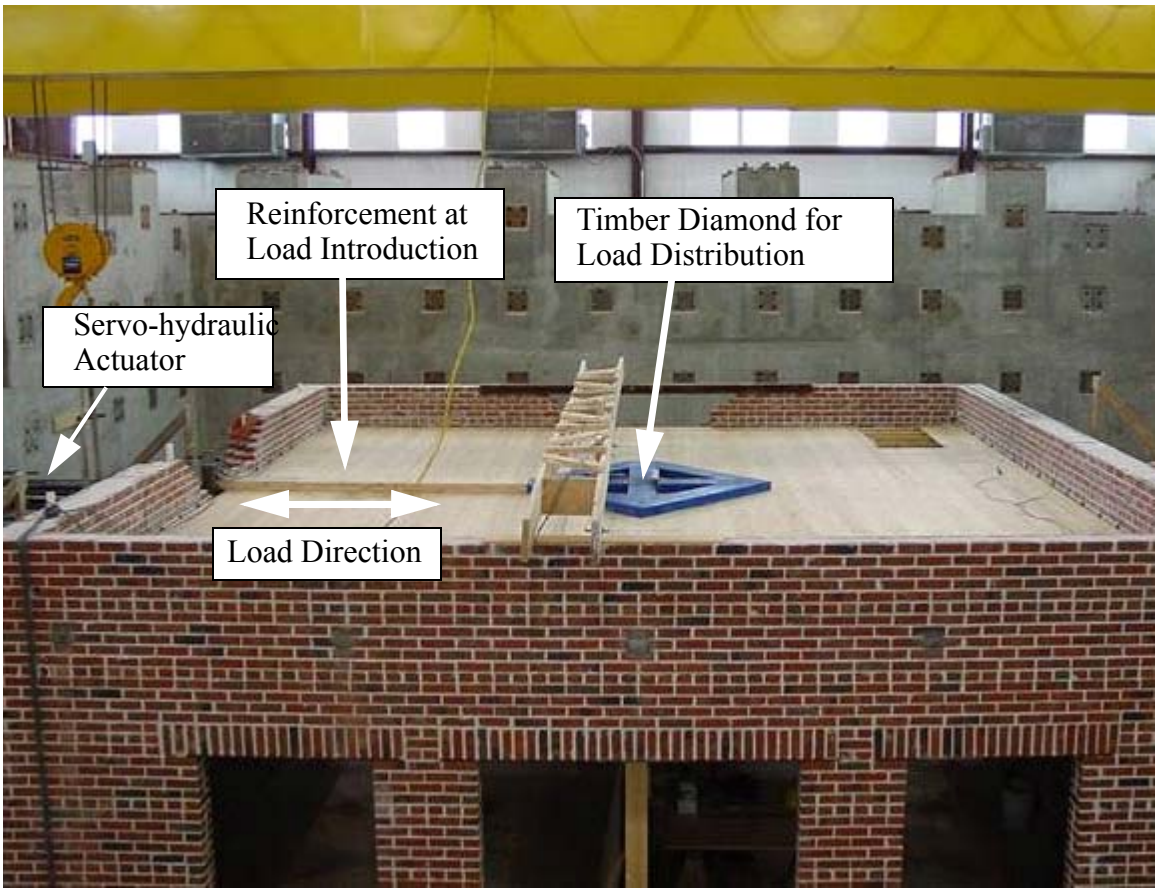

Figure 3.18. Photograph of diaphragm and out-of-plane wall test setup

3.3.2 In-Plane Wall Tests

The second portion of the experimental program subjected the in-plane walls to cyclic displacements. The initial in-plane wall tests were conducted on the structure in an unreinforced state. The primary objective of this portion of the test was to investigate global characteristics such as coupling between in-plane walls, damage progression, flange participation, and the effects of overturning moment. Following these cycles the walls were strengthened with the techniques described in Section 3.2.2 and retested. The primary goals of these tests were to (1) investigate the behavior of the strengthening techniques and identify failure modes and (2) assess the effectiveness of each technique in

terms of strengthening, energy dissipation capacity. Figure 3.19 shows the in-plane test sequence.

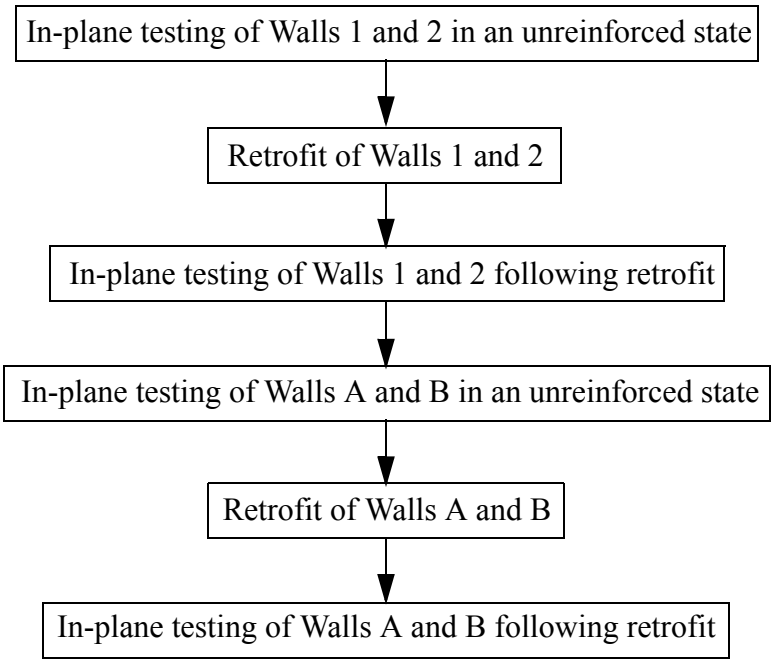

Figure 3.19. In-plane test sequence.

Loading of the structure was accomplished by imposing lateral displacements at the floor and roof levels of each in-plane wall via four servo-hydraulic actuators (see Figure 3.20). To introduce load into the structure, the in-plane walls at both the floor diaphragm and roof diaphragm levels were post-tensioned horizontally. The actuators were then bolted to the bearing plate used for post-tensioning. This allowed the actuators to induce displacements in both directions without causing local damage to the URM walls. Note that this type of loading fixture induced horizontal compression in the spandrels of the in-plane walls, thus suppressing diagonal cracking. Detailed drawings of the in-plane wall test setup can be found in Appendix A.

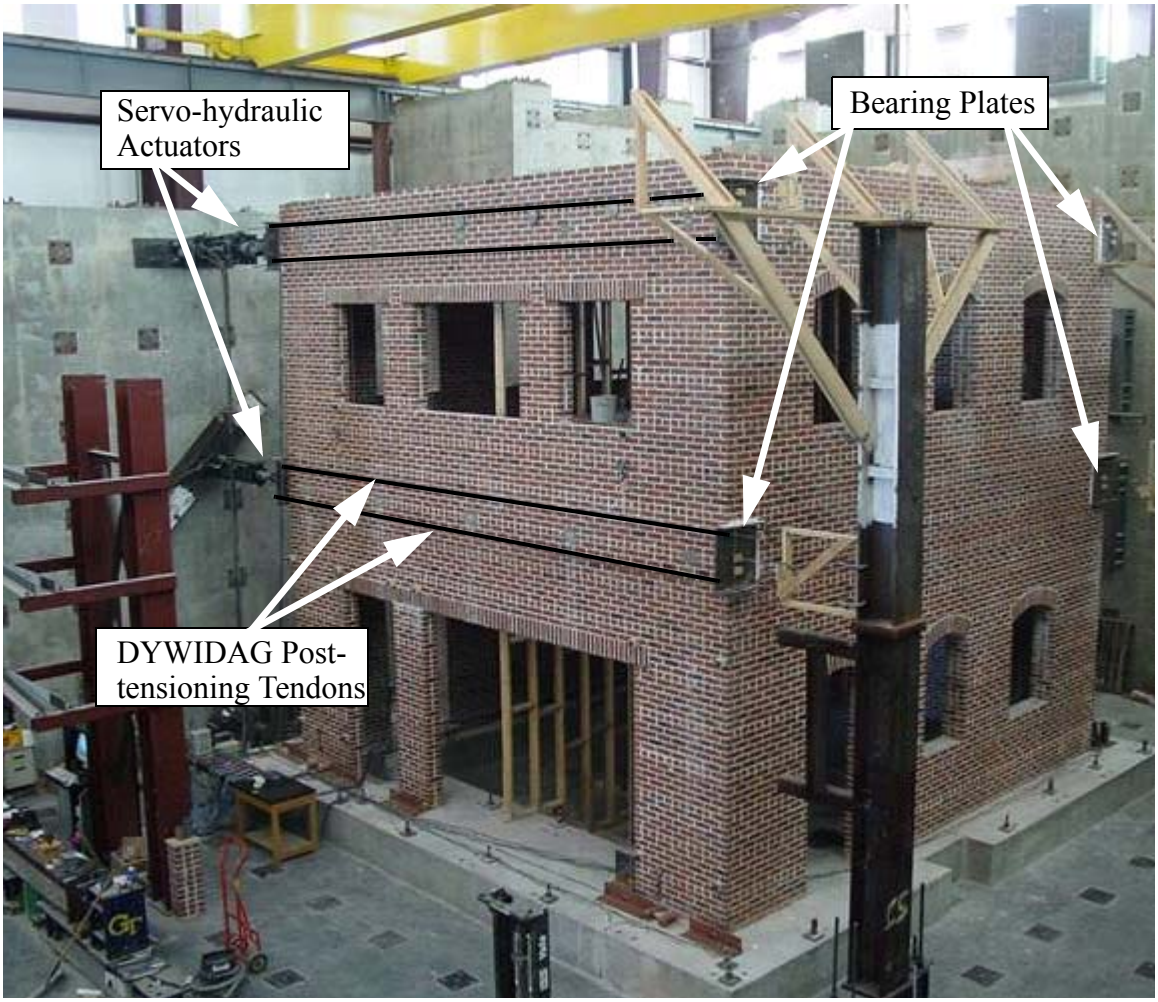

Figure 3.20. Photograph of in-plane wall test setup.

A modified stiffness control scheme was employed to approximate the seismic forces on the structure. The concept of this control scheme is described in Figure 3.21. Based on past experimental research (Clough et al., 1979; Tomazevic et al., 1993; and Costley and Abrams, 1996), it is reasonable to assume that the first vibration mode dominates the response of low-rise URM buildings. However, the first vibration mode changes throughout loading due to damage accumulation, which results in a decrease in stiffness. Therefore, in order to apply realistic displacements to the structure, the evolution

of the first mode shape must be addressed.

To accomplish this, the loading sequence for each of the walls began by imposing small displacements in order to determine the elastic stiffness of each floor. Stiffness matrices were then calculated for each in-plane wall assuming a two-degree of freedom shear building. By assuming mass matrices for the in-plane walls based on tributary area (i.e. $2m$ at the second floor and m at the roof), the first mode shape was calculated. The structure was then displaced in this profile to obtain the next desired target roof displacement $u1^{i+1}$. As damage occurred, the response of the corresponding floor became nonlinear and the stiffness was taken as the secant stiffness. This allowed major modifications in the response, such as the formation of a soft story, to be captured. At each level of displacement a minimum of two cycles were imposed to investigate stiffness and strength degradation prior to increasing roof drift. In cases where the response of the structure varied substantially during cycles at the same roof drift, the structure was subjected to additional cycles until the response became repeatable.

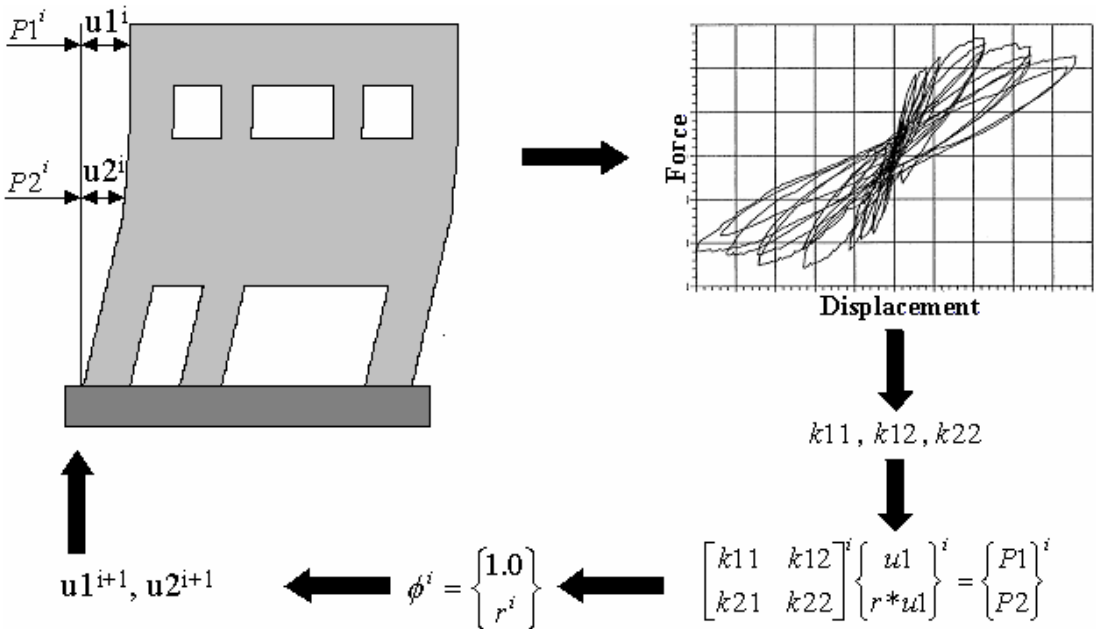

Figure 3.21. Schematic of the modified stiffness control scheme

3.3.3 Instrumentation

To measure the response of the test structure during loading, linear variable displacement transducers (LVDTs), potentiometers, strain gages, and load cells were employed. Specifically, the measured responses included:

- Applied lateral force
- Lateral and vertical deformations of the roof diaphragm
- In-plane, out-of-plane, and vertical deformations of the masonry walls
- Flexural, shear and axial deformations of individual piers
- Shear deformations of selected spandrels
- Axial strain of FRP overlays

Detailed drawings of the instrumentation plan can be found in Appendix A. In addition, the location and designation of specific instrumentation is provided in the main body of this thesis as it is referenced.

CHAPTER 4

EXPERIMENTAL RESULTS

The results of the quasi-static test conducted on the test structure before and after retrofit are summarized in this chapter. The design of the test structure and each retrofit scheme along with descriptions of the test set up, test sequence, loading protocol, and instrumentation are provided in Chapter 3. Detailed documentation of the response of the test structure prior to retrofit can be found in Yi (2004) and a detailed description of the response after retrofit can be found in Appendices C through F.

This chapter is structured as follows. Sections 4.1 through 4.4 present descriptions of the in-plane response of each wall before and after retrofit. These descriptions focus on the force-displacement response, damage progression, overall wall behavior, and the response of the retrofitting system. The discussion of each wall concludes with a brief comparison between the performance before and after retrofit. Section 4.5 gives results obtained with regards to coupling between the in-plane walls of the test structure. Section 4.6 presents a brief description of the testing conducted on the roof diaphragm, primarily with regard to the diaphragm-to-wall connection. Section 4.7 gives a summary of the principal findings of the experimental program. This summary focuses on the three primary objectives of this study which were to investigate (1) the effectiveness of each retrofit technique, (2) the behavior of each retrofit system, and (3) the global characteristics of low-rise URM structures.

4.1 Response of Wall 1

A summary of the in-plane displacements imposed on Wall 1 is given in Table 4.1 along with the test run and cycle designation. Figure 4.1 shows a graphical representation of the loading history imposed before and after retrofit. Prior to retrofit, Wall 1 was subjected to increasing cyclic displacements up to 6.35 mm (0.25 in.) in each loading direction. Based on the observed failure modes, the resulting maximum drifts corresponded to the Life Safety performance level (ATC, 2000). Following the application of GFRP overlays the wall was subjected to increasing cyclic displacements up to 19 mm (0.75 in.). No performance levels are currently available for GFRP strengthened masonry; however, if the performance levels provided for URM are employed, the imposed displacements exceeded the Collapse Prevention performance level (ATC, 2000).

Table 4.1 Summary of displacements imposed on Wall 1

	Test Run	Target Roof Displacement mm (in)	Target Second Floor Displacement mm (in)
URM	3	+/- 0.4 (0.015)	+/- 0.24 (0.009)
	4	+/- 0.5 (0.02)	+/- 0.3 (0.012)
	5	+/- 1 (0.04)	+/- 0.6 (0.026)
	6	+/- 1.5 (0.06)	+/- 0.9 (0.036)
	7	+/- 2.5 (0.1)	+/- 1.5 (0.06)
	8	+/- 3.8 (0.15)	+/- 2.3 (0.09)
	9*	+/- 2.5 (0.1)	+/- 1.5 (0.06)
	10	+/- 6.4 (0.25)	+/- 3.8 (0.15)

Table 4.1 Continued

Post-Retrofit	11	+/- 0.5 (0.02)	+/- 0.3 (0.012)
	12	+/- 1 (0.4)	+/- 0.6 (0.024)
	13	+/- 1.5 (0.6)	+/- 0.9 (0.036)
	14	+/- 2.5 (0.1)	+/- 1.5 (0.06)
	15	+/- 3.8 (0.15)	3.0 (0.12), -2.8 (- 0.11)
	16	+/- 6.4 (0.25)	5.4 (0.212), -5.7 (- 0.225)
	17	+/- 9.5 (0.375)	8.4 (0.33), -9.0 (-0.356)
	18	+/- 12.7 (0.5)	11.9 (0.47), -12.1 (-0.475)
	19	+/- 19.1 (0.75)	17.9 (0.705), -18.1 (-0.713)

* Wall 2 was held at zero displacement

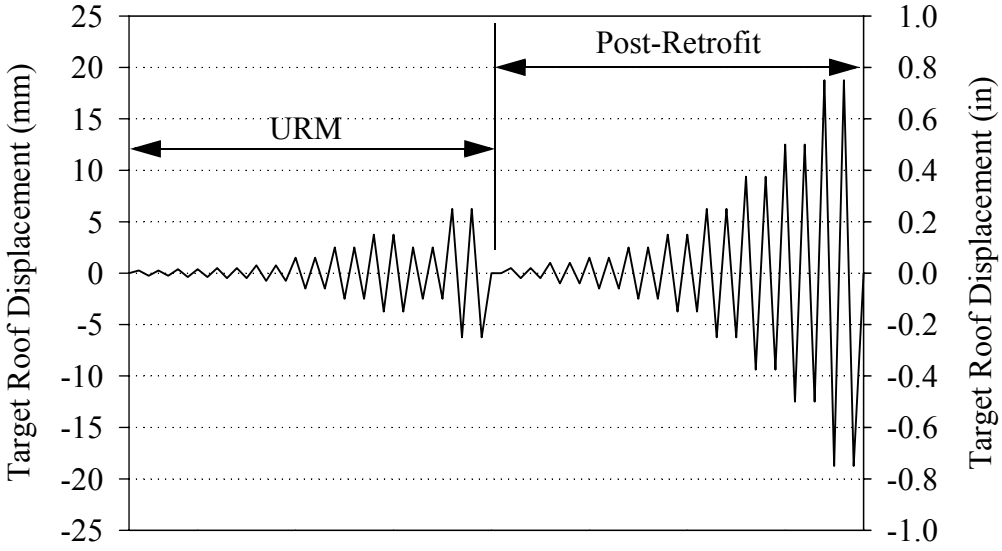

Figure 4.1. Loading history applied to Wall 1.

4.1.1 Response Prior to Retrofit

4.1.1.1 Force-Displacement Behavior

Table 4.2 shows the measured elastic stiffness of each story of Wall 1 in each direction. Each stiffness corresponds to a roof drift of 0.25 mm (0.01 in.) and each was

determined by dividing the shear force in each story by the relative displacement of each story.

Table 4.2. Elastic Stiffness of Wall 1.

	Positive Direction	Negative Direction
First Story Initial Stiffness	982 kN/mm (5610 kip/in)	919 kN/mm (5250 kip/in)
Second Story Initial Stiffness	614 kN/mm (3510 kip/in)	394 kN/mm (2250 kip/in)

Figure 4.2 shows the recorded base shear versus roof displacement response of Wall 1 prior to retrofit. The maximum strength of Wall 1 was 267 kN (60 kip) in the positive direction and 245 kN (55 kip) in the negative direction. The corresponding roof displacements were approximately 1 mm (0.04 in.) in each direction. As apparent from Figure 4.2, the hysteresis of Wall 1 displayed a great deal of pinching up to a roof displacement of approximately 4 mm (0.15 in.). As the imposed displacement increased beyond this level the response of Wall 1 displayed a more open hysteresis (particularly for the negative direction).

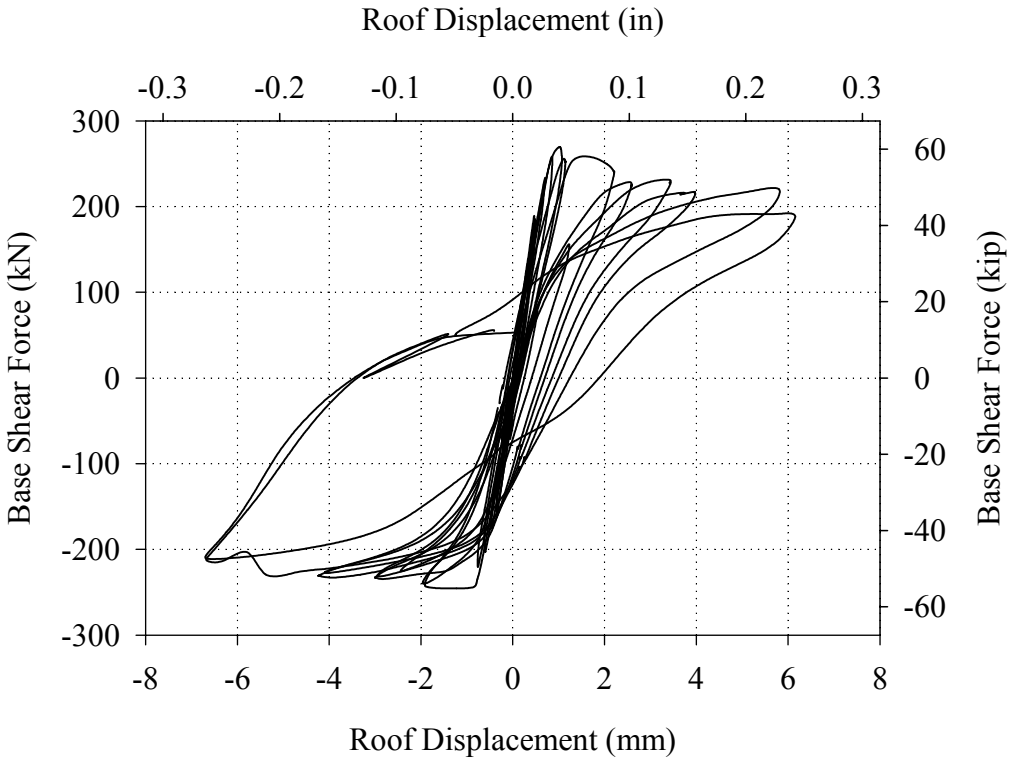

Figure 4.2. Base shear force versus roof displacement response of Wall 1 prior to retrofit.

4.1.1.2 Damage Progression and Wall Behavior

The crack pattern of Wall 1 and out-of-plane Walls A and B following Test Run 10 are shown in Figures 4.3 through 4.5. Figure 4.6 and 4.7 show schematics illustrating the behavior of Wall 1 and out-of-plane Walls A and B prior to retrofit in the positive and negative directions, respectively.

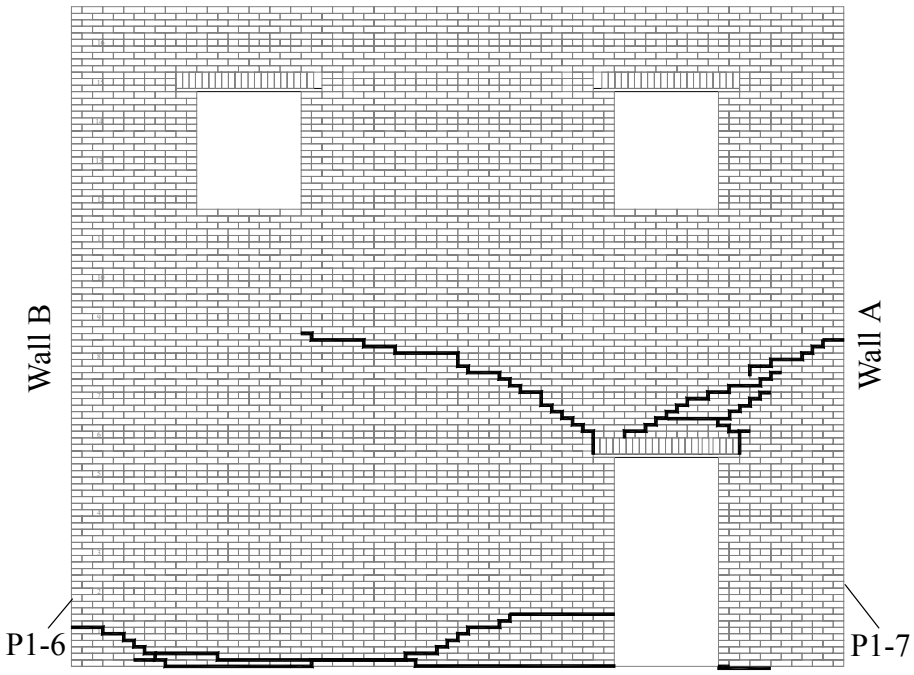

Figure 4.3. Crack pattern of Wall 1 following Test Run 10.

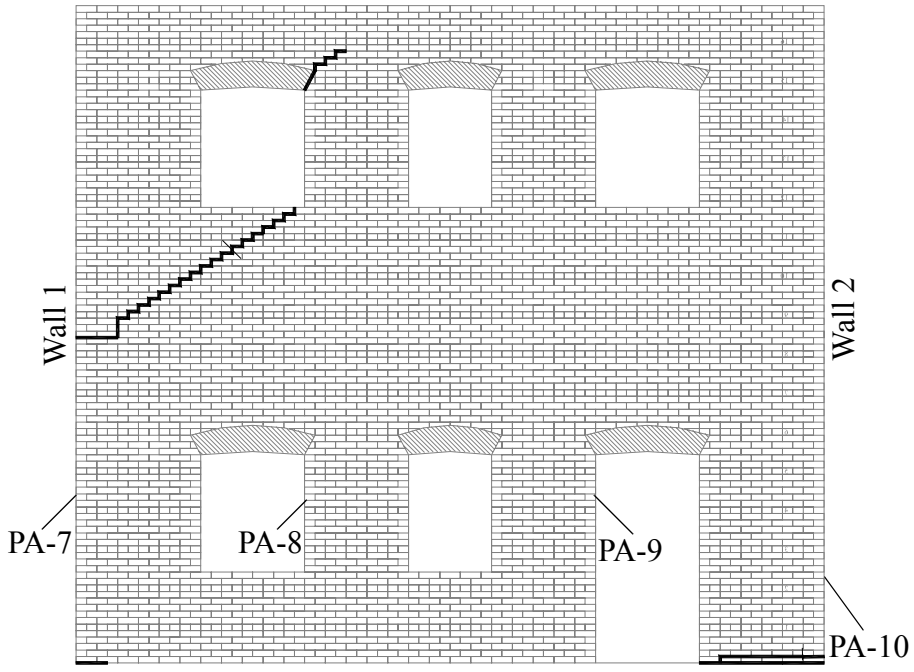

Figure 4.4. Crack pattern of Wall A following Test Run 10.

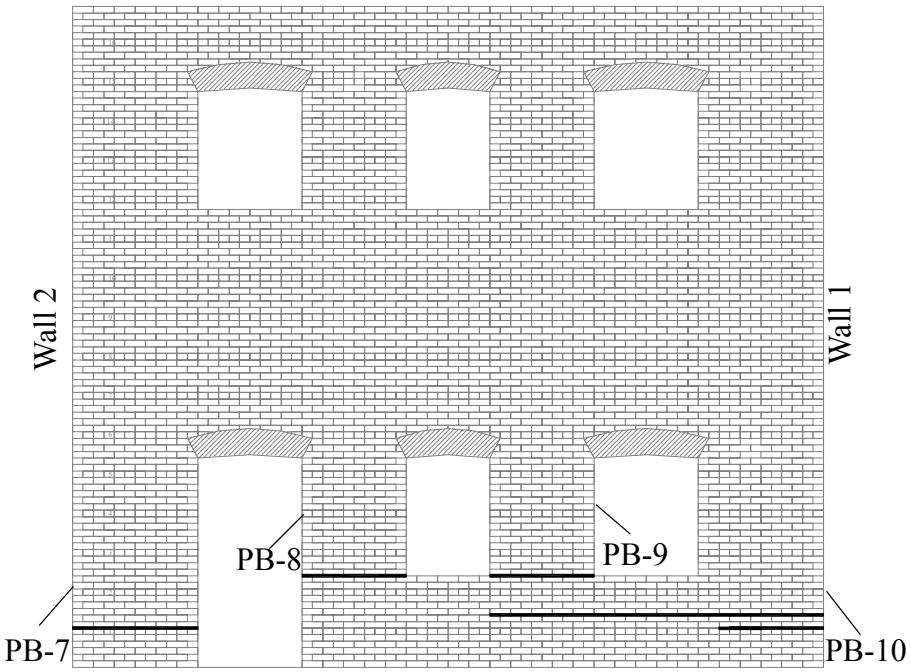

Figure 4.5. Crack pattern of Wall B following Test Run 10.

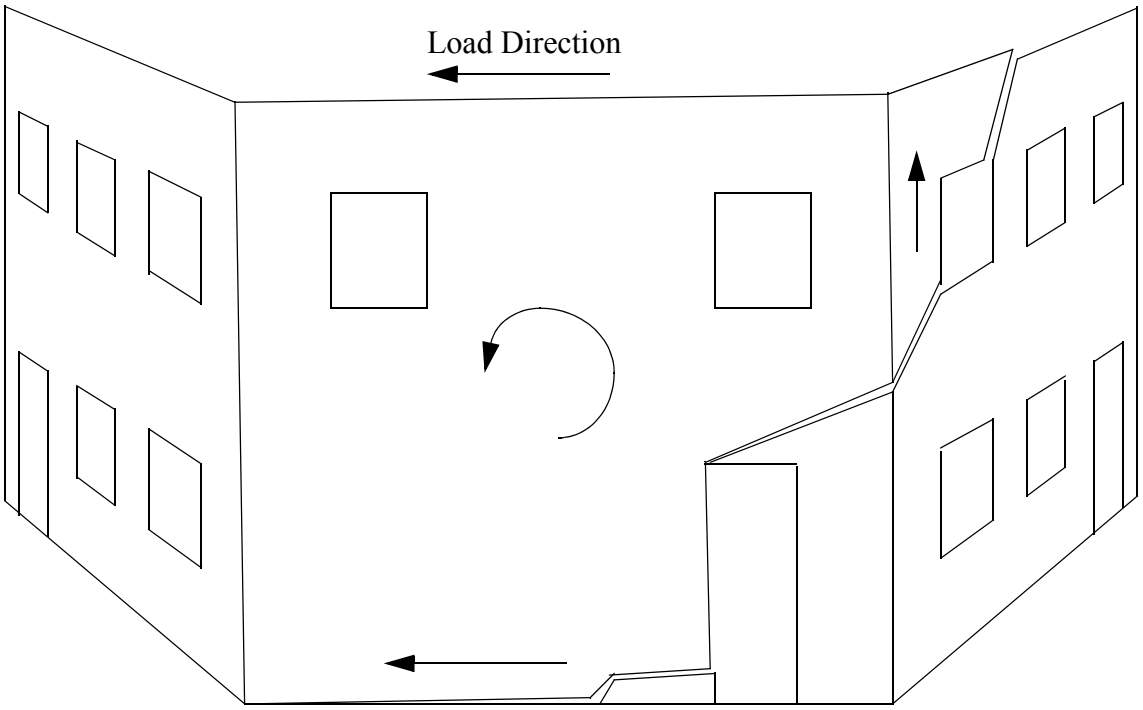

Figure 4.6. Exaggerated Schematic illustrating the response of Wall 1 and out-of-plane Walls A and B in the positive direction prior to retrofit.

In the positive loading direction, no cracks were observed in Wall 1 through Test Run 6 (i.e. roof displacement of 1.5 mm (0.06 in.)). During Test Run 7 a stair-stepped along the bottom right portion of pier P1-6 and a diagonal crack above the door opening were observed. The diagonal crack above the door opening propagated into out-of-plane Wall A and diagonally up to the roof during the initial cycle of Test Run 8 (see Figure 4.4). Following the formation of these cracks, Wall 1 along with the upper right portion of Wall A responded as a single rigid body rotating about the lower left corner of pier P1-6.

No additional cracks were observed in the positive direction during Test Run 10; however, the response changed slightly. Specifically, a moderate degree of sliding deformation was observed at the base of pier P1-6. However, due to the stair-stepped nature of the crack at the lower left corner of pier P1-6, a fully developed sliding plane did not exist during loading in the positive direction. The observed sliding deformation acted to close the crack in this region which had been opened due to sliding deformation in the negative loading direction (discussed subsequently). Once the residual crack opening at the lower left corner of pier P1-6 was closed, the response essentially reverted to the response observed during Test Run 8 (i.e. global rocking). This is consistent with the measured response shown in Figure 4.2, which indicates that during the final cycles Wall 1 displayed an increase in energy dissipation, albeit with some pinching is still visible.

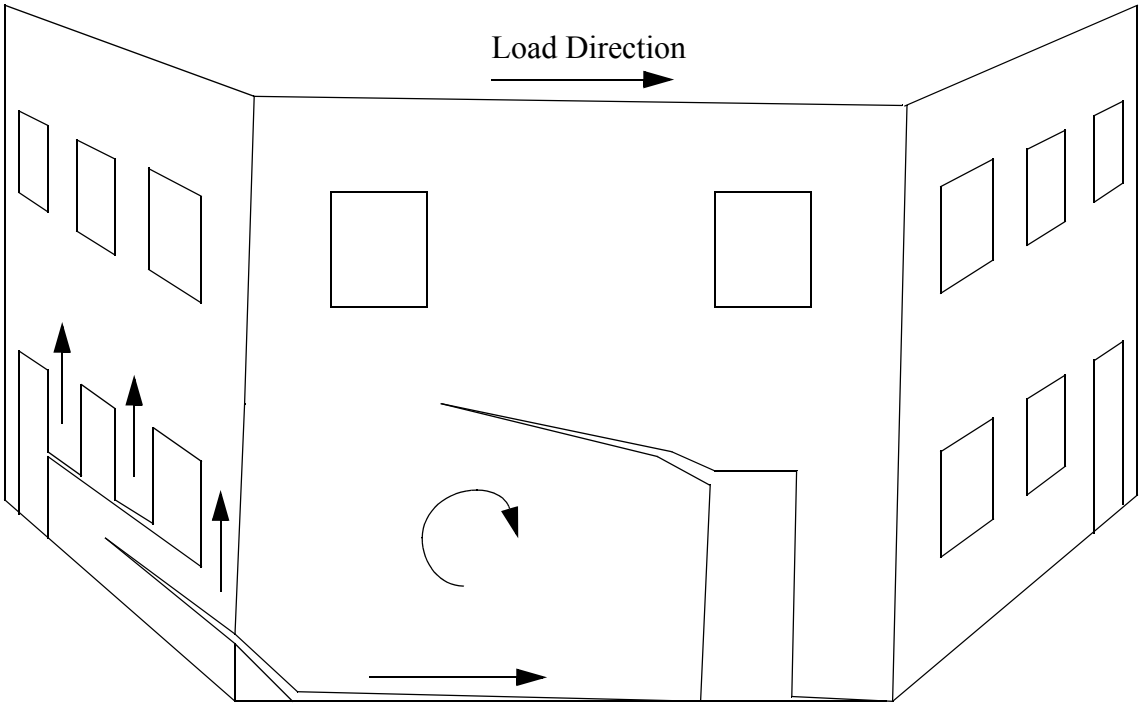

Figure 4.7. Exaggerated Schematic illustrating the behavior of Wall 1 and out-of-plane Walls A and B in the negative direction prior to retrofit.

In the negative loading direction, no cracks were observed through Test Run 5 (i.e. roof displacement of 0.75 mm (0.03 in.)). During Test Run 6 a diagonal crack formed at the lower left corner of pier P1-6 and propagated horizontally across approximately 70% of Wall B to the door opening (see Figures 4.3 and 4.5). During Test Run 7, a diagonal crack formed and propagated, extending from the corner of the door opening across the upper right portion of pier P1-6. Following the formation of these cracks it was noted that pier P1-6 and 70% of Wall B were rotating as a single rigid body about the lower right corner of pier P1-6. This caused the remaining portion of Wall 1 to rotate as a single rigid body about the lower right corner of pier P1-7. This mechanism was observed through Test Run 9.

As the roof displacement approached 5 mm (0.2 in.) during the initial cycle of Test

Run 10, a horizontal crack at the base of pier P1-6 propagated to the door opening. As a result, pier P1-6 abruptly rotated downward and began to slide. This sudden change in behavior is reflected in Figure 4.2 as a small drop in base shear force followed by a large increase in energy dissipation. In addition, this sliding deformation resulted in residual crack opening along the diagonal crack at the lower left corner of pier P1-6, which allowed some sliding deformation in the positive loading direction.

4.1.2 Response after Retrofit

4.1.2.1 Force-Displacement Behavior

Figure 4.8 shows the recorded base shear versus roof displacement response of Wall 1 after retrofit. The maximum strength of Wall 1 was 222 kN (50 kip) in the positive direction and 218 kN (49 kip) in the negative direction. The corresponding roof displacements were approximately 6 mm (0.24 in.) in both directions. As apparent from Figure 4.8, the peak resistance recorded after Test Run 16 (i.e. roof displacement greater than 6 mm (0.25 in.)) decreased with increasing roof displacement. At a roof displacement of 19 mm (0.75 in.) the measured resistances dropped approximately 28% in the positive direction and 20% in the negative direction compared to the maximum strength recorded. Also apparent from Figure 4.8, the hysteresis recorded during Test Runs 11 through 14 displayed some pinching; however, as the base shear resistance began to decrease Wall 1 displayed significant energy dissipation.

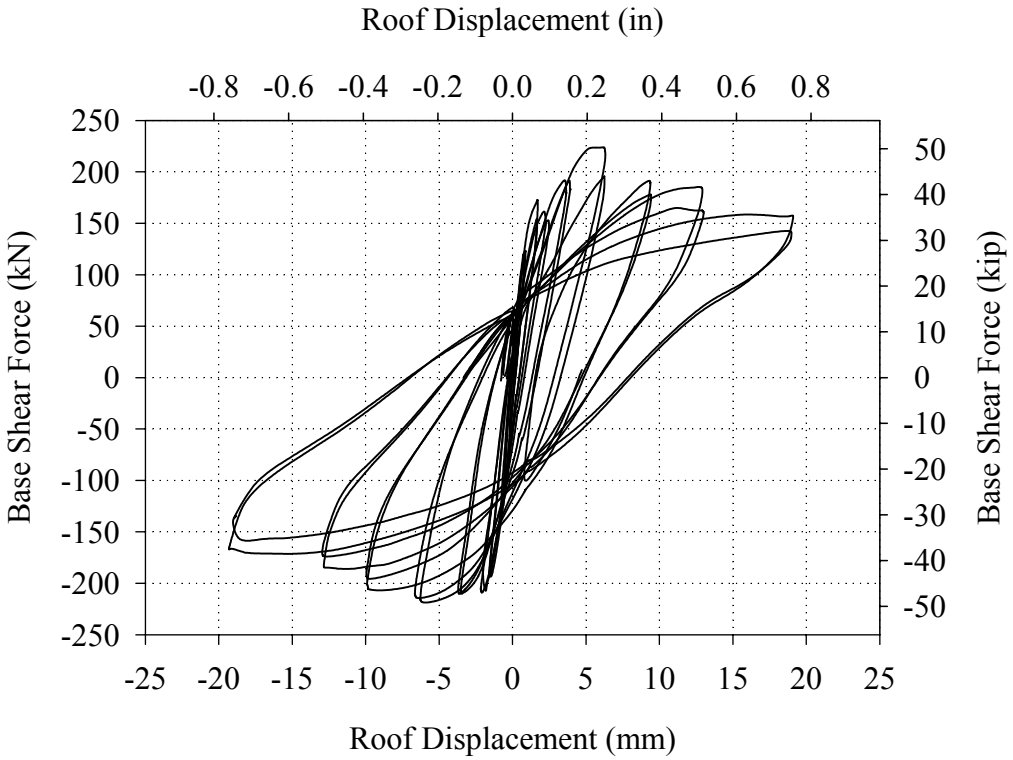

Figure 4.8. Base shear force versus roof displacement response of Wall 1 following retrofit.

4.1.2.2 Damage Progression and Wall Behavior

The crack pattern of Wall 1 and out-of-plane Walls A and B following these cycles are shown in Figures 4.9 through 4.11. Note that the cracks that formed prior to retrofit are shown in gray and the cracks observed following retrofit are shown in black. Figure 4.12 and 4.16 show schematics illustrating the behavior of Wall 1 and out-of-plane Walls A and B after retrofit in the positive and negative directions, respectively.

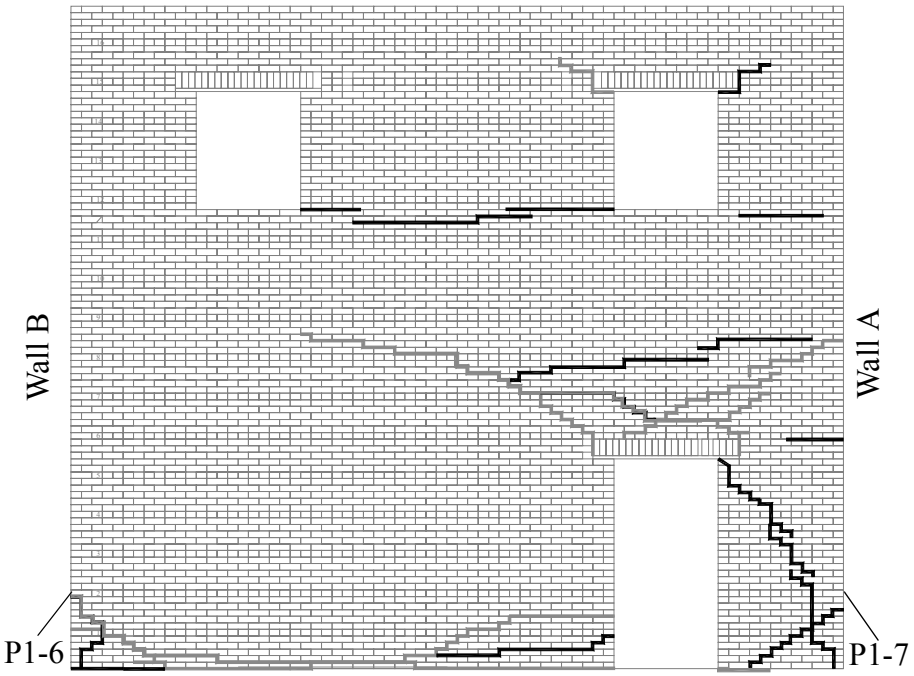

Figure 4.9. Crack pattern in Wall 1 following Test Run 19.

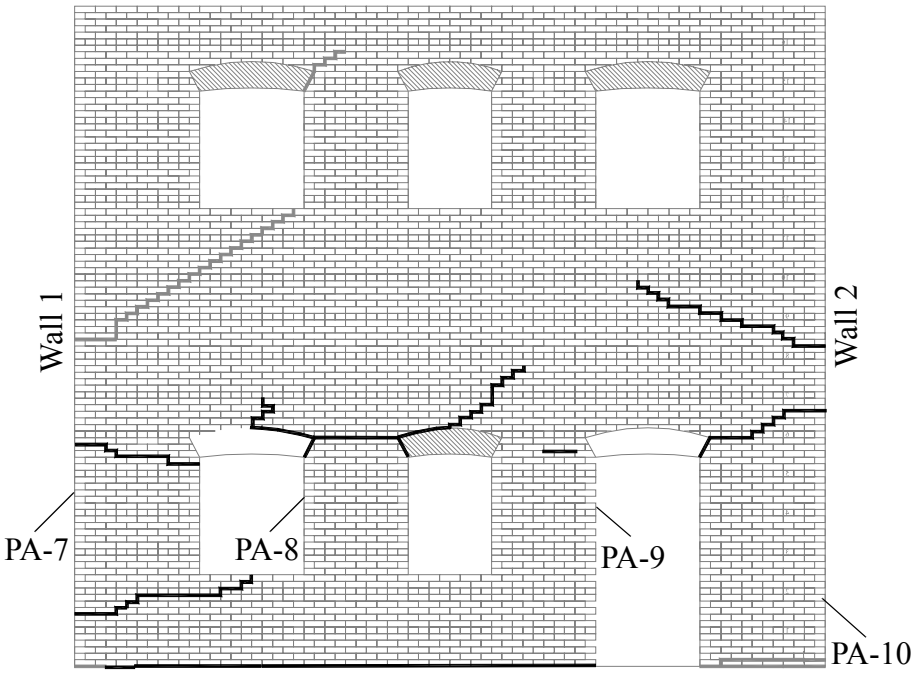

Figure 4.10. Crack pattern in Wall A following Test Run 19.

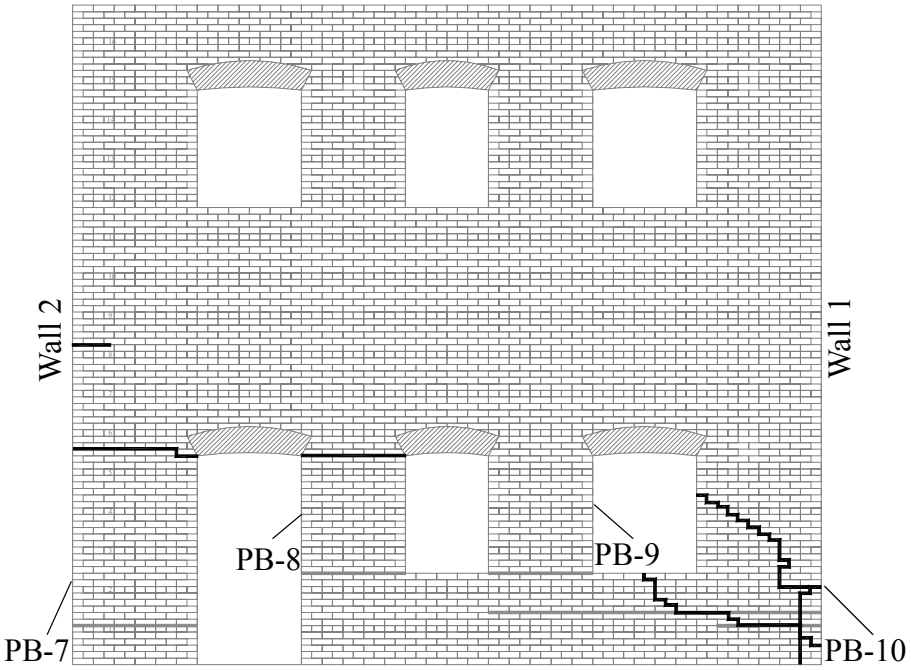

Figure 4.11. Crack pattern in Wall B following Test Run 19.

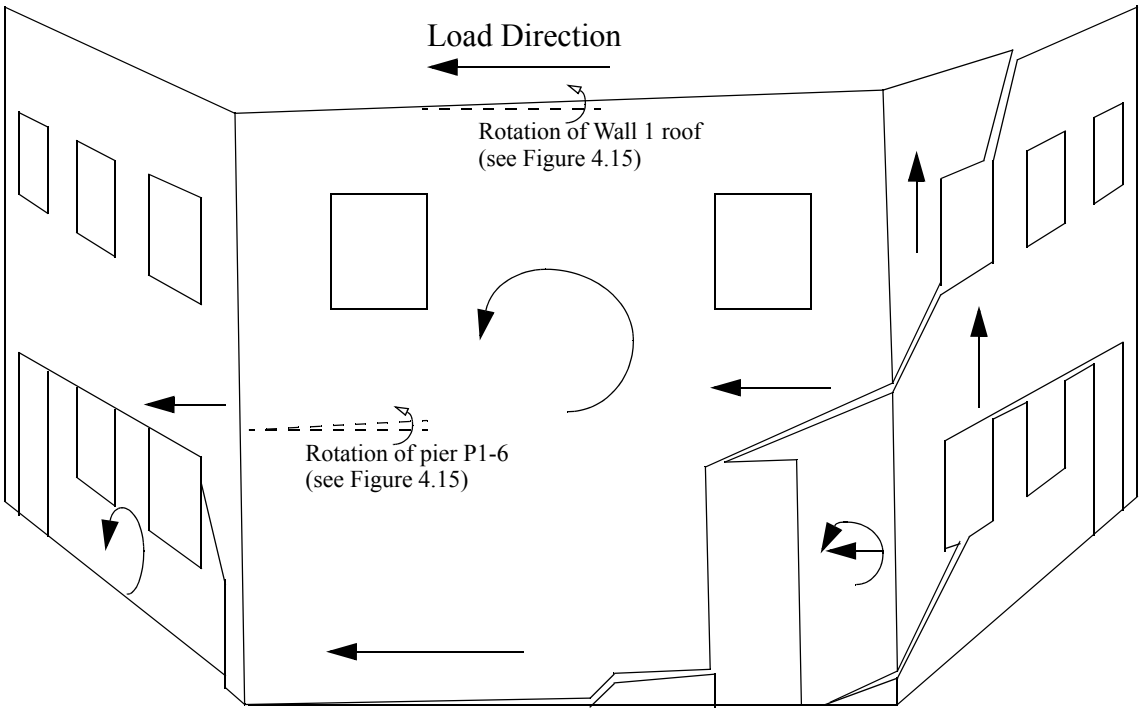

Figure 4.12. Exaggerated schematic illustrating the behavior of Wall 1 and out-of-plane Walls A and B in the positive direction following retrofit.

In the positive loading direction, the response of Wall 1 was consistent with the behavior observed prior to retrofit during Test Runs 11 through 14 (roof displacement of 2.5 mm (0.1 in.)). That is, the response consisted primarily of global rocking with a small degree of sliding. No additional cracks were observed during this level of loading.

During Test Run 15, the existing crack at the base of pier P1-6 propagated to Wall B thus providing a fully developed sliding plane. Following this damage the primary mode of pier P1-6 began to switch from rocking to bed-joint sliding. During subsequent cycles, the sliding deformation of pier P1-6 increased proportionally with roof displacement to approximately 12.5 mm (0.5 in.) during Test Run 19 in both the positive and negative directions. In addition, following Test Run 15 pier P1-7 displayed a combined rocking/ sliding mode and participated to a greater degree in the response of Wall 1. This increased component-type response was likely caused by the decreased global rocking deformation and subsequent increase in interstory shear deformation.

During Test Run 17 the sliding deformation of pier P1-6 caused the lower eight courses of Wall 1 to punch through Wall B (see Figure 4.12). A photograph of this damage following Test Run 19 is shown in Figure 4.13. During Test Run 18 a crack along the base of pier P1-7 formed and propagated into out-of-plane Wall A. During Test Run 19, an additional crack formed diagonally in pier PB-10 and propagated horizontally along the top of the first story piers in Wall B.

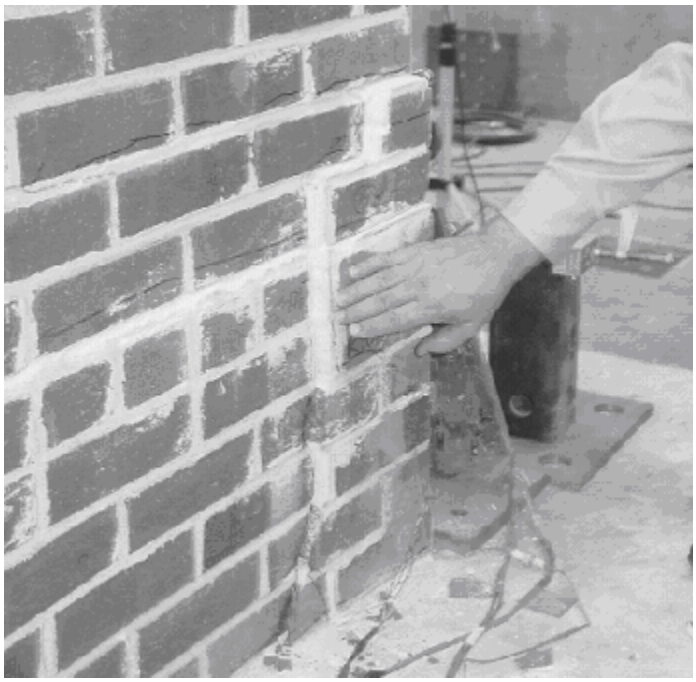

Figure 4.13. Pier P1-6 punching through Wall B.

The final mechanism of Wall 1 in the positive direction consisted of a small degree of global rocking coupled with sliding along the base of pier P1-6 and local rocking/ sliding of pier P1-7. As illustrated by Figure 4.12 the additional cracks that formed in Wall B allowed the upper portion of Wall B to translated with pier P1-6, while the lower portion of Wall B rocked out-of-plane. In addition, the vertical displacement associated with the observed rocking deformation of pier P1-7 lifted a portion of Wall A (see Figure 4.12).

Figure 4.14 shows a photograph taken of pier P1-6 along the inside of the door opening during Test Run 19. This figure illustrates that the observed sliding deformation reduced the mortar in the adjacent bed-joint to a white powder. This powder was observed along the entire base of pier P1-6. One possible explanation for the decrease in base shear capacity during these cycles is that this damage to the bed-joint along the sliding plane

decreased the coefficient of friction at the base of the wall.

In addition, this figure illustrates that the wythes in pier P1-6 separated during loading. Note that this separation occurred below the first header course (sixth course). This separation was likely caused by the GFRP reinforcement only being applied to the inside wythe and highlights the need for such reinforcement to be developed into multiple wythes. Above the sixth course no separation was observed, and thus it is concluded that the header courses provided sufficient shear transfer between wythes.

Figure 4.14. Photograph showing the sliding deformation of pier P1-6 along the inside of the door opening.

The observed evolution from global rocking deformation to bed-joint sliding was captured by several gages. Consider Figure 4.15 which shows a plot of the maximum rotation of pier P1-6 and the roof of Wall 1 for each test run versus roof displacement. From this figure it is apparent that the measured rotations of these two sections were

identical during all test runs. This implies that pier P1-6 and the second story of Wall 1 deformed as a single rigid body. In addition, the decrease in measured rotation observed for roof displacements larger than 6.35 mm (0.25 in.) corresponds roughly to the increased sliding deformation of Wall 1. Furthermore, this decrease in rotation also corresponds to a decrease in base shear capacity which further supports the contention that the increased sliding deformation resulted in the observed decrease in base shear capacity.

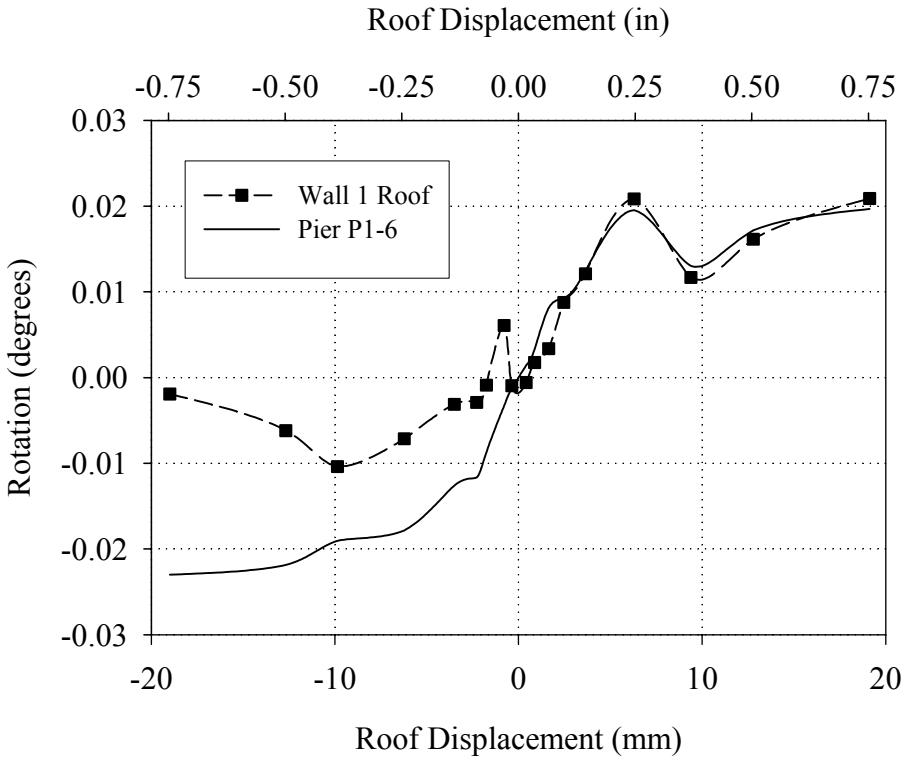

Figure 4.15. Maximum rotation of pier P1-6 and the roof of Wall 1 for each test run versus roof displacement.

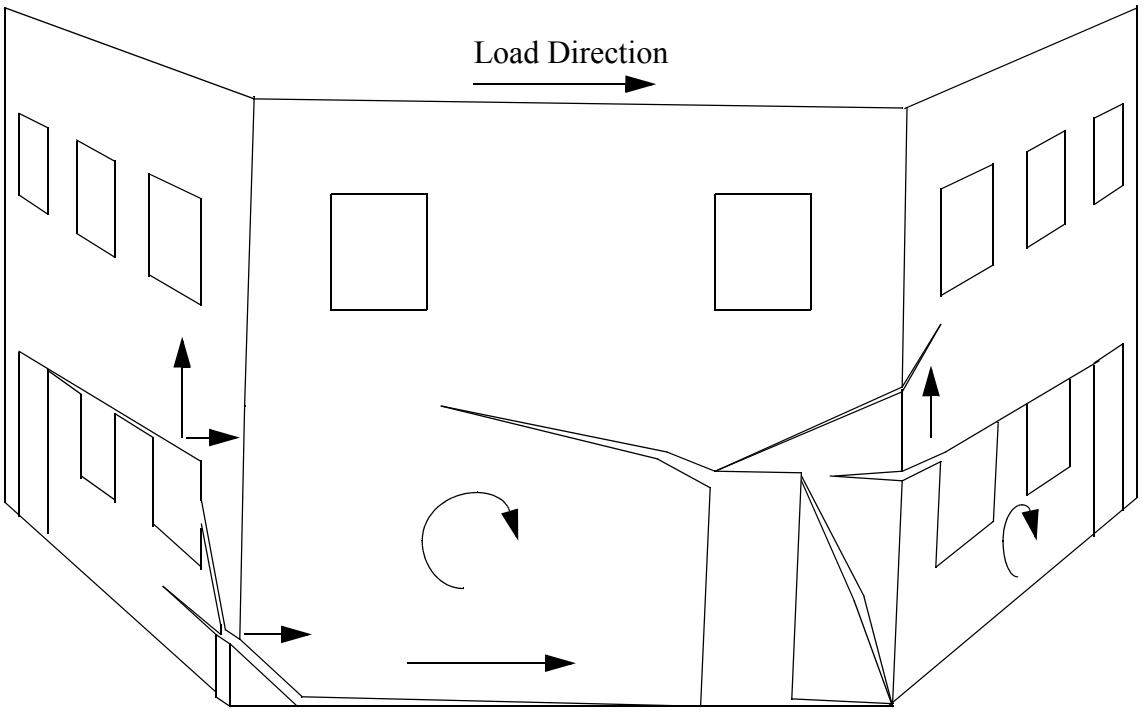

Figure 4.16. Exaggerated schematic illustrating the behavior of Wall 1 and out-of-plane Walls A and B in the negative direction following retrofit.

In the negative loading direction, the response of Wall 1 during Test Runs 11 through 14 (2.5 mm (0.1 in.) roof displacement) was very similar to the initial response observed prior to retrofit. That is, the deformation was mainly caused by the separate rocking of pier P1-6 and the remainder of Wall 1 (see Figure 4.7). Similar to the behavior in the positive direction, the propagation of the horizontal crack at the bottom of pier P1-6 during Test Run 15 caused the response of pier P1-6 to switch from rocking to sliding (see Figure 4.14). Recall that similar behavior was observed during Test Run 10; however, following the application of the external reinforcement the existing sliding plane was blocked. That is, horizontal strips H4 and H5 tied the base of pier P1-6 to uncracked portions of the wall. During Test Runs 16 and 17 the wall response remained unchanged

and no additional cracks were observed in the negative direction.

During the initial cycle of Test Run 18, a horizontal crack formed along the top of pier P1-7 and propagated into Wall A (see Figures 4.9 and 4.10). Following the formation of this crack pier P1-7 was visibly rocking. As the wall was displaced further during the initial cycle of Test Run 18 the development of a diagonal crack was observed in the center of the pier. This crack did not propagate substantially during the redundant cycle of Test Run 18; however, it fully developed during the initial cycle of Test Run 19. In addition, during Test Run 19 a horizontal crack formed in Wall B along the top of the first story piers (see Figure 4.11).

The final mechanism of Wall 1 in the negative loading direction consisted primarily of local pier response (see Figure 4.16). The primary mode of deformation of pier P1-6 was sliding. However, some low-level rocking deformation was also observed, which lifted up a large portion of Wall B above the window openings. In addition, pier P1-7 displayed a combined rocking/diagonal tension mode during the final test run. The vertical displacement associated with the rocking deformation of pier P1-7 lifted up a portion of Wall A above the window openings.

Figure 4.17 shows a photograph of the diagonal crack that formed in pier P1-7 taken after Test Run 19. Based on the observed evolution from rocking deformation to diagonal cracking it is likely that the vertical stress in pier P1-7 increased during these cycles. This increase was likely caused by two reasons: (1) in the negative loading direction overturning moment placed this pier into compression and (2) the observed local rocking of pier P1-7 caused a vertical displacement which lifted up a portion of Wall A thus increasing the vertical stress in the pier.

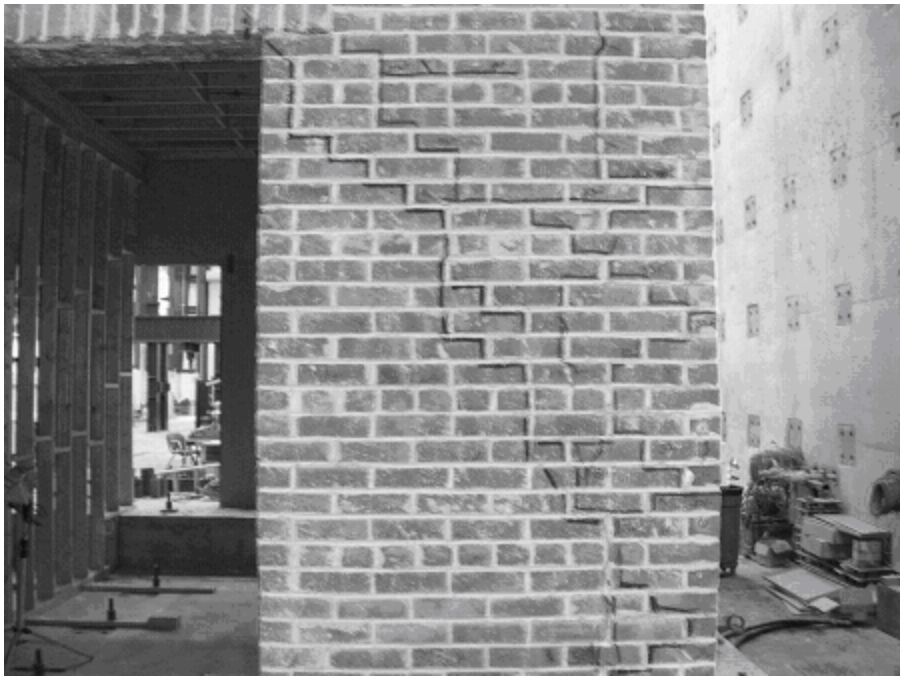

Figure 4.17. Photograph showing the diagonal crack in pier P1-7 following Test Run 19.

Although the behavior of pier P1-6 was fairly symmetric following Test Run 15 (i.e. mostly sliding) a different sliding crack was activated in each direction at the lower left corner of pier P1-6 (see Figures 4.12 and 4.16). This resulted in a progressive crack opening in this region. Figure 4.18 shows a photograph of this crack following Test Run 19. The residual crack opening following Test Run 19 was approximately 38 mm (1.5 in.), which underscores the progressive nature of this phenomenon since the maximum imposed roof displacement was 19 mm (0.75in.).

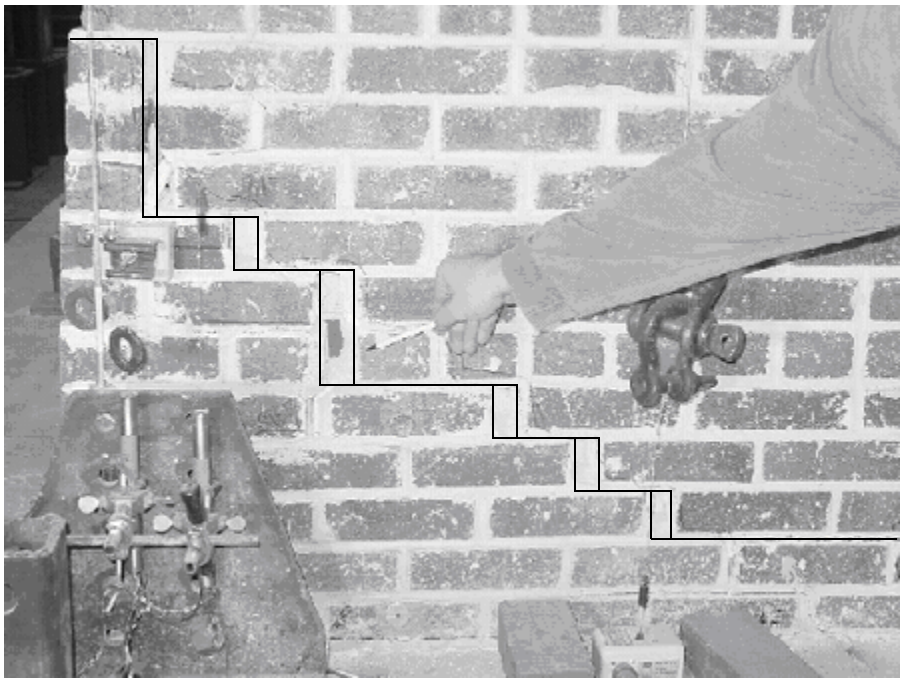

Figure 4.18. Photograph showing the offset at the corner of Wall 1 and Wall B due to the sliding deformation of pier P1-6 in the negative direction

4.1.2.3 Response of External Reinforcement

During the testing of Wall 1 following the application of GFRP, no damage to the external reinforcement and no debonding from the masonry substrate was observed. The lack of damage observed in the GFRP overlays was likely caused by the formation of the sliding plane that allowed the majority of the deformation to occur at the base of the wall thus limiting the strain in the GFRP overlays. Recall that the formation and activation of this sliding plane was the primary objective of this retrofit.

The formation of the sliding crack at the base of pier P1-6 during Test Run 15 indicated that the horizontal strips applied to the base of pier P1-6 performed as intended. Recall that these strips were employed to tie the base of pier P1-6 together and force a smooth sliding plane in each direction. Figure 4.19 shows a plot of the maximum strain

measured in these strips during each test run versus roof displacement. Note that these gages were placed directly adjacent to existing cracks in the masonry (see Figure 4.20). This plot shows that the measured strain in these strips decreased beyond Test Run 16 (i.e. 6.35 mm (0.25 in.) roof displacement) in the positive direction. Recall that a fully developed sliding plane was observed just prior to this displacement level. This suggests that the observed sliding crack allowed translation of the entire base of pier P1-6 and thus diminished the amount of strain in these strips.

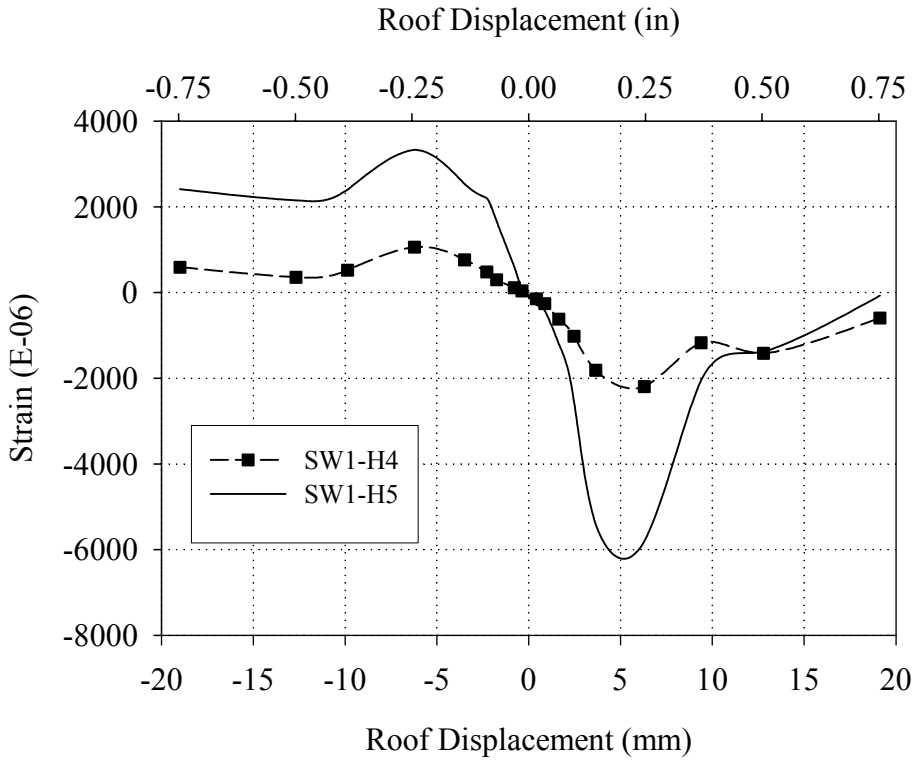

Figure 4.19. Maximum strain recorded in GFRP strips H4 and H5 during each test run versus roof displacement (see Figure 4.20 for gage locations).

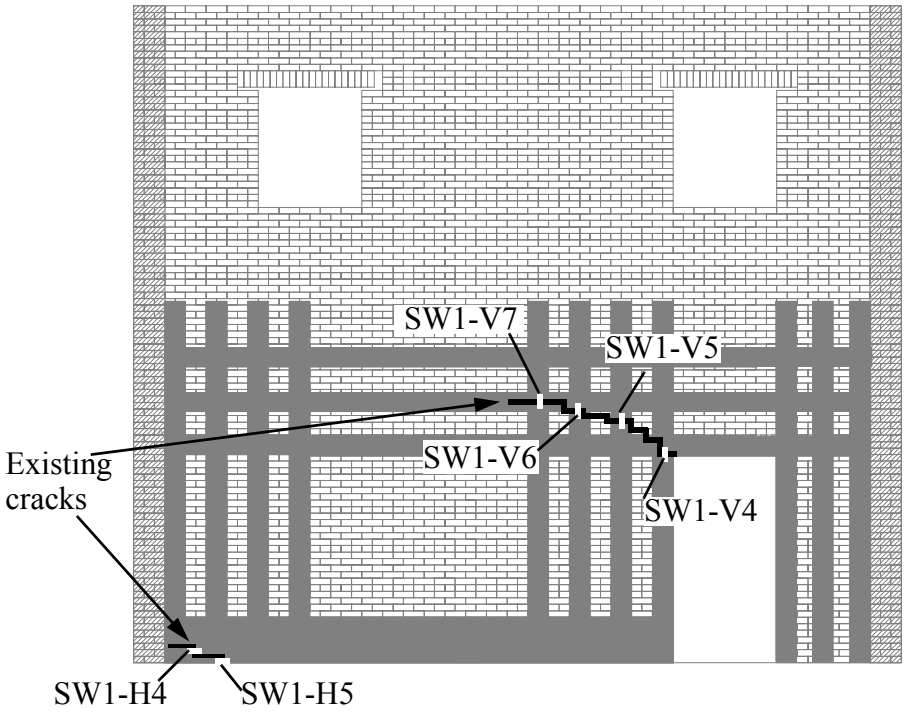

Figure 4.20. Locations of strain gages placed on the external reinforcement applied to Wall 1.

In addition, to the strips at the base of pier P1-6, the vertical strips along the inside of pier P1-6 were also engaged during loading. Figure 4.21 shows a plot of the maximum strain recorded in strips V4 through V7 during each test run versus base shear. This plot clearly shows that the rocking deformation of pier P1-6 in the negative direction was resisted by these strips throughout all cycles. Notice that in the positive loading direction negligible strain was measured due to the adjacent crack closing and allowing compression to be transferred through the masonry.

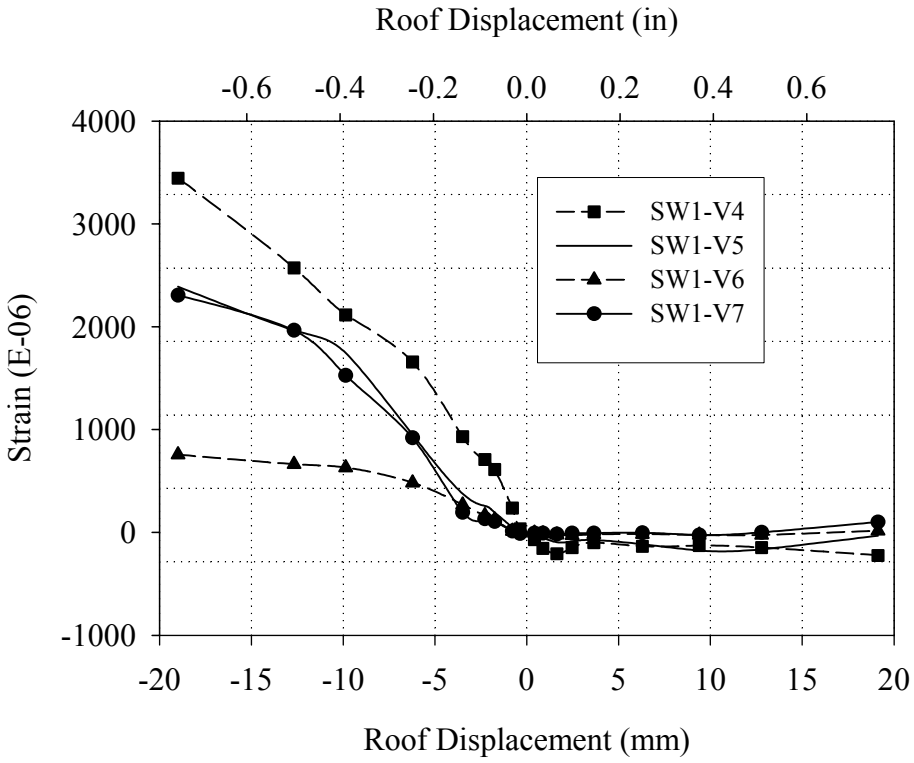

Figure 4.21. Maximum strain recorded in GFRP strips V4 through V7 during each test run versus roof displacement (see Figure 4.20 for gage locations).

4.1.3 Comparison between the Response of Wall 1 before and after Retrofit

Figure 4.22 shows the base shear versus roof displacement response for Wall 1 before and after retrofit up to 6.35 mm (0.25 in.) roof displacement. Figure 4.23 shows the complete base shear versus roof displacement response for Wall 1. Table 4.3 summarizes the peak resistance and displacement at peak resistance for Wall 1 both prior to and after retrofit. These figures and table show that the strength of Wall 1 diminished following retrofit. However, based on Figure 4.22 it is evident that the force-displacement response recorded after retrofit was nearly identical to the force-displacement response of the last cycle conducted prior to retrofit. In particular, the base shear resistances at 6.35 mm (0.25 in.) roof displacement before and after retrofit were essentially equal.

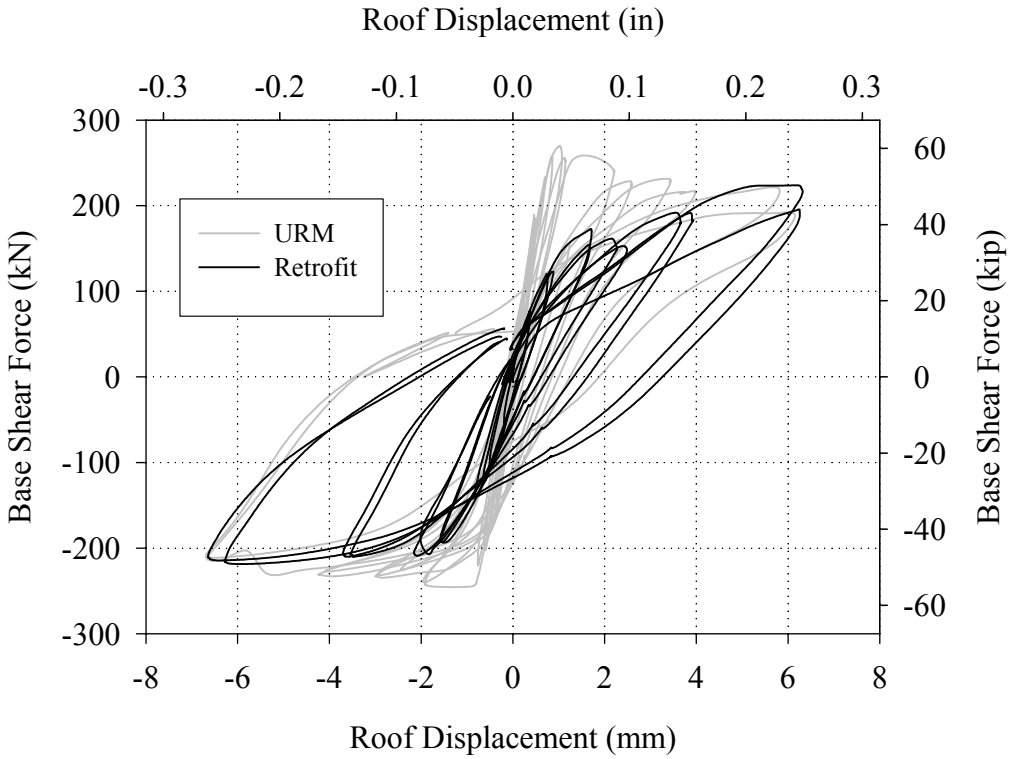

Figure 4.22. Base shear versus roof displacement response of Wall 1 before and after retrofit up to 6.35 mm (0.25 in.) roof displacement

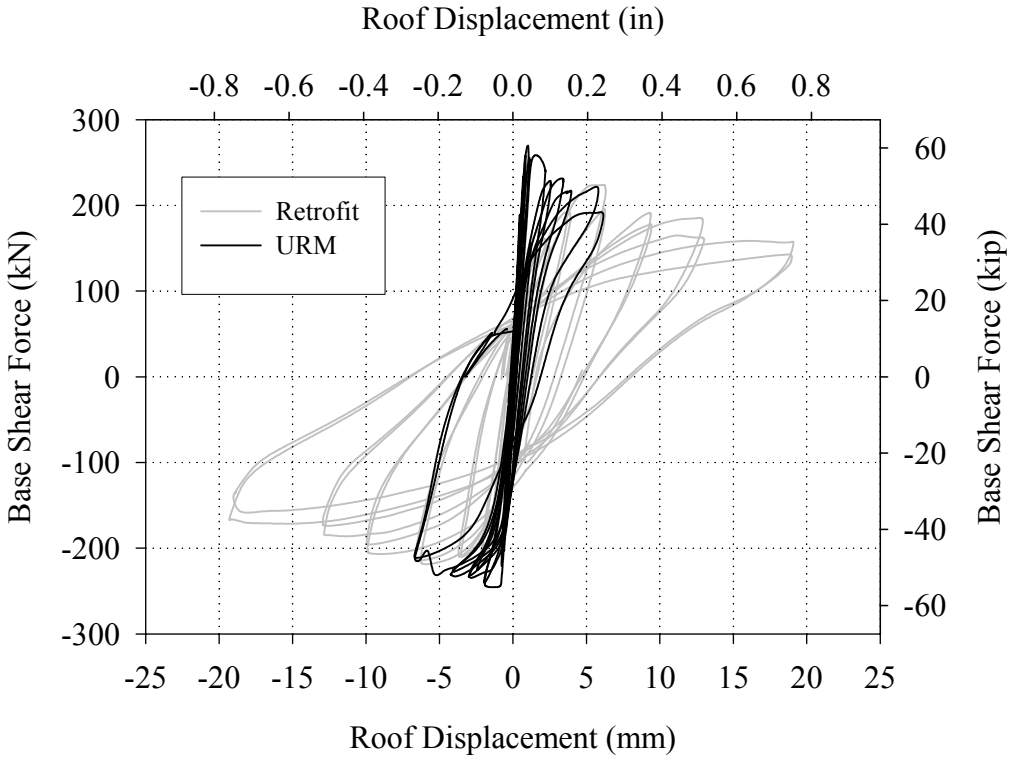

Figure 4.23. Complete base shear versus roof displacement response of Wall 1 before and after retrofit.

Table 4.3. Comparison of base shear capacity of Wall 1 before and after retrofit.

	URM		Post-Retrofit	
	Positive Direction	Negative Direction	Positive Direction	Negative Direction
Base Shear Capacity	267 kN (60 kip)	245 kN (55 kip)	222 kN (50 kip)	218 kN (49 kip)
Roof Displacement at Peak Resistance	1 mm (0.04 in.)	1 mm (0.04 in.)	6 mm (0.25 in.)	6 mm (0.25 in.)

As mentioned previously the decrease in base shear resistance is primarily attributed to the grinding of the mortar joint along the active sliding plane shown in Figure 4.14. Another factor that likely contributed to the strength decrease was the

additional damage observed in the out-of-plane walls after retrofit. This damage likely reduced the participation of the out-of-plane walls and thus reduced the base shear capacity of Wall 1.

To gain further insight into the behavior of Wall 1 before and after retrofit, the force-displacement responses for both the first and second stories were numerically integrated to obtained the energy dissipated during each test run. Figure 4.24 shows the energy dissipated by both stories of Wall 1 before and after retrofit. For comparison purposes the energy dissipated by the first story of Wall 1 was divided by the maximum possible energy dissipation, which was defined as the area of a rectangle that encompasses the force displacement response. The specifics of the procedure used to obtain this plot is given in Appendix B. Figure 4.25 shows the percentage of energy dissipated by the first story of Wall 1 before and after retrofit (note the due to the small amount of energy dissipated by the second story of Wall 1 (see Figure 4.24) only the first story was included in this plot).

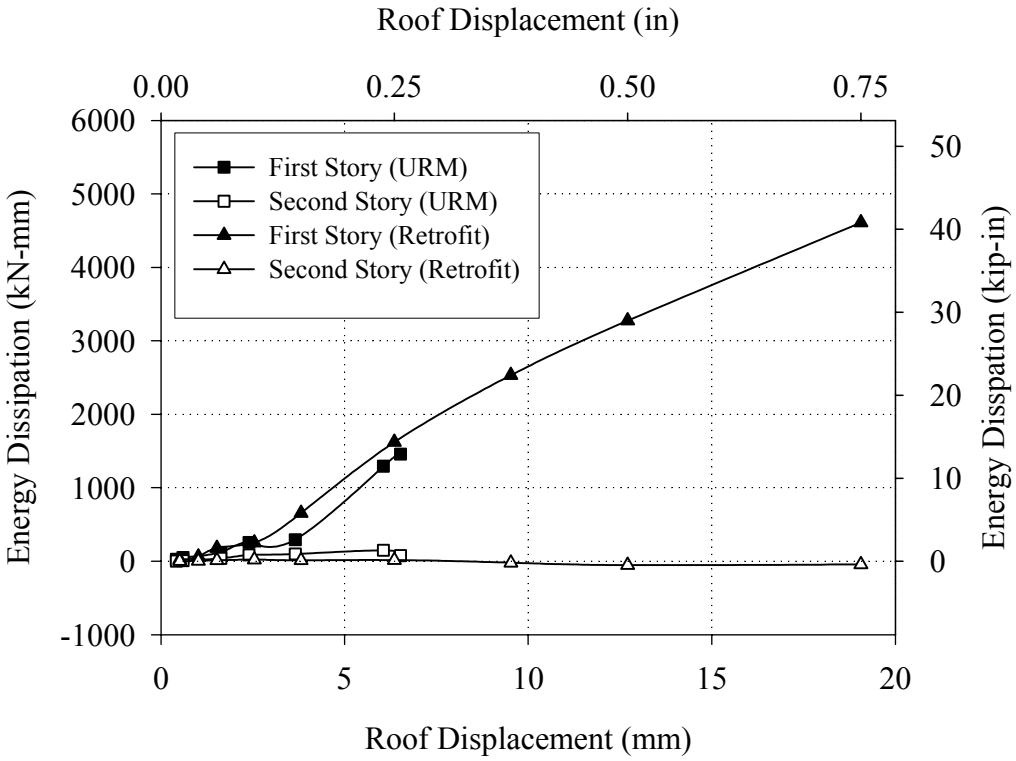

Figure 4.24. Energy dissipated by each story of Wall 1 before and after retrofit.

From Figure 4.24 it is clear that the majority of the energy was dissipated by the first story. In addition, the energy dissipated following retrofit was slightly larger than before retrofit. This was likely caused by the formation of a sliding plane in the negative direction during Test Run 10, which allowed more sliding deformation to occur during the initial cycles conducted after retrofit. Figure 4.25 shows that the abrupt change from primarily rocking deformation to sliding deformation prior to retrofit resulted in an increase in the percentage of energy dissipated. After retrofit the wall underwent a similar evolution; however, based on this figure the change was more gradual in nature. While the horizontal strips at the base of pier P1-6 aided in the formation of a smooth sliding crack in both directions, the earlier onset of sliding was likely due the damage induced into Wall 1 prior to retrofit.

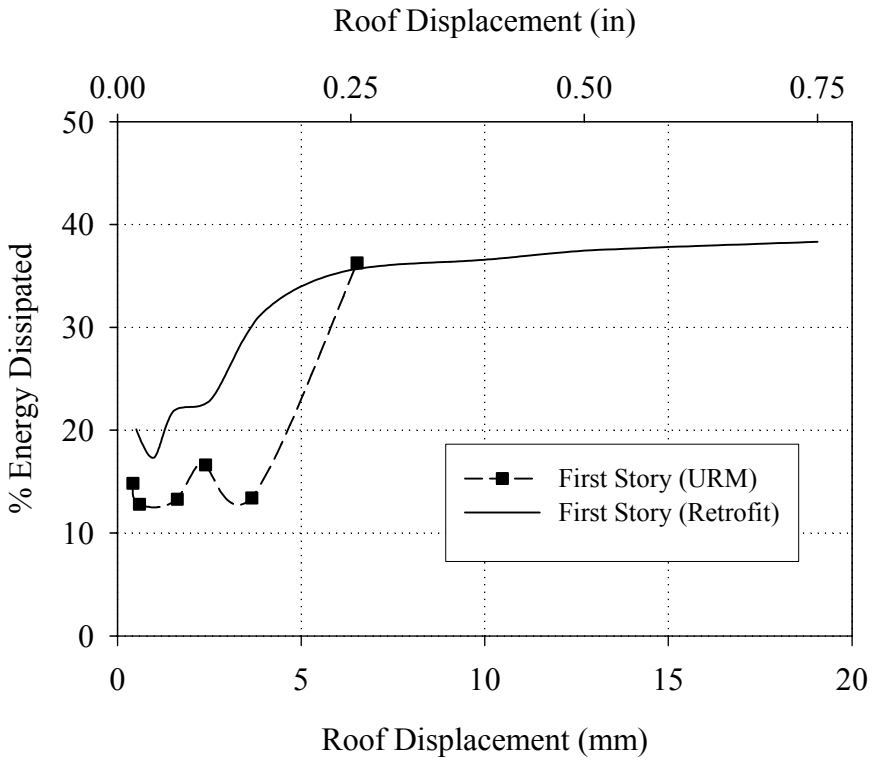

Figure 4.25. Percentage of energy dissipated by the first story of Wall 1 before and after retrofit.

4.2 Response of Wall 2

A summary of the in-plane displacements imposed on Wall 2 is given in Table 4.4 along with test run and cycle designation. Figure 4.1 shows a graphical representation of the loading history imposed before and after retrofit. Prior to retrofitting, Wall 2 was subjected to increasing cyclic displacements up to 6.35 mm (0.25 in.) in each loading direction. Based on the observed failure modes, the resulting maximum drifts exceeded the Immediate Occupancy performance level (ATC, 2000). Following the application of the external reinforcement the wall was subjected to increasing cyclic displacements up to 19 mm (0.75 in.). No performance levels are currently available for masonry walls retrofit with fiber reinforcement cement; however, if the performance levels provided for URM

are employed the imposed displacements fall half-way between the Life Safety and Collapse Prevention performance levels (ATC, 2000).

Table 4.4 Summary of displacements imposed on Wall 2

	Test Run	Target Roof Displacement mm (in)	Target Second Floor Displacement
URM	3	+/- 0.4 (0.015)	+/- 0.32 (0.012)
	4	+/- 0.5 (0.02)	+/- 0.4 (0.016)
	5	+/- 1 (0.4)	+/- 0.8 (0.032)
	6	+/- 1.5 (0.6)	+/- 1.2 (0.048)
	7	+/- 2.5 (0.1)	+/- 2.0 (0.08)
	8	0	0
	9	+/- 3.8 (0.15)	+/- 3.0 (0.12)
	10	+/- 6.4 (0.25)	+/- 5.1 (0.20)
Post-Retrofit	11	+/- 0.5 (0.02)	+/- 0.3 (0.012)
	12	+/- 1 (0.4)	+/- 0.8 (0.032)
	13	+/- 1.5 (0.6)	+/- 1.2 (0.048)
	14	+/- 2.5 (0.1)	+/- 2.0 (0.08)
	15	+/- 3.8 (0.15)	+/- 3.1 (0.12)
	16	+/- 6.4 (0.25)	+/- 5.1 (0.2)
	17	+/- 9.5 (0.375)	+/- 7.9 (0.311)
	18	+/- 12.7 (0.5)	+/- 10.4 (0.41)
	19	+/- 19.1 (0.75)	16 (0.63), -15.8 (-0.623)

4.2.1 Response Prior to Retrofit

4.2.1.1 Force-Displacement Behavior

Table 4.5 shows the measured elastic stiffness of each story of Wall 2 in each direction. Each stiffness corresponds to a roof drift of 0.25 mm (0.01 in.) and each was

determined by dividing the shear force in each story by the relative displacement of each story.

Table 4.5. Elastic stiffness of Wall 2.

	Positive Direction	Negative Direction
First Story	200 kN/mm (1140 kip/in)	154 kN/mm (880 kip/in)
Second Story	286 kN/mm (1630 kip/in)	240 kN/mm (1370 kip/in)

Figure 4.26 shows the recorded base shear versus roof displacement response of Wall 2 prior to retrofit. The maximum strength of Wall 2 was 128 kN (28.8 kip) in the positive direction and 111 kN (25.0 kip) in negative direction. The corresponding roof displacements were approximately 6.2 mm (0.24 in.) in each direction. As apparent from Figure 4.26, the hysteresis of Wall 2 displayed significant pinching throughout all cycles. In addition, little degradation was observed during the redundant cycles of the each test run, and the resistance of the wall increased with increasing roof displacement.

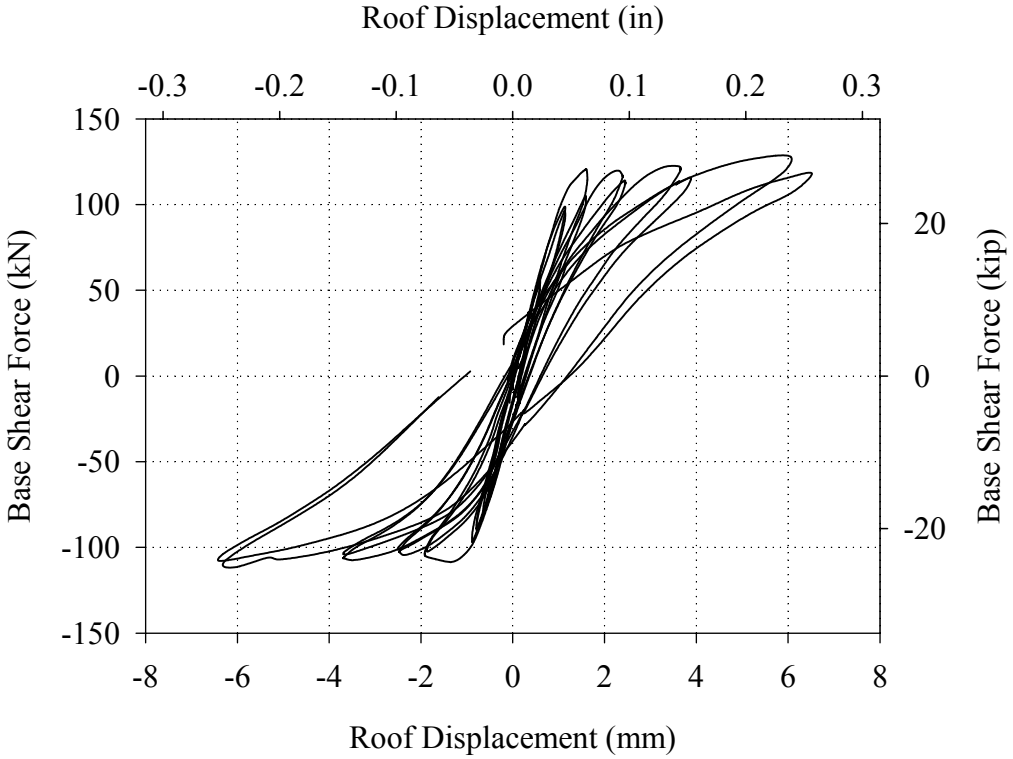

Figure 4.26. Base shear force versus roof displacement response of Wall 2 prior to retrofit.

4.2.1.2 Damage Progression and Wall Behavior

The crack pattern of Wall 2 and out-of-plane Walls A and B following Test Run 10 are shown Figures 4.27 through 4.29. A schematic illustrating the behavior of Wall 2 and out-of-plane Walls A and B in the positive direction prior to retrofit is shown in Figure 4.30. As indicated by the fairly symmetric crack pattern shown in Figure 4.27, the response of Wall 2 was essentially identical in both directions and thus the schematic shown in Figure 4.30 also applies for the negative loading direction.

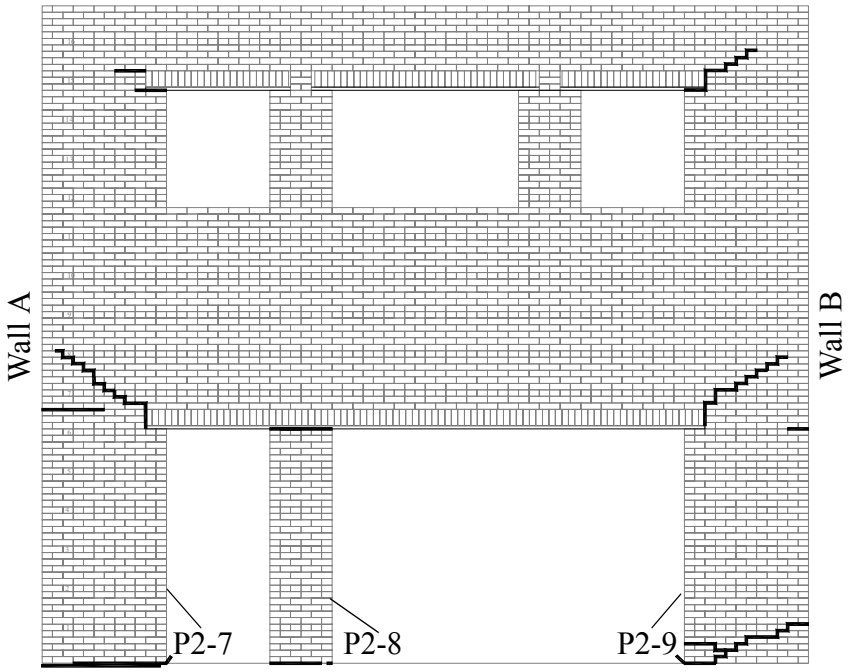

Figure 4.27. Crack pattern of Wall 2 following Test Run 10.

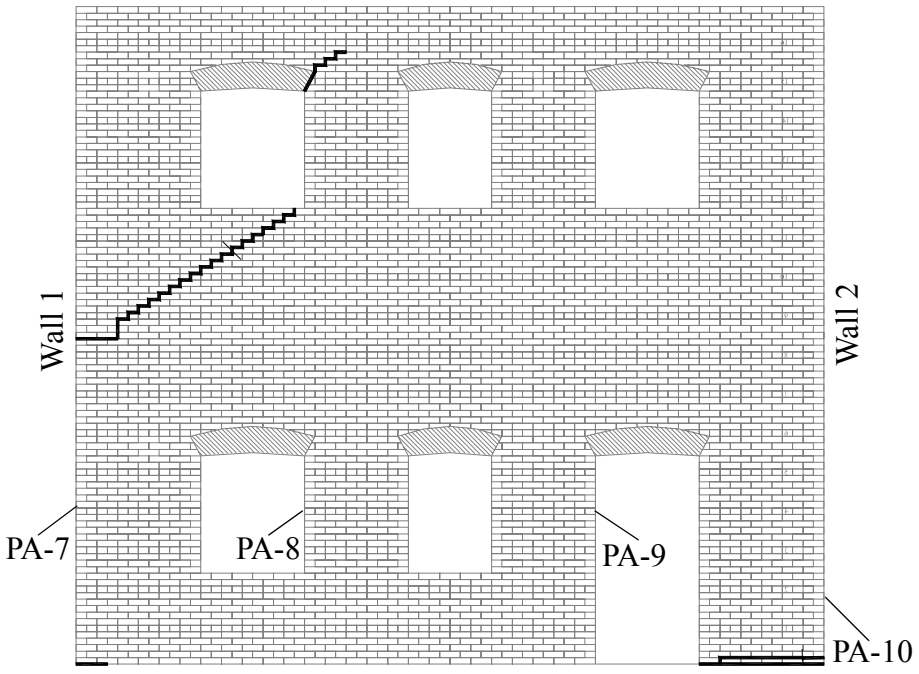

Figure 4.28. Crack pattern of Wall A following Test Run 10.

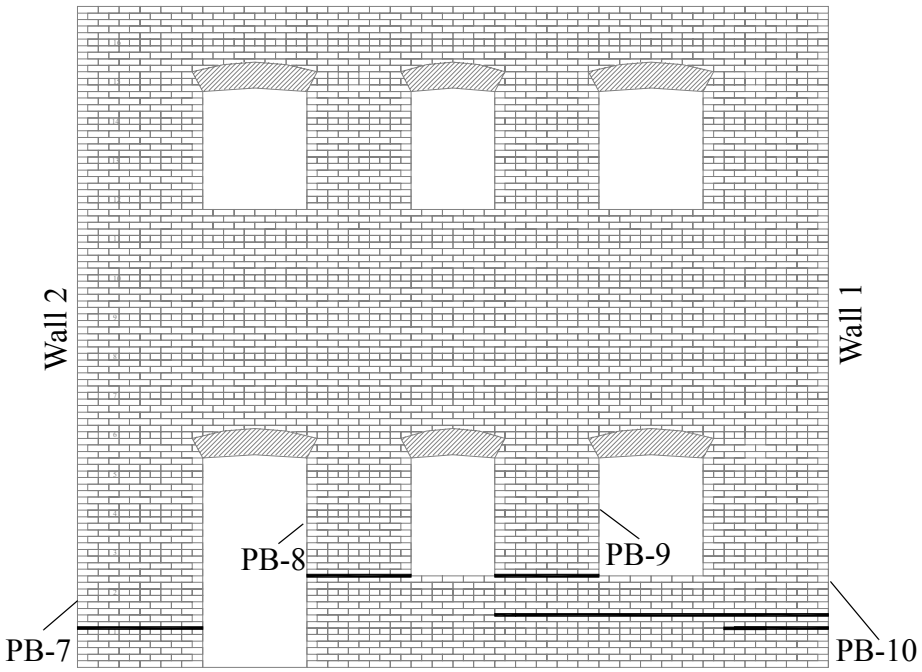

Figure 4.29. Crack pattern of Wall B following Test Run 10.

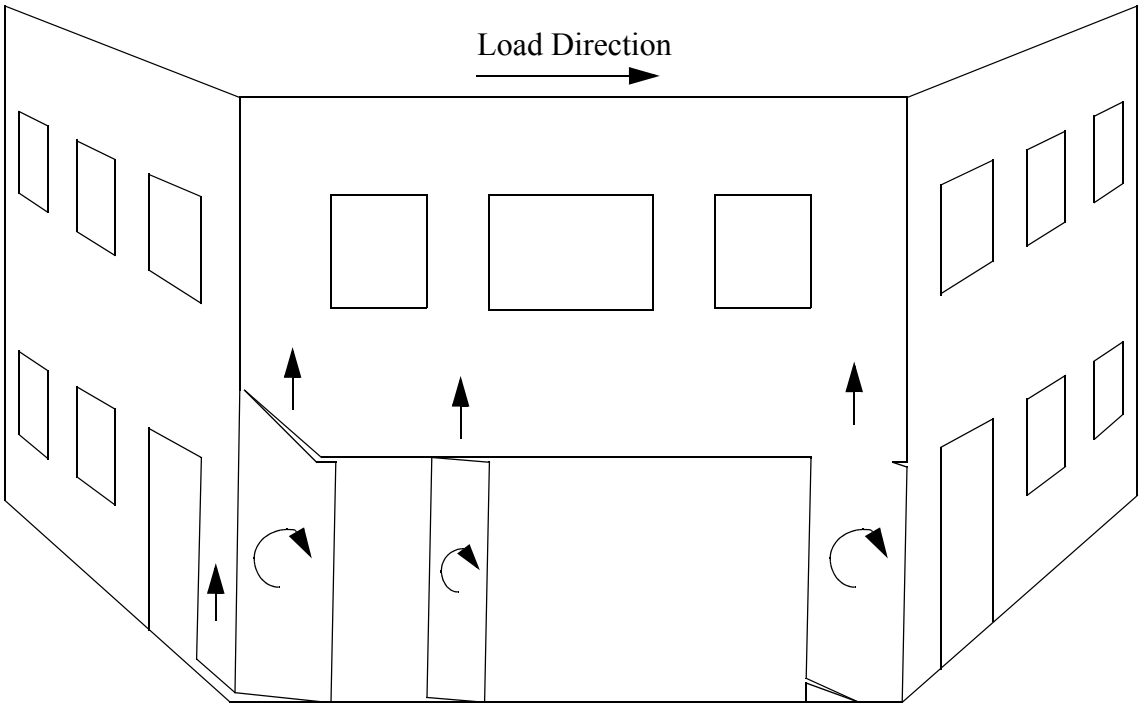

Figure 4.30. Exaggerated schematic illustrating the response of Wall 2 and out-of-plane Walls A and B in the positive direction prior to retrofit.

In both loading directions, no cracks were observed through Test Run 5. During Test Run 6, horizontal cracks formed at the base of the first floor piers and propagated into the out-of-plane walls along the base of piers PA-10 and PB-7 (see Figures 4.28 and 4.29). During Test Run 7, diagonal cracks initiated at the corner of the door openings at the top of pier P2-7 in the positive direction and at the top of pier P2-9 in the negative direction. These cracks propagated to the length shown in Figure 4.27 during Test Runs 8 and 10. In addition, during Test Run 10 a horizontal crack at the top of pier P2-7 formed in the negative loading direction.

The final mechanism of Wall 2 prior to retrofit consisted primarily of the local rocking deformation of the first story piers. In the positive direction, the rocking of pier P2-7 lifted up the adjacent portion of Wall A. Similar behavior was observed in the negative loading direction for pier P2-9. Figure 4.30 shows that piers P2-7 and P2-9 displayed different effective heights in the positive loading direction. That is, the active rocking crack at the top of pier P2-7 extended diagonally upwards from the adjacent door opening whereas the active rocking crack at the top of pier P2-9 was essentially horizontal. Based on the crack pattern shown in Figure 4.32, it is apparent that similar behavior was observed in the negative loading direction. This cracking pattern was likely caused by the different pier boundaries as defined by the out-of-plane walls and by the door opening within Wall 2.

4.2.2 Response after Retrofit

4.2.2.1 Force-Displacement Behavior

Figure 4.31 shows the recorded base shear versus roof displacement response of

Wall 2 after retrofit. The maximum strength of Wall 2 was 142 kN (32 kip) in the positive direction and 130 kN (29 kip) in the negative direction. The corresponding roof displacements were approximately 19 mm (0.74 in.) in the positive direction and 18 mm (0.70 in.) in the negative direction. Overall the hysteresis of Wall 2 was very similar to the recorded behavior prior to retrofit in that significant pinching was observed. In addition, the response showed little degradation during the redundant cycles and an increase in base shear resistance as the roof displacement increased.

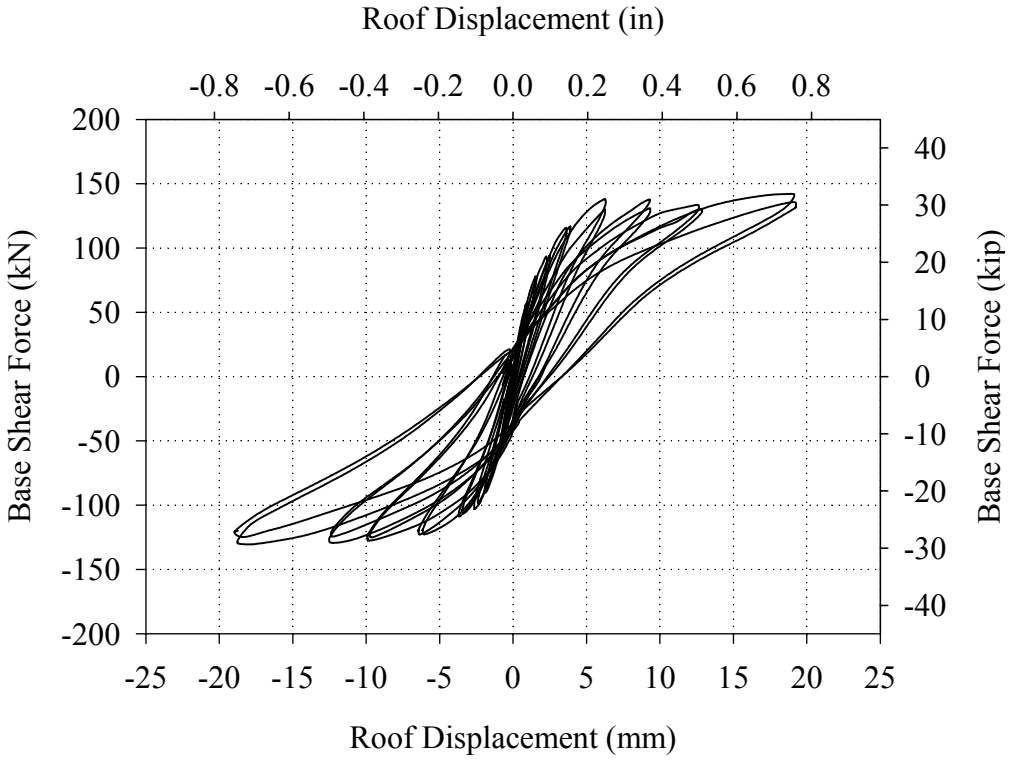

Figure 4.31. Base shear force versus roof displacement response of Wall 2 following retrofit.

4.2.2.2 Damage Progression and Wall Behavior

The crack pattern of Wall 2 and out-of-plane Walls A and B following these cycles are shown Figures 4.32 through 4.34. Note that the cracks that formed prior to retrofit are

shown in gray and the cracks observed following retrofit are shown in black. Figures 4.35 shows a schematic illustrating the final mechanism of Wall 2 and out-of-plane Walls A and B after retrofit in the positive direction. Similar to the behavior prior to retrofit, the response of Wall 2 was very symmetric and thus this figure is also representative of the behavior in the negative loading direction.

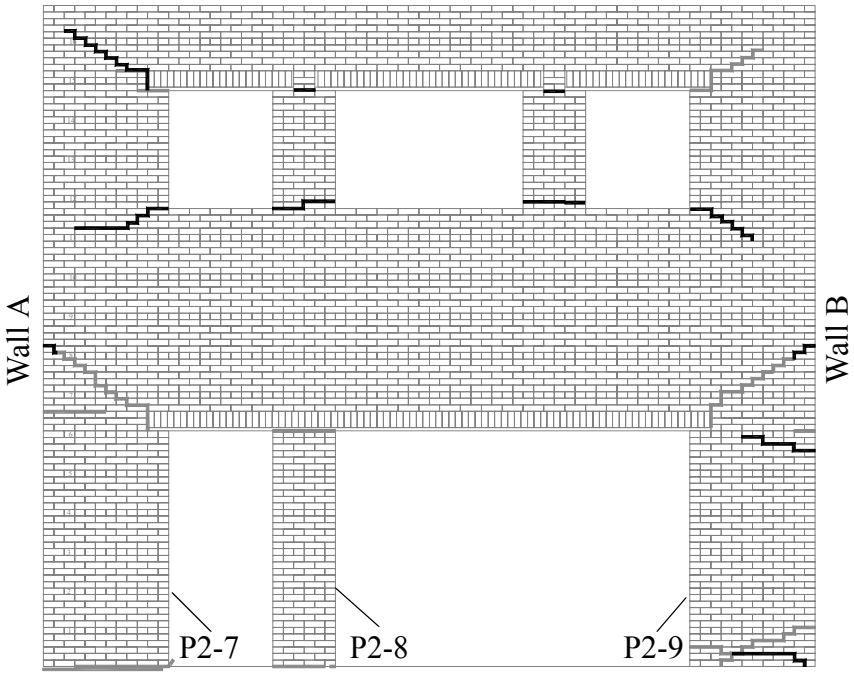

Figure 4.32. Crack pattern in Wall 2 following Test Run 19.

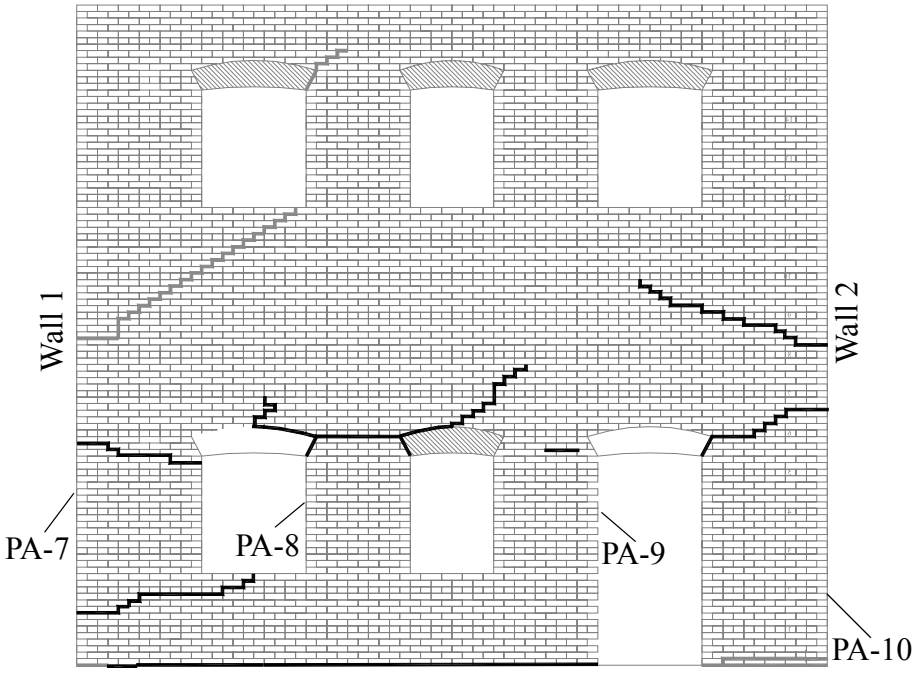

Figure 4.33. Crack pattern in Wall A following Test Run 19.

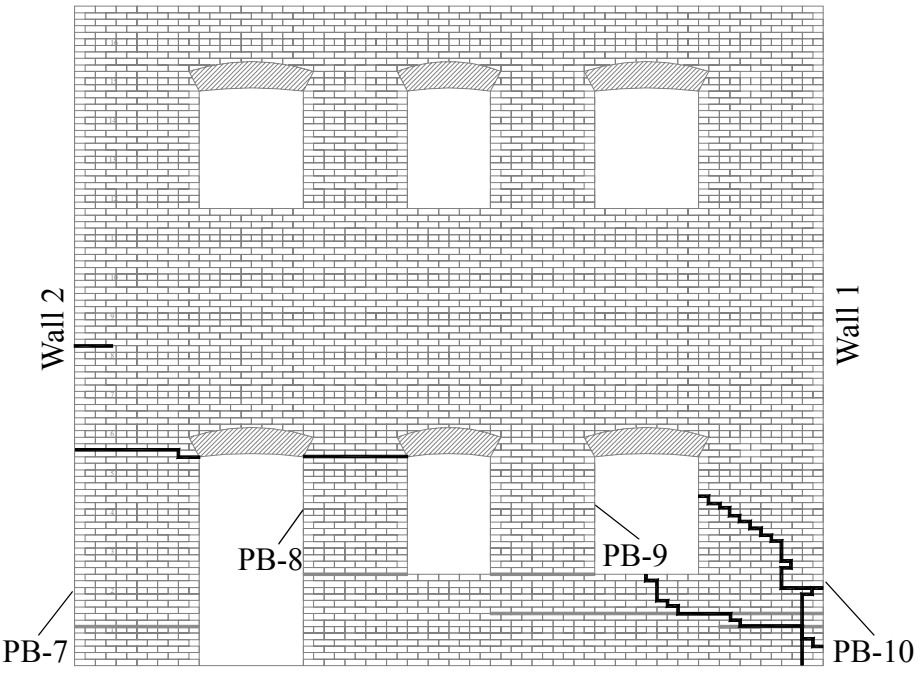

Figure 4.34. Crack pattern in Wall B following Test Run 19.

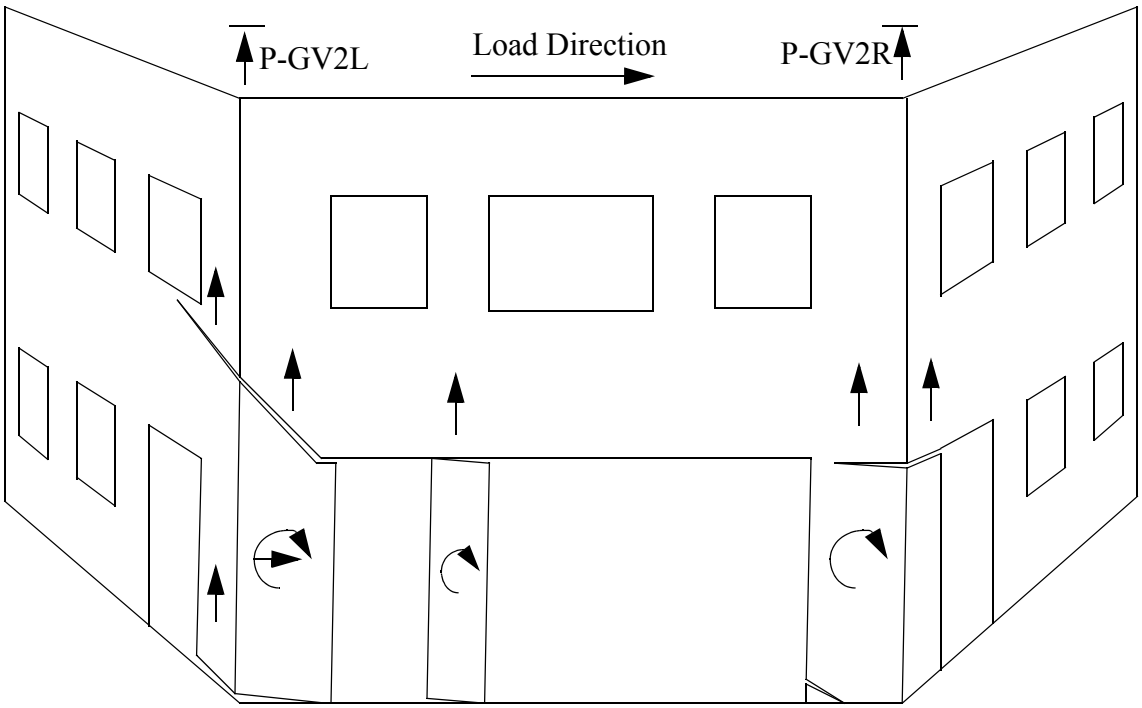

Figure 4.35. Exaggerated schematic illustrating the behavior of Wall 2 and out-of-plane Walls A and B in the positive direction following retrofit.

During Test Runs 11 through 16 no additional cracks were observed in either loading direction and the response of Wall 2 was very similar to the behavior observed prior to retrofit. That is, the response consisted primarily of local rocking deformation of the first story piers. During Test Run 17 in the positive direction, the diagonal crack above pier P2-7 propagated into the Wall A beneath pier PA-5. In addition, during this test run in the negative loading direction the horizontal crack along the top of pier P2-7 propagated into Wall A across the top of pier PA-10. During Test Run 18 a similar crack formed in pier P2-9 and propagated into Wall B across pier PB-7 (see Figures 4.32 and 4.34).

Similar to the behavior prior to retrofit, the final mechanism of Wall 2 after retrofit consisted primarily of the local rocking of the first story piers. The most notable difference

in the response after retrofit was the participation of out-of-plane Walls A and B. In the positive direction, the rocking of pier P2-9 resulted in a small uplift that displaced the adjacent portion of Wall B upwards (see Figure 4.35). Similar behavior was observed in the negative direction for pier P2-7 and out-of-plane Wall A (note, Wall A was not post-tensioned during the testing of Walls 1 and 2 in-plane).

Figure 4.36 shows a plot of the vertical displacements of both sides of the roof of Wall 2 versus lateral roof displacement for Cycle 19a (see Figure 4.35 for gage locations). The uplift caused by the rocking deformation of the first story piers is clearly visible in this figure. In addition, the differential displacement of each side of the roof suggests that a small amount of rotation was also occurring. This rotation is consistent with the direction of overturning moment and likely represents a global rotation of the entire wall about the base. Since the aspect ratio of the wall is approximately 1.0, the difference in measured uplift of each side of the wall corresponds roughly to lateral displacement caused by global rocking (if rigid body rotation about the base is assumed). Following these assumptions, the rotation implied by Figure 4.36 accounted for approximately 1.5 mm (0.06 in.) or 8% of the roof displacement during Cycle 19a. While this displacement is fairly modest, it does suggest that the response of Wall 2 did have a global component. This is further substantiated by the diagonal crack below pier PA-5 which is consistent with global overturning.

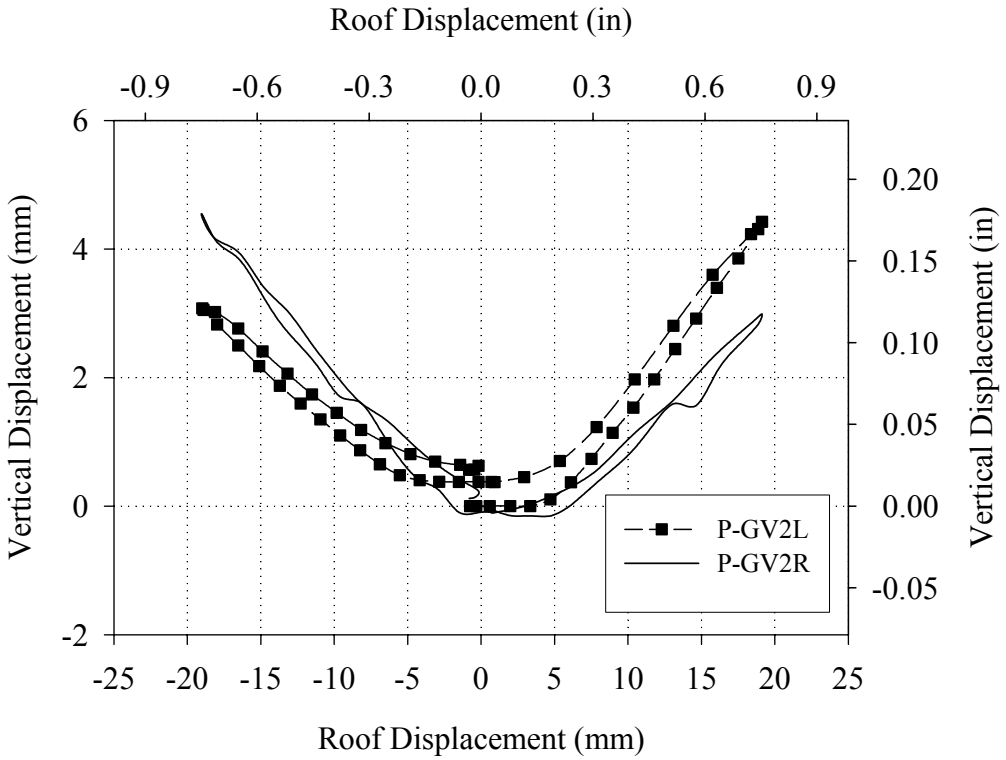

Figure 4.36. Vertical displacement of both sides of the roof of Wall 2 versus lateral roof displacement (Cycle 19a).

4.2.2.3 Response of External Reinforcement

Figure 4.37 shows a schematic illustrating the crack pattern in the external reinforcement following Test Run 19. As apparent from the figure, the observed cracks in the reinforcement formed directly adjacent to existing cracks in the masonry substrate (see Figure 4.32). In particular, during Test Run 13, horizontal hairline cracks appeared in the reinforcement at the top of pier P2-8 and diagonal cracks appeared in the reinforcement at the top of piers P2-7 (in the positive direction) and pier P2-9 (in the negative direction). Increased number of cracks were observed throughout all of the remaining test runs culminating in the crack pattern shown in Figure 4.37. In addition, a photograph showing the observed cracks in the reinforcement along the top of pier P2-7 following Test Run 19

is shown in Figure 4.38. Based on the additional cracks observed during each test run it is clear that the reinforcement was still intact and resisting the rocking deformation of the adjacent piers. Unfortunately, the observed cracks propagated through the stain gages at relatively low displacement levels and thus no meaningful strain data were obtained.

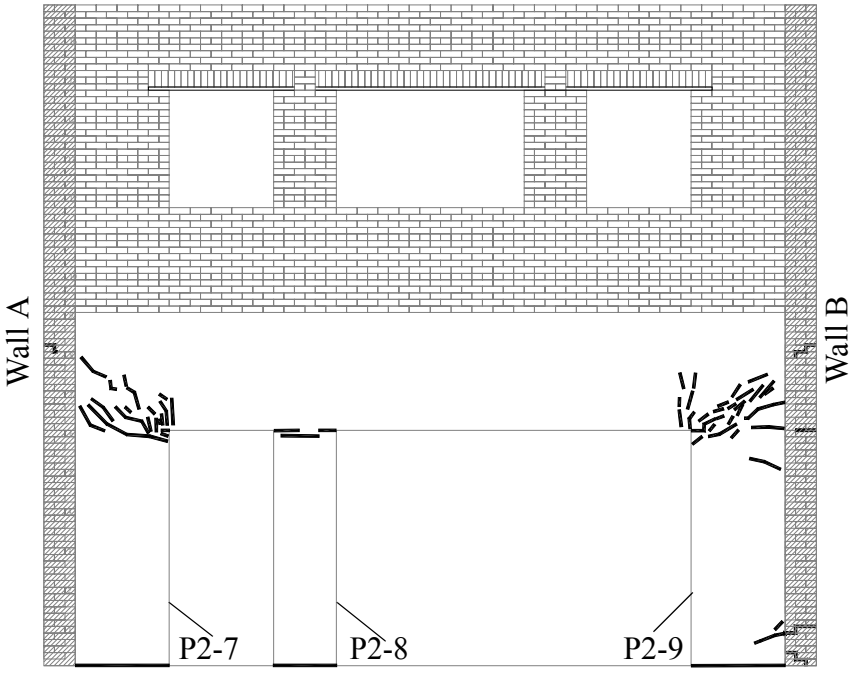

Figure 4.37. Schematic illustrating the crack pattern in the external reinforcement applied to Wall 2 following Test Run 19.

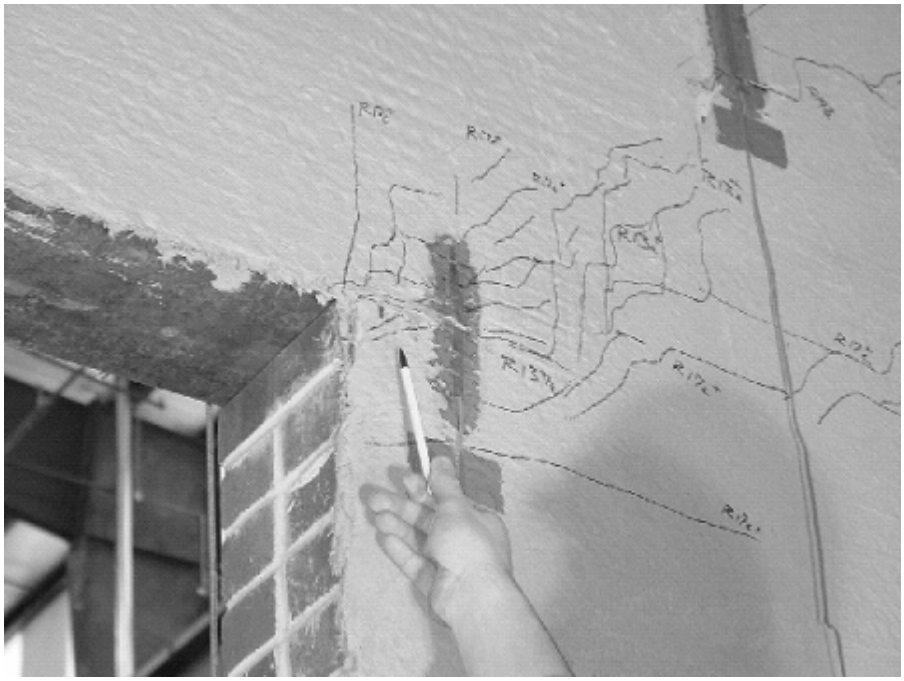

Figure 4.38. Photograph showing the damage to the external reinforcement applied to Wall 2 at pier P2-9 (taken during Test Run 19).

In addition to the formation of cracks, the reinforcement adjacent to the corner of the door opening in piers P2-7 and P2-9 was visibly buckling away from the wall when placed into compression during Test Runs 18 and 19 (see Figure 4.38). Following this observation the external reinforcement was examined for debonding by tapping it with a small wrench. The results of this evaluation suggested large regions of composite had debonded in the vicinity of the observed cracks. Figure 4.39 shows a schematic of the inside of Wall 2 illustrating the extent of the debonding following Test Run 19. In order characterize this damage, a debonded section of the external reinforcement was cut off of the wall after the testing program was completed. Figure 4.40 shows a photograph of the URM wall after the external reinforcement was removed as well as a photograph of the back of the extracted external reinforcement. These photos show that none of the

reinforcement remained bonded to the masonry substrate and that only small portions of the masonry substrate remained bonded to the external reinforcement. This indicates that the primary cause of this failure was poor adhesion between the reinforcement and the substrate.

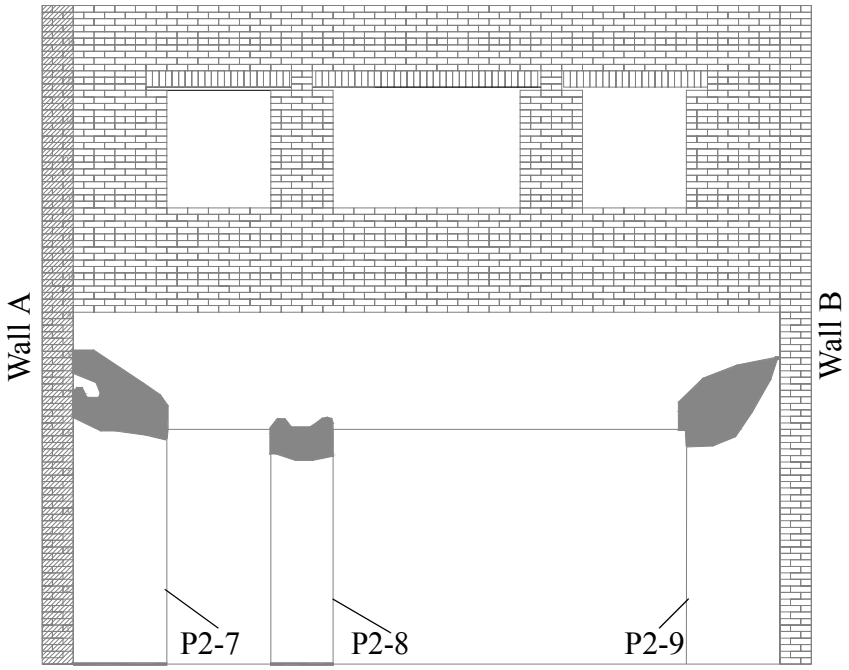

Figure 4.39. Schematic illustrating the extent of debonding following Test Run 19.

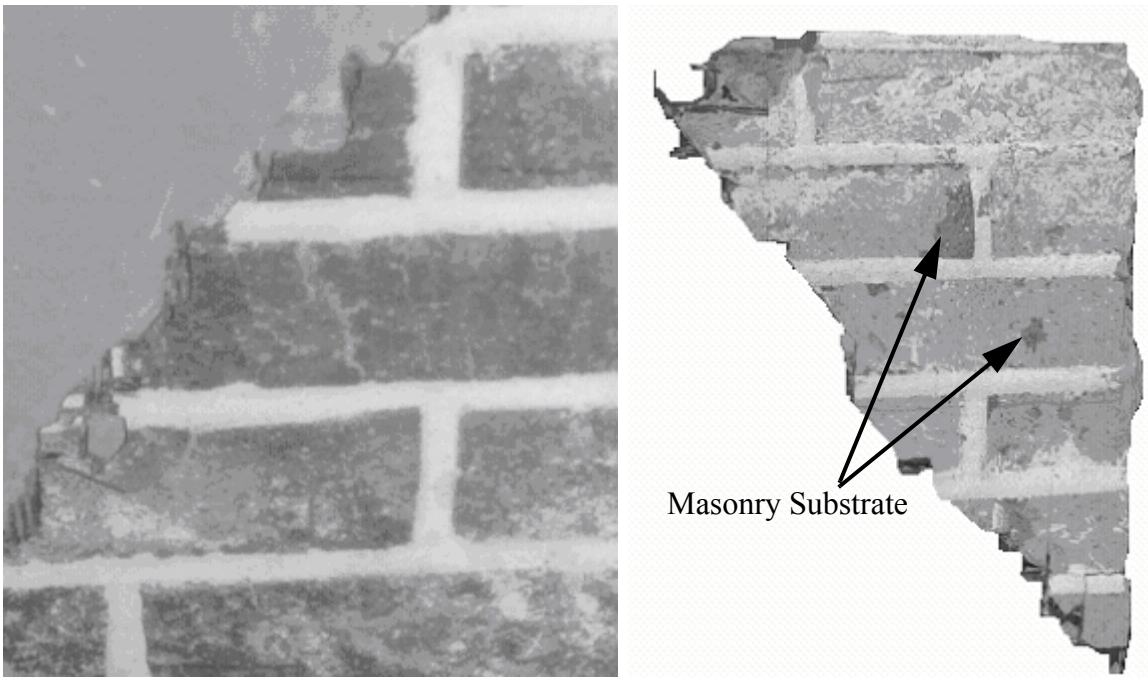

(a) (b)

Figure 4.40. Photograph of (a) the masonry wall following the extraction of the external reinforcement and (b) the back of the extracted external reinforcement.

Although no record of this debonding is available, the force-displacement response of Wall 2 shown in Figure 4.31 suggests that this damage occurred in a progressive manner. That is, as debonding occurred, the effective length of the reinforcement increased thus decreasing the effective stiffness. As a result, during each cycle a larger displacement was required to generate a similar level of resistance from the reinforcement. This phenomenon likely resulted in the highly nonlinear pseudo-ductile behavior illustrated by the overall force-displacement response.

4.2.3 Comparison between the Response of Wall 2 before and after Retrofit

Figure 4.41 shows the base shear versus roof displacement response for Wall 2

before and after retrofit up to 6.35 mm (0.25 in.) roof displacement. Figure 4.42 shows the complete base shear versus roof displacement response for Wall 2. Based on these figures, it is clear that the force-displacement response of Wall 2 after retrofit was similar to the response of Wall 2 before retrofit. Recall, that the observed deformation and behavior modes were nearly identical as well. In addition, Figure 4.41 shows that the response of the strengthened wall up to a roof displacement of 6.35 mm (0.25 in.) essentially followed the final cycle conducted on the structure prior to retrofitting. That is, the external reinforcement did not substantially affect the stiffness of the wall.

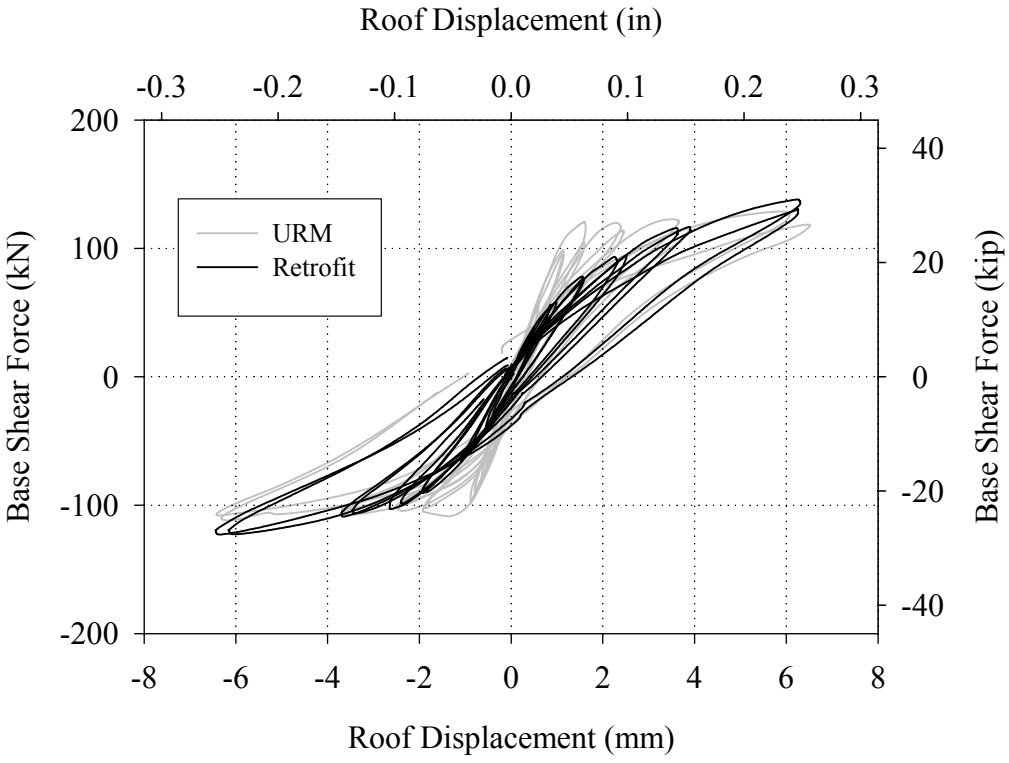

Figure 4.41. Base shear versus roof displacement response of Wall 2 before and after retrofit up to 6.35 mm (0.25 in.) roof displacement.

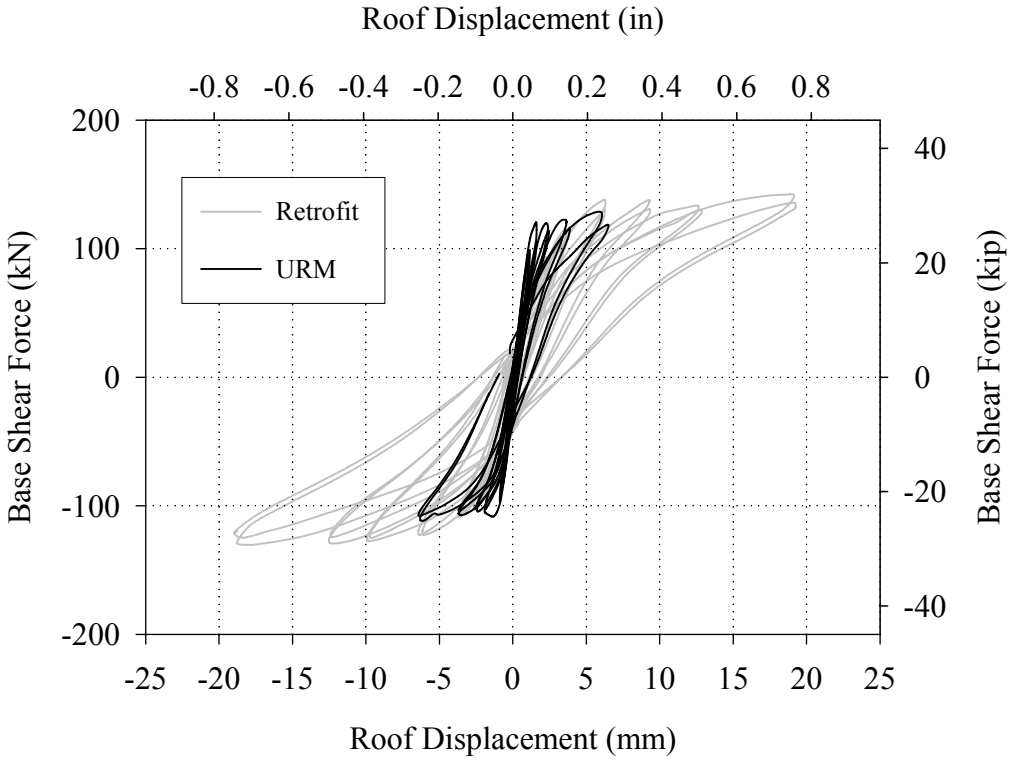

Figure 4.42. Complete base shear versus roof displacement response of Wall 2 before and after retrofit.

Table 4.6 summarizes the peak resistance and displacement at peak resistance for Wall 2 both prior to and after retrofit. This table indicates that the maximum strength of Wall 2 increased following retrofit by approximately 11% in the positive direction and 17% in the negative direction. However, these levels of base shear force were not attained until a roof displacement of roughly 18 mm (0.71 in.). Since this level of displacement is farther than Wall 2 was displaced prior to retrofit, it is unclear if the strength increase was caused by the reinforcement. To obtain a lower bound on the effectiveness of the retrofit system the base shear resistance of Wall 2 before and after retrofit at a roof displacement of 6.35 mm (0.25 in.) were compared. The retrofit system resulted in a strength increase of 7% in the positive direction and 10% in the negative direction.

Table 4.6. Comparison of base shear capacity of Wall 2 before and after retrofit.

	URM		Post-Retrofit	
	Positive Direction	Negative Direction	Positive Direction	Negative Direction
Base Shear Capacity	128 kN (29 kip)	111 kN (25 kip)	142 kN (32 kip)	130 kN (29 kip)
Roof Displacement at Peak Resistance	6.1 mm (0.24 in.)	6.3 mm (0.25 in.)	18.8 mm (0.74 in.)	17.8 mm (0.70 in.)

Figure 4.43 shows the energy dissipated by both stories of Wall 2 before and after retrofit during each test run versus roof displacement. For comparison purposes the energy dissipated by the first story of Wall 2 was divided by the maximum possible energy dissipation, which was defined as the area of a rectangle that encompasses the force displacement response. Figure 4.44 shows the percentage of energy dissipated by the first floor of Wall 2 before and after retrofit (note the due to the small amount of energy dissipated by the second story of Wall 2 only the first story was included in this plot).

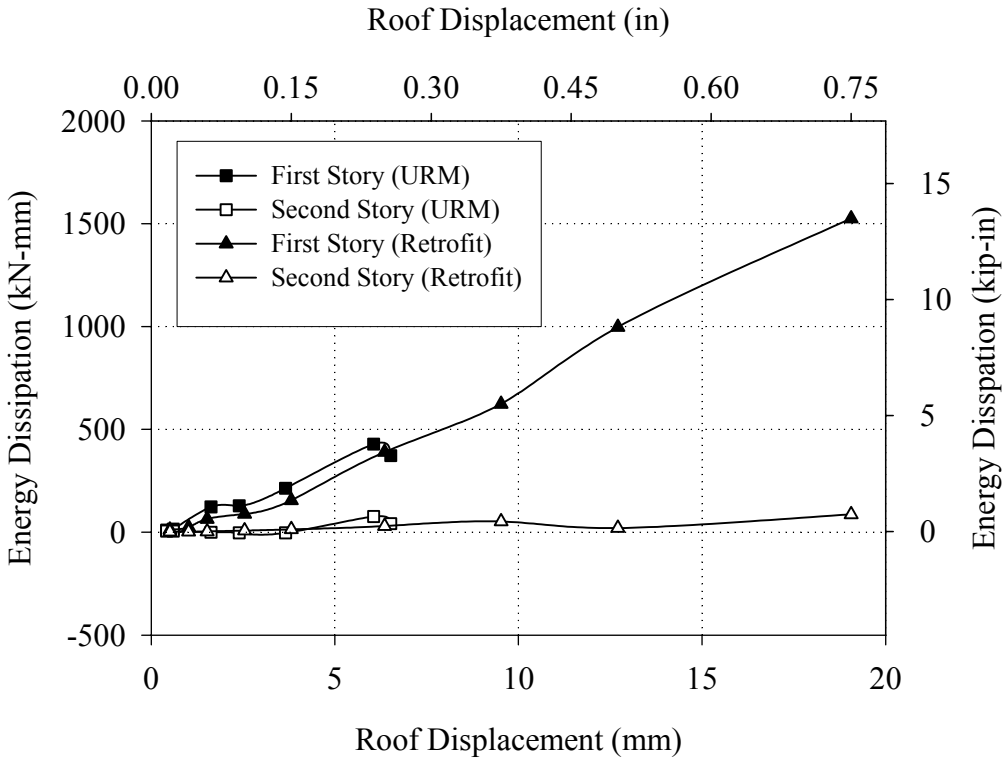

Figure 4.43. Energy dissipated by each story of Wall 2 before and after retrofit.

Figure 4.43 shows that the majority of the energy dissipation was due to the response of the first story. In addition, the energy dissipated following retrofit was slightly smaller than before retrofit, which was likely caused by the damage induced during testing prior to retrofit. Unlike the response of Wall 1, the fairly consistent percentage of energy dissipated by Wall 2 suggests that the response remained similar for all cycles. This is consistent with the unvarying failure modes displayed by the wall.

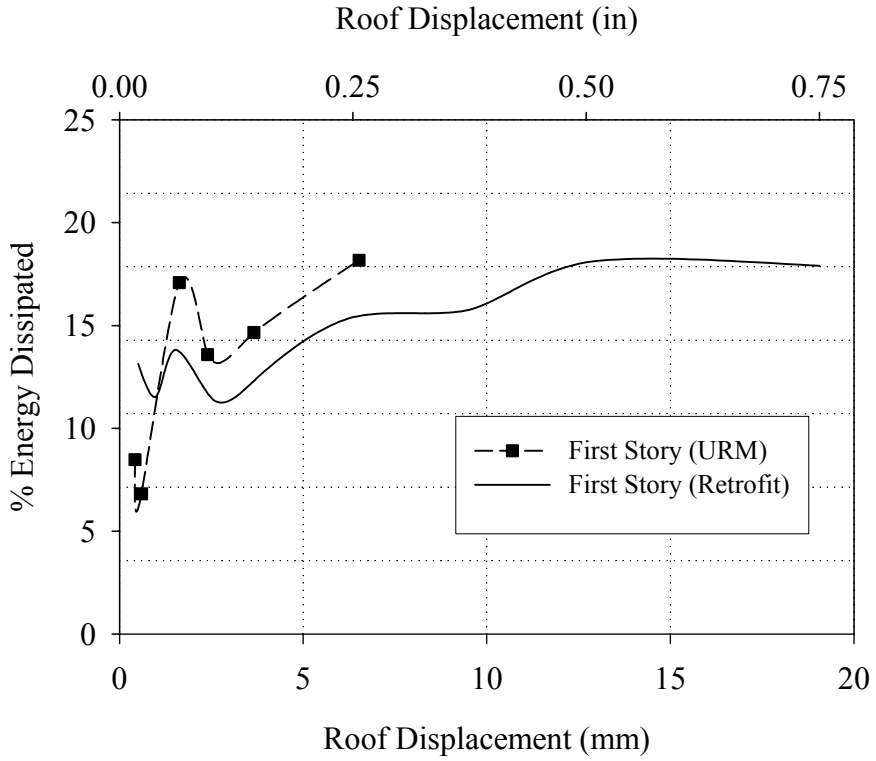

Figure 4.44. Percentage of energy dissipated by the first story of Wall 2 before and after retrofit.

4.3 Response of Wall A

A summary of the in-plane displacements imposed on Wall A is given in Table 4.7 along with test run and cycle designation. Figures 4.45 and 4.46 show a graphical representation of the loading history imposed before and after retrofit, respectively. Prior to post-tensioning Wall A, cyclic displacements up to 12.7 mm (0.5 in.) in each loading direction were imposed. Based on the observed failure modes, the resulting maximum drifts exceeded the Collapse Prevention performance level for certain piers (ATC, 2000). Following these cycles, the wall was subjected to two series of increasing cyclic displacements up to 12.7 mm (0.5 in.) and 19 mm (0.75 in.) to assess the effect of different levels of post-tensioning force (i.e. 111 kN (25 kip) and 222 kN (50 kip)). According to

FEMA 356 the performance levels provided for in-plane URM walls are applicable to URM walls post-tensioned with unbonded tendons. As a result, the displacements imposed on the structure for each level of post-tensioning force exceeded the Collapse Prevention performance level (ATC, 2000).

Table 4.7 Summary of displacements imposed on Wall A

	Test Run	Target Roof Displacement mm (in)	Target Second Floor Displacement mm (in)
URM	20	+/- 0.3 (0.01)	+/- 0.24 (0.008)
	21	+/- 0.8 (0.03)	+/- 0.64 (0.024)
	22	+/- 1.8 (0.07)	+/- 1.44 (0.056)
	23	+/- 2.5 (0.1)	+/- 2.0 (0.08)
	24	+/- 3.8 (0.15)	+/- 3.0 (0.12)
	25	+/- 6.4 (0.25)	5.8 (0.23), -4.8 (-0.19)
	26	+/- 12.7 (0.5)	10.2 (0.4), -8.9 (-0.35)
Post-Retrofit (PT = 111 kN (25 kip))	27	+/- 1 (0.04)	+/- 0.8 (0.03)
	28	+/- 1.5 (0.06)	+/- 1.4 (0.054)
	29	+/- 2.5 (0.1)	+/- 2.4 (0.093)
	30	+/- 3.8 (0.15)	+/- 3.5 (0.138)
	31	+/- 6.4 (0.25)	+/- 6.0 (0.235)
	32	+/- 9.5 (0.375)	8.9 (0.352), -9.0 (-0.356)
	33	+/- 12.7 (0.5)	+/-12.1 (0.475)
Post-Retrofit (PT = 222 kN (50 kip))	34	+/- 1.3 (0.05)	+/- 1.2 (0.0475)
	35	+/- 3.8 (0.15)	+/-3.6 (0.143)
	36	+/- 6.4 (0.25)	+/- 6.1 (0.24)
	37	+/- 9.5 (0.375)	9.3 (0.368), -9.2 (-0.364)
	38	+/- 12.7 (0.5)	+/- 12.3 (0.485)
	39	+/- 19.1 (0.75)	16.2 (0.638), -17.9 (-0.705)

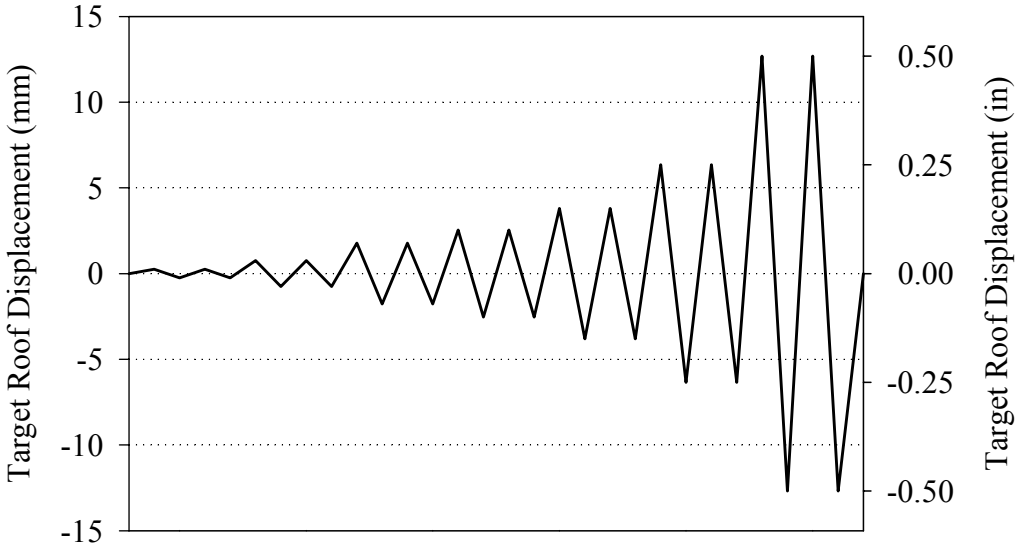

Figure 4.45. Loading history applied to Wall A prior to post-tensioning.

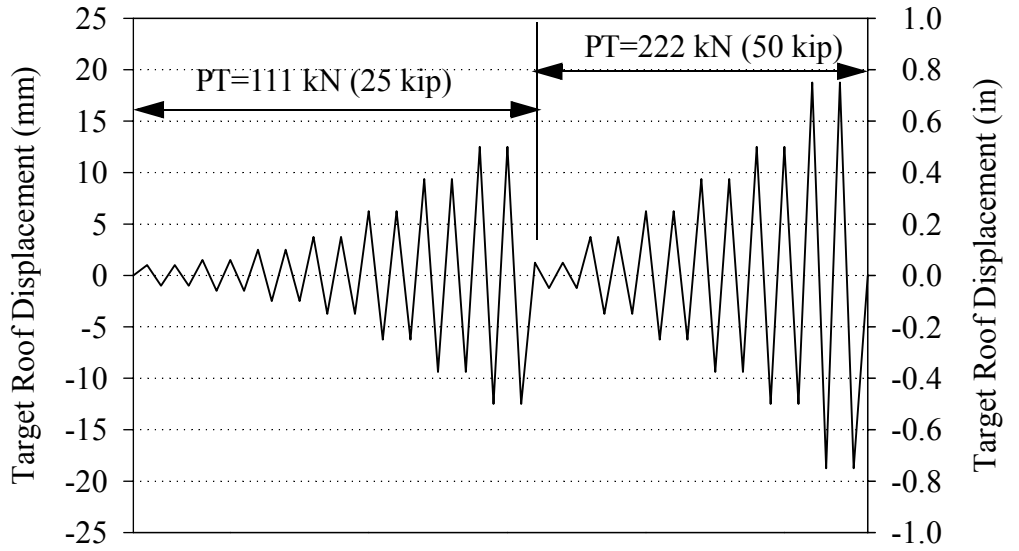

Figure 4.46. Loading history applied to Wall A following post-tensioning.

4.3.1 Response Prior to Retrofit

4.3.1.1 Force-Displacement Behavior

Table 4.8 shows the initial stiffness calculated for Wall A in each loading direction. Each stiffness corresponds to a roof drift a 0.25 mm (0.01 in.) and was determined by dividing the base shear force by the roof displacement. In contrast to the elastic stiffnesses reported for Walls 1 and 2, these stiffnesses do not reflect the elastic response of Walls A as significant cracking was induced during the loading of Walls 1 and 2 in-plane (see Sections 4.1 and 4.2).

Table 4.8. Initial Stiffness of Wall A prior to post-tensioning.

	Positive Direction	Negative Direction
Wall A	144 kN/mm (820 kip/in)	154 kN/mm (880 kip/in)

Figure 4.47 shows the recorded base shear versus roof displacement response of Wall A prior to post-tensioning. The maximum strength of Wall A was 159 kN (36 kip) in the positive direction and 182 kN (41 kip) in the negative direction. The corresponding roof drifts were approximately 6 mm (0.24 in.) in each direction. As apparent from Figure 4.47, the hysteresis of Wall A displayed a great deal of pinching up to a roof displacement of approximately 3.8 mm (0.15 in.) in both loading directions. As the imposed displacements increased beyond this level, the response of Wall A displayed more energy dissipation, although significant pinching was still observed.

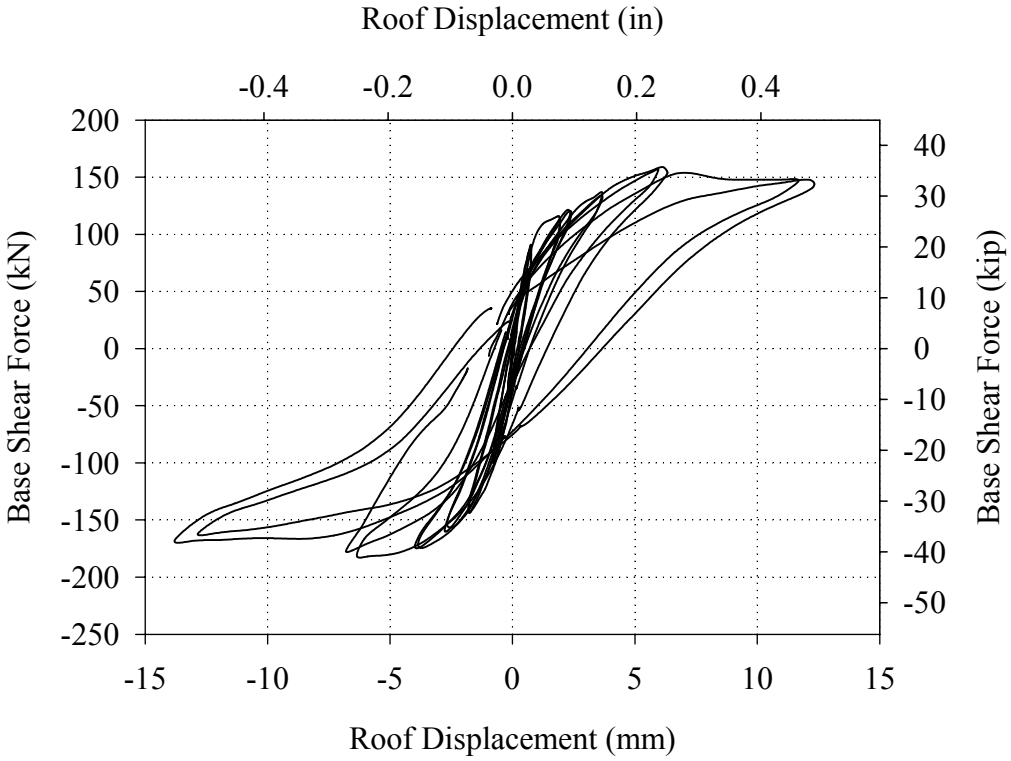

Figure 4.47. Base shear force versus roof displacement response of Wall A prior to retrofit.

4.3.1.2 Damage Progression and Wall Behavior

The crack pattern of Wall A and out-of-plane Walls 1 and 2 following Test Run 26 are shown Figures 4.48 through 4.50. Note that the cracks that formed during Test Runs 20 through 26 are shown in black and those that formed during past cycles are shown in gray. Figures 4.51 and 4.52 show schematics illustrating the final mechanism of Wall A and out-of-plane Walls 1 and 2 prior to post-tensioning in the positive and negative directions, respectively.

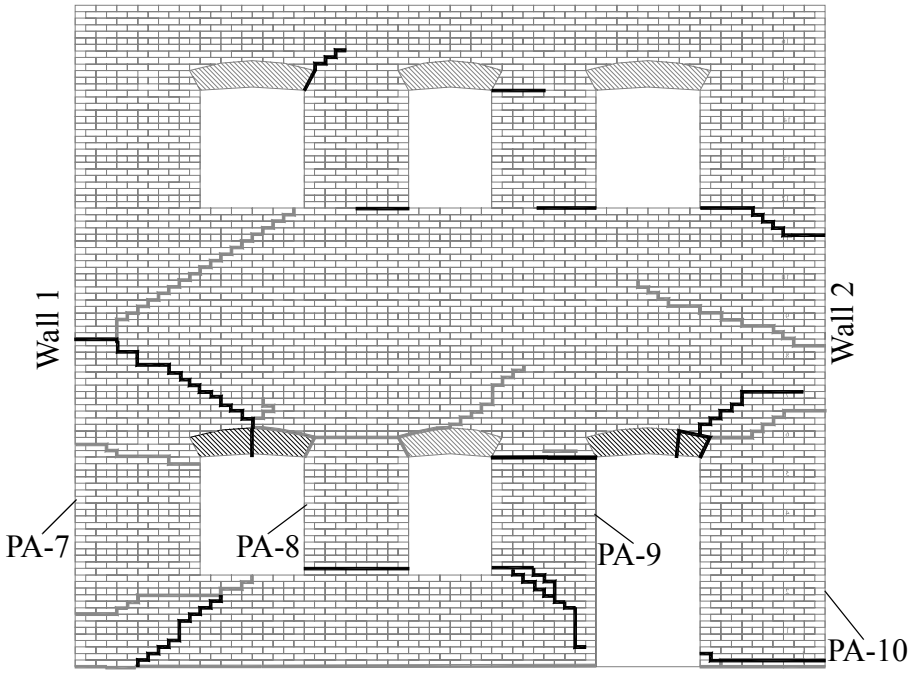

Figure 4.48. Crack pattern of Wall A following Test Run 26.

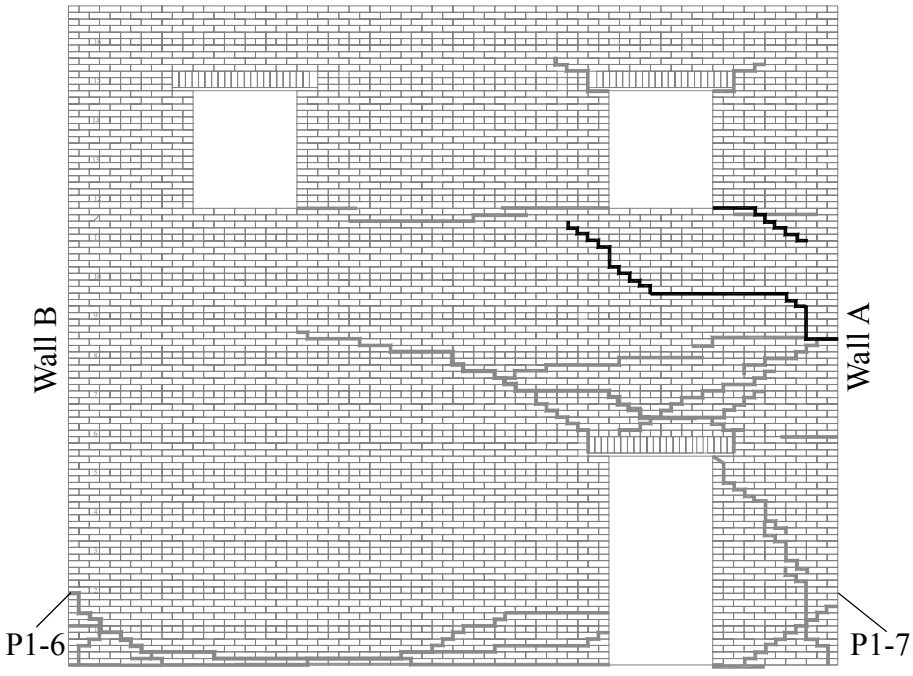

Figure 4.49. Crack pattern of Wall 1 following Test Run 26.

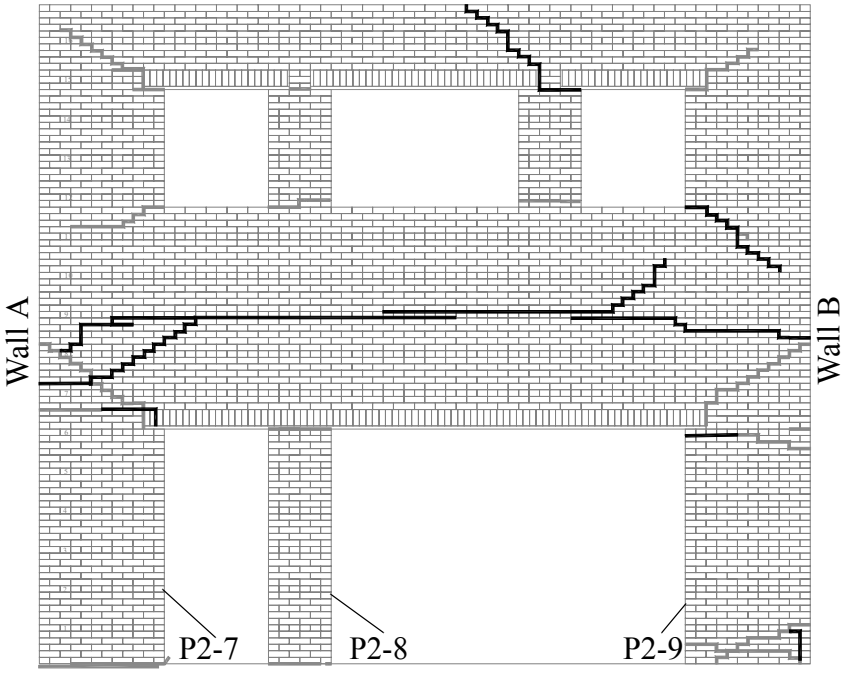

Figure 4.50. Crack pattern of Wall 2 following Test Run 26.

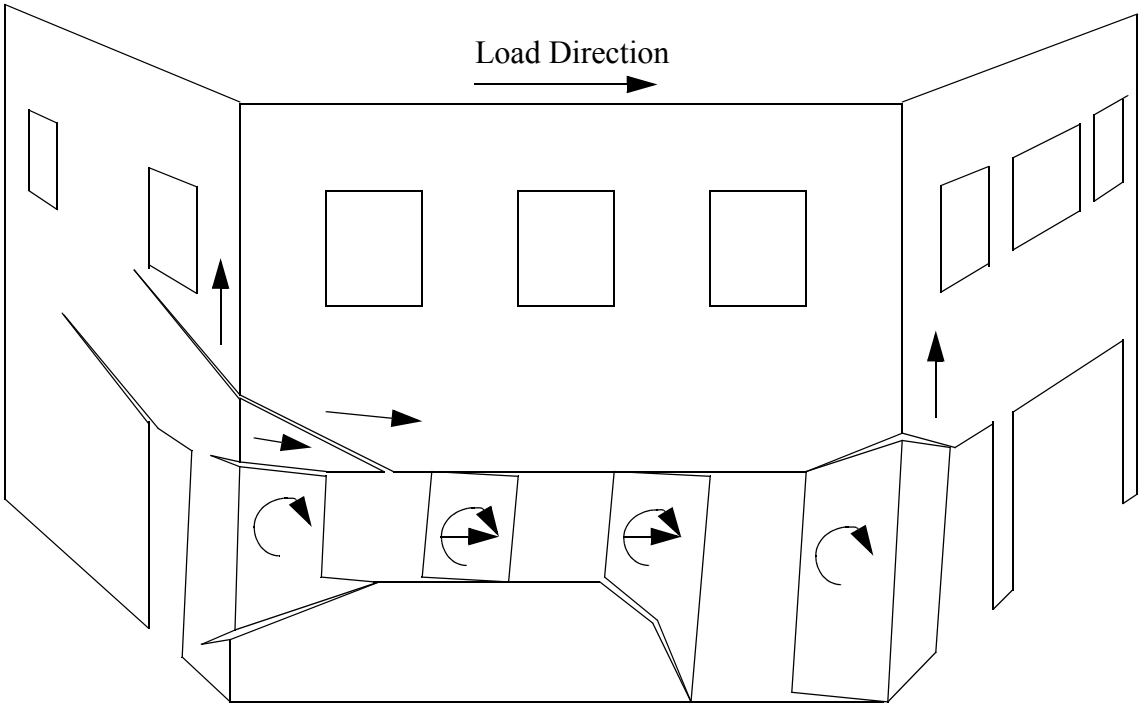

Figure 4.51. Exaggerated schematic illustrating the response of Wall A and out-of-plane Walls 1 and 2 in the positive direction prior to post-tensioning.

In the positive loading direction no new cracks were observed during Test Runs 20 and 21. During Test Run 22 a diagonal crack above pier PA-7 formed and opened in a sliding mode during subsequent cycles (see Figure 4.51). In addition, during this test run a horizontal crack below pier PA-8 and a small horizontal crack along the lower left corner of pier PA-9 were observed. During Test Runs 23 and 24, all of the first story piers displayed low-level rocking deformation.

During Test Run 25 and 26 the rocking mechanism of pier PA-9 became fully developed as the existing crack at the base propagated diagonally downward to the door opening and a horizontal crack formed along the top of the pier (see Figures 4.48 and 4.51). In addition, during these test runs additional cracks formed in out-of-plane Walls 1 and 2. In Wall 1 a crack below pier P1-4 as well as a crack extending diagonally from the base of the second floor actuator to the bottom right corner of pier P1-3 were observed. In Wall 2, the existing horizontal crack along the top of pier P2-7 propagated to the corner of the door opening.

The final mechanism of Wall A in the positive direction prior to retrofit consisted primarily of local rocking of the first story piers (see Figure 4.51). However, significant sliding deformation along the diagonal crack above pier PA-7 was also observed. This sliding deformation was likely a result of the reduced vertical stress in this portion of the wall due to overturning moment. In addition, the uplift associated with local pier rocking cracked out-of-plane Walls 1 and 2 and engaged a portion of their weight.

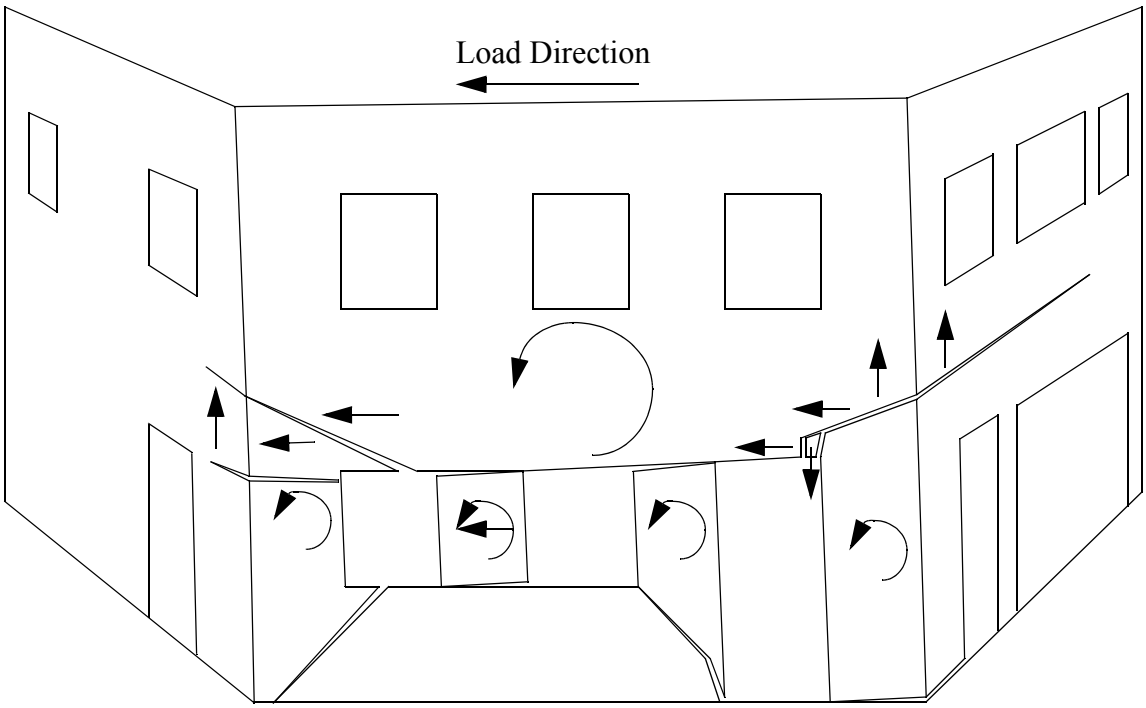

Figure 4.52. Exaggerated schematic illustrating the behavior of Wall A and out-of-plane Walls 1 and 2 in the negative direction prior to post-tensioning.

In the negative direction no new cracks were observed during Test Runs 20 through 24. The deformation of the wall during these cycles focused primarily on the rocking deformation of the first story piers. During Test Run 25 an additional diagonal crack at the base of pier PA-7 was observed. This crack subsequently became the active rocking crack of pier PA-7 (see Figures 4.48 and 4.52). Also during this test run a diagonal crack initiated above pier P2-7 at the second floor level of Wall 2. This crack extended approximately 1830 mm (72 in.) at the end of Test Run 25 and propagated across approximately 80% of Wall 2 during the initial cycle of Test Run 26 (see Figure 4.50). Also during Test Run 26 an additional diagonal crack formed above pier PA-10.

The final mechanism of Wall A in the negative direction prior to post-tensioning consisted of both local pier rocking of all first story piers as well as global rocking of the

entire wall. The global rocking portion of the deformation lifted up a large portion of out-of-plane Wall 2 (see Figure 4.52). In addition, this deformation acted to reduce the vertical stress in pier PA-10 and resulted in significant sliding deformation along the diagonal crack above this pier.

Due to the unsymmetrical response of the diagonal cracks above piers PA-7 and PA-10, significant residual crack opening was observed in these regions. Specifically, when the direction of the overturing moment acted to reduce the vertical stress in these regions, significant sliding deformation was observed. However, in the other loading direction overturning moment acted to increase the vertical stress in these regions and thus the sliding deformation was not recovered. The result was a progressive crack opening during each of the cycles. As a result of this phenomenon a portion of the arch lintel above the door opening collapsed in the negative loading direction during Test Run 26 (see Figure 4.52). Figure 4.53 shows a photograph of this lintel taken after Test Run 26. For safety reasons shoring was supplied beneath all of the first story arch lintels during the remainder of the cycles.

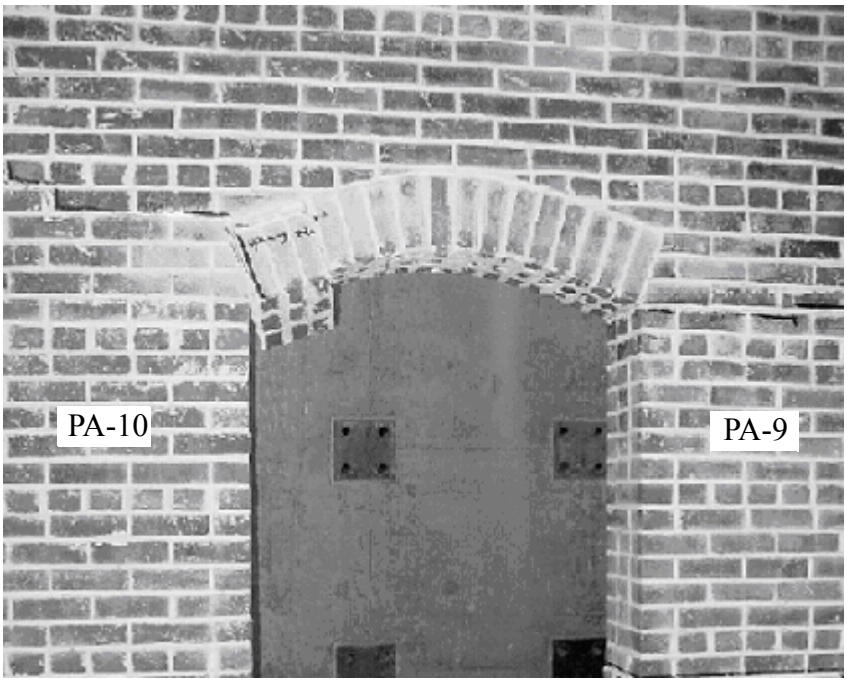

Figure 4.53. Photograph showing the collapse of a portion of the arch lintel above the door opening during Test Run 26.

4.3.2 Response after Post-tensioning

4.3.2.1 Force-Displacement Behavior

Figures 4.54 and 4.55 show the recorded base shear versus roof displacement response of Wall A during Test Runs 27 through 33 (i.e. post-tensioning force of 111 kN (25 kip or approximately 12 psi)) and Test Runs 34 through 39 (post-tensioning force of 222 kN (50 kip or approximately 24 psi)), respectively. Figure 4.56 shows the base shear versus roof displacement response of Wall A for both levels of post-tensioning force. For the 111 kN (25 kip) level of post-tensioning force the maximum strength of Wall A was 223 kN (50 kip) in the positive direction and 261 kN (59 kip) in the negative direction. The corresponding roof displacements were approximately 12.3 mm (0.5 in.) in both directions. For the 222 kN (50 kip) level of post-tensioning force the maximum strength of

Wall A was 250 kN (56 kip) in the positive direction and 294 kN (66 kip) in the negative direction. The corresponding roof displacements were approximately 12.3 mm (0.5 in.) in the positive direction and 19 mm (0.75 in.) in negative direction.

As apparent from Figures 4.54 and 4.55, the peak resistance of Wall A during each test run increased with increasing roof displacement. In addition, little degradation in terms of both stiffness and peak resistance was observed during the redundant cycles conducted during each test run. Figure 4.56 indicates that both levels of post-tensioning resulted in similar hysteresis; although, the larger post-tensioning force did result in a slight increase in energy dissipation.

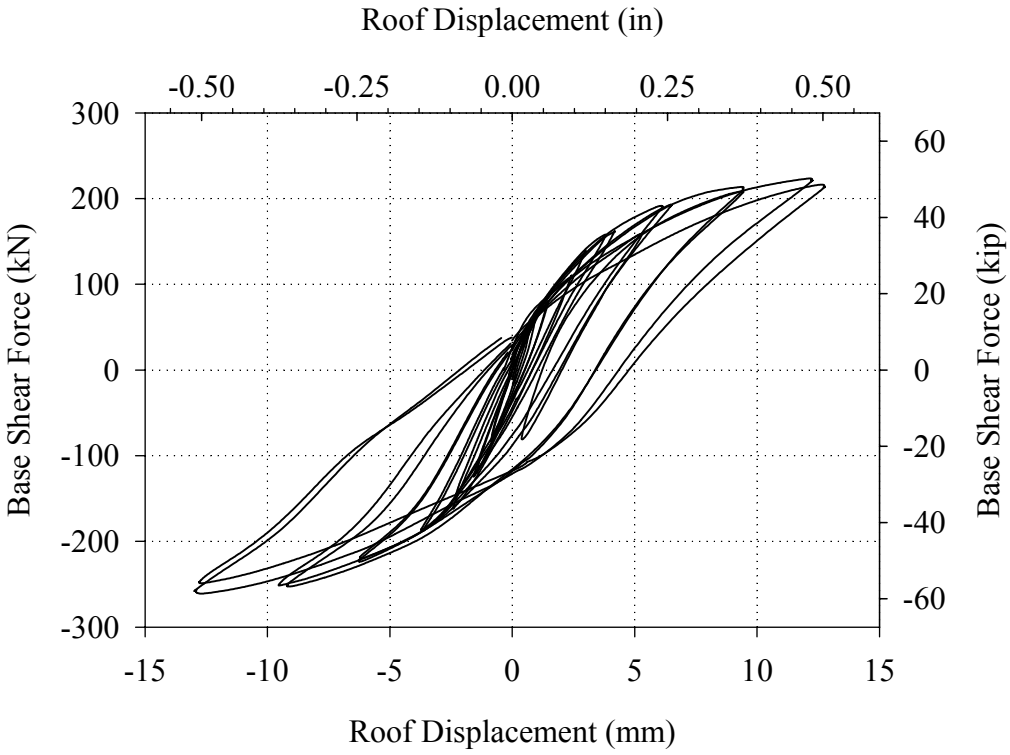

Figure 4.54. Base shear force versus roof displacement response of Wall A during Test Runs 27 through 33 (i.e. initial PT=111 kN (25 kip)).

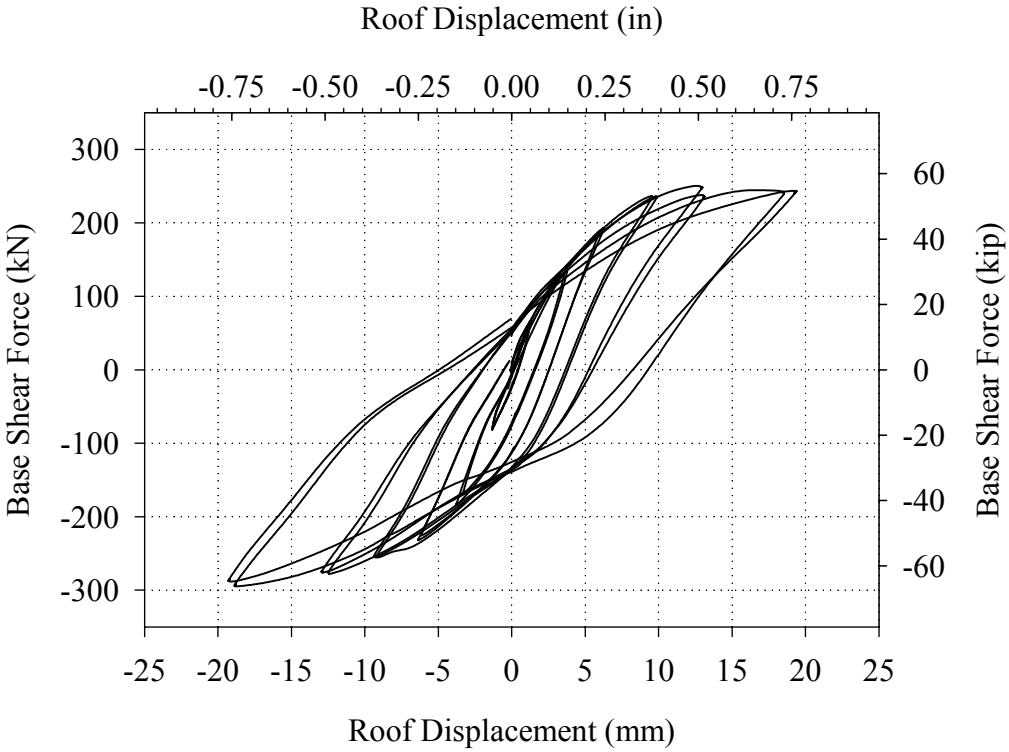

Figure 4.55. Base shear force versus roof displacement response of Wall A during Test Runs 34 through 39 (i.e. initial PT=222 kN (50 kip)).

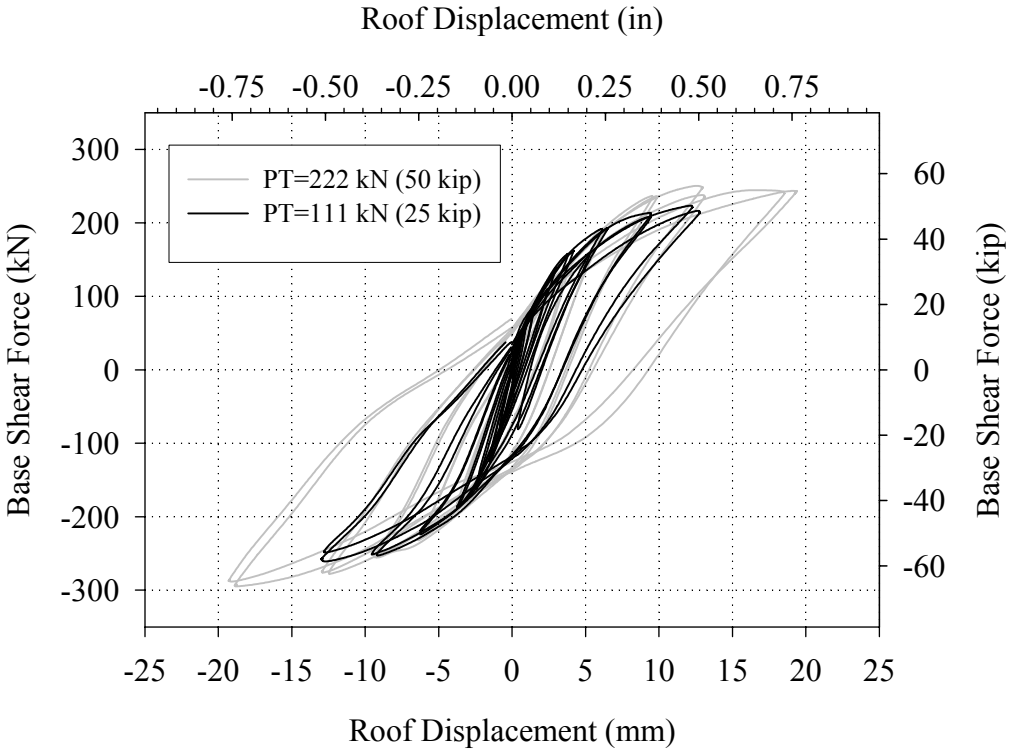

Figure 4.56. Complete base shear force versus roof displacement response of Wall A after post-tensioning.

4.3.2.2 Damage Progression and Wall Behavior

The crack pattern of Wall A and out-of-plane Walls 1 and 2 following Test Run 39 are shown in Figures 4.57 through 4.59. Note that the cracks that formed prior to retrofit are shown in gray and the cracks observed following retrofit are shown in black. Figures 4.60 and 4.62 show exaggerated schematics illustrating the final mechanism of Wall A and out-of-plane Walls 1 and 2 in the positive and negative directions, respectively.

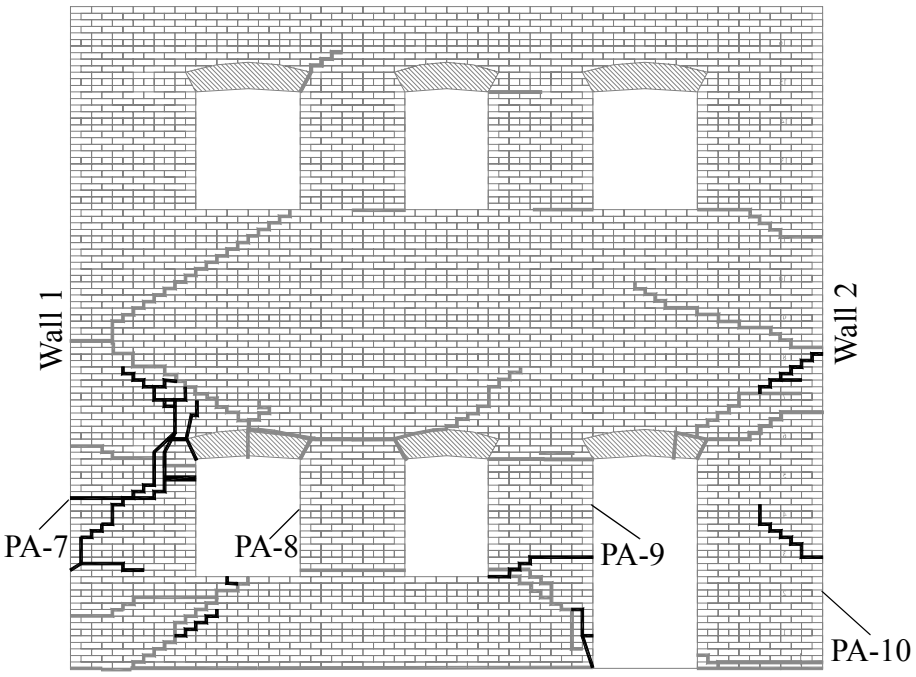

Figure 4.57. Crack pattern in Wall A following Test Run 39.

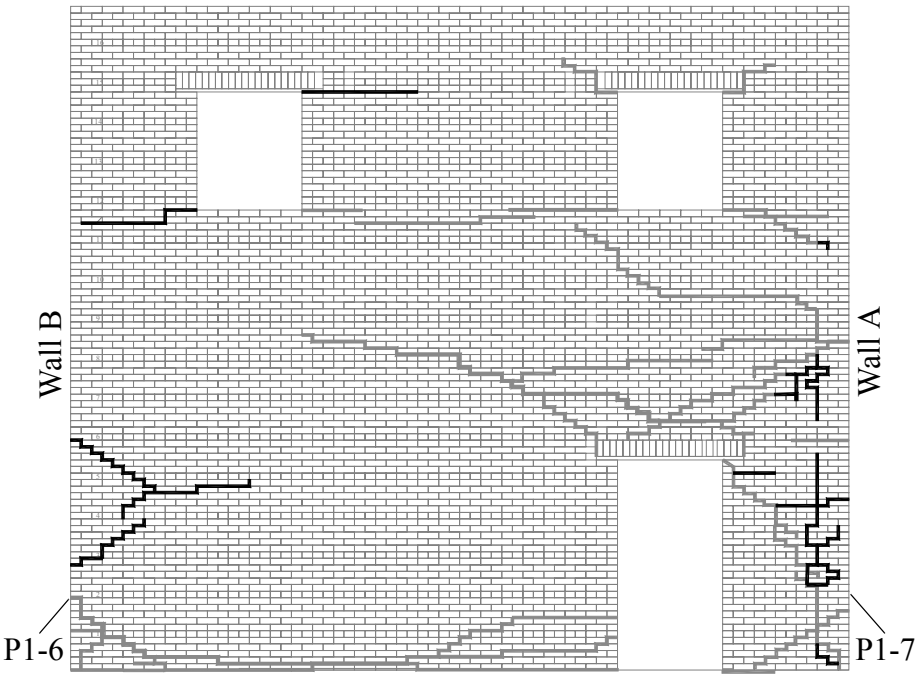

Figure 4.58. Crack pattern in Wall 1 following Test Run 39.

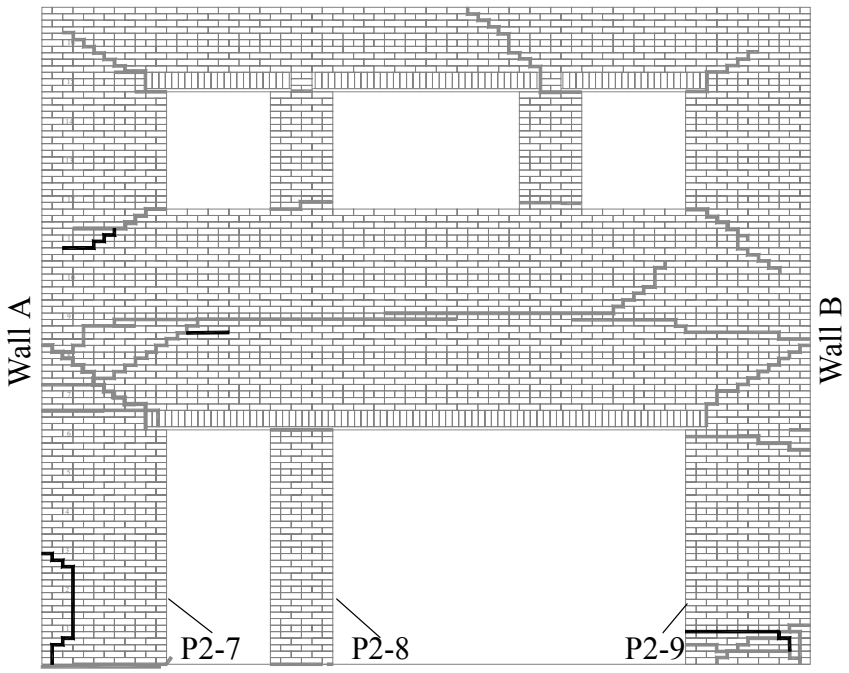

Figure 4.59. Crack pattern in Wall 2 following Test Run 39.

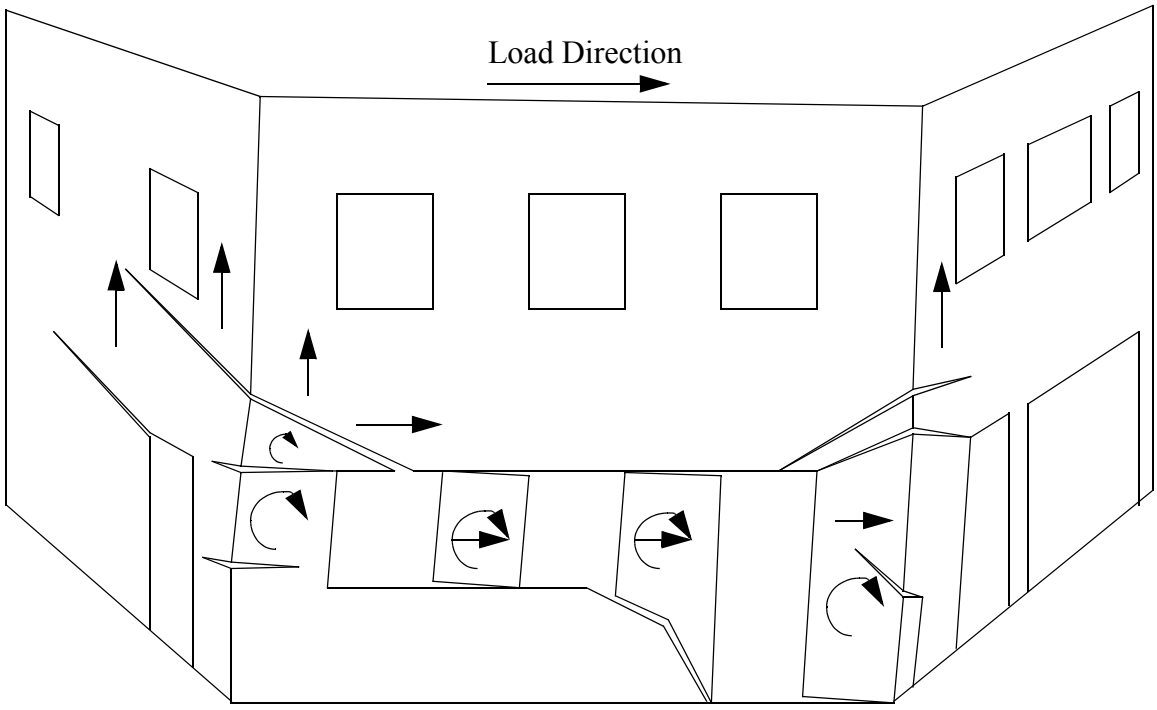

Figure 4.60. Exaggerated schematic illustrating the behavior of Wall A and out-of-plane Walls 1 and 2 in the positive direction following retrofit.

In the positive direction, the response of Wall A during Test Runs 27 through 33 (i.e. post-tensioning force of 111 kN (25 kip)) was essentially identical to the performance prior to post-tensioning (see Section 4.3.1.2). Specifically, the majority of the deformation was focused on the rocking of the first floor piers as well as some sliding along the diagonal crack above pier PA-7. The only cracks observed in the positive loading direction during these cycles were located at the base of pier PA-9 (see Figure 4.57). However, since the rocking mechanism of this pier had already fully developed, these cracks did not impact the performance.

During Test Runs 34 through 37 (i.e. post-tensioning force of 222 kN (50 kip)), the response of Wall A remained unchanged and no new cracks were observed. During Test Run 38 a horizontal crack at the base of pier PA-7 formed and subsequently became the active rocking crack of this pier (see Figures 4.57 and 4.60). During Test Run 39 a diagonal crack was observed in the center of pier PA-10. This crack propagated into Wall 2 and vertically down to the foundation suggesting that the lower portion of pier PA-10 was punching through Wall 2. As apparent from Figure 4.57 this diagonal crack did not fully develop and as a result the response of pier PA-10 remained primarily rocking. Based on the orientation and location of this crack, the presence of overturning moment was likely the primary cause. That is, the additional vertical stress applied to this pier due to overturning moment switched the failure mode from rocking to diagonal tension.

The final mechanism of Wall A in the positive direction for both levels of post-tensioning force focused primarily on the rocking deformation of the first story piers. For the majority of the cycles conducted on Wall A, negligible global rocking was observed in the positive direction; however during Test Run 39 a significant increase in global rocking

was observed. Figure 4.61 shows the rotation of the roof of Wall A at peak displacement during each test run versus roof displacement (see Appendix B for a complete description of the procedure used to generate this plot). From this figure it is apparent that the rotation of Wall A was negligible for roof displacements less than 13 mm (0.5 in.) for both levels of post-tensioning force. However, during Test Run 39 a significant increase in rotation is apparent, which suggests an increase in global rocking behavior. Based on small angle theory and assuming a rigid body rotation about the base, the rotation illustrated in Figure 4.61 translates into a roof displacement of approximately 3.8 mm (0.15 in.) or 20% of the roof displacement.

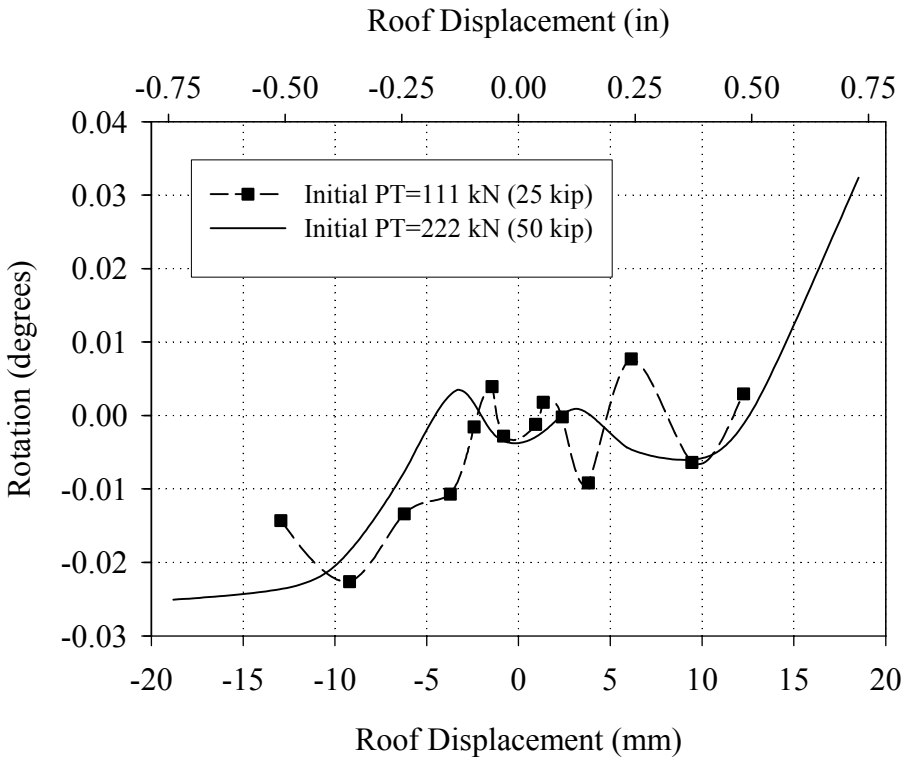

Figure 4.61. Maximum rotation of the roof of Wall A for each test run versus roof displacement.

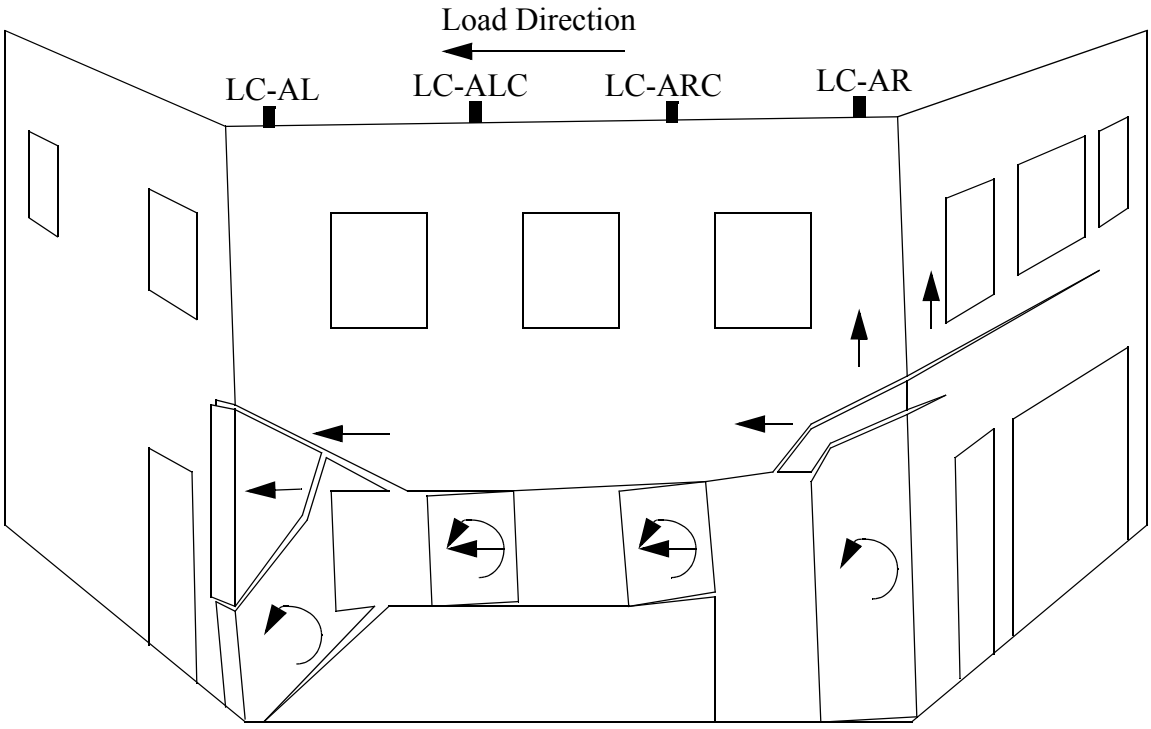

Figure 4.62. Exaggerated schematic illustrating the behavior of Wall A and out-of-plane Walls 1 and 2 in the negative direction following post-tensioning.

In the negative loading direction during Test Runs 27 through 29 (2.5 mm (0.1 in.) roof displacement), the response of Wall A was very similar to the initial response observed prior to retrofit (see Figure 4.52). No new cracks were observed during these cycles. During Test Run 30 a horizontal crack at the base of pier PA-9 formed and subsequently became the active rocking crack of this pier (see Figures 4.57 and 4.62). Figure 4.63 shows a photograph of the inside of pier PA-9 illustrating the location of these cracks.

During Test Run 31 additional cracks were observed in Wall 1 along the right side of pier P1-7. These cracks extended vertically from the foundation up to approximately half the height of pier P1-7. The location of these cracks suggested that the lower portion

of Wall A was punching through Wall 1. In addition, during Test Run 31 a diagonal crack located in the upper right portion of pier PA-7 was observed. This crack propagated during the following cycles and extended across approximately 75% of pier PA-7 at the end of Test Run 33. Following the formation of this crack, the deformation of pier PA-7 gradually switched from rocking to a combined rocking/stair-stepped bed-joint sliding mode. Similar to the diagonal crack that was observed in pier PA-10 in the positive loading direction, this crack was likely caused due to the effects of overturning moment. In particular, the presence of overturning moment acted to increase the vertical stress in this pier and thus switched the failure mode form rocking to diagonal tension.

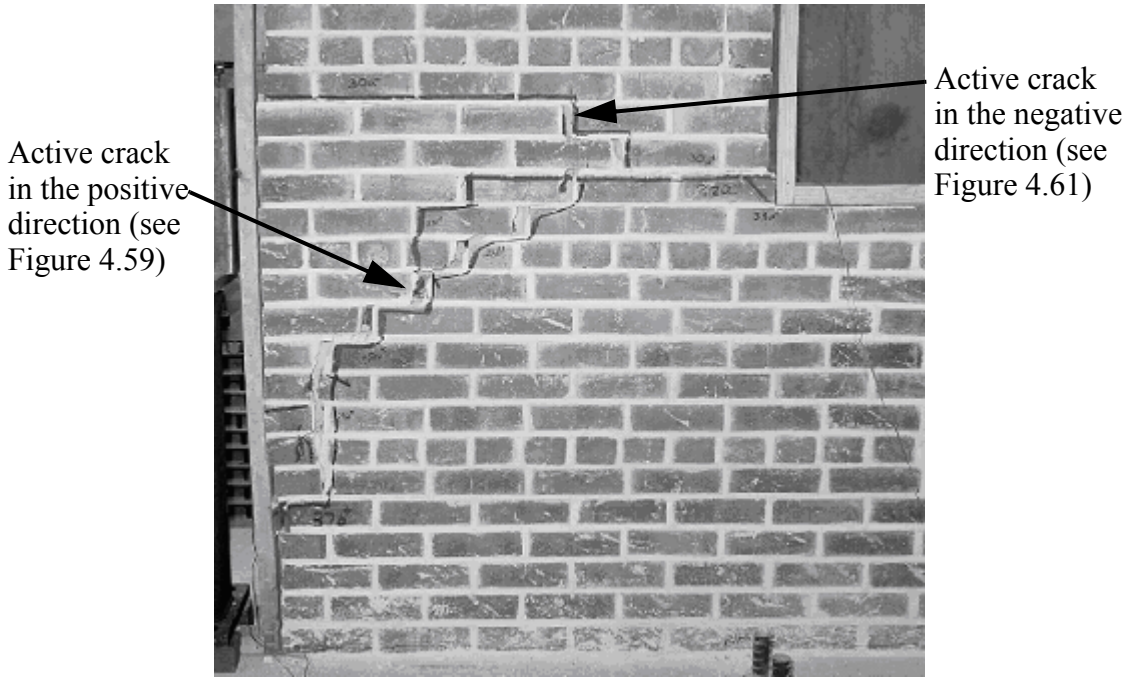

Figure 4.63. Horizontal and diagonal crack at the base of pier PA-9 following Test Run 39 (note, this photograph was taken from inside the structure).

During Test Runs 34 and 35 (i.e. a post-tensioning force of 222 kN (50 kip)) the behavior remained unchanged from past cycles and no new cracks were observed. During

Test Run 37 the diagonal crack in pier PA-7 became fully developed and propagated to the length shown in Figure 4.57. A photograph of pier PA-7 taken after Test Run 39 is shown in Figure 4.64. Additional vertical cracks were observed in Wall 1 below the second floor level during Test Run 39. These cracks extended from the bottom of the second floor actuator down to existing vertical cracks in pier P1-7 and suggested that the entire first story of Wall A was punching through Wall 1.

Figure 4.64. Diagonal Crack observed in pier PA-7 following Test Run 39.

The final mechanism of Wall A in the negative loading direction after post-tensioning was composed primarily of local pier behavior. As indicated in Figure 4.62, all of the first story piers displayed some degree of rocking/sliding deformation. In addition, sliding deformation was observed along the diagonal crack in pier PA-7 and along the diagonal crack above pier PA-10. Beyond the observed local pier deformation, some global rocking was also present throughout all test runs in the negative direction (see

Figure 4.61). Based on the rotation shown in Figure 4.61 and the assumptions outlined previously, global rocking accounted for approximately 3 mm (0.12 in.) or 16% of the roof displacement during Test Run 39. Figure 4.62 shows that this global rocking deformation coupled with the uplift caused by local pier rocking lifted up a large portion of Wall 2.

Similar to the response of Wall A prior to post-tensioning (see Section 4.3.1.2), the cyclic nature of the loading history resulted in the permanent progressive crack opening of several cracks for both levels of post-tensioning force. Figure 4.65 shows a schematic of the residual deformation of Wall A following all of the test runs. Based on visual observations this phenomenon was caused primarily by two factors: overturning moment and unsymmetrical pier behavior modes.

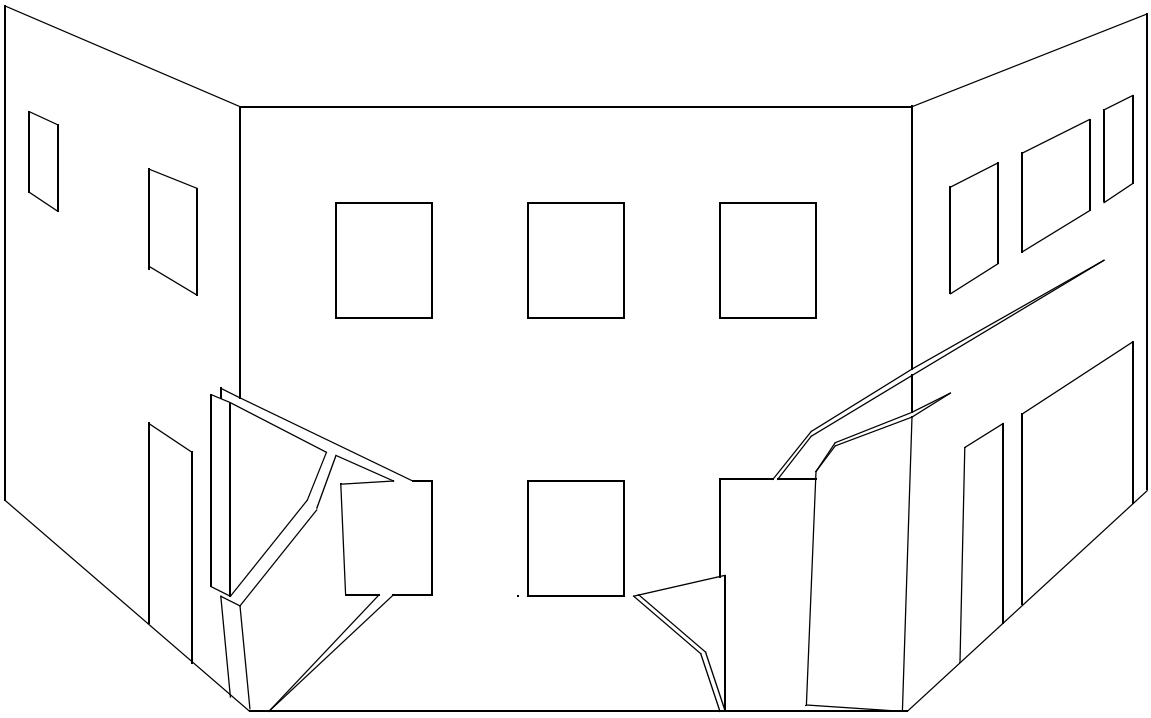

Figure 4.65. Exaggerated schematic illustrating the residual deformation of Wall A following Test Run 39.

The progressive opening of the diagonal cracks above piers PA-7 and PA-10 is attributed to overturning moment and was discussed in Section 4.3.1.2. In contrast, the progressive opening of cracks in the center of pier PA-7 and the lower portion of pier PA-9 is attributed to unsymmetrical pier behavior. In these cases overturning moment may have played a role; however, the unsymmetrical pier failure mode was the primary cause. For example, pier PA-9 displayed varying degrees of rocking/sliding behavior in both directions; however, the active cracks were different in each direction (see Figures 4.60 and 4.62). This resulted in a progressive growth of the diagonal crack at the base of pier PA-9 (see Figure 4.63). The diagonal crack in pier PA-7 opened in a similar manner and is shown in Figure 4.64.

The actual residual crack openings observed following Test Run 39 ranged up to 38 mm (1.5 in.). This magnitude clearly indicates the progressive nature of this phenomenon since the maximum roof displacement imposed was 19 mm (0.75 in.). As seen in Figure 4.65, this progressive crack opening also resulted in the permanent rotation of pier PA-7 and PA-10. Following Test Run 39 the length of Wall A was measured at approximately 915 mm (36 in.) above the foundations (i.e. along the bottom of the window openings), and it was determined that the residual displacement of the cracks had caused the length of the wall to increase approximately 51 mm (2 in.).

4.3.2.3 Response of Post-tensioning Tendons

As mention in the previous section, the observed response of Wall A resulted in a vertical displacement of the upper portion of the structure. Beyond engaging portions of Walls 1 and 2, this displacement also induced additional tensile strain in the post-

tensioning tendons and resulted in an increase in post-tensioning force during loading. Consider Figure 4.66 which shows the force in each of the post-tensioning tendons versus roof displacement during Test Run 33. From this figure it is apparent that the force in each tendon increased by approximately 50% in the positive direction and 70% in the negative direction. In addition, the low-level global rocking observed in the negative loading direction is clearly shown by the differential force in each of the tendons.

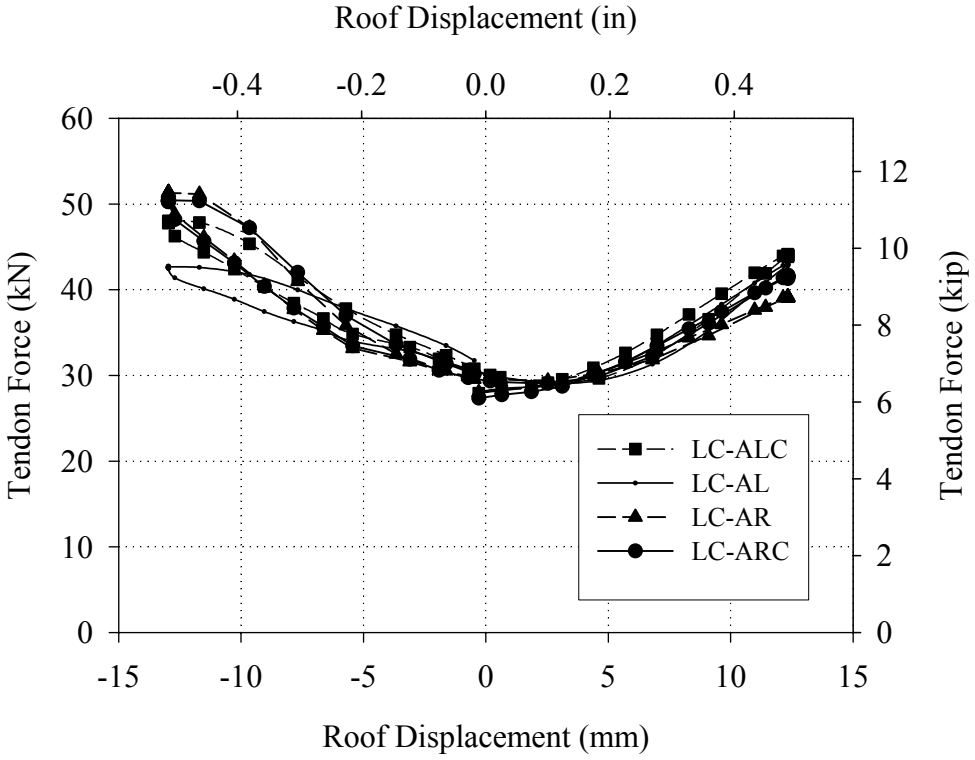

Figure 4.66. Force in each post-tensioning tendon versus roof displacement during Cycle 33a (see Figure 4.62 for gage locations).

Figure 4.67 shows the total post-tensioning force at peak displacement for each test run versus roof displacement. This plot suggests that the increase in post-tensioning force was linearly proportional to the roof displacement for nearly all cycles. This trend is expected as the uplift associated with rocking deformation is also proportional to the lateral displacement.

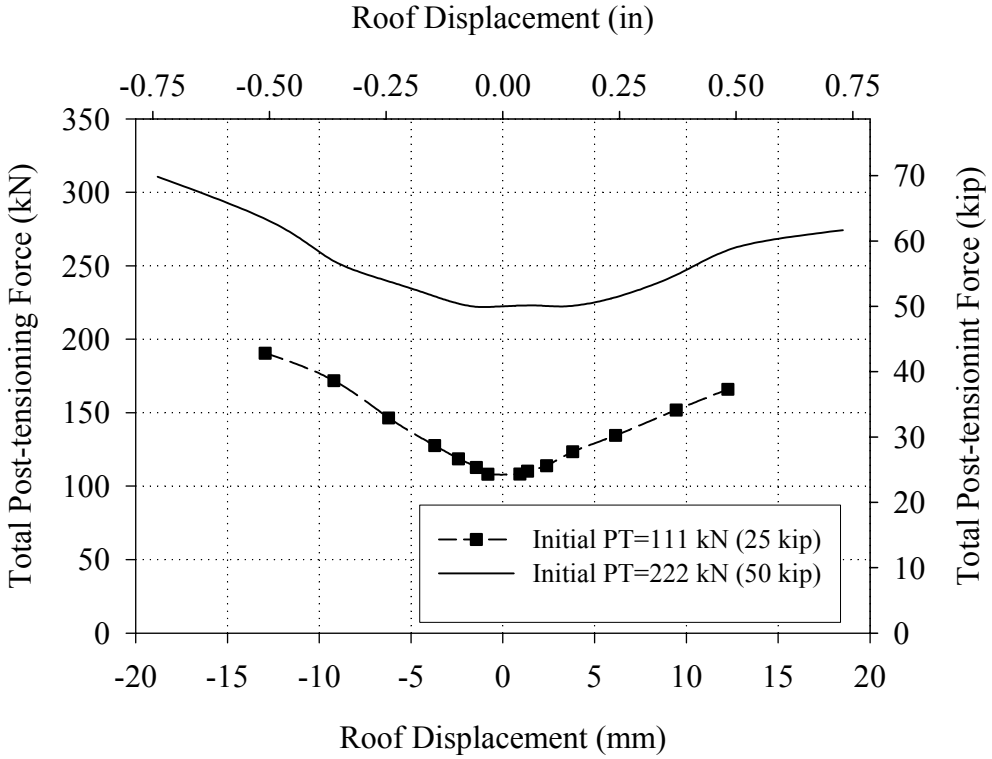

Figure 4.67. Post-tensioning force at peak displacement during each test run versus roof displacement.

4.3.3 Comparison of Wall Response before and after Retrofit

Figure 4.68 shows the base shear versus roof displacement response for Wall A in an unreinforced state and with 111 kN (25 kip) of post-tensioning force. Figure 4.69 shows the base shear versus roof displacement response for Wall A in an unreinforced state and with 222 kN (50 kip) of post-tensioning force. These figures indicate that following post-tensioning the initial stiffness of the wall remained essentially unchanged. In addition, the post-tensioned walls displayed increasing base shear resistance with increasing displacement, whereas the wall prior to post-tensioning displayed a horizontal "yield" plateau. This phenomenon is attributed to the increase in post-tensioning force observed as the roof displacement increased (see Section 4.3.2.3).

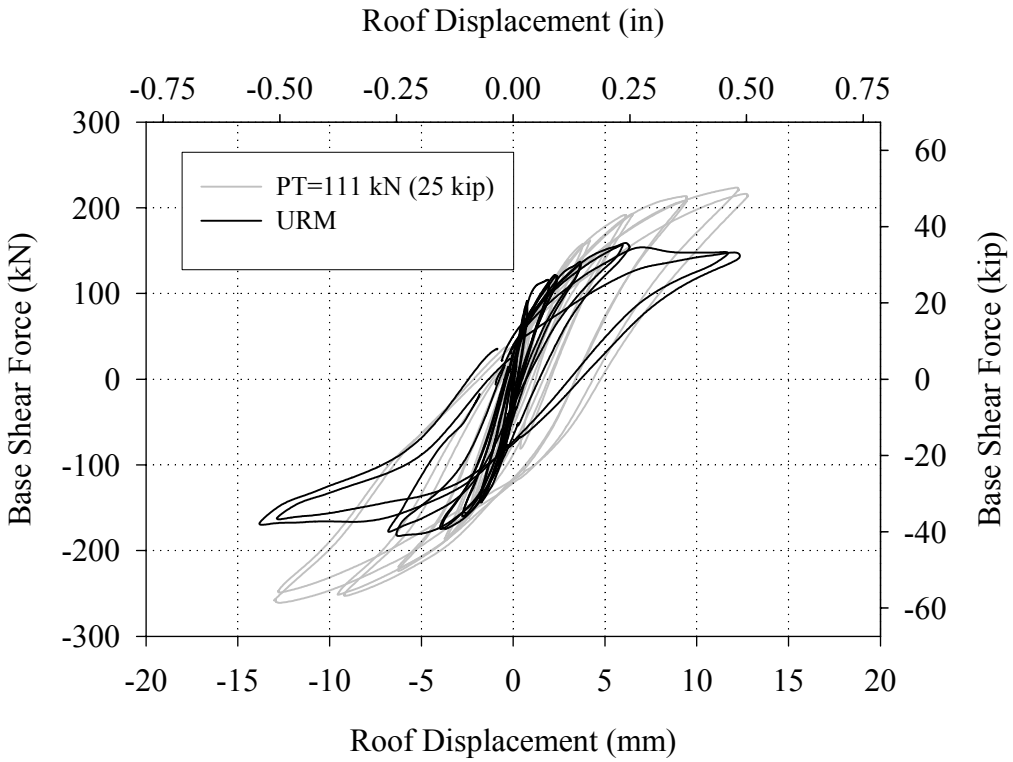

Figure 4.68. Base shear versus roof displacement response of Wall A in an unreinforced state and with 111 kN (25 kip) of post-tensioning force.

Table 4.9 summarizes the peak resistance and displacement at peak resistance for Wall A before and after retrofit. This table shows that substantial strength increases were achieved for both levels of post-tensioning. Specifically, the 111 kN (25 kip) post-tensioning level resulted in a 40% and 43% increase in base shear resistance for the positive and negative directions, respectively. The 222 kN (50 kip) post-tensioning level resulted in a 57% and 62% increase in base shear resistance for the positive and negative directions, respectively. Note that doubling the post-tensioning stress did not result in a proportional increase in the base shear capacity. This decrease in effectiveness is attributed to the change in failure modes of the outside piers from rocking to diagonal tension and underscores the potential for post-tensioning to decrease the displacement capacity of a URM wall.

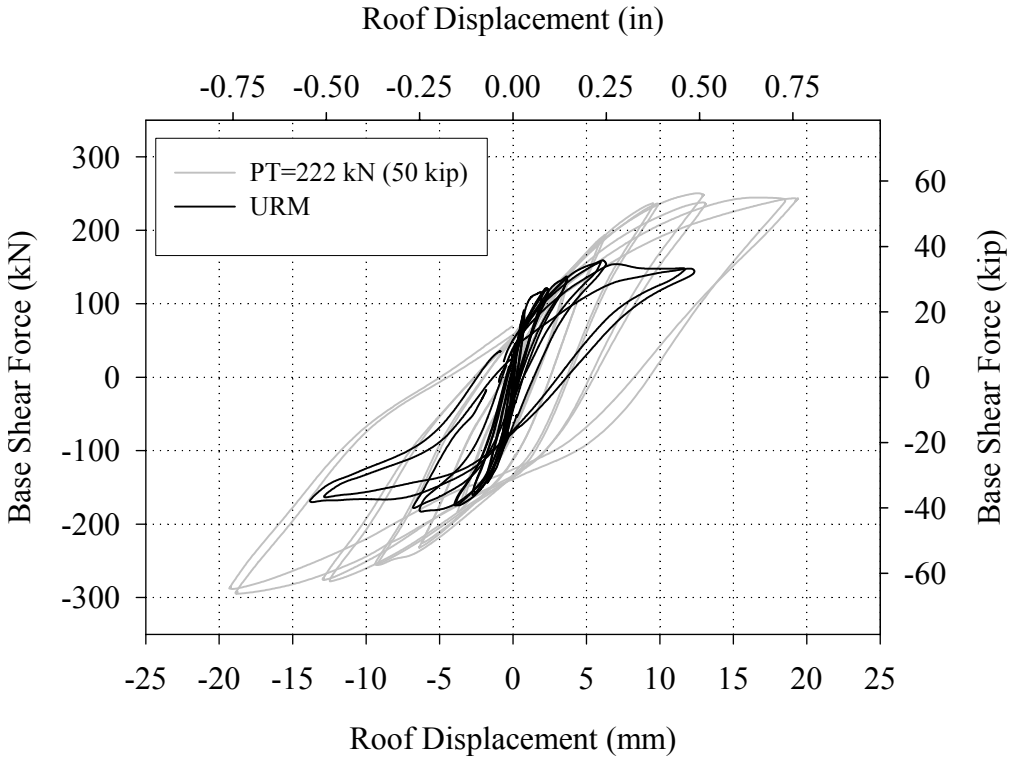

Figure 4.69. Base shear versus roof displacement response of Wall A in an unreinforced state and with 111 kN (25 kip) of post-tensioning force.

Table 4.9. Comparison of base shear capacity of Wall A before and after retrofit.

	Base Shear Capacity		Roof Displacement at Peak Resistance	
	Positive	Negative	Positive	Negative
URM	159 kN (36 kip)	182 kN (41 kip)	6 mm (0.24 in.)	6 mm (0.24 in.)
PT = 111 kN (25 kip)	223 kN (50 kip)	261 kN (59 kip)	12.3 mm (0.5 in.)	12.3 mm (0.5 in.)
PT = 222 kN (50 kip)	250 kN (56 kip)	294 kN (66 kip)	12.3 mm (0.5 in.)	19 mm (0.75 in.)

Figure 4.70 shows the energy dissipated by both stories of Wall A before and after retrofit versus roof displacement. The details of the procedure used to generate these plots is given in Appendix B. Figure 4.71 shows the percentage of energy dissipated by the first

floor of Wall A before and after retrofit (note that due to the small amount of energy dissipated by the second story of Wall A, only the first story was included in this plot).

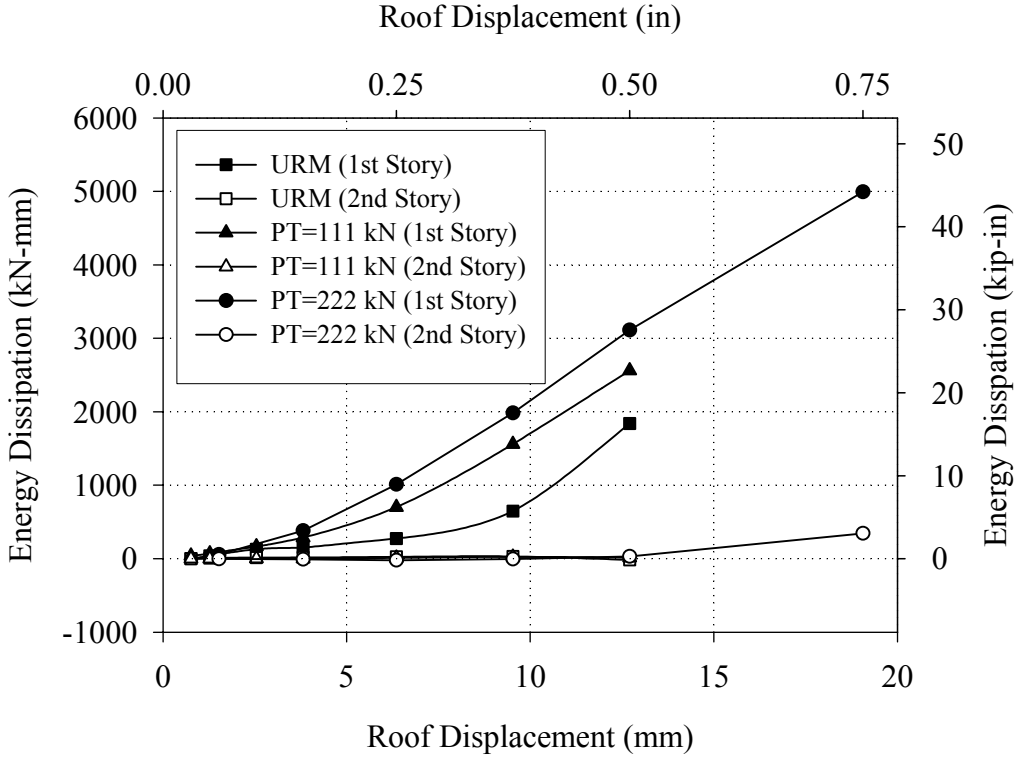

Figure 4.70. Energy dissipated by each story of Wall A before and after retrofit.

Figure 4.70 shows that the majority of the energy dissipation was due to the response of the first story. In addition, the energy dissipated as well as the percentage of energy dissipated increased slightly with increasing post-tensioning force (see Figure 4.71). This increase was likely caused by the observed evolution from primarily rocking behavior to more diagonal tension/stair-stepped bed-joint sliding deformation as the level of post-tensioning increase.

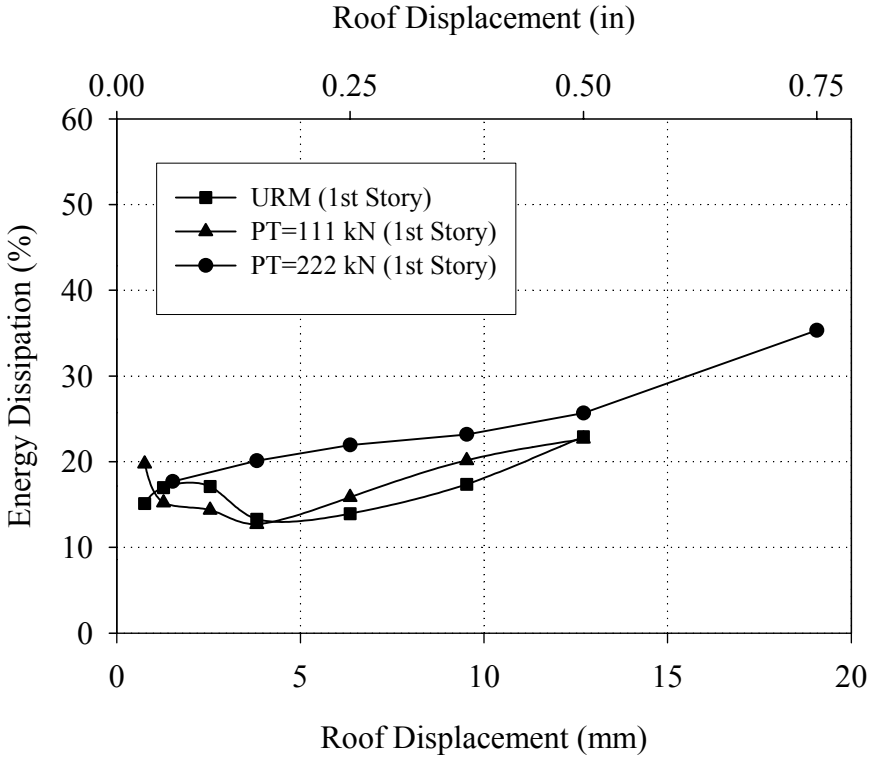

Figure 4.71. Percentage of energy dissipated by the first story of Wall A before and after retrofit.

4.4 Response of Wall B

A summary of the in-plane displacements imposed on Wall B is given in Table 4.10 along with test run and cycle designation. Figures 4.45 and 4.72 show a graphical representation of the loading history imposed before and after retrofit, respectively. Prior to retrofit Wall B, cyclic displacements up to 12.7 mm (0.5 in.) in each loading direction were imposed. Based on the observed failure modes, the resulting maximum drifts exceeded the Collapse Prevention performance level for certain piers (ATC, 2000). Following these cycles the wall was strengthened with GFRP overlays and NSM rods (see Chapter 3), and subjected to two series of increasing cyclic displacements up to 12.7 mm (0.5 in.) and 38 mm (1.5 in.). Currently no performance levels are available

for URM walls strengthened with GFRP; however, if the performance levels available for URM walls are employed the displacements imposed on the structure for each series of cycles exceeded the Collapse Prevention performance level (ATC, 2000).

Table 4.10 Summary of displacements imposed on Wall B

	Test Run	Target Roof Displacement mm (in)	Target Second Floor Displacement mm (in)
URM	20	+/- 0.3 (0.01)	+/- 0.24 (0.008)
	21	+/- 0.8 (0.03)	+/- 0.64 (0.024)
	22	+/- 1.8 (0.07)	+/- 1.44 (0.056)
	23	+/- 2.5 (0.1)	+/- 2.0 (0.08)
	24	+/- 3.8 (0.15)	+/- 3.0 (0.12)
	25	+/- 6.4 (0.25)	5.8 (0.23), -5.4 (-0.21)
	26	+/- 12.7 (0.5)	11.4 (0.45), -8.9 (-0.35)
Post-Retrofit	27	+/- 1 (0.04)	+/- 0.8 (0.03)
	28	+/- 1.5 (0.06)	+/- 1.1 (0.043)
	29	+/- 2.5 (0.1)	1.9 (0.073), -1.9 (-0.076)
	30	+/- 3.8 (0.15)	2.8 (0.111), -3.1 (-0.123)
	31	+/- 6.4 (0.25)	4.8 (0.188), -5.1 (-0.2)
	32	+/- 9.5 (0.375)	7.3 (0.289), -7.6 (-0.30)
	33	+/- 12.7 (0.5)	9.5 (0.375), -9.8 (-0.385)
	34	+/- 1.3 (0.05)	+/- 1 (0.04)
	35	+/- 3.8 (0.15)	2.9 (0.115), -3.2 (-0.125)
	36	+/- 6.4 (0.25)	5.2 (0.205), -5.3 (-0.21)
	37	+/- 9.5 (0.375)	7.6 (0.30), -7.9 (-0.311)
	38	+/- 12.7 (0.5)	10.3 (0.405), -10.5 (-0.415)
	39	+/- 19.1 (0.75)	+/- 15.8 (0.623)
	40*	+/-25.4 (1.0)	20.3 (0.8), 17.8 (-0.7)
	41*	+/- 38.1 (1.5)	30.5 (1.2), -28.7 (-1.13)

* Wall A was held at zero displacement

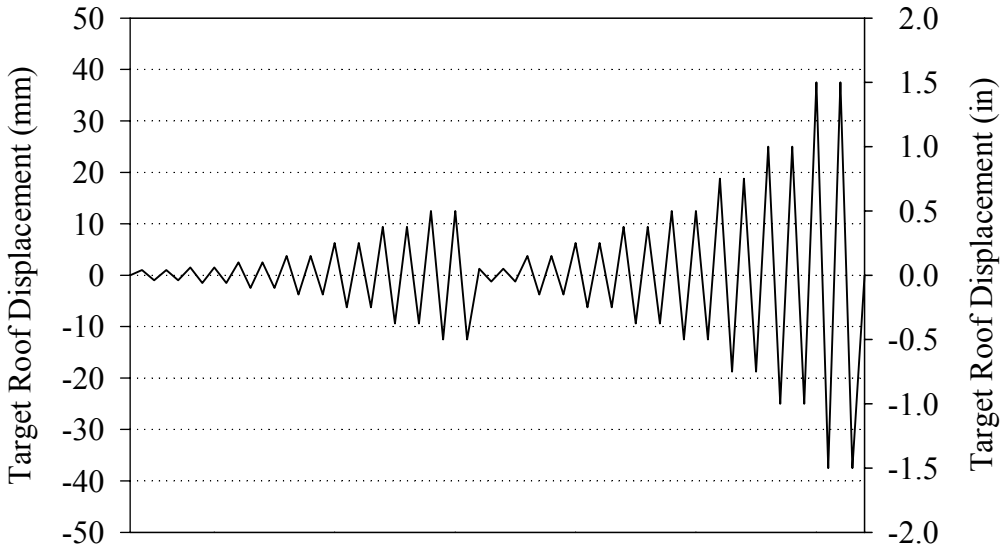

Figure 4.72. Loading history applied to Wall B after retrofit.

4.4.1 Response Prior to Retrofit

4.4.1.1 Force-Displacement Behavior

Table 4.11 shows the initial stiffness calculated for each story of Wall B in each loading direction. These stiffnesses correspond to a roof displacement of 0.25 mm (0.01 in.) and were determined by dividing the base shear force by the roof displacement. In contrast to the elastic stiffnesses reported for Walls 1 and 2, these stiffnesses do not reflect the elastic response of Walls B as significant cracking was induced during the in-plane loading of Walls 1 and 2 (see Sections 4.1 and 4.2).

Table 4.11. Initial Stiffness of Wall B prior to retrofit.

	Positive Direction	Negative Direction
Wall B	159 kN/mm (910 kip/in)	156 kN/mm (890 kip/in)

Figure 4.73 shows the recorded base shear versus roof displacement response of Wall B prior to retrofit. The maximum strength of Wall B was 191 kN (43 kip) in the positive direction and 165 kN (37 kip) in the negative direction. The corresponding roof drifts were approximately 6 mm (0.24 in.) in each direction. As apparent from Figure 4.73, the hysteresis of Wall B displayed a great deal of pinching up to a roof displacement of approximately 6 mm (0.24 in.) in both loading directions. As the imposed displacements increased beyond this level, the response of Wall B displayed a significant increase in energy dissipation, although some pinching was still observed.

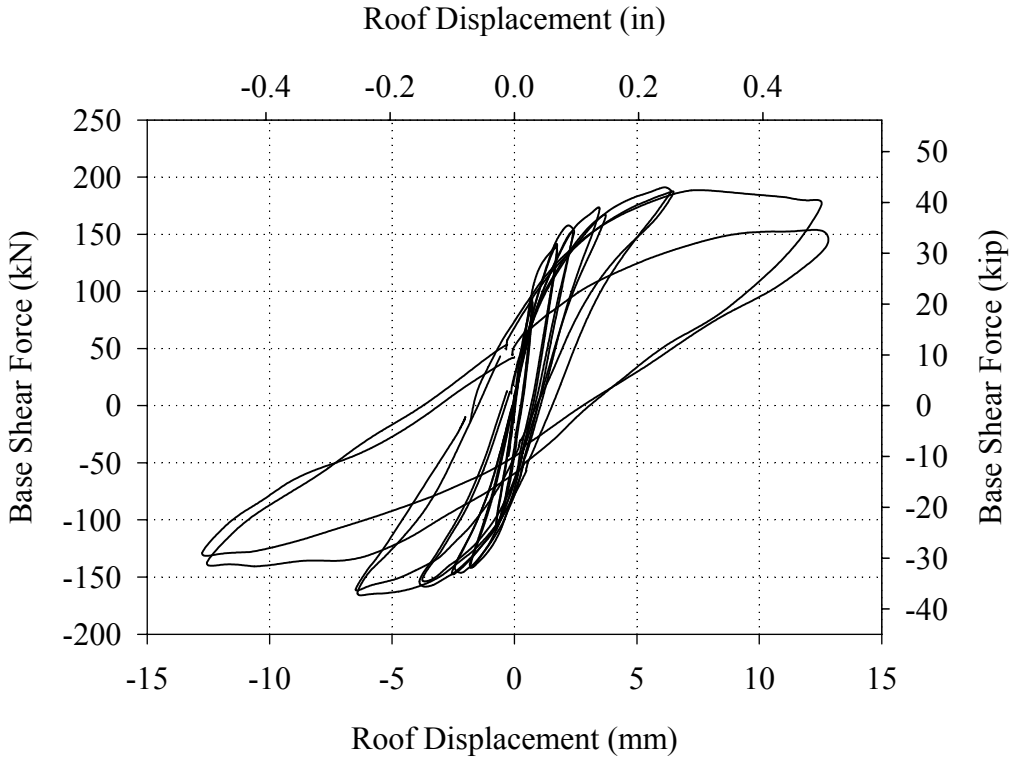

Figure 4.73. Base shear force versus roof displacement response of Wall B prior to retrofit.

4.4.1.2 Damage Progression and Wall Behavior

The crack pattern of Wall B and out-of-plane Walls 1 and 2 following Test Run 26 are shown in Figures 4.74 through 4.76. Note that the cracks that formed during Test Runs 20 through 26 are shown in black and those that formed during past cycles are shown in gray. Figures 4.77 and 4.78 show schematics illustrating the final mechanism of Wall B and out-of-plane Walls 1 and 2 prior to retrofit in the positive and negative directions, respectively.

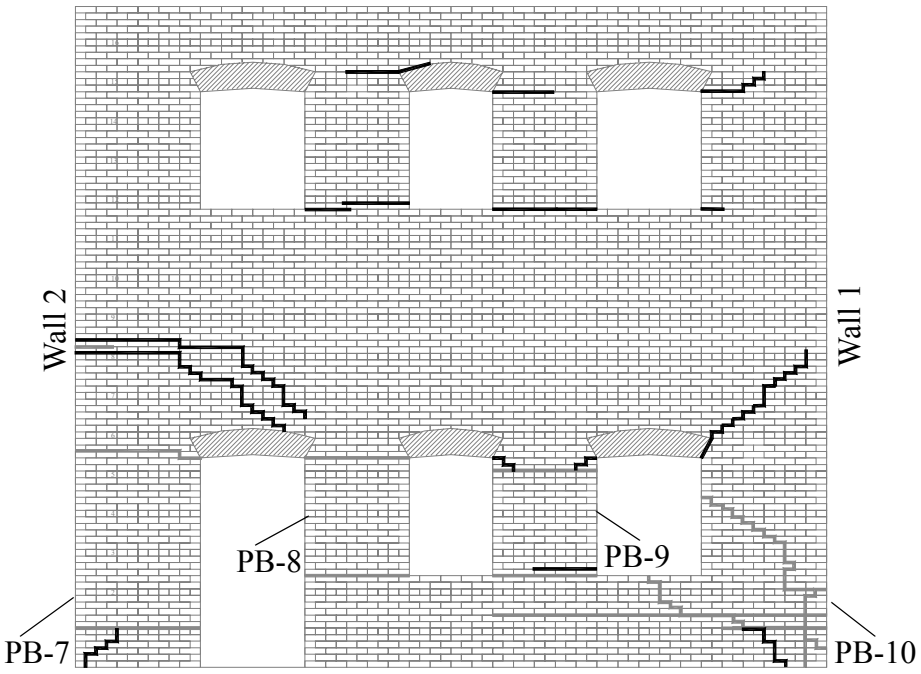

Figure 4.74. Crack pattern of Wall B following Test Run 26.

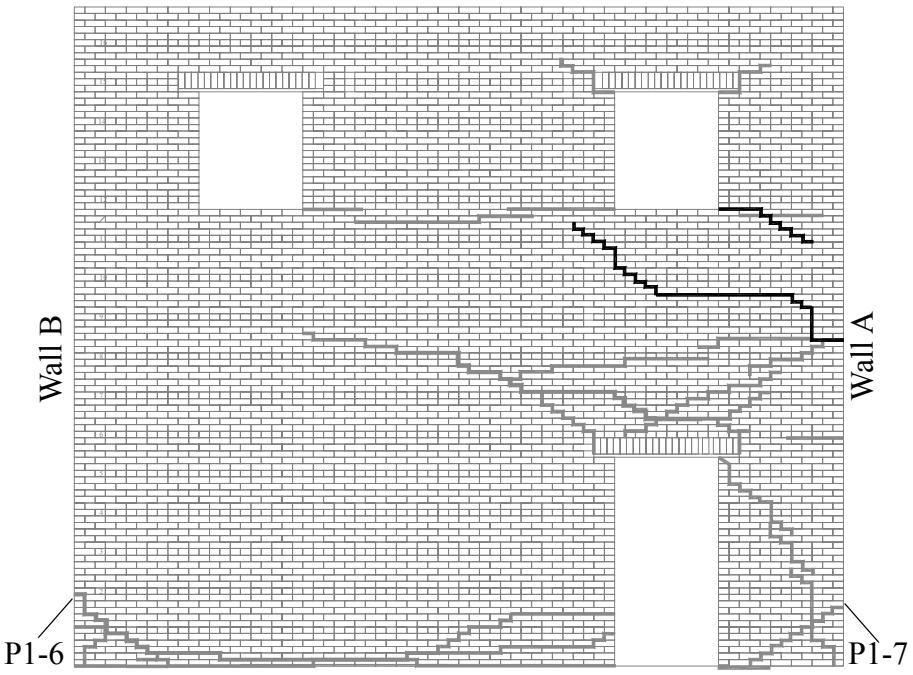

Figure 4.75. Crack pattern of Wall 1 following Test Run 26.

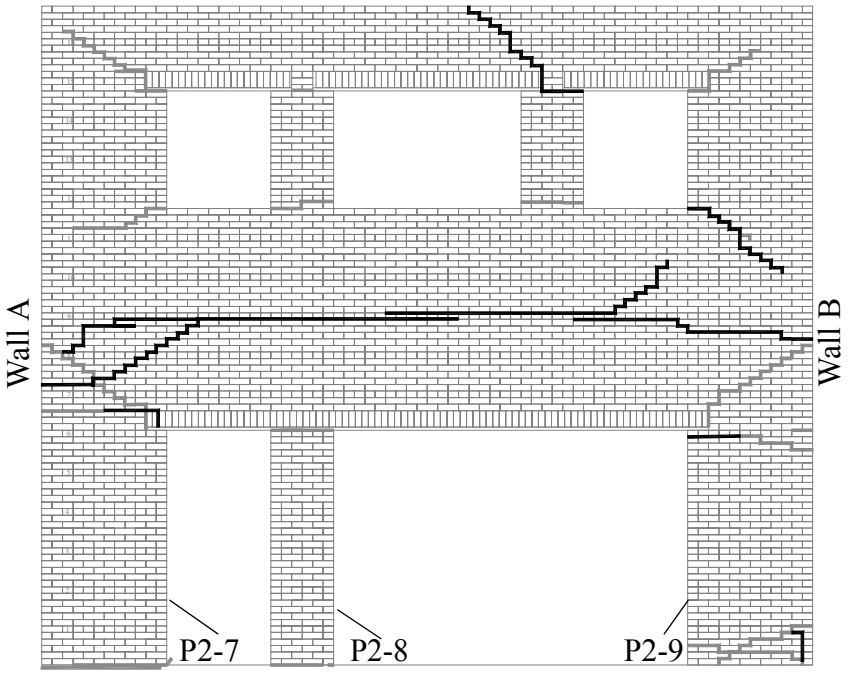

Figure 4.76. Crack pattern of Wall 2 following Test Run 26.

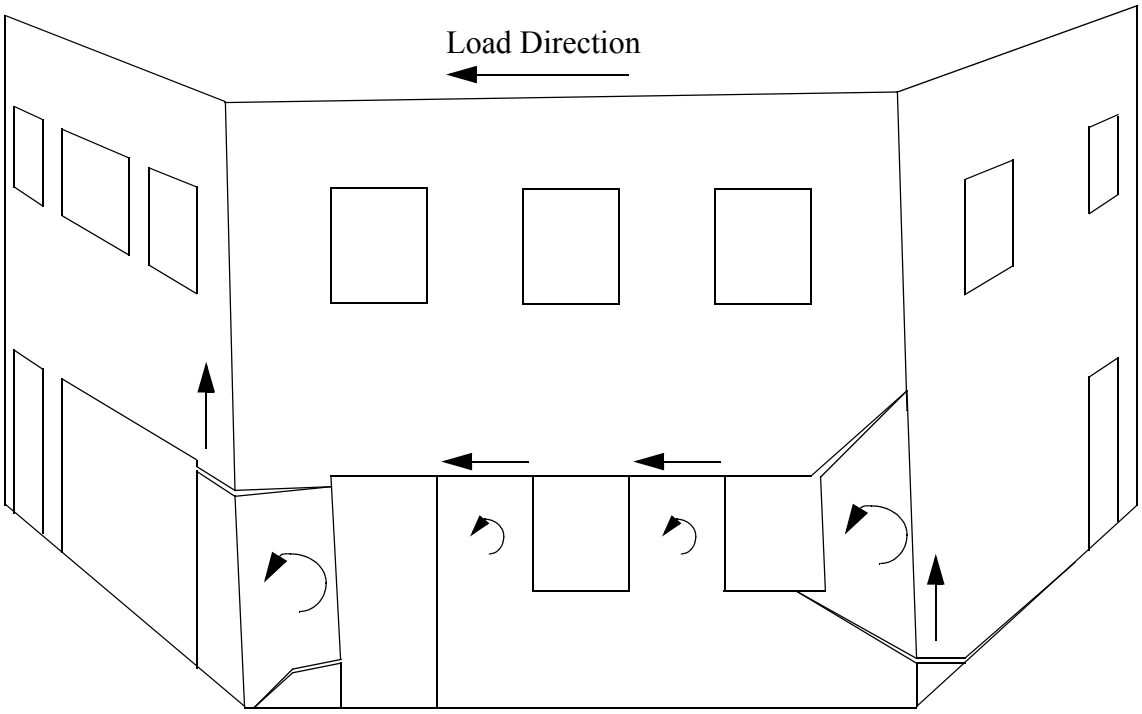

Figure 4.77. Exaggerated schematic illustrating the response of Wall B and out-of-plane Walls 1 and 2 in the positive direction prior to retrofit.

In the positive loading direction no new cracks were observed during Test Runs 20 and 21. During Test Run 22 a diagonal crack above pier PB-7 at the corner of the window opening formed. This crack propagated during the initial cycles of Test Run 23 and 24 to the length shown in Figure 4.74. During these test runs, all of the first story piers displayed low-level rocking deformation. During Test Run 26 the rocking mechanism of pier PB-7 caused the existing horizontal crack above pier P2-9 to propagate to the door opening in Wall 2 (see Figure 4.76).

The final mechanism of Wall B in the positive direction prior to retrofit consisted primarily of local pier behavior (see Figure 4.77). During Test Run 26 the behavior of the interior piers (PB-8 and PB-9) switched from rocking to primarily sliding along the upper pier boundary. Outside piers PB-7 and PB-10 continued to display rocking deformation

during these cycles. In addition, the uplift associated with the rocking deformation of piers PB-7 and PB-10 lifted up a portion of Wall 2 above pier P2-9 and a portion of Wall 1 above pier P1-6, respectively.

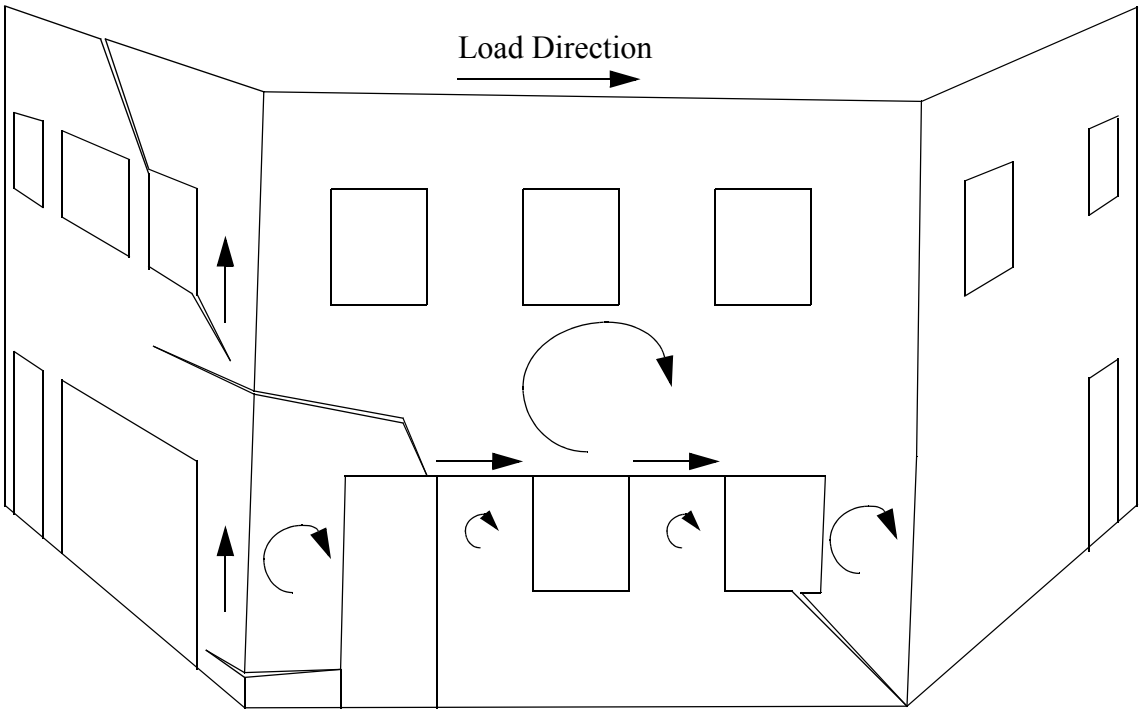

Figure 4.78. Exaggerated schematic illustrating the behavior of Wall B and out-of-plane Walls 1 and 2 in the negative direction prior to retrofit.

In the negative direction no new cracks were observed during Test Runs 20 through 22. During Test Run 23 a diagonal crack initiated below the window opening between piers PB-9 and PB-10 and propagated downward towards existing cracks during Test Runs 24 and 25 (see Figure 4.74). The deformation of the wall during these cycles was primarily due to the rocking of the first story piers. During Test Run 26 a diagonal crack initiated above pier PB-7 and propagated horizontally into Wall 2 at the second floor level (see Figure 4.76). Recall, that a similar crack propagated from Wall A during Test Run 25 and extended across approximately 80% of Wall 2 during the initial cycle of Test

Run 26 (see Section 4.3). Also during Test Run 26 a diagonal crack from the second floor actuator propagated diagonally upwards to the roof of Wall 2.

The final mechanism of Wall B in the negative direction prior to retrofit consisted of both local pier deformation as well as global rocking of the entire wall. The global rocking portion of the deformation lifted up the upper right corner of out-of-plane Wall 2 as shown in Figure 4.78. In addition, this deformation acted to reduce the vertical stress in pier PB-7 thus limiting the deformation of this pier. The local response of the interior piers (PB-8 and PB-9) consisted primarily of sliding deformation along the upper boundary although some low-level rocking deformation was also observed. Pier PB-10 displayed rocking deformation during these cycles.

4.4.2 Response after Retrofit

4.4.2.1 Force-Displacement Behavior

Figures 4.79 and show the recorded base shear versus roof displacement response of Wall B after retrofit during Test Runs 27 through 33 and Test Runs 27 through 38, respectively. Figure 4.81 shows the complete base shear versus roof displacement response of Wall B after retrofit. The maximum strength of Wall B was 253 kN (57 kip) in the positive direction and 211 kN (48 kip) in the negative direction. The corresponding roof displacements were approximately 12 mm (0.47 in.) in both directions.

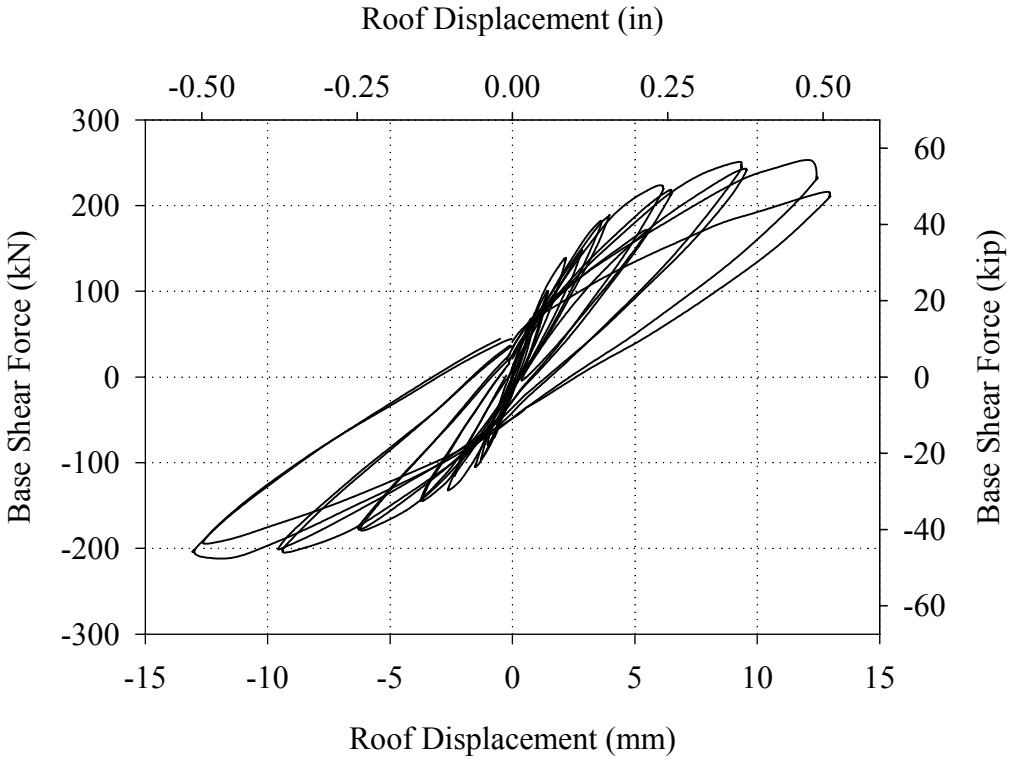

Figure 4.79. Base shear force versus roof displacement response of Wall B during Test Runs 27 through 33.

Figure 4.79 shows Wall B degraded little in terms of peak resistance through the initial cycle of Test Run 33 (i.e. a roof displacement of 12.7 mm (0.5 in.)). However, during the redundant cycle conducted at this roof displacement the resistance in the positive direction decreased by approximately 20%. From Figure it is apparent that during Test Runs 34 through 38 the response of the wall essentially followed the behavior recorded during the redundant cycle of Test Run 33. That is, little degradation in the response was observed during the second series of increasing displacements. As the imposed roof displacement increased past 12.7 mm (0.5 in.), some degradation was observed during the redundant cycles. However, during these cycles the peak resistance increased with increasing roof displacement in the positive direction and was fairly constant in the negative direction.

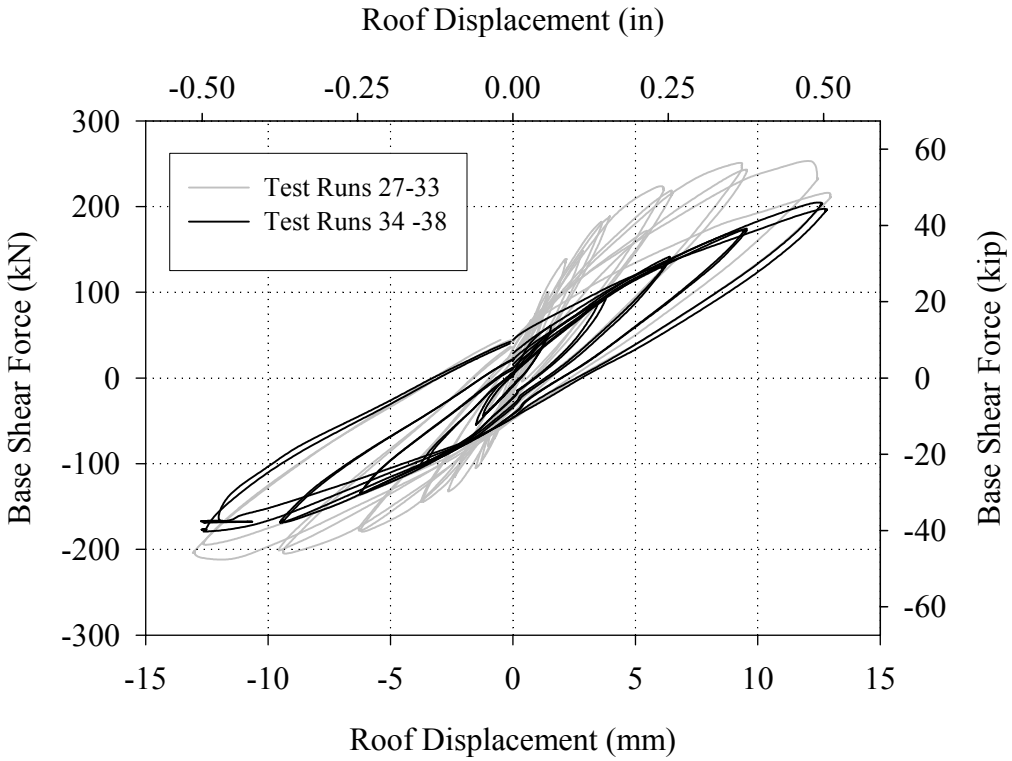

Figure 4.80. Base shear force versus roof displacement response of Wall B following retrofit during Test Runs 27 through 38.

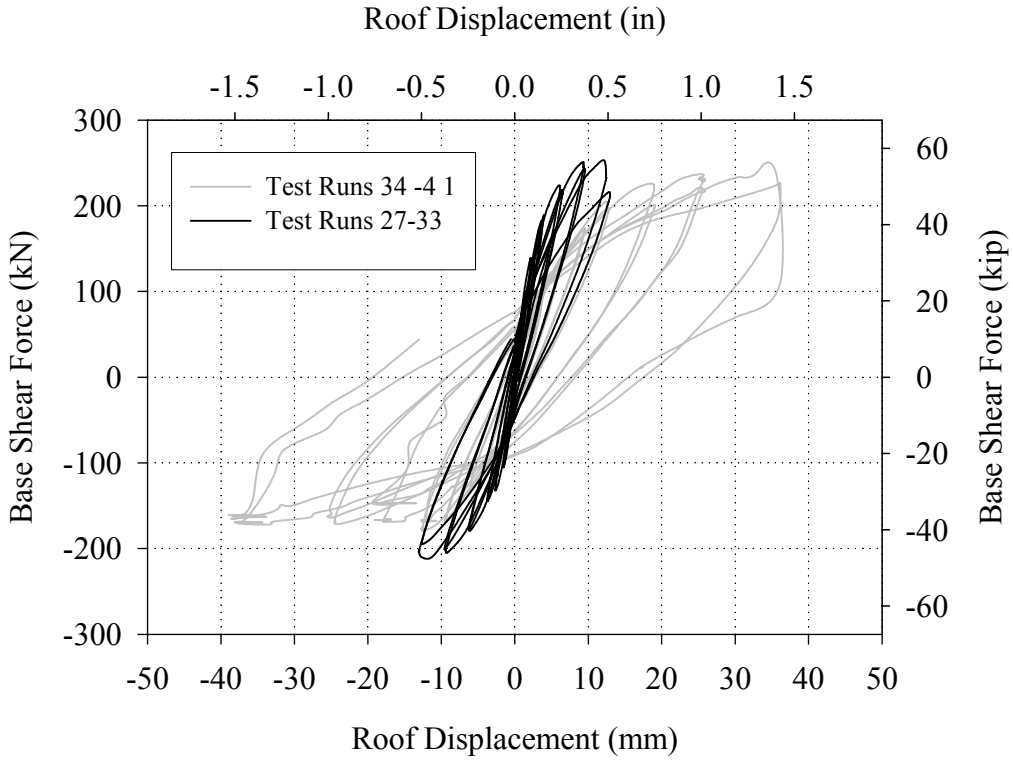

Figure 4.81. Complete base shear force versus roof displacement response of Wall B after retrofit.

4.4.2.2 Damage Progression and Wall Behavior

The crack pattern of Wall B and out-of-plane Walls 1 and 2 following Test Run 41 are shown in Figures 4.82 through 4.84. Note that the cracks that formed prior to retrofit are shown in gray and the cracks observed following retrofit are shown in black. Figures 4.85 and 4.88 show exaggerated schematics illustrating the final mechanism of Wall B and out-of-plane Walls 1 and 2 in the positive and negative directions, respectively.

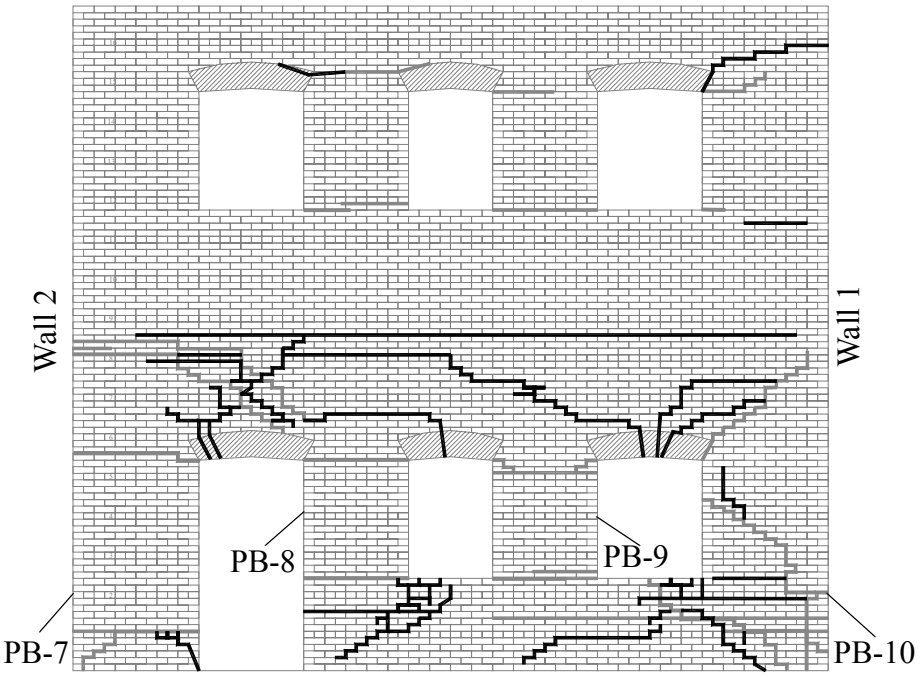

Figure 4.82. Crack pattern in Wall B following Test Run 41.

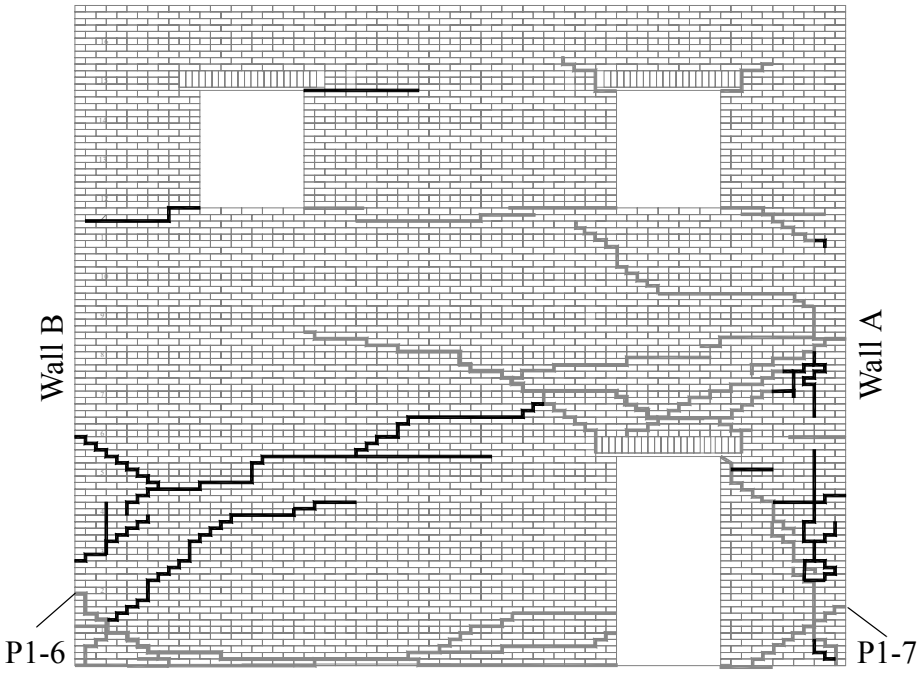

Figure 4.83. Crack pattern in Wall 1 following Test Run 41.

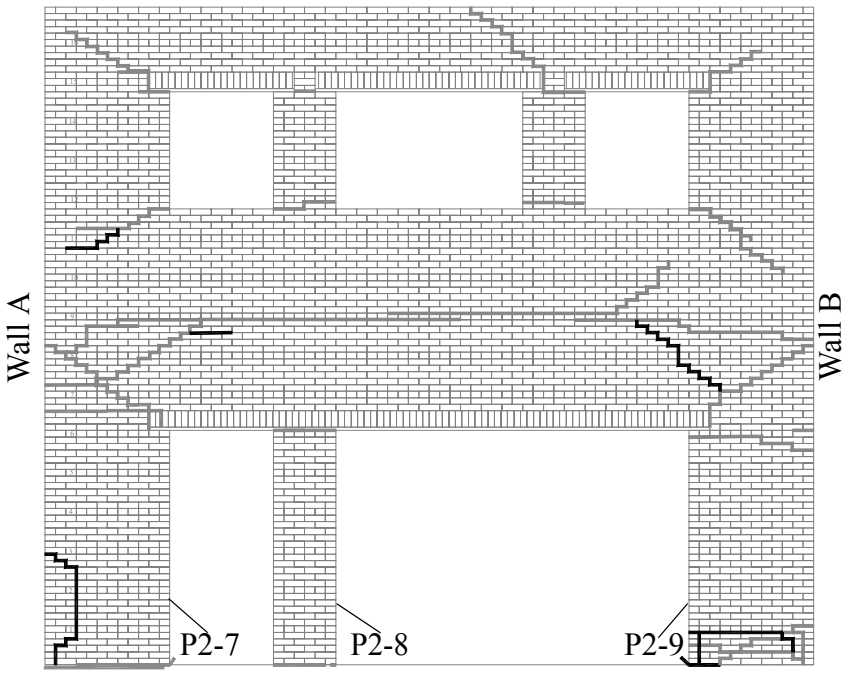

Figure 4.84. Crack pattern in Wall 2 following Test Run 41.

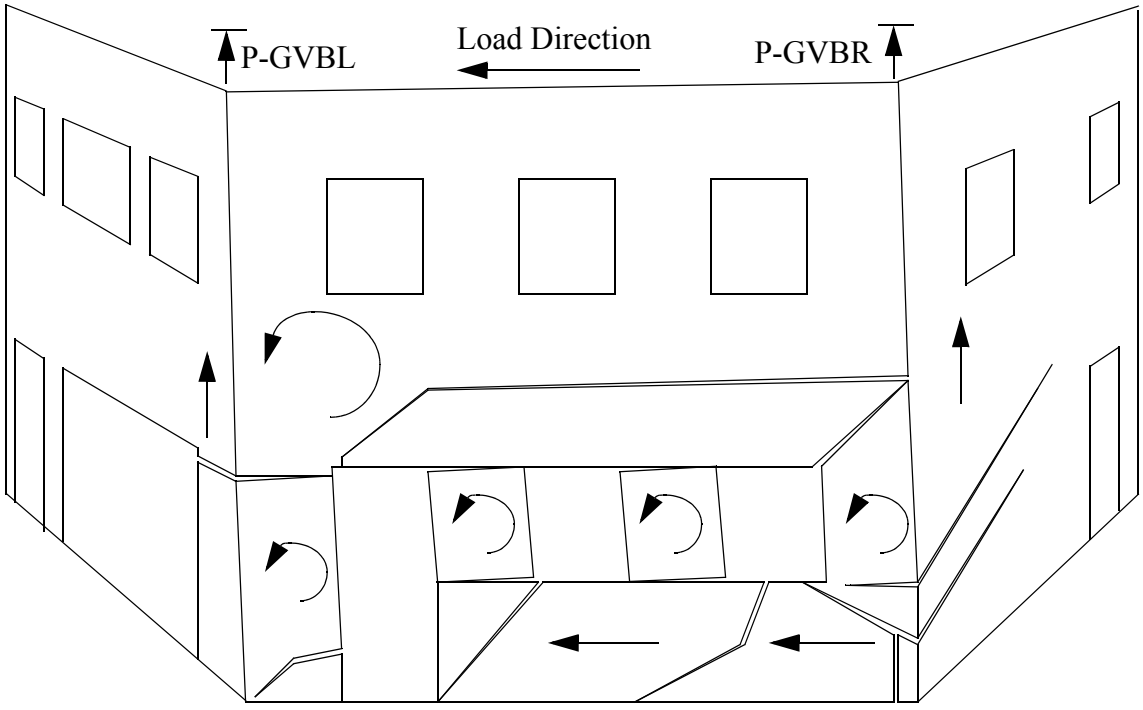

Figure 4.85. Exaggerated schematic illustrating the final mechanism of Wall 1 and out-of-plane Walls A and B in the positive direction following retrofit.

In the positive direction, the response of Wall B during Test Runs 27 through 38 was similar to the initial performance observed prior to retrofit (see Section 4.4.1). That is, the majority of the deformation focused on the rocking of the first story piers. Recall that during the final cycles conducted prior to retrofit, significant sliding deformation occurred along the top of the interior piers. This observed deformation decreased substantially after retrofit. No new cracks were observed during these cycles.

During Test Run 39 a diagonal crack formed in the spandrel above the door opening in Wall B and extended from the left side of the arch lintel upwards to the second floor level. In addition, the existing crack at the base of pier PB-10 propagated diagonally upwards approximately 2000 mm (80 in.) into out-of-plane Wall 1. During Test Run 40 this crack propagated to the length shown in Figure 4.83 and an additional crack in this area formed. Furthermore, diagonal cracks were also observed during Test Run 40 below piers PB-8 and PB-9 as well as above pier PB-10. In addition, during this test run horizontal cracks were observed across the entire wall at the second floor level and across the base of the wall below piers PB-8 through PB-10. Following the formation of the crack at the base, the wall began to slide along the foundation (see Figure 4.85). Figure 4.86 shows a photograph taken below pier PB-8 that illustrates this observed sliding deformation.

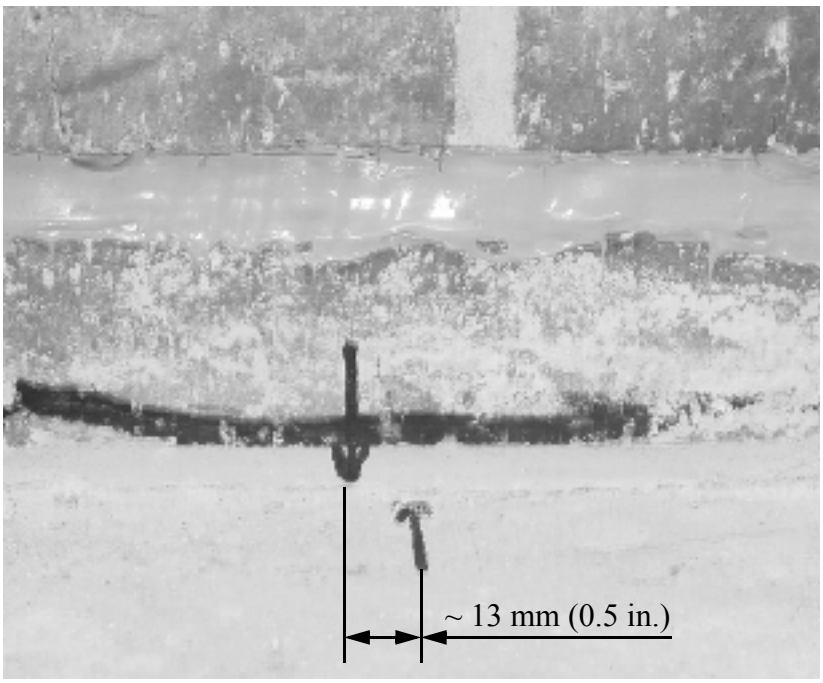

Figure 4.86. Photograph of the base of Wall B taken during Test Run 41 showing the offset caused by the sliding deformation.

The final mechanism of Wall B in the positive direction consisted primarily of sliding deformation along the foundation below piers PB-8 through PB-10 as well as local rocking of all first story piers. In general, the observed sliding deformation increased with increasing roof displacement up to approximately 12.7 mm (0.5 in.) during Test Run 41. As apparent from Figure 4.85 the uplift associated with the local rocking deformations of the first story piers lifted up portions of out-of-plane Walls 1 and 2.

Beyond the primary mechanism of Wall B, a small amount of global rocking was also observed. This observed deformation opened the horizontal crack at the second floor level and resulted in the rotation of the second story of Wall B and pier PB-7. Figure 4.87 shows the vertical displacements of the roof of each side of Wall B measured during Test Run 41 versus horizontal roof displacement (see Figure 4.85 for gage locations). Based on

the assumptions outlined in Section 4.2.2.2, the global rotation implied by this figure accounts for approximately 6 mm (0.24 in.) or 16% of the imposed roof displacement.

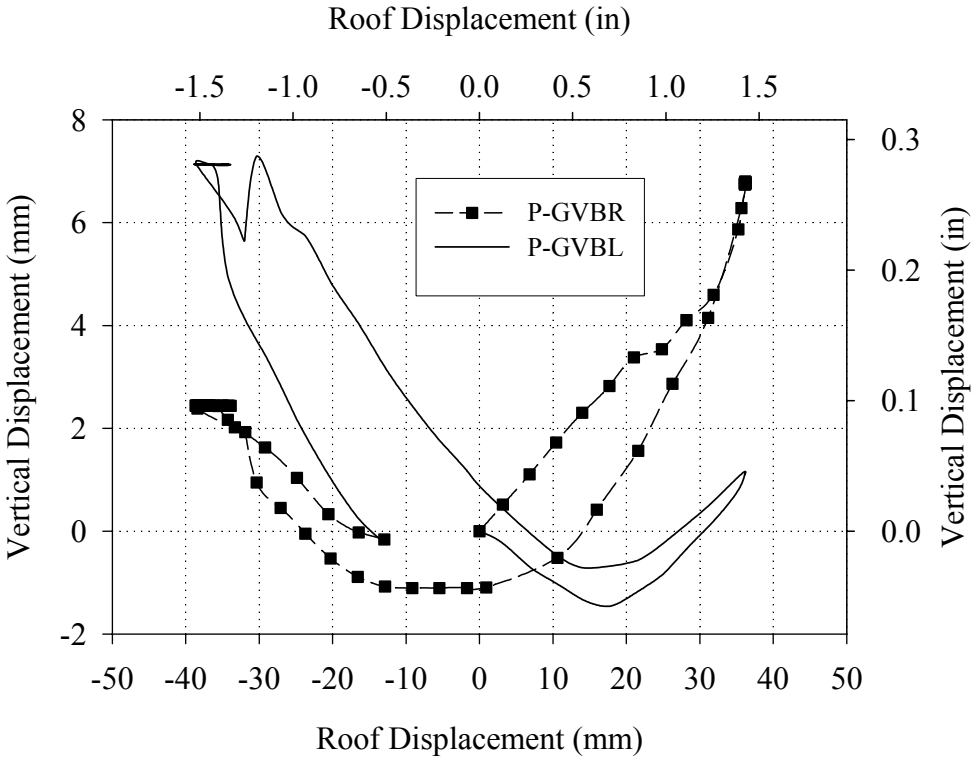

Figure 4.87. Vertical displacement of both sides of the roof of Wall B versus lateral roof displacement during Cycle 41c (see Figure 4.85 for gage locations).

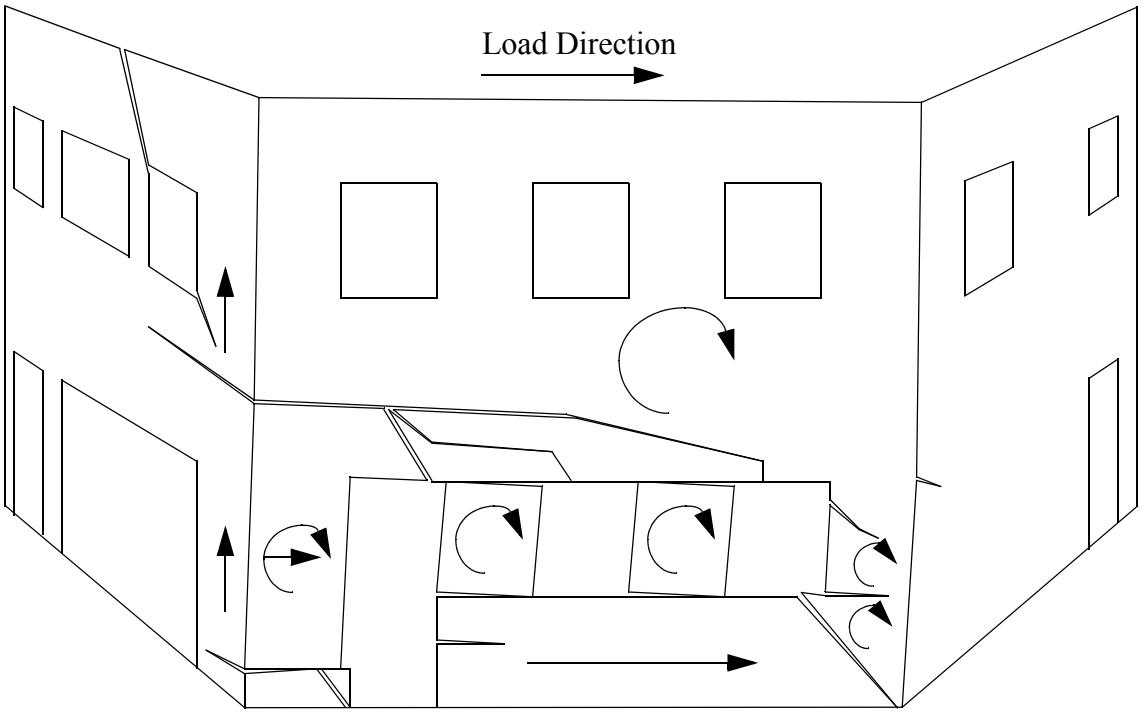

Figure 4.88. Exaggerated schematic illustrating the final mechanism of Wall 1 and out-of-plane Walls A and B in the negative direction after retrofit.

In the negative loading direction during Test Runs 27 through 38, the response of Wall B was very similar to the initial response observed prior to retrofit (see Figure 4.78). That is, the response was a combination of local pier behavior and global rocking. However similar to the positive direction, the sliding deformation observed during the final cycles conducted prior to retrofit decreased significantly and all of the first story piers displayed rocking. No new cracks were observed during these cycles.

During Test Run 39 the rocking deformation of pier PB-7 resulted in the formation of an additional horizontal crack at the base of pier P2-9. During Test Run 40 additional diagonal cracks formed in the spandrel above the door opening as well as in Wall 2 above pier P2-9. In addition, during this test run further horizontal and diagonal cracking was

observed at the base of pier PB-10. Similar to the observed behavior in the positive direction, significant sliding deformation occurred along the foundation below piers PB-8 through PB-10 during Test Runs 40 and 41.

During Test Run 41 two cracks formed in the spandrel above the door opening and propagated to the arch lintels above both window openings. Also during this test run at a roof displacement of approximately 1.3 in, the lower corner of pier PB-7 separated from the remainder of the pier causing the pier to abruptly rotate downward and slide along the base (see Figures 4.88). Essentially, the rotation of the pier was recovered and translated into sliding deformation. Figure 4.89 shows a photograph of the lower right corner of pier PB-7 taken after Test Run 41.

Figure 4.89. Horizontal and diagonal crack at the base of pier PB-7 following Test Run 41.

As indicated by Figure 4.88, the final mechanism of Wall B in the negative loading direction after retrofit consisted of sliding deformation of pier PB-7 and below piers PB-8 through PB-10, local rocking of piers PB-8 through PB-10, and low-level global rocking. In general, the sliding deformation along the foundation in the negative loading direction was approximately equal to the sliding deformation in the positive direction, thus resulting in very small residual displacements. As illustrated by Figure 4.88, the vertical deformation associated with the local rocking of the first story piers as well as the global rocking of the entire wall lifted up the upper right portion of Wall 2. Utilizing the assumptions outlined in Section 4.2.2.2 the global rotation in the negative direction implied by Figure 4.87 accounted for approximately 4.6 mm (0.18 in.) or 12% of the imposed roof displacement during Cycle 41c.

4.4.2.3 Response of the NSM Rods

During the initial cycle of Test Run 29 popping noises were heard coming from the NSM rods above piers PB-7 and PB-10. Specifically, these noises seemed to originate in the vicinity of the diagonal cracks above these piers. These noises continued during the initial cycles of Test Runs 30 through 33. In addition, during Test Runs 32 and 33, extensive visual inspection of these areas revealed several hairline cracks in the epoxy; the cracks were perpendicular to the axis of the reinforcement.

During Test Runs 34 through 38 no additional cracks were observed and no popping noises were heard. However, once the displacement increased beyond 12.7 mm (0.5 in.) during the initial cycle of Test Run 39, the popping noises resumed and additional hairline cracks were observed. During the initial cycles of the remaining test runs

additional hairline cracks were observed above piers PB-7 and PB-10 and in the region below piers PB-8 through PB-10 adjacent to active cracks.

In all cases, the observed damage to the NSM rods consisted of multiple hairline cracks spaced at approximately 25 mm (1 in.). Based on visual observations, this cracking began directly adjacent to active cracks in the masonry and progressed fairly symmetrically in both directions. Figure 4.90 shows a photograph of the region below pier PB-9 taken after Test Run 41. This progressive damage likely contributed in the highly nonlinear force-displacement response of the wall shown in Figures 4.8 through 4.55. In addition, the dispersed cracking of the masonry above piers PB-7 and PB-10 as well as below piers PB-8 through PB-10 suggests that the NSM rods remained intact during all cycles.

Figure 4.90. Photograph of the lower right portion of pier PB-8 showing the numerous hairline cracks observed in the epoxy bed-joints of the NSM rods (the short black vertical marks indicate crack locations).

4.4.2.4 Response of the GFRP Overlays

No damage to the GFRP overlays were observed during Test Runs 27 through 30. During Test Run 31 some minor debonding of the vertical GFRP strips was observed adjacent to the active rocking cracks along the top of piers PB-8 through PB-10. Additional debonding in these regions was observed during the initial cycles of Test Runs 32 and 33. Similar to the response of the NSM rods, no further damage was observed during Test Runs 34 through 37. During Test Runs 38 through 41 additional debonding occurred in these regions as well as below pier PB-8 and above PB-7. Figure 4.91 shows a schematic illustrating the extent of this debonding following Test Run 41. Note that no damage was observed in the diagonal GFRP strips.

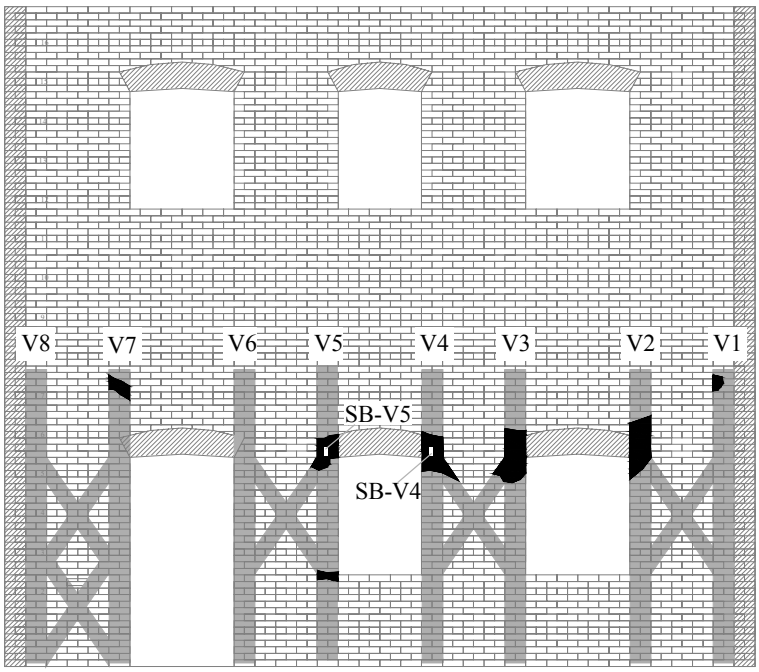

Figure 4.91. Schematic illustrating the extent of debonding (black areas) following Test Run 41 (this exterior elevation shows the GFRP reinforcement on the interior surface).

Figure 4.92 shows two photographs of a debonded region above pier PB-9 following Test Run 41. Although regions of the vertical GFRP strips debonded, no cracking or failure of the composite was visible. That is, the GFRP overlays retained their load carrying capacity throughout all cycles. The principal result of this debonding was an increased effective length of the reinforcement and thus a lower apparent stiffness. Similar to the NSM rods, this decrease in the apparent stiffness contributed to the highly nonlinear force-displacement response shown in Figures 4.79 through 4.81.

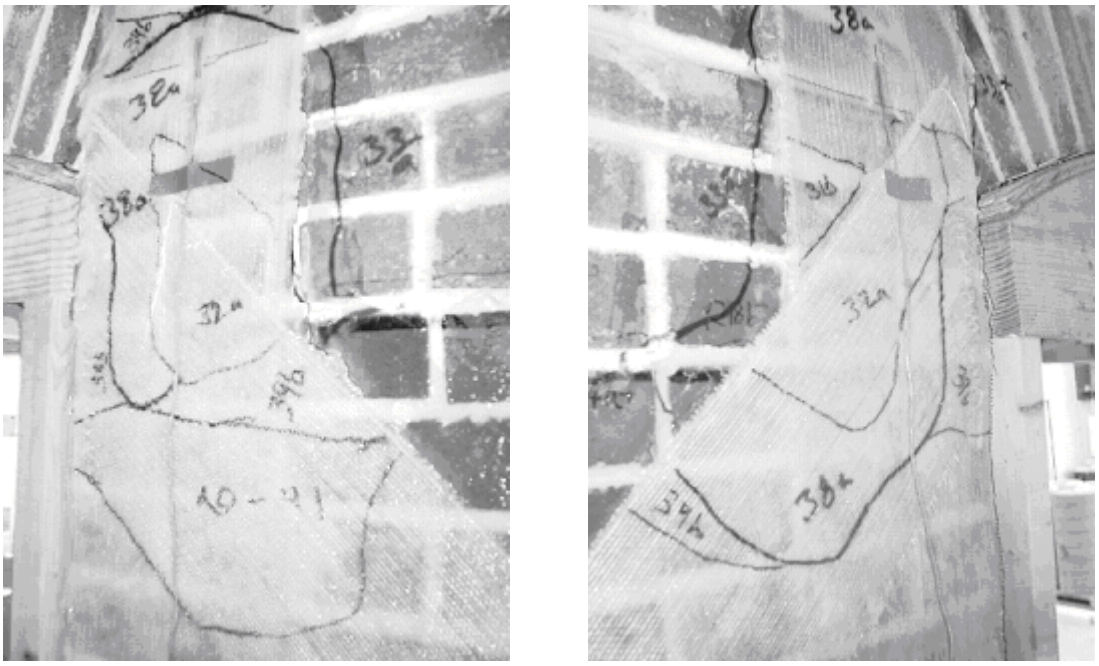

(a) (b)

Figure 4.92. Photographs showing the debonding of GFRP overlays following Test Run 41 (a) right side of pier PB-9 in Figure 4.91 (b) left side of pier PB-9 in Figure 4.91.

In addition, these GFRP overlays were monitored by strain gages throughout all cycles. Figure 4.93 shows the strain recorded at peak displacement during Test Runs 34 through 41 for the vertical GFRP strips applied to pier PB-9. The recorded strains shown in this figure are consistent with rocking deformation and suggest that the vertical GFRP

strips were activated by the observed local rocking deformation of this pier. Notice that as the roof displacement increased beyond 12.7 mm (0.5 in.) the peak strain in these strips remained fairly constant at approximately 4000 με. Recall, that this was the displacement level where the progressive debonding resumed. In addition, these measured strains suggest that upon developing approximately 4000 με in the GFRP strips, additional debonding occurred thus reducing the apparent stiffness of the reinforcement.

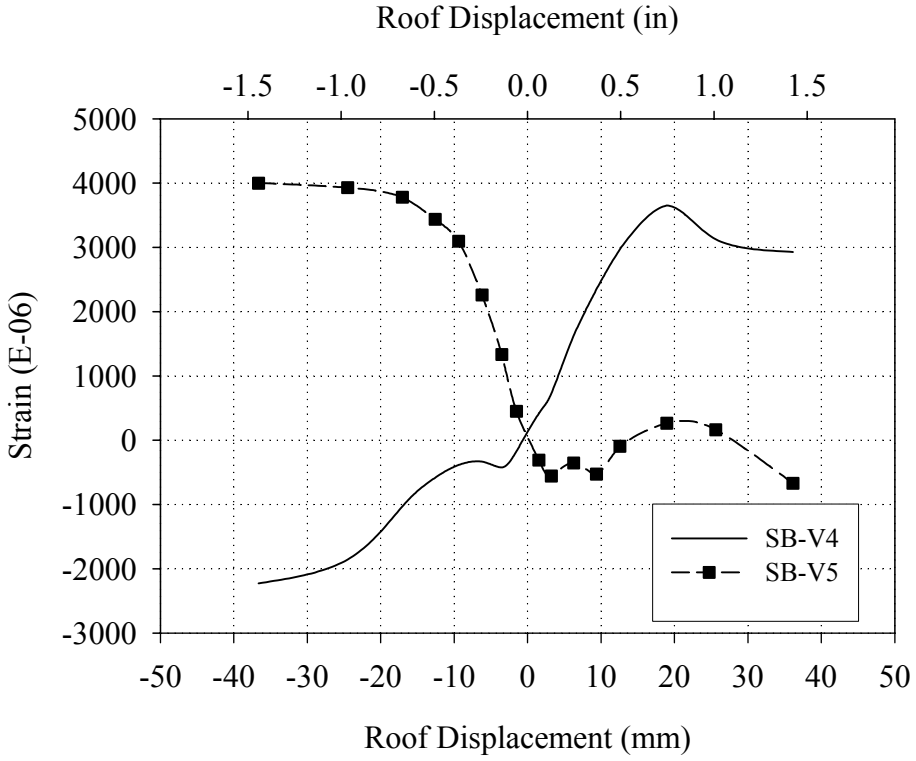

Figure 4.93. Strain recorded at peak displacement during Test Runs 34 through 41 versus roof displacement (see Figure 4.91 for gage locations).

In order characterize this damage, a debonded section of the external reinforcement was cut off of the wall after the testing program was completed. Figure 4.94 is a photograph of the back of the extracted GFRP and shows that the masonry substrate remained bonded to the GFRP. As a result, the debonding failure can be classified as a cohesive failure of the masonry substrate.

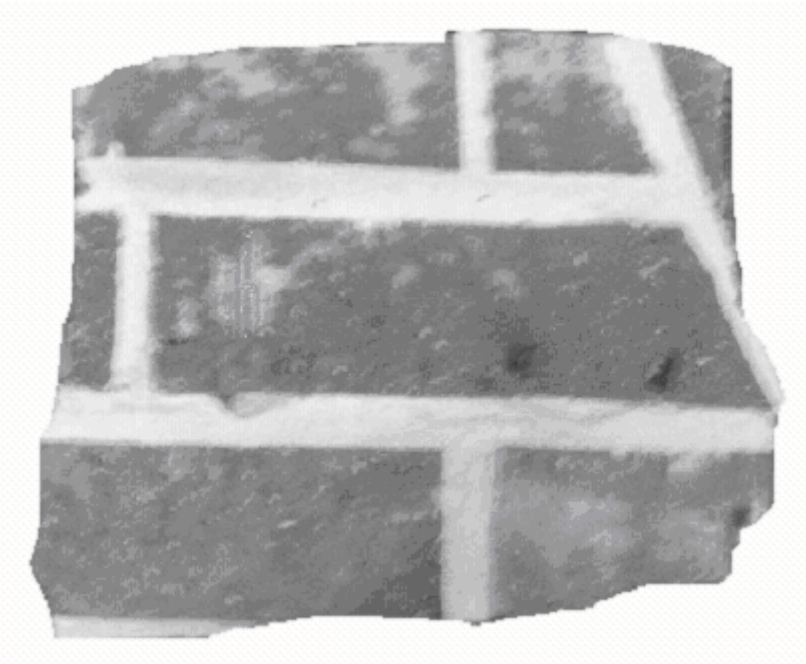

Figure 4.94. Photograph showing the back of the extracted external reinforcement.

4.4.3 Comparison of Wall B Response before and after Retrofit

Figure 4.95 shows the base shear versus roof displacement response of Wall B before and after retrofit through Test Run 33. Figure 4.96 shows the complete base shear versus roof displacement response of Wall B. These figures show that after retrofit the stiffness increased; however, the initial stiffness measured prior to retrofit was not recovered. Table 4.12 summarizes the peak resistance and displacement at peak resistance for Wall B before and after retrofit. This table shows that increases in peak resistance of approximately 32% in the positive direction and 28% in the negative direction were obtained. Note that these peak resistances occurred at different displacement levels. If the resistances before and after retrofit are compared at the 12.7 mm (0.5 in.) in each direction, strength increases of 43% in the positive direction and 50% in the negative direction are obtained.

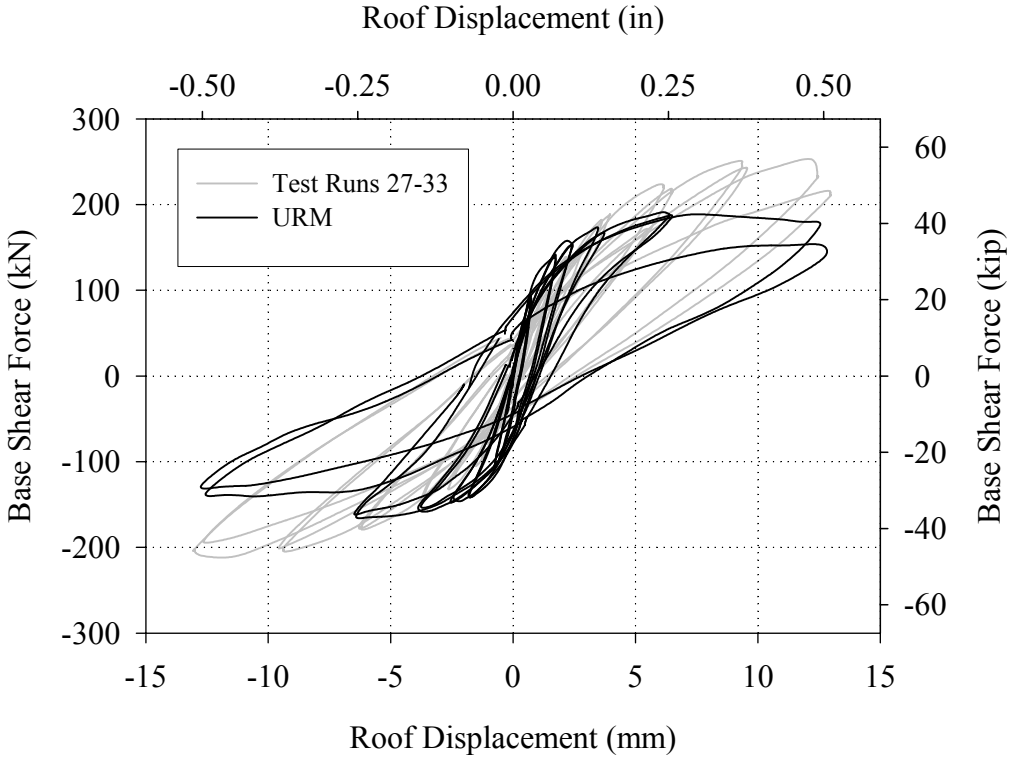

Figure 4.95. Base shear versus roof displacement response of Wall B in an unreinforced state and following the application GFRP reinforcement.

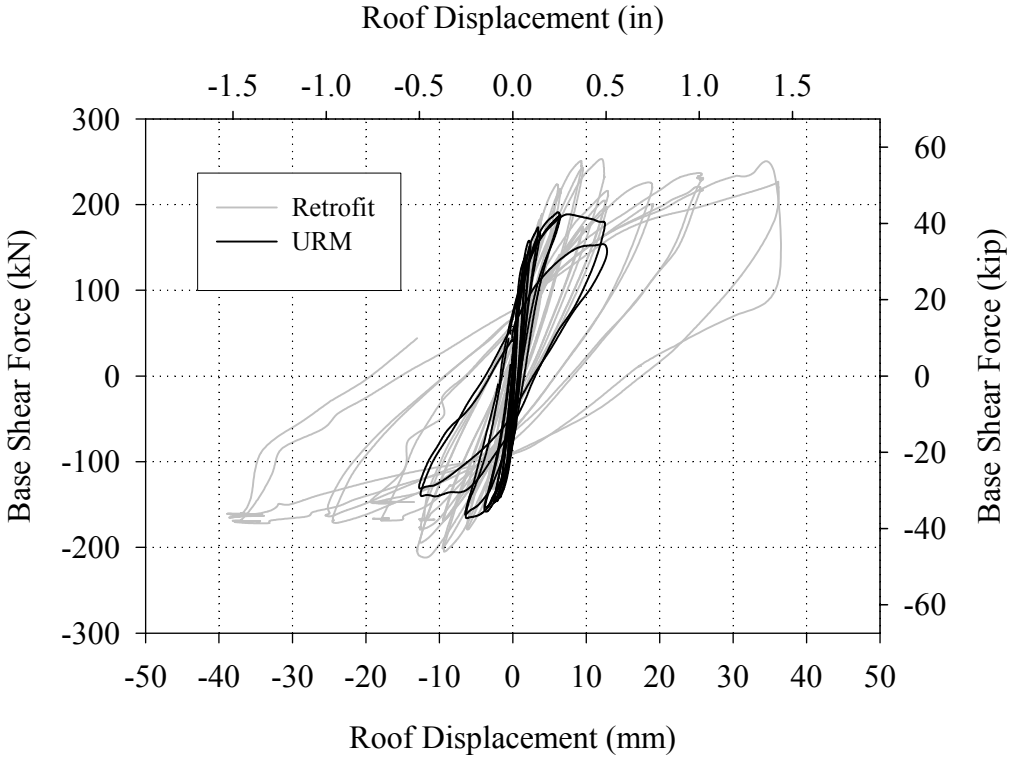

Figure 4.96. Base shear versus roof displacement response of Wall B in an unreinforced state and following the application of GFRP reinforcement.

Table 4.12. Comparison of base shear capacity of Wall B before and after retrofit.

	Base Shear Capacity		Roof Displacement at Peak Resistance	
	Positive	Negative	Positive	Negative
URM	191 kN (43 kip)	165 kN (37 kip)	6 mm (0.24 in.)	6 mm (0.24 in.)
Post-Retrofit	253 kN (57 kip)	211 kN (48 kip)	12.3 mm (0.5 in.)	12.3 mm (0.5 in.)

Figure 4.97 shows the energy dissipated by both stories of Wall B before and after retrofit versus roof displacement. Figure 4.98 shows the percentage of energy dissipated by the first floor of Wall B before and after retrofit (note that due to the small amount of energy dissipated by the second story of Wall B only the first story is included in this plot).

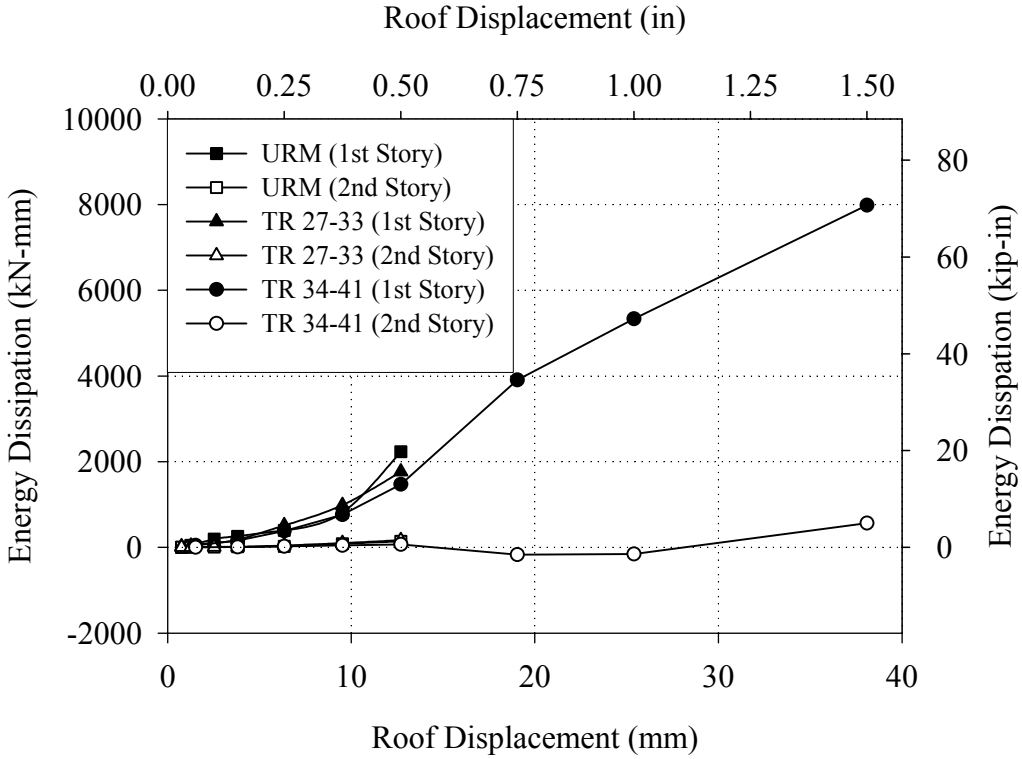

Figure 4.97. Energy dissipated by each story of Wall B before and after retrofit.

Figure 4.97 shows that the majority of the energy dissipation was due to the response of the first story. In addition, the energy dissipated by both stories were very similar before and after retrofit. However, Figure 4.98 indicates that up to a roof displacement of 12.7 mm (0.5 in.) Wall B dissipated a larger percentage of energy prior to retrofit. This larger energy dissipation was attributed to the sliding deformation observed above piers PB-8 and PB-9 that decreased substantially after retrofit. In addition, as the roof displacement increased to around 19 mm (0.75 in.), the strengthened wall dissipated a similar percentage of energy as the wall prior to retrofit. Recall, that around this displacement level, a horizontal crack formed at the base of the wall, after which significant sliding deformation was observed.

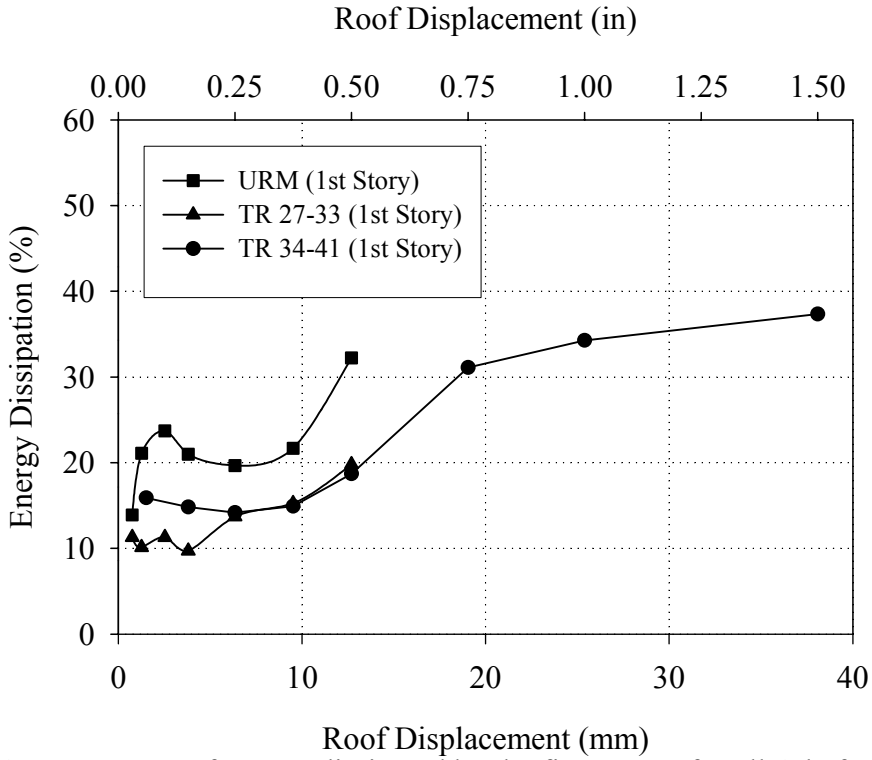

Figure 4.98. Percentage of energy dissipated by the first story of Wall A before and after retrofit.

4.5 Coupling between In-Plane Walls

The coupling between in-plane Walls A and B was investigated during Test Runs 40 and 41. During these test runs, Wall A was held at zero displacement as Wall B was displaced in-plane (see Table 4.10). Figure 4.99 shows an idealized schematic of the structure during this series of tests. Figure 4.100 shows the force-displacement response of Wall B (i.e. F_B versus Δ) and the coupling supplied by the diaphragm and out-of-plane walls (i.e. F_A versus Δ) during Test Runs 40 and 41 (see Figure 4.99 for definition of terms). While Figure 4.100 indicates that some shear force was transferred from Wall B to Wall A during these cycles, the magnitude of this shear force was small compared with the applied load. As an example, at a Wall B Δ of 25 mm, the F_B was 166 kN while the F_A force required to hold Wall A at zero displacement was 31 kN, only 19% of F_B.

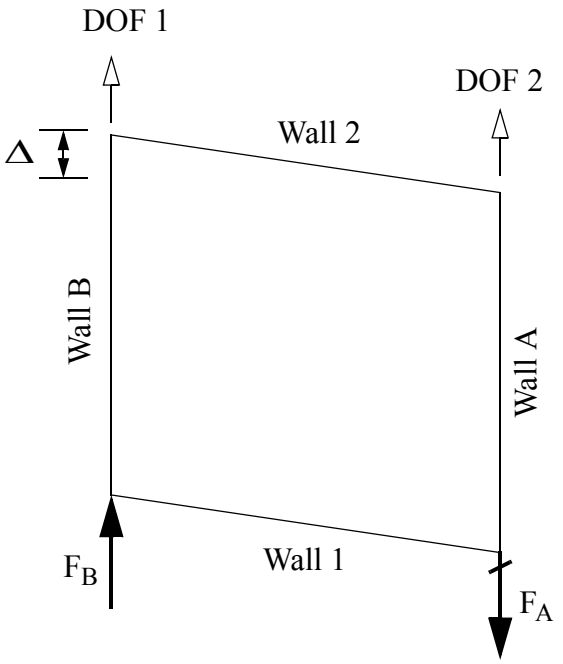

Figure 4.99. Schematic illustrating the deformed shape of the test structure during Test Runs 40 and 41.

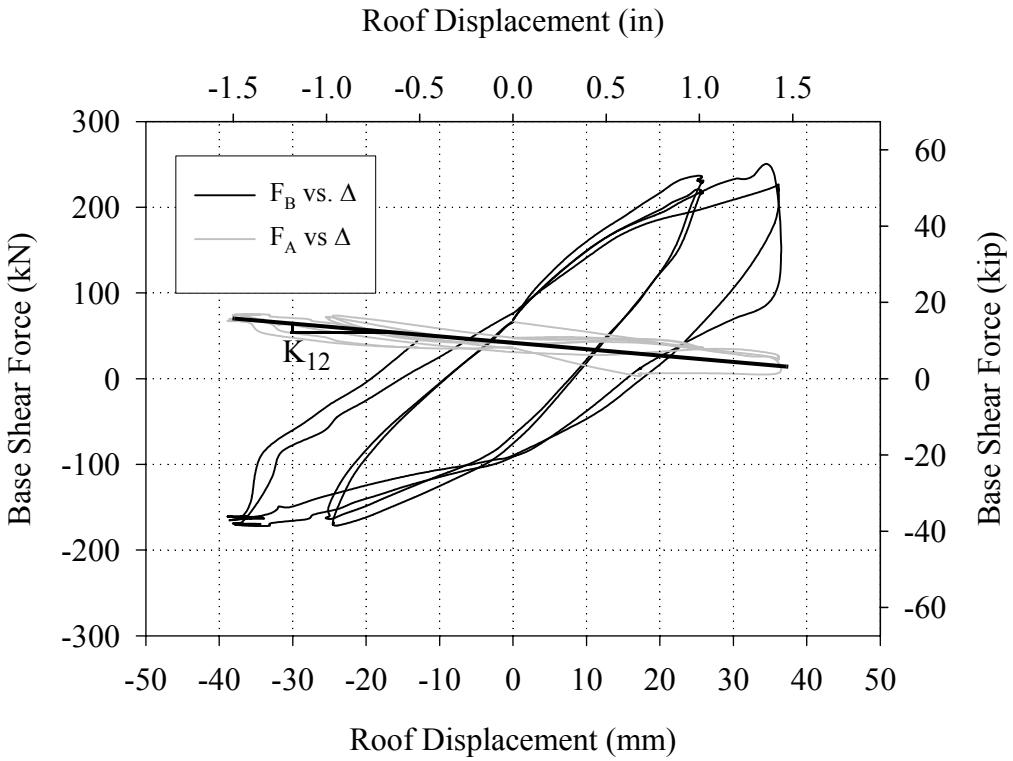

Figure 4.100. Force-displacement response recorded during Test Runs 40 and 41 (see Figure 4.99 for definition of plots)

To gain further insight into the level of coupling, the structure was modeled as a two degree of freedom system with the in-plane displacements of Walls A and B representing the degrees of freedoms shown in Figure 4.99. Following this assumption, the loading pattern illustrated in Figure 4.99 was used to solve for the first column of the stiffness matrix. Where K_{11} is the in-plane stiffness of Wall B (i.e. the stiffness of the F_B versus Δ plot) and K_{12} is the coupling stiffness (i.e. the stiffness of the F_A versus Δ plot). Since the F_A versus Δ plot was fairly linear, this response was characterized by a trendline from peak positive displacement to peak negative displacement. By averaging all of the cycles conducted during Test Runs 40 and 41 this coupling stiffness, K_{12}, was calculated as -0.85 kN/mm (-4.9 kip/in).

In contrast to the linear coupling response, the response of Wall B throughout loading was highly nonlinear, which indicates that K_{11} is dependent on the level of displacement. As a result, K_{11} was calculated for each level of imposed displacement (i.e. Test Runs 27 through 41) as the secant stiffness of Wall B (see Appendix F for the details of this calculation). For comparison purposes the absolute value of K12/K11 was plotted versus roof displacement of Wall B and is shown in Figure 4.101.

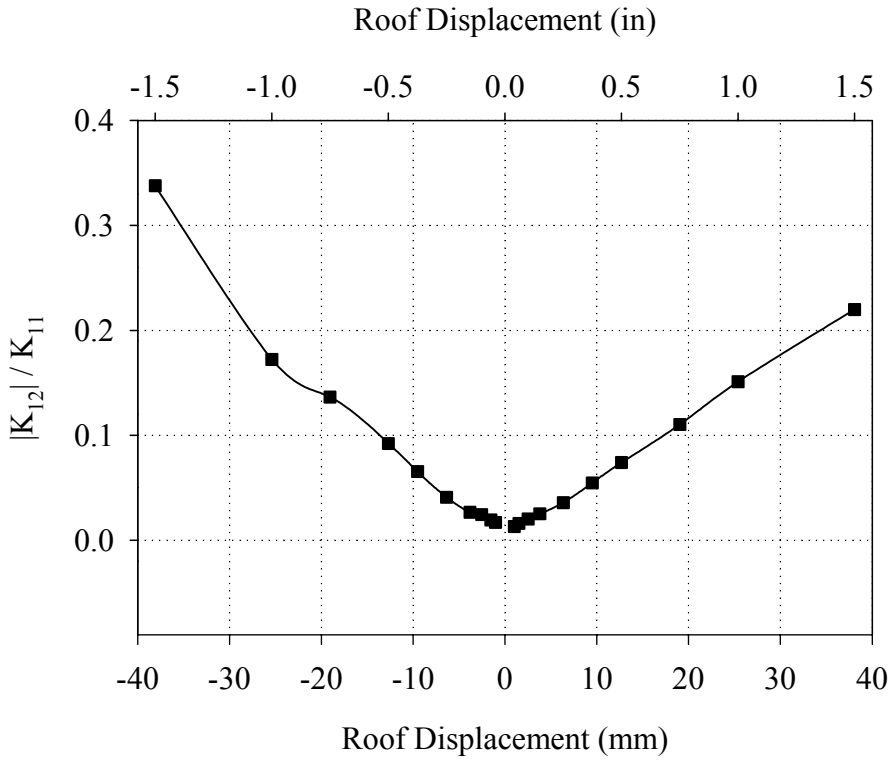

Figure 4.101. Normalized coupling stiffness versus roof displacement.

Note that the displacement axis in Figure 4.101 represents both the roof displacement of Wall B as well as the differential roof displacement between Walls A and B (i.e. Wall A was held at zero displacement). This figure shows that up to a differential roof displacement of around 13 mm (0.5 in), the coupling stiffness was below 10% of the in-plane stiffness. At larger differential displacements the coupling stiffness does exceed 10% of the in-plane stiffness; however, due to the short periods of most URM structures, this level of differential displacement between in-plane walls could be considered atypical. As a result, it is concluded that in most cases the coupling supplied by out-of-plane URM walls and timber diaphragms is negligible. This findings is consistent with past research (Clough et al., 1979; Tomazevic et al., 1993; Costley and Abrams, 1996; and Benedetti et al., 1998).

4.6 In-plane Response of Timber Diaphragm

Prior to loading the walls of the test structure in-plane, several tests were conducted on the roof diaphragm and URM walls out-of-plane (see Chapter 3 for details). The primary objectives of these tests were to (1) experimentally determine the elastic stiffness of the roof diaphragm and out-of-plane walls and (2) to gain insight into the response of typical diaphragm-to-wall connections and the effectiveness of installing joist anchors. For the sake of brevity, only results that pertain to connection behavior and retrofit are discussed here. However, a brief summary of the findings from the other portion of the testing is also presented. A complete set of the results is presented by Yi, (2004).

As outlined in Chapter 3, the testing of the roof diaphragm was carried out in both principal directions (i.e. parallel to the joists and perpendicular to the joists). All cycles were conducted in displacement control and imposed an actuator displacement of 5.1 mm (0.2 in.) in each direction. Figure 4.102 shows a graphical representation of the actuator command for each cycle imposed on the roof diaphragm. Figures 4.103 and 4.104 show schematics illustrating the test setup for each loading direction. Recall that the roof diaphragm was tested with and without the joist anchors shown in these figures. Note that the location of the LVDTs employed to measured displacements at mid-span of the out-of-plane walls and diaphragm are also shown.

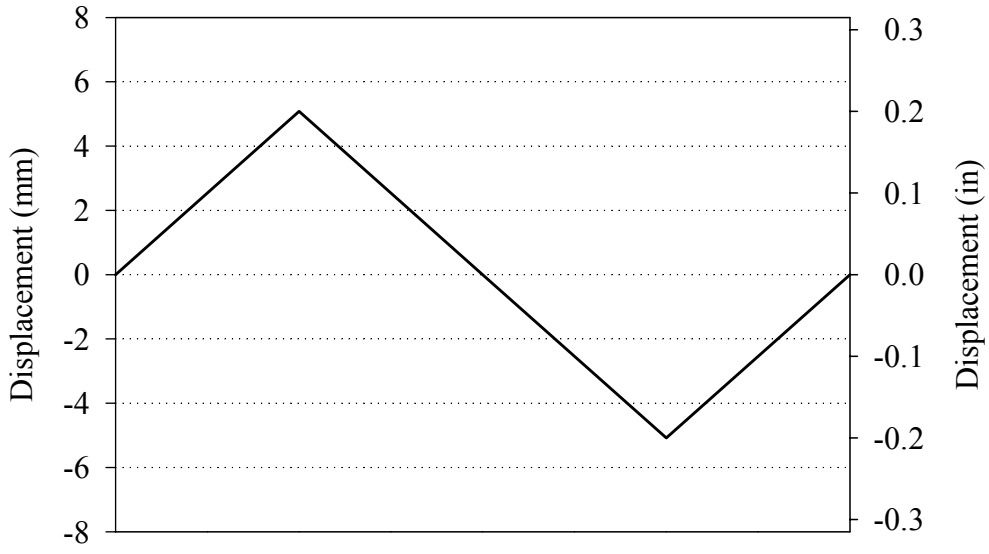

Figure 4.102. Actuator command for each cycle imposed on the diaphragm.

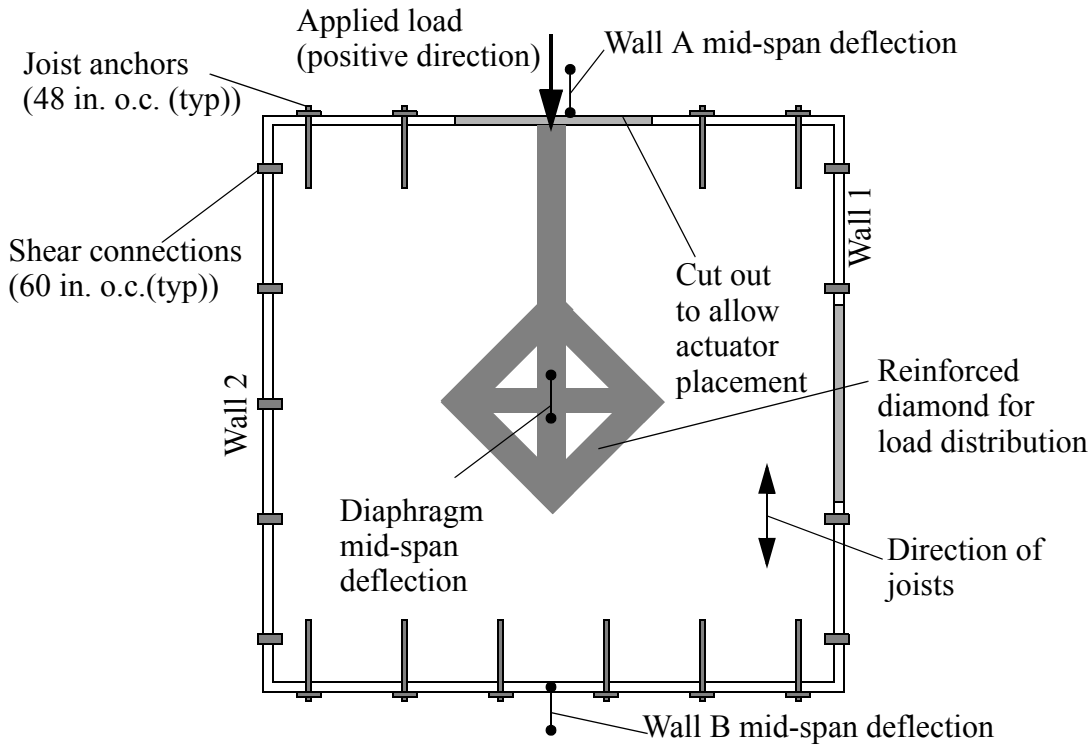

Figure 4.103. Test setup for loading parallel to joists.

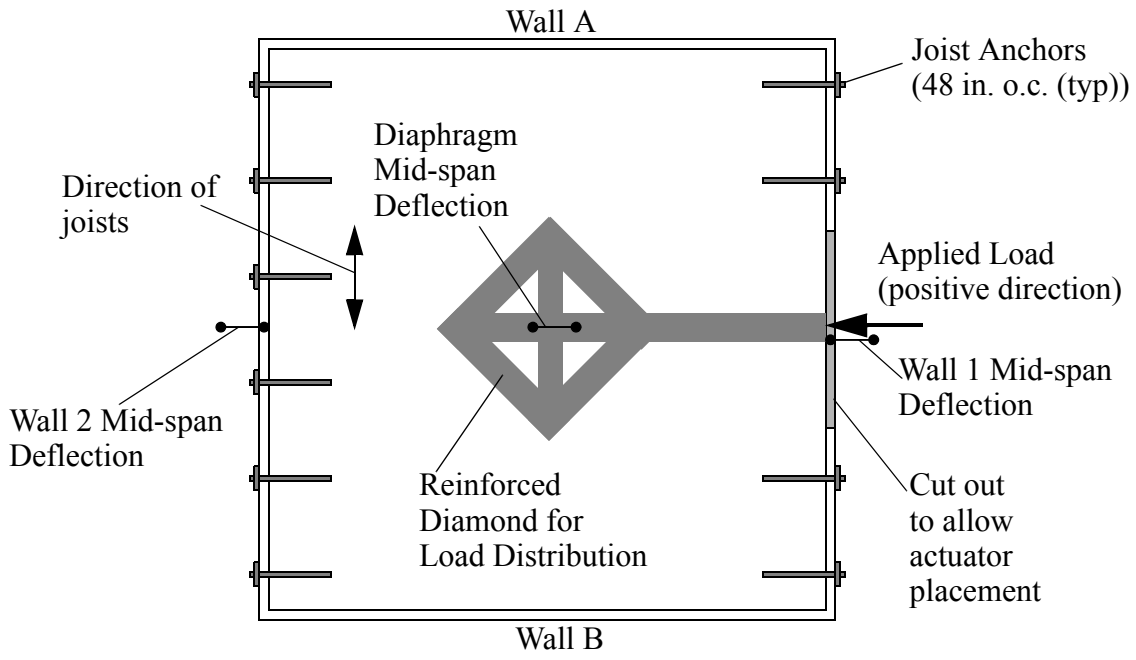

Figure 4.104. Test setup for loading perpendicular to joists.

4.6.1 Response Parallel to Joists

Figures 4.105 and 4.106 show the deflection of the diaphragm and out-of-plane walls versus the applied load before and after the installation of joist anchors, respectively. Figure 4.105 shows that the response of out-of-plane Walls A and B was not symmetric prior to the installation of joist anchors. Specifically, the deflection of Wall A in the negative direction was nearly twice as large as the deflection of Wall A in the positive direction (note, similar behavior was observed for Wall B). This suggests that in the positive direction the joists were pulling out of the pocket connection, and thus the response of Wall A was diminished. In the negative direction the diaphragm pushed against Wall A thus forcing a greater degree of participation.

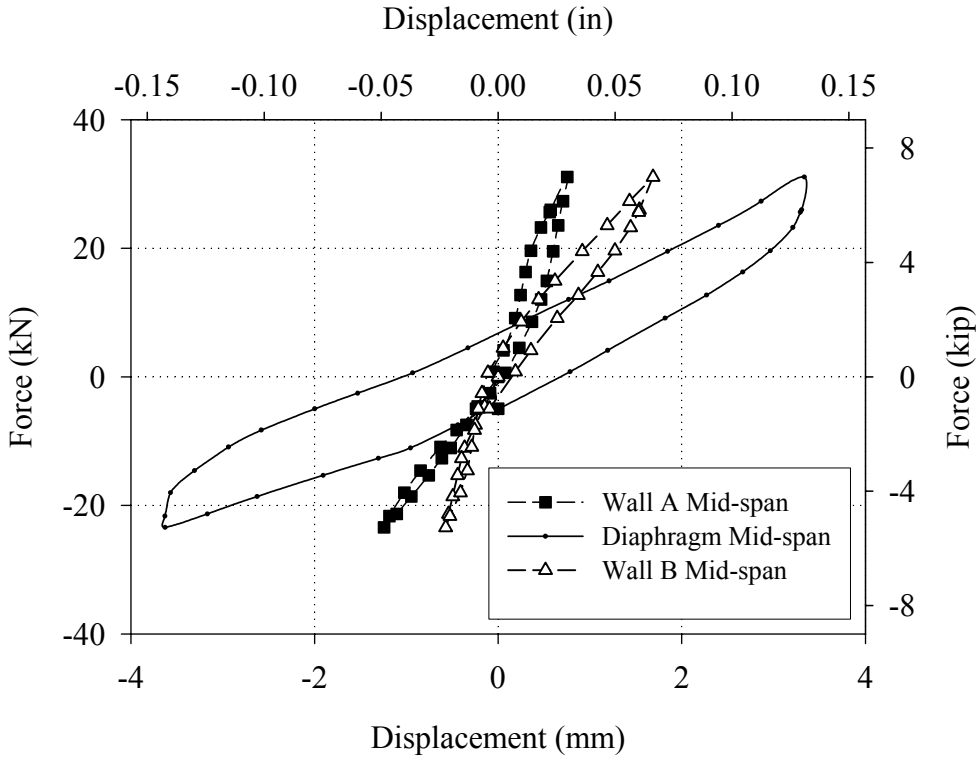

Figure 4.105. Deflection of the diaphragm and the out-of-plane Walls A and B versus applied load before the installation of joist anchors (loaded parallel to joists, perpendicular to Walls A and B, see Figure 4.103 for gage locations).

Following the installation of joist anchors the response of Walls A and B became far more symmetric (see Figure 4.106). This suggests that the joists anchors supplied enough tension capacity to keep the joists from sliding out of the pocket connections in Walls A and B. However, differential displacement between the out-of-plane walls and diaphragm was still apparent after the joist anchors were installed. This differential displacement is attributed to (1) the flexibility of the connections and (2) the axial displacement of the diaphragm.

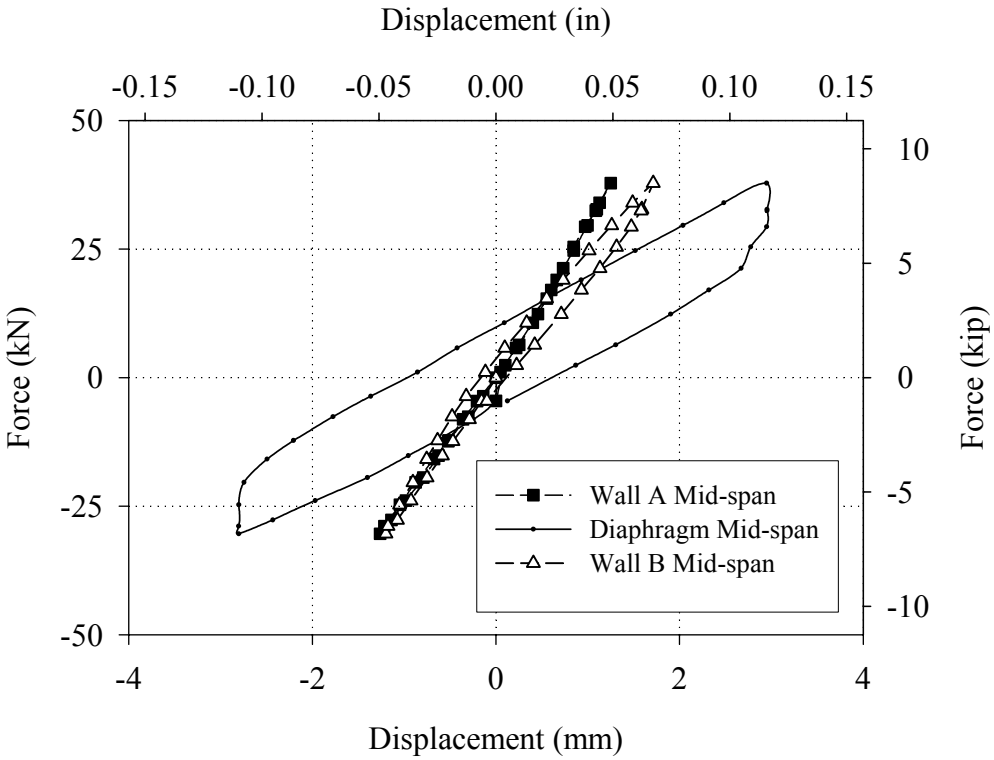

Figure 4.106. Deflection of the diaphragm and the out-of-plane Walls A and B versus applied load after the installation of joist anchors (loaded parallel to joists, perpendicular to Walls A and B, see Figure 4.103 for gage locations).

4.6.2 Response Perpendicular to Joists

Figures 4.107 and 4.108 show the deflection of the diaphragm and out-of-plane walls versus the applied load before and after the installation of joist anchors, respectively. Similar to the response parallel to the joists, Figure 4.107 shows that prior to the installation of joist anchors the response of the out-of-plane walls was unsymmetrical. Note that since the joists were supported on Walls A and B, no connection between the diaphragm and Walls 1 and 2 existed during this cycle; hence, the negligible deflection of Wall 1 in the positive direction and Wall 2 in the negative direction.

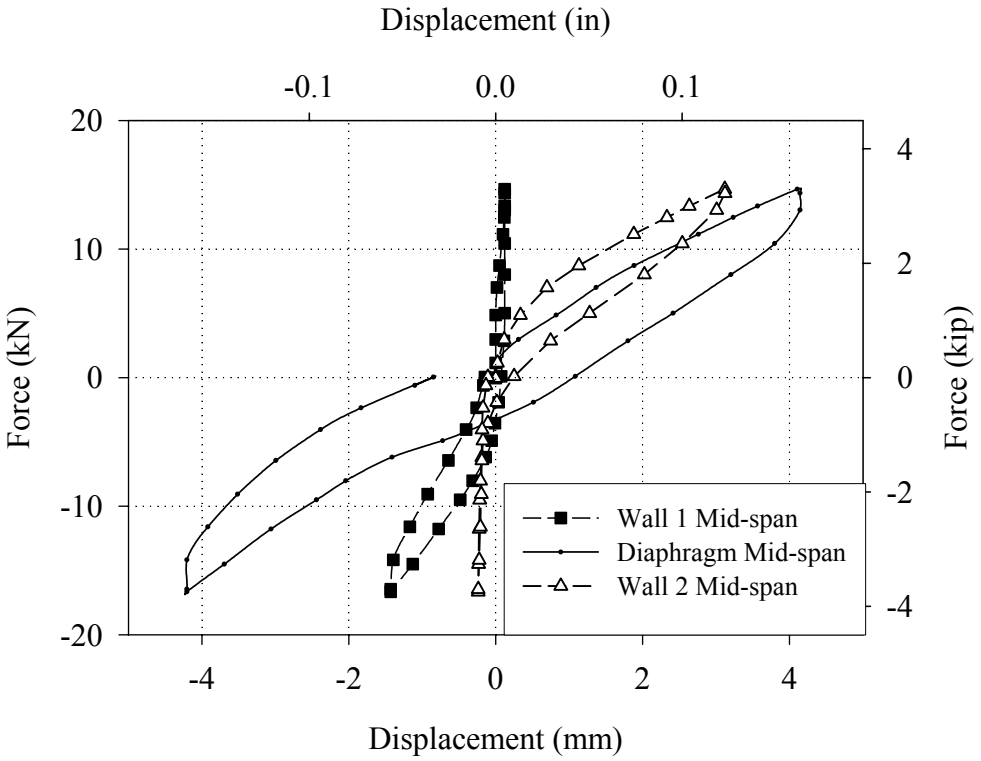

Figure 4.107. Deflection of the diaphragm and the out-of-plane Walls 1 and 2 versus applied load after the installation of joist anchors (loaded perpendicular to joists, perpendicular to Walls 1 and 2, see Figure 4.104 for gage locations).

Similar to the results obtained in the direction parallel to the joists, Figure 4.107 shows that following the installation of joist anchors, the response of Walls 1 and 2 became far more symmetric. The slight lack of symmetry apparent in the response of Wall 1 is attributed to the lack of joists anchors supplied at mid-span of Wall 1 (see Figure 4.104). Note that the cut out in Wall 1, required to position the actuator, precluded the installation of joist anchors in this region.

In addition, the differential displacement between the diaphragm and out-of-plane walls in the direction perpendicular to the joists was smaller than the differential displacement measured parallel to the joists. This is attributed to the diminished bearing force between the diaphragm and out-of-plane walls caused by the smaller stiffnesses of

Walls 1 and 2. Recall that Walls 1 and 2 were two wythes thick while Walls A and B were three wythes thick.

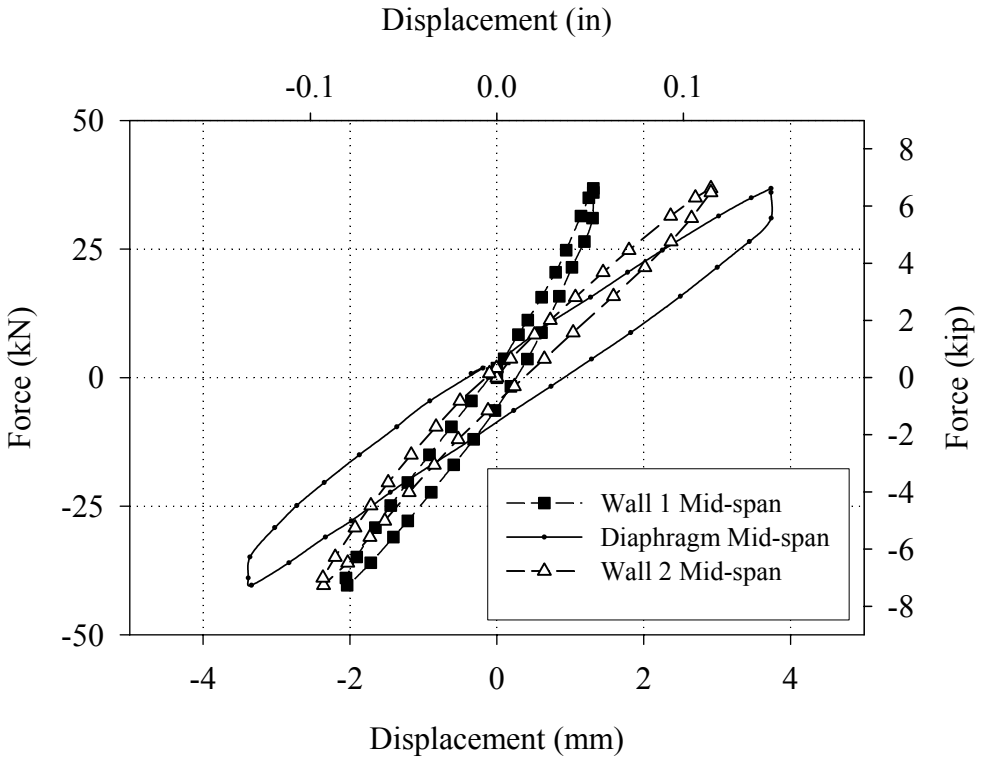

Figure 4.108. Deflection of the diaphragm and the out-of-plane Walls 1 and 2 versus applied load after the installation of joist anchors (loaded perpendicular to joists, perpendicular to Walls 1 and 2, see Figure 4.104 for gage locations).

4.6.3 Summary of Diaphragm Test

The joist anchor retrofit was successful in forcing the out-of-plane walls to participate in the response of the diaphragm in both directions. However, since the imposed displacements were fairly modest (i.e. 5.1 mm (0.2 in.)), the forces developed in the joist anchors and URM walls were far below those likely during an earthquake. Nevertheless, the experimental results indicate that, at least at low levels, the joist anchors performed as intended.

As mentioned previously several others cycles were conducted on the roof diaphragm to determine the elastic stiffnesses of the diaphragm and out-of-plane walls. For completeness a summary of these results are provided in Table 4.13. In addition, this series of test concluded that the grout typically supplied within the joist pocket connections had a negligible effect on the response of the diaphragm perpendicular to the joists. More detailed documentation of these findings including a comparison with past research can be found in Yi (2004).

Table 4.13. Summary of diaphragm test results (Yi, 2004)

Out-of-plane stiffness of Wall 1	5.4 kN/mm (31 kip/in)
Out-of-plane stiffness of Wall 2	4.2 kN/mm (24 kip/in)
Out-of-plane stiffness of Wall A	12.6 kN/mm (73 kip/in)
Out-of-plane stiffness of Wall B	12.6 kN/mm (73 kip/in)
In-plane stiffness of half diaphragm parallel to joists	1.0-1.7 kN/mm (6-10 kip/in)
In-plane stiffness of diaphragm perpendicular to joists	1.0 kN/mm (6 kip/in)
Axial stiffness of diaphragm parallel to joists	31-38 kN/mm (180-220 kip/in)

4.7 Summary of Experimental Results

The following sections summarize the principal findings of the experimental program in terms of the three primary objectives which were to (1) investigate the behavior of each retrofit technique in terms of damage progression and failure modes, (2) assess the effect of each retrofit technique on overall structure performance, and (3)

identify global characteristics of URM structures that impact the behavior of primary components. This section concludes with a brief discussion of findings that did not directly coincide with these primary objectives.

4.7.1 Behavior of Retrofit Systems

In the case of the external reinforcement systems, the primary damage observed can be classified as a progressive debonding from the masonry substrate. For the GFRP systems applied to Wall B, this debonding occurred primarily in the substrate and is classified as a cohesive failure of the masonry (see Sections 4.4.2.3 and 4.4.2.4). In the case of the GFRC system applied to Wall 2, this debonding was classified as an adhesive failure of the bond between the reinforcement and the substrate (see Section 4.2.2.3). In both cases, limited damage was observed in the reinforcement itself (aside from cracking of the GFRC matrix). As a result, this debonding did not represent a failure of the reinforcement, but rather limited the effectiveness of the reinforcement. Specifically, this damage limited the strain induced in the external reinforcement by the deformation of the wall. In the case of the system applied to Wall B this limiting strain was approximately 4000 με. The progressive debonding contributed to the highly nonlinear and apparent ductile system response.

In the case of the unbonded post-tensioning tendons, substantial increases in prestressing force was observed throughout loading. This increase was due to the uplift associated with local pier and global rocking, which induced additional tensile strain in the tendons. For both levels of post-tensioning force, increases between 50 kN (11 kip) to 100 kN (22 kip) were observed at a roof displacement of 12.7 mm (0.5 in.) in each direction

(see Section 4.3.2.3). Due to the sensitivity of URM walls to the level of vertical stress, it is likely that the observed increases in the post-tensioning force greatly impacted the behavior of the wall.

4.7.2 Effectiveness of Retrofit Systems

Table 4.14 summarizes the peak strengths recorded for each wall before and after retrofit. The apparent strengthening reported in this table should be viewed as a lower bound since all of the walls were first tested in an unreinforced state. That is, the damage induced prior to retrofit may have reduced the measured capacity after retrofit (particularly in the case of Wall 1). Nevertheless, Table 4.14 shows that, in terms of strengthening, the post-tensioning system was the most effective followed by the GFRP retrofit applied to Wall B. Due to the large differences in the observed behavior of each wall, the reader is cautioned that direct comparisons between the effectiveness of retrofit systems should be done with discretion.

Table 4.14. Base shear capacity of each wall before and after retrofit.

	Direction	Base Shear Capacity		Apparent Strengthening (%)
		URM	Post-Retrofit (PR)	$\frac{V_{PR} - V_{URM}}{V_{URM}}$
Wall 1	Positive	267 kN (60 kip)	222 kN (50 kip)	-17%
	Negative	245 kN (55 kip)	218 kN (49 kip)	-11%
Wall 2	Positive	128 kN (29 kip)	142 kN (32 kip)	11%
	Negative	111 kN (25 kip)	130 kN (29 kip)	17%
Wall A PT = 111 kN (25 kip)	Positive	159 kN (36 kip)	223 kN (50 kip)	40%
	Negative	182 kN (41 kip)	261 kN (59 kip)	43%
Wall A PT = 222 kN (50 kip)	Positive	159 kN (36 kip)	250 kN (56 kip)	57%
	Negative	182 kN (41 kip)	294 kN (66 kip)	61%
Wall B	Positive	191 kN (43 kip)	253 kN (57 kip)	32%
	Negative	165 kN (37 kip)	211 kN (48 kip)	28%

Beyond strengthening, the retrofit techniques employed in the test structure also impacted pier failure modes and overall wall performance. For the external reinforcement systems, the desired sliding mode at the base of the structure was achieved in two cases. Sliding planes were activated along the foundation during the testing of Walls 1 and B (see Sections 4.1.2 and 4.4.2). In addition, the presence of horizontal reinforcement in these retrofit schemes resulted in relatively small crack openings and a distributed cracking

pattern, which is indicative of reinforced masonry behavior. In all cases, the application of FRP overlays to only one side of the URM walls resulted in negligible out-of-plane response. This is attributed to the restraint supplied by the surrounding wall.

In the case of the post-tensioning retrofit, substantial strength increases were achieved; however, the increased vertical stress resulted in brittle failure modes. That is, the primary failure mode of the outside piers (i.e. piers PA-7 and PA-10) switched from rocking to diagonal tension after post-tensioning. In addition, the lack of horizontal reinforcement in Wall A allowed cracks to open in a progressive manner, thus substantially impacting the displacement capacity of the wall. Note that following Test Run 39, crack widths were measured up to 38 mm (1.5 in.) even though the largest imposed roof displacement was 19 mm (0.75 in.) (see Section 4.3.2).

The joist anchor retrofit was successful in forcing the out-of-plane walls to participate in the response of the diaphragm in both directions. During the testing of the diaphragm prior to installing these anchors, the out-of-plane walls only participated when the diaphragm pushed against them (see Section 4.6). However, since the imposed displacements were fairly modest (i.e. 5 mm (0.2 in.)), the forces developed in the joist anchors and URM walls were far below those likely during an earthquake. Nevertheless, the experimental results illustrated that, at least at low levels, the joist anchors performed as intended.

4.7.3 Global Characteristics of URM Structures

Several global characteristics were identified that may impact the response of primary components including: effects of overturning moment, global rocking, flange

participation, and coupling between in-plane walls. The following sections summarize the findings in each of these areas.

4.7.3.1 Effects of Overturning Moment

The effect of overturning moment was most clearly displayed by the three diagonal cracks which were observed in the test structure. These cracks were located in piers P1-7, PA-7, and PA-10 (see Section 4.1.2 and 4.3.2). In all cases these cracks formed when overturning moment was acting to increase the level of vertical stress in the pier. As described in Chapter 2, individual pier response is extremely sensitive to the level of vertical stress. Furthermore, diagonal tension failures are indicative of relatively high levels of vertical stress. These results suggest that overturning moment increased the level of vertical stress in these piers and switched the governing failure mode from rocking to diagonal tension. As a result, it is concluded that overturning moment can substantially impact the response of individual URM piers.

4.7.3.2 Global Rocking

In some cases wall response was not dominated by interstory shear deformation caused by lateral force, but rather due to a global rotation (or global rocking) of the entire wall caused by overturning moment. Varying degrees of global rocking deformation were observed during the testing of Walls 1, A, and B in-plane (see Sections 4.1, 4.3, and 4.4). In the case of Wall 1, the observed global rocking was the primary mode of deformation whereas the global rocking of Walls A and B (while significant) was secondary to the interstory shear displacement. Nevertheless, these results indicate that global rocking is a

failure mode for perforated URM walls.

4.7.3.3 Flange Participation

Substantial flange participation was observed for each in-plane wall in each loading direction. In general, the primary contribution of the observed tension flange participation was an increase in weight of the in-plane wall. Recall that in all cases, significant portions of the out-of-plane walls were engaged due to the uplift associated with local pier rocking or global rocking. This participation was effective in (1) resisting the effects of overturning moment and (2) increasing the level of vertical stress in the piers.

To gain further insight into the importance of this participation, each wall was analyzed (prior to retrofit) with and without flanges. For simplicity, all piers were assumed to rock (note, that nearly all piers displayed some degree of rocking deformation prior to retrofit). The weight on each pier was taken as the tributary weight of masonry above each pier as illustrated in Figure 4.109. As an approximation, the flange was taken as the weight of masonry above a 45 degree line extending from the active rocking crack (as observed during testing) of the adjacent in-plane pier (see Figure 4.109). To ensure that the out-of-plane wall was not counted twice, the portion of the assumed flange that extended beyond half of the out-of-plane wall was ignored. The weight of the flange was assumed to be resisted exclusively by the adjacent pier.

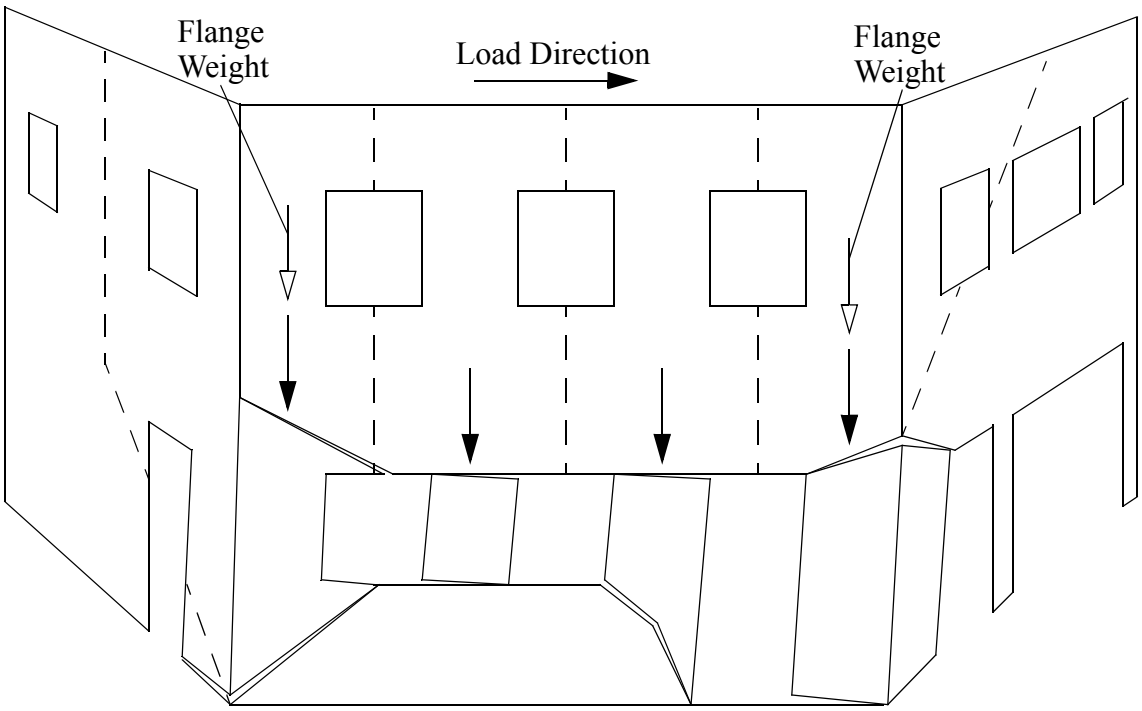

Figure 4.109. Schematic illustrating the calculation of axial compressive force.

Table 4.15 summarizes the calculated capacity of each wall prior to retrofit with and without flanges as well as the experimentally measured capacity. Table 4.16 gives the percent difference of these calculations (compared with the experimentally measured capacity) as well as the percentage of base shear strength attributed to flanges (i.e. the percent difference between the calculated capacity with and without flange participation). Both of these tables show that in all cases the approximation of flange weight significantly increased the accuracy of the predicted strength. In addition, the strength attributed to the flange participation ranged from 24 to 52% of the calculated base shear capacity.

Table 4.15. Comparison between the calculated base shear capacity of each wall with and without flange participation and the experimentally measured capacity.

	Direction	Base Shear Capacity		
		Experiment	Approximation w/o flange	Approximation w/ flange
Wall 1	Positive	267 kN (60 kip)	129 kN (29 kip)	231 kN (52 kip)
	Negative	245 kN (55 kip)	147 kN (33 kip)	307 kN (69 kip)
Wall 2	Positive	128 kN (29 kip)	45 kN (10 kip)	93 kN (21 kip)
	Negative	111 kN (25 kip)	45 kN (10 kip)	93 kN (21 kip)
Wall A	Positive	159 kN (36 kip)	107 kN (24 kip)	156 kN (35 kip)
	Negative	182 kN (41 kip)	111 kN (25 kip)	147 kN (33 kip)
Wall B	Positive	191 kN (43 kip)	107 kN (24 kip)	156 kN (35 kip)
	Negative	165 kN (37 kip)	111 kN (25 kip)	147 kN (33 kip)

Although limiting the failure mode of all piers to rocking should provide an upper bound on strength, Table 4.15 shows that for all cases (except for Wall 1 in the negative loading direction) the consideration of flange participation underpredicted the base shear capacity. This indicates that the assumed flange participation (45^o crack rule) was generally conservative. Note, that the effect of overturning moment may also have impacted the capacity of the wall and was not considered in this simple analysis. A more detailed analysis of the test structure is provided in Chapter 5.

Table 4.16. Percent difference of the calculated base shear capacity of each wall (with and without) and percentage of capacity attributed to flange participation.

	Direction	% Difference $\frac{V - V_{Exp}}{V_{Exp}}$		% of capacity attributed to flange participation
		Approximation w/o flange	Approximation w/ flange	
Wall 1	Positive	-52%	-13%	44%
	Negative	-40%	25%	52%
Wall 2	Positive	-66%	-28%	52%
	Negative	-60%	-16%	52%
Wall A	Positive	-46%	-3%	31%
	Negative	-39%	-20%	24%
Wall B	Positive	-44%	-19%	31%
	Negative	-32%	-11%	24%

4.7.3.4 Coupling between In-plane Walls

During Test Runs 40 and 41 the coupling between Walls A and B was investigated. Results showed that the coupling stiffness was less than 10% of the in-plane stiffness for differential roof displacements less than 12.7 mm (0.5 in.). As a result, it is concluded that the coupling between in-plane walls provided by flexible timber diaphragms and out-of-plane walls is negligible for typical displacement levels.

4.7.4 Other Findings

Beyond the findings associated with the primary objectives of this investigation, several other observations were made:

- For URM piers, low-level rocking impacts bed-joint sliding resistance. That is, the flexural cracking associated with low-level rocking erodes the shear strength

provided by the bed-joint. This phenomenon was displayed by the behavior of piers PB-7 and P1-6 in the negative loading direction, which switched from rocking to sliding abruptly (see Sections 4.1.1 and 4.4.2). Note that in some cases, the flexural cracks were stepped and, thus, a sliding plane was not created (e.g. pier P1-6 in the positive loading direction).

- Both the steel lintels and the shallow arch lintels performed well. However, during the testing of Walls A and B cracks formed in several arch lintels and a small portion (9 bricks) of one of the lintels collapsed. Although this appears to be cause for concern, the presence of nonstructural components such as door and window frames are likely sufficient to prevent such a collapse. This finding applies only to lintels and implies nothing about the behavior of other portions of URM structures such as parapets.
- Header courses were sufficient to transfer the force developed in the external reinforcement to the outer wythes of masonry. Below the first header course, cracks through the collar joint were observed. However, above the first header course no separation was observed indicating that the header courses provided sufficient shear transfer between wythes. Depending on the thickness of the wall, more than one header course may be required to develop external reinforcement into outer wythes.
- The hysteric response of each wall was uniform. Walls displaying primarily sliding dissipated approximately 35 to 40% of the input energy, and displayed residual displacements equal to approximately 60% of the maximum roof displacement. Walls displaying primarily rocking behavior dissipated approximately 15 to 20%

of the input energy and displayed residual displacement equal to approximately 20% of the maximum roof displacement. These findings provide a means to approximate the hysteretic response of URM walls dominated by either rocking or sliding.

CHAPTER 5

SIMPLIFIED PUSHOVER ANALYSIS

The primary objective of the analytical portion of this study was to develop a simplified model with which one could perform seismic analysis on in-plane perforated URM walls before and after retrofit with FRP overlays and vertical post-tensioning. The approach taken was to modify and extend the existing model implied by the "Prestandard for the Rehabilitation of Existing Structures", FEMA 356 (ATC, 2000). In terms of the objective of this study, the existing FEMA 356 model has two major shortcomings: (1) little guidance is provided on the analysis of URM piers strengthened with FRP overlays, and (2) the global characteristics of URM structures identified during the experimental portion of this study are not addressed. In addition to these major areas of modification, other subtle changes were made to the existing model and those changes are also outlined in this chapter.

A schematic of the model implied by FEMA 356 (ATC, 2000) for the in-plane analysis of perforated URM walls is shown in Figure 5.1. As apparent from this figure, the model employs single shear springs to capture the response of individual piers. The properties of these springs are based largely on past component tests and are dependent on the gravity stress and dimensions of each pier. In addition, the spandrels of URM walls are only considered to affect the boundary conditions of the in-plane piers (i.e. fixed-fixed or cantilever). To calculate the story response of a wall, the displacements of each pier spring (within a story) are assumed to be equal and the resistances of these springs are added

together (i.e. springs in parallel). The response of the entire wall is then determined by combining the responses of each story as springs in series.

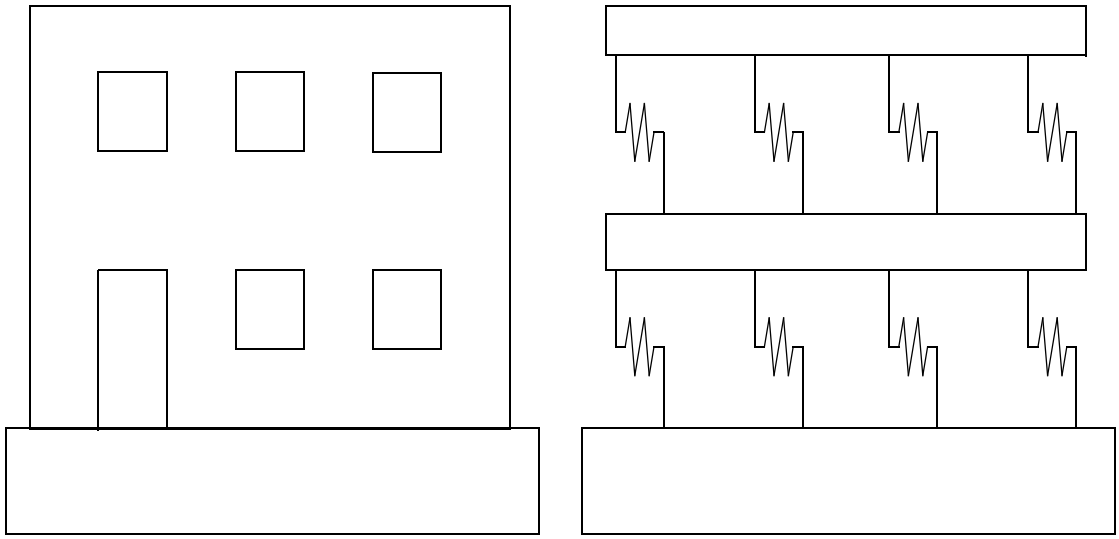

Figure 5.1. Schematic of the model presented in FEMA 356 for the in-plane analysis of perforated URM walls.

This model can be used in conjunction with both the linear static method and nonlinear static (i.e. pushover) method of evaluation. In the case of the linear static method, each spring stiffness is taken as the elastic stiffness of the corresponding pier, and the analysis is carried out to determine the demand on each pier due to the equivalent lateral load (as calculated using the elastic period and applicable design response spectrum). These forces are compared with predetermined values to assess the performance level of each pier and, ultimately, of the wall. In the case of the nonlinear static method, each spring is defined by a nonlinear force-displacement curve based on the governing failure mode. The analysis is performed by imposing increasing lateral forces or displacements to determine a pushover curve of the entire wall. Using this curve and the

applicable design response spectrum, a target displacement is defined, which is an estimate of the maximum displacement that the structure is expected to undergo during an actual earthquake. By comparing the target displacement with the pushover curve of the structure, the performance level of the individual piers can be assessed.

The modifications presented in this chapter are primarily geared towards the nonlinear static model due to its ability to capture the behavior of the structure beyond first crack. In addition, this analysis method is ideal for supporting the experimental portion of this study, since the test itself could also be characterized as nonlinear-static. However, all of the modifications proposed are equally applicable to the linear static model.

As mentioned previously, the proposed modifications primarily consist of two parts: (1) extending the pier shear springs to model the behavior of URM piers following retrofit with FRP overlays, and (2) modifying the overall model to account for the global characteristics outlined in Chapter 4. The details of the extension of the pier model to consider the effects of FRP retrofit as well as some minor modifications made to the URM pier model are discussed in detail in Section 5.1. The global issues addressed by the modified model are discussed in Section 5.2 and include pier definition and boundary conditions (Section 5.2.1), overturning effects (Section 5.2.2), global rocking (Section 5.2.3), and flange effects (Section 5.2.4). No modifications were required to consider the coupling between in-plane walls since the experimental results indicated that such coupling is negligible in the case of flexible timber diaphragms.

Utilizing the proposed modifications, a MATLAB program was developed to conduct the nonlinear pushover analysis of URM perforated walls and is discussed in

Section 5.3. This program was then employed to analyze each wall of the test structure before and after retrofit. Comparisons between the model predictions and the experimental results are provided in Sections 5.4 and 5.5.

5.1 Simplified Pier Damage Model

The simplified pier damage model described in the following sections is a modification and extension of the model outlined in FEMA 356. This model is composed of a single nonlinear translational spring which considers several failure modes. The force-drift relationship is defined based on the governing failure mode which is taken as the failure mode of least resistance at the current displacement level. The following sections outline the force-drift relationships for each of the failure modes considered for both URM piers and piers after retrofit with composite overlays. For brevity, only the details associated with either modifications and/or extensions of the recommendations given by FEMA 356 will be presented. Based on these recommendations, piers retrofit with unbonded vertical post-tensioning are considered as URM piers with an increased level of vertical stress. As a result, this retrofit technique is not recognized as requiring a separate model.

5.1.1 URM Pier Model

The in-plane behavior of URM piers has been the focus of several experimental investigations (Konig 1988; Epperson and Abrams, 1989; Abrams, 1992; Franklin et al., 2001, to cite but a few examples). In an attempt to consolidate these results, FEMA 307 (ATC, 1999b) presents a summary of experimental studies including force-displacement

responses and failure modes. The summarized experimental results suggest that aspect ratio and vertical stress are the most important factors in determining the failure mechanisms of URM piers. The four principal failure modes identified for in-plane URM piers are rocking, bed-joint sliding, diagonal tension, and toe crushing (Chapter 2 of this thesis presents a more detailed discussion of these failure modes). Corresponding to these four potential failure modes, FEMA 356 gives the capacities shown in Table 5.1.

Table 5.1. Strength equations given by FEMA 356 (ATC, 2000) for URM piers

Failure Mode	Strength (FEMA 356)
Rocking	$V_r = 0.9\alpha P\left(\frac{L}{H}\right)$
Bed-joint sliding	$V_{bjs1} = v_{me}A_n$ where $v_{me} = \frac{0.75\left(0.75v_{te} + \frac{P}{A_n}\right)}{1.5}$
Diagonal tension	$V_{dt} = f_{dt}'A_n\left(\frac{L}{H}\right)\sqrt{1 + \frac{\left(\frac{P}{A_n}\right)}{f_{dt}'}}$
Toe crushing	$V_{tc} = \alpha P\left(\frac{L}{H}\right)\left(1 - \frac{P}{0.7f_m'A_n}\right)$

where

α = 0.5 for cantilever piers and 1.0 for fixed-fixed piers

P = vertical compressive force on the pier

A_n = net area of the pier

L = length of the pier

H = effective height of the pier

v_{te} = shear strength of the bed-joint

f_{dt}' = tension strength of masonry

f_m' = compression strength of masonry

In addition, FEMA 356 provides force-drift curves for rocking and bed-joint sliding since these failure modes are considered deformation-controlled. Figure 5.2 shows the generalized force-drift relationship given by FEMA 356, and Table 5.2 shows the values required to specify this curve for specific failure modes. Note that FEMA 356 does not permit the nonlinear static analysis procedure to be used if force-controlled failure modes (i.e. toe crushing and diagonal tension) govern the response of any pier.

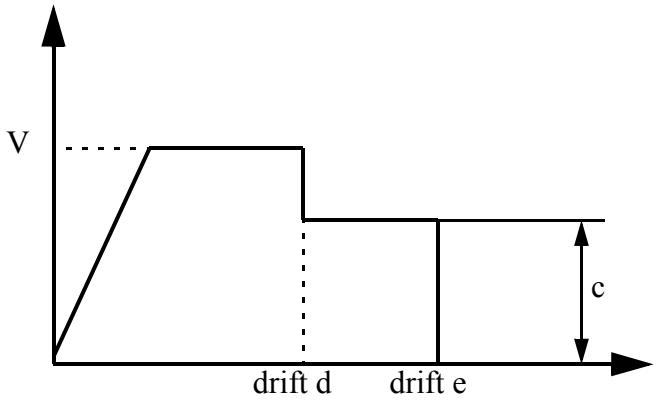

Figure 5.2. Generalized force-drift relationship given in FEMA 356.

Table 5.2. Force-drift relationships for deformation controlled failure modes given by FEMA 356 (ATC, 2000).

Failure Mode	V	d	e	c
Rocking/Toe Crushing	V_r	0.004(H/L)	0.008(H/L)	$0.6V_r$
Bed-joint Sliding	V_{bjs1}	0.004	0.008	$0.6V_{bjs1}$

The initial stiffness of the generalized relationship shown in Figure 5.2 is taken as the elastic stiffness of the pier and is given in FEMA 356 as:

$$K_{elastic} = \frac{1}{\left(\frac{H^3}{\lambda E_m I_g} + \frac{H}{A_v G_m}\right)} \quad (1)$$

where

I_g = gross moment of inertia of the pier

A_v = shear area of the pier

G_m = shear modulus of masonry (taken as $0.4E_m$)

λ = 12 for a fixed-fixed pier and 3 for a cantilever pier

For this research the most significant modification made to the FEMA 356 model was to combine the rocking and toe crushing failure modes into a single failure mode. This decision was largely based on past experimental studies on individual URM piers. Consider Table 5.3 which lists the failure modes and deformation capacities observed during the in-plane testing of several URM piers (ATC, 1999b). Based on this table, toe crushing is always preceded by either rocking or flexural cracking. Note that flexural cracking can be considered low level rocking. More specifically this implies that some rigid body rotation is required in order to cause a compressive failure at the toe of the pier, for typical ranges of vertical stress. Due to this apparent interdependency and the flexural nature of both rocking and toe crushing, these modes were combined for the analysis of walls in this study.

Table 5.3. Ultimate drift of URM piers corresponding to different failure modes

Failure mode	Ultimate drift (%)	Reference
Rocking	0.6% to 1.3%	Anthoine (1995), Magenes & Calvi (1995), Costley & Abrams (1996)
Rocking/Toe Crushing	0.8%	Abrams & Shah (1992)
Flexural Cracking / Toe Crushing / Bed-joint Sliding	0.8% to 1.3%	Manzouri et al (1995)
Flexural Cracking/ Diagonal tension	0.5% to 0.8%	Anthoine (1995), Magenes & Calvi (1992), Magenes & Calvi (1995)
Flexural Cracking/ Toe crushing	0.2% to 0.4%	Abrams & Shah (1992), Epperson and Abrams (1989)

The combined rocking/toe crushing failure mode proposed utilizes the curve given by FEMA 356 through the elastic range. However, once the pier goes into the nonlinear range, the assumed force-drift curve changes substantially. Specifically, the value for drift *d* is taken as the drift at which compressive failure initiates, and the value for residual strength *c* is taken as the toe crushing capacity. In order to obtain an approximation of these values the following assumptions were made:

- Axial vertical strain along the length of the pier is assumed to vary linearly
- The tensile strength of clay masonry is assumed to be negligible
- The ultimate compressive strain of masonry is assumed to be 0.0035 (ACI 530-02/ ASCE 5-02/TMS 402-02, 2002)
- The portion of masonry in compression is assumed to have a constant stress of $0.8f_m'$ over an equivalent compression zone equal to 80% of the distance from the fiber of maximum compression to the neutral axis (ACI 530-02/ASCE 5-02/TMS

402-02, 2002)

- The curvature along the height of the pier is assumed to vary linearly

Based on these assumptions, the shear strength associated with compressive failure can be calculated as:

$$V_{tc} = \alpha P\left(\frac{L - a_{tc}}{H}\right) \tag{2}$$

where

$$a_{tc} = \frac{P}{0.8 f_m' t_m} \tag{3}$$

t_m = thickness of pier.

Note that the strength expression obtained for toe crushing differs from that proposed by FEMA 356 in that the the compression strength is multiplied by 0.8 as opposed to 0.7 (i.e. FEMA 356 assumed the compressive stress was constant at $0.7f_m'$). Since FEMA 356 does not address the depth of the compression block, the design assumptions given by ACI 530-02/ASCE 5-02/TMS 402-02, (2002) were employed. By making use of the assumed ultimate masonry compressive strain, the following expression can be obtained for the curvature at compressive failure.

$$\phi_{tc} = \frac{(0.8)(0.0035)}{a_{tc}} \tag{4}$$

In order to obtain an approximation of the displacement at which compressive failure initiates, the assumption of linearly varying curvature along the height of the pier is utilized. Specifically, the maximum curvature is set equal to ϕ_{tc} and the curvature at the inflection point is set to zero. By integrating this assumed curvature distribution twice and making use of appropriate boundary conditions (i.e. zero displacement and zero rotation at

the base of the pier) the following expression is obtained:

$$\Delta_{tc} = \phi_{tc} H^2 \left(\frac{1}{2} - \frac{1}{6\gamma} \right) \tag{5}$$

where

γH = height of the inflection point above the base of the pier.

For drifts beyond this point the lateral resistance of the pier is assumed to rapidly decrease to zero. For simplicity the additional drift past Δ_{tc}/H is taken as the elastic drift of the pier. This was done in order to recognize the potentially brittle nature of toe crushing.

Figure 5.3 shows the proposed generalized force-drift curve for a URM pier. This curve differs from the one given in FEMA 356 in that it does not contain any sharp drops. This variation was made in order to better estimate past experimental results as well as to avoid any numerical convergence problems during analysis. Table 5.4 gives the modified values used for each of the failure modes to specialize the generalized force-drift relationship shown in Figure 5.3.

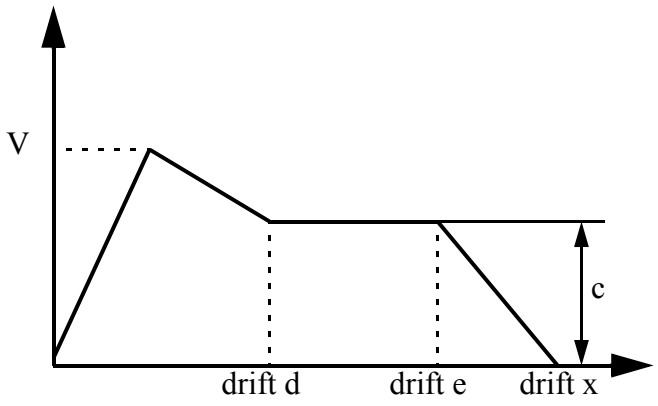

Figure 5.3. Generalized force-drift curve for the analysis of URM piers.

Table 5.4. Force-drift relationships for URM pier failure modes.

Failure Mode	V	d	e	x	c
Rocking/Toe Crushing	V_r	$(\Delta_{tc})/H$	–	$(\Delta_{tc}+\Delta_{elastic})/H$	V_{tc}
Bed-joint Sliding	V_{bjs1}	0.004	0.008	0.012	$V_{bjs2}=\mu f_a A_n$ (friction)
Diagonal Tension	V_{dt}	-	-	$2(\Delta_{elastic})/H$	0

Table 5.4 includes minor modifications made to the sliding and diagonal tension failure modes. In the case of bed-joint sliding, the residual strength value *c* is taken as the frictional resistance of the pier instead of $0.6V_{bjs1}$. This approach was also adopted in FEMA 306 (ATC, 1999a). However, FEMA 306 recommends that the coefficient of friction be divided by 1.5 to account for the elastic shear stress distribution in a rectangular pier. Since bed-joint sliding is an inelastic phenomenon, this "1.5" factor is omitted.

In the case of diagonal tension, a force-drift relationship was assumed since FEMA 356 supplies no guidance on the nonlinear response of this failure mode. The assumed curve is linear up to V_{dt} and then decreases rapidly to zero at twice the elastic drift. While there is no physical basis for this choice, it does reflect the potentially brittle nature of the failure mode and alleviates numerical convergence problems.

5.1.2 FRP Retrofit Pier Model

Several experimental studies have been conducted in order to investigate the effectiveness of FRP overlays as a retrofitting method for in-plane URM piers as discussed in Chapter 2. In general, two approaches have emerged for the in-plane retrofit of URM piers with FRP. The first employs sheets of FRP that are bonded over the entire

area of the pier. The second involves the use of FRP strips bonded in specific locations to strengthen the pier. For simplicity, only the FRP retrofit involving the use of strips is considered for this model.

Based on the results of past experiments, the most efficient configuration of FRP consists of vertical and diagonal strips as shown in Figure 5.4. Recall, that similar configurations were employed to strengthen Walls 1 and B of the test structure. The locations of the strips were determined in order to mitigate the rocking and diagonal tension failure modes discussed in Section 5.1.1.

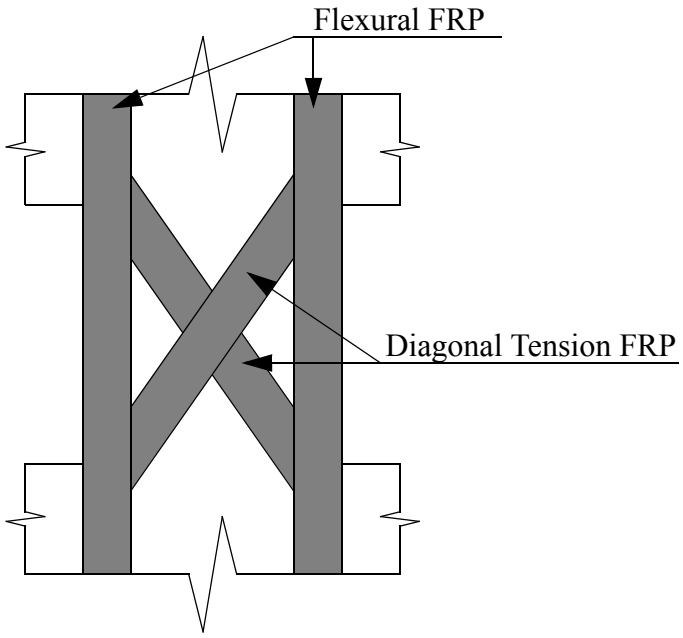

Figure 5.4. URM retrofit with FRP strips

As mentioned previously, the pier model presented in FEMA 356 does not explicitly address the behavior of piers retrofit with FRP overlays. Although, if FRP overlays are assumed to fall within the general category of external coatings, then FEMA 356 recommends that (1) the strengthened masonry wall be considered to behave as a

composite section as long as adequate anchorage is provided; (2) The difference in elastic moduli for each material be considered to determined stresses in the masonry and coating; and (3) if stresses exceed the strength of the coating, the coating should be considered ineffective.

Utilizing these recommendations the pier model presented in FEMA 356 was extended to predict the response of URM piers following the application of FRP overlays. The following sections detail the derivation of the strength and displacement response of each of the failure modes considered by the model, which were:

- Tension failure of flexural FRP
- Debonding of flexural FRP
- Compressive failure of masonry
- Shear failure of flexural FRP (bed-joint sliding)
- Tension failure of diagonal tension FRP
- Debonding of diagonal tension FRP

5.1.2.1 Tension Failure of Flexural FRP

In order to determine the capacity associated with the tension failure of flexural FRP, the pier was analyzed as a beam-column. The strength and drift expressions were determined by employing the same simplifying assumptions used in Section 5.1.1 with the exception that masonry stress-strain behavior is assumed to be linear in compression. In addition, when placed into tension the external reinforcement was assumed to be linear-elastic and to act at a single line located at the centroid of the strip. The contribution of the external reinforcement in compression was neglected due to the relatively large

compression stiffness and strength supplied by the masonry. A schematic illustrating the assumed internal stress and strain distributions is given Figure 5.5.

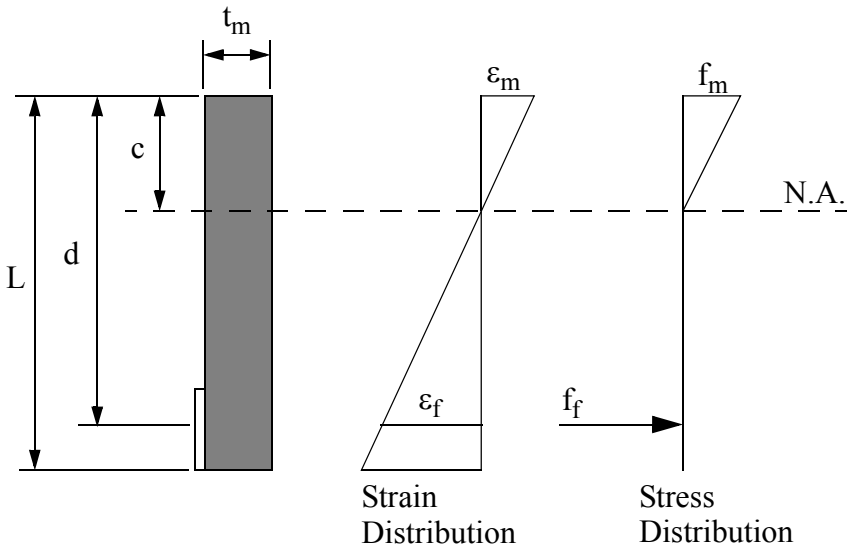

Figure 5.5. Internal stress and strain distribution assuming masonry is linear in compression.

By using strain compatibility and equilibrium the following expression for the distance from the extreme compression fiber of masonry to the elastic neutral axis, *c*, was determined.

$$c = \frac{-y + \sqrt{y^2 - 4xz}}{2x} \tag{6}$$

where

$$x = \frac{f_f t_m}{2n} \tag{7}$$

$$y = f_f w_f t_f + P \tag{8}$$

$$z = -d(P + f_f w_f t_f) \tag{9}$$

f_f = stress in the FRP

n = ratio of FRP modulus to masonry modulus

w_f = width of the flexural FRP

t_f = thickness of the flexural FRP

d = distance from extreme compression fiber to the centroid of reinforcement

Substituting the ultimate tensile strength of the FRP, f_{fu}, into Eqn. 6 through 9, the location of the neutral axis at tension failure of the FRP, c_{tf}, can be obtained. Summing moments about the centerline of the pier, in order to eliminate *P*, yields the moment corresponding to the tension failure of FRP as:

$$M_{tf} = \frac{f_{fu} t_m c_{tf}^2}{2n(d - c_{tf})}\left(\frac{L}{2} - \frac{c_{tf}}{3}\right) + f_{fu} w_f t_f \left(d - \frac{L}{2}\right) \tag{10}$$

The shear capacity associated with the tension failure of flexural FRP can be obtained by summing moments about the base of the pier and is written as:

$$V_{tf} = \frac{2\alpha M_{tf}}{H} \tag{11}$$

In order to calculate the drift associated with the tension failure of the flexural FRP, a linear curvature distribution was assumed. By integrating this assumed distribution twice and making use of appropriate boundary conditions (i.e. fixed condition at the pier base), the following expression for the displacement at tension failure of flexural FRP can be obtained.

$$\Delta_{tf} = \frac{f_{fu} H^2}{nE_m(d - c_{tf})}\left(\frac{1}{2} - \frac{1}{6\gamma}\right) \tag{12}$$

The resulting force drift relationship is shown in Figure 5.6. It is assumed that prior to reaching the rocking capacity of the URM pier, the pier behaves as if it were unreinforced. In addition, once the flexural FRP has failed, it is assumed that the force-drift relationship reverts to the force-drift curve associated with rocking/toe crushing of a URM pier.

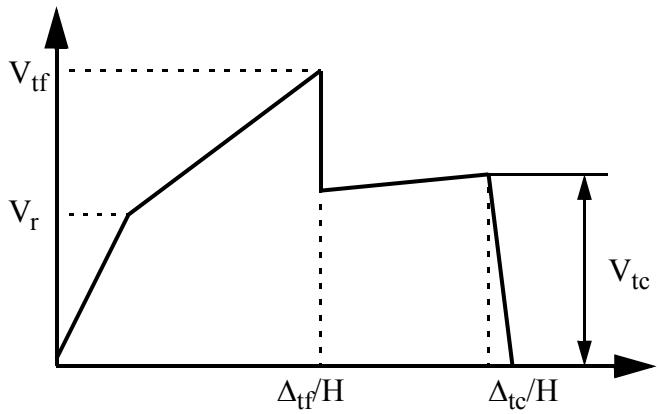

Figure 5.6. Force-drift relationship associated with the tension failure of flexural FRP.

5.1.2.2 Debonding of Flexural FRP

In order to estimate the strength associated with the debonding of flexural FRP, an expression for the bond strength between FRP overlays and masonry must be obtained. While a reliable expression is not currently available for masonry, extensive research has been conducted on the bond strength between FRP overlays and concrete. These models may provide a reasonable starting point; however, several issues exist which may jeopardize the applicability of these models to masonry, such as:

- The differential stiffness between bed-joints and units
- Geometric discontinuities caused by tooled bed-joints and/or the misalignment of masonry courses

• Surface texture and absorption capacity

Clearly, additional research in this area is required to investigate the effect of these characteristics; however, for the current study it is assumed that the debonding models developed for concrete are applicable to masonry. In general, the models available to predict the bond strength between concrete and FRP overlays can be classified as either empirical models, fracture mechanics based models, or design models (Chen and Teng, 2001). Empirical models and design models tend to trade off accuracy for efficiency and conservatism, and in many cases lack a scientific foundation. However, these models are easy to use and typically rely are readily available material properties. In contrast, models based on fracture mechanics, while more accurate, require more effort in terms of computation and determination of material properties. For the current study both a model based on fracture mechanics and a design/empirical model were considered.

Neubauer and Rostasy (1997) developed a model based on nonlinear fracture mechanics that has been shown to be accurate for predicting the bond strength between carbon FRP (CFRP) and concrete. The basis for this model is the assumption that the shear-slip relationship can be represented by a triangular distribution as shown in Figure 5.7.

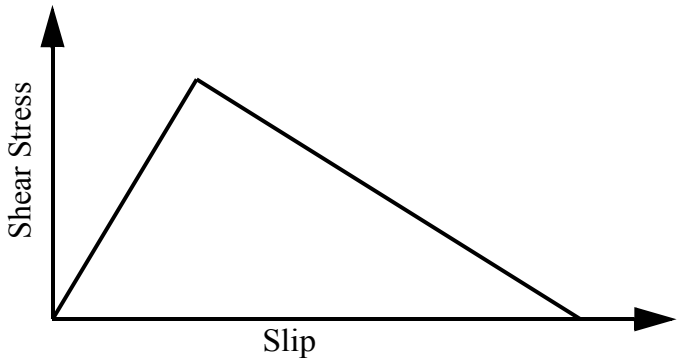

Figure 5.7. Shear-slip model for the bond strength between CFRP and concrete (Neubauer and Rostasy, 1997).

As a result of this assumption, expressions for the tensile force in the FRP at bond failure can be derived. For the case where the bond length of the reinforcement, L_f, is greater than the development length, L_d, the tensile force in the FRP at bond failure can be written as:

$$T_u = 0.64 k_p w_f \sqrt{E_f t_f f_{ctm}} \tag{13}$$

For cases where the bond length of the reinforcement is less than the development length, the tensile force in the FRP at bond failure becomes:

$$T_u = 0.64 k_p w_f \sqrt{E_f t_f f_{ctm}} \left(\frac{L_f}{L_d}\right)\left(2 - \frac{L_f}{L_d}\right) \tag{14}$$

where

$$L_d = \sqrt{\frac{E_f t_f}{2 f_{ctm}}} \tag{15}$$

T_u = tension force in the FRP at bond failure

k_p = factor that account for influence of FRP width relative to the width of the substrate

E_f = elastic modulus of the FRP

f_{ctm} = surface tensile strength of the substrate

L_f = bond length of the FRP

L_d = required bond length to maximize the bond strength

Neubauer and Rostasy (1997) noted that k_p can be estimated as 1.0. Although this model is based on fracture mechanics, the "0.64" factor employed in Eqn. 13 and 14 was determined experimentally.

As a simple alternative to the Neubauer and Rostasy model, an empirical model developed for design and presented in ACI 440.2R-02 (2002) was also considered. In this approach the strain associate with debonding is taken as:

$$\varepsilon_{db} = k_m \varepsilon_{fu} \tag{16}$$

where

$$k_m = \frac{1}{60\varepsilon_{fu}}\left(1 - \frac{mE_f t_f}{2,000,000}\right) \le 0.9 \text{ for } mE_f t_f \le 1,000,000 \text{ psi} \tag{17}$$

$$k_m = \frac{1}{60\varepsilon_{fu}}\left(\frac{500,000}{mE_f t_f}\right) \le 0.9 \text{ for } mE_f t_f > 1,000,000 \text{ psi} \tag{18}$$

ε_{fu} = ultimate tensile strain of the FRP

m = number of plies

To derive a strength expression associated with the debonding failure of flexural FRP, the procedure outlined in Section 5.1.2.1 was used; however, the tensile stress in the FRP was taken as the stress associated with debonding (as obtained from either the Neubauer and Rostasy (1997) model or the ACI 440.2R-02 (2002) model). The resulting expressions for moment and shear force at debonding can be written as:

$$M_{db} = \frac{f_{db} t_m c_{db}^2}{2n(d - c_{db})}\left(\frac{L}{2} - \frac{c_{db}}{3}\right) + f_{db} w_f t_f \left(d - \frac{L}{2}\right) \quad (19)$$

$$V_{db1} = \frac{2\alpha M_{db}}{H} \quad (20)$$

where

f_{db} = the tensile stress associated with FRP debonding taken as $T_u/(t_f w_f)$ or $E_f(k_m e_{fu})$.

c_{db} = the location of the neutral axis determined by substituting f_{db} into Eqn. 6 through Eqn. 9.

Similarly, the displacement associated with the debonding of flexural FRP can be written as:

$$\Delta_{db1} = \frac{f_{db} H^2}{E_f(d - c_{db})}\left(\frac{1}{2} - \frac{1}{6\gamma}\right) \quad (21)$$

Based on the experimental portion of this study as well as past research, it can be concluded that while debonding does limit the effectiveness of FRP overlays, in many cases it does not render the reinforcement useless. Rather the debonding, which typically occurs in a progressive manner, allows the retrofit pier to exhibit pseudo-ductile behavior. That is, the progressive debonding causes a decrease in the apparent stiffness of the reinforcement, it does not render the reinforcement useless. However, as the debonding propagates, brittle failure of the FRP overlays has been observed. This brittle failure is considered a secondary effect and is likely due to out-of-plane displacement of the reinforcement caused by the substrate sliding along the rough fracture surface (Neubauer and Rostasy, 1997).

For simplicity, this secondary effect is ignored, and the debonding of FRP overlays

is treated as a plastic mechanism. The displacement capacity of this failure mode is then limited by the onset of masonry compressive failure. To calculate the strength and displacement associated with this failure the assumptions outlined in Section 5.1.1 were employed (see Figure 5.8).

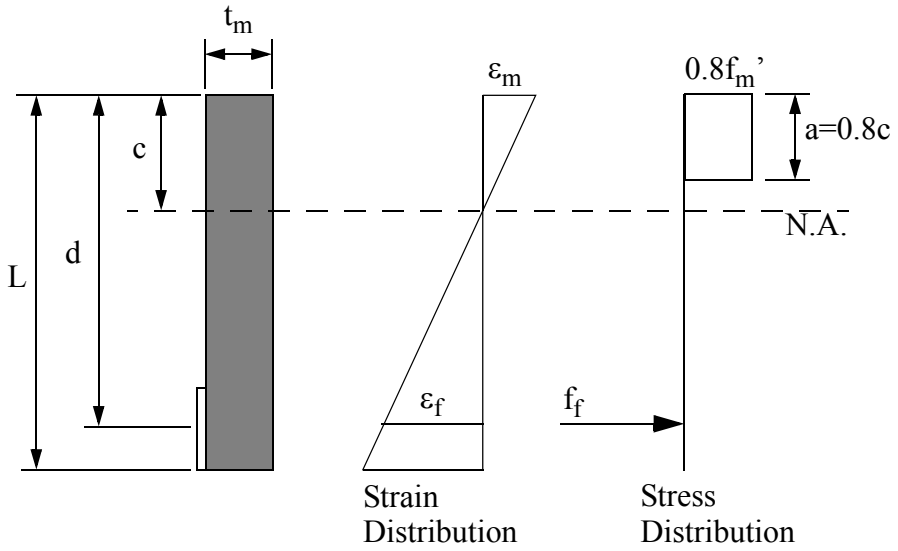

Figure 5.8. Internal stress and strain distribution utilizing a rectangular stress block for masonry in compression.

By setting the tensile stress in the reinforcement equal to the debonding stress, f_{db}, the moment associated with the onset of compressive failure after debonding can be written as:

$$M_{db2} = (f_{db} w_f t_f)\left(d - \frac{L}{2}\right) + (0.8 f_m' t_m a_{db})\left(\frac{L - a_{db}}{2}\right) \tag{22}$$

where

$$a_{db} = \frac{P + f_{db} w_f t_f}{0.8 f_m' t_m} \tag{23}$$

The corresponding shear capacity can be obtained by summing moments about the

base of the pier and is written as:

$$V_{db2} = \frac{2\alpha M_{db2}}{H} \tag{24}$$

Again, utilizing the assumptions given in Section 5.1.1, the displacement at which compression failure occurs is given by:

$$\Delta_{db2} = \left(\frac{0.0035(0.8)}{a_{db}}\right)(H)^2\left(\frac{1}{2} - \frac{1}{6\gamma}\right) \tag{25}$$

The resulting force drift relationship for the debonding of flexural FRP is shown in Figure 5.9.

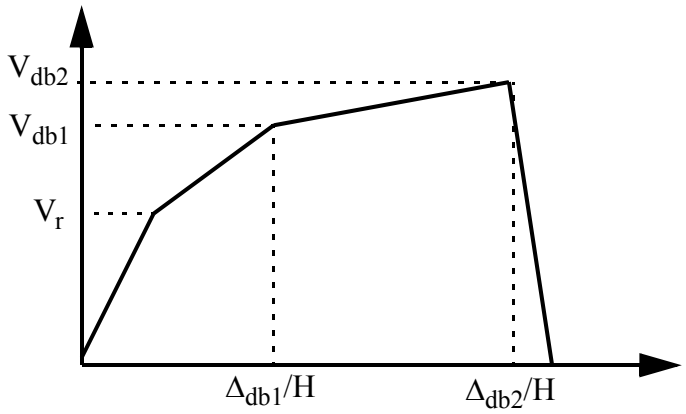

Figure 5.9. Force-drift relationship associated with the debonding of flexural FRP

5.1.2.3 Compressive Failure of Masonry

To determine the force-drift relationship associated with the compression failure of masonry, the internal stress strain relationship shown in Figure 5.8 was used. The resulting expressions for strength and displacement are summarized as:

$$M_{cf} = 0.8 f_m' a_{cf} t_m \left(\frac{L - a_{cf}}{2} \right) + f_f t_f w_f \left(d - \frac{L}{2} \right) \tag{26}$$

$$V_{cf} = \frac{2\alpha M_{cf}}{H} \tag{27}$$

$$\Delta_{cf} = \left(\frac{0.0035(0.8)}{a_{cf}} \right) (H)^2 \left(\frac{1}{2} - \frac{1}{6\gamma} \right) \tag{28}$$

where

$$f_f = \left(\frac{0.0035(0.8) E_f}{a_{cf}} \right) \left(d - \frac{a_{cf}}{0.8} \right) \tag{29}$$

$$a_{cf} = \frac{-y + \sqrt{y^2 - 4xz}}{2x} \tag{30}$$

$$x = 0.8 f_m' t_m \tag{31}$$

$$y = 0.0035 E_f w_f t_f - P \tag{32}$$

$$z = (0.8)(0.0035) E_f t_f w_f d \tag{33}$$

The resulting force drift relationship for the compressive failure of masonry is shown in Figure 5.10. Due to the potential brittle nature of a compressive failure, the force-drift relationship is assumed to decrease rapidly after the onset of compressive failure.

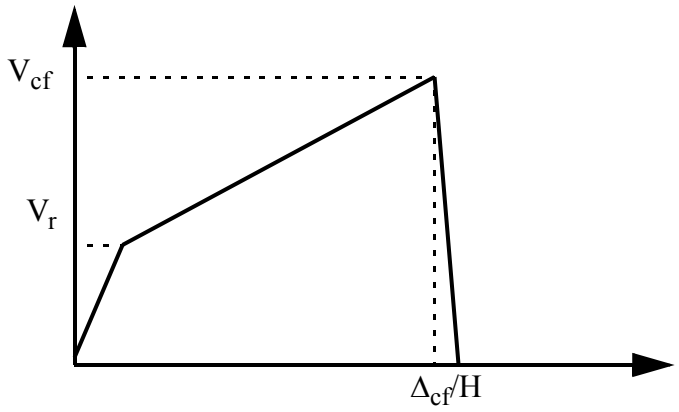

Figure 5.10. Force-drift relationship associated with the compressive failure of masonry.

5.1.2.4 Shear Failure of Flexural FRP (Bed-joint Sliding)

To obtain an expression for shear capacity due to the shear failure of flexural FRP, the entire bed joint is assumed to be cracked. This assumption is reasonable when one considers the area and stiffness of the FRP compared with that of the masonry. That is, the FRP is not "activated" until the masonry has cracked. Following this assumption, the resistance due to friction is additive to the shear strength of the flexural FRP and the following expression is obtained:

$$V_{sf} = \mu P + \tau_f w_f t_f \tag{34}$$

where

τ_f = shear strength of the flexural FRP in the transverse direction

The displacement associated with this failure mode is quite difficult to approximate. Unidirectional FRP is common for URM retrofit and in this loading case the fibers are being sheared transverse to their axis. The behavior of FRP composites loaded in this manner has been reported to be highly nonlinear (Vinson, 1998). Due to the complexity of this issue, the drift associated with this failure mode was assumed to be

0.4%, which is the drift *e* suggested by FEMA 356 for bed-joint sliding. The resulting force-drift relationship is given in Figure 5.11.

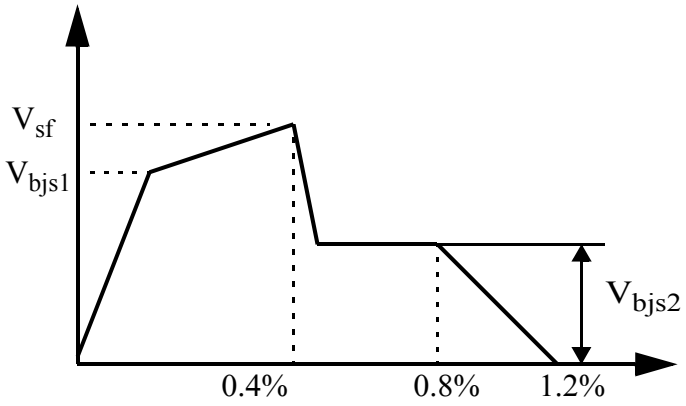

Figure 5.11. Force-drift relationship associated with the shear failure of flexural FRP.

5.1.2.5 Tension Failure of Diagonal Tension FRP

To obtain a force-drift relationship for the tension failure of the diagonal FRP, the contribution of the FRP is added to the diagonal tension capacity of the pier as given by FEMA 356. Although diagonal tension failure of URM piers is considered brittle, displacement capacities of 0.5% are not uncommon (ATC, 1999b). Due to the stiffness of typical FRP systems, this drift level is likely sufficient to engage the tension capacity of the diagonal FRP. These assumptions, coupled with the overly conservative alternative assumption of ignoring the contribution of the pier, resulted in the decision to approximate the capacity by adding the capacities of the FRP and masonry together. To calculate the contribution of the FRP, the pier was assumed to be completely cracked. The shear capacity corresponding to the failure of the diagonal tension FRP is obtained by considering the diagonal FRP as a tension tie, as shown in Figure 5.12.

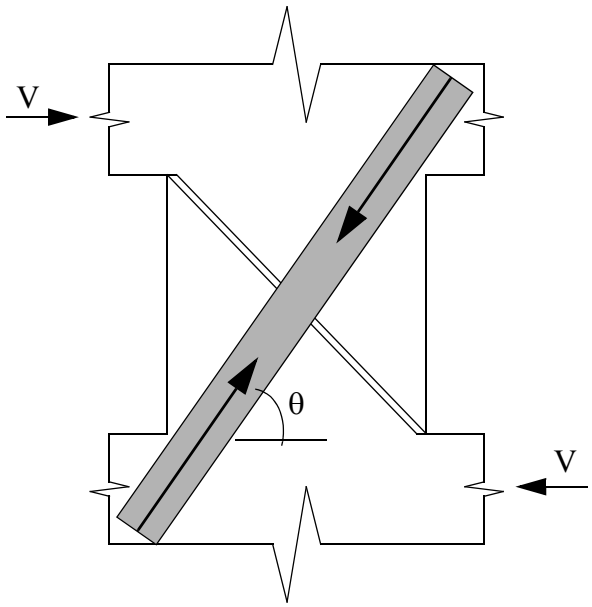

Figure 5.12. Model used to obtain diagonal tension strength associated with diagonal FRP strips

By utilizing statics, the contribution of the diagonal FRP can be obtained. This capacity is then added to the diagonal tension strength of URM piers (see Section 5.1.1) to obtain the following expression:

$$V_{dttf} = f_{dt}'Lt_m\left(\frac{L}{H}\right)\sqrt{1+\frac{P}{A_n f_{dt}'}} + f_{fu}w_{dt}t_{dt}\cos(\theta) \qquad (35)$$

where

w_{dt} = width of the diagonal FRP

t_{dt} = thickness of the diagonal FRP

θ = angle of diagonal tension FRP as defined in Figure 5.12

The force-drift relationship adopted to model the tension failure of the diagonal FRP is shown in Figure 5.13. As seen from this figure, the force-drift relationship was assumed to be linear until the reaching the capacity, V_{dttf}. Once the diagonal tension

capacity of the pier is overcome, the lateral resistance decreases rapidly to zero. The intent was to obtain a simplified relationship that recognized the potential brittle nature of this failure mode.

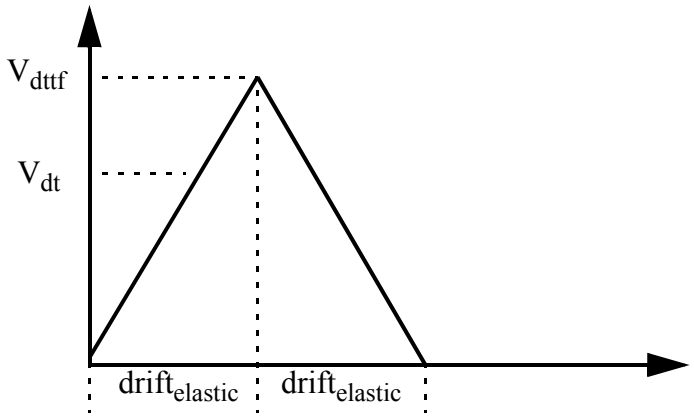

Figure 5.13. Force-drift relationship associated with the tension failure of diagonal FRP.

5.1.2.6 Debonding of Diagonal Tension FRP

Following the same procedure outlined in the previous section, an approximation of the force-drift relationship for the debonding of diagonal FRP can be obtained. The shear capacity associated with the debonding of diagonal FRP is obtained by substituting the debonding stress (as determined from Eqn. 13 and 14 or Eqn. 16) into Eqn. 35 for the tensile strength of the FRP as:

$$V_{dtdb1} = f_{dt}'Lt_m\left(\frac{L}{H}\right)\sqrt{1+\frac{P}{A_n f_{dt}'}} + f_{db}w_{dt}t_{dt}\cos(\theta) \qquad (36)$$

The force-drift relationship corresponding to debonding of diagonal FRP is shown in Figure 5.14. This relationship does exhibit some displacement capacity, which recognizes the pseudo-ductility that often results from FRP debonding (see Section 5.1.2.2). The first descending portion of the curve corresponds to a progressive

debonding of the diagonal FRP. The decrease in lateral resistance is a result of the contribution of the masonry decreasing rapidly. As a result, the total resistance of the pier is taken as V_{dtdb2} which is the shear capacity corresponding to the debonding of the diagonal FRP alone (i.e. the second term of Eqn. 36). The displacement associated with the complete debonding of the diagonal FRP can be calculated as:

$$\Delta_{dtdb} = \frac{f_{db}}{E_f}\sqrt{L^2 + H^2}(\cos(\theta)) \tag{37}$$

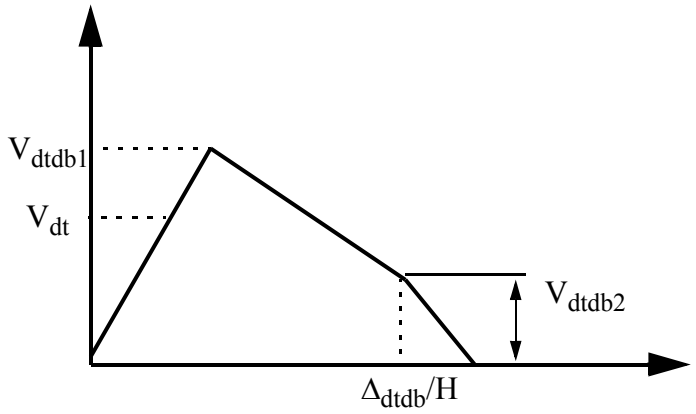

Figure 5.14. Force-drift relationship associated with the debonding of diagonal FRP.

5.2 Proposed Global Modifications

The current FEMA 356 model primarily relies upon the type of component models discussed in the previous sections to describe the behavior of the in-plane walls. While this is a common engineering approach, it neglects the important global characteristics of URM structures identified during the experimental portion of this study. Specifically, FEMA 356 provides little or no guidance for the consideration of the following issues: definition of pier dimensions and boundary conditions, effects of overturning moment, global rocking deformation, and flange participation. The following sections briefly

discuss the importance of each of these issues and describe the approach used to modify the existing model to allow them to be considered. The approaches adopted in this study should not be viewed as unique, but rather as examples of how such issues could be considered. Figure 5.15 shows a schematic illustrating some of the proposed modifications discussed in the following sections (note some modifications are difficult to represent visually).

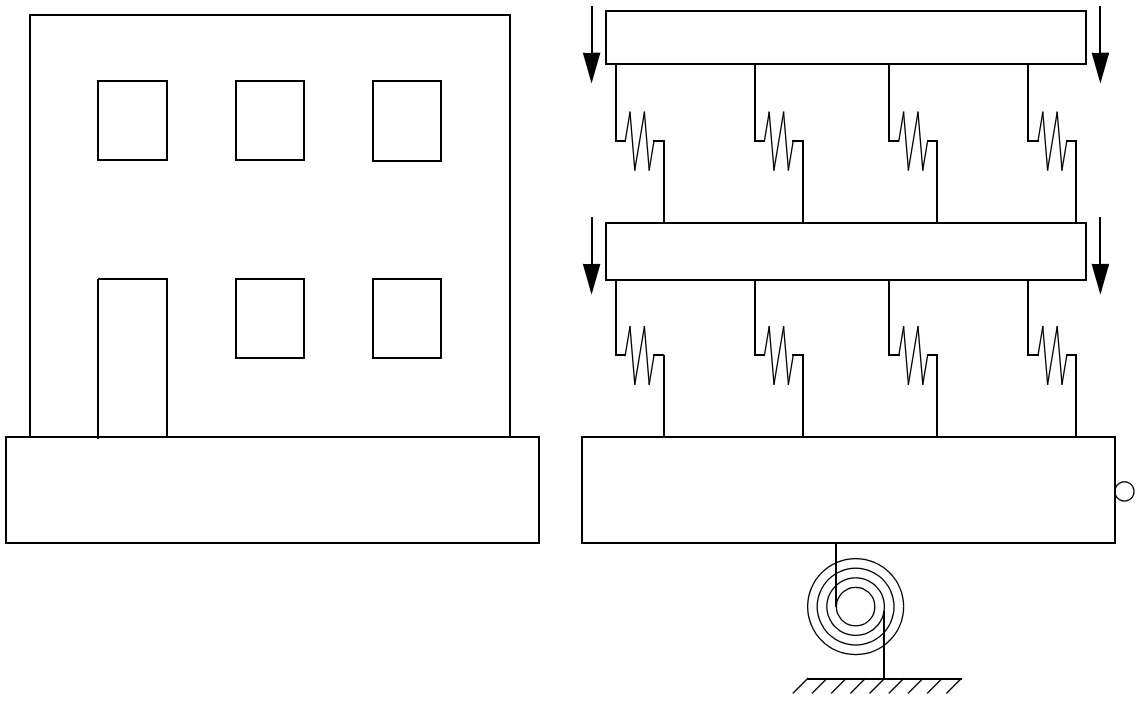

Figure 5.15. Schematic of the existing in-plane wall model given in FEMA 356 with the proposed modifications

5.2.1 Definition of Piers and Boundary Conditions of Piers

As apparent from the discussion of pier models in the Section 5.1, flexural behavior of in-plane piers is strongly dependant on the assumed effective height and boundary conditions. In the case of past component tests, this issue was easily resolved as

such tests have typically created highly idealized pier configurations. In contrast, typical wall configurations often render the definition of effective height and boundary conditions less straightforward. While this issue is critical to the accurate analysis of URM walls, FEMA 356 provides little guidance for appropriate choices. Specifically, the method outlined in FEMA 356 requires that piers be designated as either fixed-fixed or cantilevered, and that the effective height be defined as the height of adjacent openings. Clearly, such an approach cannot be used to define the effective height of a pier between two openings of different heights (i.e. door and window). In addition, no guidance is provided on how to choose the appropriate boundary conditions.

As a result of these shortcomings, a simple yet versatile method, based on the experimental portion of this study, was developed to provide an approximation of the effective height and boundary conditions of in-plane URM piers within a perforated wall. The proposed method defines the effective height of a pier as the height over which a compression strut is likely to develop (as shown in Figure 5.16). The compression strut is defined by assuming that flexural cracks can develop either horizontally or at a 45 degree angle. In addition, the strut is assumed to develop at the steepest possible angle. That is, the likely compression strut is taken as the strut which offers the minimum lateral resistance. Note that by following this simple method all of the flexural cracks observed in the test structure can be be predicted (see Chapter 4).

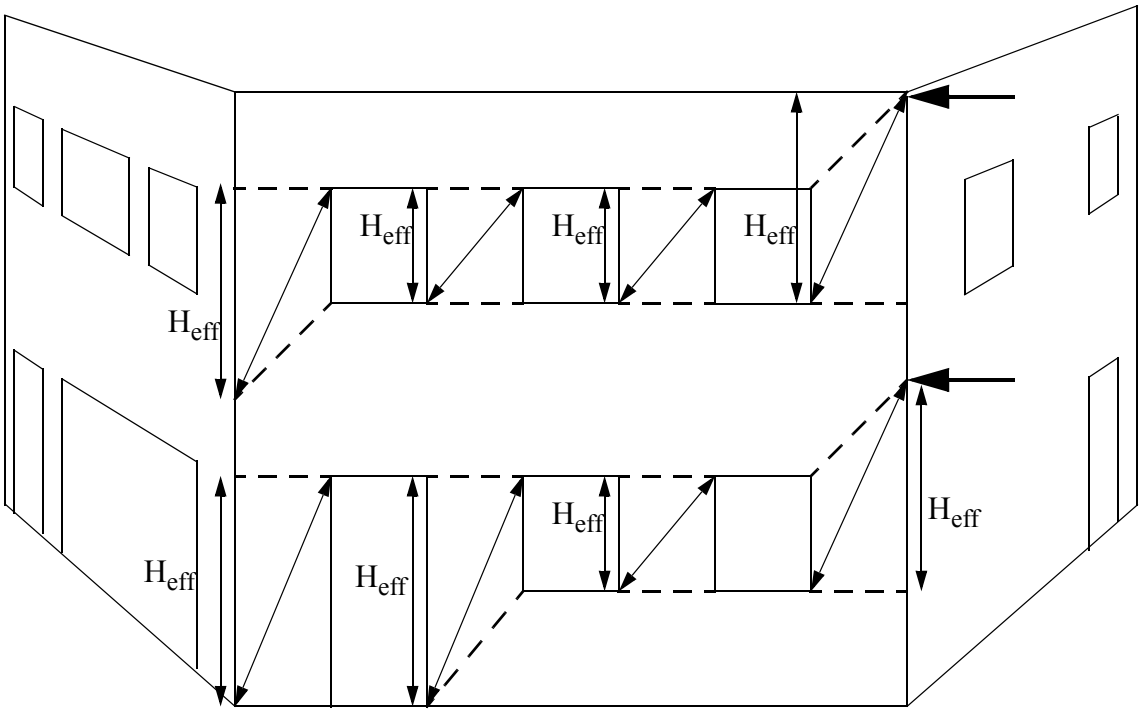

Figure 5.16. Definition of pier effective height based on the development of a compression strut.

Recall that only flexural failure modes (i.e. rocking/toe crushing) are dependent on the effective height and boundary conditions of the pier. Furthermore, if the assumed compression strut develops, then the end moments of the pier are equal which is consistent with a fixed-fixed boundary condition. As a result, the effective height as defined previously should always be used in conjunction with a fixed-fixed boundary condition. While such an assumption is only valid at ultimate (i.e. once flexural cracks have developed above and below the pier), for simplicity this assumption is employed for the elastic range as well.

Based on this method, the geometry of a pier may change based on the direction of loading. For example, for the loading direction shown in Figure 5.16, the effective height of the pier in between the door and window is taken as the height of the door opening. If

the load was applied in the other direction, the effective height of this pier would be the height of the window opening.

5.2.2 Overturning Moment

In most URM walls, the primary effect of overturning moment is to alter the vertical stresses in the piers and flanges (note global rocking displacement will be discussed in the following section). Based on the development of component models in Section 5.1, it is apparent that the behavior of in-plane piers is very sensitive to the level of vertical stress. Therefore, the effects of overturning moment must be considered for cases where substantial changes in the vertical stress distribution can be expected. These cases include structures where the height of the building is similar to the length, i.e., where the overturning moment is relatively large compared with the moment of inertia of the in-plane walls. This is the case for numerous low-rise URM structures, including the test structure used in this research. Recall, that during the experimental portion of this study three diagonal cracks were observed in the test structure. In all cases these cracks formed when the effects of overturning moment were acting to increase the level of vertical stress in the pier. Clearly, this underscores the potential impact of overturning moment on pier failure modes and ultimately on the response of the entire wall.

Although, the need to consider the effects of overturning moment is recognized by FEMA 356 as a general requirement for all analysis, little guidance is provided with respect URM structures. In order to include this effect in the FEMA 356 model, a relationship between overturning moment and the average vertical stress in the piers and flanges must be obtained (flange participation will be discussed in Section 5.2.4). To

accomplish this, cross-sections at each floor level of the in-plane wall are analyzed using a fiber model. This analysis is carried out by dividing each section into a number of strips and applying an incrementally increasing curvature to the cross-section. If plane sections are assumed to remain plane after bending, then the incremental change in strain of each fiber can be written as:

$$d\varepsilon_{i,j} = d\phi_j d_i + d\varepsilon_{c,j} \tag{38}$$

where

$d\varepsilon_{i,j}$ = incremental change in the axial strain of fiber i at step j

$d\phi_j$ = incremental increase in the curvature of the cross-section at step j

d_i = distance between the centroid of the cross-section and fiber i

$d\varepsilon_{c,j}$ = incremental change in the centroid strain of the cross-section at step j

Figure 5.17 shows a schematic illustrating this assumed strain distribution.

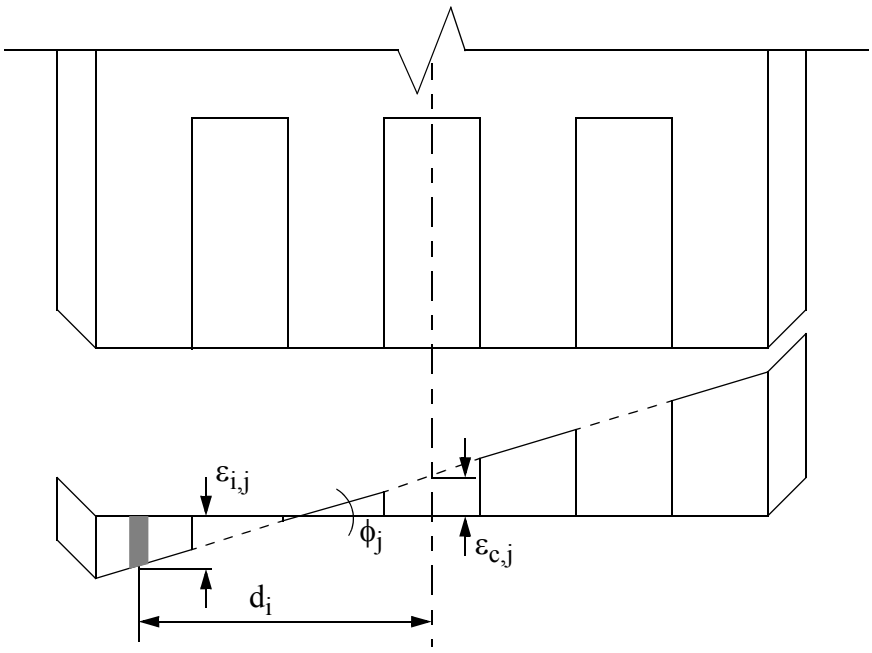

Figure 5.17. Illustration of the assumed strain distribution.

Based on the assumed strain distribution the incremental change in moment and axial force on the cross-section can be determined as:

$$dP_j = d\phi_j \left(\sum_{i=1}^{n} A_i E_{i,j} d_i \right) + d\varepsilon_{c,j} \left(\sum_{i=1}^{n} A_i E_{i,j} \right) \tag{39}$$

$$dM_j = d\phi_j \left(\sum_{i=1}^{n} A_i E_{i,j} d_i^2 \right) + d\varepsilon_{c,j} \left(\sum_{i=1}^{n} A_i E_{i,j} d_i \right) \tag{40}$$

where

dP_j = incremental change in the axial force applied to the cross-section at step j;

n = total number of fibers;

A_i = area of fiber i;

$E_{i,j}$ = tangent modulus of elasticity of fiber i at step j; and

dM_j = incremental change in the moment applied to the cross-section at step j.

For the analysis at hand, the applied axial load (i.e. the weight of the structure) is assumed to be constant. As a result, Eqn. 39 can be used to approximate the incremental change in centroid strain as:

$$d\varepsilon_{c,j} = \frac{d\phi_j \left(\sum_{i=1}^{n} A_i E_{i,j} d_i \right)}{\left(\sum_{i=1}^{n} A_i E_{i,j} \right)} \tag{41}$$

For the determination of $E_{i,j}$, the tensile strength of masonry is ignored and the material model is taken as linear elastic in compression. The solution procedure can be

summarized as follows:

(1) Discretize the cross-section into *n* fibers.

(2) Set the initial strain in each fiber equal to the strain induced by gravity load, *P*.

(3) Add a small incremental curvature to the previous value.

(4) Estimate the centroid strain for the current step from Eqn. 41 using the tangent moduli from the previous step.

(5) Solve Eqn. 39 and Eqn. 40 for the incremental change in moment and axial load.

(6) If the incremental change in axial load is sufficiently close to zero (as specified by some tolerance), continue the analysis (i.e. return to step 3).

(7) If the incremental change in axial load is not sufficiently close to zero, return to step 4 and re-estimate the centroid strain by using the current tangent moduli.

Once the analysis of the cross-section is completed, the stresses in the fibers at each step can be calculated by:

$$\sigma_{i,j} = E_{i,j}(d\phi_j d_i + d\varepsilon_{c,j}) \tag{42}$$

The average vertical stress in each pier and flange is then calculated by averaging the stresses for all of the fibers that reside within the component.

Note that the moment calculated above does not correspond to the overall overturning moment. Rather, this moment is the portion of the overturning moment that is resisted through the altering of vertical stress in piers and flanges. In order to obtain the correct vertical stresses the total overturning moment has to be reduced by the local moments at the base of each pier. To illustrate how the simplified pushover analysis accomplishes this, consider the perforated masonry wall shown in Figure 5.18. The

moments at the base of each pier can be calculated as $v_i \gamma h_i$. Thus, the reduced overturning moment that is resisted through altering the vertical stresses in piers and flanges can be written as:

$$M = \sum_{s=1}^{2} P_s H_s - \sum_{i=1}^{n} v_i \gamma_i h_i \tag{43}$$

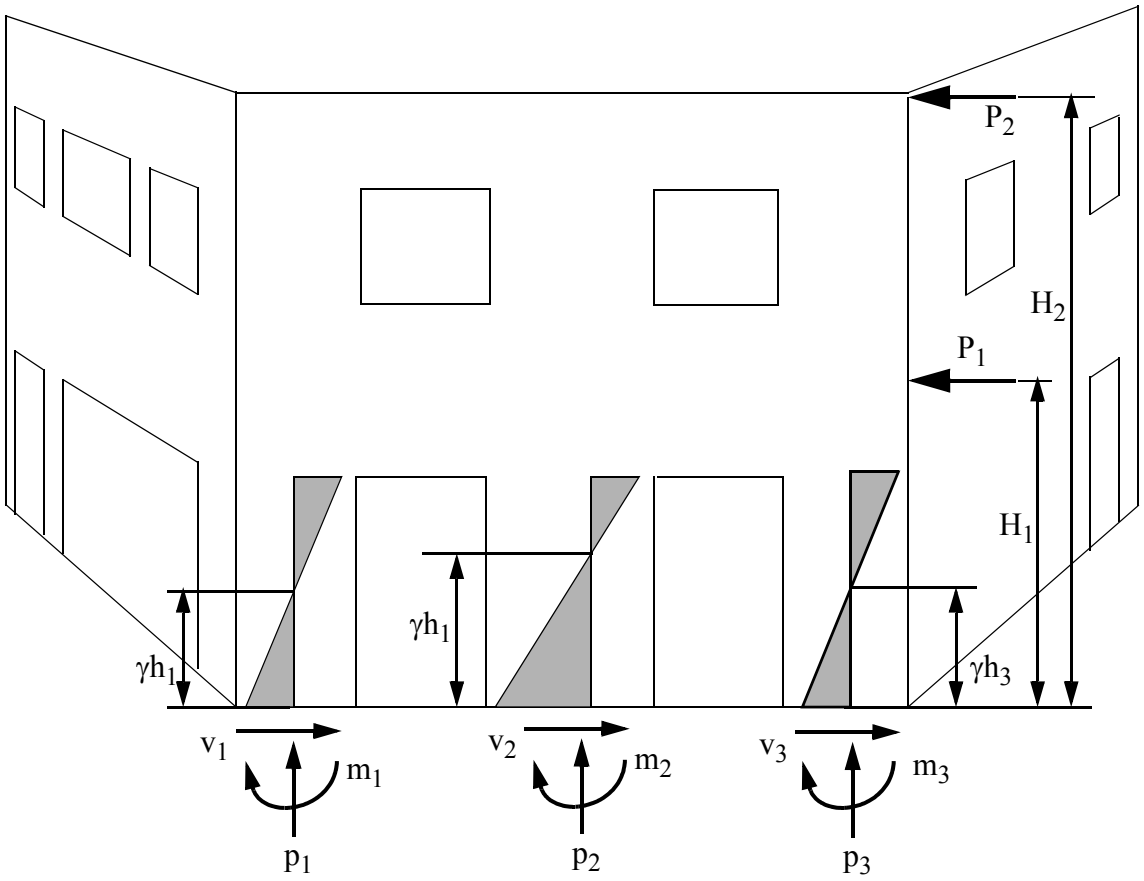

Figure 5.18. Schematic of a perforated URM wall illustrating how overturning moment is calculated.

5.2.3 Global Rocking

Thus far, the description of the simplified model has focused primarily on the response of the in-plane piers to interstory shear force/displacement. However, in some

cases wall response is not dominated by interstory shear deformation caused by lateral force, but rather due to a global rotation of the entire wall caused by overturning moment. Recall that varying degrees of global rocking deformation were observed during the testing of Walls 1, A, and B in-plane as discussed in Chapter 4. Based on these results, it is concluded that global rocking is a viable failure mode for perforated URM walls and as such must be considered in the analysis of such walls. While this failure mode is not addressed in FEMA 356, FEMA 306 (ATC, 1999a) does consider global rocking as a potential failure mode for solid in-plane walls.

In order to modify the FEMA 356 model to capture this type of behavior, a rotational spring was supplied between the base of the model and the foundation (see Figure 5.15). The characteristics of this rotational spring are defined based on the analysis conducted in the previous section. Recall, that to consider overturning moment, cross-sections of the in-plane walls (including flanges) were analyzed using a fiber model. As a result of this analysis, a moment-curvature relationship was developed for the base of the structure. In order to convert this relationship into a moment-rotation relationship, the curvature was assumed to vary linearly from ϕ_j at the base of the structure to zero at the top of the first story. By integrating this curvature distribution over the height of the first story and enforcing zero rotation at the base, the following expression is obtained:

$$\theta_j = \frac{\phi_j H_1}{2} \tag{44}$$

where

θ_j = rotation at the top of the first story

H_1 = the height of the first story.

The assumption of curvature distribution implies that the rotation of the cross-section varies parabolically throughout the height of the first story. For simplicity, the rotation of the cross-section is assumed to be constant throughout the height of the first story, thus the angle defined by Eqn. 44 is the rotation of the base rotational spring. This rotation coupled with the moment, M_j, as defined in the previous section, fully defines the base rotational spring.

5.2.4 Flange Participation

For the current study a flange is defined as the portion of the out-of-plane wall that participates with the in-plane wall to resist lateral loads. Based on the experimental results presented in Chapter 4, substantial flange participation was observed for each in-plane wall in each loading direction. To modify the current FEMA 356 model to consider this effect, the observed flanges were classified into three categories:

- Compression flanges - the portion of the out-of-plane wall that resists compressive stresses generated by the rocking of the adjacent pier
- Global tension flange - the portion of the out-of-plane wall that is lifted up due to global rocking.
- Component tension flange - the portion of the out-of-plane wall that is lifted up by the vertical displacement associated with local pier rocking

The following sections detail the modifications proposed to allow the current FEMA 356 model to consider the effect of each of these flanges.

5.2.4.1 Compression Flanges

In most cases, the participation of a compression flange has a minor effect on the shear capacity associated with a toe crushing failure of the adjacent pier. However, typically such a flange acts to substantially increase the rotational displacement at which this type of failure occurs. As a result, neglecting such participation can result in overly conservative estimates of wall performance.

During the experimental portion of this investigation strain gages were employed to monitor the response of the out-of-plane walls with the intent of determining the effective length of the compression flanges. However, due to large variations in material properties and extensive cracking, the reliability of the data obtained from these gages is questionable (see Appendix C through F). As a result, the design provisions of ACI 530-02/ASCE 5-02/TMS 402-02 (2002) are employed. According to these provisions the length of a compression flange may be taken as six times the thickness of the in-plane wall or the actual length of the flange, whichever is smaller. Based on the commentary of this document, this provision is applicable to unreinforced masonry walls constructed in an interlocking running bond configuration, which is consistent with the test structure.

To address the participation of a compression flange, the failure modes associated with compression failure are modified in the pier damage model. For simplicity the compression zone of the pier is assumed to reside entirely within the flange. As a result, the length of the flange, L_{flange}, is substituted for the thickness of the pier, t_m, in Eqn. 3, 22, 23, 26, and 31. Note that this modification is only appropriate when the adjacent flange is located at the toe of the pier.

5.2.4.2 Global Tension Flanges

A global tension flange, as defined previously, impacts the response of URM walls through supplying additional weight. This weight is effective in (1) resisting the effects of overturning moment and (2) increasing the level of vertical compressive stress in the piers. As a result, these tension flanges can substantially affect both the strength of the wall as well as the governing failure modes of the individual components.

During the experimental portion of this study, Walls 1, A, and B all displayed varying degrees of global rocking. In all cases similar global tension flanges were engaged. Consider Figure 5.18, which shows an exaggerated schematic of the deformation of Wall 1 and out-of-plane Walls A and B prior to retrofit. From this figure it is apparent that the global tension flange was defined by a 45 degree crack from the second floor of Wall 1 to the roof of Wall A (similar cracks were observed during the testing of Walls A and B in-plane (see Chapter 4)). As a result, the simplified pushover model defines a global tension flange as the portion of the out-of-plane wall located above a 45 degree crack from the second floor to the roof level. To ensure that the out-of-plane walls are not counted twice, the portion of a global tension flange that extends beyond the centerline of the out-of-plane wall is ignored.

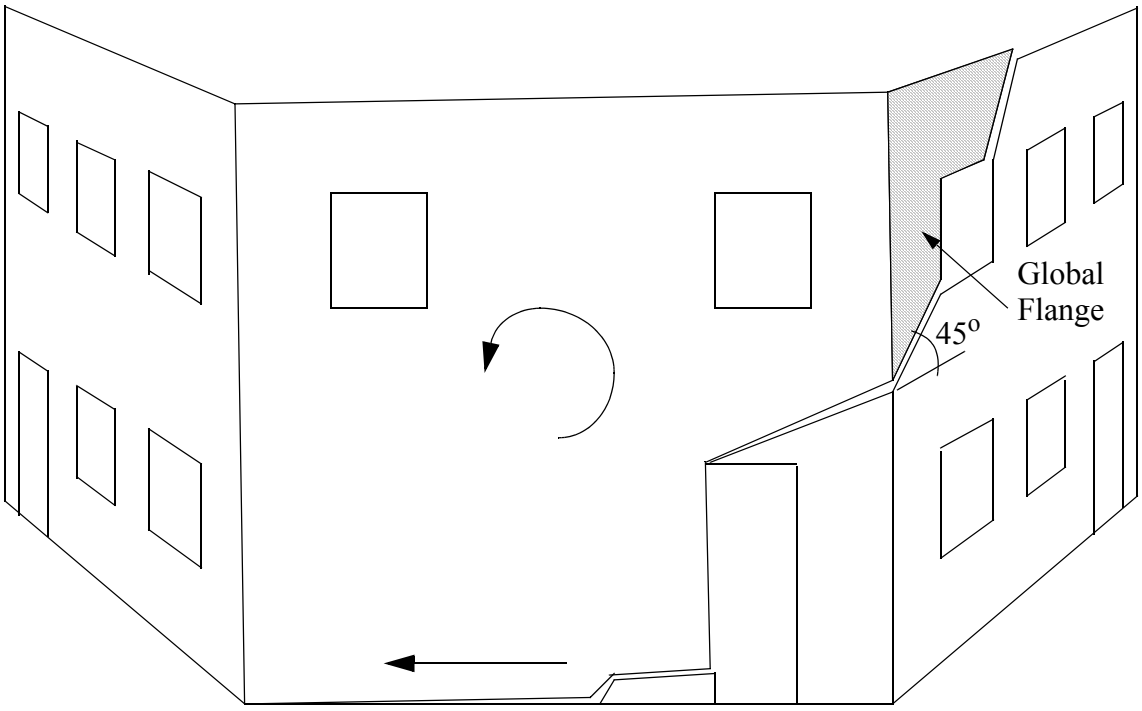

Figure 5.19. Schematic illustrating the definition of global tension flanges.

To consider the effect of global tension flanges on wall behavior, they are included in the cross-section used to calculate the effect of overturning moment and global rocking displacement (see Sections 5.2.2 and 5.2.3). However, for these calculations the global tension flanges need to be converted into an equivalent prismatic flange. That is, a flange with a constant length over the height of the structure. To accomplish this conversion, the initial vertical stress in the flange is assumed to be equal to that of the adjacent pier. Since the total weight of the flange is known, the equivalent length can be calculated as:

$$L_{gf} = \frac{W_{gf}}{t_{gf} f_{flange}} \tag{45}$$

where

W_{gf} = weight of the global tension flange

t_{gf} = thickness of the out-of-plane wall

f_{flange}= initial vertical stress in the flange

In addition to considering the impact of global tension flanges on the effects of overturning moment, the weight of the global tension flange is also assumed to increase the vertical stress in the adjacent pier. For each displacement step, the vertical stress in the flange (i.e. as calculated by the procedure outlined in Section 5.2.2) is added to the vertical load on the adjacent pier.

5.2.4.3 Component Tension Flanges

Similar to global tension flanges discussed in the previous section, component tension flanges are assumed to act primarily as a source of additional weight. However, a component tension flange is only considered to increase the vertical stress in the adjacent pier and not to affect the way overturning moment is resisted. Nevertheless, such flange can substantially alter the behavior of the adjacent piers and, thus, must be considered in the analysis.

Recall that during the experimental portion of this study, the uplift associated with pier rocking deformation engaged significant portions of the out-of-plane walls. Figure 5.20 shows a schematic illustrating the deformed shape of Wall 2 and out-of-plane Walls A and B. Note that similar flange participation was observed during the testing of Walls 1, A and B (see Chapter 4). In addition, Figure 5.20 shows the assumed component tension flanges used in the proposed model.

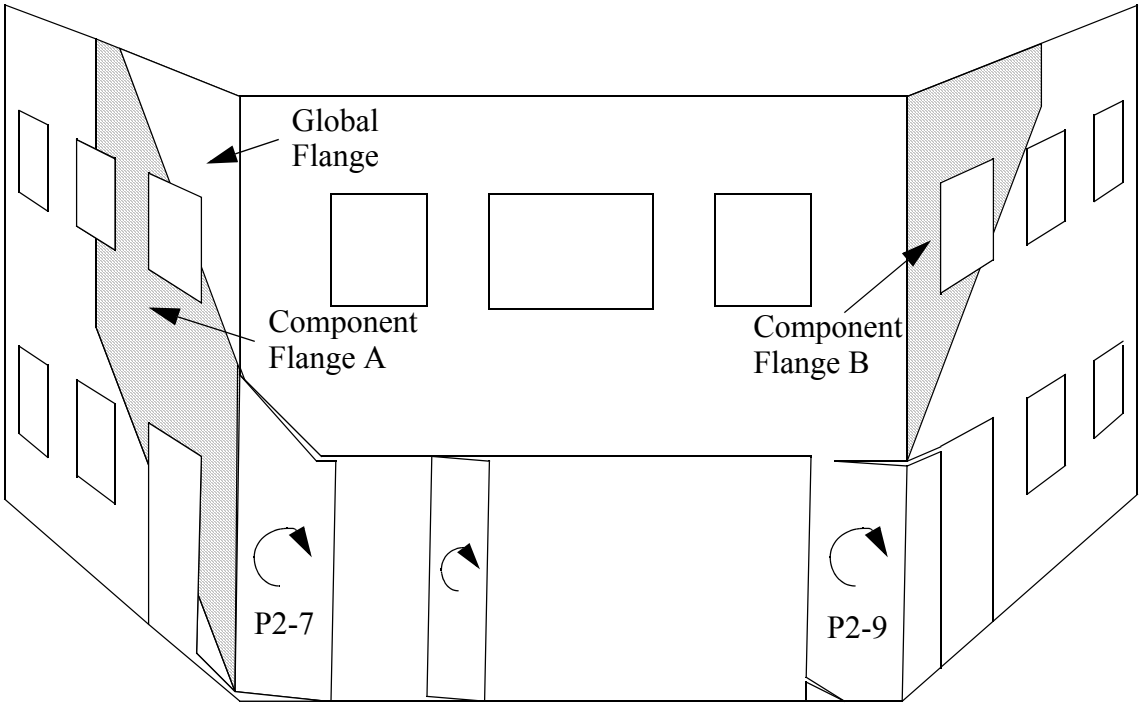

Figure 5.20. Schematic illustrating the definition of component tension flanges.

For a pier located at the heel of the wall, the component tension flange is defined by a 45 degree crack from the base of the pier to roof of the out-of-plane wall. To ensure that the out-of-plane wall is not counted twice the portion of the component tension flange that extends beyond half of the out-of-plane wall is ignored. In addition, the portion of the component tension flange that coincides with the global tension flange is also ignored (see Figure 5.20). For a pier located at the toe of the wall, the component tension flange is defined by a 45 degree crack from the top of the pier up to the roof of the out-of-plane wall. Again, the portion of this flange that extends beyond half of the out-of-plane wall is ignored.

To consider the impact of these flanges, the weight of the component tension flange is added to the weight of the adjacent pier. For example, the weight of component

tension flange A is added to the weight of pier P2-7. The only exception to this rule is made for the calculation of sliding resistance for piers located at the heel of the wall. In these cases only the weight of the global tension flange is assumed to be active. This modification was made due to the sliding deformation that occurred above the piers located at the heel of Walls A and B during the experimental portion of this study. This observed behavior illustrated that only the global tension flange is active in resisting this deformation.

5.3 Coding of Proposed Model

Based on the proposed modifications discussed in the previous sections, a MATLAB program was developed to conduct the nonlinear pushover analysis of URM perforated walls. A flow chart of this program is shown in Figure 5.21.

As apparent from this figure, the analysis begins by developing the moment-rotation and moment-vertical stress relationships for the entire wall as defined in Sections 5.2.2 and 5.2.3. Following this step, lateral displacements are applied to the model based on the selected type of pushover (Section 5.3.2 describes the various types of displacement distributions available). Then the secant stiffness and corresponding lateral shear force of each pier are calculated based on the nonlinear force-drift relationships defined in Section 5.1 (Section 5.3.1 describes the coding of the individual pier models). The restoring forces at the second floor and roof level are then obtained by summing up the resistances of all piers in each story. Based on these forces the overturning moment for each floor is calculated, and the vertical stresses in each pier are updated based on the relationship defined Section 5.2.2. The program then iterates by recalculating the secant

stiffness of each pier until the lateral forces at each floor level converge (based on some allowable "error" value). Once these values converge, the final overturning moment at the base of the structure is used to calculate the global rocking displacements as per Section 5.2.3. The total displacements for the current step are then obtained by adding the interstory displacements to the global rocking displacements. This procedure is repeated with incrementally increasing story displacements until the desired roof displacement is achieved. The program output includes the following: overall force-displacement curves, interstory force-displacement curves, global rocking force-displacement curves, individual pier failure modes, pier failure sequence; and variation of vertical stress in each pier during loading.

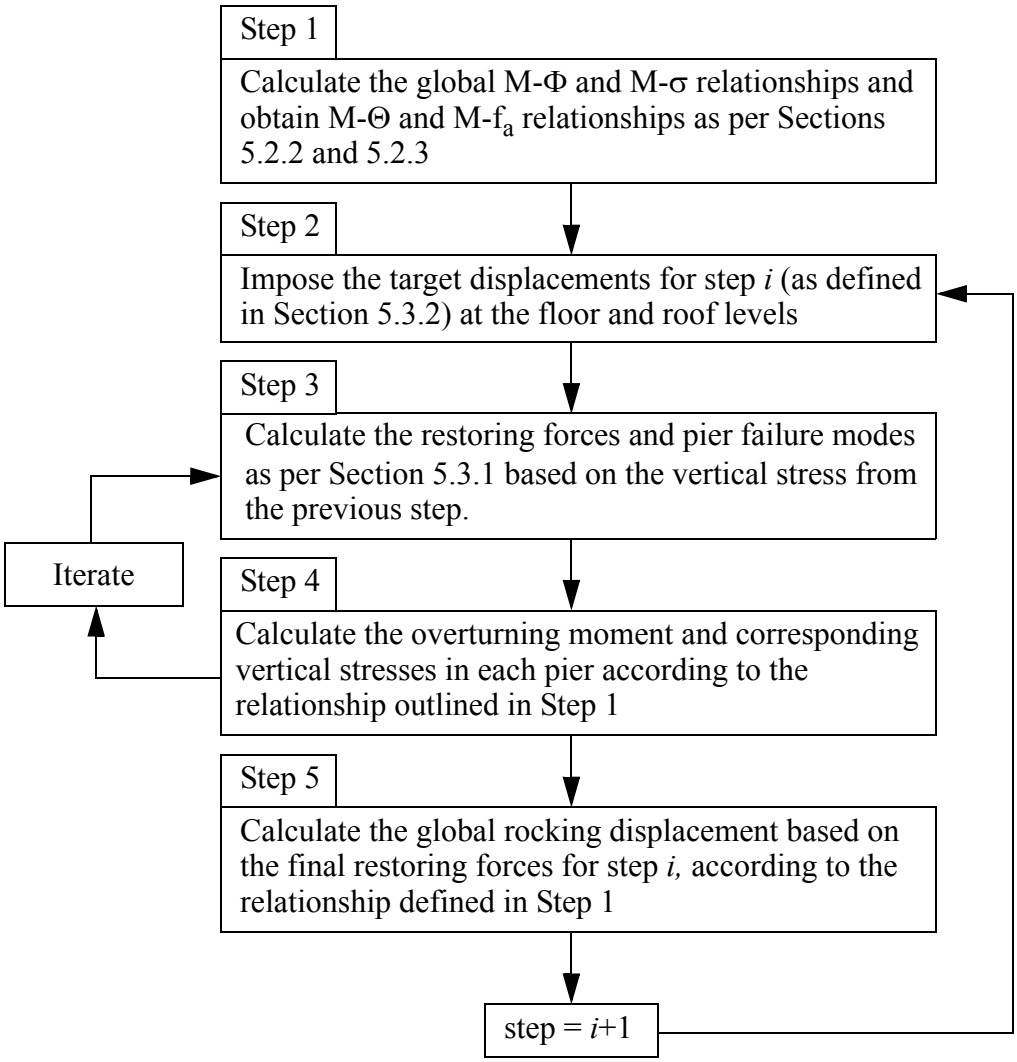

Figure 5.21. Flow chart depiction of the simplified pushover analysis program.

5.3.1 Pier Model

Based on the pier model discussed in Section 5.1, a MATLAB program was developed which is utilized as a subroutine within the overall pushover analysis program discussed in the previous section. Similar to the overall program, the analysis of each pier is conducted in displacement control. At each displacement level, each of the curves described in either Section 5.1.1 or 5.1.2 are formed for the pier being analyzed. Based on

these curves, a governing failure mode is selected, and the pier is assumed to follow that force-drift behavior for the current displacement step.

In order to define the governing failure mode, the FEMA classification of force-controlled and displacement-controlled failure modes is adopted. Due to the potential for brittle behavior, failure modes associated with diagonal tension and compression failure are assumed to be force-controlled. That is, these failure modes will govern only when the force in the pier exceeds the capacity of these modes. All other failure modes are considered to be displacement controlled. A displacement controlled mode governs the response when the resistance of the mode, at the current displacement level, is less than the resistance of all other modes. Following these rules, the failure modes are allowed to change throughout the analysis and are updated at every displacement step. This was done in an attempt to capture a progression of failure modes commonly observed during past experiments (ATC, 1999b).

5.3.2 Loading History

The pushover program utilizes three types of displacement-controlled pushover analysis. The first imposes a predetermined ratio of displacement for the first and second story as defined by the user. Typically this type of pushover analysis applies increasing displacements to the structure in the same profile as the elastic first mode shape. Previous research has revealed that, for structures with rather low natural periods, such as low-rise URM buildings, the first vibration mode dominates its lateral displacement under seismic excitation (Paulson, 1990 and Costley and Abrams,1996).

The second type of displacement-controlled pushover analysis imposes

displacements based on the relative story stiffnesses in order to maintain a constant force ratio between the floors. FEMA 356 recommends the use of either an inverted triangular lateral load pattern or equal force distributions on all stories, which are indicative of the elastic first mode.

The third, and most realistic method, imposes displacements based on the current first mode. That is, at each analysis step the stiffness of each floor is updated, and the first mode is recalculated. The ensuing displacement is then imposed based on the profile of the new first mode. This type of pushover recognizes the fact that, while the response of URM low-rise buildings are dominated by the first mode, the mode shape changes throughout loading due to damage accumulation. This is illustrated by Figure 5.22, which shows the measured lateral force distribution during a dynamic test of a ¼-scale URM structure (Paulson and Abrams, 1990).

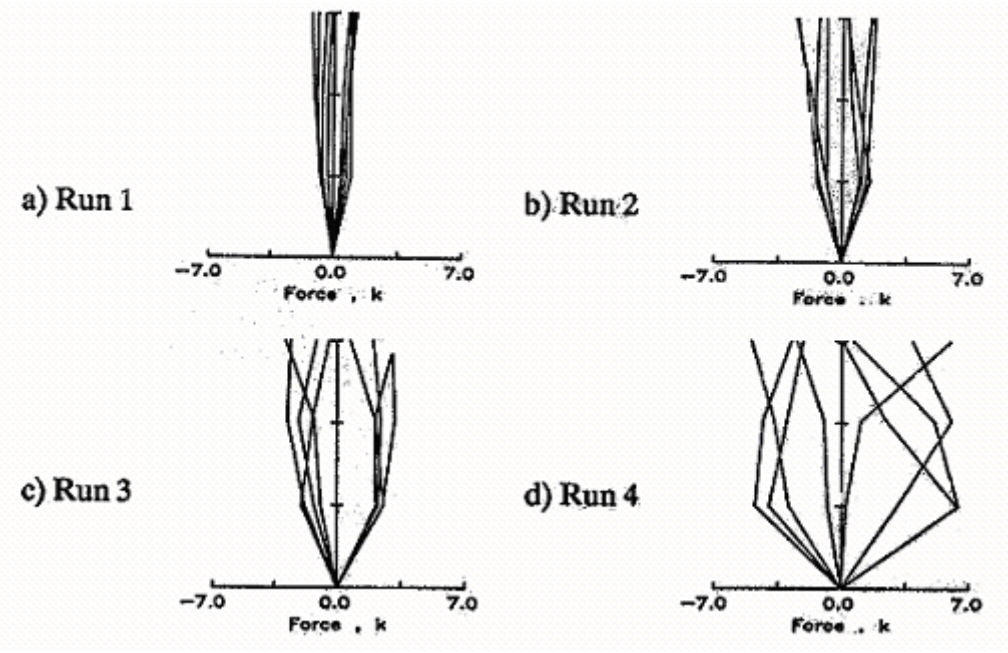

Figure 5.22. Lateral force distributions reported by Paulson and Abrams (1990).

The initial runs show essentially the elastic force distribution of an inverted triangle, which suggests little damage was occurring. However, as the ground accelerations increased, more damage occurred and the force distribution became fairly uniform, as seen in the results of Run 3. Finally, at large ground accelerations, after the structure had experienced substantial damage, force distributions became irregular (Paulson, 1990). This shift in lateral force distribution causes changes of shear force distribution as well as overturning moment, which can be important for the analysis of URM buildings.

5.4 Analysis of Test Structure Prior to Retrofit

Using the pushover analysis program discussed in the previous sections, each wall of the test structure was analyzed. The initial vertical stress in each pier was determined through a three dimensional elastic finite element analysis detailed in Yi (2004). However, for the analysis of Wall 2, pier P2-8 was ignored due to the continuous lintel, which distributed the weight above this pier to piers P2-7 and P2-9 (see Chapter 3 and 4). The pushover analysis conducted on each wall utilized a constant force profile. The specific profile chosen was set equal to the imposed force profile measured during the experimental portion of this study. This approach was adopted since the intent of this portion of the study was to assess the ability of the proposed model to capture the response of the test structure; it was not to predict the loading profile imposed on the structure.

The material properties used in all analyses are given in Table 5.5. Recall, the compression strength and bed-joint shear strength were determined through material tests as reported in Chapter 3. The coefficient of friction was assumed to be 0.75, which is

consistent with the equation provided for v_{me} by FEMA 356 (see Table 5.1). As apparent from Table 5.5, the bed-joint shear strength was ignored for the calculation of v_{me}. This modification is recommended by FEMA 306 (ATC, 1999a) for the analysis of piers after bed-joint cracks occur. In the case of the test structure, all of the first story piers displayed flexural cracking at low displacement levels, which eroded the shear strength of the bed-joint. To consider this interaction between rocking and sliding, only friction is assumed to resist sliding. Also, Table 5.5 shows that the elastic modulus was taken as 550 times the compression strength (ATC, 2000); and the diagonal tension strength was taken as, v_{me} (ATC, 2000). Notice that the equation for f_{dt} in Table 5.5 does not contain a 0.75 reduction factor for v_{te} as recommended by FEMA 356 (see Table 5.1). This reduction factor is intended to cancel out the contribution of the collar joint for cases where v_{te} is determined from an in-place shove test. Since a four brick assemblage test was used to determined v_{te}, the 0.75 factor is inappropriate.

Table 5.5. Masonry material properties

Property	Mean
Masonry compressive strength (f'_m)	10.1 MPa (1460 psi)
Bed-joint shear strength (v_{te})	0.41 MPa (60 psi)
Bed-joint coefficient of friction (μ)	0.75
Expected bed-joint sliding shear strength (v_{me})	$v_{me} = \mu \frac{P}{A_n}$
Elastic modulus of masonry (E_m)	5550 MPa (800 ksi)
Diagonal tension strength of masonry (f_{dt})	$f_{dt} = \frac{0.75\left(v_{te} + \frac{P}{A_n}\right)}{1.5}$

Figures 5.23 through 5.26 show the base shear versus roof displacement response of each wall prior to retrofit along with results from the proposed model. The predicted strength given by FEMA 356 (ATC, 2000) is also shown in these figures. The details of this calculation can be found in Yi (2004). In addition, Tables 5.6 through 5.9 give the predicted failure modes of each first floor pier as well as the experimentally observed failure modes. All of these analyses were carried out as described previously. In addition, Wall 1 was also analyzed with the entire flange of Wall B (i.e. adjacent to pier P1-6) as a global tension flange. That is, the entire flange of Wall B was assumed to resist the effects of overturning moment and the sliding of pier P1-6. This additional analysis was conducted due to observations made during the experimental portion of the analysis that indicated the entire flange of Wall B participated as a global tension flange in the negative direction.

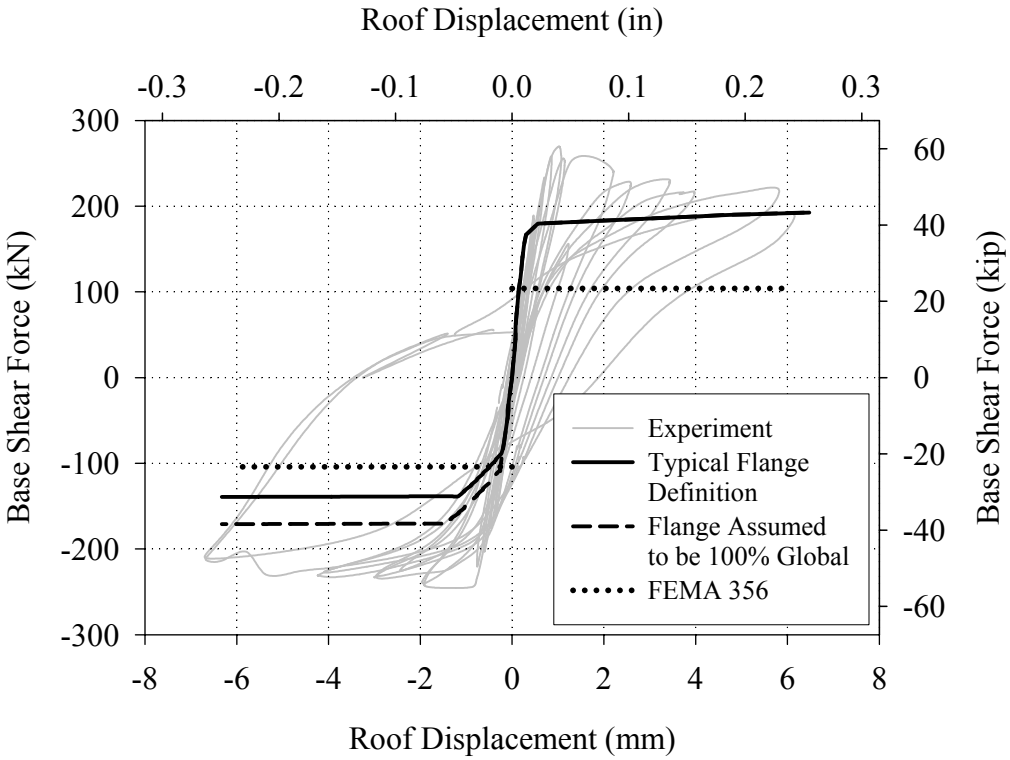

Figure 5.23. Comparison between the proposed model and the base shear versus roof displacement response of Wall 1 prior to retrofit.

Table 5.6. Comparison between observed and predicted pier failure modes.

Pier	Positive Direction Failure Mode		Negative Direction Failure Mode	
	Experiment	Proposed Model	Experiment	Proposed Model
P1-6	Global rocking/ Sliding	Global rocking	Rocking/ Sliding	Sliding
P1-7	Global rocking	Global rocking	Rocking	Rocking

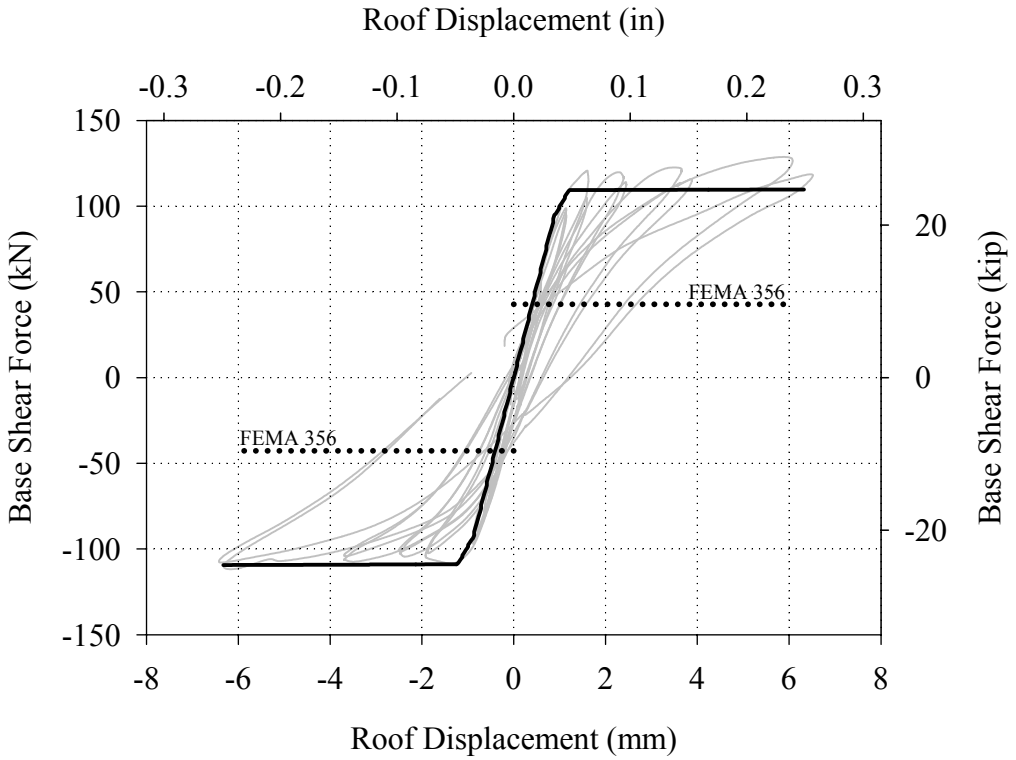

Figure 5.24. Comparison between the proposed model and the base shear versus roof displacement response of Wall 2 prior to retrofit.

Table 5.7. Comparison between observed and predicted pier failure modes.

Pier	Positive Direction Failure Mode		Negative Direction Failure Mode	
	Experiment	Proposed Model	Experiment	Proposed Model
P2-7	Rocking/ Sliding	Sliding	Rocking	Rocking
P2-9	Rocking	Rocking	Rocking/ Sliding	Sliding

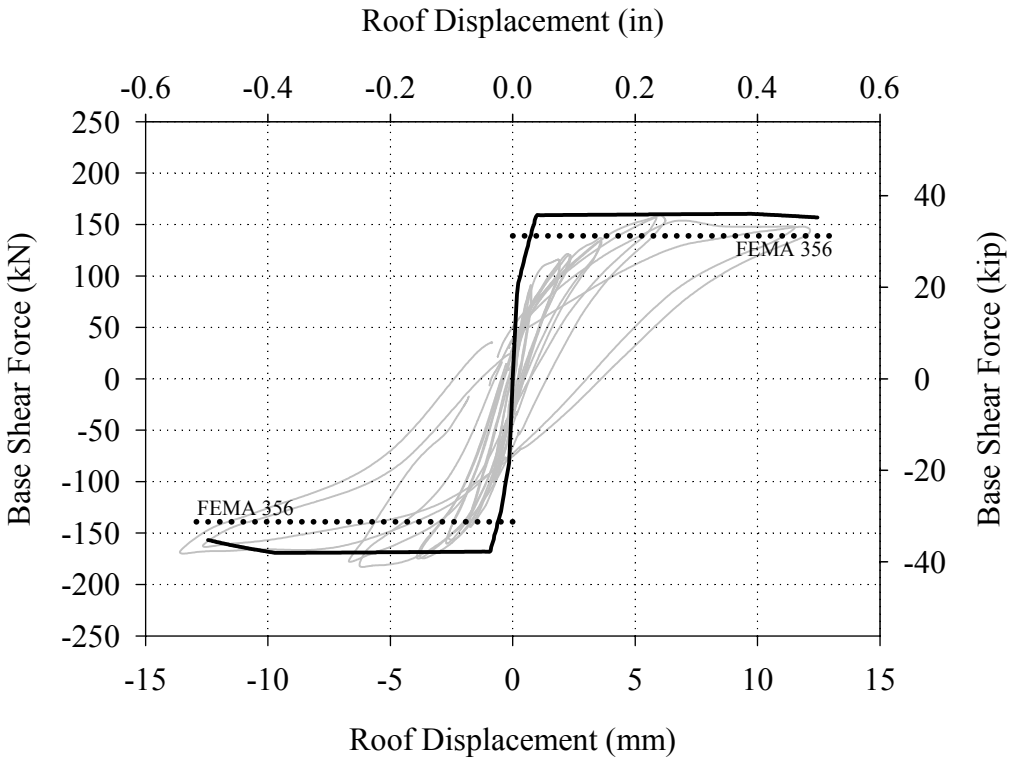

Figure 5.25. Comparison between the proposed model and the base shear versus roof displacement response of Wall A prior to post-tensioning.

Table 5.8. Comparison between observed and predicted pier failure modes.

Pier	Positive Direction Failure Mode		Negative Direction Failure Mode	
	Experiment	Proposed Model	Experiment	Proposed Model
PA-7	Rocking/ Sliding	Sliding	Rocking	Rocking
PA-8	Rocking/ Sliding	Sliding	Rocking/ Sliding	Sliding
PA-9	Rocking/ Sliding	Rocking	Rocking	Sliding
PA-10	Rocking	Rocking	Rocking/ Sliding	Sliding

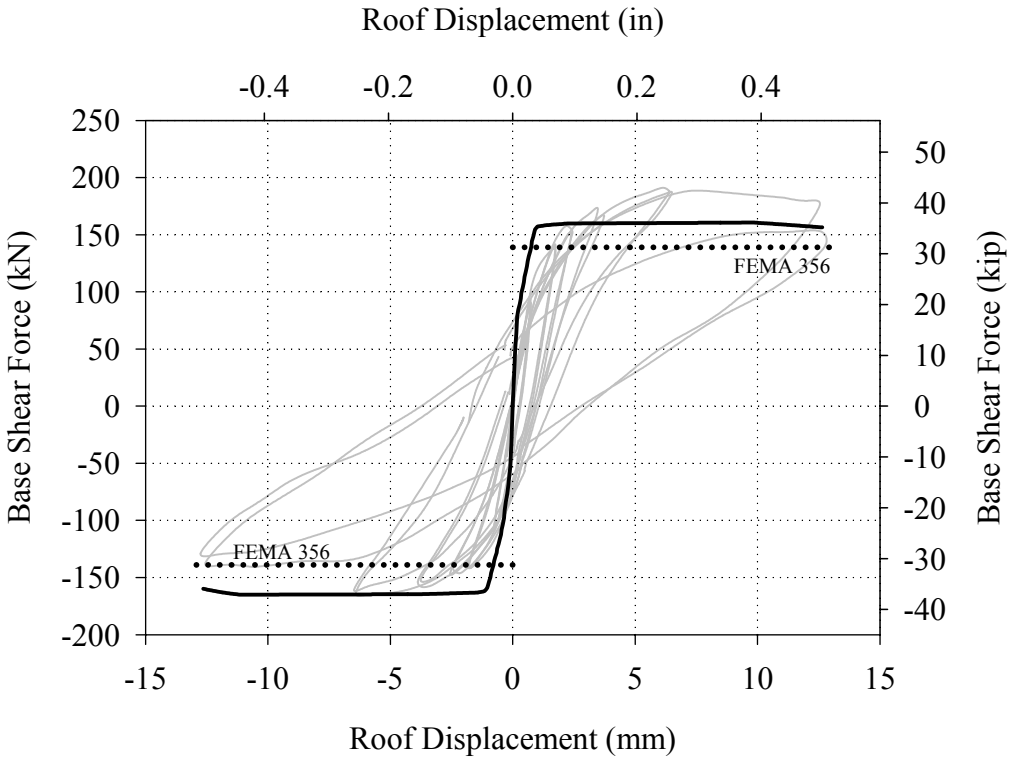

Figure 5.26. Comparison between the proposed model and the base shear versus roof displacement response of Wall B prior to retrofit.

Table 5.9. Comparison between observed and predicted pier failure modes.

Pier	Positive Direction Failure Mode		Negative Direction Failure Mode	
	Experiment	Proposed Model	Experiment	Proposed Model
PB-7	Rocking	Rocking	Rocking	Sliding
PB-8	Rocking/ Sliding	Rocking	Rocking/ Sliding	Sliding
PB-9	Rocking/ Sliding	Sliding	Rocking/ Sliding	Sliding
PB-10	Rocking	Sliding	Rocking	Rocking

Figures 5.23 through 5.26 show that the proposed model was able to predict the strength of each wall with a reasonable amount of accuracy. Table 5.10 shows a comparison between the experimentally measured and analytically predicted base shear capacity of each wall. All of the predictions were conservative and within 20% of the measured capacity with the exception of Wall 1.

The large error associated with the Wall 1 prediction is primarily attributed to the resistance supplied by the masonry prior to cracking. As apparent from Sections 5.1 and 5.2, the model largely ignores the tensile strength of masonry and assumes cracks have already formed (aside from the treatment of diagonal tension). As a result, the model is only capable of capturing the ultimate response following the formation of a mechanism. Due to the relatively large cracks that formed in Wall 1 (see Chapter 4), significant resistance was offer by the tensile strength of masonry prior to cracking. This contention is supported by the decrease in resistance shown in Figure 5.23 as the wall was displaced beyond peak strength. Note, that the prediction of base shear capacity is within 20% of the measured strength at a roof displacement of 6.4 mm (0.25 in).

In addition, the assumption of flange participation also contributed to the error associated with the prediction of Wall 1 in the negative direction. If the entire flange of Wall B is assumed to act as a global tension flange (as was observed in the experiment) the base shear capacity of the wall becomes 168 kN (38 kip), which is within 20% of the measured capacity of Wall 1 at 12.7 mm (0.25 in) of roof displacement (see Figure 5.23).

Table 5.10. Comparison between the measure and predicted base shear capacity of each wall prior to retrofit (negative percent difference is conservative).

	Direction	Base Shear Capacity		% Difference $\left(\frac{V - V_{Exp}}{V_{Exp}}\right)$
		Experiment	Proposed Model	
Wall 1	Positive	267 kN (60 kip)	191 kN (43 kip)	-28%
	Negative	245 kN (55 kip)	169 kN (32 kip)	-42%
Wall 2	Positive	128 kN (29 kip)	111 kN (25 kip)	-13%
	Negative	111 kN (25 kip)	111 kN (25 kip)	0%
Wall A	Positive	159 kN (36 kip)	159 kN (36 kip)	0%
	Negative	182 kN (41 kip)	169 kN (38 kip)	-7%
Wall B	Positive	191 kN (43 kip)	159 kN (36 kip)	-17%
	Negative	165 kN (37 kip)	165 kN (37 kip)	0%

In addition, the results presented in Tables 5.6 through 5.9 indicate that the model was capable of predicting the observed failure modes fairly well. In particular, the rotational spring supplied at the base of the model correctly captured the global rocking behavior of Wall 1 in the positive direction. In addition, the model correctly predicted that the behavior of all other walls would be dominated by the interstory shear displacement. In terms of pier failure modes, the biggest shortcoming of the proposed model was its inability to capture combined modes such as rocking/sliding.

Table 5.11 summarizes the predicted initial stiffness of each wall along with the experimentally measured initial stiffness of each wall. The model substantially over

predicted the stiffness of Walls A and B as shown in Figures 5.25 and 5.26. This is primarily attributed to the substantial cracks induced into these walls during the testing of Walls 1 and 2 (see Chapter 4). However even in the case of Walls 1 and 2, the stiffness predicted by the proposed model contained large errors. These errors are likely due to two simplifying assumptions employed within the model. First, the method used to determine the pier height and boundary conditions is only valid once cracks have fully developed at the top and bottom of the pier. In the elastic range these assumptions cause the pier stiffness to be over estimated. Second, the treatment of flanges completely ignores any impact on stiffness; disregarding the flange results in a more flexible system.

Table 5.11. Comparison between measured and predicted stiffness of each wall prior to retrofit.

	Direction	Initial Stiffness		% Difference $\left(\frac{K - K_{Exp}}{K_{Exp}}\right)$
		Experiment	Proposed Model	
Wall 1	Positive	385 kN/mm (2200 kip/in)	595 kN/mm (3400 kip/in)	45%
	Negative	280 kN/mm (1600 kip/in)	385 kN/mm (2200 kip/in)	38%
Wall 2	Positive	117 kN/mm (670 kip/in)	112 kN/mm (640 kip/in)	-5%
	Negative	95 kN/mm (540 kip/in)	112 kN/mm (640 kip/in)	19%
Wall A	Positive	144 kN/mm (820 kip/in)	490 kN/mm (2800 kip/in)	240%
	Negative	154 kN/mm (880 kip/in)	560 kN/mm (3200 kip/in)	260%
Wall B	Positive	159 kN/mm (910 kip/in)	490 kN/mm (2800 kip/in)	210%
	Negative	156 kN/mm (890 kip/in)	560 kN/mm (3200 kip/in)	260%

Table 5.12 gives the base shear capacity of each wall determined according to FEMA 356 (ATC, 2000) and the proposed model. In addition, the percent difference between these predictions and the measured capacity is also given. This table indicates that the predictions of the proposed model were between 11% and 60% more accurate than FEMA 356. This increased accuracy is attributed primarily to the consideration of global effects and is further examined in Section 5.6. Note that the FEMA 356 model neglects all of the global effects addressed by the proposed model.

Table 5.12. Comparison between the predicted strength of the proposed model and FEMA 356 for each wall prior to retrofit (negative percent difference is conservative).

	Direction	Proposed Model		FEMA 356	
		Base Shear Capacity	% Difference $\left(\frac{V - V_{Exp}}{V_{Exp}}\right)$	Base Shear Capacity	% Difference $\left(\frac{V - V_{Exp}}{V_{Exp}}\right)$
Wall 1	Positive	191 kN (43 kip)	-28%	102 kN (23 kip)	-62%
	Negative	169 kN (32 kip)	-42%	102 kN (23 kip)	-58%
Wall 2	Positive	111 kN (25 kip)	-13%	44 kN (10 kip)	-66%
	Negative	111 kN (25 kip)	0%	44 kN (10 kip)	-60%
Wall A	Positive	159 kN (36 kip)	0%	138 kN (31 kip)	-14%
	Negative	169 kN (38 kip)	-7%	138 kN (31 kip)	-24%
Wall B	Positive	159 kN (36 kip)	-17%	138 kN (31 kip)	-28%
	Negative	165 kN (37 kip)	0%	138 kN (31 kip)	-16%

5.5 Analysis of Test Structure After Retrofit

Using the pushover analysis program discussed in the previous sections, Walls 1, A and B of the test structure were analyzed after retrofit. Since the behavior of URM piers strengthened with full-coverage systems was not addressed in the current study, Wall 2 was not analyzed after retrofit. These analyses were carried out with the same loading protocol and masonry material properties described in the previous section. In the case of Wall A, the vertical stress in each pier was increased based on the maximum measured post-tensioning force during testing (see Table 5.13). This simplification was made to alleviate the necessity to increase the post-tensioning force as the model was displaced. The initial vertical stresses in all other walls were identical to those used for the analysis prior to retrofit.

Table 5.13. Assumed increase in vertical stress of all piers in Wall A for each level of post-tensioning force.

	PT = 111 kN (25 kip)		PT 222 kN (50 kip)	
	Positive	Negative	Positive	Negative
Increase in vertical stress	0.124 MPa (18 psi)	0.138 MPa (20 psi)	0.200 MPa (29 psi)	0.228 MPa (33 psi)

The additional material properties required for the analysis of the test structure after retrofit are given in Table 5.14. All of the material properties of the FRP reinforcement systems were normalized by the thickness. This simplification along with assuming that the matrix provides no strength, eliminates the dependence on FRP thickness which is difficult to control and typically varies. For this analysis, the properties of the 18oz/yd^2 structural grid were taken as those provided by the manufacturer (TECH FAB, 2003). The properties used for the 27 oz/yd^2 unidirectional system were determined

through material tests conducted at the Construction Engineering Research Laboratory under MAE Center Project ST-45 (Marshall et al., 2000). The modulus and tensile strength were determined through coupon tests and the shear strength was determined through the testing of three-brick assemblages as described in Chapter 2. The debonding stress of FRP overlays was determined by multiplying the debonding strain determined from Eqn. 16 by the elastic modulus of the FRP.

Table 5.14. FRP material properties.

18 oz/yd^2 glass/epoxy fiber structural grid (Wall 1)	Tensile stiffness per width ($E_f t_f$)	7.5 kN/mm (43 kip/in)
	Tensile strength per width ($f_{fu} t_f$)	0.21 kN/mm (1.2 kip/in)
	Debonding strength per width ($f_{db} t_f$)	0.12 kN/mm (0.7 kip/in)
27 oz/yd^2 glass/epoxy unidirectional FRP (Wall B)	Tensile stiffness per width ($E_f t_f$)	27 kN/mm (154 kip/in)
	Tensile strength per width ($f_{fu} t_f$)	0.74 kN/mm (4.2 kip/in)
	Debonding strength per width ($f_{db} t_f$)	0.40 kN/mm (2.3 (kip/in)
	Shear strength per width ($\tau_f t_f$)	0.16 kN/mm (0.94 kip/in)

Figures 5.27 through 5.30 show the base shear versus roof displacement response of Walls 1, A and B after retrofit along with results from proposed model. In addition, Tables 5.15 through 5.18 give the predicted failure modes of each first floor pier as well as the experimentally observed failure mode. All of these analyses were carried out as described previously.

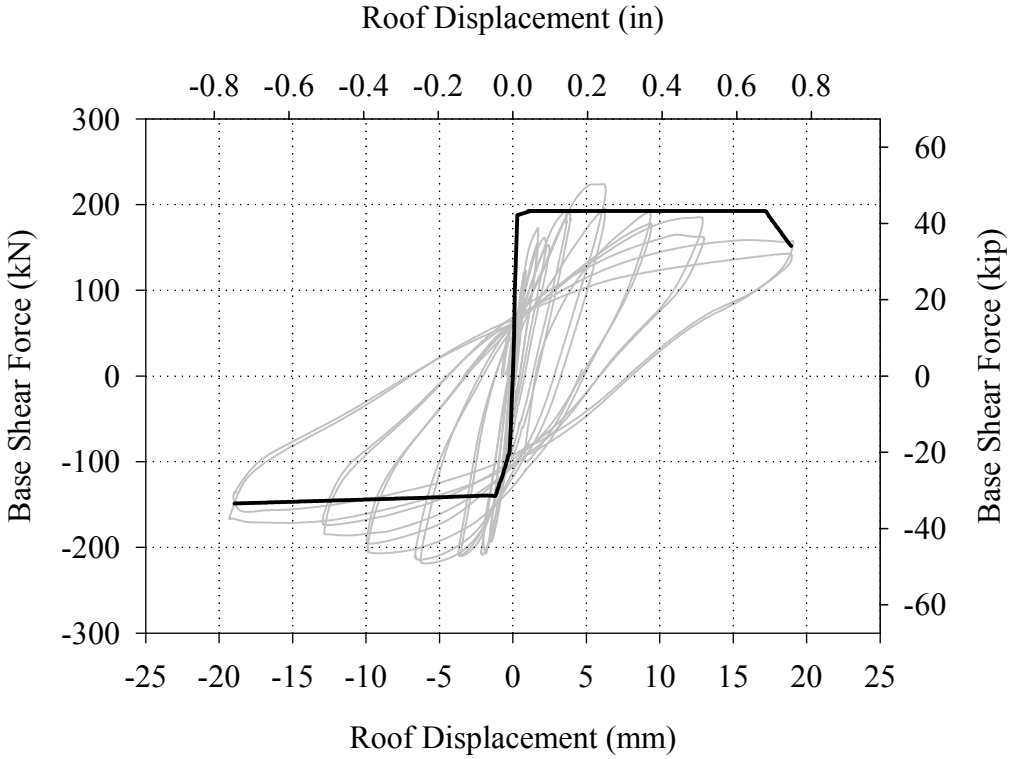

Figure 5.27. Comparison between the proposed model and the base shear versus roof displacement response of Wall 1 after retrofit.

Table 5.15. Comparison between observed and predicted pier failure modes.

Pier	Positive Direction Failure Mode		Negative Direction Failure Mode	
	Experiment	Proposed Model	Experiment	Proposed Model
P1-6	Sliding/ Global rocking	Sliding/ Global rocking	Sliding/ Rocking	Sliding
P1-7	Rocking/ Global rocking	Global rocking	Rocking/ Diagonal tension	Rocking

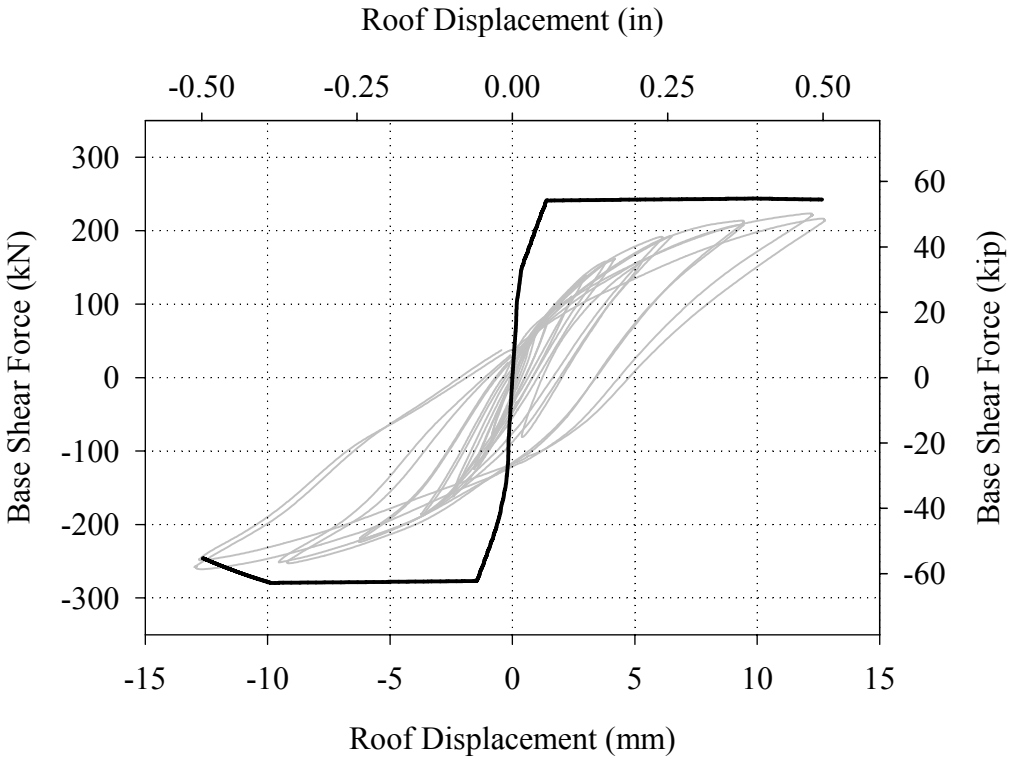

Figure 5.28. Comparison between the proposed model and the base shear versus roof displacement response of Wall A with a post-tensioning force of 111 kN (25 kip).

Table 5.16. Comparison between observed and predicted pier failure modes.

Pier	Positive Direction Failure Mode		Negative Direction Failure Mode	
	Experiment	Proposed Model	Experiment	Proposed Model
PA-7	Sliding/ Rocking	Rocking	Diagonal tension/ Rocking	Rocking
PA-8	Sliding/ Rocking	Sliding/ Rocking	Sliding/ Rocking	Sliding
PA-9	Sliding/ Rocking	Rocking	Sliding/ Rocking	Sliding
PA-10	Rocking	Rocking	Sliding/ Rocking	Rocking

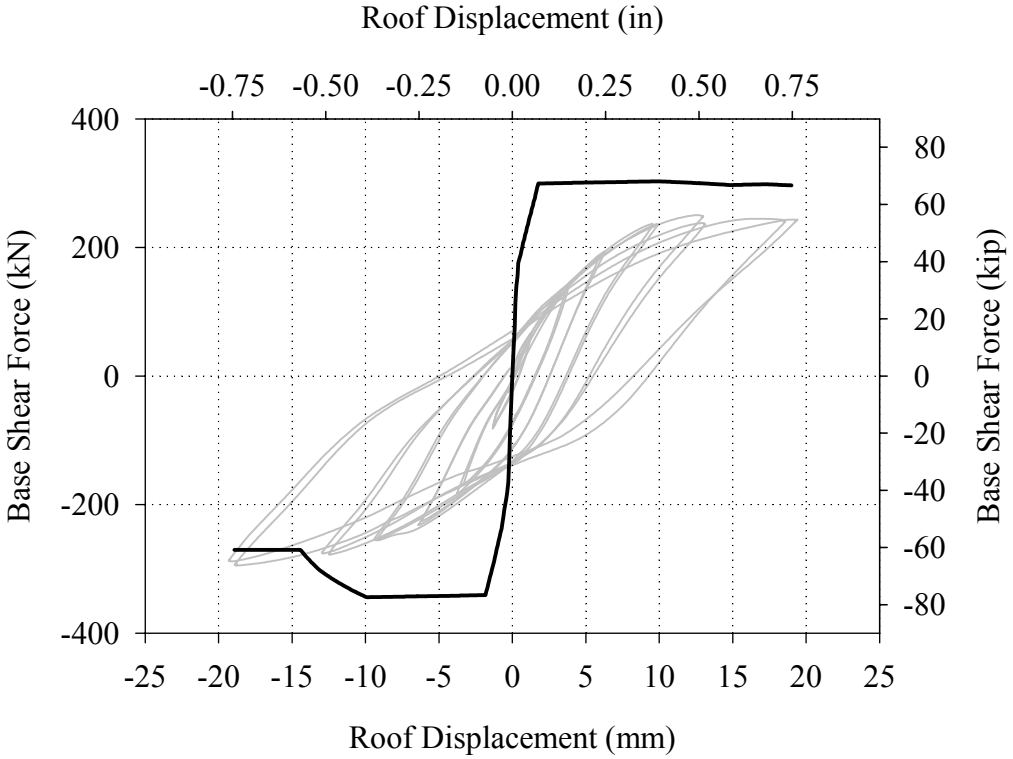

Figure 5.29. Comparison between the proposed model and the base shear versus roof displacement response of Wall A with a post-tensioning force of 222 kN (50 kip).

Table 5.17. Comparison between observed and predicted pier failure modes.

Pier	Positive Direction Failure Mode		Negative Direction Failure Mode	
	Experiment	Proposed Model	Experiment	Proposed Model
PA-7	Sliding/ Rocking	Rocking	Diagonal tension/ Rocking	Rocking
PA-8	Sliding/ Rocking	Sliding	Sliding/ Rocking	Sliding
PA-9	Sliding/ Rocking	Rocking	Sliding/ Rocking	Sliding
PA-10	Rocking/ Diagonal tension	Rocking	Sliding/ Rocking	Sliding

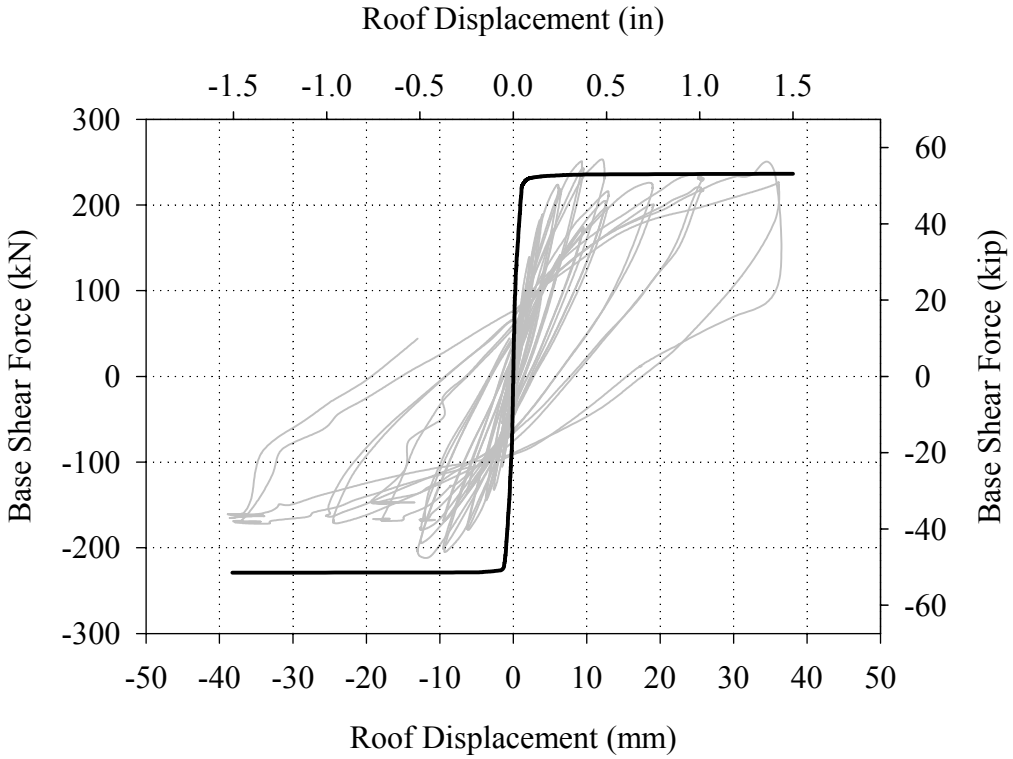

Figure 5.30. Comparison between the proposed model and the base shear versus roof displacement of Wall B prior to retrofit.

Table 5.18. Comparison between observed and predicted pier failure modes.

Pier	Positive Direction Failure Mode		Negative Direction Failure Mode	
	Experiment	Proposed Model	Experiment	Proposed Model
PB-7	Rocking/ Sliding	Global rocking	Rocking/ Sliding	Global rocking
PB-8	Flexural FRP debonding/ Sliding	Global rocking	Flexural FRP debonding/ Sliding	Global rocking
PB-9	Flexural FRP debonding/ Sliding	Global rocking	Flexural FRP debonding/ Sliding	Global rocking
PB-10	Flexural FRP debonding/ Sliding	Global rocking	Rocking/ Sliding	Global rocking

Table 5.19 shows a comparison between the experimentally measured and analytically predicted base shear capacity of each wall. As apparent from this table, all of the strength predictions were within 20% of the measured capacity with the exception of Wall A. The larger error associated with the predicted base shear capacity of Wall A is attributed primarily to the calculation of pier diagonal tension strength. As apparent from Tables 5.16 and 5.17, the observed diagonal tension failure modes were not properly predicted by the model. As a result, a mode of greater resistance was assumed to govern, thus causing an overestimate of base shear capacity. In addition, Figures 5.28 and 5.29 show that the model substantially over predicted the strength of Wall A at displacements below the peak displacement. This overprediction is attributed to the assumption that the vertical post-tensioning force was constant throughout loading. If the post-tensioning force was incrementally increased as observed during the experiment, the predicted curve would likely have been closer to the measured response. However, the model would still have overestimated the base shear capacity.

Table 5.19. Comparison between the measure and predicted base shear capacity of each wall after retrofit

	Direction	Base Shear Capacity		% Difference $\left(\frac{V - V_{Exp}}{V_{Exp}}\right)$
		Experiment	Proposed Model	
Wall 1	Positive	222 kN (50 kip)	191 kN (43 kip)	-14%
	Negative	218 kN (49 kip)	182 kN (34 kip)	-31%
Wall A PT = 111 kN (25 kip)	Positive	223 kN (50 kip)	245 kN (55 kip)	10%
	Negative	261 kN (59 kip)	280 kN (63 kip)	7%
Wall A PT = 222 kN (50 kip)	Positive	250 kN (56 kip)	302 kN (68 kip)	21%
	Negative	294 kN (66 kip)	342 kN (77 kip)	17%
Wall B	Positive	253 kN (57 kip)	236 kN (53 kip)	-7%
	Negative	211 kN (48 kip)	231 kN (52 kip)	10%

Although the model correctly predicted several failure modes, the results presented in Tables 5.15 through 5.18 indicate that the model was unable to accurately predict some failure modes in Walls A and B. In the case of Wall A, as mentioned previously, the model was unable to accurately predict the observed diagonal tension failures. This shortcoming is likely due to the poor accuracy of the FEMA 356 approach. According to FEMA 306 (ATC, 1999a) "there is a great deal of uncertainty in diagonal tension strength calculations" due to the difficulty in determining the diagonal tension strength of masonry. Note, currently no direct test is available to determine the diagonal tension strength of masonry. In addition, the calculation of overturning moment and assumptions of flange

participation could have contributed to this error.

In the case of Wall B, the model erroneously predicted that global rocking would govern the response in both the positive and negative direction. While some global rocking displacement was observed in the experiment (see Chapter 4), the primary mode of the first floor piers was the debonding of flexural FRP. This error is attributed to (1) the shortcomings of the model used to predict the debonding strength as outlined in Section 5.1.2.2 and (2) the assumptions of flange participation since they greatly impact the calculation of global rocking resistance.

5.6 Effect of Global Characteristics

To investigate the effect of the global characteristics included in the proposed model, the test structure was analyzed with each of these characteristics neglected. Specifically, each wall of the test structure was analyzed before and after retrofit without:

(1) Flange participation (FP), i.e the contributions of compression flanges, global tension flanges, and component tension flanges were ignored.

(2) The effects overturning moment (OM), i.e. the vertical stress in all piers and flanges was assumed to be constant throughout loading and equal to the gravity stress.

(3) Global rocking (GR), i.e. only interstory shear deformation was considered.

(4) The pier height definition presented in Section 5.2.1 (PD), i.e. the pier height was taken as the height of the adjacent opening (for cases where a pier was between openings of different heights (e.g. PA-9) the pier definition defined in Section 5.2.1 was used).

The results of these analyses are summarized in Table 5.20. Table 5.21 gives the percent difference between the analysis conducted without each of the global characteristics and the analysis conducted utilizing the total model.

5.6.1 Effect of Flange Participation

Tables 5.20 and 5.21 show that in all cases the flange participation acted to increase the base shear capacity of the wall. This is primarily attributed to the additional vertical compressive stress applied to the piers by the component tension flanges and global tension flanges. Note that for all of the failure modes considered, additional vertical compressive stress results in larger capacity.

For the analysis of the walls prior to retrofit, the flanges accounted for between 22% and 42% of the base shear capacity. In addition, Table 5.21 shows that the contribution of the flanges to the strength of Walls 1 and 2 was greater than the contribution of the flanges to the strength of Walls A and B. This was a result of the different thicknesses of these walls. Recall Walls A and B were three wythes thick whereas Walls 1 and 2 were two wythes thick. As a result, the flanges supplied by Walls A and B represented a relatively large portion of the total weight of Walls 1 and 2. Conversely, the flanges supplied by Walls 1 and 2 represented a relatively small portion of the weight of Walls A and B.

Table 5.20. Summary of analyses conducted without consideration of global characteristics.

		V_{Exp}	Total Model	w/o FP	w/o OM	w/o GR	w/o PD
Wall 1 (URM)	(+)	267 kN (60 kip)	193 kN (43 kip)	140 kN (32 kip)	191 kN (43 kip)	192 kN (43 kip)	193 kN (43 kip)
	(-)	245 kN (55 kip)	141 kN (32 kip)	100 kN (23 kip)	173 kN (39 kip)	141 kN (32 kip)	141 kN (32 kip)
Wall 2 (URM)	(+)	129 kN (29 kip)	109 kN (25 kip)	64 kN (14 kip)	88 kN (20 kip)	109 kN (25 kip)	109 kN (25 kip)
	(-)	111 kN (25 kip)	109 kN (25 kip)	64 kN (14 kip)	88 kN (20 kip)	109 kN (25 kip)	109 kN (25 kip)
Wall A (URM)	(+)	160 kN (36 kip)	161 kN (36 kip)	125 kN (28 kip)	165 kN (37 kip)	161 kN (36 kip)	161 kN (36 kip)
	(-)	182 kN (41 kip)	169 kN (38 kip)	133 kN (30 kip)	172 kN (39 kip)	169 kN (38 kip)	230 kN (52 kip)
Wall B (URM)	(+)	191 kN (43 kip)	161 kN (36 kip)	126 kN (28 kip)	165 kN (37 kip)	161 kN (36 kip)	161 kN (36 kip)
	(-)	165 kN (37 kip)	166 kN (37 kip)	134 kN (30 kip)	173 kN (39 kip)	166 kN (37 kip)	217 kN (49 kip)
Wall 1 (PR)	(+)	222 kN (50 kip)	193 kN (43 kip)	140 kN (32 kip)	180 kN (40 kip)	193 kN (43 kip)	193 kN (43 kip)
	(-)	218 kN (49 kip)	149 kN (34 kip)	110 kN (25 kip)	170 kN (38 kip)	149 kN (34 kip)	148 kN (33 kip)
Wall A PT=111 kN	(+)	222 kN (50 kip)	244 kN (55 kip)	213 kN (48 kip)	260 kN (59 kip)	244 kN (55 kip)	244 kN (55 kip)
	(-)	262 kN (59 kip)	279 kN (63 kip)	245 kN (55 kip)	282 kN (63 kip)	279 kN (63 kip)	373 kN (84 kip)
Wall A PT=222 kN	(+)	249 kN (56 kip)	303 kN (68 kip)	271 kN (61 kip)	320 kN (72 kip)	303 kN (68 kip)	303 kN (68 kip)
	(-)	294 kN (66 kip)	344 kN (77 kip)	312 kN (70 kip)	350 kN (79 kip)	344 kN (77 kip)	450 kN (101 kip)
Wall B (PR)	(+)	254 kN (57 kip)	236 kN (53 kip)	191 kN (43 kip)	236 kN (53 kip)	286 kN (64 kip)	236 kN (53 kip)
	(-)	214 kN (48 kip)	231 kN (52 kip)	196 kN (44 kip)	228 kN (51 kip)	273 kN (61 kip)	231 kN (52 kip)

Table 5.21. Percent difference between the total model and the capacity obtained when each of the global characteristics were neglected (negative percentage is conservative).

		% difference w/o flanges	% difference w/o OM	% difference w/o GR	% difference w/o PD
		$\left(\frac{V_{nF}-V_{total}}{V_{total}}\right)$	$\left(\frac{V_{nOM}-V_{total}}{V_{total}}\right)$	$\left(\frac{V_{nGR}-V_{total}}{V_{total}}\right)$	$\left(\frac{V_{nPD}-V_{total}}{V_{total}}\right)$
Wall 1 (URM)	(+)	-27%	-1%	0%	0%
	(-)	-29%	23%	0%	0%
Wall 2 (URM)	(+)	-42%	-20%	0%	0%
	(-)	-42%	-20%	0%	0%
Wall A (URM)	(+)	-22%	3%	0%	0%
	(-)	-22%	2%	0%	35%
Wall B (URM)	(+)	-22%	3%	0%	0%
	(-)	-19%	4%	0%	31%
Wall 1 (PR)	(+)	-27%	-7%	0%	0%
	(-)	-26%	14%	0%	-1%
Wall A (PT=111 kN)	(+)	-13%	7%	0%	0%
	(-)	-12%	1%	0%	33%
Wall A (PT=222 kN)	(+)	-10%	6%	0%	0%
	(-)	-9%	2%	0%	31%
Wall B (PR)	(+)	-19%	0%	21%	0%
	(-)	-15%	0%	18%	0%

After retrofit, the contribution of the flanges to the strength of Wall 1 remained relatively unchanged (see Table 5.21), which was expected since the behavior of Wall 1 was similar both before and after retrofit. In the case of Walls A and B, the percentage of strength attributed to flange participation diminished after retrofit. For Wall A, the contribution of the flanges decreased as the post-tensioning force increased. This was

caused by the weight of the flanges becoming less significant relative to the total vertical load on the wall. For Wall B, the decrease in the percentage of strength supplied by the flanges was attributed to the increased capacity provided by the FRP overlays. Nevertheless, the flange contribution accounted for between 15% and 20% of the base shear capacity of Wall B after retrofit.

5.6.2 Effect of Overturning Moment

The effect of overturning moment altered the base shear capacity of the walls between -20% and 23%. Unlike flange participation, this effect can act to either increase or decrease the capacity of the wall. Specifically, if overturning moment acts to transfer vertical compressive stress from a stocky pier to a slender pier, the base shear capacity decreases (e.g. the response of Wall 1 in the negative direction). For cases where overturning moment acts to transfer vertical compressive stress from a slender pier to a stock pier, the base shear capacity increases (e.g. the response of Wall 1 in the positive direction).

In addition to strength, the change in vertical stress due to overturning moment can substantially impact failure modes. However, due to the inability of the pier model to accurately predict diagonal tension failures (see Section 5.5), the change in failure modes was limited to rocking and sliding. Note that during the experimental portion of this study the orientation of the observed diagonal tension failures was consistent with the direction of overturning moment.

5.6.3 Effect of Global Rocking

Tables 5.20 and 5.21 show that neglecting global rocking affected the strength of Wall B after retrofit by approximately 20%. This was expected since global rocking was the primary failure mode of this wall. Similarly, one would expect that neglecting global rocking would result in an increase in the base shear capacity of Wall 1 in the positive direction. However, since the sliding strength of Wall 1 was nearly identical to the global rocking strength, the capacity was essentially unchanged.

Although the predicted global rocking of Wall B was erroneous (likely due to an overestimation of the debonding strength of the FRP overlays), the results of this analysis highlights the potentially unconservative assumption of ignoring global rocking. Note that since global rocking represents a potential failure mode, considering global rocking is always conservative.

5.6.4 Effect of Pier Definition

The pier definition proposed in Section 5.2.1 had a major effect on the base shear capacity of Walls A and B in the negative direction (see Tables 5.20 and 5.21). For these cases, the definition of pier height as per FEMA 356 differed from the procedure outlined in Section 5.2.1 for the piers located at the toe of the wall. Specifically, the height of piers PA-7 and PB-10, as defined by the method outlined in Section 5.2.1, was 2.1 m (84 in.), whereas FEMA 356 takes the height as 1.2 m (48 in.). By defining the pier height as 1.2 m (48 in.) the strength associated with rocking/toe crushing increases substantially, thus resulting in an overprediction of strength. In all other cases the differences between pier definitions occurred only at piers located at the heel of the wall. Since sliding governed the

response of these piers, no impact on strength was observed.

5.7 Effect of Material Properties

To investigate the effect of material properties on the base shear capacity of low-rise URM structures, several walls of the test structure were analyzed with a range of material properties. For this investigation, masonry compressive strength was varied from 500 psi to 1500 psi, masonry shear strength was varied from 0 psi to 100 psi (an upper bound according to FEMA 356), and the bed-joint coefficient of friction was varied from 0.5 to 1.0 (note that only one property was varied at a time). To assess the effect of wall openings on the influence of these properties, Walls 1, 2, and A were analyzed prior to retrofit. In addition, to assess the effect of different levels of vertical stress, Wall A was analyzed with 0 kN, 111 kN (25 kip), and 222 kN (50 kip) of post-tensioning force. Figures 5.31 through summarize the results of these analyses.

Figure 5.31a shows that masonry compressive strength has little effect on the base shear capacity of URM walls with low levels of vertical stress, regardless of the opening ratio. However, as the vertical stress increases, masonry compressive strength does impact the wall capacity to a greater extent (see Figure 5.31b). This is due to the fact that URM piers are more prone to compression failures at larger levels of vertical stress. However, since the compressive strength of masonry has little effect on the toe crushing capacity (see Eqn. 2), the influence of masonry compressive strength on wall capacity is still minor.

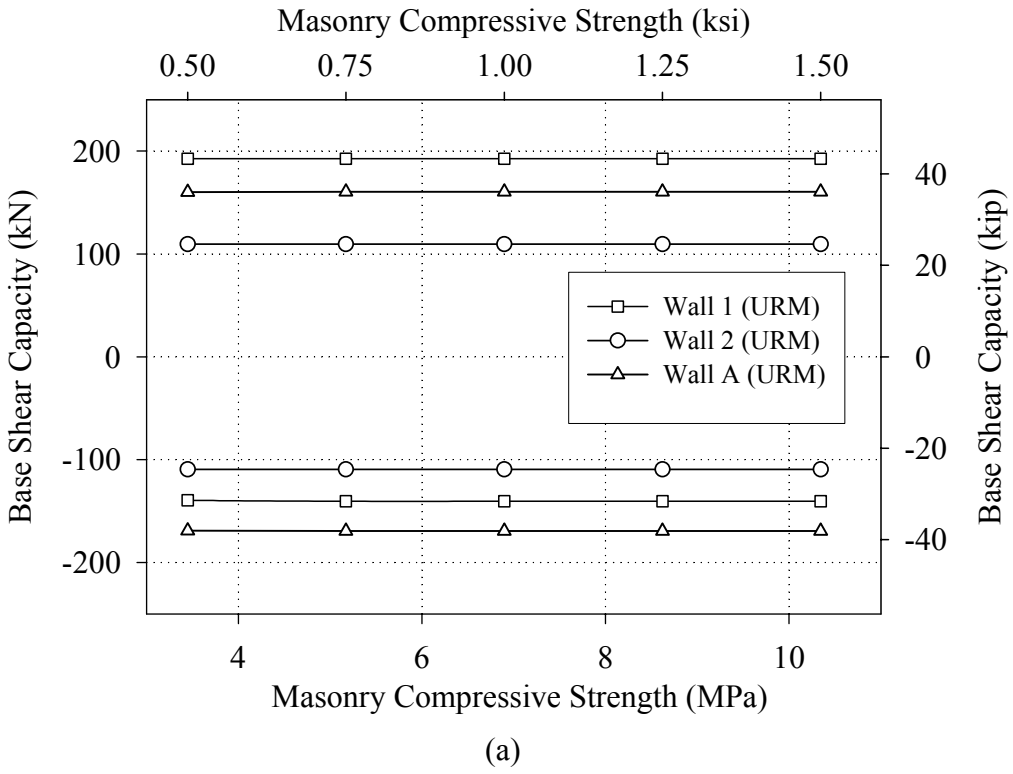

(a)

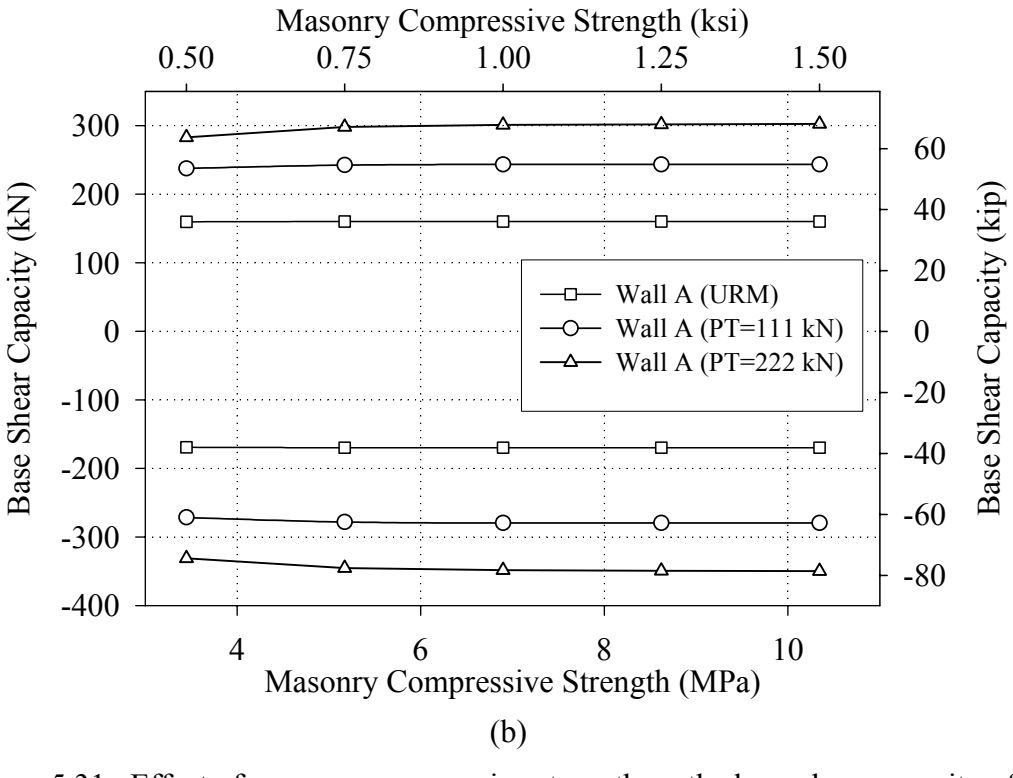

(b)

Figure 5.31. Effect of masonry compressive strength on the base shear capacity of (a) walls with different opening ratios and (b) walls with different levels of vertical stress.

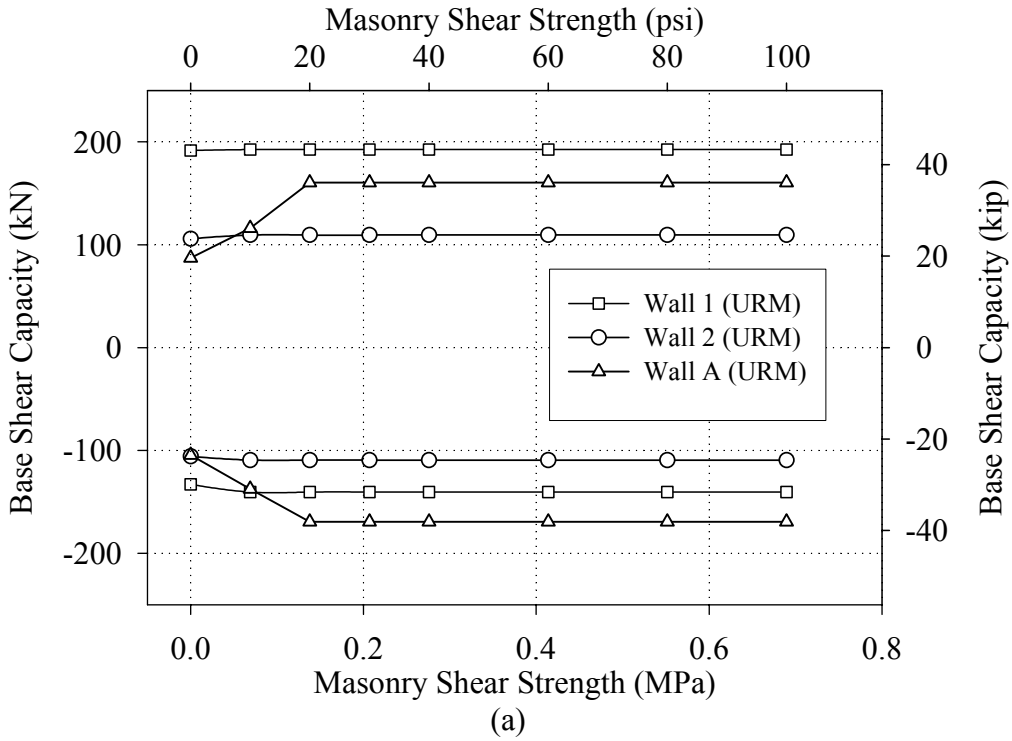

Figure 5.32. Effect of masonry shear strength on the base shear capacity of (a) walls with different opening ratios and (b) walls with different levels of vertical stress.

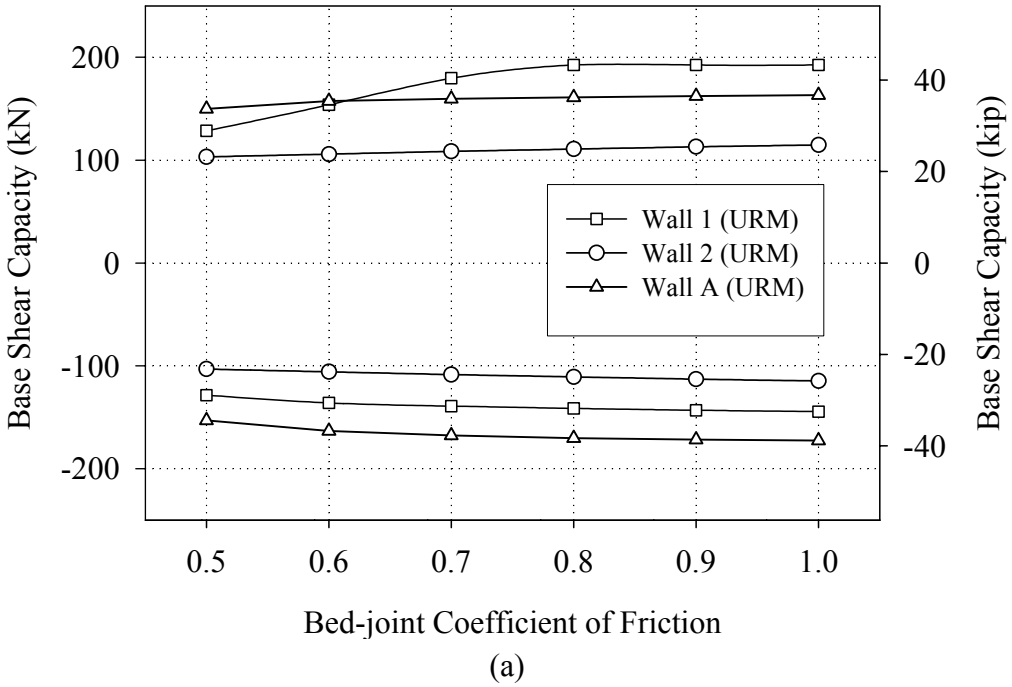

(a)

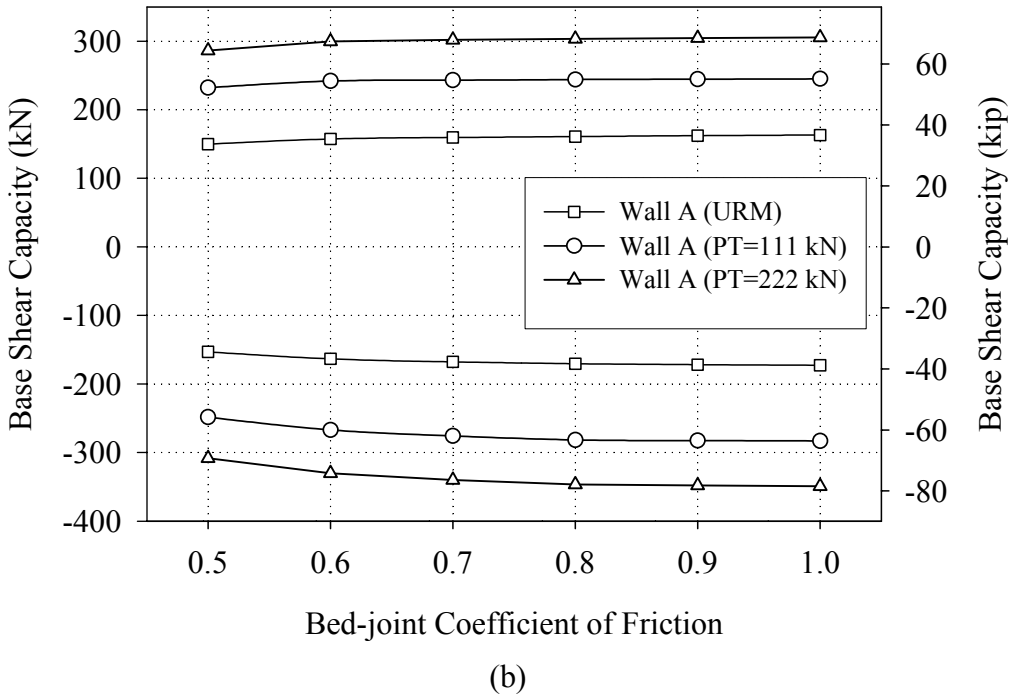

(b)

Figure 5.33. Effect of bed-joint coefficient of friction on the base shear capacity of (a) walls with different opening ratios and (b) walls with different levels of vertical stress.

Figure 5.32 shows that masonry shear strength influences the base shear capacity of several walls. In the current model, masonry shear strength only affects the calculation of diagonal tension capacity, since bed-joint sliding resistance is assumed to be supplied exclusively by friction (see Table 5.5). Note that the equation used for f_{dt} considers both masonry shear strength and frictional resistance. As a result, when the masonry shear strength is neglected (i.e. v_{te}= 0), resistance to diagonal tension is still provided by friction. The plot shown in Figure 5.32a indicates that for low levels of masonry shear strength (below 20 psi), Wall A displayed some sensitivity to this property. This sensitivity is attributed to the stockier piers employed in Wall A, which are more likely to display diagonal tension failures. Figure 5.32b shows that as the vertical stress was increased, the base shear capacity of Wall A became more sensitive to masonry shear strength. This trend was expected since URM piers are more prone to diagonal tension failures at higher levels of vertical stress.

Figure 5.33 shows that for nearly all of the walls, the influence of the bed-joint friction coefficient was minor. The one exception was the behavior of Wall 1 in the positive direction (see Figure 5.33a). For friction coefficients less than 0.7, the response of pier P1-6 (i.e. the large pier in Wall 1) was sliding, and thus very sensitive to friction. However as the coefficient of friction increased beyond this point, global rocking governed the response, and this sensitivity decreased. In all other cases, bed-joint sliding occurred only in piers that were at the heel of the wall (i.e. where overturning moment acted to decrease the level of vertical stress). As a result, the resistance of these piers did not represent a significant portion of the base shear capacity of the wall; therefore, the effect of the friction coefficient was relatively minor.

5.8 Summary

The model implied by FEMA 356 was modified to (1) consider the effect of FRP overlays on pier response, and (2) consider the global effects identified during the experimental portion of this research. Comparing the results obtained from the proposed model with the experimental results showed a reasonable amount of accuracy with an improvement over the current model from 15% to 66%. The two primary shortcomings of the proposed model were (1) the inability to accurately predict diagonal tension failures for URM piers, and (2) the inability to accurately predict debonding of FRP overlays from masonry.

Results of sensitivity analyses indicated that the global effects identified during the experimental portion of this study greatly impact the base shear capacity of low-rise URM buildings. Flange participation was the most important effect in terms of base shear capacity accounting for up 42% of the in-plane wall strength. Results also showed that material properties such as masonry compression strength, masonry shear strength, and the bed-joint coefficient of friction tend to play a smaller role in determining strength. However, as the level of vertical stress increases these properties influence the base shear capacity to a greater degree.

CHAPTER 6

SUMMARY AND CONCLUSIONS

The focus of this study was on the seismic retrofit of low-rise URM structures found in the Mid-America region. A summary of both the experimental and analytical portions of this research is presented in this chapter with an emphasis on findings. In addition, recommendations derived from the findings of this study are also presented. This chapter concludes with a brief description of the significance of this work as well as several areas where future research is recommended.

6.1 Summary of Experimental Work

Throughout the experimental portion of this study three primary objectives were followed. Specifically these objectives were to (1) investigate the behavior of several retrofit techniques in terms of damage progression and failure modes, (2) assess the effect of several retrofit techniques on overall structure performance in terms of strength, stiffness, energy dissipation, damage progression, and failure modes, and (3) identify global effects of URM structures that impact the behavior of primary components.

To satisfy these objectives, a full-scale two story URM structure was designed and built following construction practices consistent with those used in Mid-America prior to 1950. The structure was composed of four URM walls, flexible timber diaphragms and interior stud walls. Initial testing subjected both the roof diaphragms and in-plane walls (in an unreinforced state) to slowly applied lateral load reversals. Following this series of

tests, each masonry wall was retrofit and retested in-plane to assess the effectiveness of several retrofit techniques, which included the use of FRP overlays, NSM rods, and vertical unbonded post-tensioning. The goal of the FRP techniques was to activate a sliding plane adjacent to the foundation. The following sections present a summary of the conclusions of this research in terms of the three primary objectives.

6.1.1 Behavior of Retrofit Techniques

The findings of this study with regard to the behavior of the retrofit systems are summarized as follows:

- The primary damage to the FRP reinforcement systems was a progressive debonding from the masonry substrate. Both a cohesive failure of the masonry substrate (see Section 4.4.2.4) and an adhesive failure of the bond between the reinforcement and masonry substrate were observed (see Section 4.2.2.3).
- Progressive debonding of FRP reinforcement systems acts as a fuse which limits damage to the reinforcement itself. As a result, debonding allows the reinforcement to remain effective at large displacement levels and contribute to a highly nonlinear and apparent ductile system response (see Sections 4.2.2 and 4.4.2).
- Uplift of in-plane URM walls associated with local pier and global rocking induces additional tensile strain into unbonded post-tensioning tendons, which resulted in increases in prestressing force up to 50% during loading (see Section 4.3.2.3).

6.1.2 Effectiveness of Retrofit Techniques

In terms of the effectiveness of the retrofit systems investigated, the following conclusions are drawn:

- FRP reinforcement has the ability to greatly increase base shear capacity of URM buildings. In general, the effectiveness of these systems, in terms of strengthening, was limited by either debonding or the formation of a sliding plane (see Section 4.7.2).
- FRP retrofit systems that successfully aid in the formation of a sliding plane substantially increase the energy dissipation capacity of the in-plane wall (see Sections 4.1.3 and 4.4.3).
- The application of FRP reinforcement to only one side of URM walls results in negligible out-of-plane response. This is attributed to the restraint supplied by the transverse walls (see Section 4.7.2).
- The presence of both vertical and horizontal reinforcement in retrofit schemes results in small crack openings and a distributed cracking pattern, which is indicative of reinforced masonry behavior (see Sections 4.1.2.2 and 4.4.2.2).
- Lack of horizontal reinforcement in retrofit schemes allows cracks to open in a progressive manner during cyclic loading, thus substantially decreasing the displacement capacity of the wall (see Section 4.3.2.2).
- Vertical unbonded post-tensioning resulted in strength increases up to 60% greater than displayed prior to post-tensioning (see Section 4.3.3).
- The increase in vertical compressive stress imposed by a post-tensioning retrofit tends to alter pier failure modes from a ductile rocking/sliding to a more brittle

diagonal tension (see Section 4.3.2.2).

- Joist anchor retrofits are capable of forcing out-of-plane URM walls to participate in the response of the diaphragm in both directions (for the small displacement level investigated) (see Section 4.6).

6.1.3 Global Effects

Findings pertaining to the global effects of low-rise URM buildings can be summarized as follows:

- Out-of-plane URM walls participate to a large degree in the response of in-plane URM walls. The primary contribution of this tension flange participation is the additional weight imposed on the in-plane wall. Note that this participation requires sufficient connection between orthogonal walls (see Section 4.7.3.3).
- Defining flange weight by a 45^{o} crack extending upwards from the active rocking crack of the adjacent in-plane wall is generally conservative (see Section 4.7.3.3).
- The effect of overturning moment greatly impacts pier failure modes through altering the vertical stress applied to individual piers (see Section 4.7.3.1).
- In-plane URM walls respond to lateral loads by either interstory shear deformation caused by lateral force, a global rotation (global rocking) of the entire wall caused by overturning moment (see Section 4.7.3.2), or a combination of both mechanisms.
- Flexible timber diaphragms provide negligible coupling between in-plane URM walls (see Section 4.5).

6.1.4 Other Findings

Other important findings that did not directly coincide with specific objectives are summarized as follows:

- For URM piers, low-level rocking impacts bed-joint sliding resistance by cracking the bed-joint and, thus, reducing the shear resistance to friction alone (Sections 4.1.1 and 4.4.2).
- Both steel lintels and shallow arch lintels perform well; however, shallow arch lintels are prone to collapse if non-structural components such as window and door frames are not present (see Section 4.3.1.2).
- Header courses are sufficient to transfer the force developed in external reinforcement to the other wythes of masonry (see Section 4.7.4).
- Rocking dominated behavior results in the dissipation of approximately 20% of the input energy and residual displacements around 20% of the maximum imposed displacement (see Section 4.7.4).
- Sliding dominated behavior results in the dissipation of approximately 40% of the input energy and residual displacements up to 60% of the maximum imposed displacement (see Section 4.7.4).

6.2 Summary of Analytical Work

The analytical portion of this study was centered around three primary objectives, which were to: (1) investigate the ability of simplified models based on component behavior to predict overall structure response, (2) investigate the influence of global effects on the response of low-rise URM walls, and (3) investigate the influence of

masonry material properties on the response of low-rise URM walls.

To satisfied these objectives, the model implied by FEMA 356 (ATC, 2000) was modified to consider both the effect of FRP overlays on pier response and the global effects identified during the experimental portion of this study. The resulting model was then validated through comparisons with the measured response of the structure. The influence of global effects and masonry material properties on the base shear capacity of low-rise URM structures was then assessed.

Based on the results of this analytical study, the following conclusions are made:

- Simplified models, such as the pushover model presented in Chapter 5, can provide accurate predictions of the response of low-rise URM structures both before and after retrofit (see Sections 5.4 and 5.5).
- The model proposed in Chapter 5 gave strength estimates with errors ranging from 0% to 42% (with an averaging 13%) when compared with experimental results. The model implied by FEMA 356 (ATC, 2000) gave strength estimates with errors ranging from 14% to 66% (with an average of 41%) when compared with experimental results. The predictions of both models were conservative in all cases. The improved accuracy of the proposed model is primarily attributed to the consideration of global effects (see Section 5.4).
- Results of sensitivity analyses indicated that the global effects identified during the experimental portion of this study greatly impact the base shear capacity of low-rise URM buildings both before and after retrofit (see Section 5.6).
- For low-rise URM buildings, the consideration of tension flange participation always results in an increase in base shear capacity that is proportional to the

tension flange weight compared with the weight of the in-plane wall (see Section 5.6.1).

- Neglecting the effects of overturning moment can result in either conservative or unconservative strength estimates depending on the relative sizes of the piers within the wall (see Section 5.6.2).
- Consideration of global rocking as a potential failure mode is always conservative in terms of base shear capacity (see Section 5.6.3).
- Defining pier height as the height of adjacent openings can result in unconservative strength estimates (see Section 5.6.4).
- Material properties such as masonry compression strength, masonry shear strength, and the bed-joint coefficient of friction have a small influence on strength for low-levels of vertical stress. As the level of vertical stress increases, the influence of these properties (particularly the shear strength of masonry) also increases (see Section 5.7).

6.3 Recommendations

Based on the findings of this research the following recommendations are made:

- For the calculation of sliding resistance, the shear strength of the bed-joint should be neglected for cases where rocking deformation is expected to occur.
- In-plane wall retrofits should employ both vertical and horizontal reinforcement to prevent the progressive opening of cracks during cyclic loading.
- The condition of header courses should be assessed if resistance provided by external reinforcement is assumed to be transferred to inner wythes.

- FRP overlays employed as in-plane retrofits should be properly developed to allow the highly nonlinear pseudo-ductile response associated with progressive debonding to be exploited.
- The effective height of piers should be defined as the height over which a compression strut is likely to form, not the height of adjacent openings.
- For the analysis of unbonded post-tensioned masonry, the structure may be analyzed as a URM structure with increased compressive vertical stress; however, the increase in post-tensioning force caused by local pier and global rocking deformation should be considered.
- In conjunction with vertical post-tensioning of URM walls, additional reinforcement should be provided to suppress diagonal tension failures.
- For the analysis of low-rise URM buildings before and after retrofit, global effects such as flange participation, the effects of overturning moment, and global rocking should be addressed.
- Flange participation should only be considered for cases where sufficient connection between orthogonal walls is present (i.e. interlocking units).
- All URM structure retrofits should contain sufficient connections between the diaphragm and out-of-plane walls.

6.4 Significance

The research outlined in this thesis will make significant contributions to the structural engineering community for a number of reasons, which are summarized as follows:

- The identification of global effects (currently not address in the current prestandard (ATC, 2000)) greatly improves the understanding URM structure response. In addition, these findings allow the large knowledge base of URM component behavior, both before and after retrofit, to be utilized more effectively.
- The analysis procedure presented in Chapter 5 represents the first simplified model, applicable for design, that considers flange participation, overturning moment, and global rocking. This represents an improvement over the current guidelines and prestandards (ATC, 1997 and ATC, 2000), which are based almost entirely on past research that has focused on component behavior.
- The detailed documentation of the experimental results provides a means to validate analytical models and current code provisions, thus increasing the accuracy of tools available to practicing engineers.
- This study represents the first time that several modern retrofit techniques have been assessed through the testing of a full-scale structure. The results presented provide insight into how these techniques contribute to the overall building response, which is required to permit their safe and effective application for seismic upgrading of URM facilities.

6.5 Future Work

Throughout this study several areas which require further work were uncovered, these areas are summarized as follows:

- The global effects outlined in this study need to be investigated with a structure subjected to dynamic loading. Results from the parallel investigation (Project ST-

22) conducted at CERL will provided insight into the effect of dynamic loading. However, due to scaling issues and mass distribution a full-scale dynamic test of a similar test structure is recommended.

- The impact of the global effects on the behavior of individual piers needs to be assessed. This could be accomplished by subjecting a series of corner URM piers (i.e. with flanges) to cyclic lateral displacements while varying the level of vertical stress to account for overturning effects.
- A model capable of accurately predicting the debonding of FRP from masonry is required. Such a model is needed to develop models capable of accurately predicting of the response of URM piers following retrofit with FRP overlays.
- The accuracy of the spring model, developed for the analysis URM piers after retrofit, should be assessed through comparisons with past component tests. Due to the lack of a reliable debonding model, such a comparison was not included in this research. Once this model is validated, the influence of various FRP properties on the effectiveness of URM pier retrofit can be investigated.
- A more accurate method of determining the diagonal strength of URM piers is required. Such a model should include a method to separate diagonal tension failures that occur through units with those that occur in a stair-stepped pattern to allow for the large differences in displacement capacity to considered.

APPENDIX A

TEST SETUP

A.1 In-Plane Testing of Walls 1 and 2

This section contains drawings of the instrumentation plan for the in-plane testing of Walls 1 and 2. Figures A.1 through A.3 show the location of load cells; Figures A.4 through A.8 show the location of LVDTs; Figures A.9 through A.11 show the location of potentiometers; Figures A.12 through A.15 show the location of strain gages; and Figures A.16 through A.17 show the location of strain gages attached to the external reinforcement applied to Walls 1 and 2. Note that final crack pattern of each wall is also shown.

Figure A.1 Elevation view of Wall 1 showing the location of load cells.

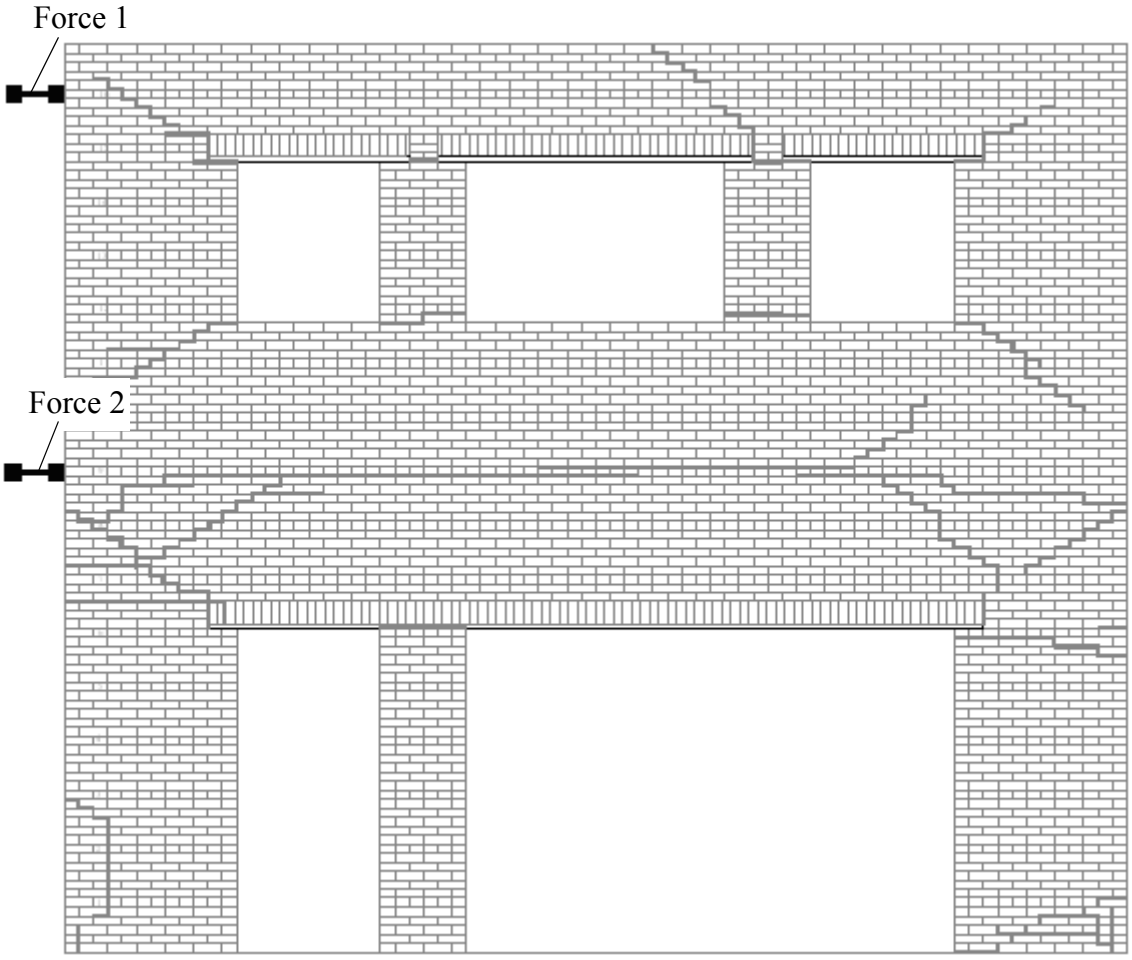

Figure A.2 Elevation of Wall 2 illustrating the location of load cells.

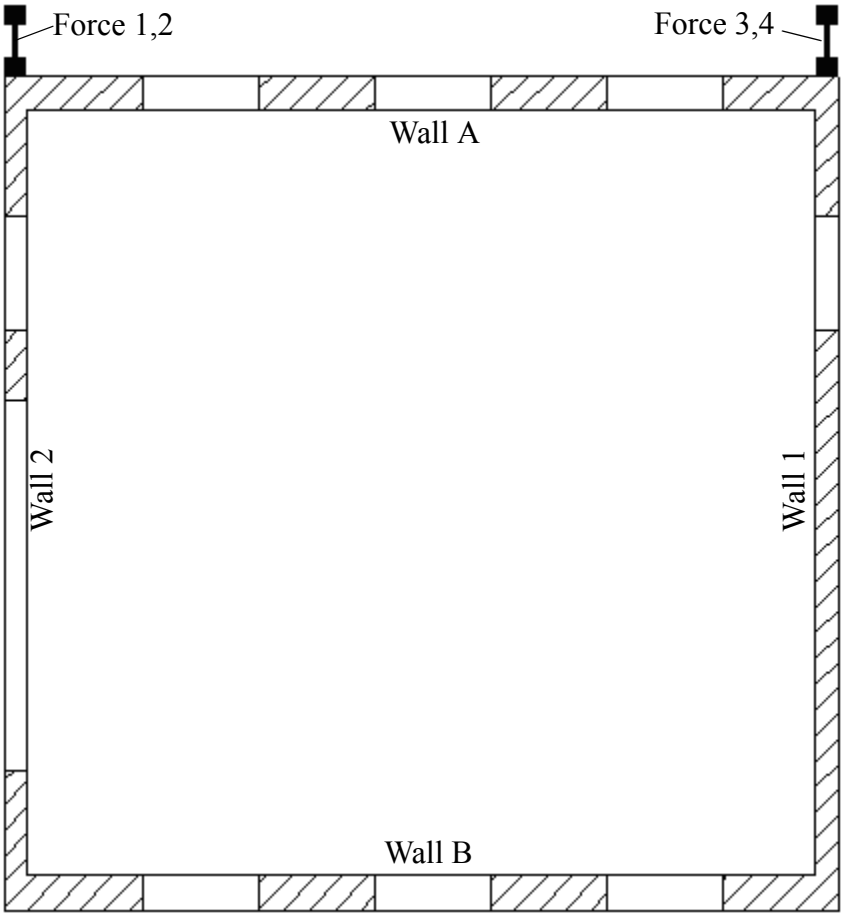

Figure A.3 Plan view illustrating the location of load cells.

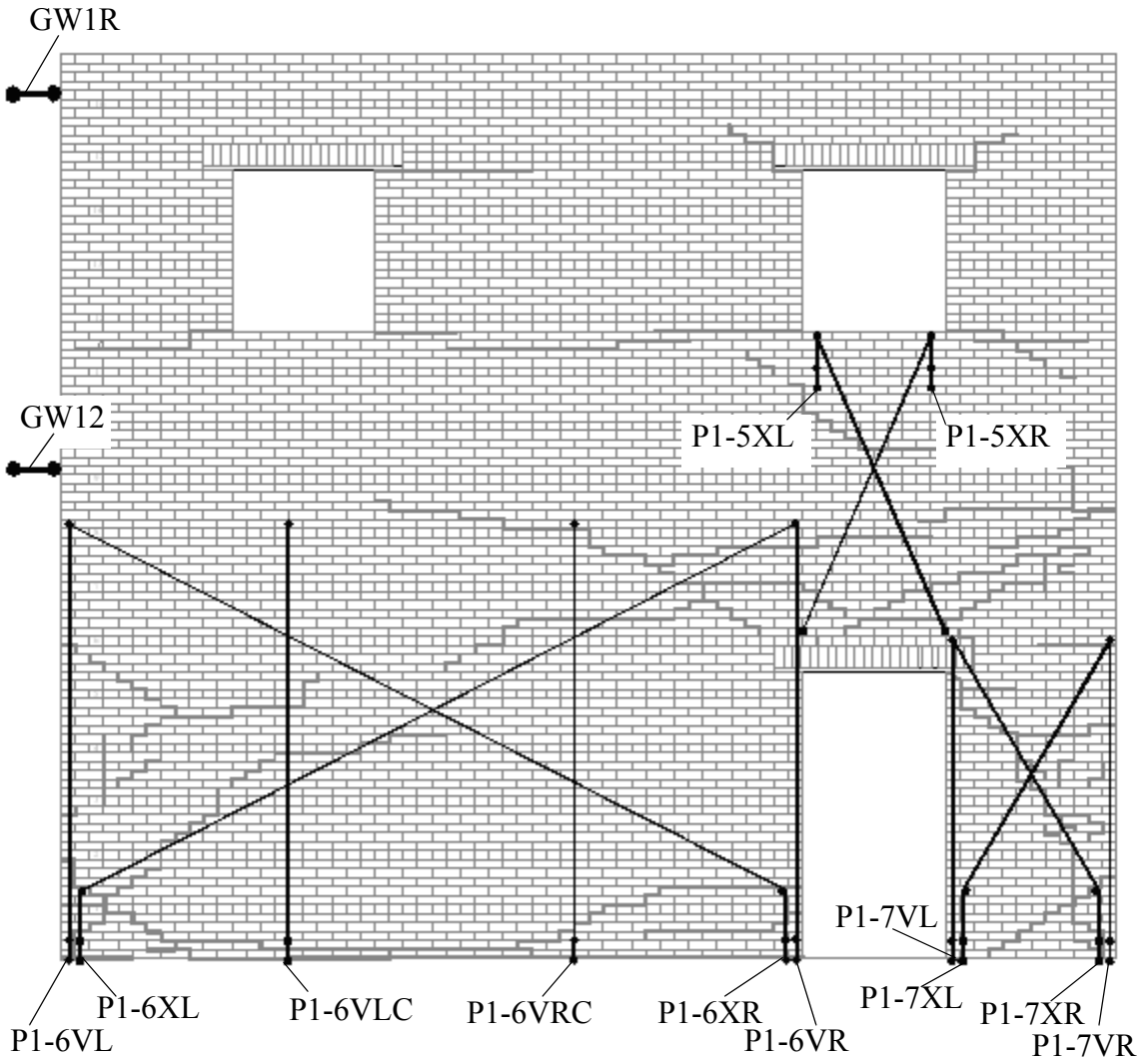

Figure A.4 Elevation view of Wall 1 illustrating the location of LVDTs.

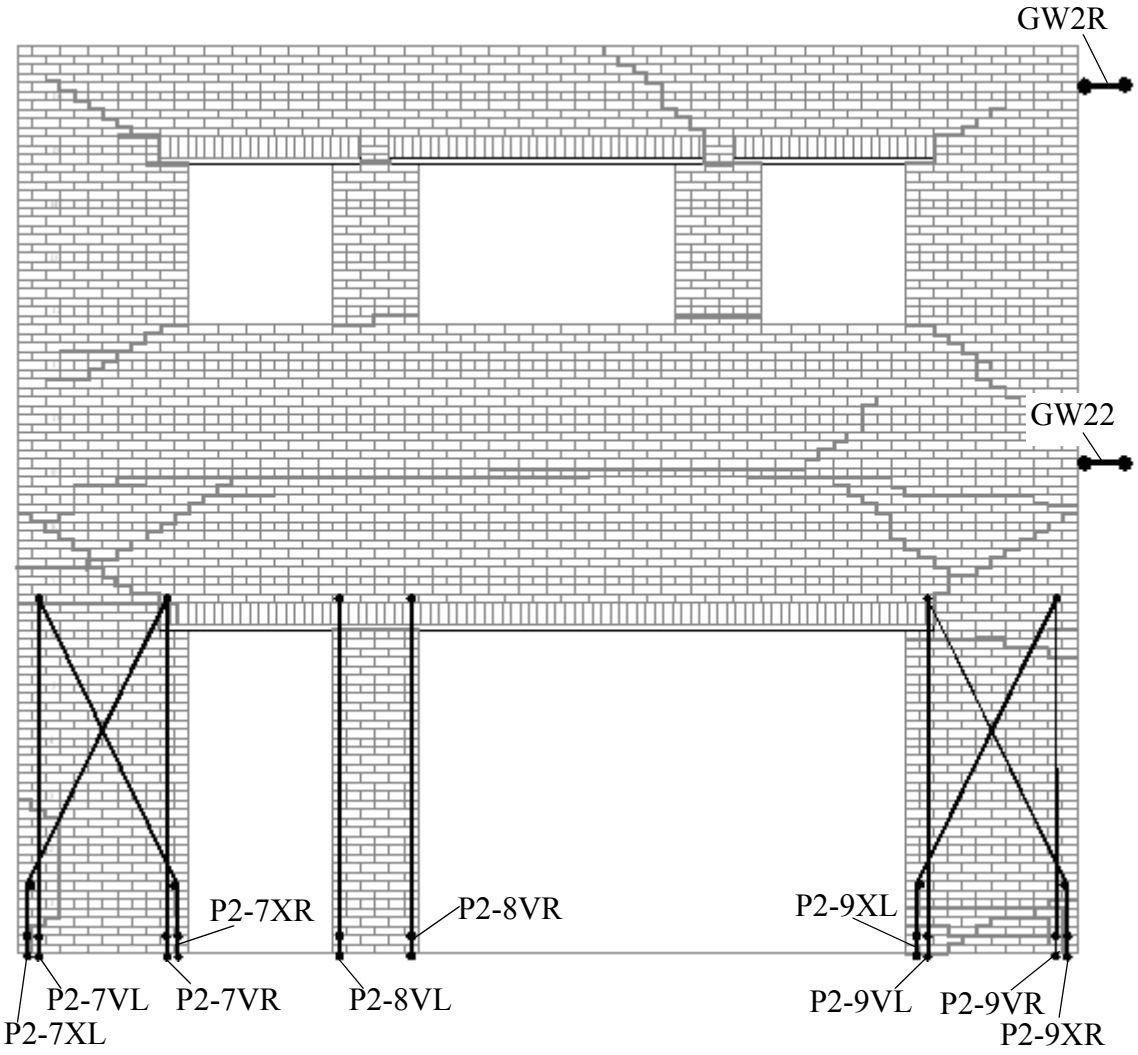

Figure A.5 Elevation view of Wall 2 illustrating the location of LVDTs

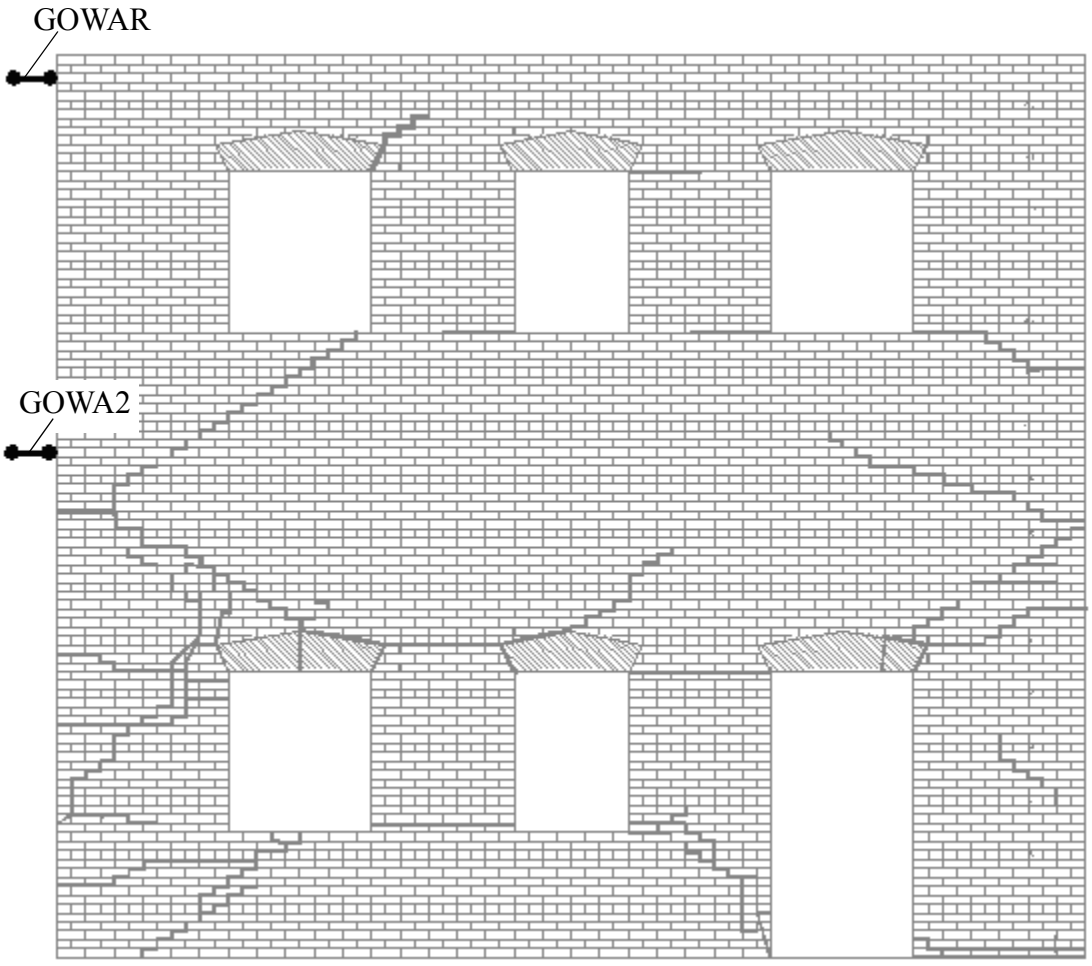

Figure A.6 Elevation view of Wall A illustrating the location of LVDTs.

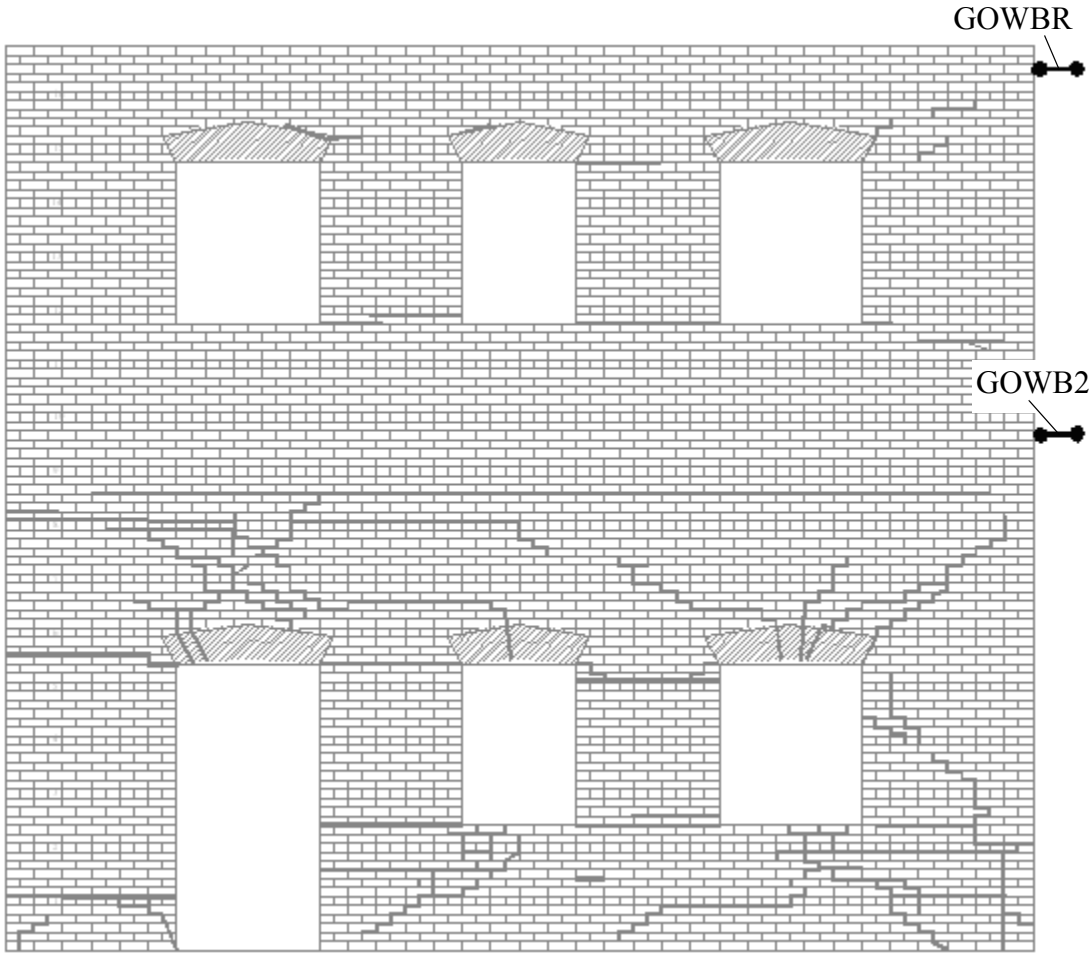

Figure A.7 Elevation view of Wall B illustrating the location of LVDTs.

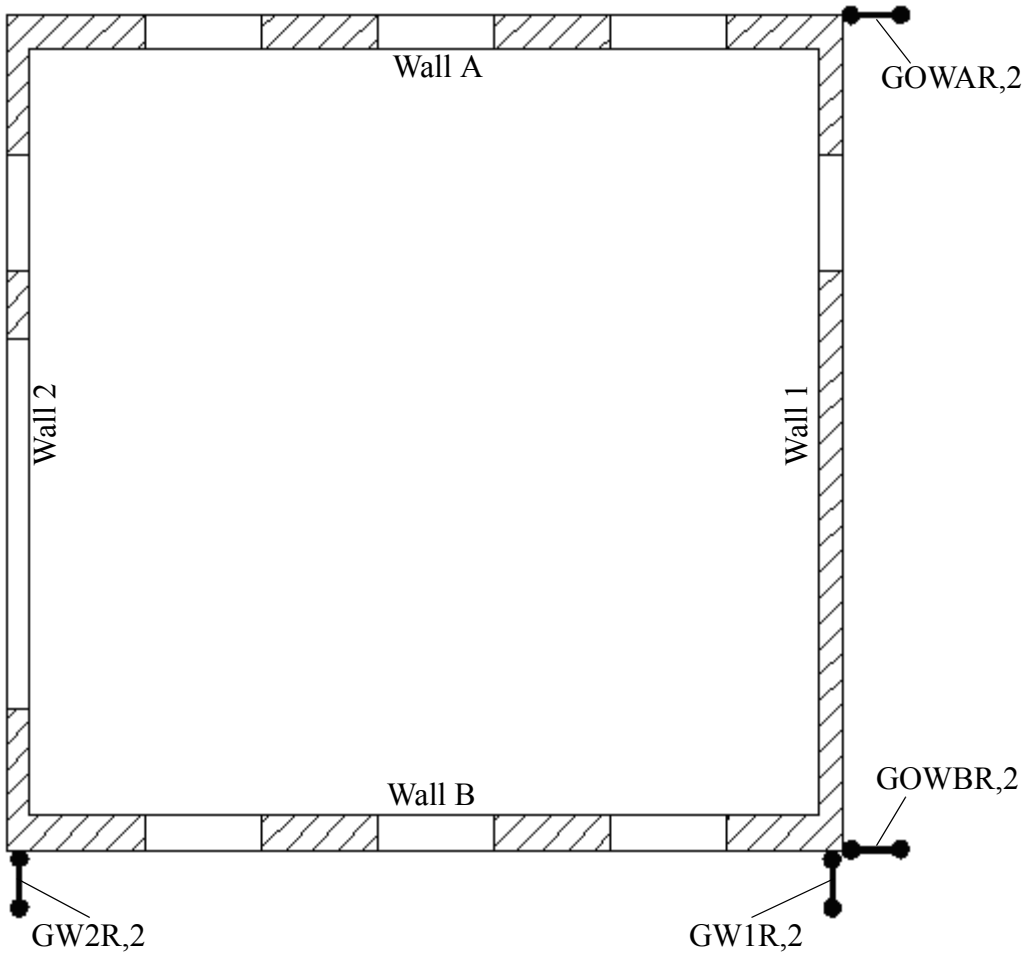

Figure A.8 Plan view illustrating the location of LVDTs.

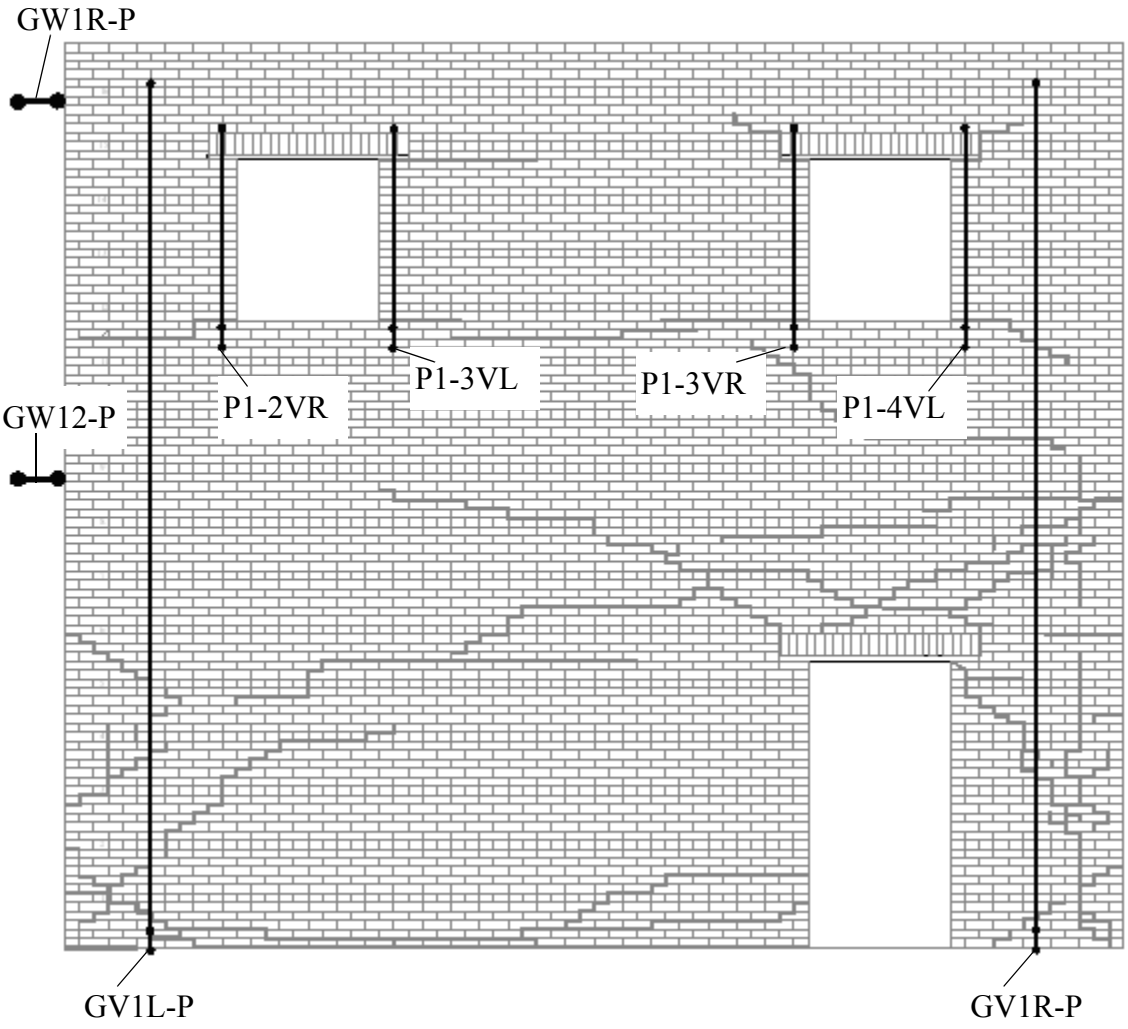

Figure A.9 Elevation view of Wall 1 illustrating the location of potentiometers.

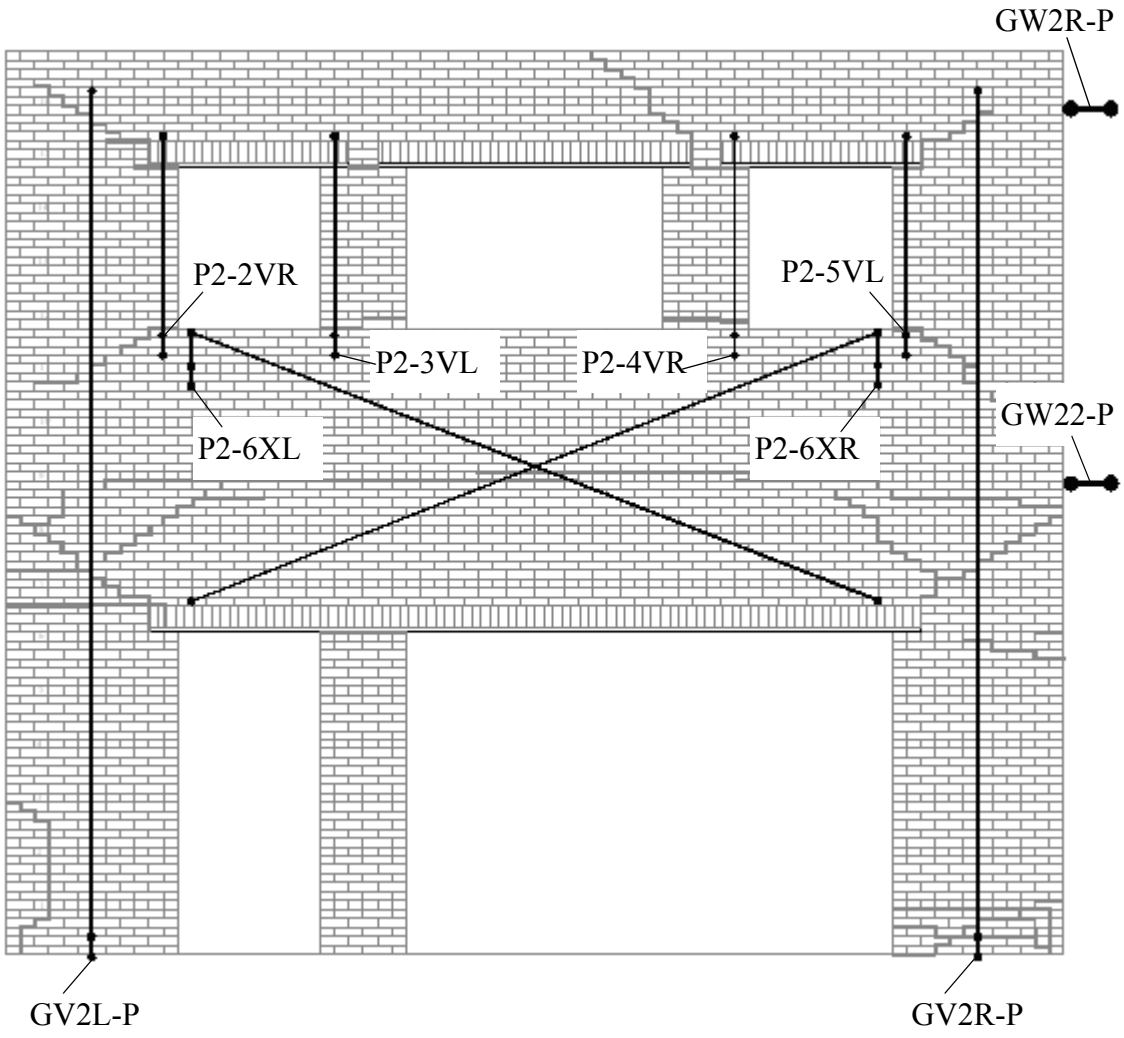

Figure A.10 Elevation view of Wall 2 illustrating the location of potentiometers.

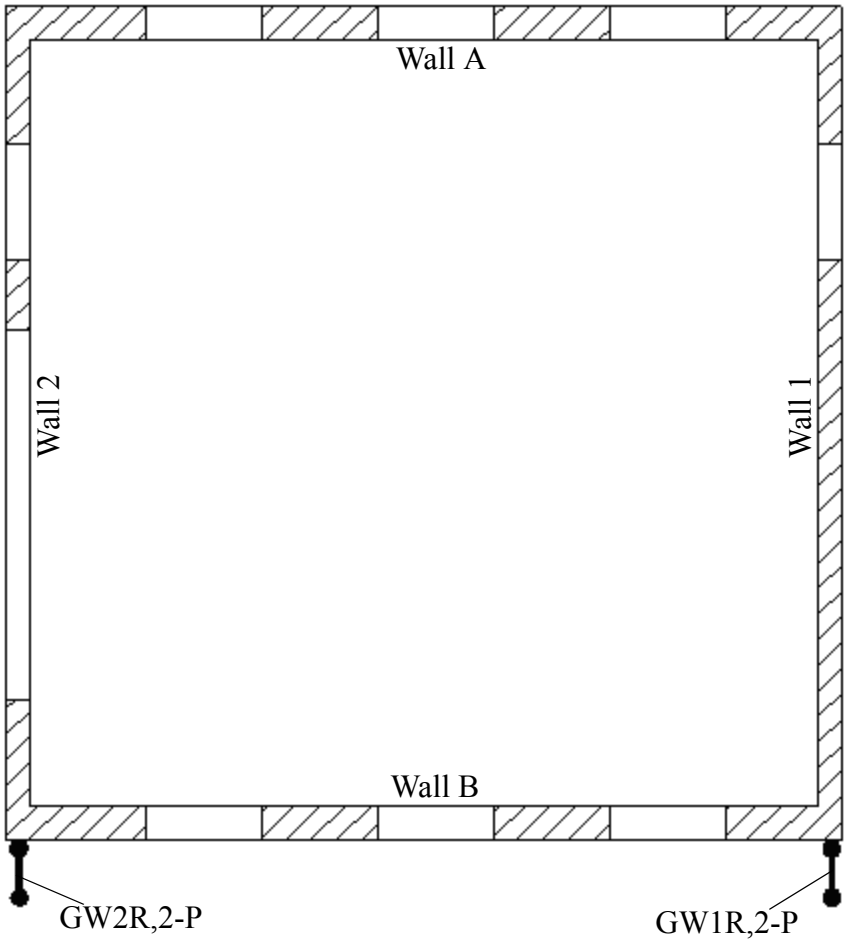

Figure A.11 Plan view illustrating the location of potentiometers.

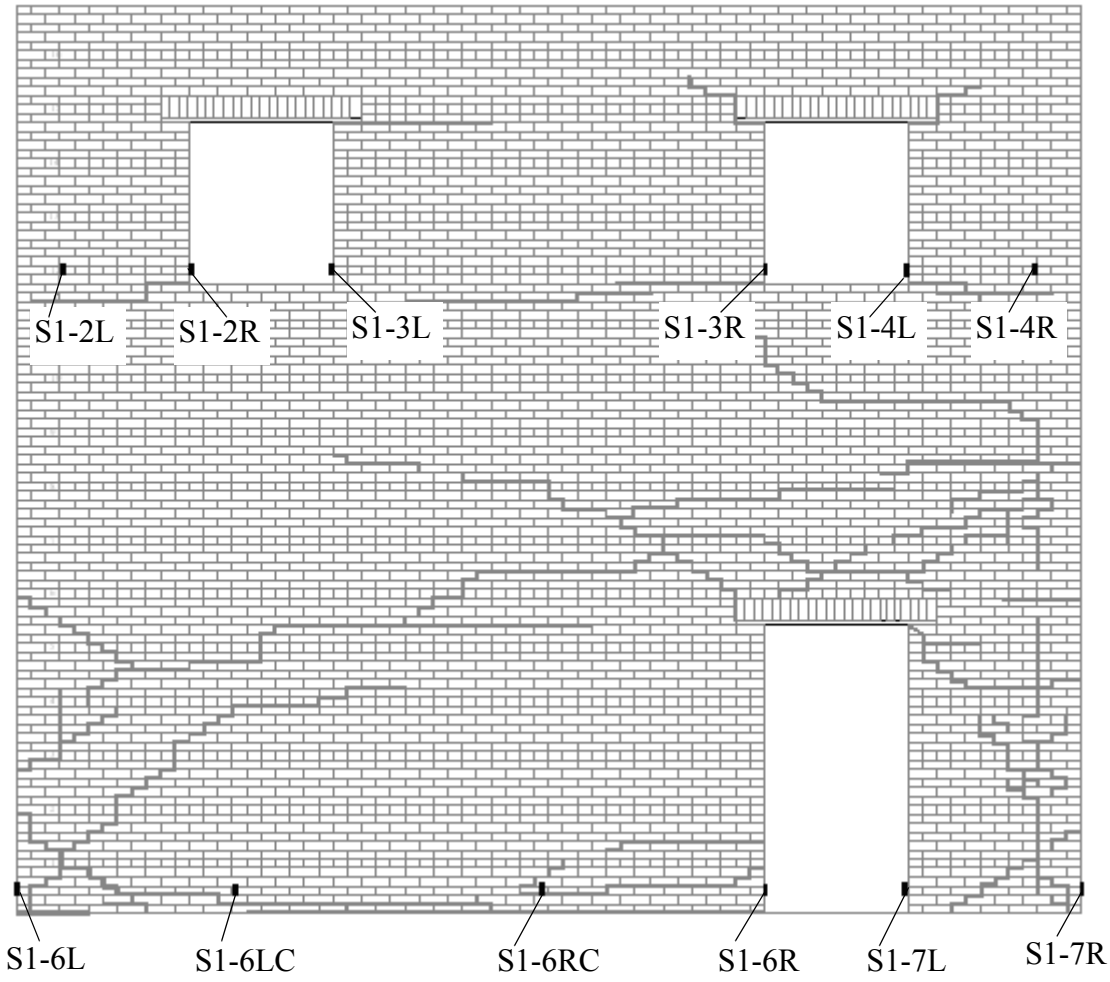

Figure A.12 Elevation of Wall 1 illustrating the location of strain gages.

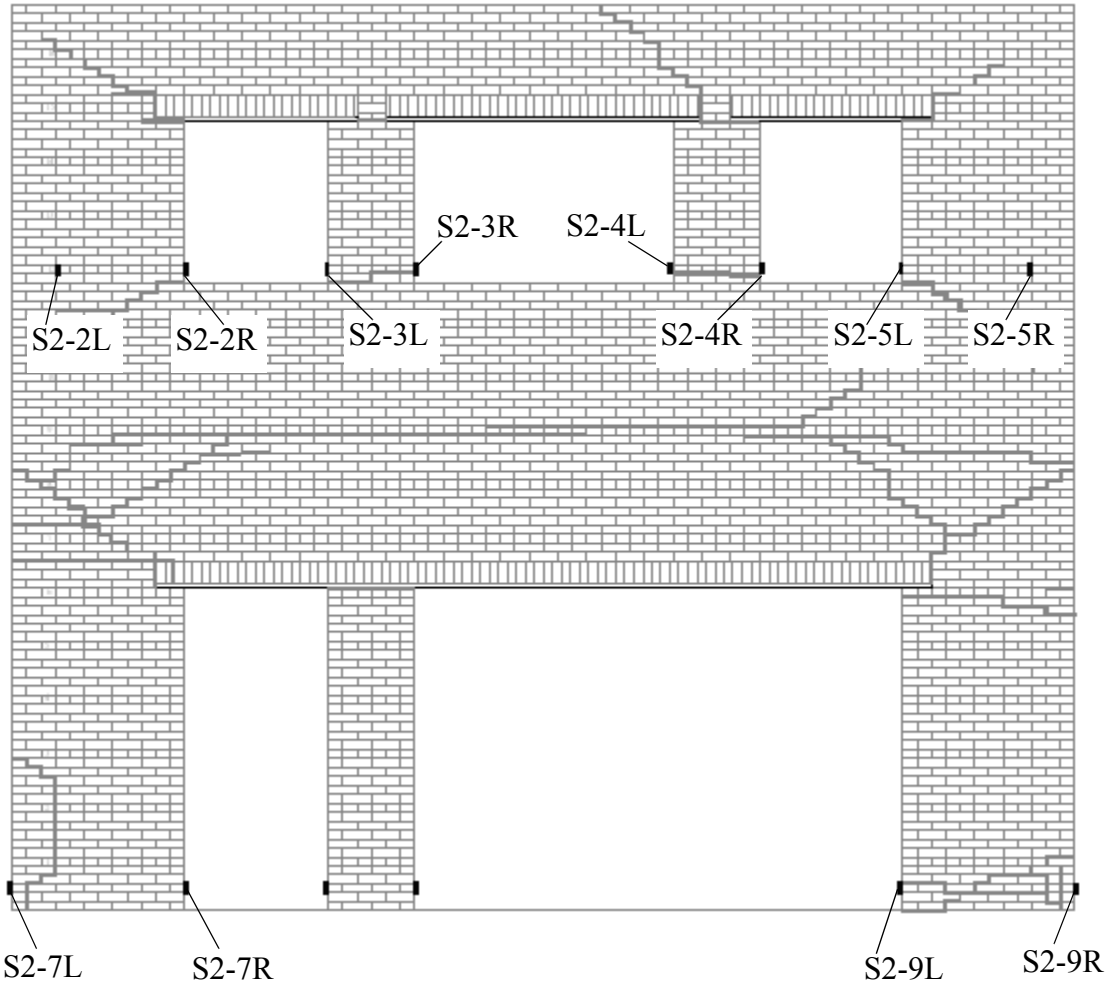

Figure A.13 Elevation of Wall 2 illustrating the location of strain gages.

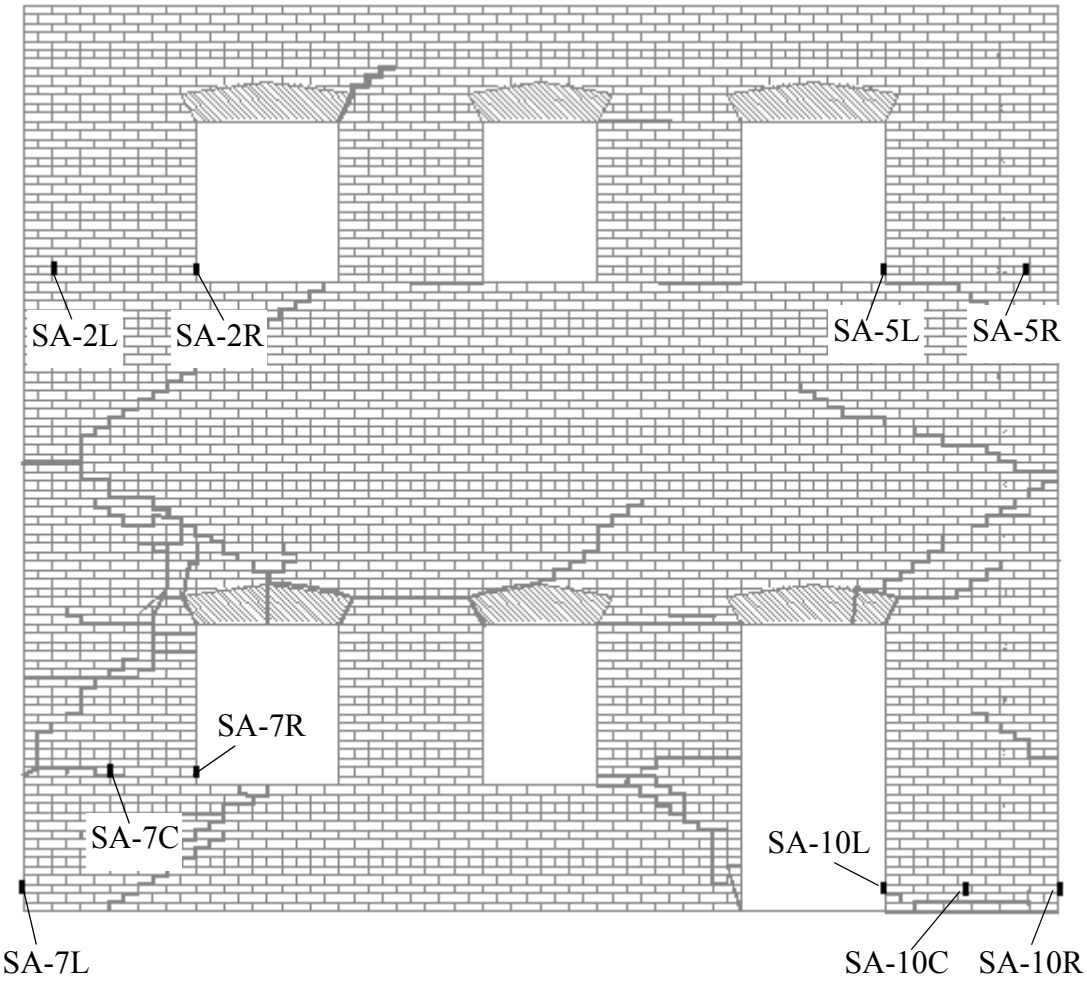

Figure A.14 Elevation of Wall A illustrating the location of strain gages.

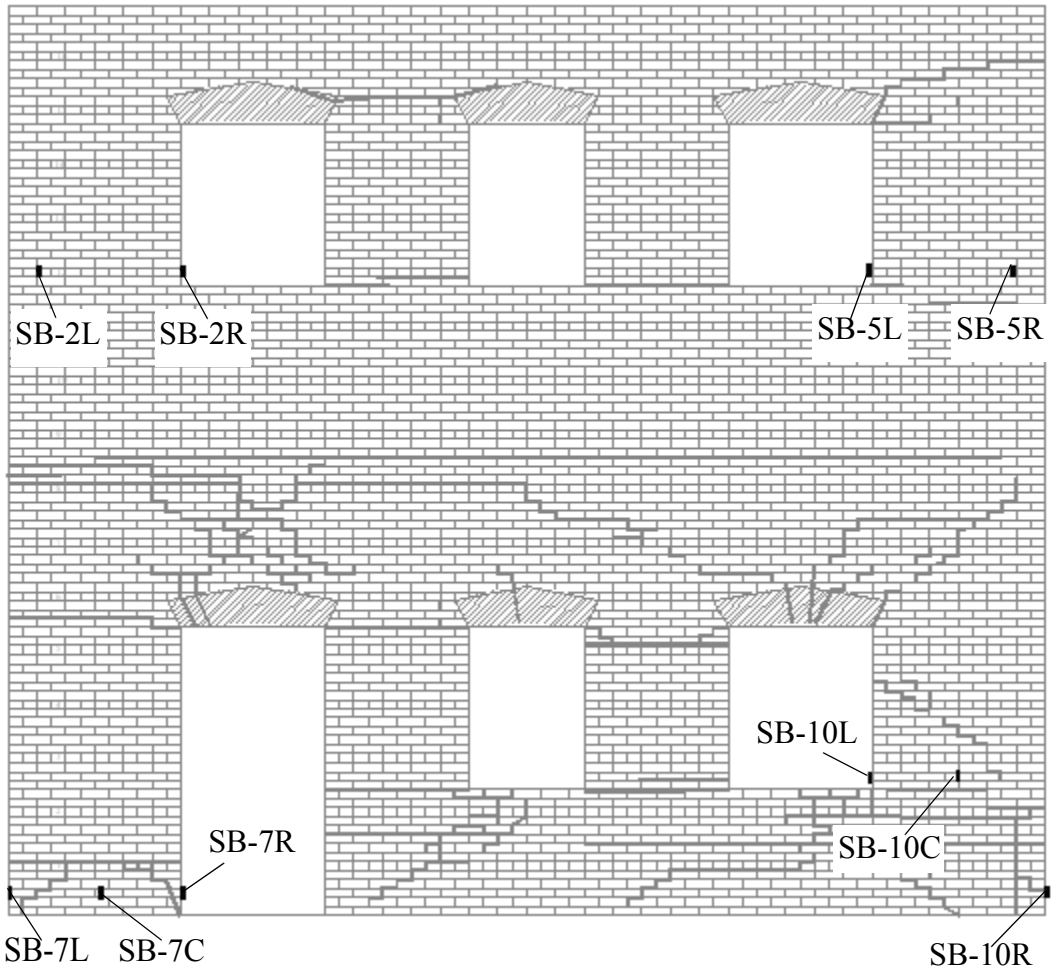

Figure A.15 Elevation of Wall B illustrating the location of strain gages.

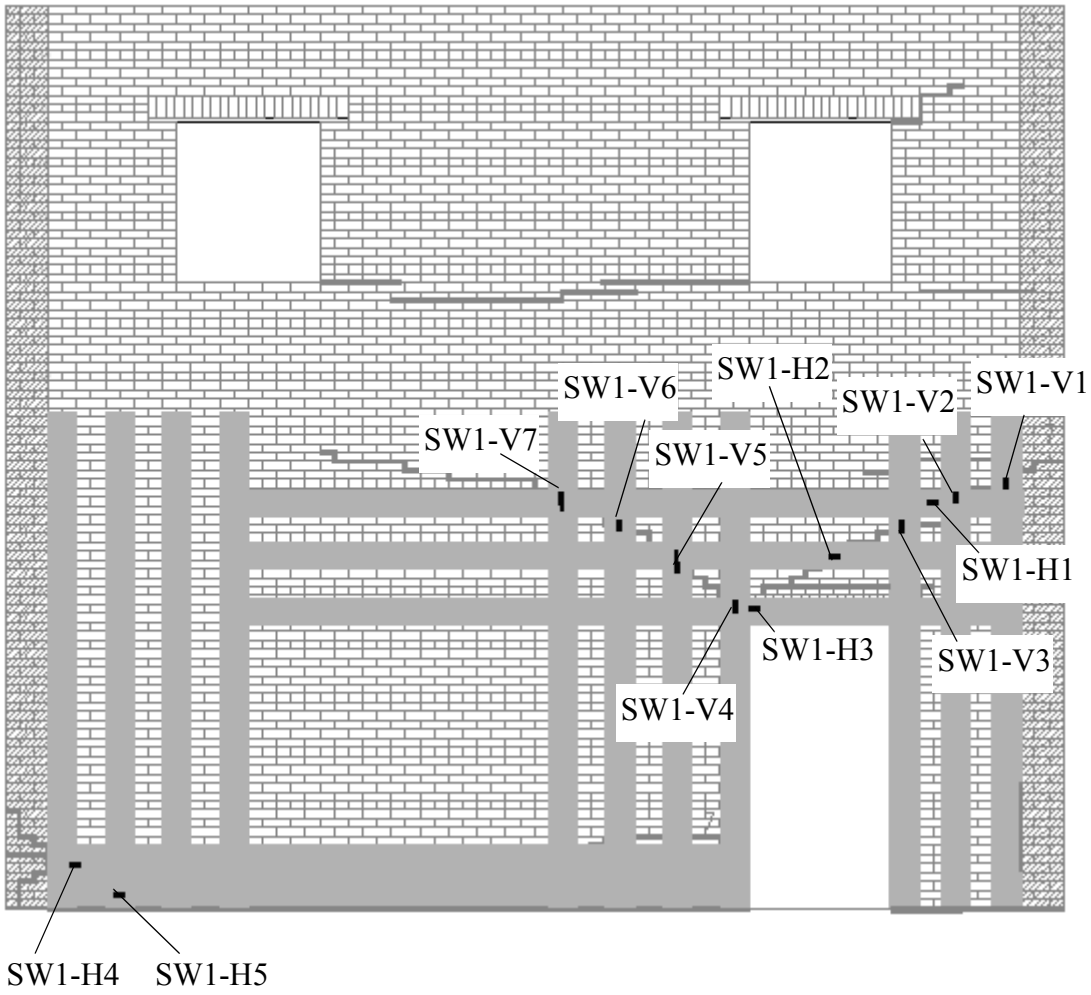

Figure A.16 Elevation of Wall 1 illustrating the location of strain gages attached to the FRP overlays.

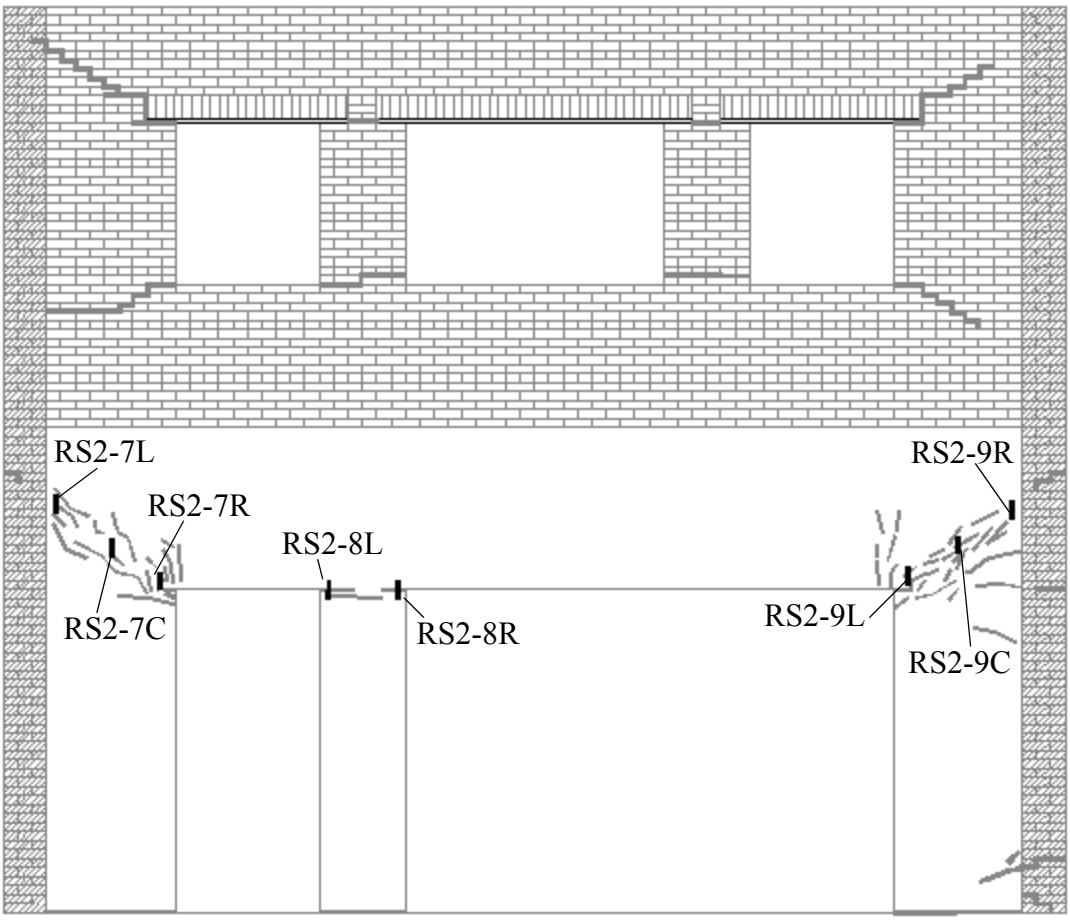

Figure A.17 Elevation of Wall 2 illustrating the location of strain gages attached to the external reinforcement system.

A.2 In-Plane Testing of Walls A and B

This section contains drawings of the instrumentation plan for the in-plane testing of Walls A and B. Figures A.18 through A.20 show the location of load cells; Figures A.21 through A.25 show the location of LVDTs; Figures A.26 through A.28 show the location of potentiometers; Figures A.29 through A.32 show the location of strain gages; and Figures A.33 through A.34 show the location of instrumentation attached to the retrofit systems applied to Walls A and B. Note that final crack pattern of each wall is also shown.

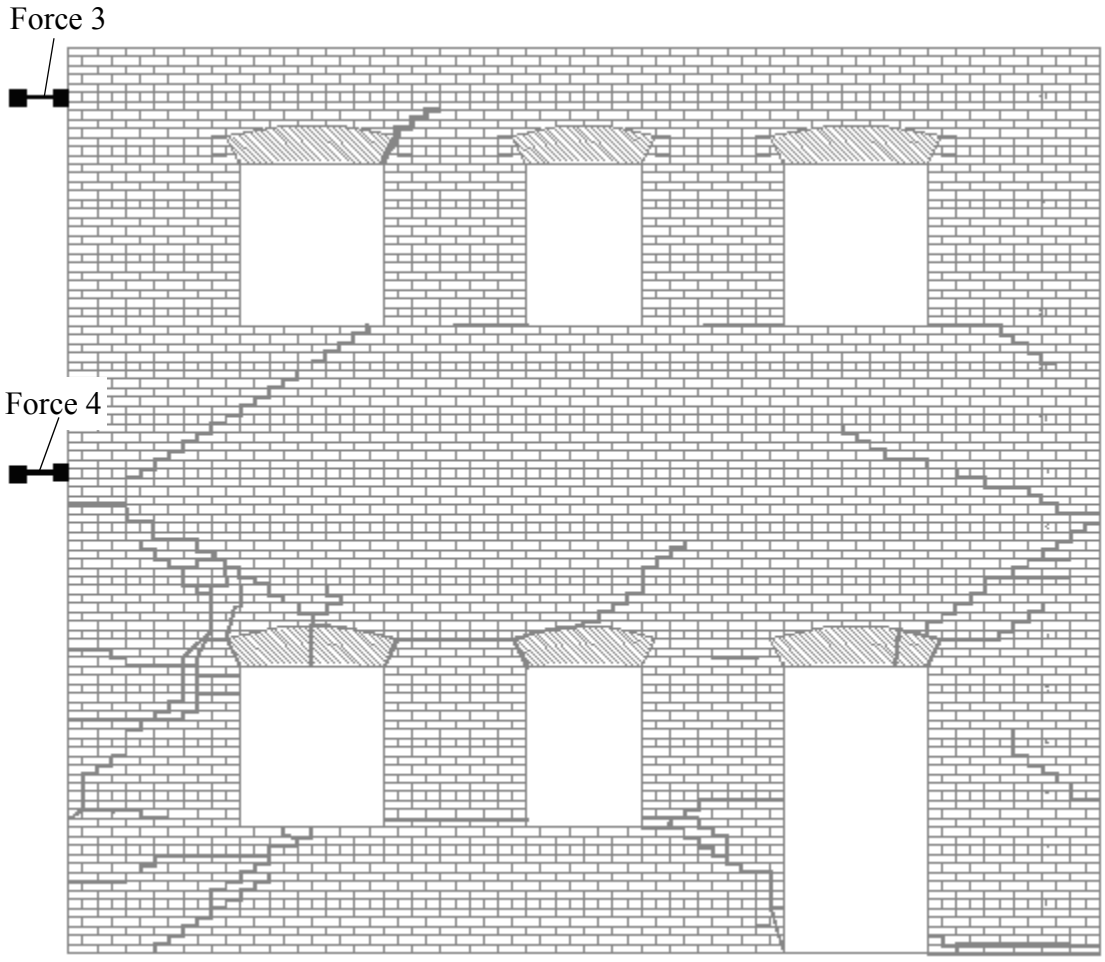

Figure A.18 Elevation view of Wall A showing the location of load cells.

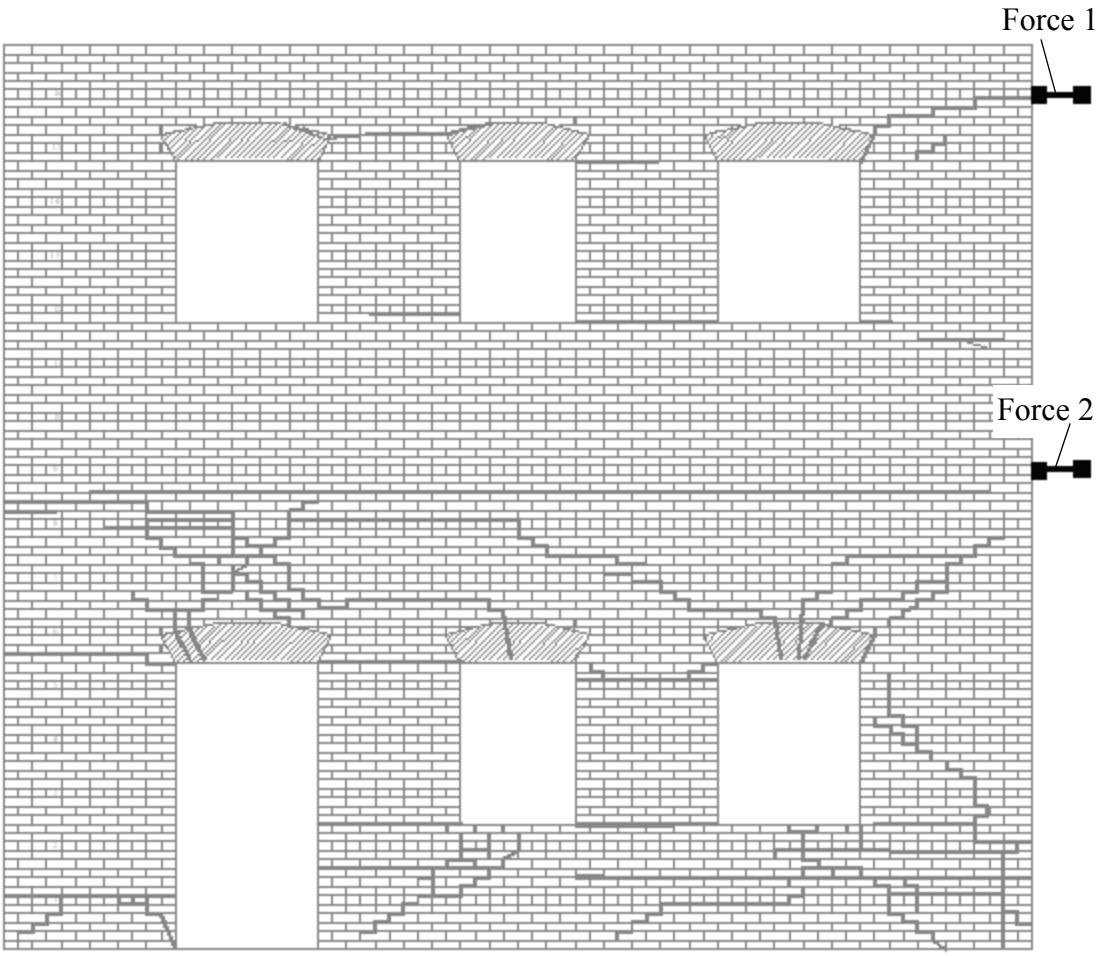

Figure A.19 Elevation of Wall B illustrating the location of load cells.

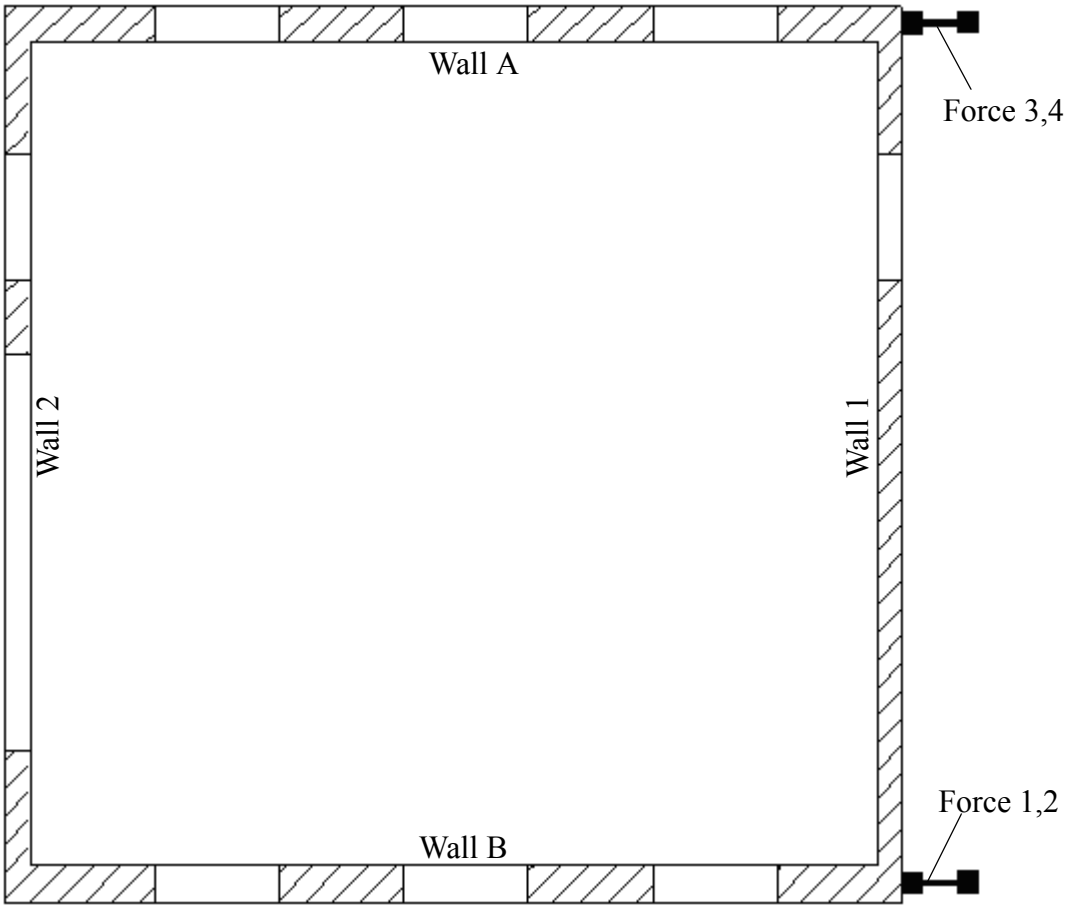

Figure A.20 Plan view illustrating the location of load cells.

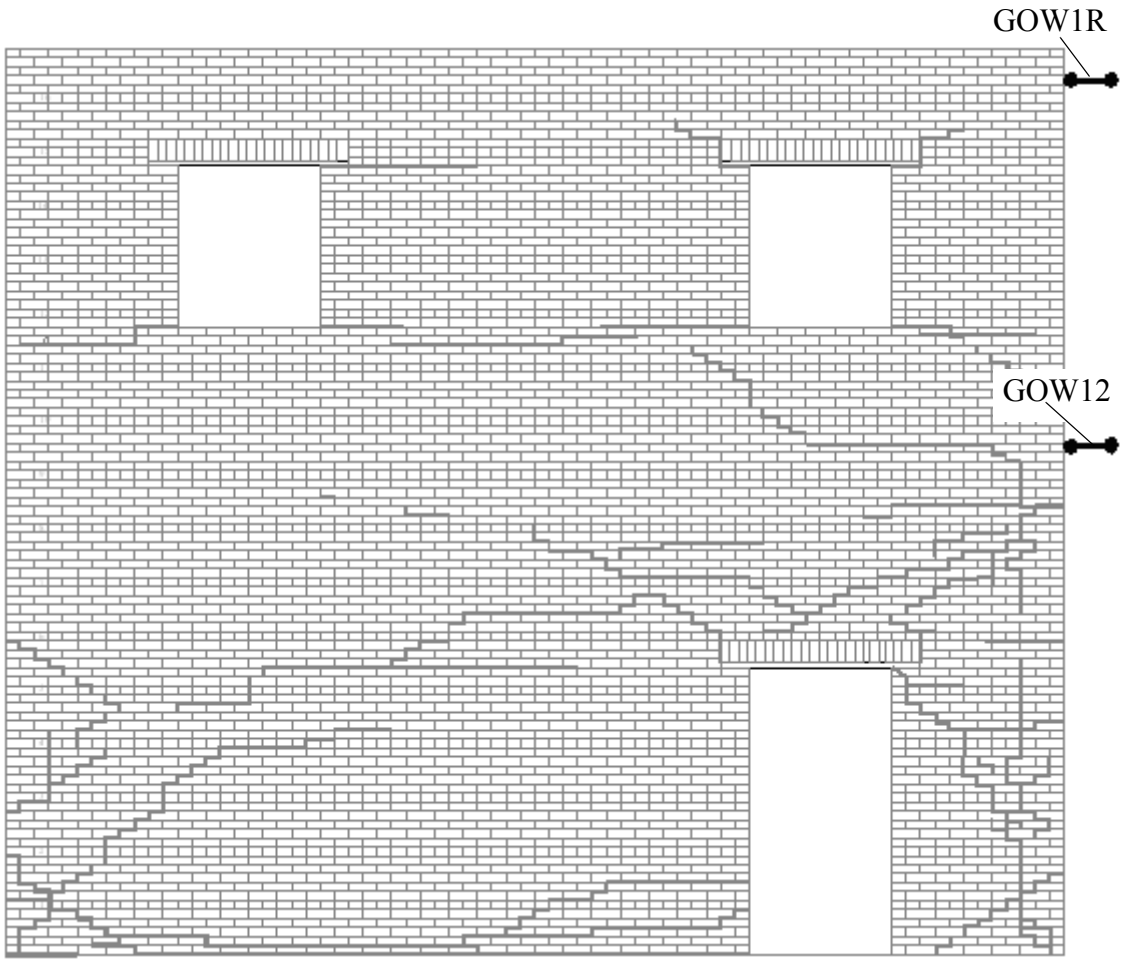

Figure A.21 Elevation view of Wall 1 illustrating the location of LVDTs.

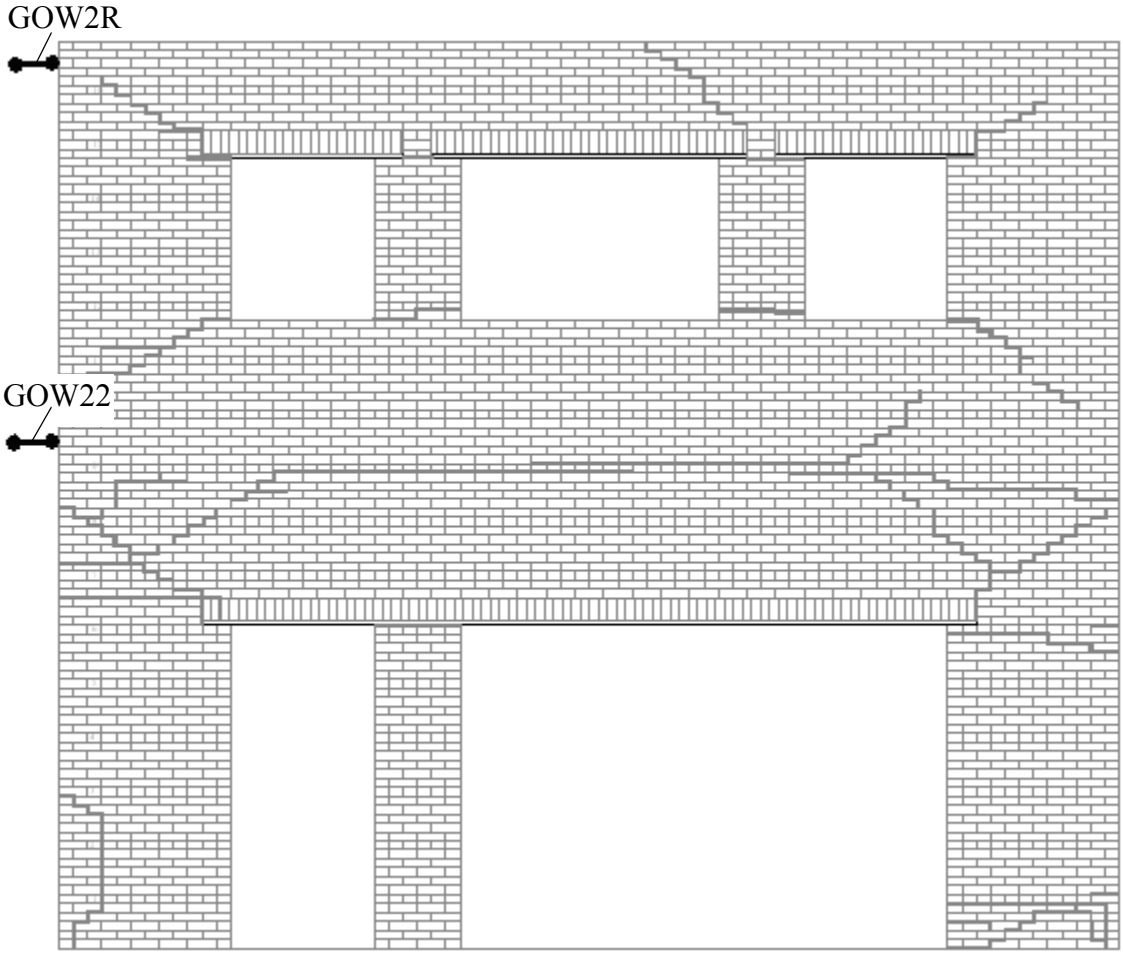

Figure A.22 Elevation view of Wall 2 illustrating the location of LVDTs

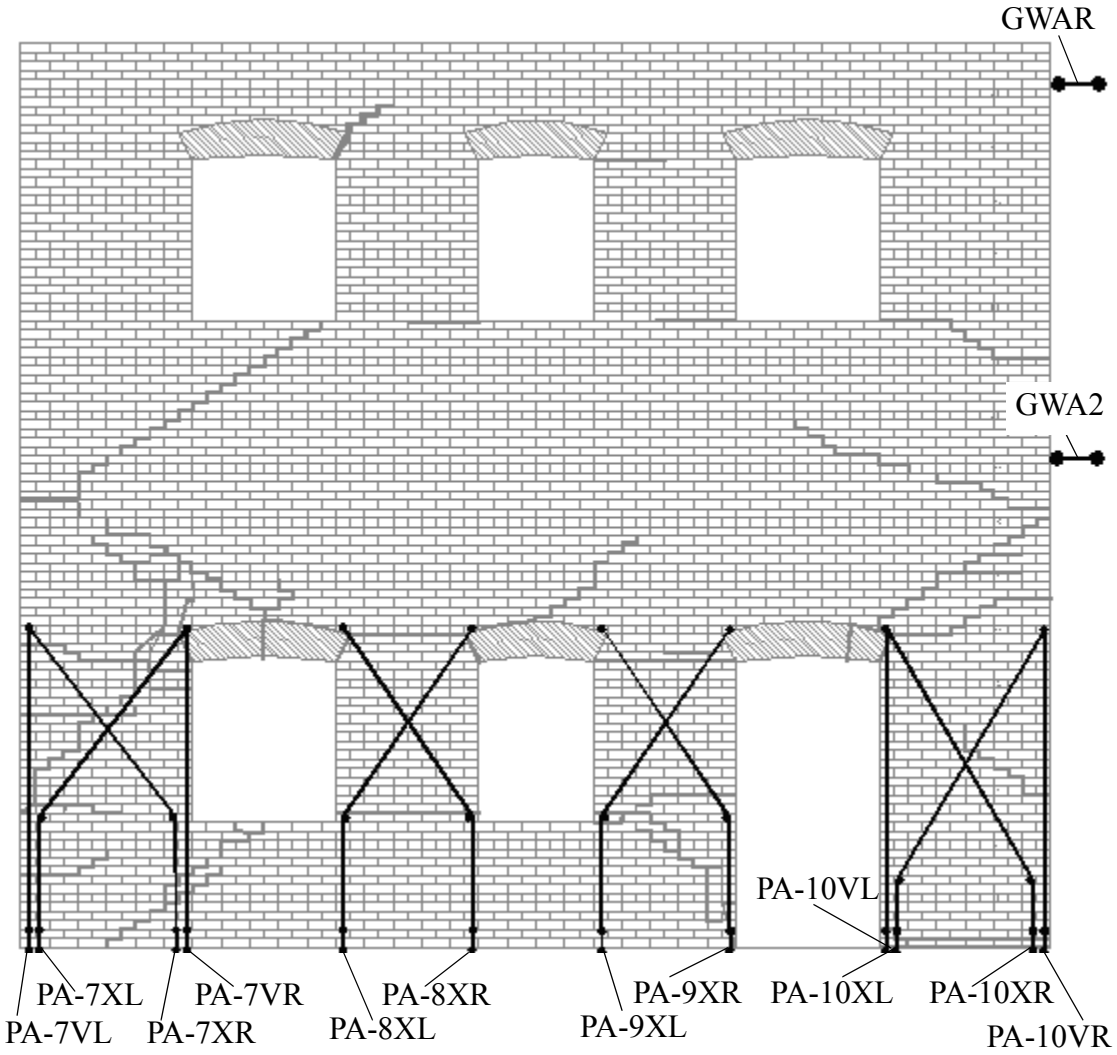

Figure A.23 Elevation view of Wall A illustrating the location of LVDTs.

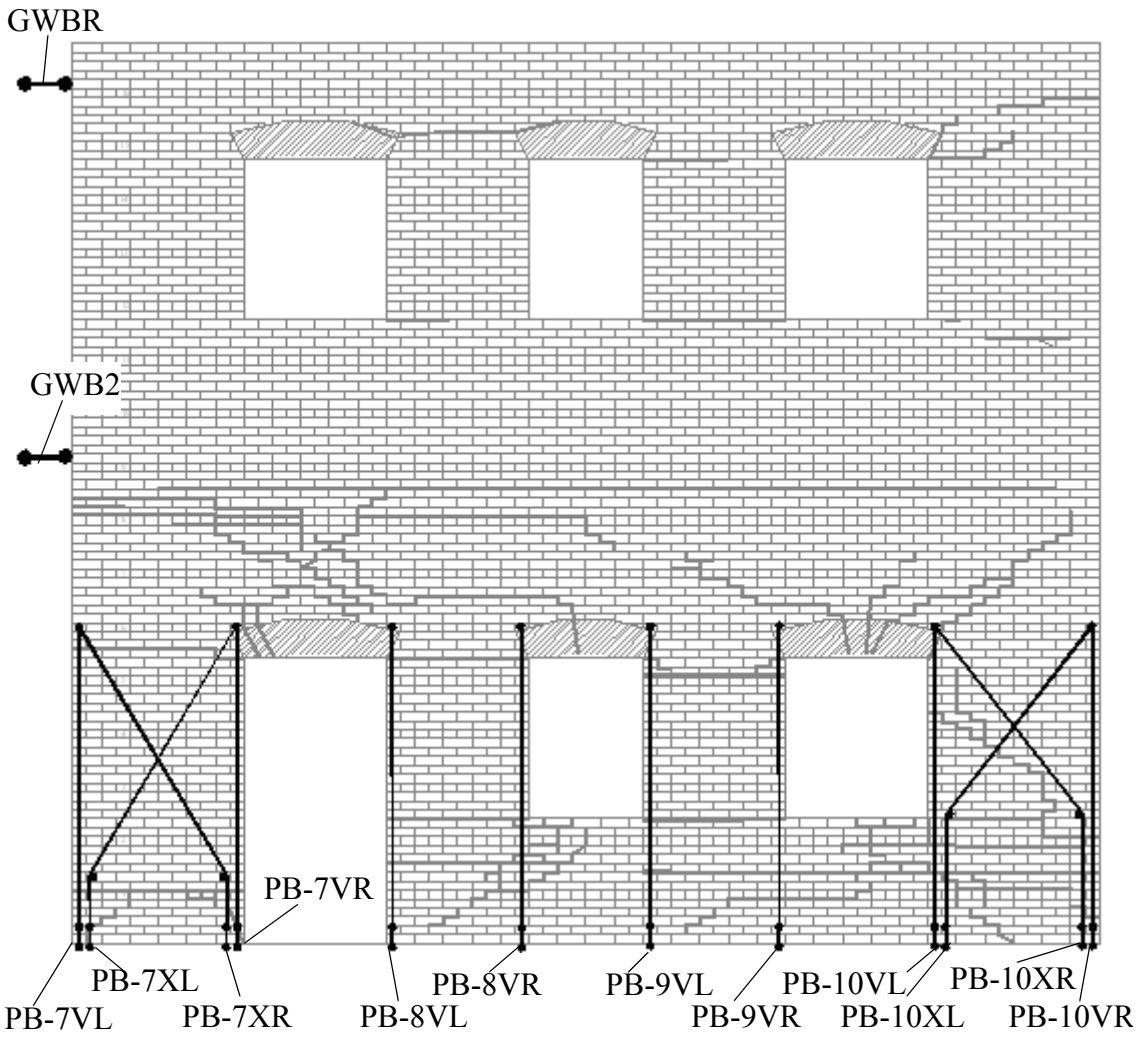

Figure A.24 Elevation view of Wall B illustrating the location of LVDTs.

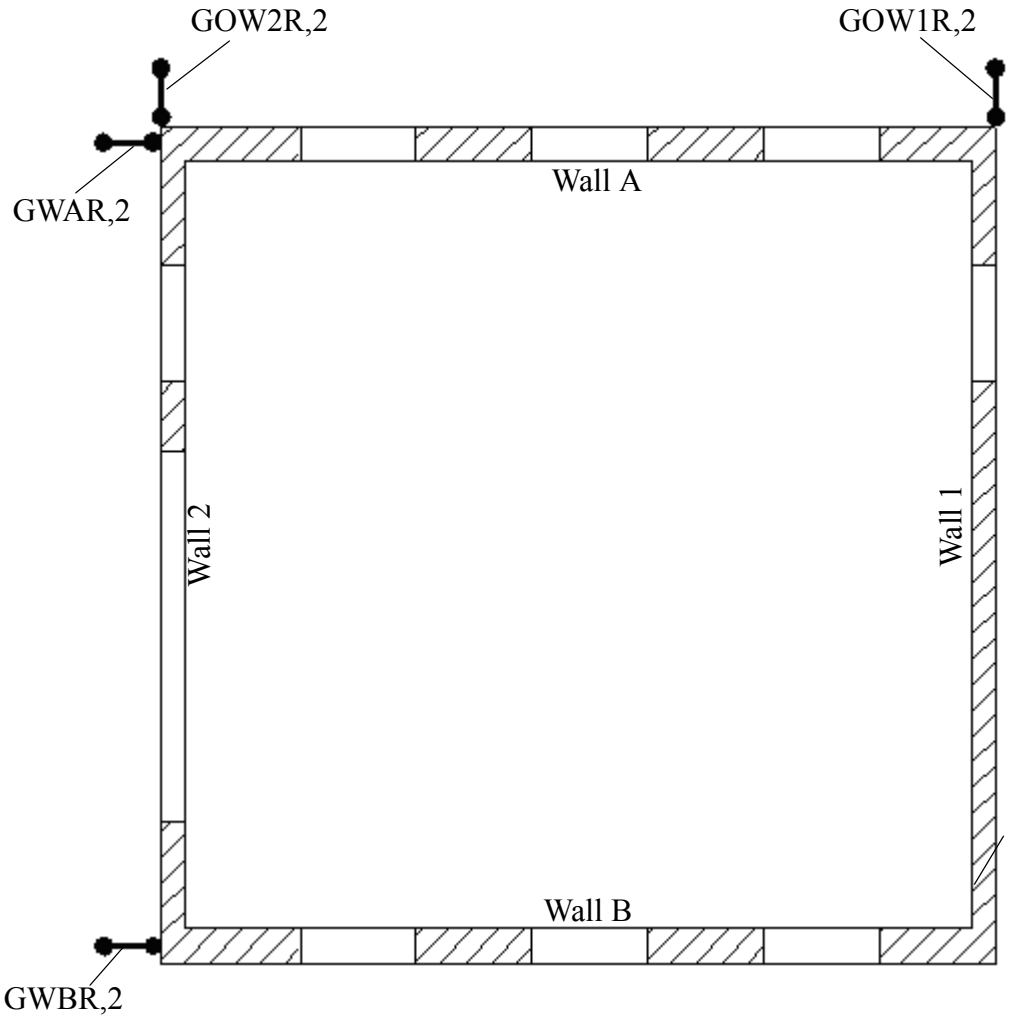

Figure A.25 Plan view illustrating the location of LVDTs.

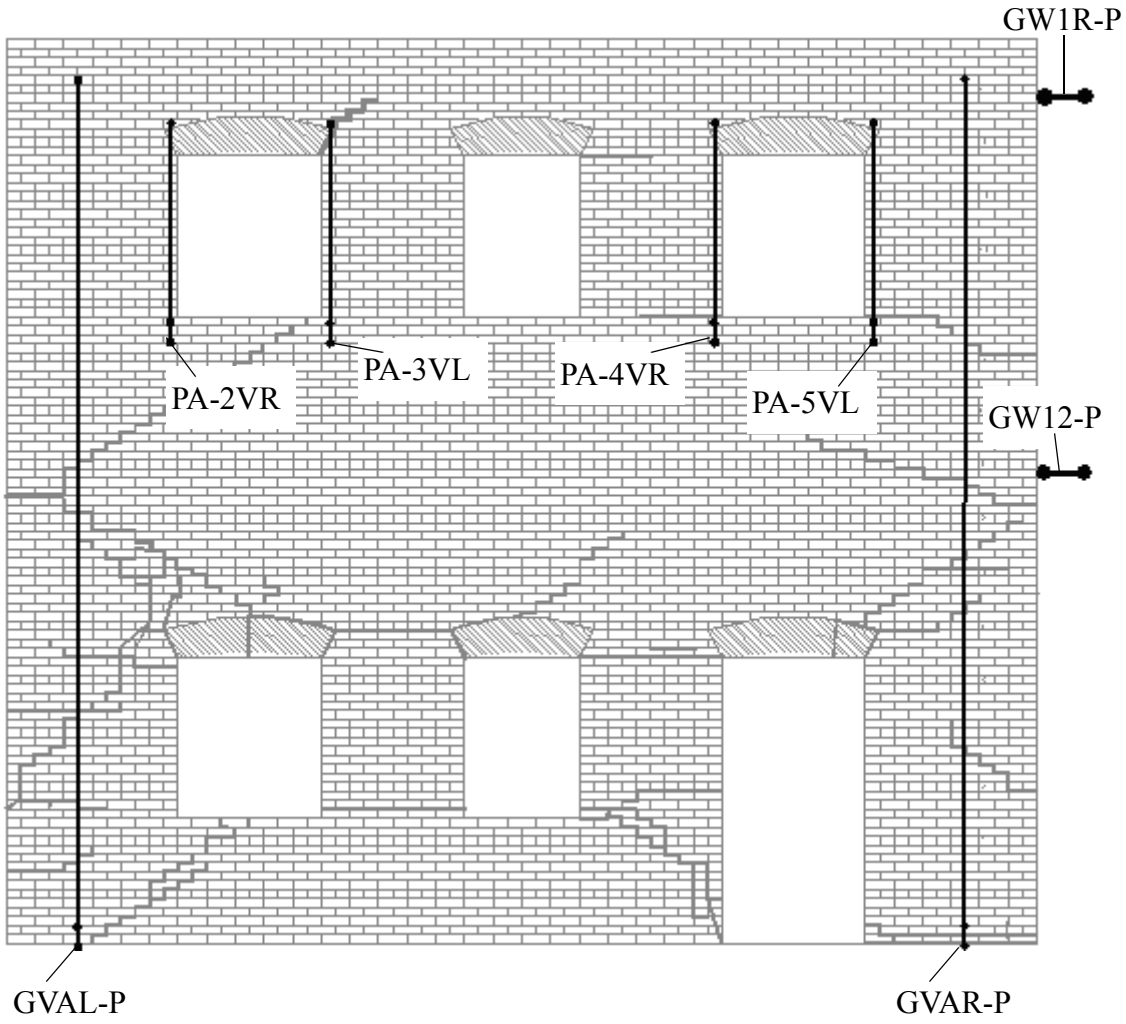

Figure A.26 Elevation view of Wall A illustrating the location of potentiometers.

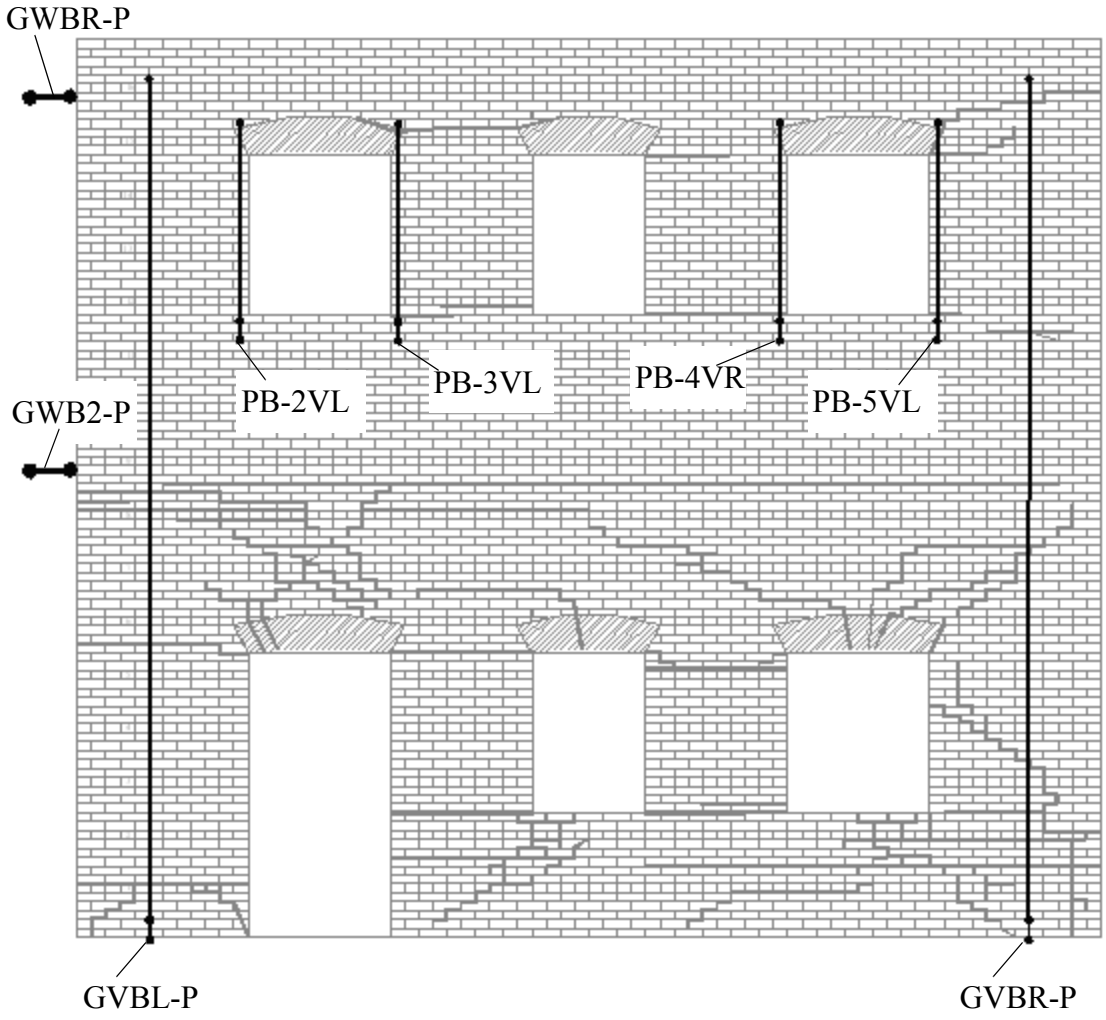

Figure A.27 Elevation view of Wall B illustrating the location of potentiometers.

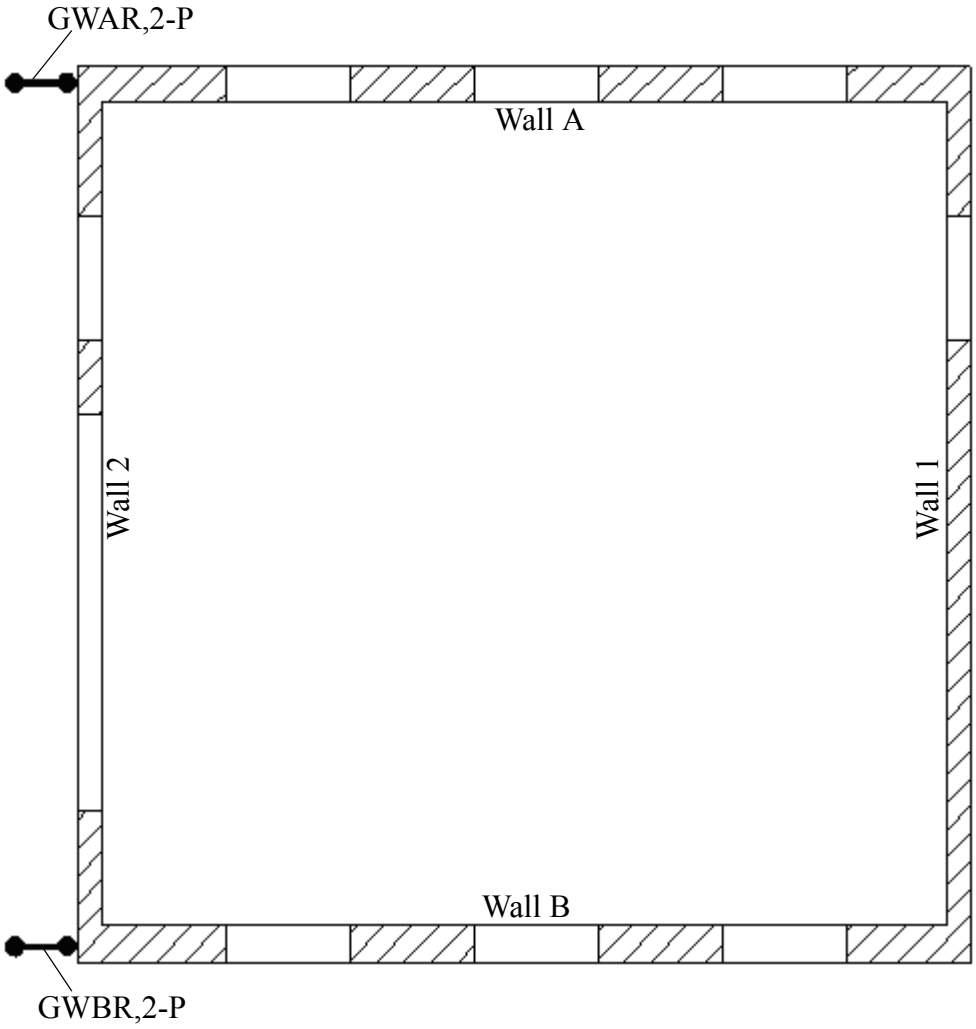

Figure A.28 Plan view illustrating the location of potentiometers.

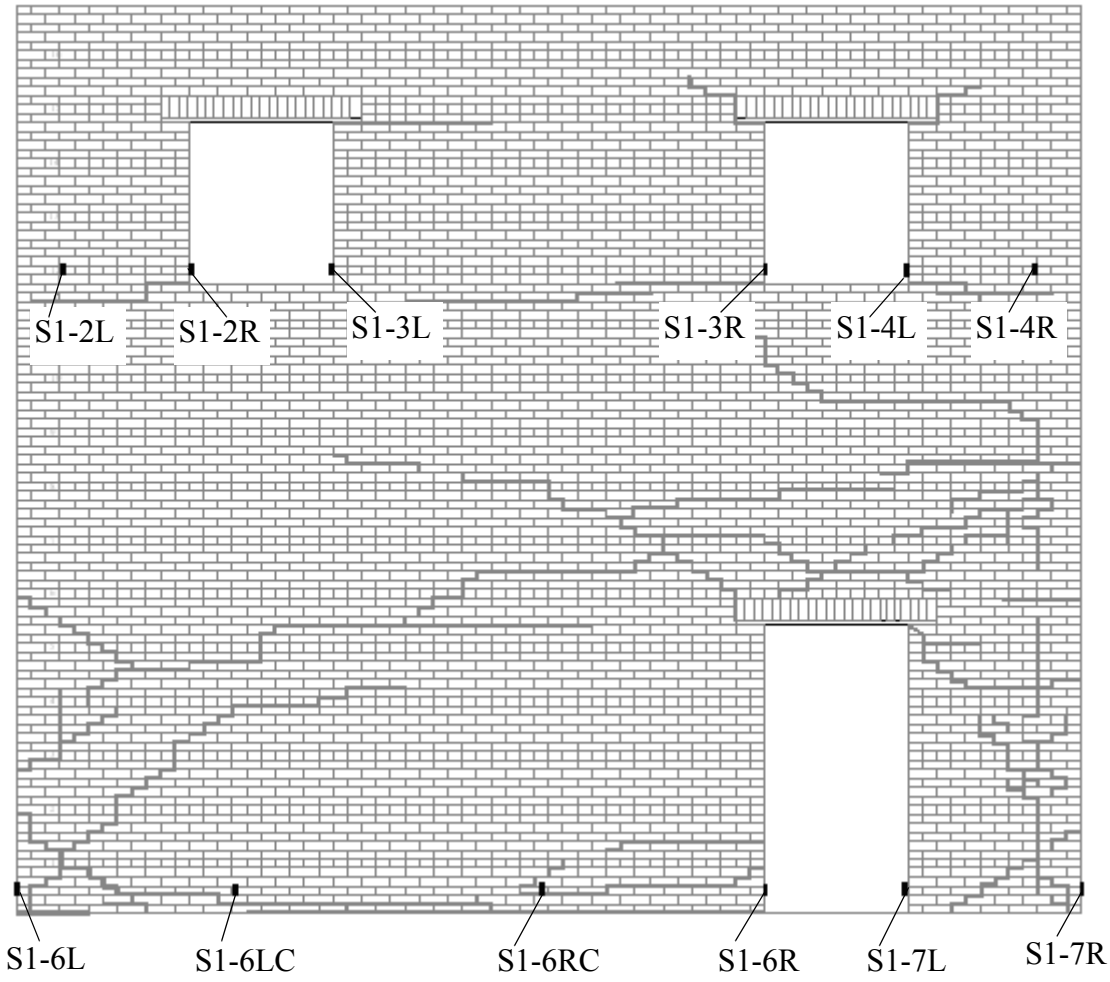

Figure A.29 Elevation of Wall 1 illustrating the location of strain gages.

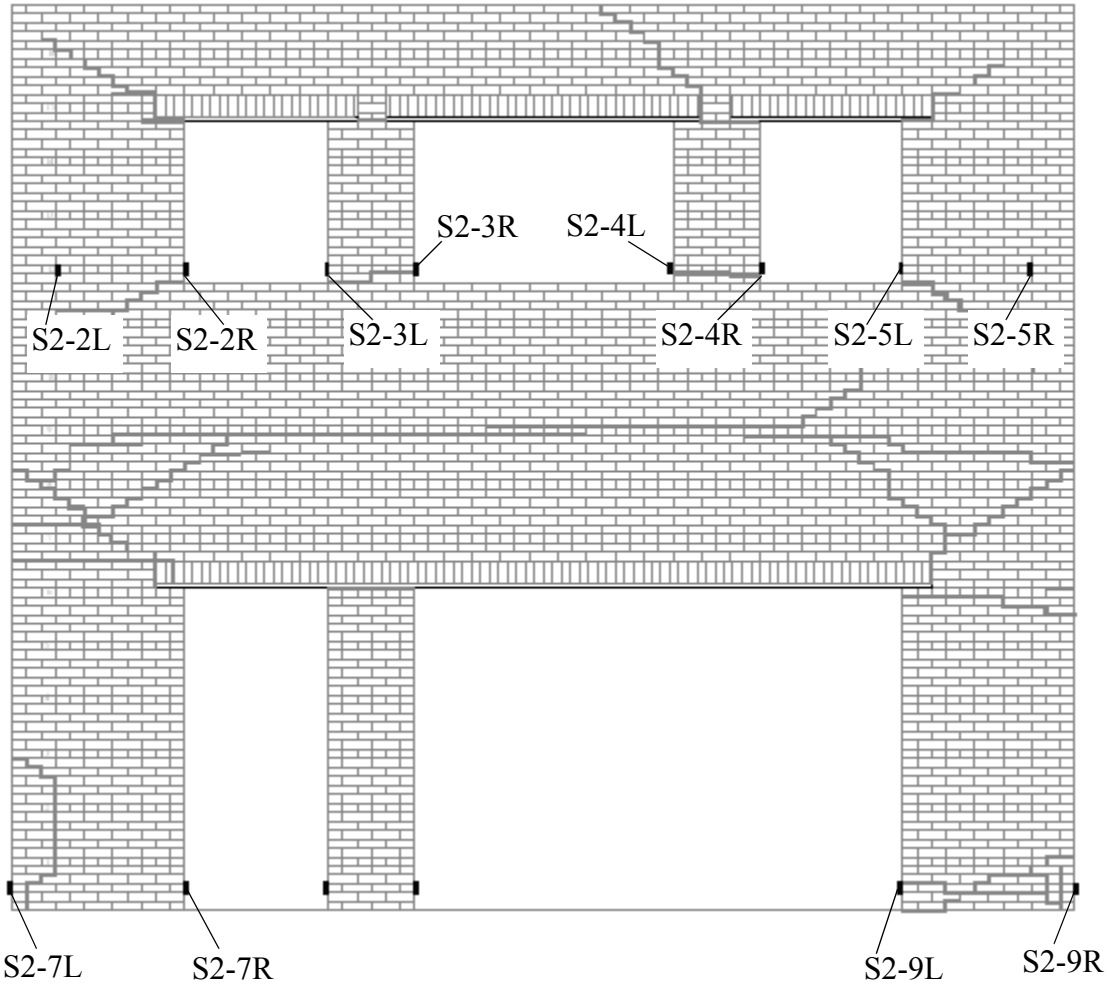

Figure A.30 Elevation of Wall 2 illustrating the location of strain gages.

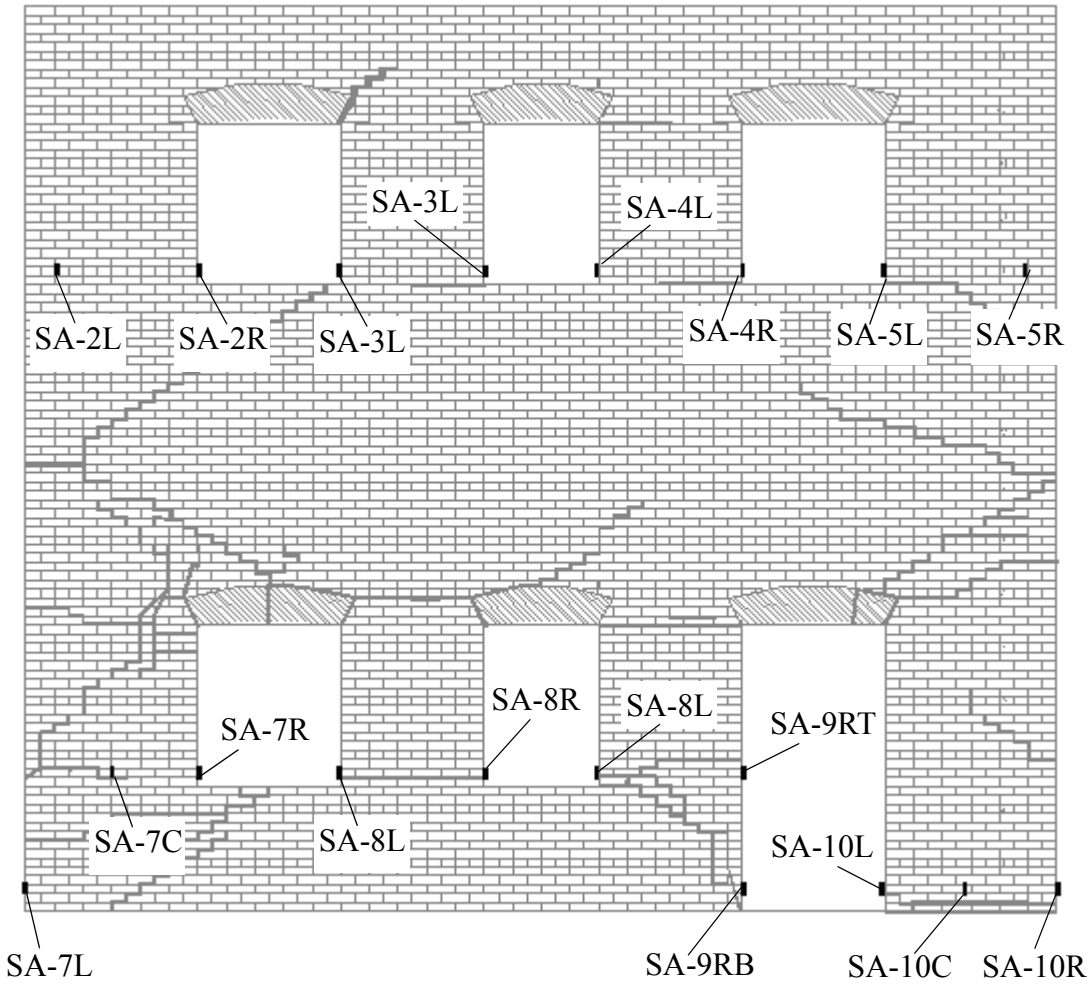

Figure A.31 Elevation of Wall A illustrating the location of strain gages.

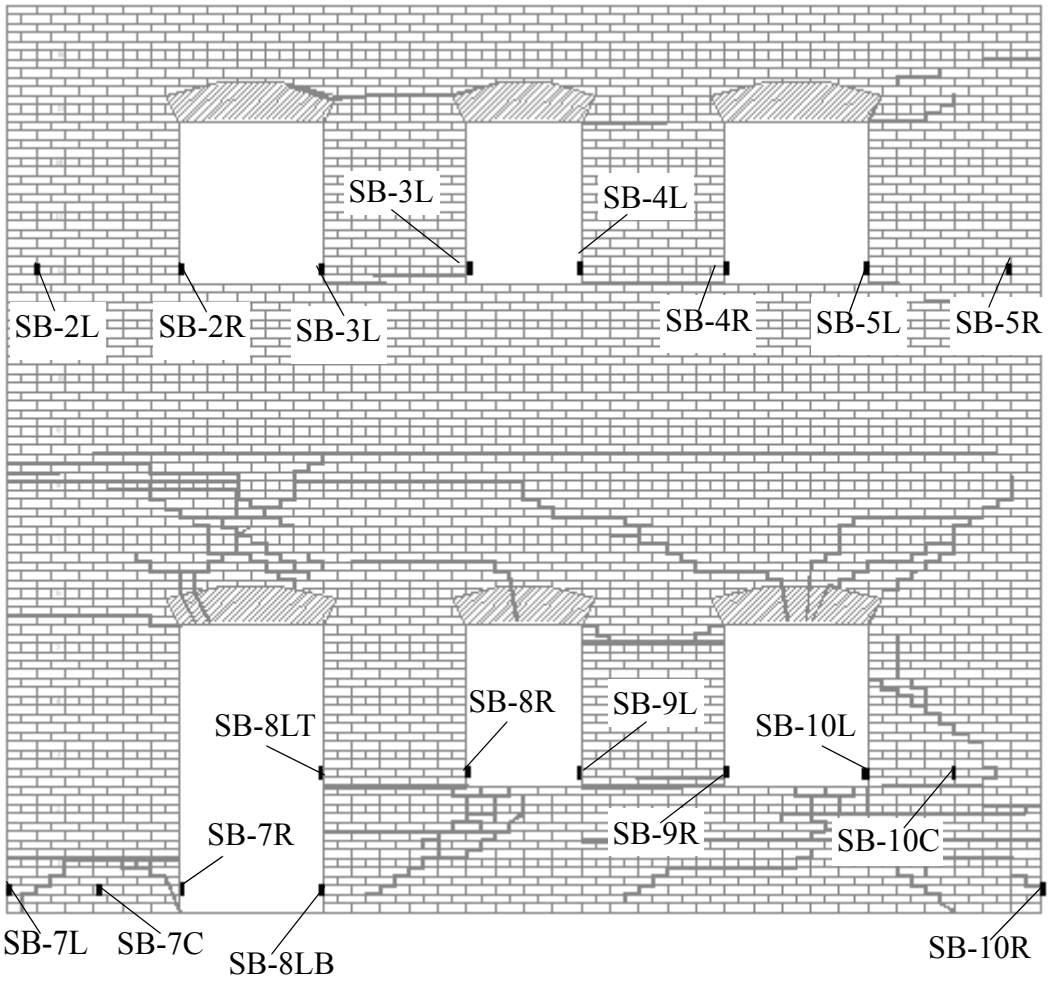

Figure A.32 Elevation of Wall B illustrating the location of strain gages.

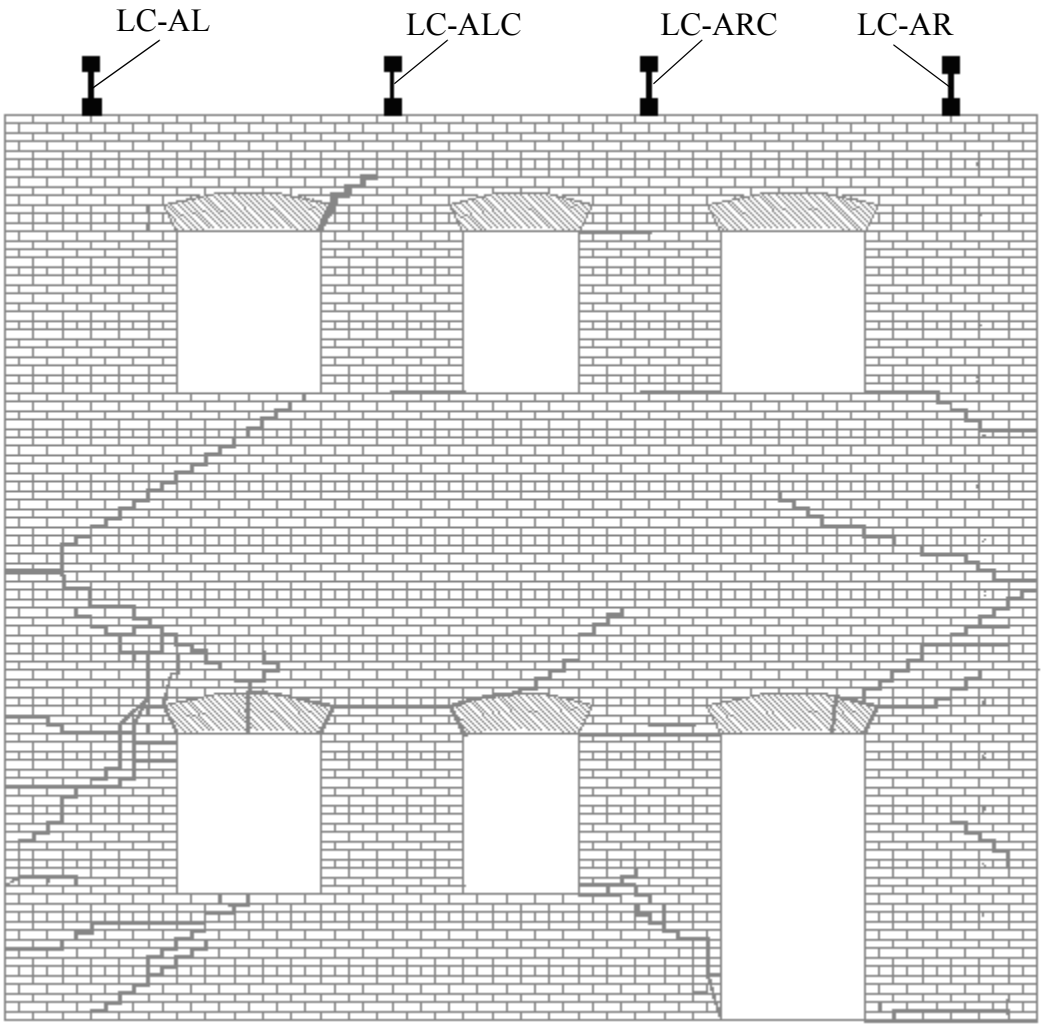

Figure A.33 Elevation of Wall A illustrating the load cells on each post-tensioning tendon

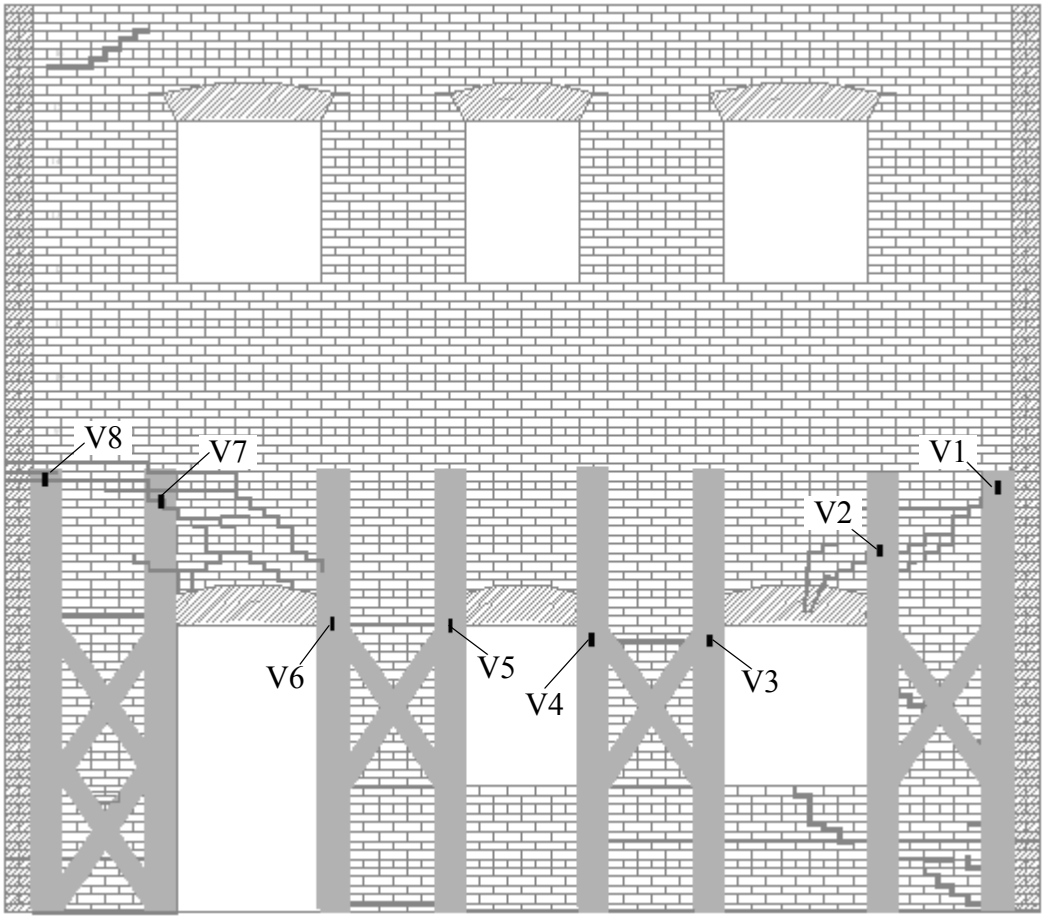

Figure A.34 Elevation of Wall B illustrating the location of strain gages attached to the FRP overlays.

APPENDIX B

DATA REDUCTION AND MANIPULATION

This appendix contains details of the procedures used to reduce and manipulate test data in order to generate plots.

B.1 Data Reduction

Due to the large amount of data recorded during each cycle, the data files were reduced in order to facilitate plotting. This reduction was accomplished by first plotting the entire data set to identify benchmarks (BM), which were data points retained in the reduced data set. Benchmarks were chosen to ensure peak point data as well as all important behavior characteristics such as a rapid drop in load were preserved. Note that peak points were chosen to retain displacement peak points, and as a result small errors may be observed for force peak points. However, all strengths reported were taken directly from the unreduced data files and hence are not subject to this error. The data reduction was achieved by dividing the data between benchmarks into *n* number of data sets. These data sets were then averaged and a single data point was returned for each set. Figure B.1 shows a schematic illustrating this procedure.

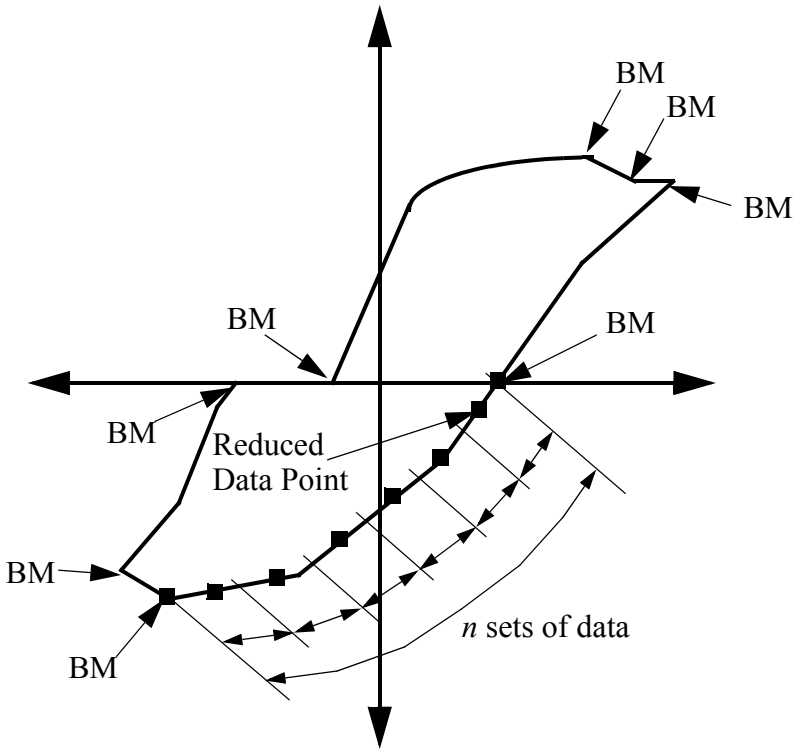

Figure B.1. Schematic illustrating the procedure used to reduce the test data.

B.2 Data Manipulation

B.2.1 Force-Displacement Response

To obtain force-displacement plots for each story of the in-plane walls, the relative displacement was calculated by subtracting the measured displacement at the base of the story with the measured displacement at the top of the story. Note that this procedure does not distinguish between lateral shear displacement and lateral displacement due to a rotation of the entire wall. For example, global rocking displacement of a wall will result in a relative displacement of the second story. As a result, this displacement should not be viewed strictly as an interstory shear displacement. Figure B.2 shows a schematic illustrating the location of lateral force and displacement transducers for each in-plane wall. Table B.1 summarizes the procedure used to generate the force-displacement plots.

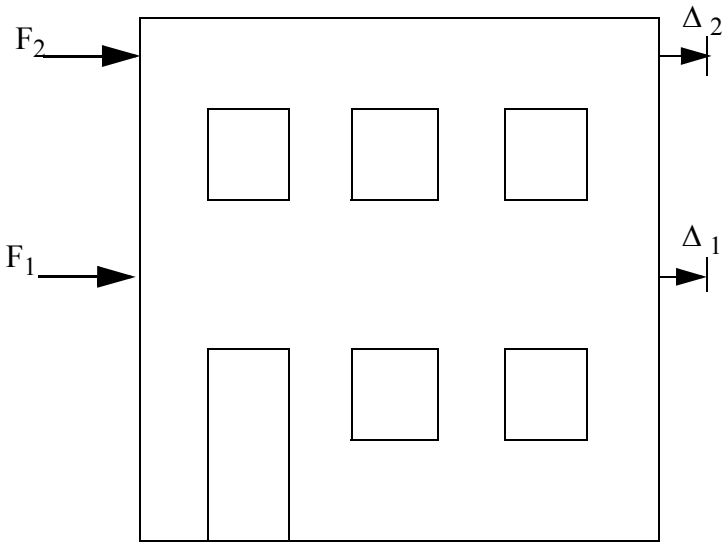

Figure B.2. Location of lateral force and displacement transducers for each in-plane wall.

Table B.1. Procedure used to generate force-displacement for each in-plane wall.

Story	Force vs. Displacement
First Story	(F_1+F_2) vs. Δ_1
Second Story	F_2 vs. $(\Delta_2-\Delta_1)$
Base Shear - Roof Displacement	(F_1+F_2) vs. Δ_2

B.2.2 Rotation

To calculate the rotational displacement of certain portions of the test structure, the relative displacement recorded from displacement transducers were divided by the distance between the transducers. Figure B.3 and Eqn B.1 illustrate this procedure.

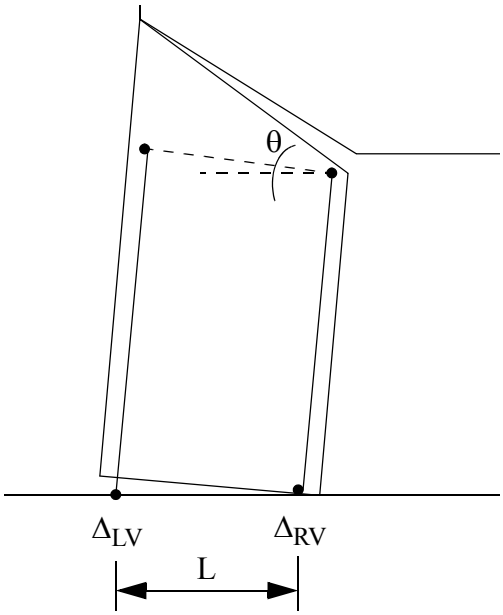

Figure B.3. Schematic of a deformed pier illustrating the location of vertical displacement transducers.

$$\theta[\text{rad}] = \frac{\Delta_{LV} - \Delta_{RV}}{L} \tag{B.1}$$

B.2.3 Energy Dissipation

To determine the energy dissipation of each story, the force-displacement responses generated by the procedure outlined in Section B.2.1 were integrated numerically. Eqn B.2 and Figure B.4 give the specific procedure used to determined the energy dissipated. Note that due to the procedure used to calculate the interstory displacement, the calculated energy dissipation for the second story may be negative. This error occurs in cases where the second story relative displacement is a combination of shear displacement (caused by the applied load at the roof) and global rocking (caused by overturning moment resulting from applied loads at both the roof and second floor).

$$\text{Energy} = \sum_{i=1}^{n} \left(\frac{(F_{i+1} + F_i)}{2} \right) (\Delta_{i+1} - \Delta_i) \qquad \text{(B.2)}$$

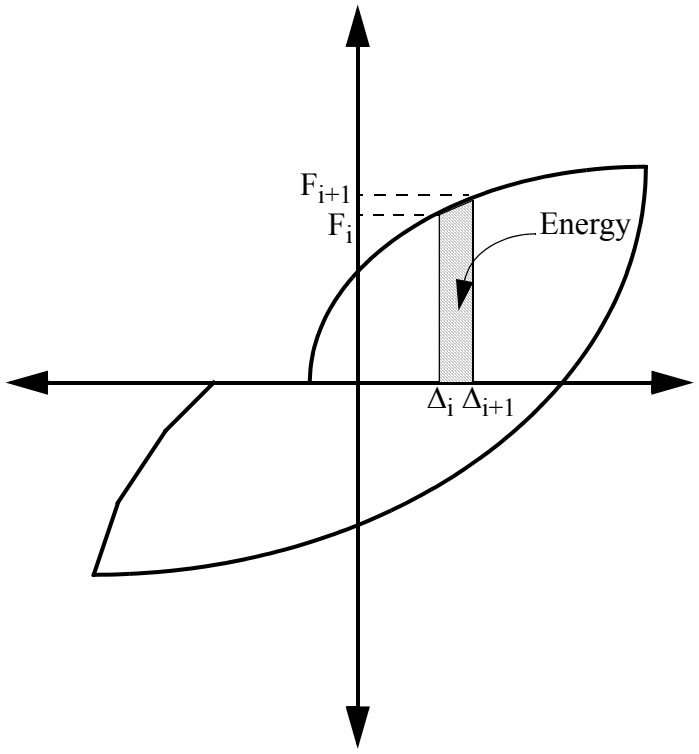

Figure B.4. Schematic illustrating the procedure used to calculate the energy dissipation of each story of the in-plane walls.

B.2.4 Normalized Energy Dissipation

For comparison purposes, the energy dissipation of each story (calculated as outlined in Section B.2.3) was normalized. This was done by dividing the calculated energy dissipation by the area of a rectangle encompassing the entire force-displacement plot. Figure B.5 illustrates this procedure.

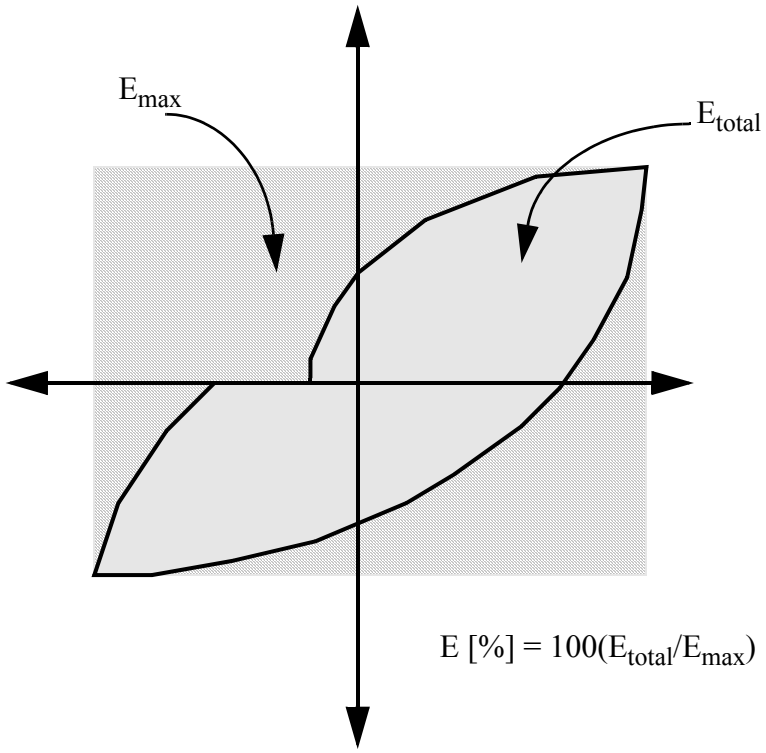

Figure B.5. Schematic illustrating the procedure used to normalize the energy dissipation of each story of the in-plane walls.

B.2.5 Secant Stiffness

The stiffness of each story of the in-plane walls was taken as the slope of a line from the peak displacement point (both positive and negative) and the displacement corresponding to no lateral load (i.e. the point at which the plot crosses the x-axis). This procedure is illustrated by Figure B.6.

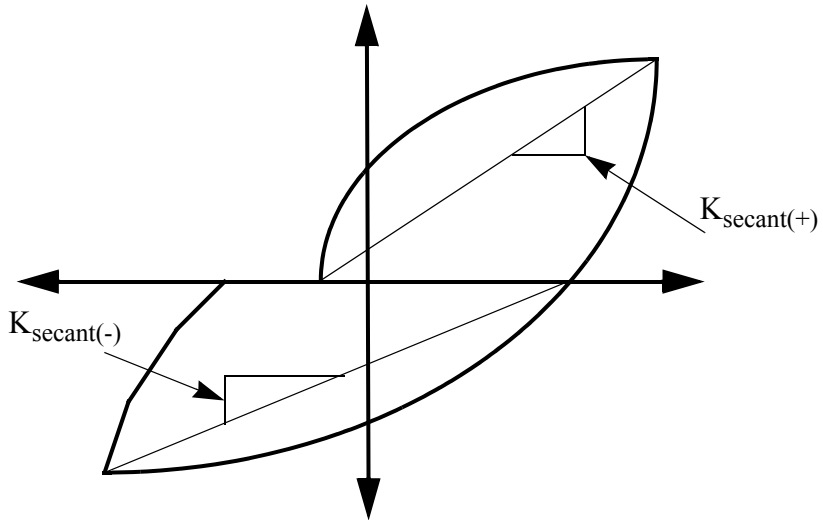

Figure B.6. Schematic showing the definition of secant stiffness.

B.2.6 Residual Displacement

The residual displacement of each story was taken as the permanent displacement resulting from half of a loading cycle (i.e. zero load to peak load to zero load). For comparison purposes the calculated residual displacement was normalized. This was done by dividing the calculated residual displacement by the maximum lateral displacement. A schematic that illustrates this procedure is given in Figure B.7.

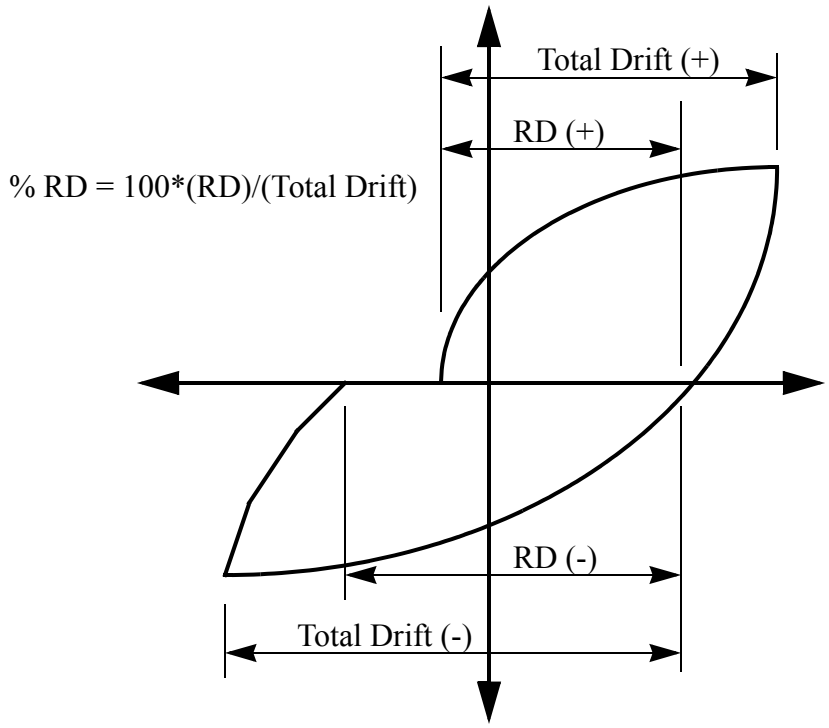

Figure B.7. Schematic illustrating the process used to determine the residual displacement of the first floor of Wall 1 in terms of a percentage of story drift

APPENDIX C

EXPERIMENTAL RESULTS OF WALL 1

C.1 Introduction

The behavior of Wall B following the application of the Clark Schwebel Tech-Fab unidirectional glass grid is discussed in this appendix. Further details on the retrofit, test setup, instrumentation, and loading scheme can be found in Chapter 3. A summary of the displacements imposed on Wall 1 are shown in Table C.1 along with the test run and cycle designation. As apparent from the table, Wall 1 was subjected to at least two cycles at each displacement level, which allows degradation and damage accumulation to be assessed. For certain comparisons it is necessary to limit the number of cycles considered. In these cases the cycles in italics are used since these cycles were the most complete in terms of instrumentation and target displacements.

Table C.1 Summary of displacements imposed on Wall 1

Test Run	Cycle	Target Roof Displacement (in)	Target Second Floor Displacement (in)
11	*a*,b	+/- 0.02	+/- 0.012
12	*a*,b,c	+/- 0.04	+/- 0.024
13	*a*,b	+/- 0.06	+/- 0.036
14	a,*b*,c,e	+/- 0.1	+/- 0.06
15	*a*,b	+/- 0.15	0.12, - 0.11
16	*a*,b	+/- 0.25	0.212, - 0.225
17	a,b,*c*	+/- 0.375	0.33, -0.356
18	*a*,b	+/- 0.5	0.47, -0.475
19	*a*,b	+/- 0.75	0.705, -0.713

The appendix begins by discussing the general force-displacement behavior of Wall 1 for both the first and second stories. This behavior is quantified for each Test Run in terms of secant stiffness, secant mode shape, energy dissipation and residual displacement. Next the damage progression and wall behavior are discussed including a discussion of the reinforcement behavior and observed damage. For this task, the behavior of the wall was divided into three sections: Group 1 cycles (Test Run 11 through Test Run 14), Group 2 cycles (Test Run 15 through Test Run 17) and Group 3 cycles (Test Run 18 through Test Run 19). Finally, the appendix concludes with a brief summary of the behavior of Wall 1.

C.2 Force-Displacement Response

The lateral displacement of Wall 1 was measured through LVDTs referenced to the structure at the second floor and roof levels (see Appendix A). Due to the importance of these measurements, linear potentiometers were also employed for redundancy. During Test Runs 18 and 19 the stroke of the second floor LVDT was exhausted and thus the readings of the potentiometer were used. Figures C.1 through C.3 show plots of roof displacement versus base shear for the Test Runs 11 through 14, Test Runs 11 through 17, and all of the cycles conducted on Wall 1, respectively.

From Figures C.1 and C.2 it is apparent that the response of Wall 1 was stable through Test Run 15. During most of these test runs negligible degradation was observed during the redundant cycles and the peak resistance of the wall increased with increasing displacement. The exception to this was degradation in peak resistance measured during Cycle 13b (approximately 10%). In contrast, during Test Runs 16 through 17 Wall 1

displayed significant degradation during the redundant cycles in term of peak resistance (see Figure C.3). Furthermore, the peak resistance during these cycles decreased with increasing lateral displacement. This decrease in peak resistance was likely caused by damage to the base bed-joint that resulted from extensive sliding deformation. This is discussed in more detail in Section C.3.

In addition, Figures C.1 through C.3 show that the energy dissipated by Wall 1 increased with wall displacement throughout loading. This suggests that the amount of bed-joint sliding deformation increased with increasing roof displacement.

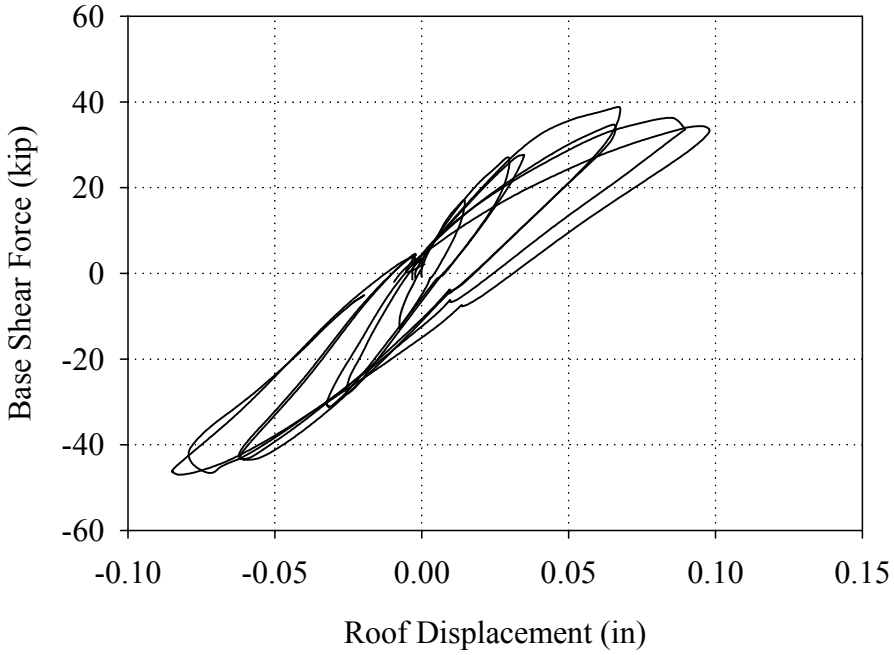

Figure C.1 Base shear versus roof displacement response of Wall 1 recorded during Test Runs 11 through 14.

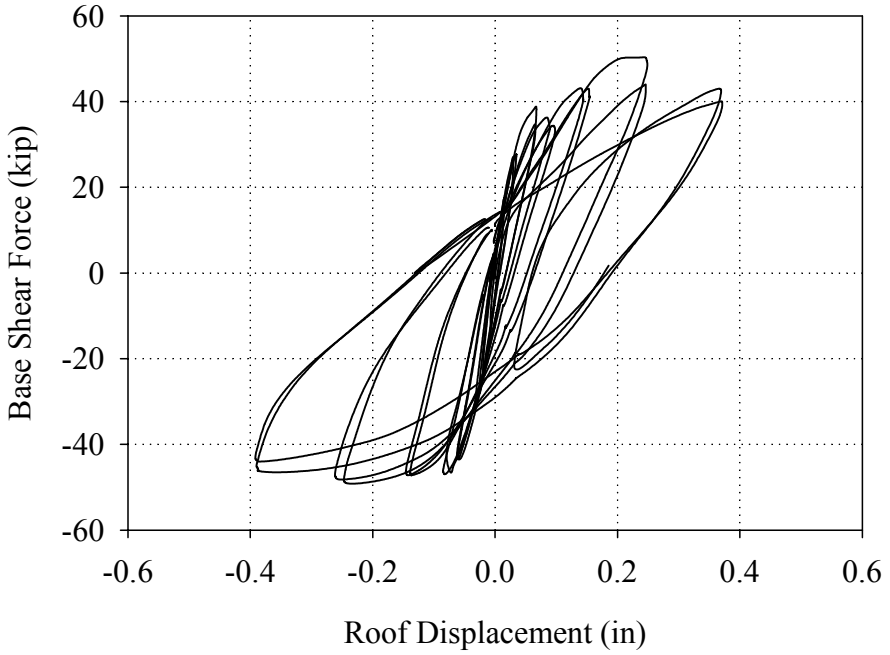

Figure C.2 Base shear versus roof displacement response of Wall 1 recorded during Test Runs 11 through 17.

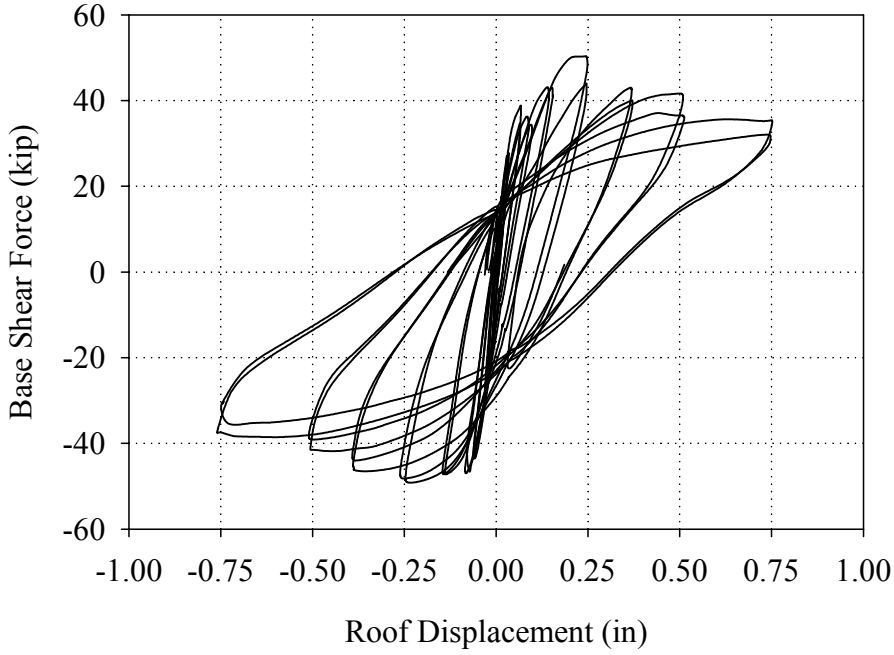

Figure C.3 Base shear versus roof displacement response of Wall 1 recorded during Test Runs 11 through 19.

The force-displacement response of the first story of Wall 1 is shown in Figures C.4 through C.6 for Test Runs 11 through 14, Test Runs 11 through17, and all of the cycles conducted on Wall 1, respectively. Figures C.7 through C.9 show the force-displacement response of the second story of Wall 1 for Test Runs 11 through 14, Test Runs 11 through17, and all of the cycles conducted on Wall 1, respectively.

From these plots it is apparent that the energy dissipation displayed in Figures C.2 and C.3 was due to the behavior of the first floor. In general, the discussion provided in regards to the base shear versus roof displacement response applies directly to the first story. In addition, Figures C.7 through C.9 show that the behavior of the second story of Wall 1 was essentially nonlinear-elastic throughout all of the cycles. This behavior is attributed mainly to the global rocking of the entire wall. This phenomenon is discussed in more detail in Section C.3.

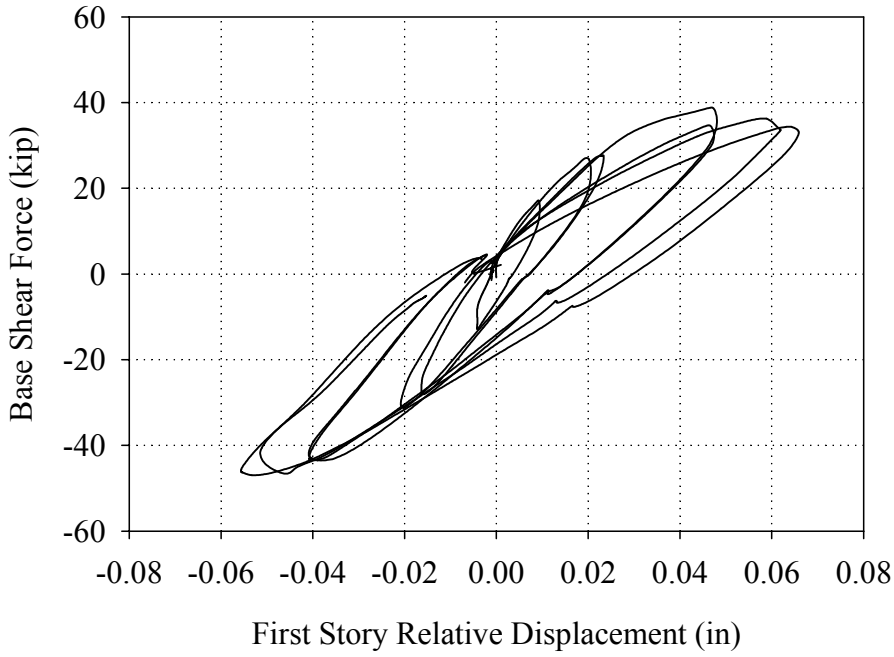

Figure C.4 Force-displacement response of the first story of Wall 1 recorded during Test Runs 11 through 14.

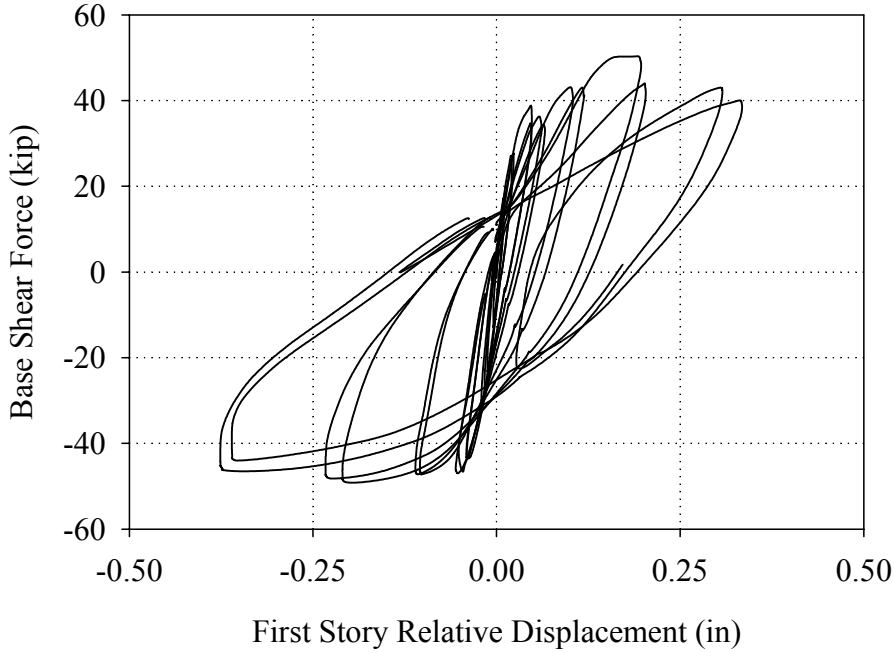

Figure C.5 Force-displacement response of the first story of Wall 1 recorded during Test Runs 11 through 17.

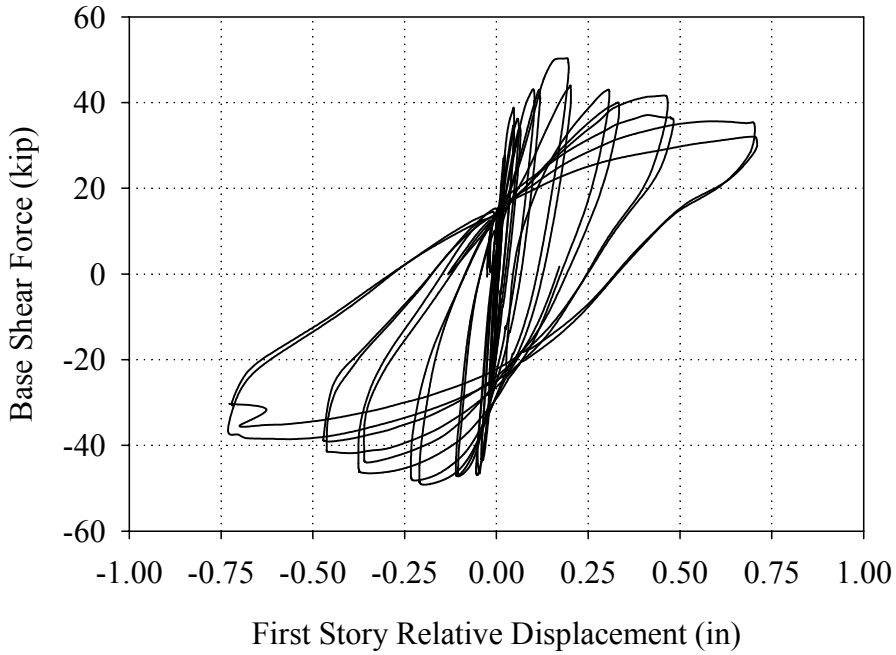

Figure C.6 Force-displacement response of the first story of Wall 1 recorded during Test Runs 11 through 19.

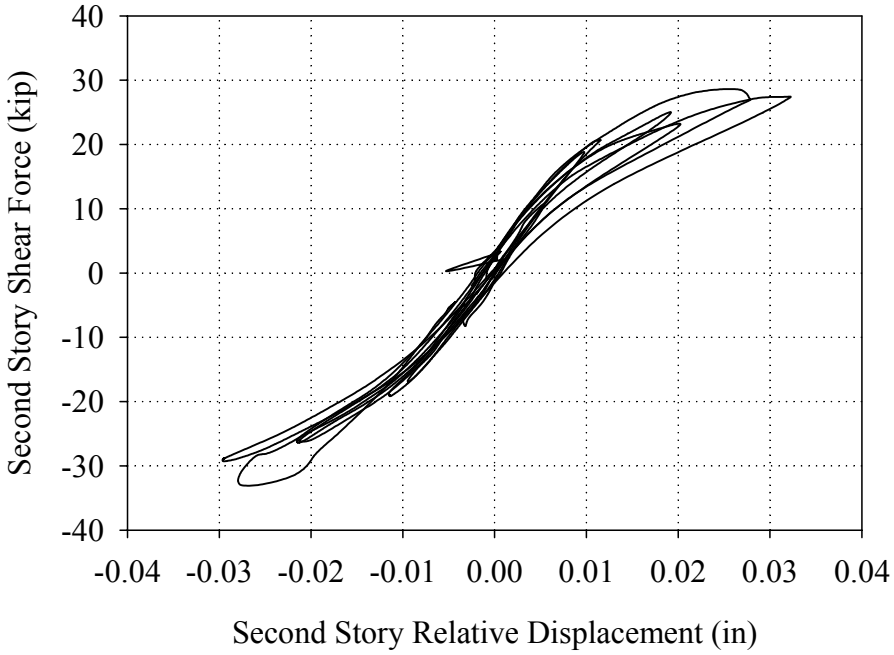

Figure C.7 Force-displacement response of the second story of Wall 1 recorded during Test Runs 11 through 14.

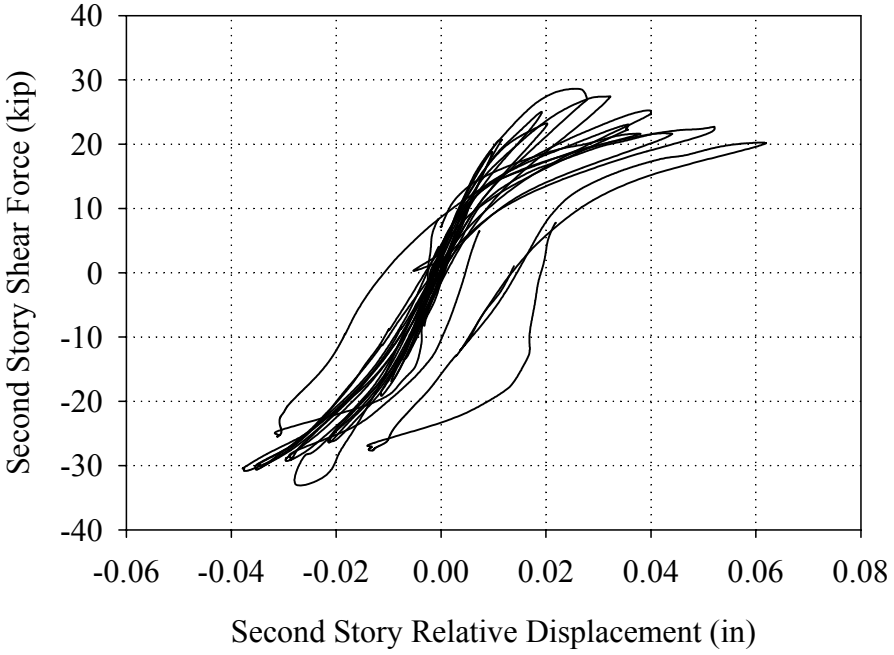

Figure C.8 Force-displacement response of the second story of Wall 1 recorded during Test Runs 11 through 17.

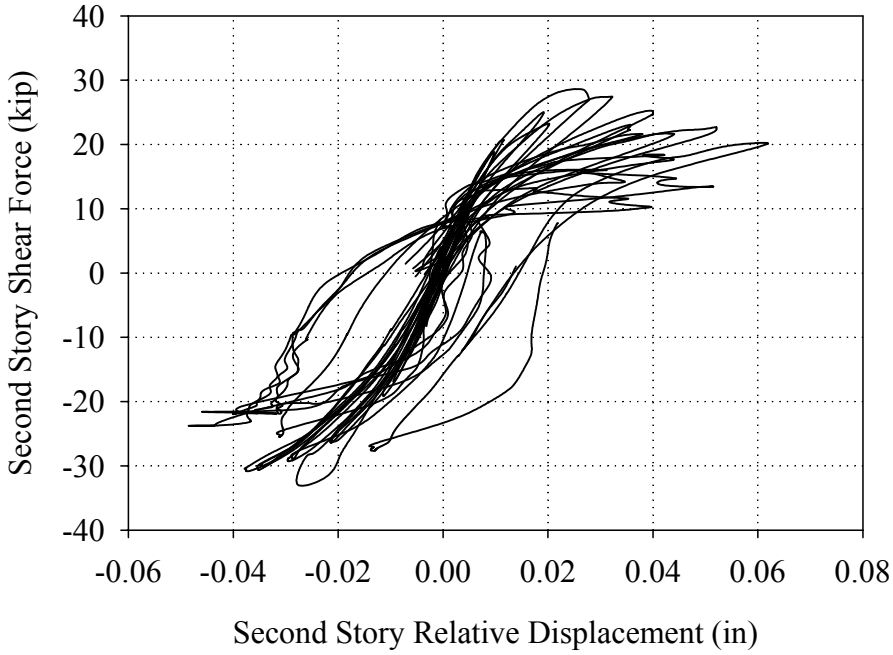

Figure C.9 Force-displacement response of the second story of Wall 1 recorded during Test Runs 11 through 19.

C.2.1 Stiffness and Mode Shapes

For each of the test runs conducted on Wall 1, the secant stiffness' were determined for both the first and second stories. The secant stiffness of a structure represents an average tangent stiffness and as such can be used as an indication of damage. The stiffness' were taken as the slope of a line connecting the peak displacement point (both positive and negative) and the point at which the plot crosses x-axis. This procedure is discussed in detail in Appendix B. Table C.2 shows the calculated secant stiffness' for the first and second stories of Wall 1 in the positive and negative direction during each test run.

Table C.2 Secant stiffness of Wall 1 for each Test Run

Test Run	Story	Positive Secant Stiffness (kip/in)	Negative Secant Stiffness (kip/in)
11	First	1611	1638
	Second	2091	2127
12	First	1214	1166
	Second	1658	1732
13	First	793	817
	Second	1087	704
14	First	434	554
	Second	779	905
15	First	368	284
	Second	592	862
16	First	220	149
	Second	332	829
17	First	88	79
	Second	381	1278
18	First	67	58
	Second	234	749
19	First	48	34
	Second	205	670

From this table it is apparent that the secant stiffness of both stories decrease during each cycle. This is expected since the secant stiffness can also be used as a measure of nonlinear response. Based on the relative decrease between the first and second stories, these stiffness' suggest that the majority of the damage focused on the first story of Wall 1. The apparent decreased in secant stiffness of the second floor of Wall in the positive direction is attributed to the observed global rocking behavior (see Section C.3). That is,

due to the simple way in which the story drift is calculated (see Appendix B), the global rotation of Wall 1 leads to an apparent relative displacement of the second story, which causes a decrease in the calculated secant stiffness.

To gain more insight into the seismic behavior of Wall 1, the secant mode shapes were determined for each test run and are listed in Table C.3 (see Appendix B for a detailed description of this calculation and associated assumptions). Figure C.10 shows the calculated secant mode shapes normalized to roof displacement for all of the cycles conducted on Wall 1.

Table C.3 Fundamental secant mode shapes of Wall 1 normalized to 1.0.

Test Run	Positive Fundamental Secant Mode Shape	Negative Fundamental Secant Mode Shape
11	$\{1.0, 0.77\}^T$	$\{1.0, 0.77\}^T$
12	$\{1.0, 0.78\}^T$	$\{1.0, 0.80^T$
13	$\{1.0, 0.78\}^T$	$\{1.0, 0.68\}^T$
14	$\{1.0, 0.83\}^T$	$\{1.0, 0.82\}^T$
15	$\{1.0, 0.81\}^T$	$\{1.0, 0.90\}^T$
16	$\{1.0, 0.80\}^T$	$\{1.0, 0.94\}^T$
17	$\{1.0, 0.93\}^T$	$\{1.0, 0.98\}^T$
18	$\{1.0, 0.91\}^T$	$\{1.0,0.98\}^T$
19	$\{1.0, 0.93\}^T$	$\{1.0, 0.98\}^T$

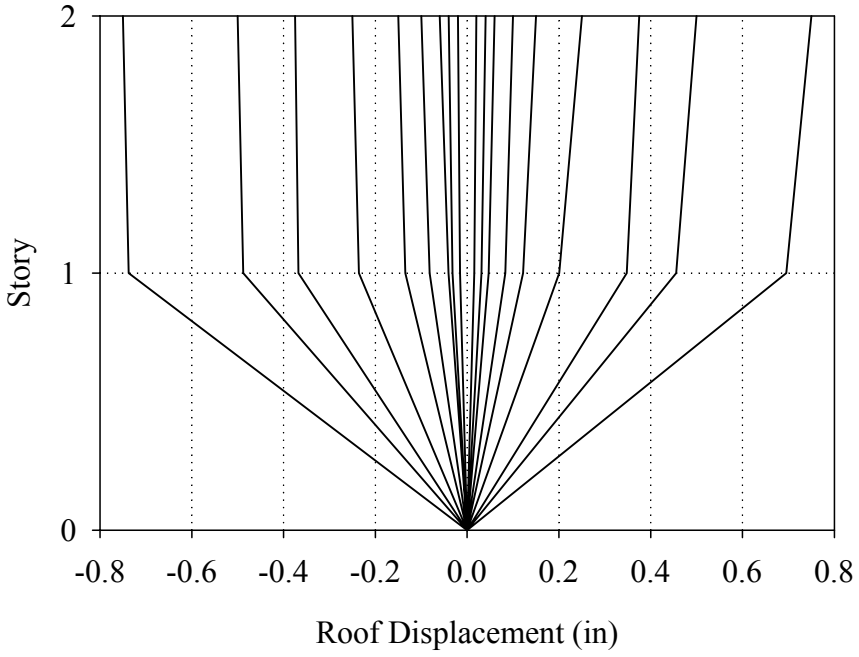

Figure C.10 Fundamental secant mode shapes of Wall 1 normalized to target roof displacement.

As apparent from this table and figure, the initial fundamental mode shapes in the positive direction (up to around 0.25 in roof displacement, Test Run 16) corresponded to approximately 75% of the roof displacement applied at the second floor. As the roof displacement increased beyond this point, the fundamental mode shapes in the positive direction suggest that a soft story was forming (see Table C.3). This change in mode shape reflects a decrease in global rocking displacement and an increase in sliding displacement at the base of the wall (see Section C.3).

In the negative direction, the calculated mode shapes follow a similar trend with one notable exception. Namely, that the formation of the soft story in the negative direction was far more gradual in nature suggesting a less abrupt change in wall behavior. This is consistent with observed behavior (see Section C.3).

C.2.2 Energy Dissipation

The energy dissipated by each floor of Wall 1 was calculated for each of the cycles conducted. This was accomplished by numerically integrating the force-displacement plots shown in Figures C.4 through C.9 (see Appendix B). For comparison purposes, the calculated values were divided by the maximum possible energy dissipated, which was defined as the area of a rectangle encompassing the force-displacement plot. Figure C.11 shows the percentage of energy dissipated by each floor versus roof displacement. In addition, Figure C.12 shows the actual energy dissipated by each floor versus roof displacement.

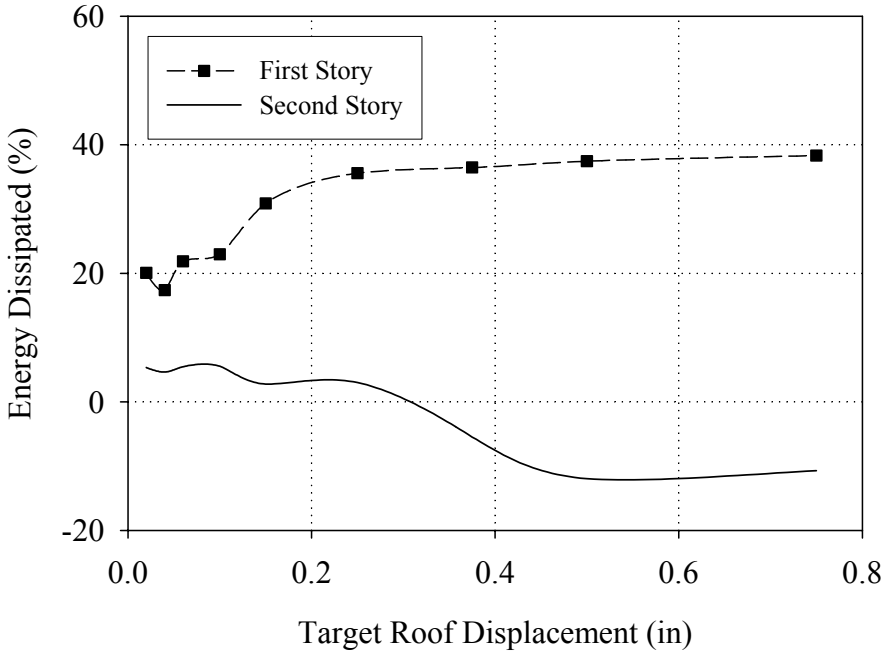

Figure C.11 Percentage of energy dissipated by each story of Wall 1 versus target roof displacement.

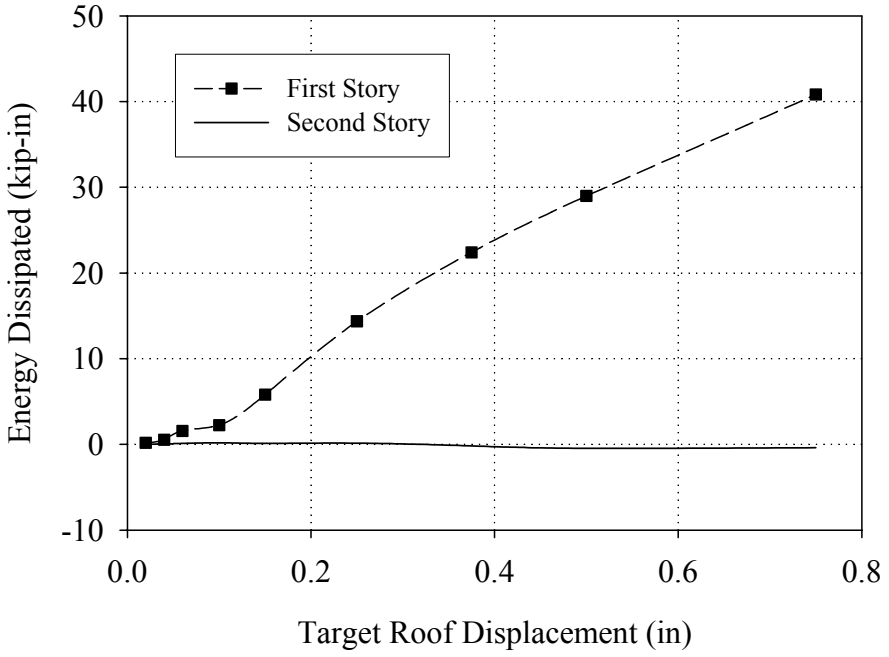

Figure C.12 Energy dissipated by each story of Wall 1 versus target roof displacement.

As apparent from Figure C.11, the percentage of energy dissipated by the first floor through Test Run 13 (i.e. approximately 0.1 in roof displacement) was relatively constant at 20%, which is consistent with rocking dominated behavior. During the following test runs, the percentage energy dissipated by the first floor increased substantially to approximately 40%. This increase suggests a change in the response of the first story from rocking to primarily sliding behavior. In addition, during these cycles the percentage of energy dissipated by the second floor became negative. This erroneous measurement is attributed to the global rotation of the entire wall as well as the relatively small displacements imposed on the second story (see Table C.1).

From Figure C.12, it is apparent that the first story of Wall 1 dissipated orders of magnitude more energy than the second story. As a result, the apparent negative percentage of energy dissipated by the second story is trivial (see Figure C.11).

C.2.3 Residual Displacement

The residual displacement of the first story of Wall 1 was calculated for each test run according to the procedure outlined in Appendix B. Due to the small displacements imposed on the second story the residual displacements measured were negligible and are not discussed. The calculated first story residual displacements are present in Table C.4 as a percentage of the story drift. In addition, Figure C.13 shows the residual displacement for the first story (as a percentage of the first story drift) versus first story drift.

Table C.4 Residual Displacement of Wall 1

Test Run	+ Residual Displacement (% of Story Drift)	- Residual Displacement (% of Story Drift)
11	36	59
12	40	45
13	36	39
14	48	44
15	53	60
16	64	62
17	65	58
18	61	58
19	56	56

From this figure and Table C.4 it is apparent that for small roof displacements (i.e. less than 0.05 in) the residual displacement of the first floor remained fairly small suggesting rocking dominated response. However, as the roof displacement increased the residual displacements increased substantially in both directions up to approximately 60%. This suggests that response of the first story change to primarily sliding deformation

during the larger cycles. This is consistent with the discussion of energy dissipation presented in Section C.2.2.

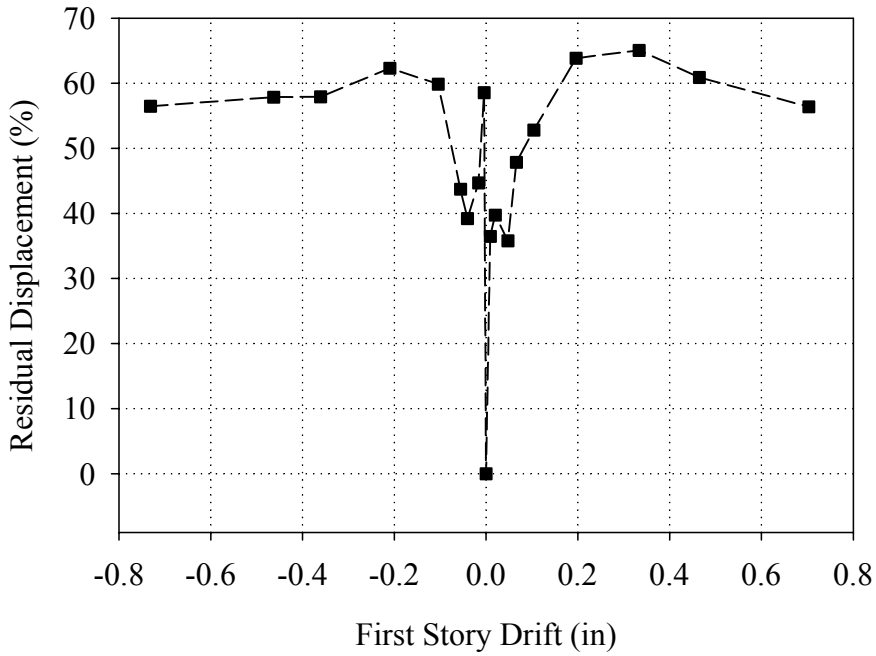

Figure C.13 Residual displacement as a percentage of story drift for the first story of Wall 1 versus story drift.

C.3 Damage Progression and Wall Behavior

The following sections describe the behavior of Wall 1 during each of the three groups of cycles defined in Section C.1. For each group of cycles the general behavior of the wall is first described in terms of crack pattern, visually observed behavior, and representative instrumentation. Next, a description of the external reinforcement behavior is presented including strain gage readings. Finally, the specific behavior of the in-plane piers are described and representative plots of the instrumentation attached to the piers are presented.

C.3.1 Group 1 Cycles (Test Run 11-Test Run 14)

C.3.1.1 Overall Wall Behavior

During the Group 1 cycles no new cracks were observed and no existing cracks appeared to open. Figures C.14 through C.16 show schematics of the crack pattern in Wall 1 and out-of-plane Walls A and B following the these cycles. The cracks shown in these figures formed during the in-plane testing of Walls 1 and 2 prior to retrofitting. For a complete discussion of the testing prior to strengthening the reader is directed to I (2003).

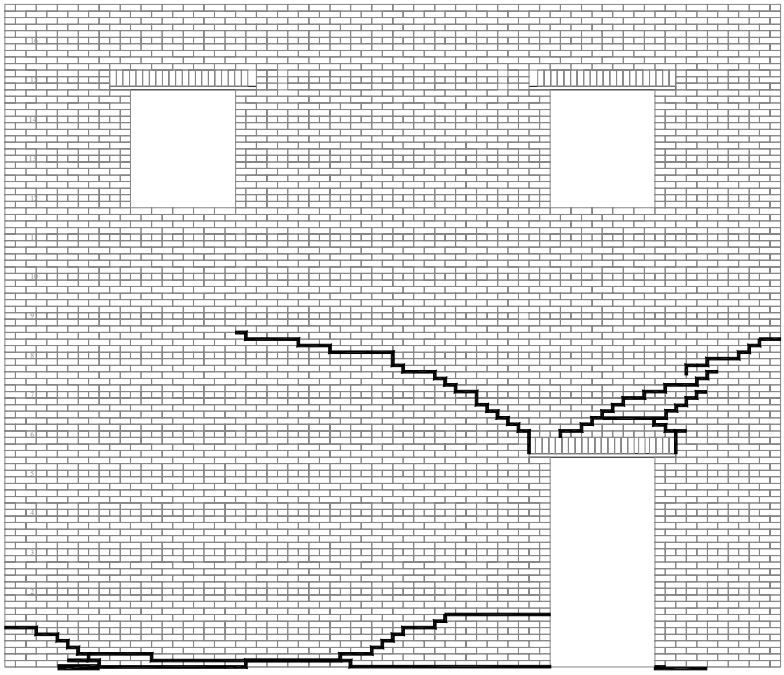

Figure C.14 Crack Pattern of Wall 1 following the Group 1 Cycles.

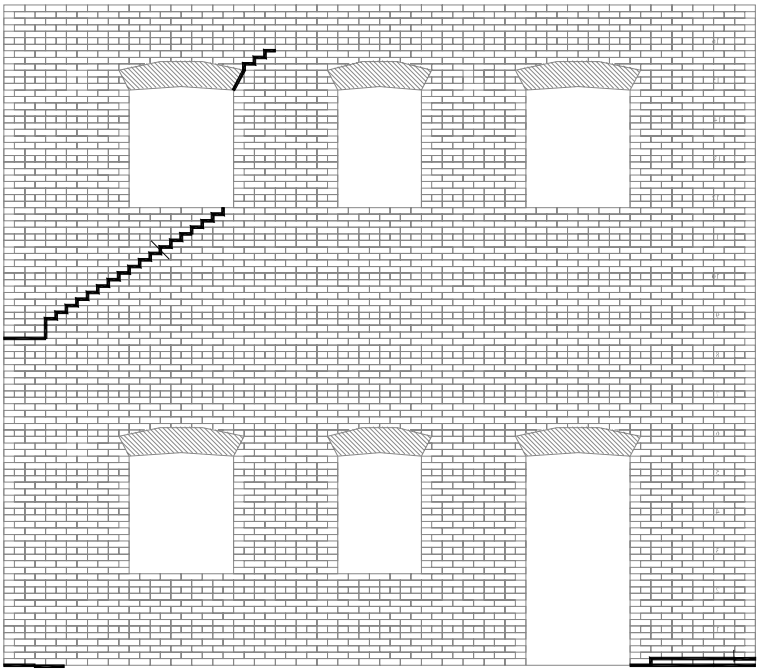

Figure C.15 Crack pattern of Wall A following the Group 1 cycles.

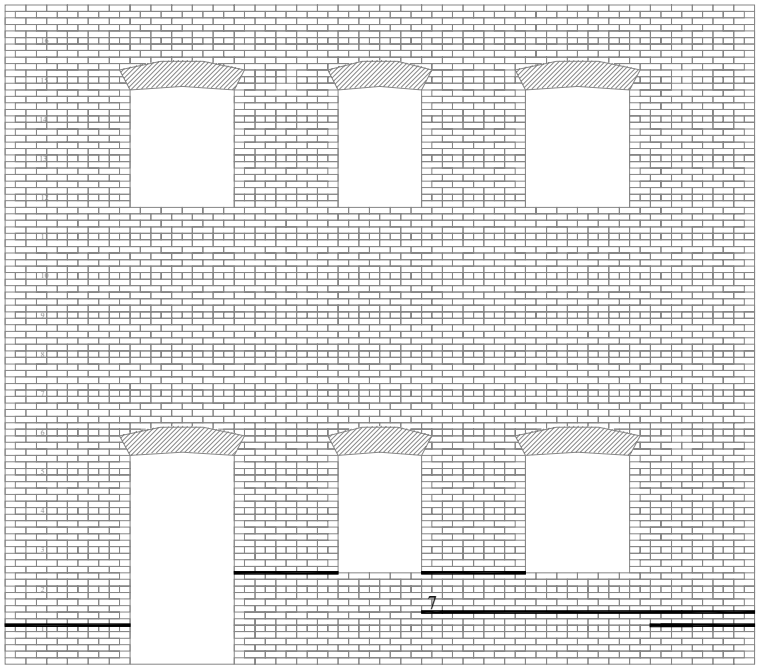

Figure C.16 Crack pattern of Wall B following the Group 1 cycles.

Figure C.17 shows a schematic illustrating the behavior of Wall 1 in the positive direction (Note that the location of the LVDT reference points are also shown). From this figure it is apparent that Wall 1 primarily behaved as a single rigid body rotating about the lower left corner of pier P1-6. Figure C.18 shows a plot of the vertical roof displacement of each side of Wall 1 versus lateral roof displacement for Cycle 14b. Since the aspect ratio of the wall is approximately 1.0, the difference between the vertical displacements shown correspond roughly to the lateral roof displacement that resulted from this observed global rocking (assuming rigid body rotation about the base). Following this logic the global rocking displacement of Wall 1 accounted for approximately 0.04 in or 40% of the roof displacement. Furthermore, Figure C.19 shows a plot of the roof rotation as well as the rotation of pier P1-6 versus base shear for Cycle 14b (see Appendix B for calculation procedure). From this figure it is apparent that during loading in the positive direction, both of these rotations were nearly identical, which represents further evidence that the majority of Wall 1 was deforming as a single rigid body.

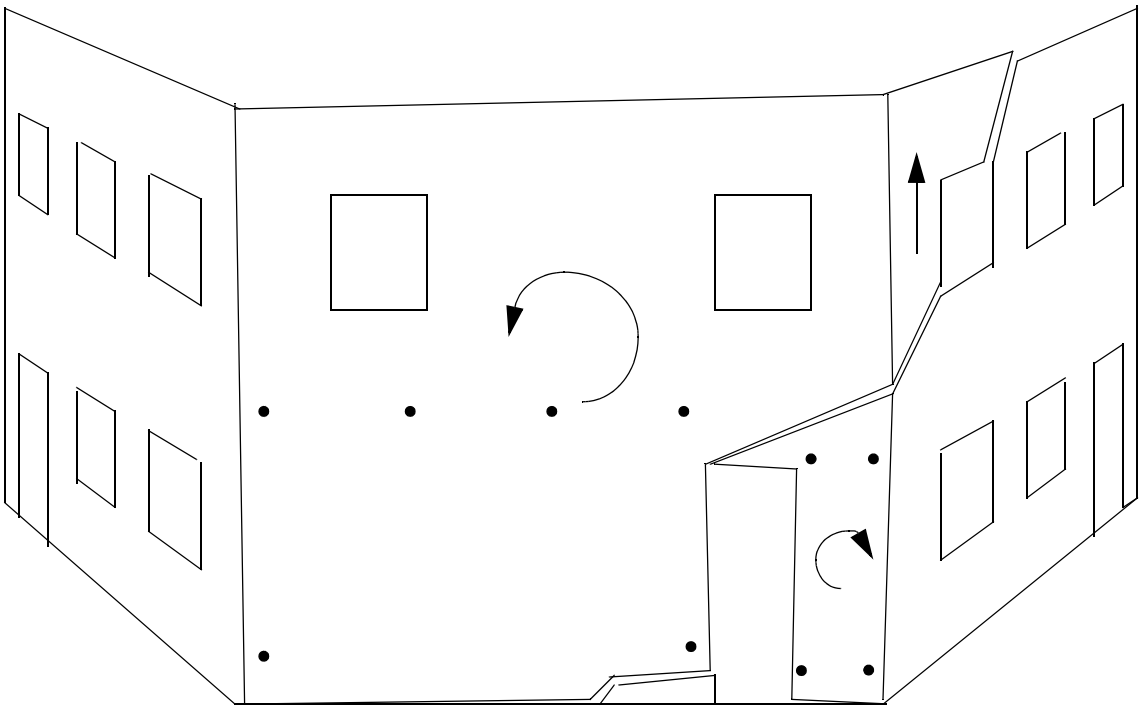

Figure C.17 Exaggerated schematic of the observed behavior of Wall 1 and out-of-plane Walls A and B in the positive loading direction during the Group 1 cycles.

In addition to this primary mechanism, the behavior of Wall 1 in the push direction provided some insight into pier interaction. As apparent from Figure C.17, the observed global rocking of Wall 1 resulted in a clockwise rotation of pier P1-7 (also see Section C.3.1.3). This apparently bizarre behavior was likely caused by a number of factors. First, the global rocking displacement resulted in a vertical displacement of the upper portion of pier P1-7. This displacement engaged vertical reinforcement strips V1 through V3 essentially lifting pier P1-7. However, the resultant of these forces did not coincide with the center of pier P1-7 (see Chapter 3), and thus resulted in a clockwise moment. In addition, the presence of the flange on the right side of pier P1-7 also resisted this uplift and added to the clockwise moment.

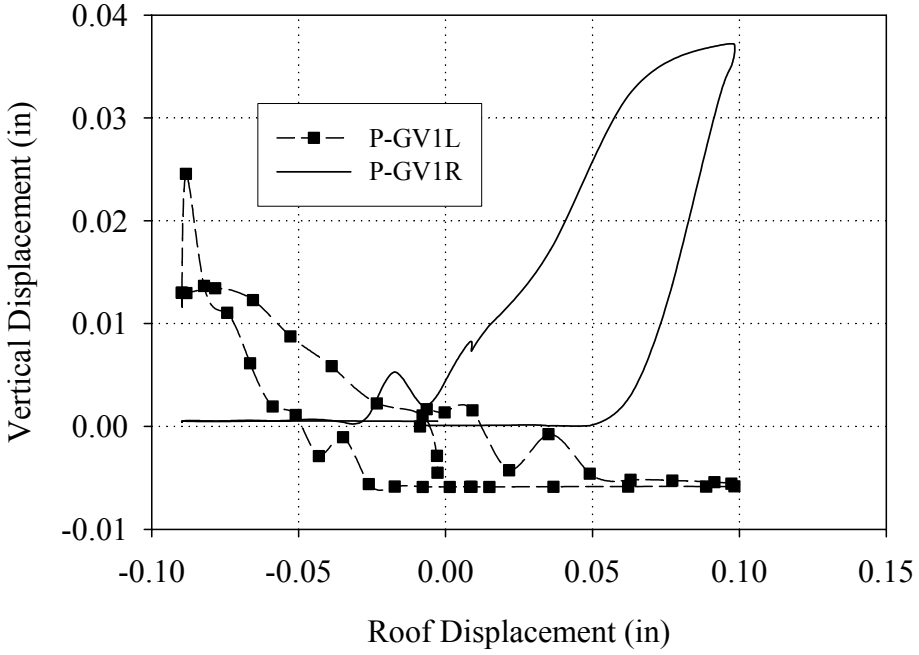

Figure C.18 Vertical displacements of both sides of Wall 1 versus roof displacement (Cycle 14b)

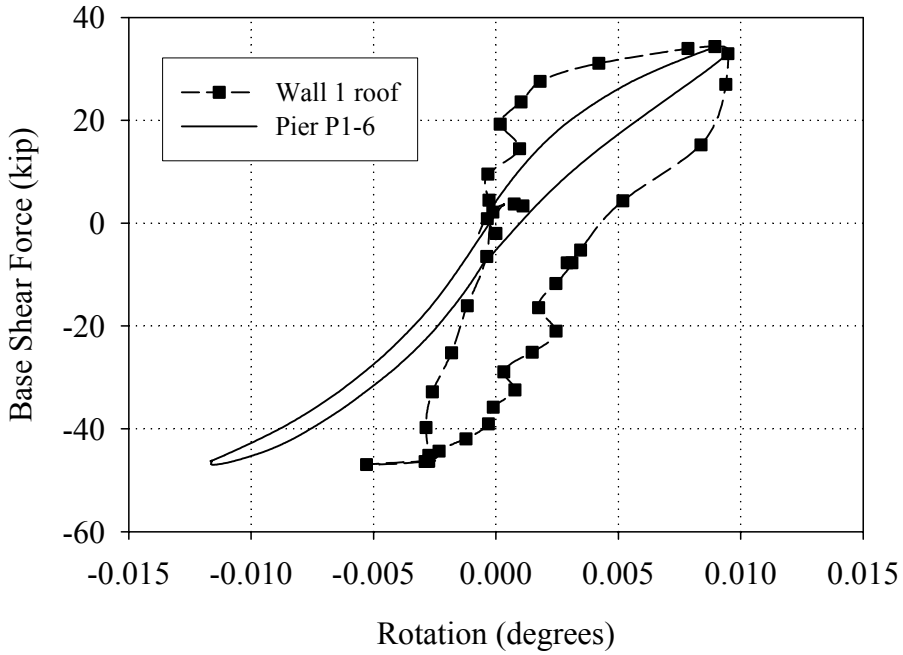

Figure C.19 Comparison between roof rotation and rotation of pier P1-6 (Cycle 14b)

In addition to the observed in-plane behavior, the global rotation of Wall 1 likely engaged the upper portion of Wall A shown in Figure C.17. While this participation was not visible due to the small displacements imposed during this level of testing, the existing crack pattern, measured response (i.e. global rocking), and the behavior observed during past cycles (Yi, 2004) all suggest that the upper corner of Wall A was likely participating in the response.

Figure C.20 shows the base strains recorded at the peak positive displacement during Cycle 14e. As apparent from this figure, the uplift of pier P1-7 was clearly captured by these gages. Furthermore, the strains recorded in out-of-plane pier PA-7 suggest that the vertical stress in this portion of the wall was decreasing, which supports the contention of flange participation. However, the small magnitude of the strains measured in pier P1-6 is inconsistent with the observed global rocking deformation and is attributed to damage induced during the testing prior to strengthening. The reader is cautioned that due to large variations in material properties, numerous cracks, and uncertainties inherent in strain gage measurements obtained from masonry, only a qualitative discussion of the strain data is appropriate.

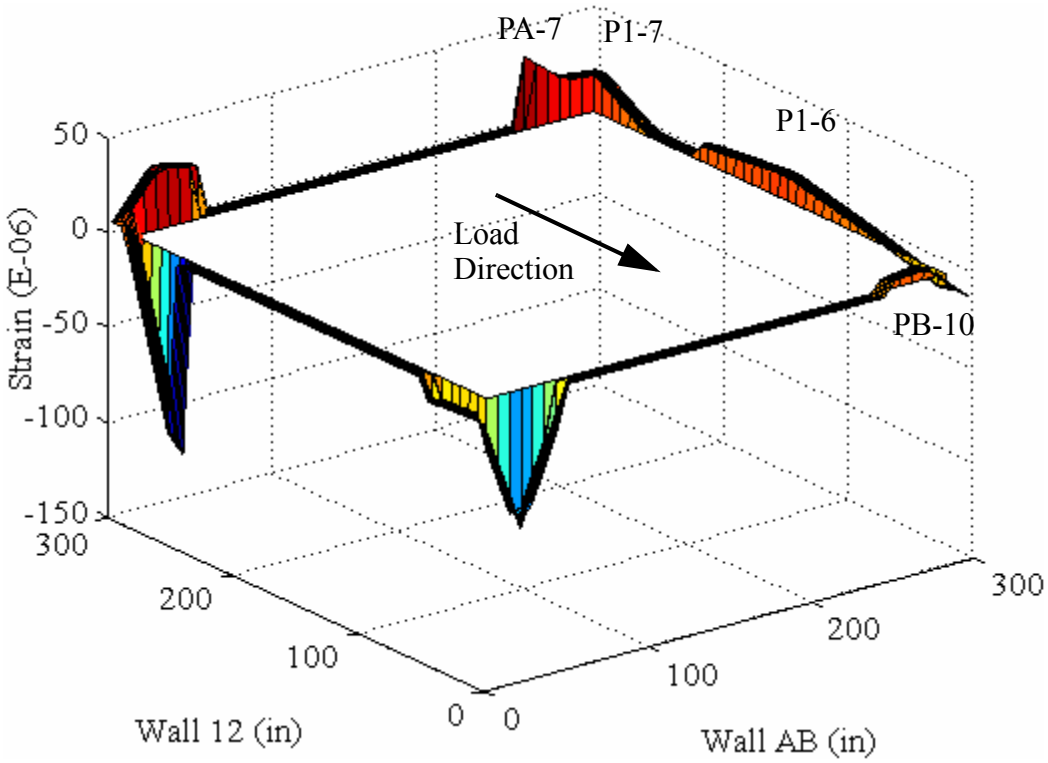

Figure C.20 Base strains recorded at peak positive displacement (Cycle 14e).

Figure C.21 shows a schematic illustrating the behavior of Wall 1 in the negative direction (note that the LVDT reference points are also shown). From this figure it is apparent that primary mode of deformation of the wall was the rocking of pier P1-6. In contrast to the behavior in the positive direction, the rocking of pier P1-6 in the negative direction was independent of the entire wall. Consider Figure C.19 which shows the rotation of pier P1-6 as well as the roof rotation of Wall 1 versus base shear. Notice that in the negative direction these plots diverge suggesting differential rotation, which is consistent with the local rocking behavior shown in Figure C.21. In addition, the local rocking of pier P1-6 resulted in a relatively large vertical displacement due to the small aspect ratio of the pier (i.e. approximately 0.4). This vertical displacement was captured by LVDTs and is shown in Figure C.18. Although the rotation suggested by this figure was

not a result of global rocking per se, this rotation did result in lateral roof displacement.

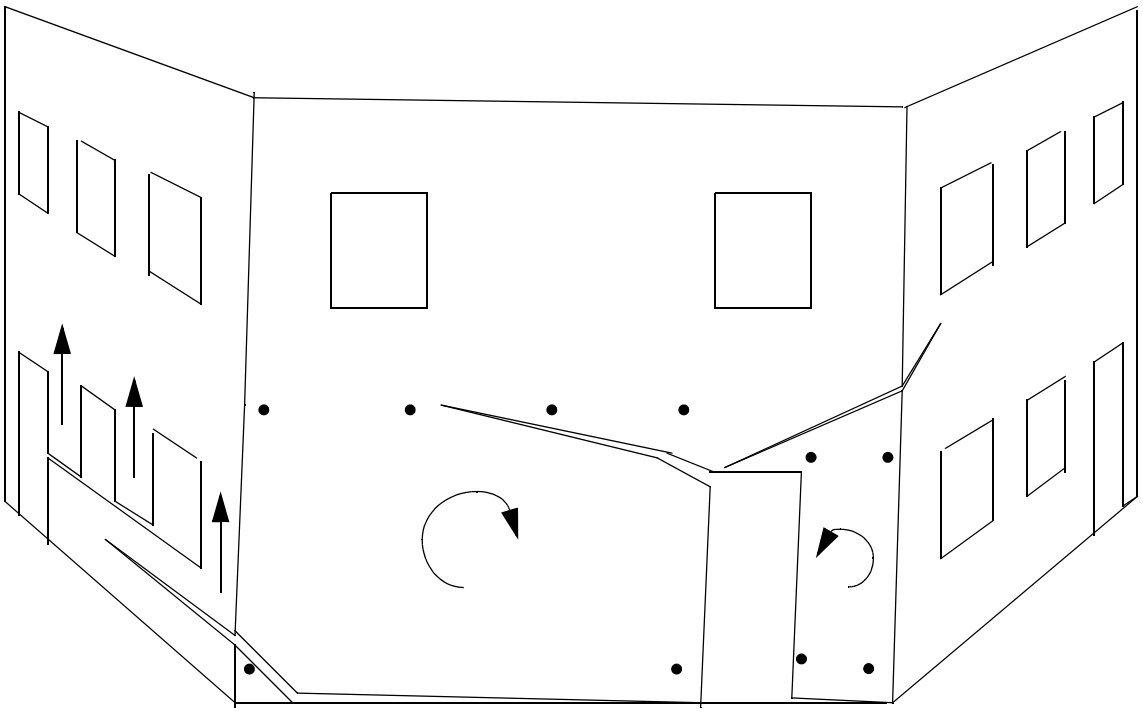

Figure C.21 Exaggerated schematic of the observed behavior of Wall 1 and out-of-plane Walls A and B in the negative loading direction during the Group 1 cycles.

Similar to the response in the positive direction, the rotation of pier P1-7 in the negative direction was somewhat counter intuitive (see Figure C.21). Again, in this direction the cause of this seemingly bizarre behavior is attributed to pier interaction. As illustrated in Figure C.21, the rotation of pier P1-7 in the positive direction was not fully recovered upon unloading. That is, the bottom left corner of pier P1-7 was not in contact with the foundation at the end of the positive loading cycle. Similar behavior was observed during the cycles conducted prior to strengthening and the reader is directed to Yi (2004) for further explanation. As a result of this deformation, pier P1-7 was loaded exclusively through the upper left corner as shown in Figure C.21. The force transferred to

pier P1-7 at this location resulted in a counterclockwise moment at the top of pier P1-7 which resulted in the observed rotation.

In addition to the observed in-plane behavior, the uplift associated with the rocking of pier P1-6 likely engaged the large portion of Wall B above the horizontal crack shown in Figure C.14. Of course at this small displacement level no visual observations could be made; however, this behavior is consistent with the existing crack pattern as well as previous cycles Yi (2004).

Figure C.22 shows the base strains recorded at peak displacement in the negative direction during Cycle 14e. From this figure it is apparent that the recorded strain profiles of pier P1-6 and out-of-plane pier PB-10 were consistent with the behavior illustrated in Figure C.21. In addition, the gages mounted to pier P1-7 and out-of-plane pier PA-7 measured nearly exclusively compressive strains. This not only is consistent with the described behavior but it also suggests that overturning moment was increasing the vertical stress at the toe of the wall.

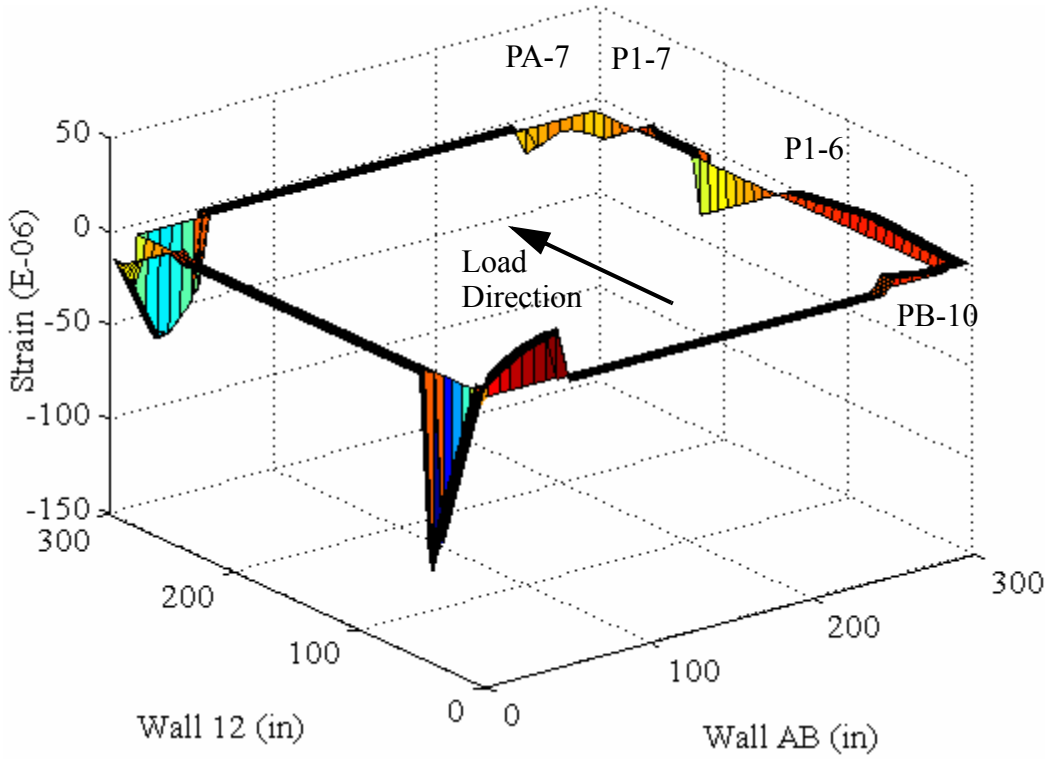

Figure C.22 Base strains recorded at peak negative displacement (Cycle 14e).

C.3.1.2 Behavior of External Reinforcement

During this level of testing no visual damage was observed in any of the FRP overlays applied to the inside of Wall 1. The behavior of several FRP strips were monitored throughout loading by strain gages placed directly adjacent to existing cracks (see Appendix A).

Figures C.23 and C.24 show the recorded strains in the vertical FRP strips versus base shear for Cycle 14b. In general, the response shown in these figures is consistent with the observed behavior. That is, the tensile strain induced into strips V1 through V3 by the global rocking of Wall 1 in the positive direction was clearly captured by gages SW1-V1 through SW1-V3 (see Figure C.23). In addition, the resistance to the rocking deformation of pier P1-6 supplied by vertical strips V4 through V7 is illustrated by tensile strains in the

negative direction in Figure C.24. Also notice the relatively small strains measured in strips V1 through V3 in the negative direction and strips V4 through V7 in the positive direction. These negligible strains suggest that the crack adjacent to the strain gages closed, thus allowing compression stress to be transferred through the masonry.

Figures C.25 and C.26 show the recorded strains in the horizontal FRP strips versus base shear for Cycle 14b. From Figure C.25 it is apparent that the measured response of the horizontal strips above the door opening in Wall 1 was somewhat erratic. In particular, the strain measurements supplied by gage SW1-H2 were somewhat inconsistent with the previously described response of the wall. However, the magnitude of the strains measured in this region were fairly small (compared to the other reinforcement) and thus this bizarre behavior is considered trivial. As illustrated by Figure C.26, the largest strains recorded during Cycle 14b were measured in the horizontal strips at the base of pier P1-6. The compression strains displayed in this figure were likely due to residual crack opening following the cycles on the structure prior to retrofit (see Yi, 2004).

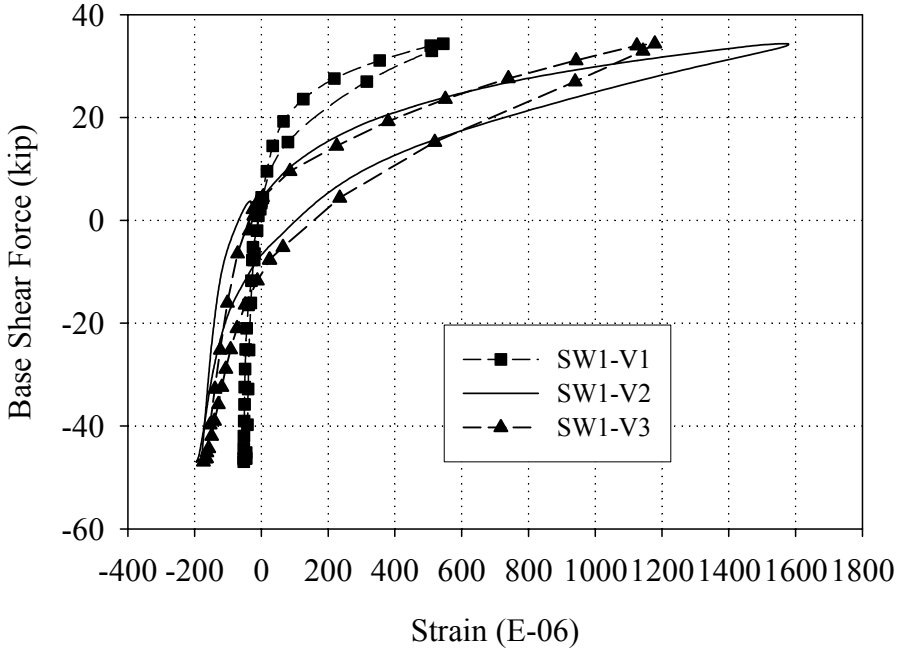

Figure C.23 Strains measured in the vertical FRP overlays applied to the inside of pier P1-7 versus base shear force (Cycle 14b).

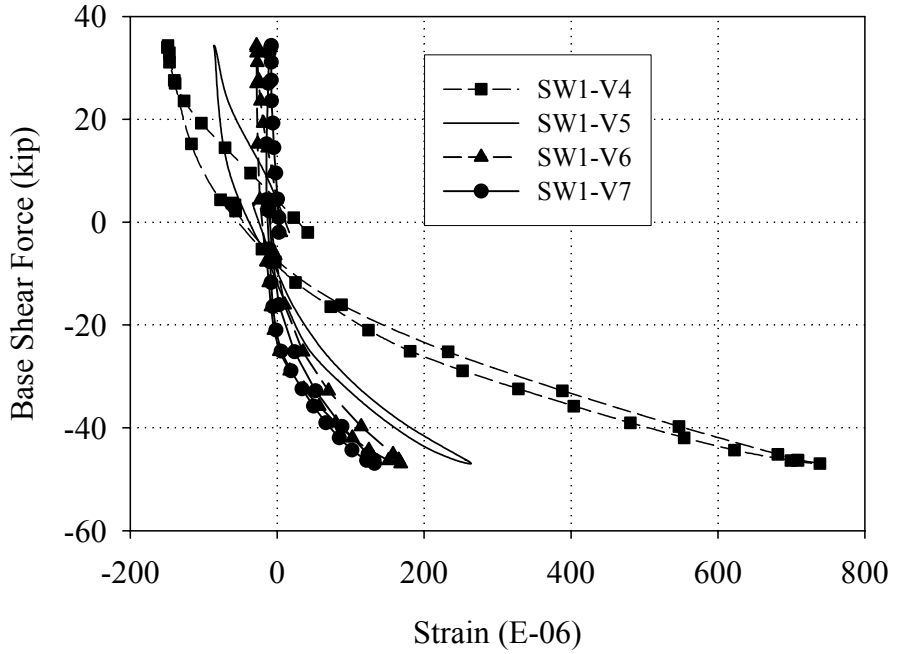

Figure C.24 Strains measured in the vertical FRP overlays applied to the inside of pier P1-6 versus base shear force (Cycle 14b).

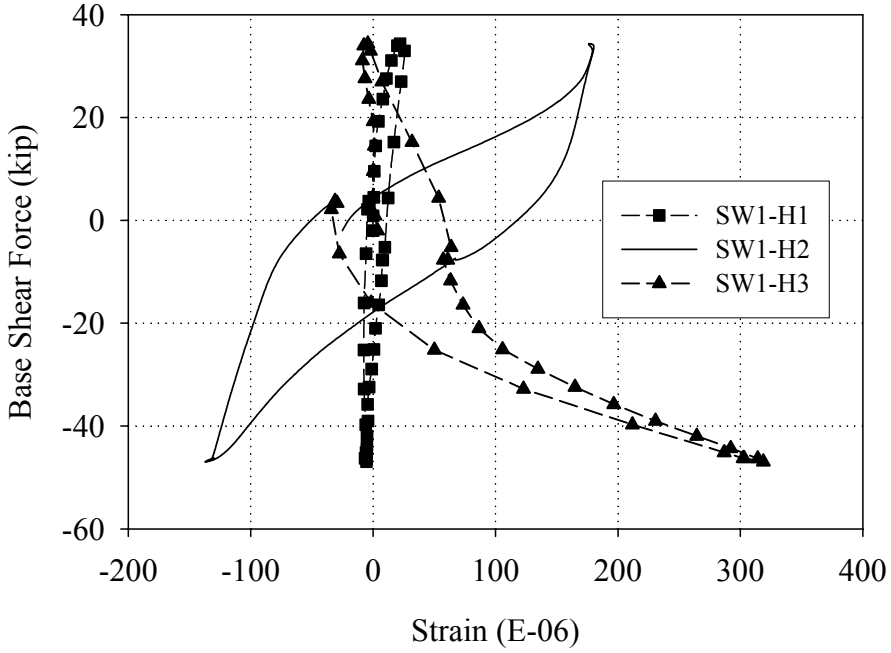

Figure C.25 Strains measured in the horizontal FRP overlays applied to the inside of spandrel P1-5 versus base shear force (Cycle 14b).

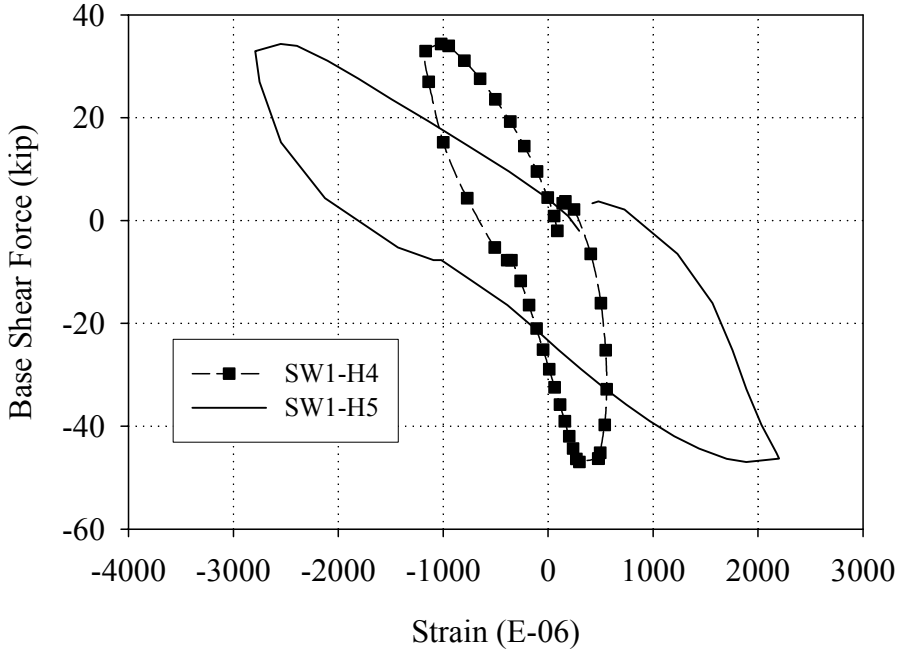

Figure C.26 Strains measured in the horizontal FRP overlays applied to the base of pier P1-6 versus base shear force (Cycle 14b).

C.3.1.3 Local Pier Behavior

Due to the observed crack opening of the first floor piers, the location of the LVDT reference points relative to the active crack is of paramount importance. As a result, the interpretation of LVDT measurements must utilize Figures C.17 and C.21, which show the location of the LVDTs in reference to the displaced shape. Since all of the piers displayed similar behavior during the Group 1 cycles, the data obtained during Cycle 14b will be used to illustrate the behavior of each pier.

Figures C.27 and C.28 show the readings obtained from the LVDTs attached to pier P1-6 (note LVDT P1-6VR was read improperly during Cycle 14b). Figures C.29 and C.30 show the readings obtained from the LVDTs attached to pier P1-7. In many cases, the LVDTs attached to the in-plane traversed several cracks (see Figures C.17 and C.21), thus a precise determination of each piers rotation and translation cannot be obtained. As a result, only a qualitative discussion will be presented.

In general, the measurements shown in Figures C.27 through C.30 indicate that the deformation of the piers was almost entirely recoverable upon unloading, which is consistent with the observed rocking dominated behavior. In addition, these readings are consistent with the previously described wall behavior. In particular, the vertical displacement of the upper boundary of pier P1-7 was upwards in the positive direction and downward n the negative direction. This is clearly consistent with the previously described behavior and underscores the pronounced overturning effect observed in the response of Wall 1. In addition, based on the relative displacements of each side of pier P1-7 the bizarre rotations discussed in Section C.3.1.1 are also apparent.

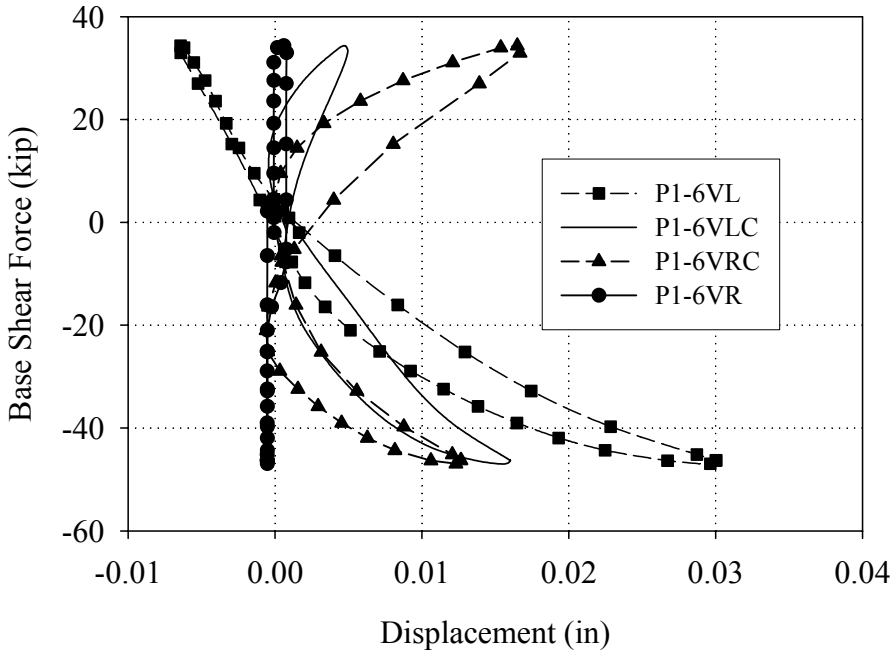

Figure C.27 Readings of the vertical LVDTs attached to pier P1-6 versus base shear force (Cycle 14b).

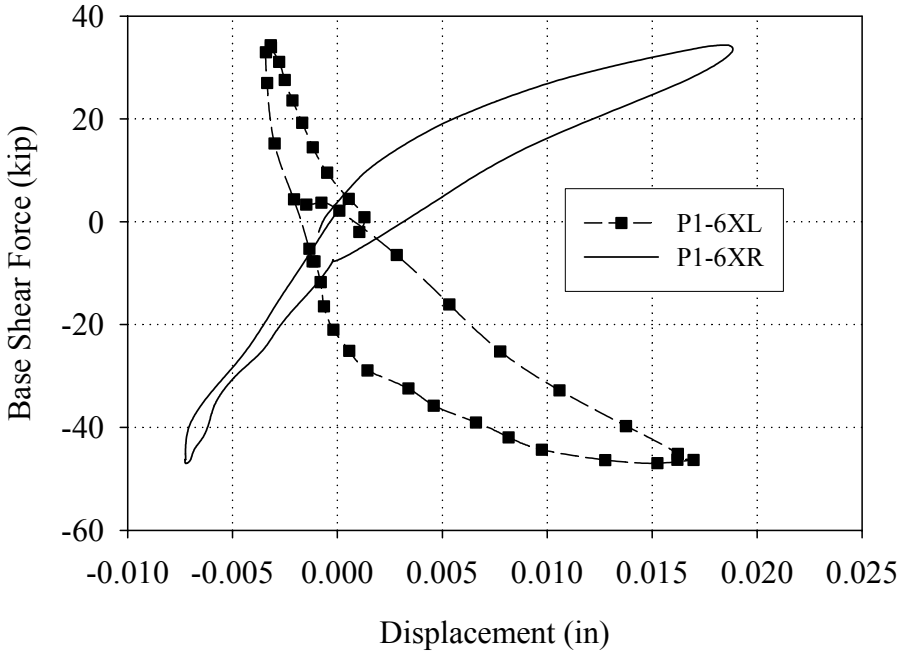

Figure C.28 Readings of the diagonal LVDTs attached to pier P1-6 versus base shear force (Cycle 14b).

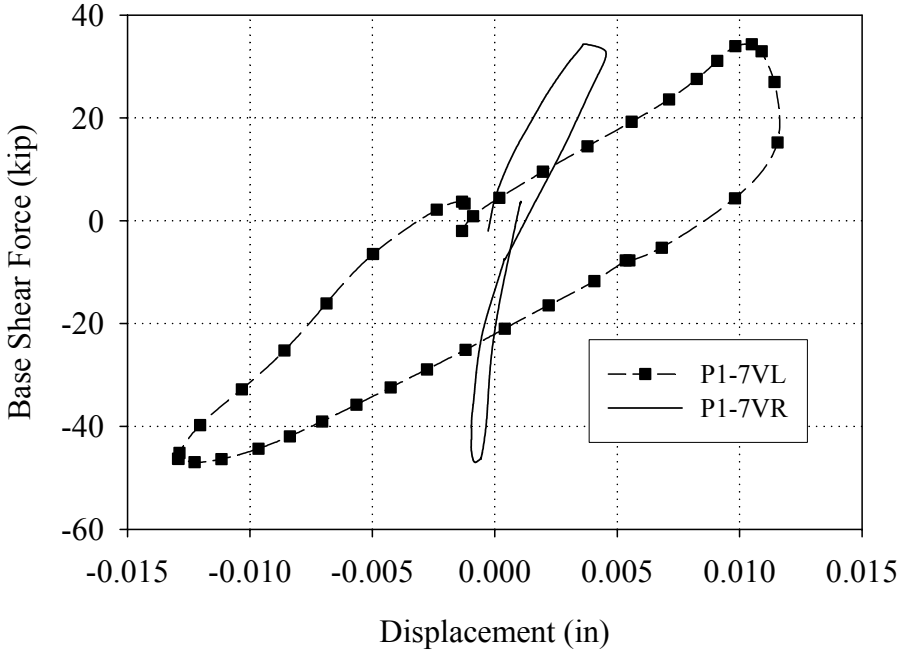

Figure C.29 Readings of the vertical LVDTs attached to pier P1-7 versus base shear force (Cycle 14b).

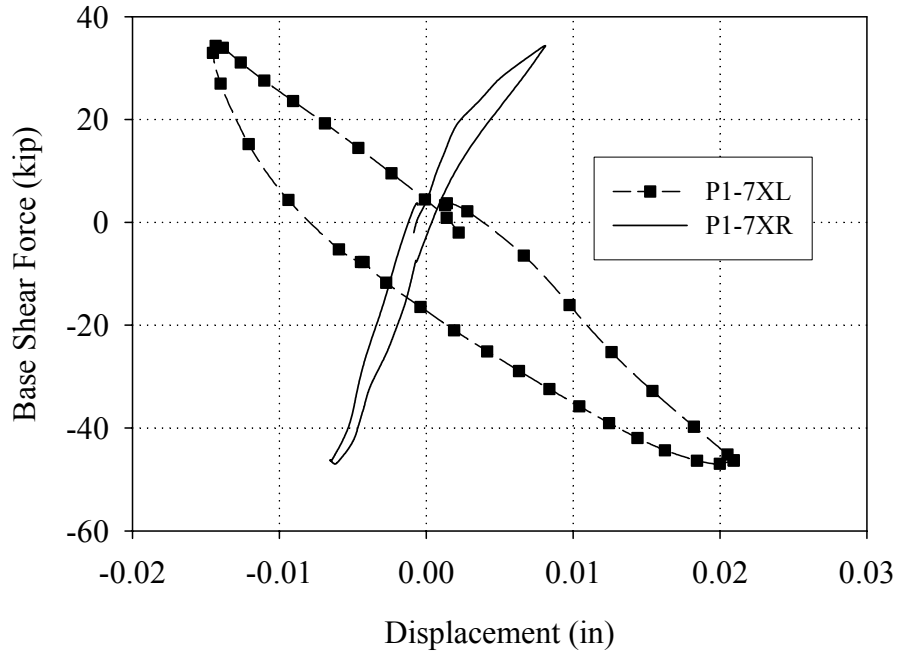

Figure C.30 Readings of the diagonal LVDTs attached to pier P1-7 versus base shear force (Cycle 14b).

C.3.2 Group 2 Cycles (Test Run 15 - Test Run 17)

C.3.2.1 Overall Wall Behavior

Figures C.31 through C.33 show the crack patterns in Wall 1 and out-of-plane Walls A and B following the Group 2 cycles. During Test Run 15, a crack at the base of pier P1-3 formed in both the positive and negative directions. In the positive direction during Test Run 16 a shallow diagonal crack formed in the lower right corner of pier P1-6. In addition, during Test Run 17 additional cracking in the spandrel above the door opening was observed in the positive direction. The largest amount of damage observed was focused on the corner of Wall 1 and Wall B. Cracks observed in this area suggested that pier P1-6 was punching through Wall B in the positive loading direction.

In addition to the cracks illustrated in these figures, a crack at the base of pier P1-6 along the inside of the wall was observed during these cycles. This crack formed in the positive direction and initiated at the door opening during Test Run 14. By the end of Test Run 15 this crack had propagated the entire length of pier P1-6. The formation and propagation of this crack was consistent with the measured flexural response of pier P1-6 in the positive direction.

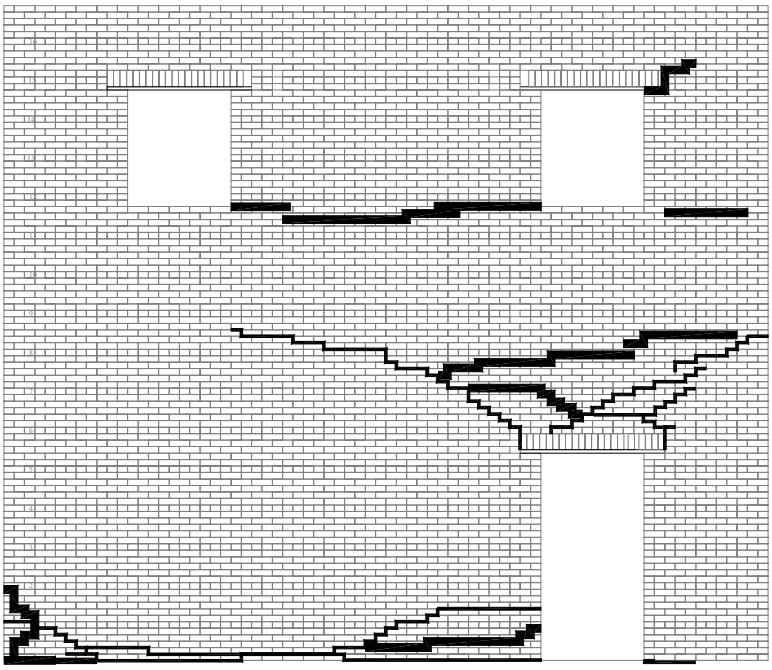

Figure C.31 Crack Pattern of Wall 1 following the Group 2 Cycles.

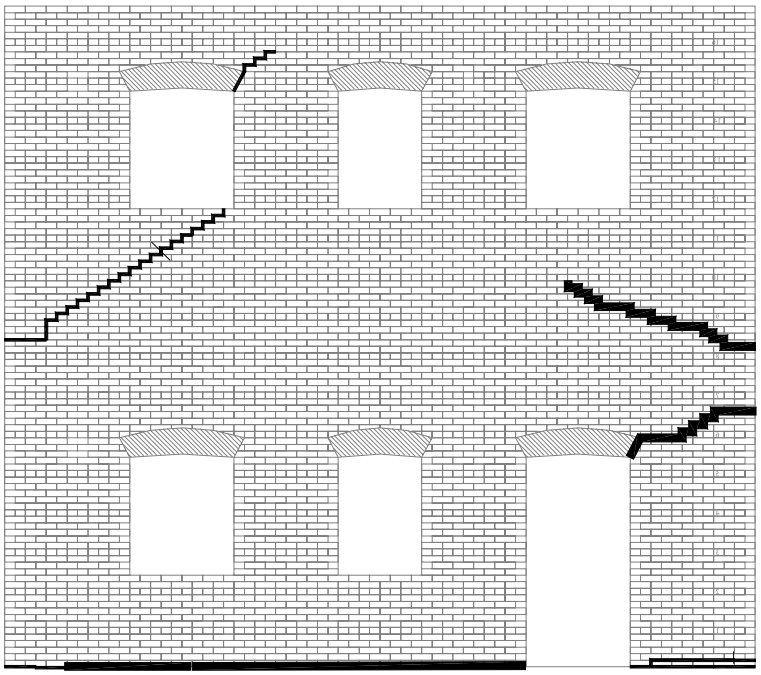

Figure C.32 Crack pattern of Wall A following the Group 2 cycles.

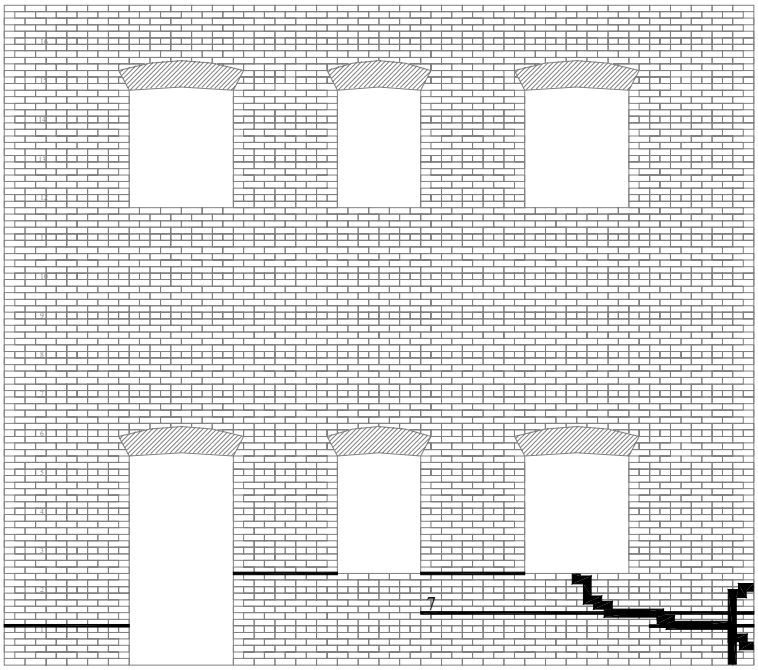

Figure C.33 Crack pattern of Wall B following the Group 2 cycles.

Figure C.34 shows an exaggerated schematic illustrating the response of Wall 1 and out-of-plane Walls A and B in the positive direction during the Group 2 cycles (note that the LVDT reference points are also shown in the figure). Based on visual observations the primary mode of deformation switched during these cycles from primarily global rocking to a combined global rocking/sliding mode. Following the formation of the base crack on the inside of pier P1-6 during Test Run 15, pier P!-6 was visibly sliding in both directions. Figure C.35 shows a plot of the sliding deformation of pier P1-6 versus base shear during Cycle 15a (unfortunately, the sliding deformation beyond this cycle could not be captured as it exceeded the stroke of the potentiometer). The sliding deformation suggested by this plot is also supported by the by the calculated energy dissipation and residual displacement plots shown in Figures C.11 through C.13.

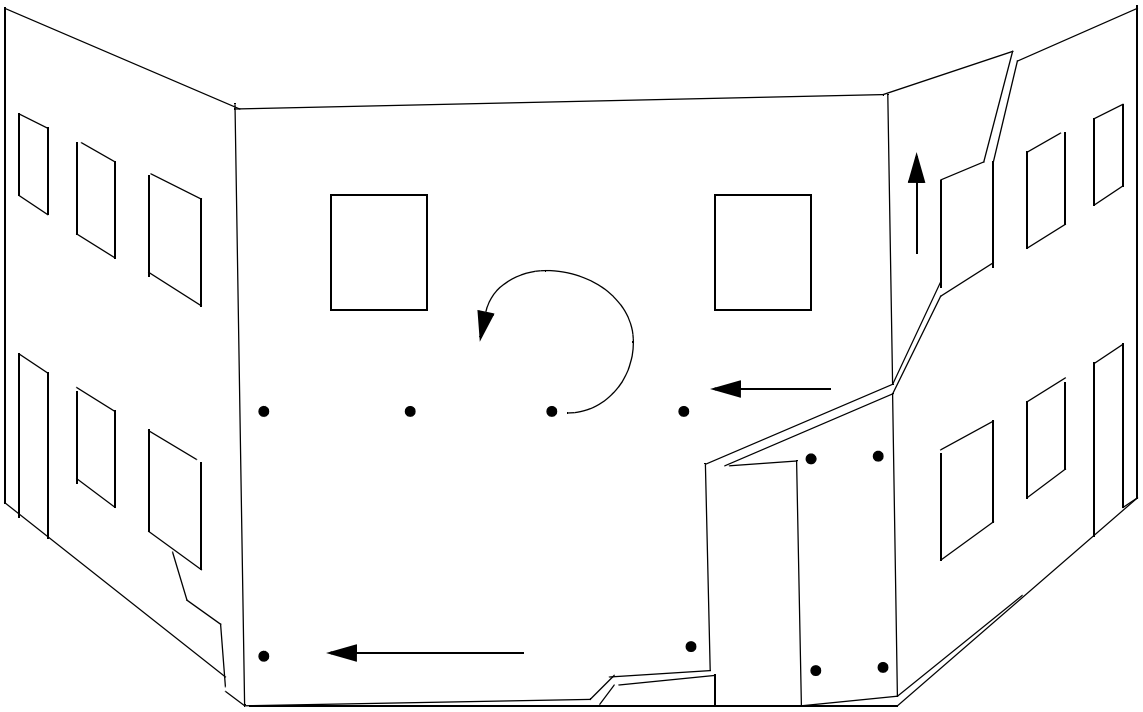

Figure C.34 Exaggerated schematic of the observed behavior of Wall 1 and out-of-plane Walls A and B in the positive direction during the Group 2 cycles.

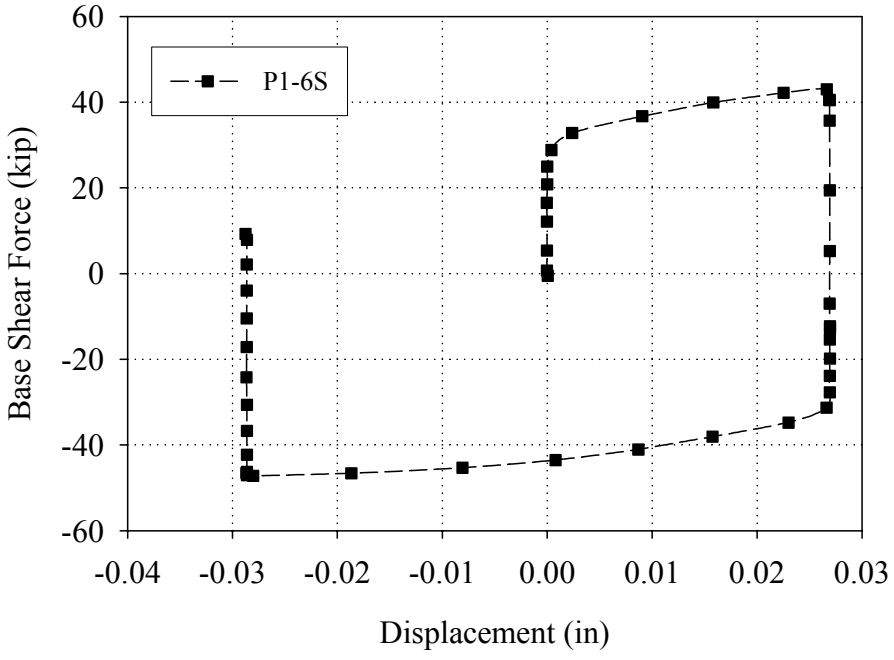

Figure C.35 Sliding displacement of pier P1-6 versus base shear (Cycle 15a).

Based on Figure C.35, it is apparent that while the sliding deformation of pier P1-6 substantially increased during Test Run 15, it still only represented approximately 30% of the imposed first story displacement. The majority of the roof displacement of Wall 1 was still likely caused by global rocking. Consider Figure C.36 which shows the vertical displacements of each side of Wall 1 versus roof displacement for Cycle 15a. Utilizing the simplifying assumptions outlined in Section C.3.1.1, the global rocking displacement implied by this figure accounted for approximately 0.06 in or 40% of the imposed roof displacement during Cycle 15a. In addition, consider Figure C.37 which shows the vertical displacements of each side of Wall 1 versus roof displacement for Cycle 17c. Based on this figure the implied roof displacement due to global rocking was approximately 0.05 in or 13% of the imposed roof displacement during Cycle 17c. As a result, it can be concluded that during the Group 2 cycles the behavior of Wall 1 exhibited a decreasing percentage of global rocking displacement thus implying an increase in sliding deformation. While this increase in sliding deformation was not quantified, it is supported by visual observations as well as the calculated energy dissipation and residual displacements (see Figures C.11 through C.13).

Beyond this primary mechanism a slight change in behavior of pier P1-7 was also observed during the Group 2 cycles. Essentially, the decrease in global rocking displacement resulted in a more local response of this pier. As illustrated in Figure C.34 pier P1-7 exhibited low-level rocking in the positive direction.

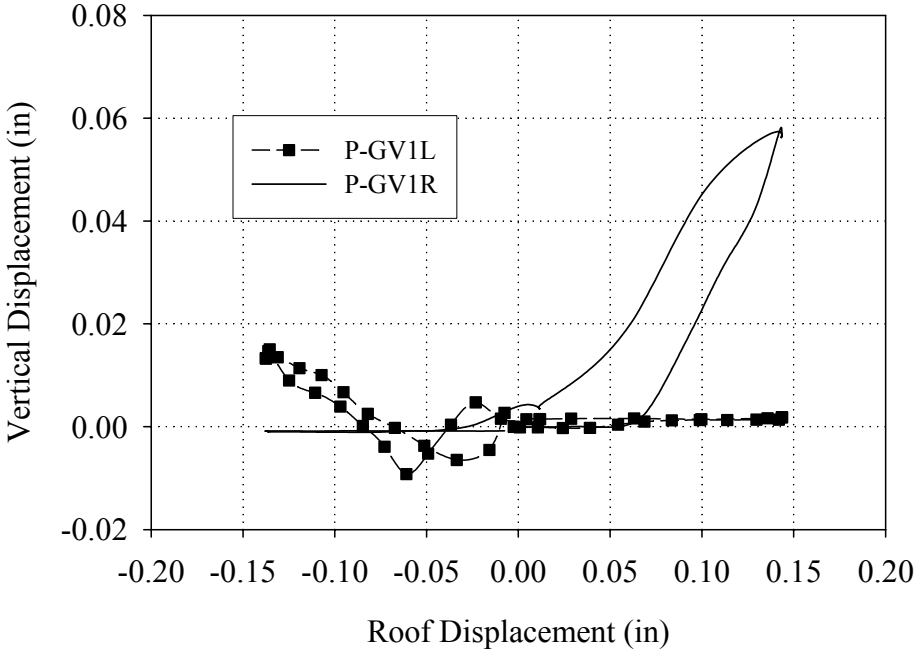

Figure C.36 Vertical displacements of both sides of Wall 1 versus roof displacement (Cycle 15a)

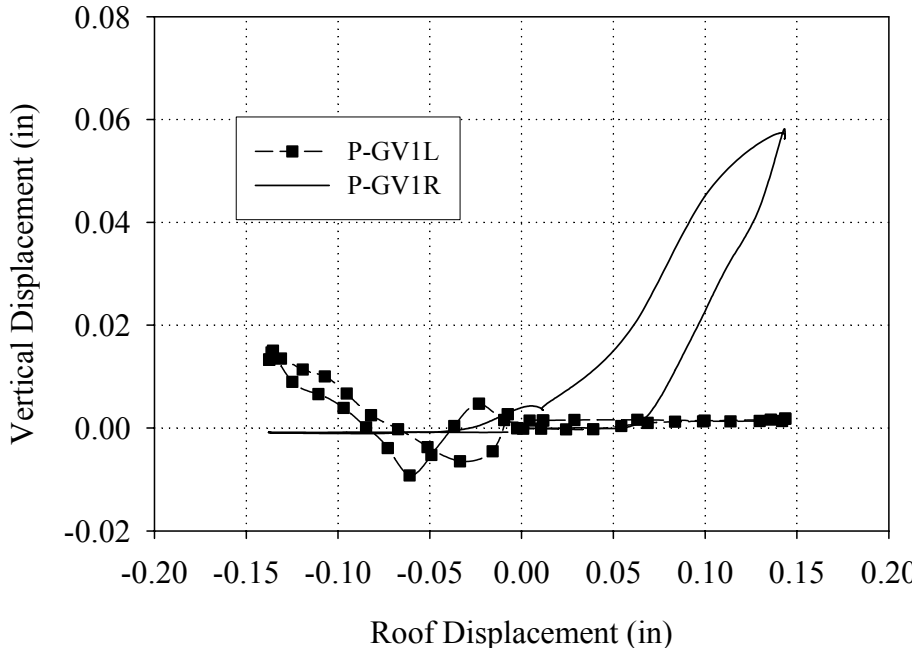

Figure C.37 Vertical displacements of both sides of Wall 1 versus roof displacement (Cycle 17c)

Similar to the response during the Group 1 cycles, the observed global rocking behavior engaged the upper corner of Wall A. In addition, the low-level rocking of pier P1-7 cracked Wall A at the base. Figure C.38 shows the base strains recorded at peak positive displacement during Cycle 17c. Form this figure it is clear that the observed local rocking of pier P1-7 was captured by these strain gages. Furthermore, the strain profile measure in pier PA-7 supports the contention that a portion of out-of-plane Wall A was participating in the response. The relatively small strains measured in piers P1-6 and PB-10 are attributed to the large amount of damage sustained directly adjacent to the gages.

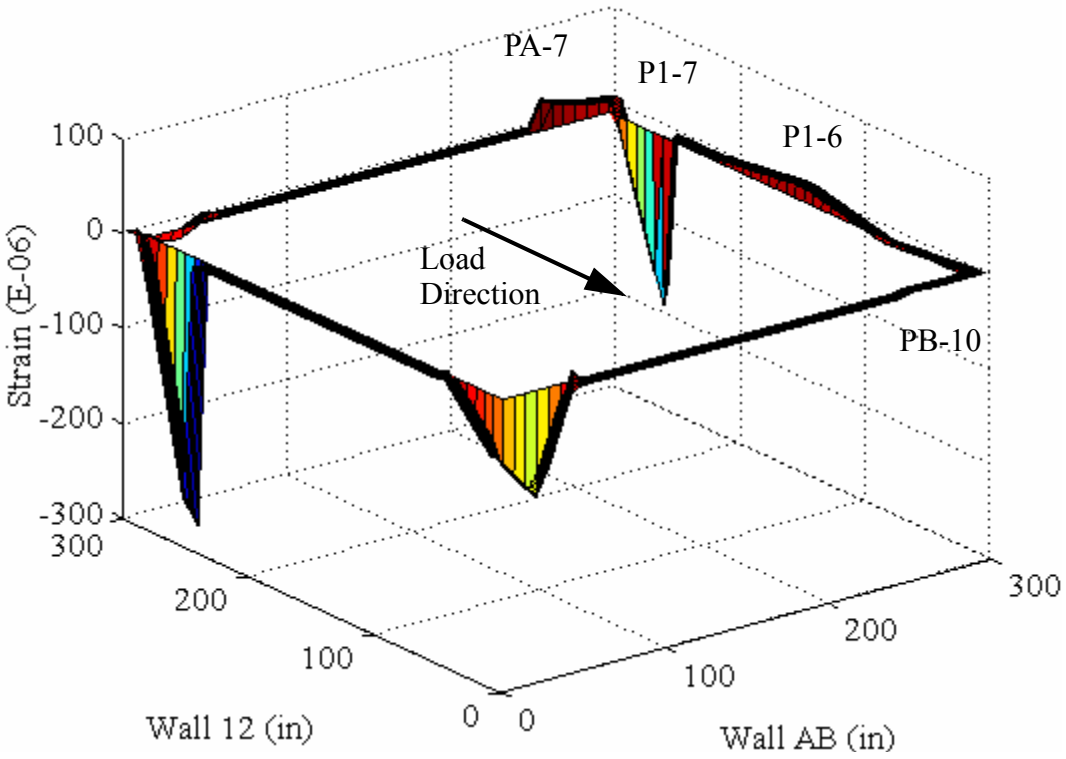

Figure C.38 Base strains recorded at peak positive displacement (Cycle 17c).

Figure C.39 shows a schematic illustrating the behavior of Wall 1 and out-of-plane Walls A and B in the negative direction during the Group 2 cycles (note that the location of the LVDT reference points are also shown). Similar to the behavior in the positive

direction, the response of Wall 1 in the negative direction changed from primarily rocking to a combined rocking/sliding mode during the Group 2 cycles. The sliding deformation at the base of pier P1-6 was captured by a potentiometer and is shown in Figure C.35 versus base shear force. As apparent from the Figure C.35, the measured sliding deformation accounted for approximately 30% of the lateral displacement imposed on the first story, which suggests that rocking deformation was also present. In addition to visual observations, this increased sliding deformation is apparent from the calculated energy dissipation and residual displacement of the first story of Wall 1 (see Figures C.11 through C.13).

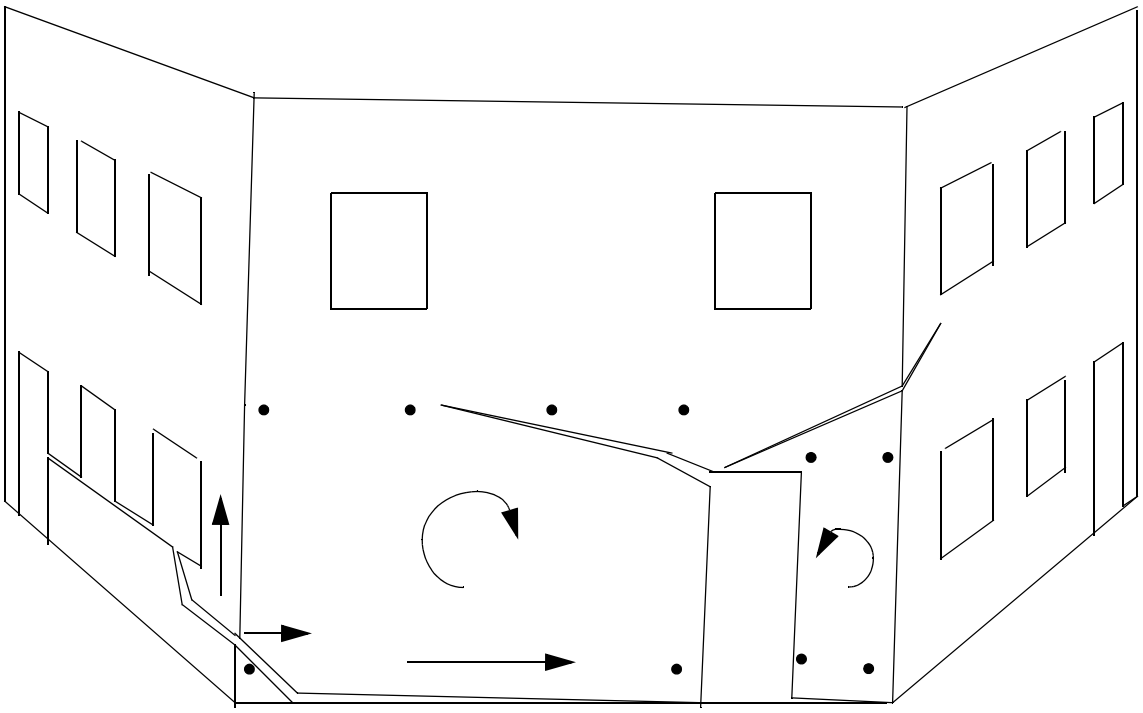

Figure C.39 Exaggerated schematic of the observed behavior of Wall 1 and out-of-plane Walls A and B in the negative direction during the Group 2 cycles.

In addition, the increased sliding deformation of pier P1-6 resulted in a change in the behavior of Wall B during the Group 2 cycles. Recall that during past cycles, the

rocking of pier P1-6 lifted up the large portion of Wall B above the horizontal crack below the window opening. During the Group 2 cycles this vertical displacement was still observed; however, it was also accompanied by a horizontal translation. This translation primarily occurred above the 6th course in Wall B. Following Test Run 17, this offset was approximately 0.25in (see Figure C.40). It was noted that this offset diminished to zero approximately 2 ft from the corner.

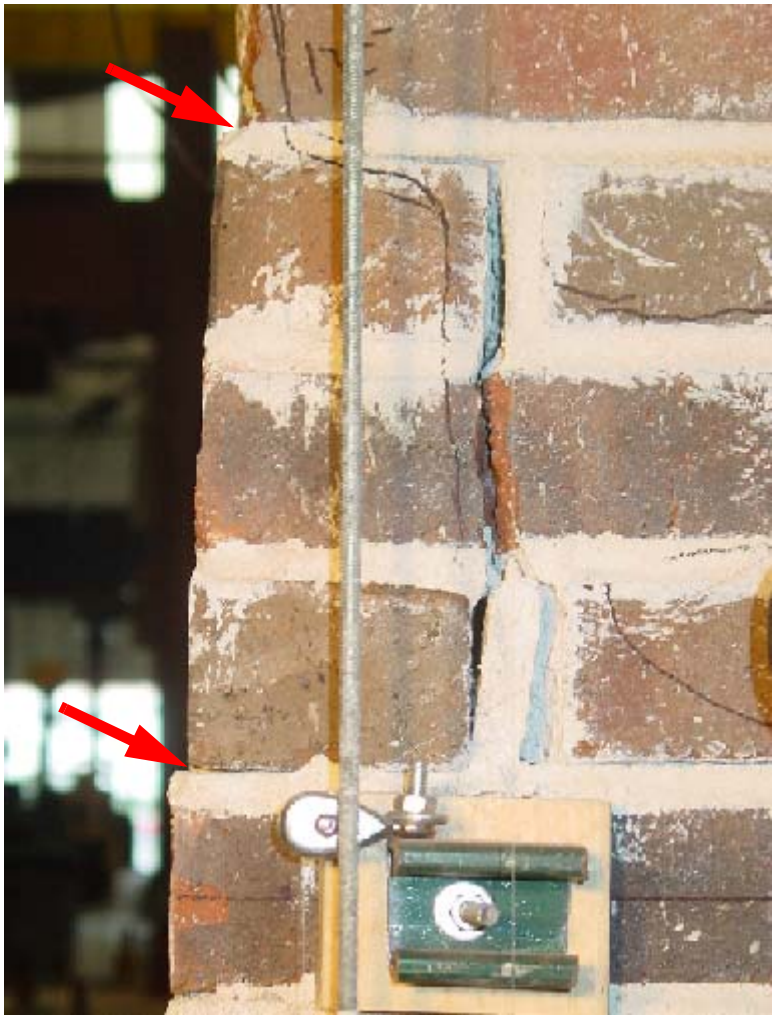

Figure C.40 Photograph showing the offset at the corner of Wall 1 and Wall B due to the sliding deformation of pier P1-6 in the negative direction

Figure C.41 shows the base strains recorded at peak negative displacement during Cycle 17c. From this figure it is apparent that the measured strain profiles are somewhat erratic and the strain magnitudes are fairly small. This is attributed to the diminished flexural response of the pier as well as the relatively large amount of damage that accumulated during the Group 2 cycles.

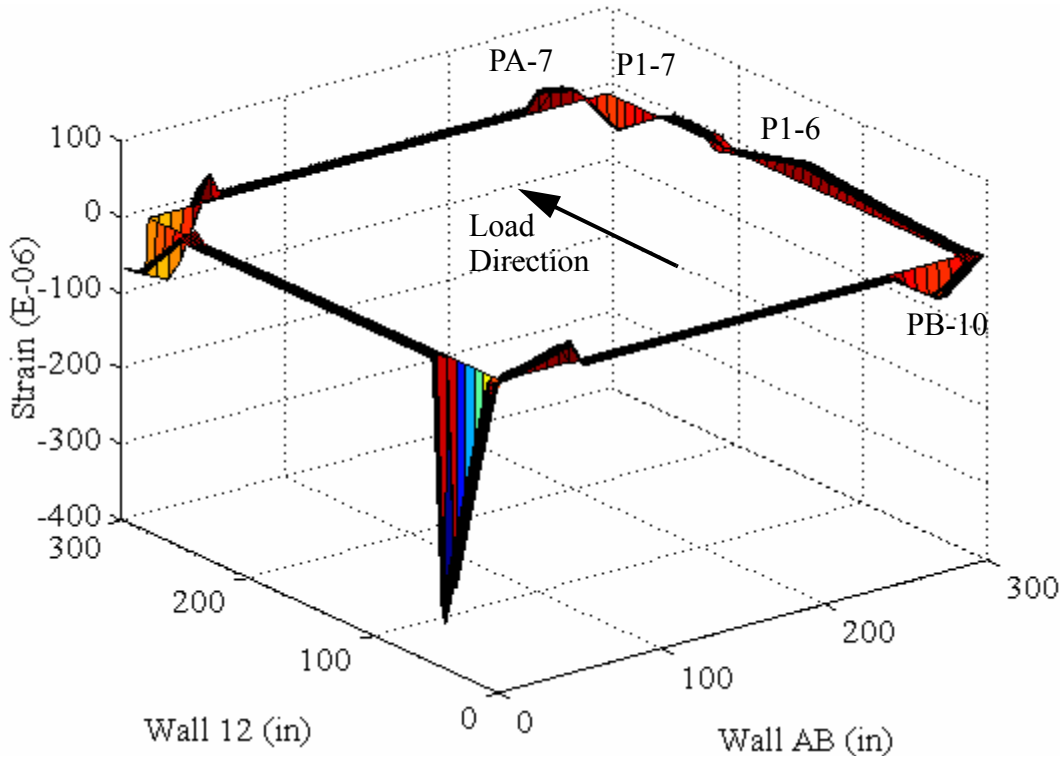

Figure C.41 Base strains recorded at peak negative displacement (Cycle 17c).

C.3.2.2 Behavior of External Reinforcement

During the Group 2 cycles no visual damage was observed in any of the FRP overlays applied to the inside of Wall 1. The behavior of several FRP strips were monitored throughout loading by strain gages placed directly adjacent to existing cracks (see Appendix A).

Figures C.42 and C.43 show the recorded strains in the vertical FRP strips versus

base shear for Cycle 17c. In general, the response shown in these figures is consistent with past cycles. That is, the measured strains clearly indicate that vertical strips V1 through V3 were engaged due to the global rocking of Wall 1 in the positive direction. Furthermore, the strains measured in vertical strips V4 through V7 indicate that these strips resisted the local rocking deformation of pier P1-6 in the negative direction.

Figures C.44 and C.45 show the recorded strains in the horizontal FRP strips versus base shear for Cycle 17c. From Figure C.44 it is apparent that the horizontal strips above the door opening in Wall 1 were resisting the lateral deformation of the this spandrel. This is also apparent from the distributed cracking pattern observed during the Group 2 cycles.

From Figure C.45 it is apparent that strips H4 and H5 were active in tying the base of pier P1-6 together. In addition, this figure indicates that the maximum strains recorded during Cycle 17c were very similar to the maximum strains recorded during Cycle 14b (see Figure C.26). This is consistent with the formation of a smooth sliding crack which acted as a fuse thus limiting the amount of strain in these strips. Based on this instrumentation as well as visual observations it can be concluded that strips H4 and H5 were effective in tying the bottom courses together and forcing a smooth horizontal crack that established a sliding plane in both directions.

However, this smooth crack only formed on the inside wythe. Since the first header course was located at the sixth course, the reinforcement was not developed in the outer wythe below this point. The result was a vertical crack through the collar joint below the first header course. This crack allowed independent movement of the wythes at the base of the pier. This was observed most clearly at the door opening (see Figure C.46);

however, based on observed crack opening this phenomenon was likely occurring at the lower left corner of pier P1-6 as well. Above the sixth course no separation of the wythes was observed, which suggests that the header courses performed properly throughout loading.

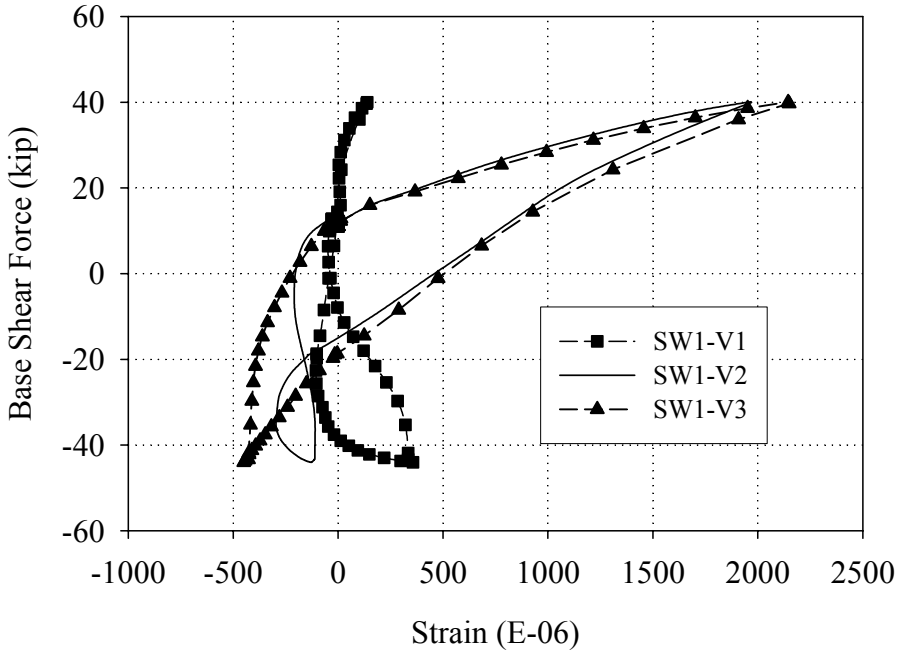

Figure C.42 Strains measured in the vertical FRP overlays applied to the inside of pier P1-7 versus base shear force (Cycle 17c).

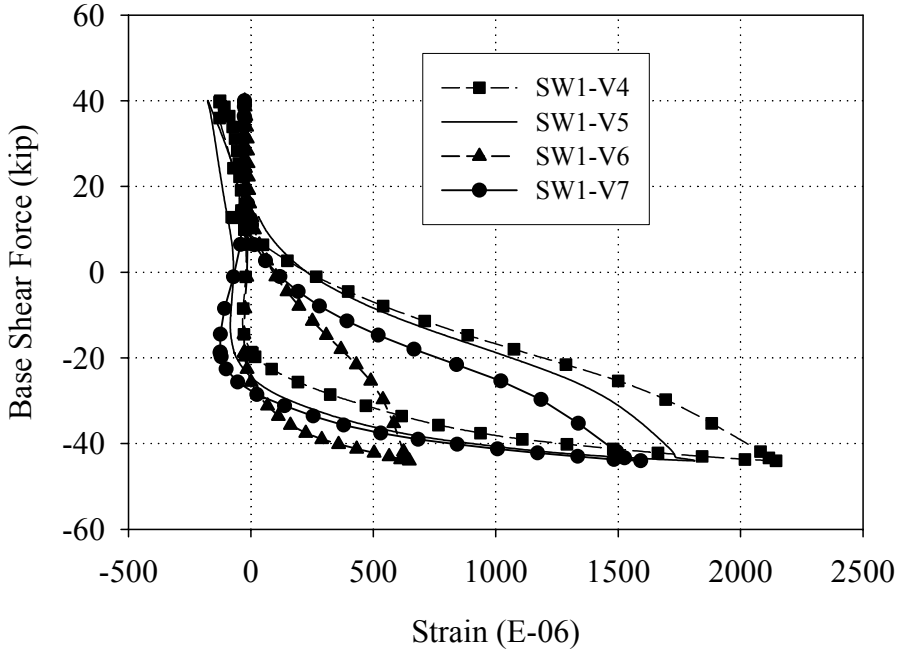

Figure C.43 Strains measured in the vertical FRP overlays applied to the inside of pier P1-6 versus base shear force (Cycle 17c).

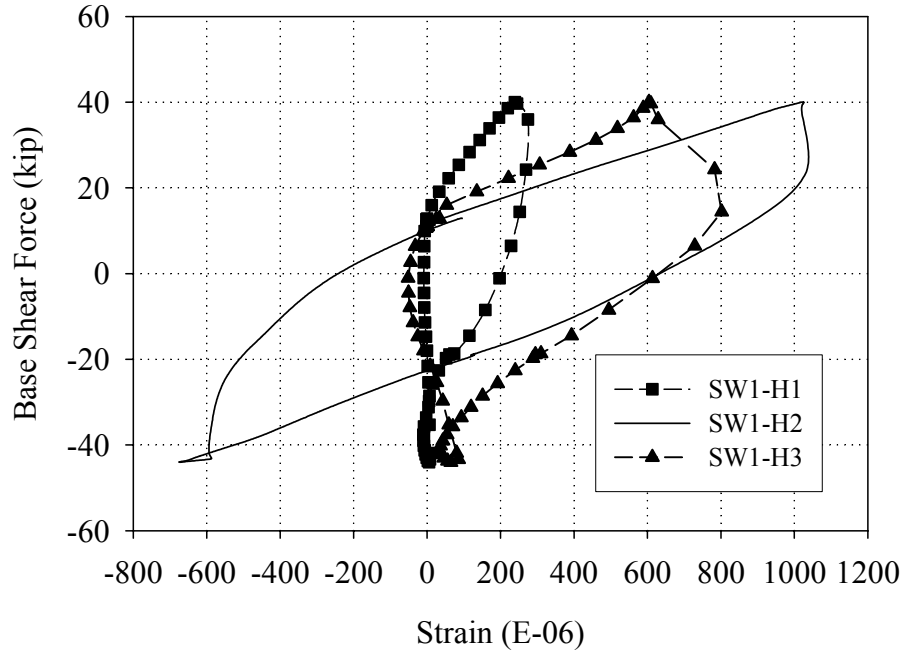

Figure C.44 Strains measured in the horizontal FRP overlays applied to the inside of spandrel P1-5 versus base shear force (Cycle 17c).

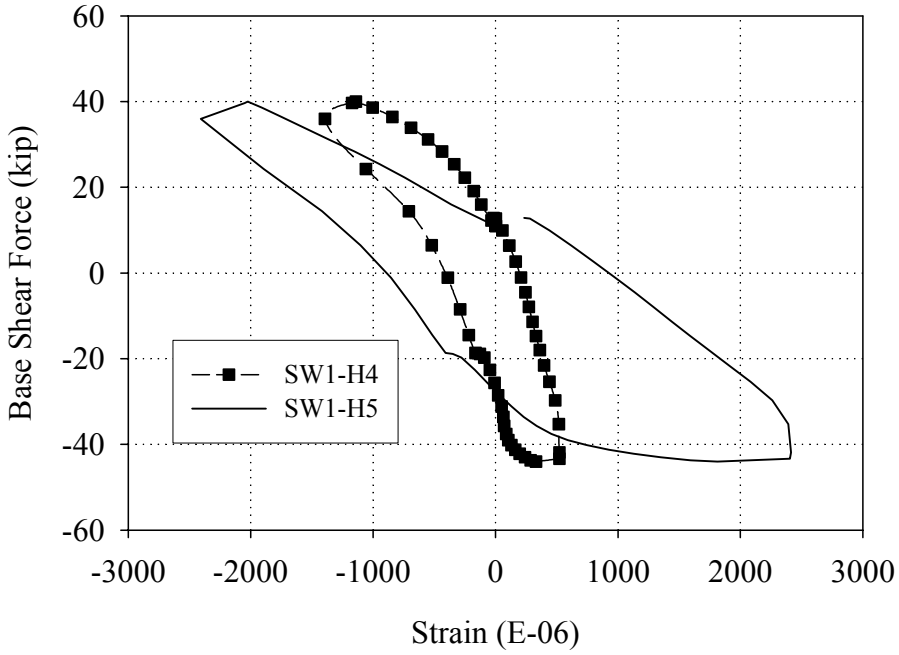

Figure C.45 Strains measured in the horizontal FRP overlays applied to the base of pier P1-6 versus base shear force (Cycle 17c).

Figure C.46 Photograph showing the separation of the wythes below the first header course.

C.3.2.3 Local Pier Behavior

Due to the observed crack opening of the first floor piers, the location of the LVDT reference points relative to the active crack is of paramount importance. As a result, the interpretation of LVDT measurements must utilize Figures C.34 and C.39, which show the location of the LVDTs in reference to the displaced shape. Since all of the piers displayed similar behavior during the Group 2 cycles, the data obtained during Cycle 17c will be used to illustrate the behavior of each pier.

Figures C.47 and C.48 show the readings obtained from the LVDTs attached to pier P1-6. Figures C.49 and C.50 show the readings obtained from the LVDTs attached to pier P1-7. In many cases, the LVDTs attached to the in-plane traversed several cracks (see Figures C.34 and C.39), thus a precise determination of each piers rotation and translation cannot be obtained. As a result, only a qualitative discussion will be presented.

In general, the measurements shown in Figures C.47 through C.50 are fairly consistent with the pier behavior observed during the Group 1 cycles (see Section C.3.1.3). The principal difference is the large amount of residual displacement measured by the diagonally mounted LVDTs (see Figures C.48 and C.50). This residual displacement suggests an increased sliding deformation which is consistent with the observed wall behavior described previously.

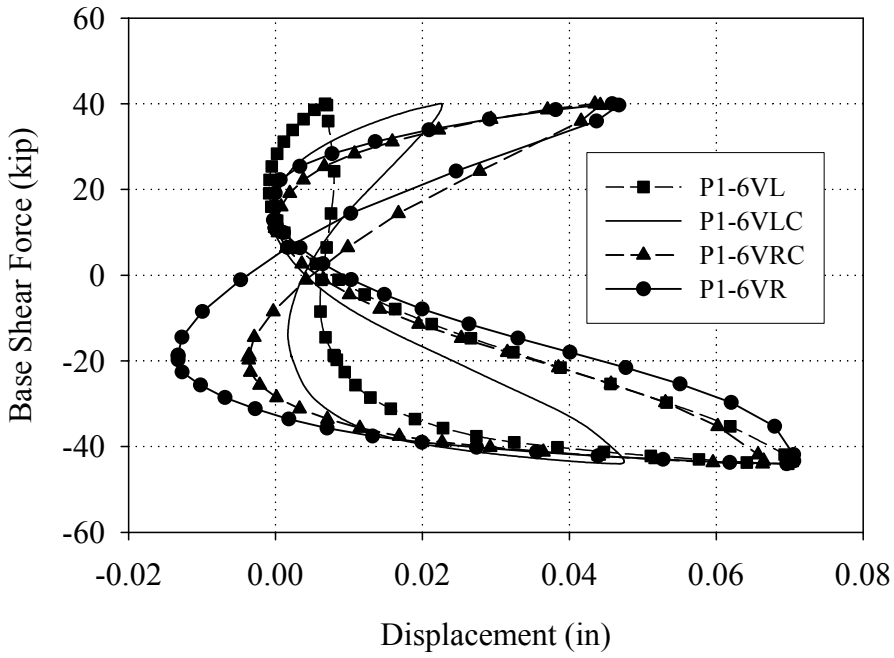

Figure C.47 Readings of the vertical LVDTs attached to pier P1-6 versus base shear force (Cycle 17c).

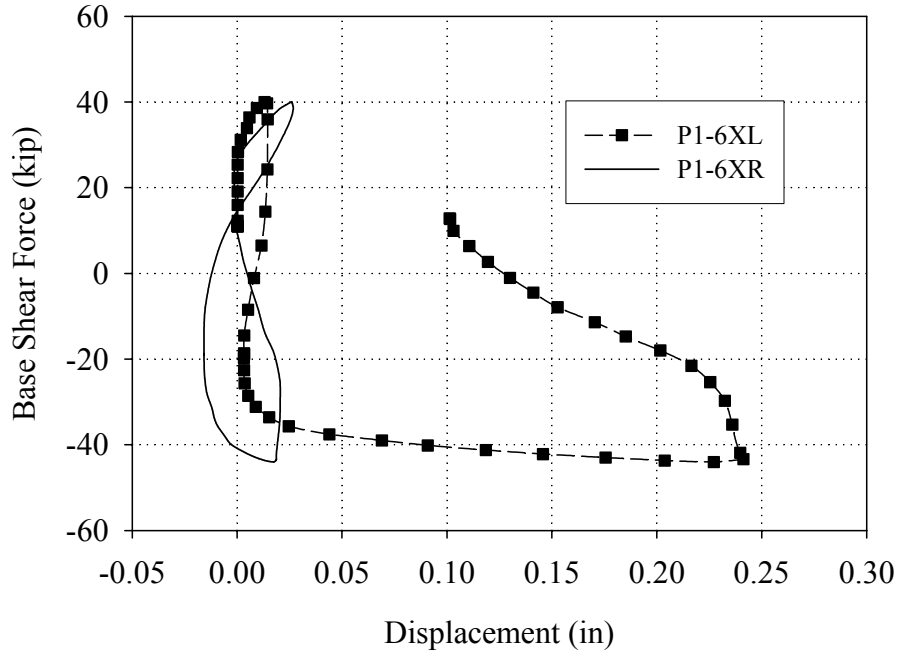

Figure C.48 Readings of the diagonal LVDTs attached to pier P1-6 versus base shear force (Cycle 17c).

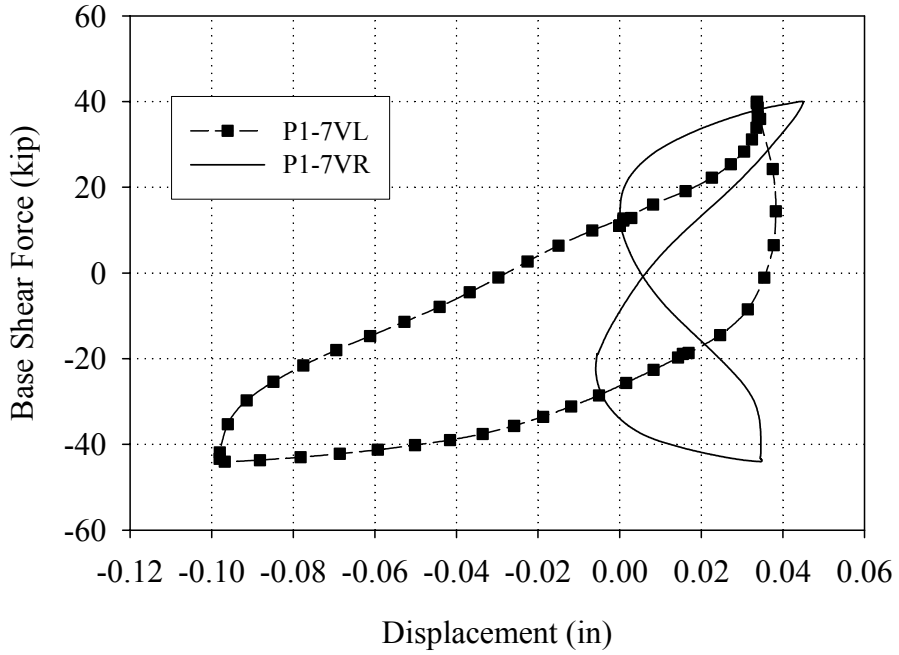

Figure C.49 Readings of the vertical LVDTs attached to pier P1-7 versus base shear force (Cycle 17c).

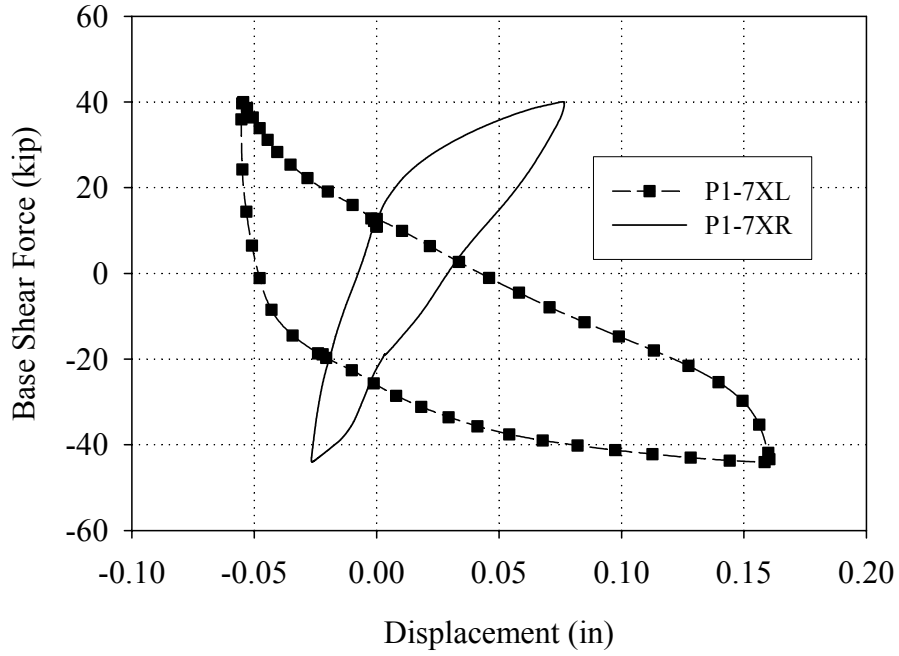

Figure C.50 Readings of the diagonal LVDTs attached to pier P1-7 versus base shear force (Cycle 17c).

C.3.3 Group 3 Cycles (Test Run 18 - Test Run 19)

C.3.3.1 Overall Wall Behavior

Figures C.51 through C.53 illustrate the crack pattern in Wall 1 and out-of-plane Walls A and B following the Group 3 cycles (note the cracks that formed during the Group 3 cycles are shown in bold). As apparent from these figures several cracks were observed in out-of-plane Walls A and B during these cycle. In the positive loading direction, the cracks below pier PA-7, above piers PA-8 and PA-9, and diagonally through pier PB-10 were observed. In the negative direction, the horizontal cracks above piers PA-7, PB-8 and PB-9 were observed. In addition, during Cycle 18a in the negative direction a diagonal crack was observed in the center of pier P1-7, this crack fully developed during Cycle 19a.

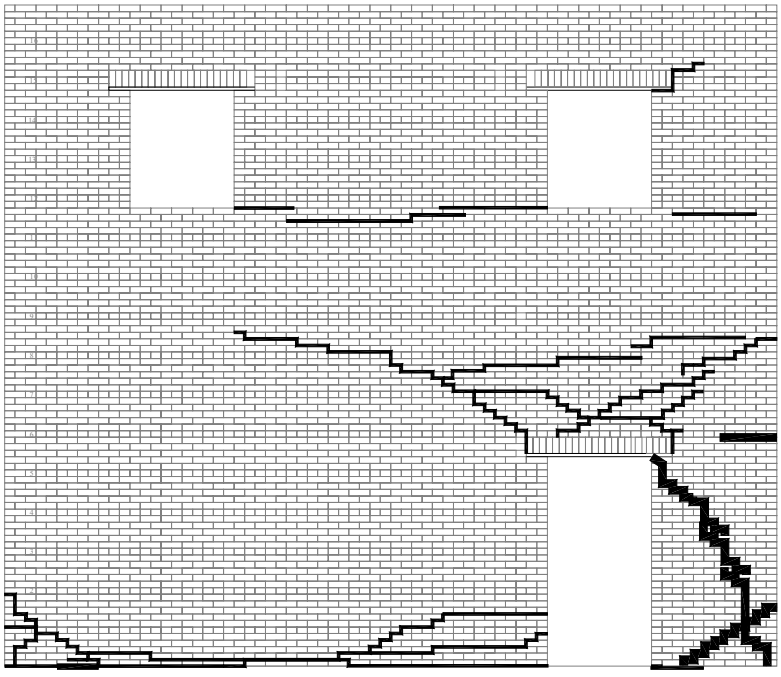

Figure C.51 Crack Pattern of Wall 1 following the Group 3 Cycles.

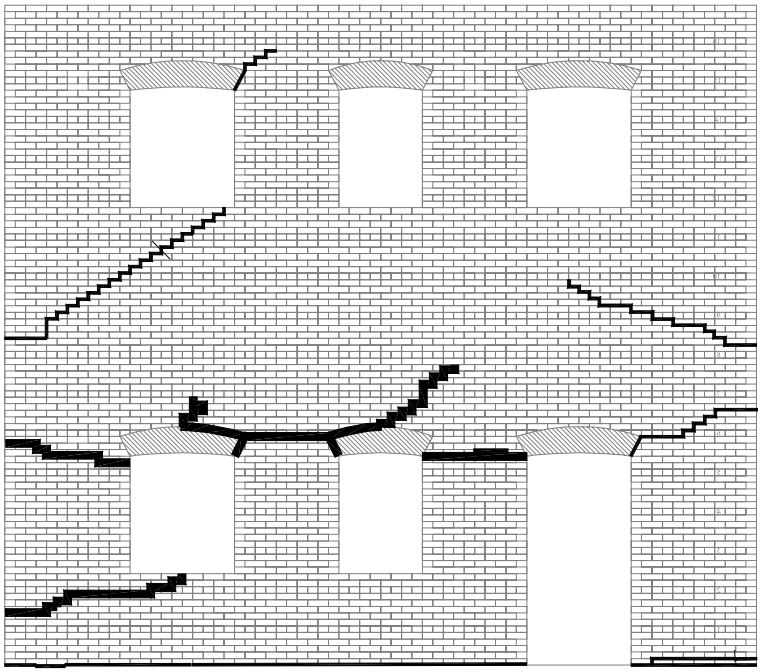

Figure C.52 Crack pattern of Wall A following the Group 3 cycles.

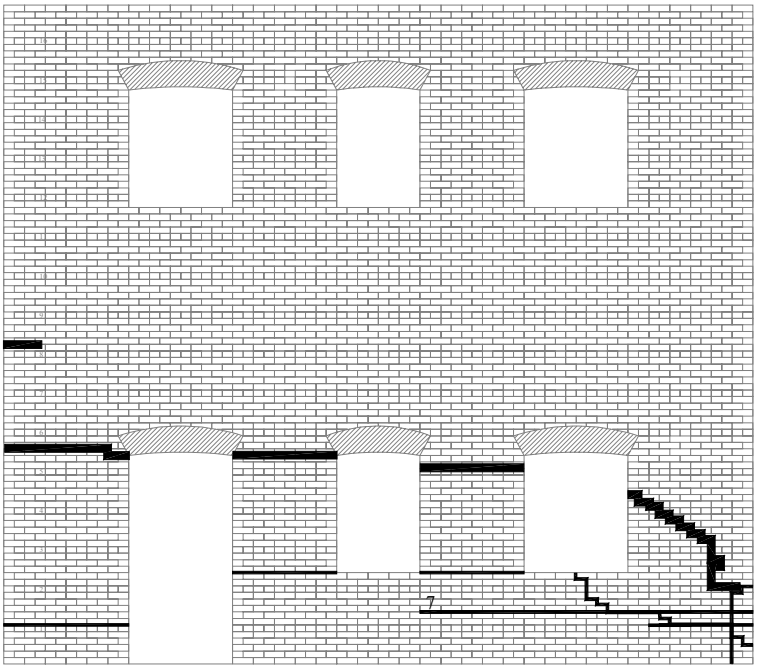

Figure C.53 Crack pattern of Wall B following the Group 3 cycles.

Figure C.54 shows an exaggerated schematic of the behavior of Wall 1 in the positive direction (note that the location of the LVDT reference points are also shown). Similar to past cycles instrumentation and observations suggested that pier P1-6 exhibiting a combined rocking/sliding mode in the positive direction. However, during the Group 3 cycles visual observations suggested that the behavior of pier P1-6 was dominated by sliding. It was noted that the pier was visibly sliding approximately 0.5 in. in both the positive and negative direction. This sliding deformation reduced the mortar in the adjacent bed-joint to a white powder (see Figure C.55). One possible explanation for the decrease in base shear capacity during these cycles is that this powder was decreasing the coefficient of friction at the base of the wall. It should be pointed out that this phenomenon has not been observed in the past.

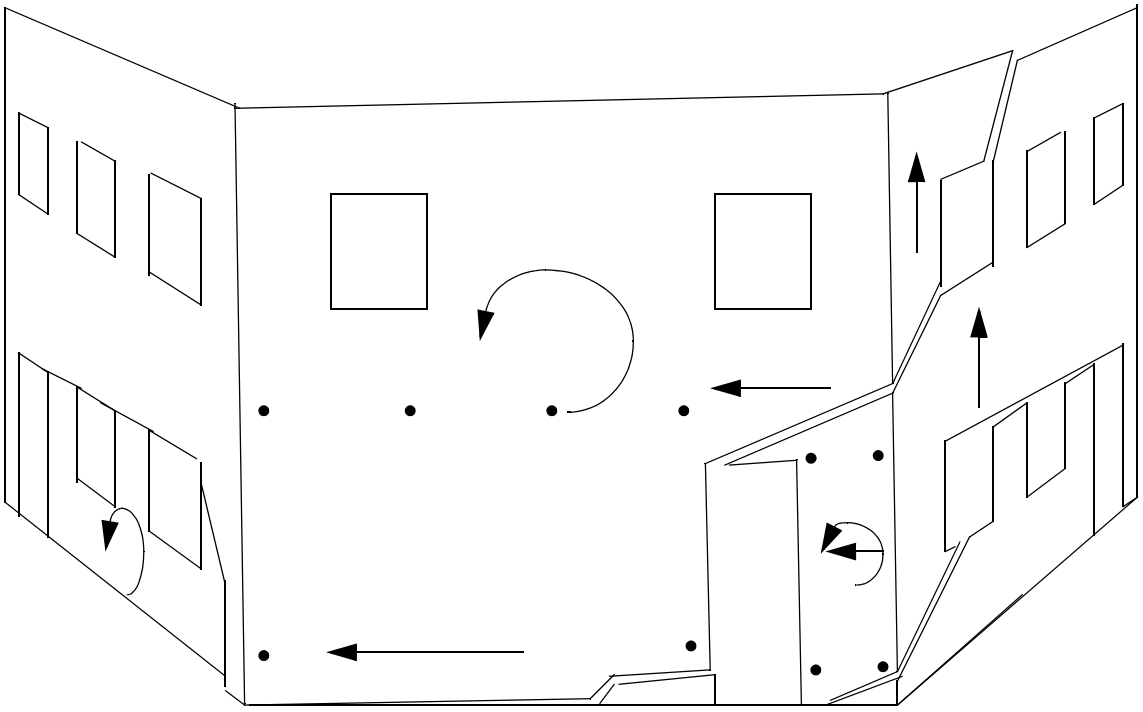

Figure C.54 Exaggerated schematic illustrating the behavior of Wall 1 and out-of-plane Walls A and B in the positive direction during the Group 3 cycles.

Figure C.55 Photograph showing the resulting white powder from the bed-joint at the base of pier P1-6

Figure C.56 shows the vertical displacement of each side of Wall 1 versus roof displacement for Cycle 19a. Based on the assumptions outlined in Section C.3.1.1, the global rocking deformation suggested by this plot accounted for approximately 0.1 in. or 13% of the imposed roof displacement. This relatively small global rocking displacement supports the contention that sliding deformation dominated the response. In addition, this reduced global displacement of Wall 1 resulted in a more local response for pier P1-7. Recall that due to the observed global rocking displacement during the Group 1 cycles, pier P1-7 did not fully participate in the response. In contrast during the Group 3 cycles this pier displayed a combined rocking/sliding behavior (see Figure C.54).

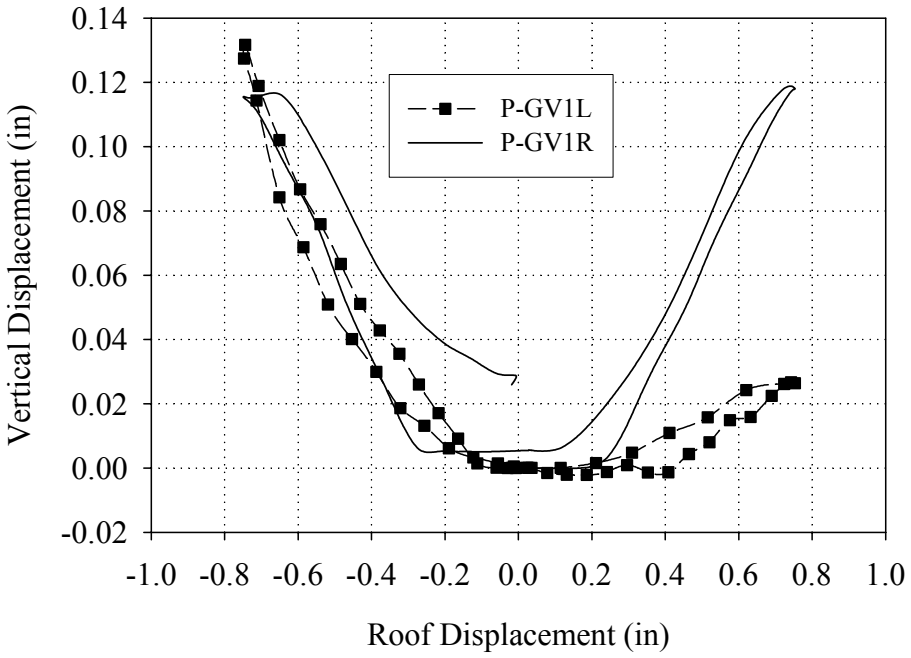

Figure C.56 Vertical displacements of both sides of Wall 1 versus roof displacement (Cycle 19a).

In addition to the in-plane behavior of Wall 1, out-of-plane Walls A and B also participated in the response. Based on visual observations the participation of Wall A was due to both global rocking as well as the local rocking of pier P1-7. In particular the vertical displacement associated with these modes lifted up portions of Wall A (see Figure C.54). In the case of Wall B, the increased sliding deformation of Wall 1 acted to punch the lower eight courses of pier P1-6 through Wall B (see Figure C.54). Figure C.57 shows a photograph of this region following Test Run 19. Although heavy damage can be seen in this location, the connection between the walls was still intact above this point. In fact, the portion of Wall B located below the horizontal cracks along the top of piers PB-8 and PB-9 was visibly rocking out-of-plane during loading in the positive direction (see Figure C.54).

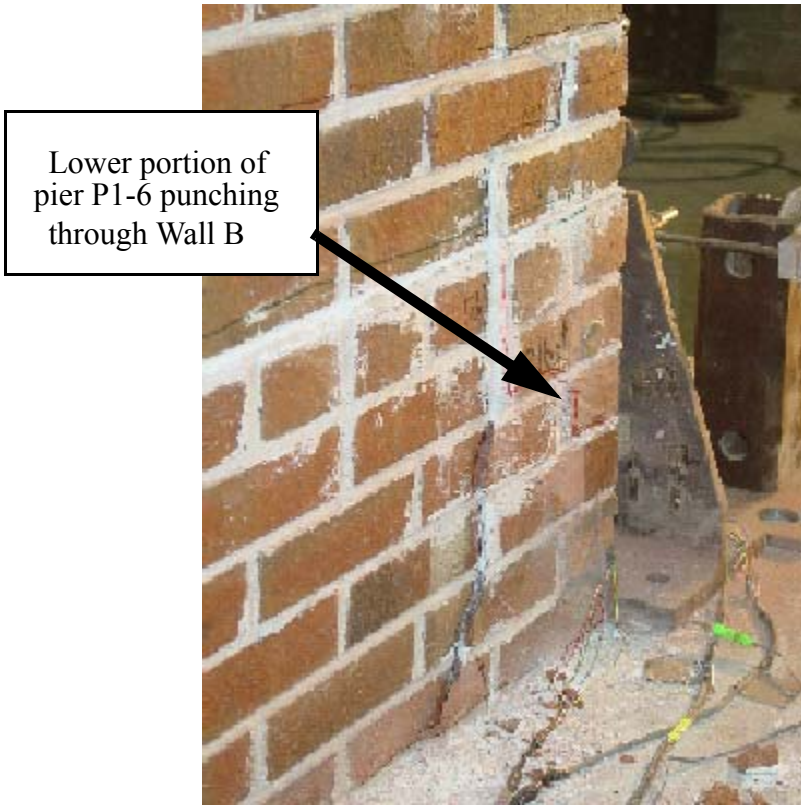

Figure C.57 Photograph showing the damage to the lower corner between Walls 1 and B following Test Run 19.

Figure C.58 shows a plot of the base strains recorded at peak positive displacement during Cycle 19a. The strain profiles shown in the figure are consistent with the observed local rocking behavior of pier P1-7 and the participation of pier PA-7. The relatively small strains measured in pier P1-6 and PB-10 are attributed to an increase in sliding behavior as well as the large amount of damage observed directly adjacent to the strain gages.

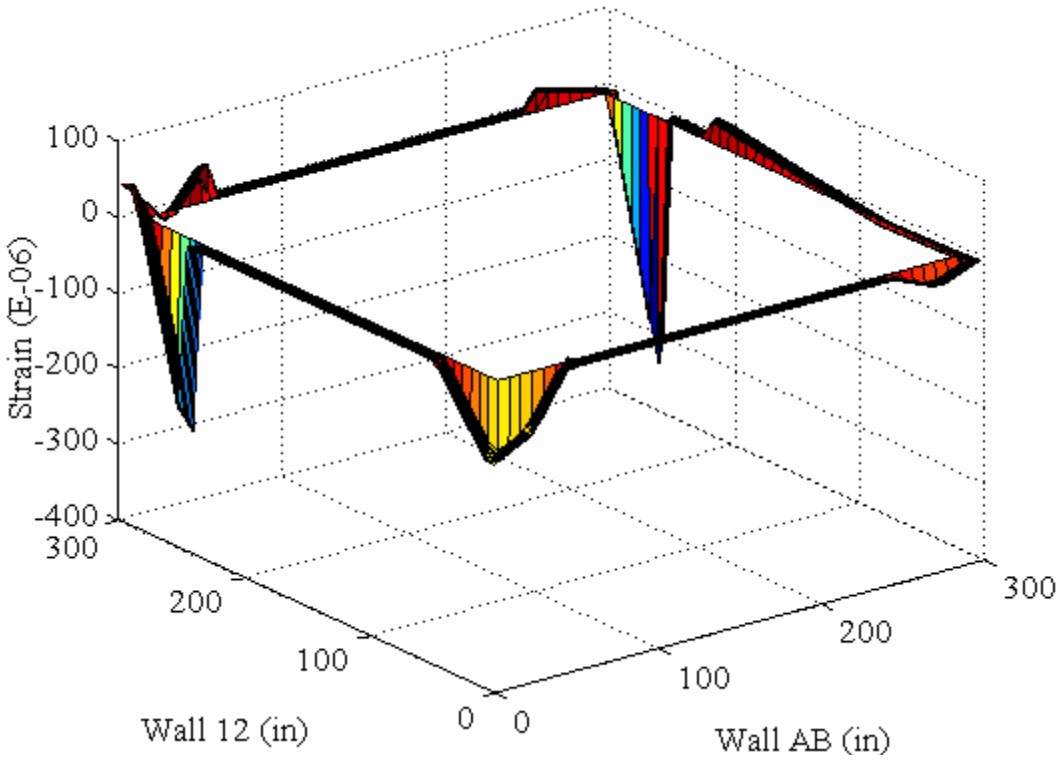

Figure C.58 Base strains recorded at peak positive displacement (Cycle 19a).

Figure C.59 shows an exaggerated schematic illustrating the behavior of Wall 1 in the negative direction (note that the location of the LVDT reference points are also shown). As apparent from this figure, pier P1-7 underwent a major change in behavior during the Group 3 cycles in the negative direction. During the initial portion of Cycle 18a, a horizontal crack formed along the top of the pier and propagated into Wall A. Following the formation of this crack pier P1-7 was visibly rocking. As the wall was displaced further the development of a diagonal crack was observed in the center of the pier. This crack did not propagate substantially during Cycle 18b; however, it fully developed during Cycle 19a.

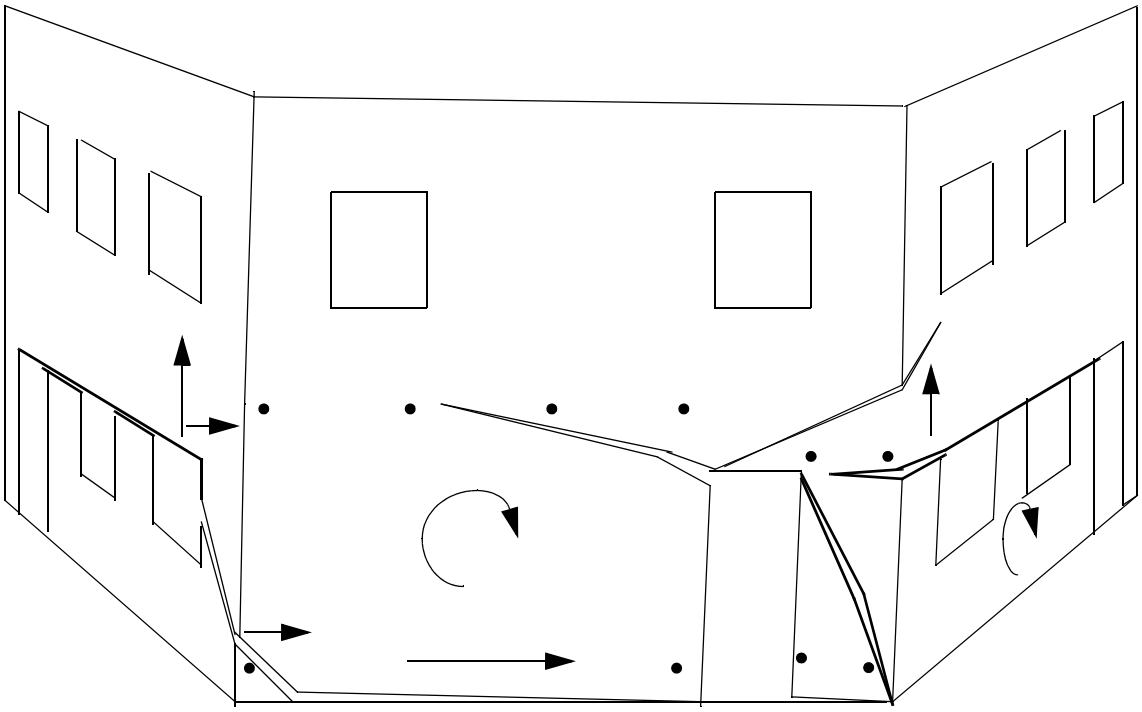

Figure C.59 Exaggerated schematic illustrating the behavior of Wall 1 and out-of-plane Walls A and B in the negative loading direction during the Group 3 cycles.

Based on the observed evolution from rocking deformation to diagonal cracking it is likely that the vertical stress in pier P1-7 increased during the Group 3 cycles. This increase was likely caused by two reasons: (1) in the negative loading direction overturning moment placed this pier into additional compression and (2) the observed local rocking of pier P1-7 caused a vertical displacement which lifted up a portion of Wall A thus increasing the vertical stress in the pier. In addition, the presence of the vertical reinforcement strips also could have promoted a diagonal tension failure since they strengthened the rocking mode.

Aside from the change in behavior of pier P1-7, the response of Wall 1 was very similar to the behavior observed during the Group 2 cycles. That is, the primary mechanism was the combined rocking/sliding of pier P1-6. However, based on visual

observations and the energy dissipation and residual displacement displayed during the Group 3 cycles (see Figures C.11 through C.13), the sliding deformation of pier P1-6 was likely far greater than the rocking deformation.

During the Group 3 cycles, the participation of Wall B was similar to that observed during the Group 2 cycles. Specifically, the portion of Wall B above the first floor piers was lifted up; however, the magnitude of this uplift diminished from previous cycles. This indicated that pier P1-6 displayed a lower level of rocking deformation but was still engaging a large portion of Wall B as a flange. In addition, the offset in Wall B (discussed in Section C.3.2.1) was continually increasing during this level of testing. Following Test Run 19 the offset had increased to nearly 0.5 in. Similar to observations made during the Group 2 cycles, this offset was confined to within 3 ft of the corner between Wall 1 and Wall B.

C.3.3.2 Behavior of External Reinforcement

During the Group 3 cycles no visual damage was observed in any of the FRP overlays applied to the inside of Wall 1. The behavior of several FRP strips were monitored throughout loading by strain gages placed directly adjacent to existing cracks (see Appendix A).

Figures C.60 and C.61 show the recorded strains in the vertical FRP strips versus base shear for Cycle 19a. In general, the response shown in these figures is consistent with past cycles. That is, the measured strains clearly indicate that vertical strips V1 through V3 were engaged due to the global rocking of Wall 1 in the positive direction. Furthermore, the strains measured in vertical strips V4 through V7 indicate that these

strips resisted the local rocking deformation of pier P1-6 in the negative direction.

Figures C.62 and C.63 show the recorded strains in the horizontal FRP strips versus base shear for Cycle 19a. From Figure C.62 it is apparent that the horizontal strips above the door opening in Wall 1 were resisting the lateral deformation of the this spandrel. From Figure C.46 it is apparent that strips H4 and H5 were active in tying the base of pier P1-6 together. In addition, this figure indicates that the maximum strains recorded during Cycle 19a were smaller than during past cycles (see Figures C.26 and C.45). This is consistent with the formation of a smooth sliding crack which acted as a fuse thus limiting the amount of strain in these strips.

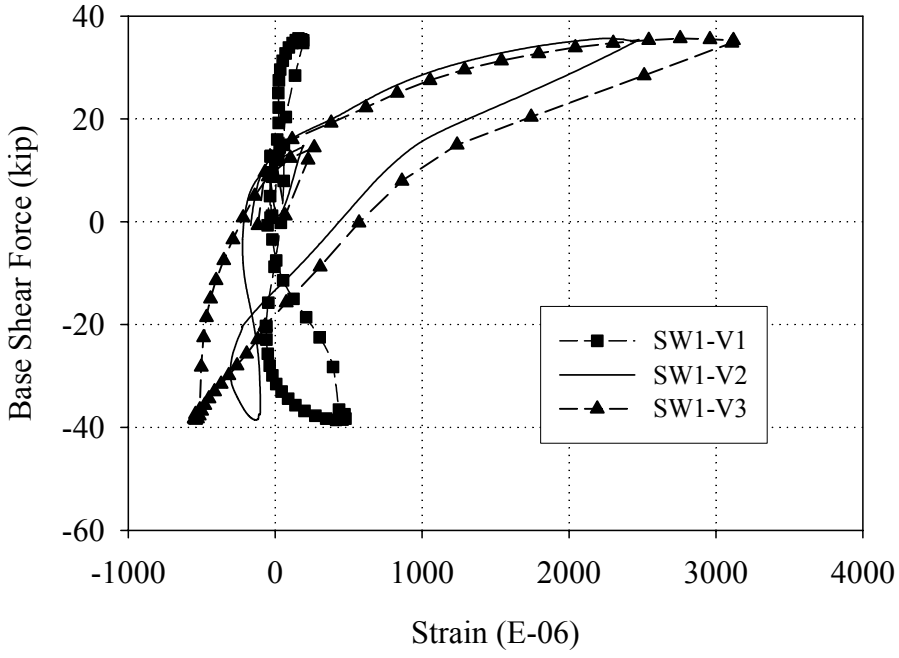

Figure C.60 Strains measured in the vertical FRP overlays applied to the inside of pier P1-7 versus base shear force (Cycle 19a).

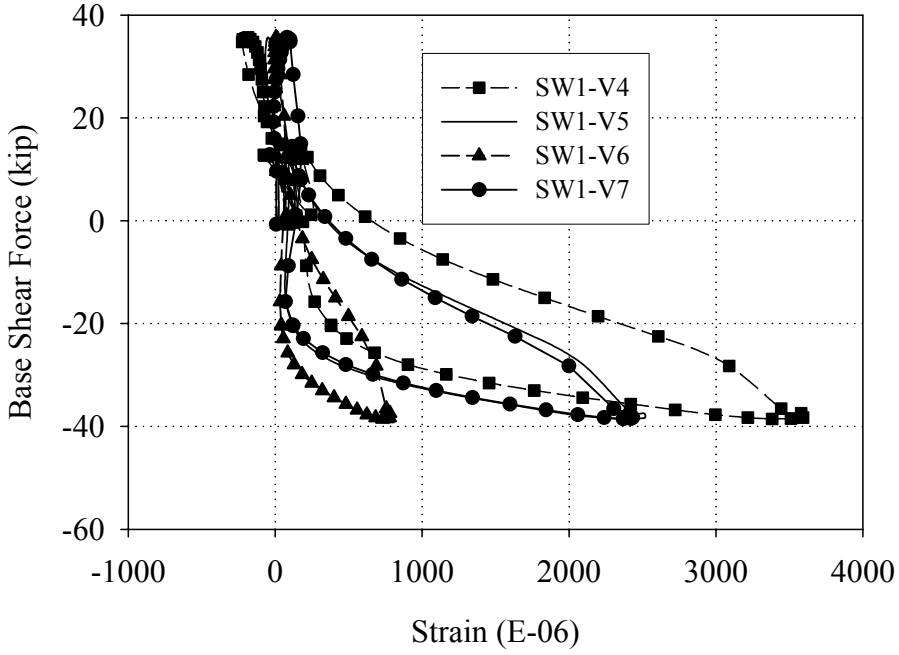

Figure C.61 Strains measured in the vertical FRP overlays applied to the inside of pier P1-6 versus base shear force (Cycle 19a).

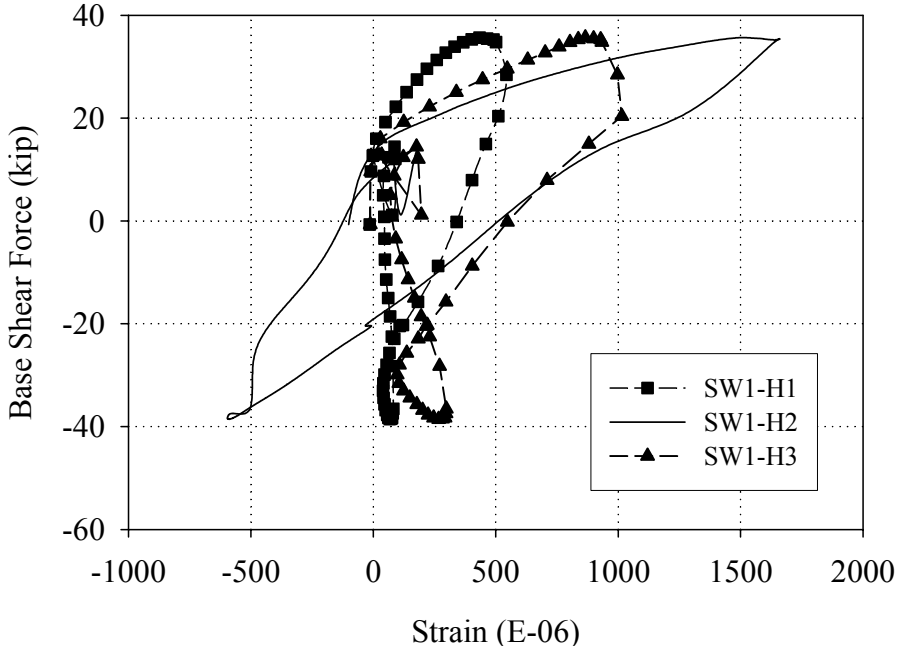

Figure C.62 Strains measured in the horizontal FRP overlays applied to the inside of spandrel P1-5 versus base shear force (Cycle 19a).

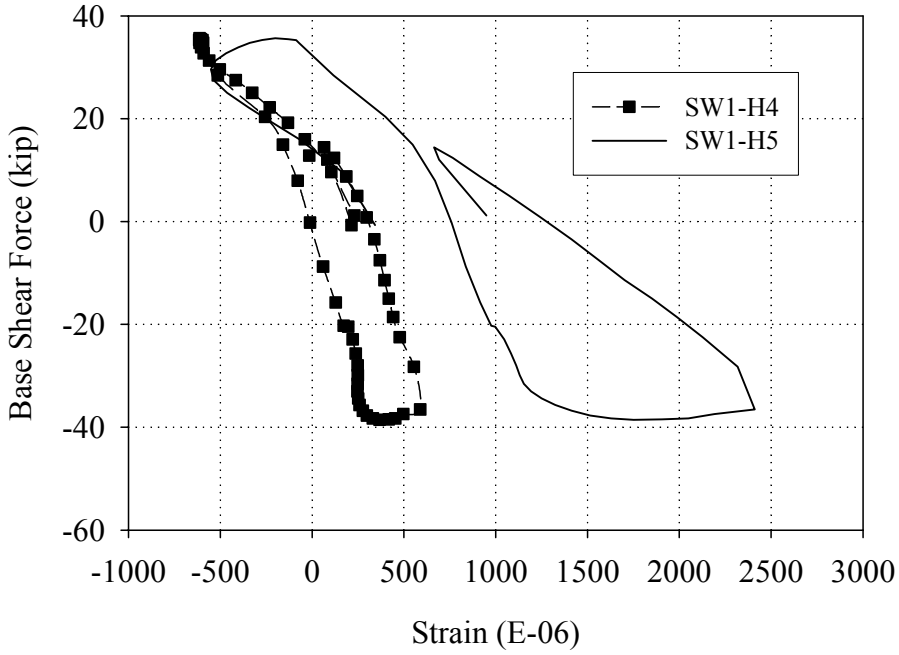

Figure C.63 Strains measured in the horizontal FRP overlays applied to the base of pier P1-6 versus base shear force (Cycle 19a).

C.3.3.3 Local Pier Behavior

Due to the observed crack opening of the first floor piers, the location of the LVDT reference points relative to the active crack is of paramount importance. As a result, the interpretation of LVDT measurements must utilize Figures C.54 and C.59, which show the location of the LVDTs in reference to the displaced shape. Since all of the piers displayed similar behavior during the Group 3 cycles, the data obtained during Cycle 19a will be used to illustrate the behavior of each pier.

Figures C.64 and C.65 show the readings obtained from the LVDTs attached to pier P1-6. Figures C.66 and C.67 show the readings obtained from the LVDTs attached to pier P1-7. In general, the response shown in these figures is consistent with past cycles. The reader is directed to Section C.3.2.3 for further discussion.

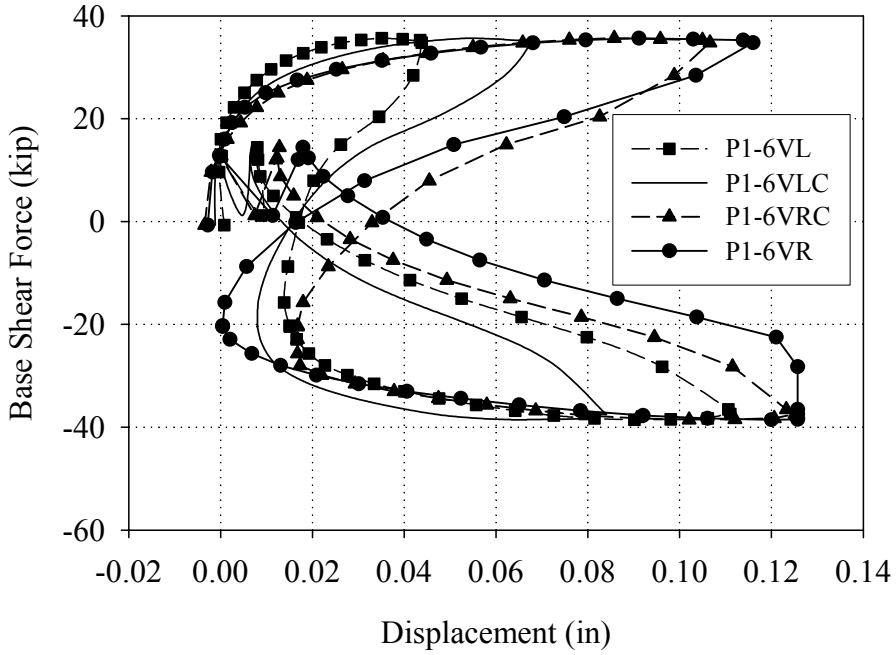

Figure C.64 Readings of the vertical LVDTs attached to pier P1-6 versus base shear force (Cycle 19a).

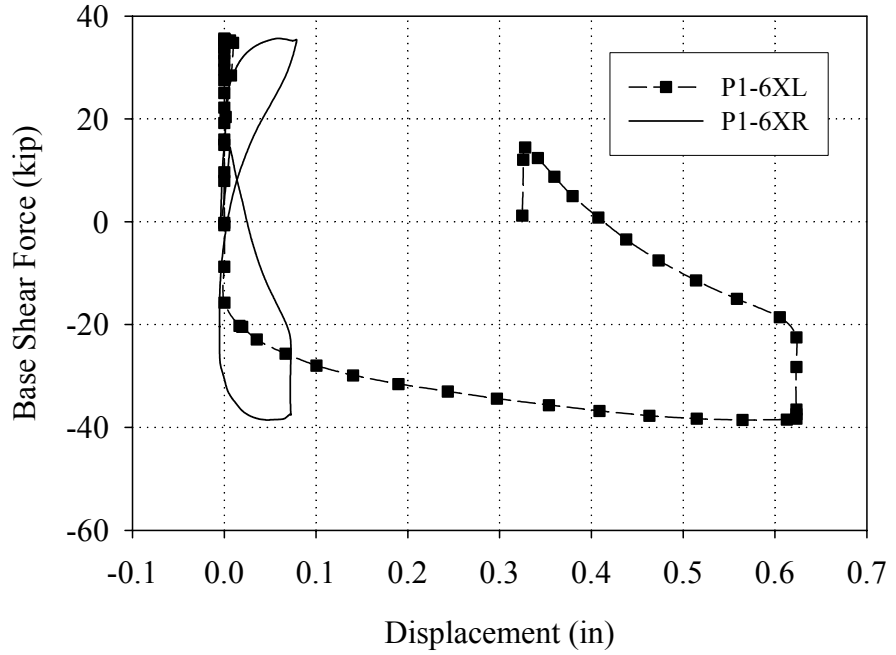

Figure C.65 Readings of the diagonal LVDTs attached to pier P1-6 versus base shear force (Cycle 19a).

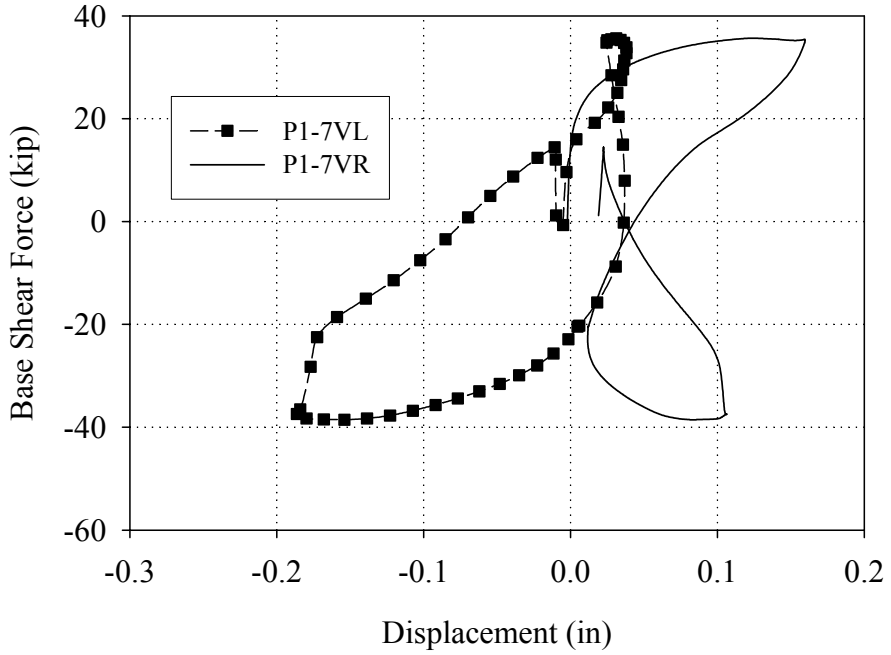

Figure C.66 Readings of the vertical LVDTs attached to pier P1-7 versus base shear force (Cycle 19a).

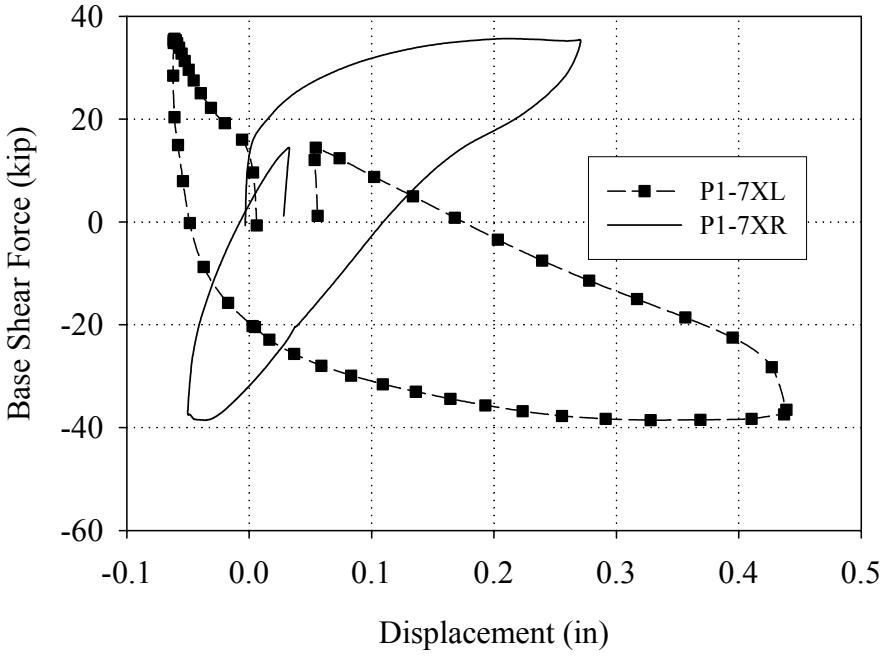

Figure C.67 Readings of the diagonal LVDTs attached to pier P1-7 versus base shear force (Cycle 19a).

APPENDIX D

EXPERIMENTAL RESULTS OF WALL 2

D.1 Introduction

The behavior of Wall 2 following the application of the Saint-Gobain bi-directional glass reinforcement system is discussed in this appendix. Details on the retrofit, test setup, instrumentation, and loading scheme can be found in Chapter 3. A summary of the displacements imposed on Wall 2 are shown in Table D.1 along with the test run and cycle designation. As apparent from the table, Wall 2 was subjected to at least two cycles at each displacement level, which allows degradation and damage accumulation to be assessed. However, for certain comparisons it was necessary to limit the number of cycles considered to one at each displacement level. In these cases the cycles in italics were used since these cycles were the most complete in terms of instrumentation and target displacements.

Table D.1. Summary of displacements imposed on Wall 2

Test Run	Cycle	Target Roof Displacement (in)	Target Second Floor Displacement (in)
11	*a*,b	+/- 0.02	+/- 0.012
12	*a*,b,c	+/- 0.04	+/- 0.032
13	*a*,b	+/- 0.06	+/- 0.048
14	a,*b*,c,e	+/- 0.1	+/- 0.08
15	*a*,b	+/- 0.15	+/- 0.12
16	*a*,b	+/- 0.25	+/- 0.2
17	a,b,*c*	+/- 0.375	+/- 0.311
18	*a*,b	+/- 0.5	+/- 0.41
19	*a*,b	+/- 0.75	+ 0.63, -0.623

The appendix begins with a discussion of the general force-displacement behavior of Wall 2 for both the first and second stories. This behavior is quantified for each test run in terms of secant stiffness, secant fundamental mode shape, energy dissipation and residual displacement. Next the damage progression and wall behavior are described including discussions of reinforcement behavior and observed damage. For this task, the behavior of the structure was divided into three portions: Group 1 cycles (Test Runs 11 through 14), Group 2 cycles (Test Runs 15 through 17) and Group 3 cycles (Test Runs 18 through 19). The appendix concludes with a brief summary of the behavior of Wall 2.

D.2 Force-Displacement Response

The lateral displacement of Wall 2 was measured through LVDTs referenced to the structure at the second floor and roof levels. Due to the importance of these measurements, linear potentiometers were also employed for redundancy. During Test

Runs 18 and 19 the stroke of the second floor LVDT was exhausted and thus the readings of the potentiometers were used. Figures D.1 through D.3 show plots of roof displacement versus base shear for Test Runs 11 through 14, Test Runs 11 through 17, and all of the cycles conducted on Wall 2, respectively.

From these figures it is apparent that the response of Wall 2 was essentially linear elastic for cycles up to 0.15 in roof displacement. Following these cycles the response of the wall became nonlinear with a significant amount of pinching. This type of nonlinear-elastic response is consistent with rocking deformation. In addition, negligible degradation was observed for the redundant cycles conducted at each displacement level in terms of peak resistance. As the roof displacement level increased the base shear capacity of the wall remained relatively constant after 0.25 in roof displacement for both the positive and negative directions. In addition, the response of the wall was fairly symmetric in both directions.

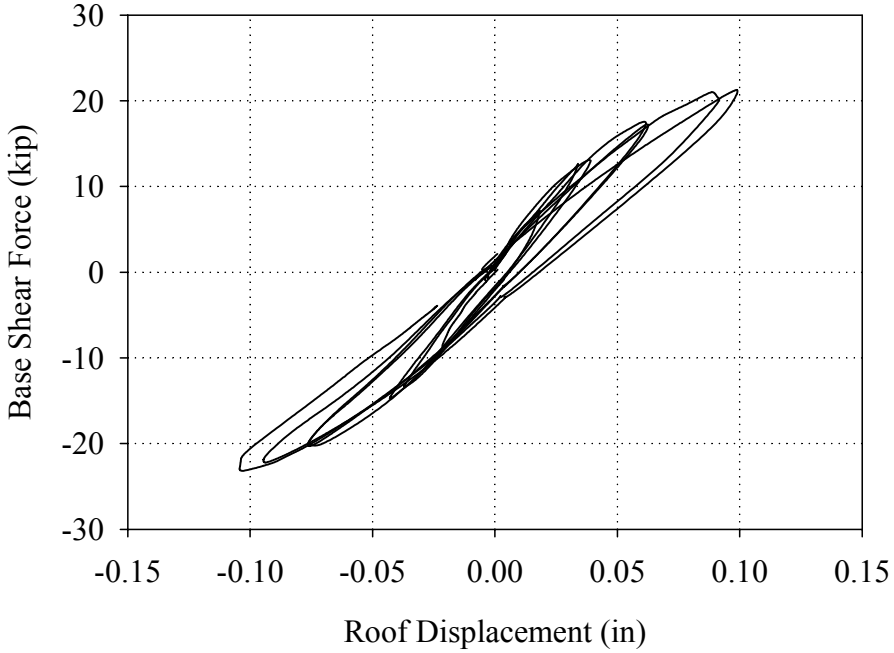

Figure D.1. Base shear versus roof displacement response of Wall 2 recorded during Test Runs 11 through 14.

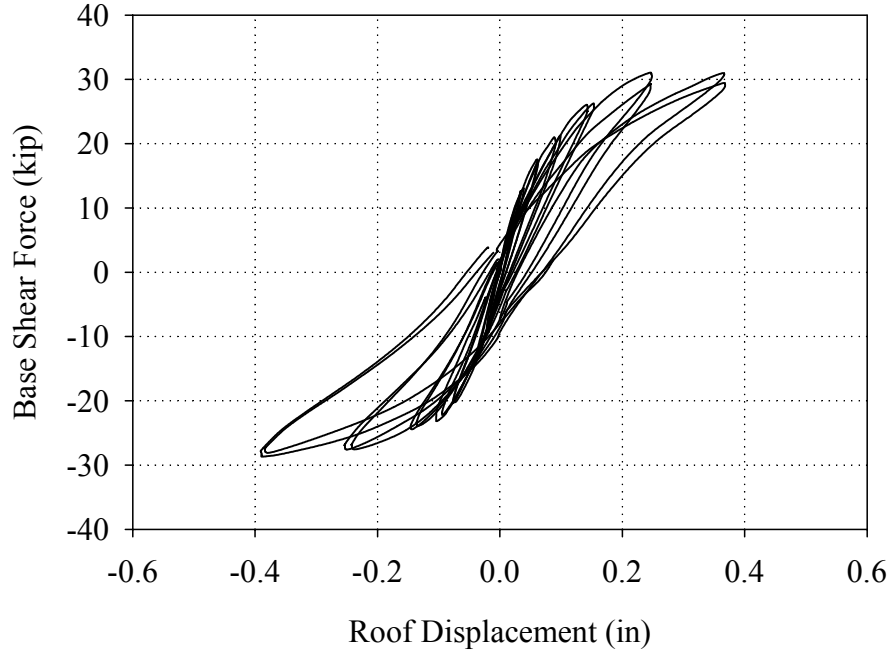

Figure D.2. Base shear versus roof displacement response of Wall 2 recorded during Test Runs 11 through 17.

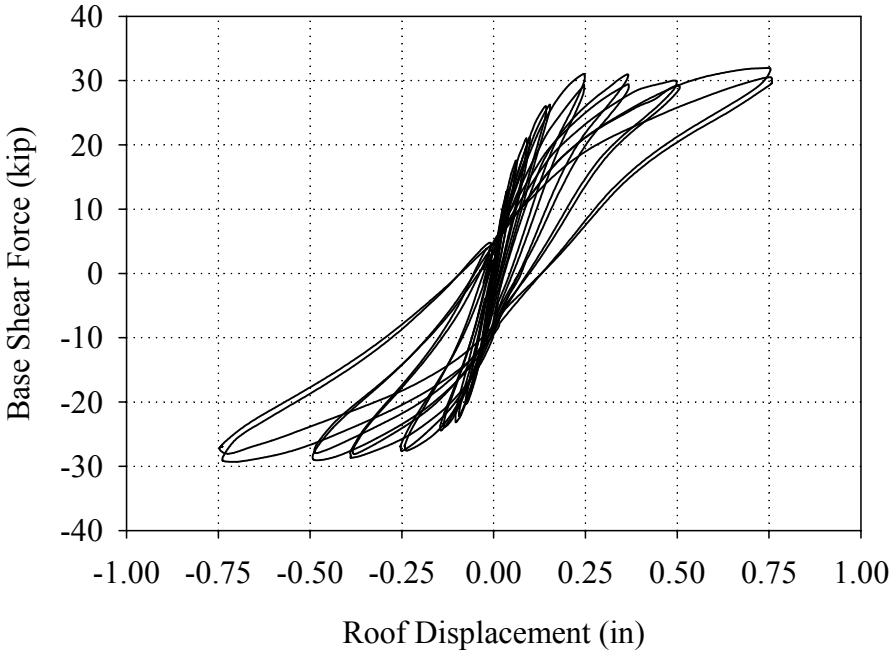

Figure D.3. Base shear versus roof displacement response of Wall 2 recorded during Test Runs 11 through 19.

The force-displacement response of the first story of Wall 2 is shown in Figures D.4 through D.6 for Test Runs 11 through 14, Test Runs 11 through 17, and all of the cycles conducted on Wall 2, respectively. Figures D.7 through D.9 show the force-displacement response of the second story of Wall 2 for Test Runs 11 through 14, Test Runs 11 through 17, and all of the cycles conducted on Wall 2, respectively.

In general these figures show that both the first and second stories of Wall 2 exhibited nonlinear behavior with a significant amount of pinching. However, based on these figures it is clear that the small amount of energy dissipation shown in Figures D.2 and D.3 was focused on the first story of Wall 2. The somewhat erratic response of the second story (measured during the larger cycles) is attributed to a small amount of rotation of the first story, which resulted in an apparent second story drift.

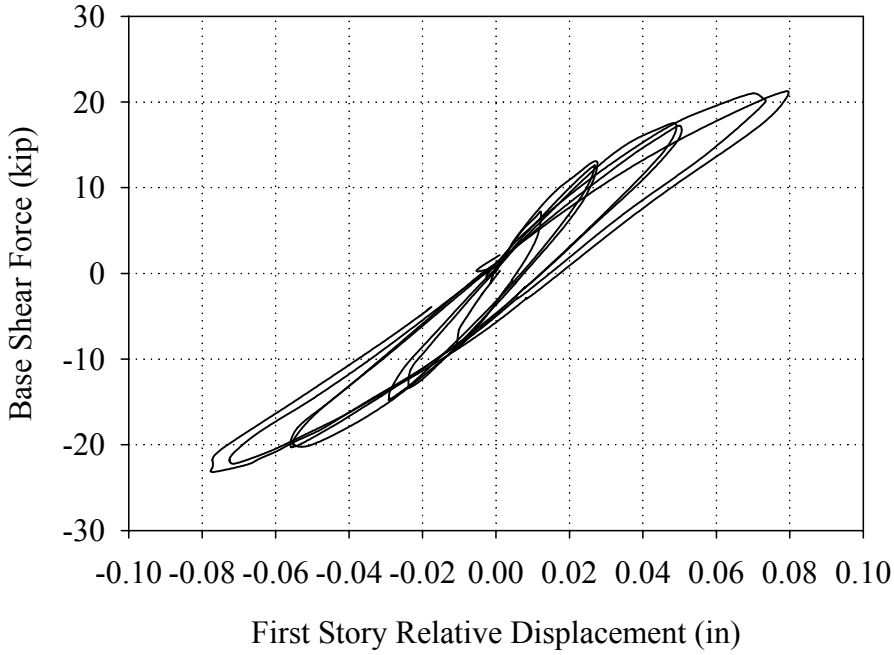

Figure D.4. Force-displacement response of the first story of Wall 2 recorded during Test Runs 11 through 14.

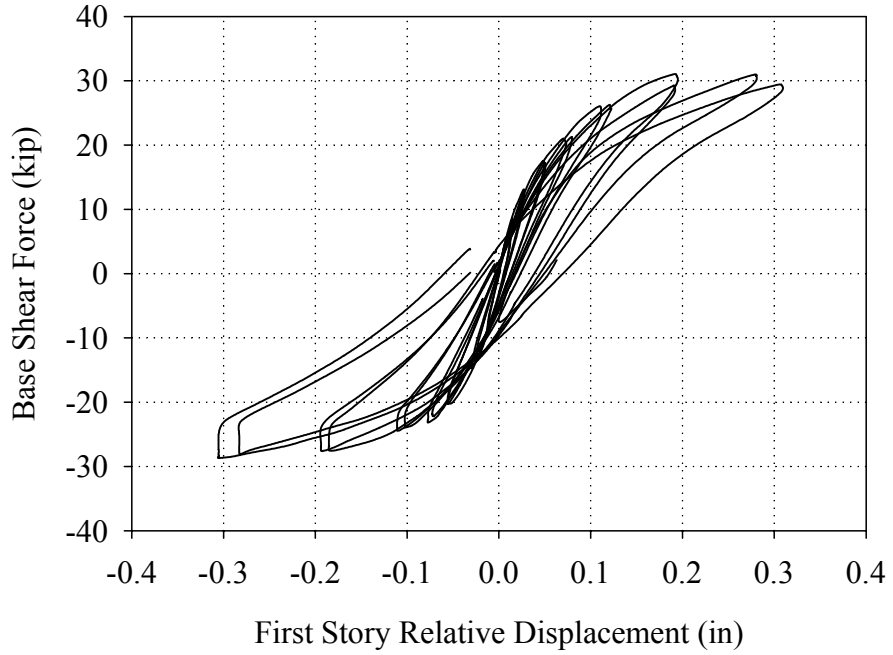

Figure D.5. Force-displacement response of the first story of Wall 2 recorded during Test Runs 11 through 17.

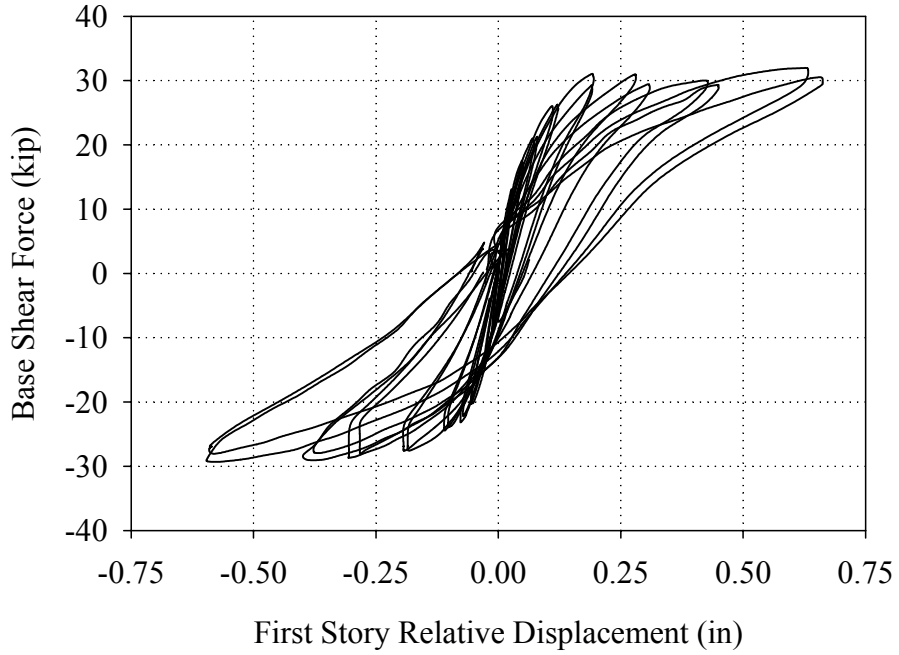

Figure D.6. Force-displacement response of the first story of Wall 2 recorded during Test Runs 11 through 19.

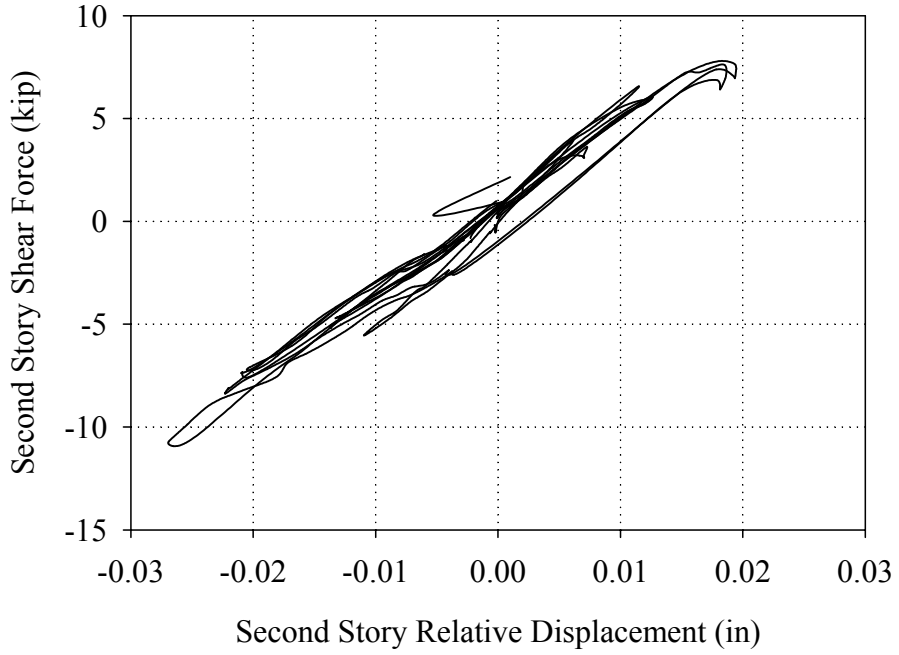

Figure D.7. Force-displacement response of the second story of Wall 2 recorded during Test Runs 11 through 14.

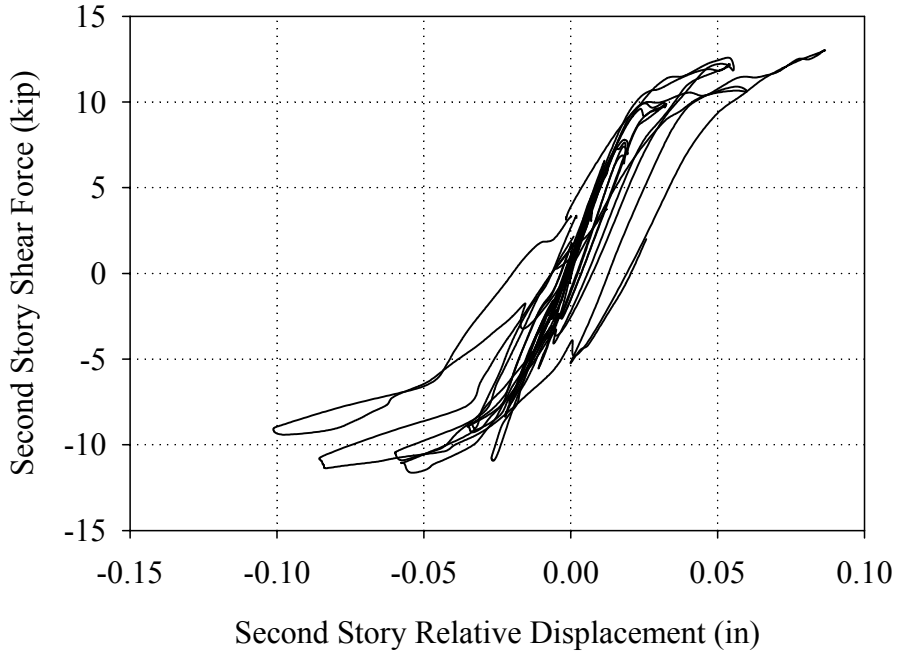

Figure D.8. Force-displacement response of the second story of Wall 2 recorded during Test Runs 11 through 17.

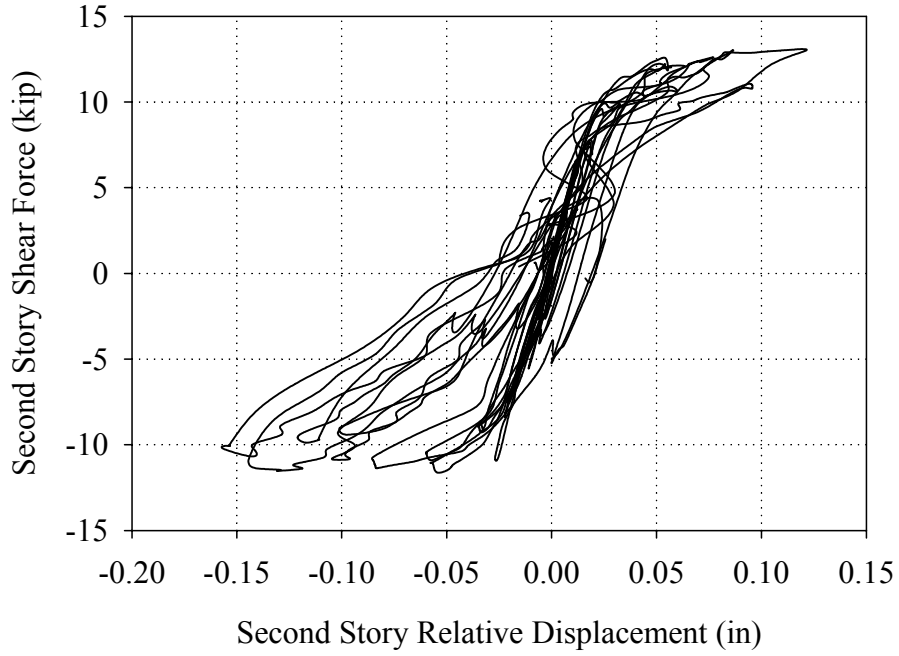

Figure D.9. Force-displacement response of the second story of Wall 2 recorded during Test Runs 11 through 19.

D.2.1 Stiffness and Mode Shapes

For each of the test runs conducted on Wall 2, the secant stiffness' were determined for both the first and second stories. The secant stiffness represents an average tangent stiffness, and as such can be used as an indication of damage. The stiffness' were taken as the slope of a straight line connecting the peak displacement point (both positive and negative) and the point at which the plot crosses the x-axis. This procedure is discussed in detail in Appendix B. Table D.2 shows the calculated secant stiffness for both the first and second stories of Wall 2 in the positive and negative direction for each test run.

From this table it is apparent that the secant stiffness of both the first and second stories decreased during each cycle. In addition, this decrease was similar for each story and in each loading direction. This suggests a somewhat balanced damage progression for Wall 2.

Table D.2. Secant stiffness of Wall 2 for each Test Run

Test Run	Story	Positive Secant Stiffness (kip/in)	Negative Secant Stiffness (kip/in)
11	First	554	658
	Second	536	514
12	First	461	507
	Second	414	383
13	First	345	463
	Second	293	340
14	First	251	381
	Second	270	362
15	First	227	321
	Second	193	232
16	First	146	208
	Second	122	180
17	First	83	135
	Second	76	107
18	First	54	140
	Second	55	117
19	First	50	100
	Second	38	72

To gain more insight into the seismic behavior of Wall 2, the secant fundamental mode shapes were determined for each test run and are listed in Table D.3 (see Appendix B for a detailed description of this calculation and associated assumptions). Figure D.10 shows the calculated fundamental secant mode shapes normalized to roof displacement for all of the cycles conducted on Wall 2.

Table D.3. Fundamental secant mode shapes of Wall 2 normalized to 1.0.

Test Run	Positive Fundamental Secant Mode Shape	Negative Fundamental Secant Mode Shape
11	$\{1.0, 0.76\}^T$	$\{1.0, 0.70\}^T$
12	$\{1.0, 0.74\}^T$	$\{1.0, 0.70\}^T$
13	$\{1.0, 0.78\}^T$	$\{1.0, 0.75\}^T$
14	$\{1.0, 0.80\}^T$	$\{1.0, 0.78\}^T$
15	$\{1.0, 0.79\}^T$	$\{1.0, 0.76\}^T$
16	$\{1.0, 0.79\}^T$	$\{1.0, 0.80\}^T$
17	$\{1.0, 0.82\}^T$	$\{1.0, 0.79\}^T$
18	$\{1.0, 0.88\}^T$	$\{1.0,0.86\}^T$
19	$\{1.0, 0.85\}^T$	$\{1.0, 0.84\}^T$

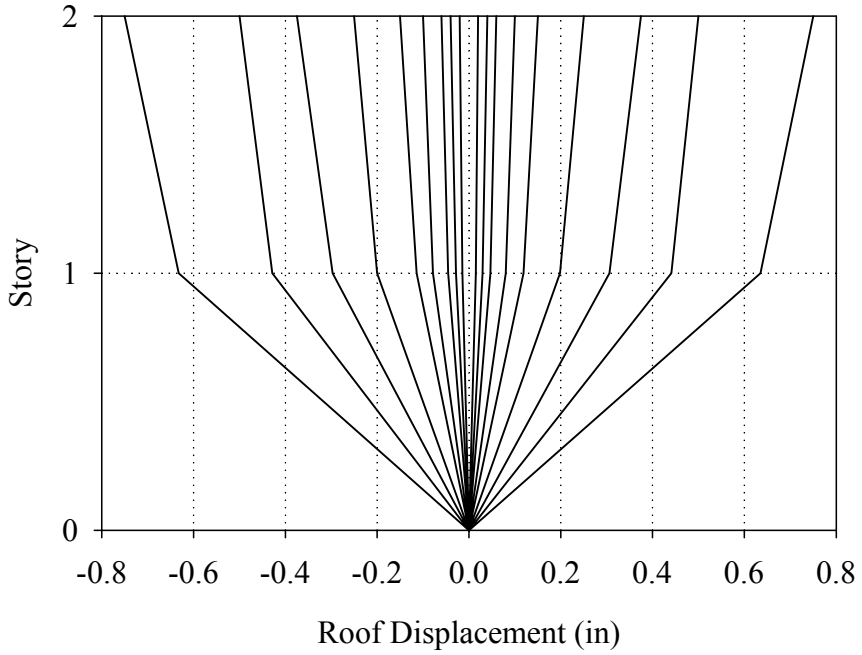

Figure D.10. Fundamental secant mode shapes of Wall 2 normalized to target roof displacement.

From these figures and tables, it is apparent that the fundamental mode shape of Wall 2 changed slightly as the roof displacement was increased. Specifically, Wall 2 began to form a soft story in both loading directions. This evolution of the fundamental mode shape was fairly moderate. This suggests that the behavior of Wall 2 did not undergo any substantial changes throughout loading. This is consistent with the relatively constant force-displacement behavior of the wall as the amplitude of the cycles increased.

D.2.2 Energy Dissipation

The energy dissipated by each story of Wall 2 was calculated for each of the cycles conducted. This was accomplished by numerically integrating the force-displacement plots shown in Figures D.4 through D.9 (see Appendix B). For comparison purposes, the calculated values were divided by the maximum possible energy dissipated, which was defined as the area of a rectangle encompassing the force-displacement plot. Figure D.11 shows the percentage of energy dissipated by each story versus roof displacement and Figure D.12 shows the actual energy dissipated by each story versus roof displacement.

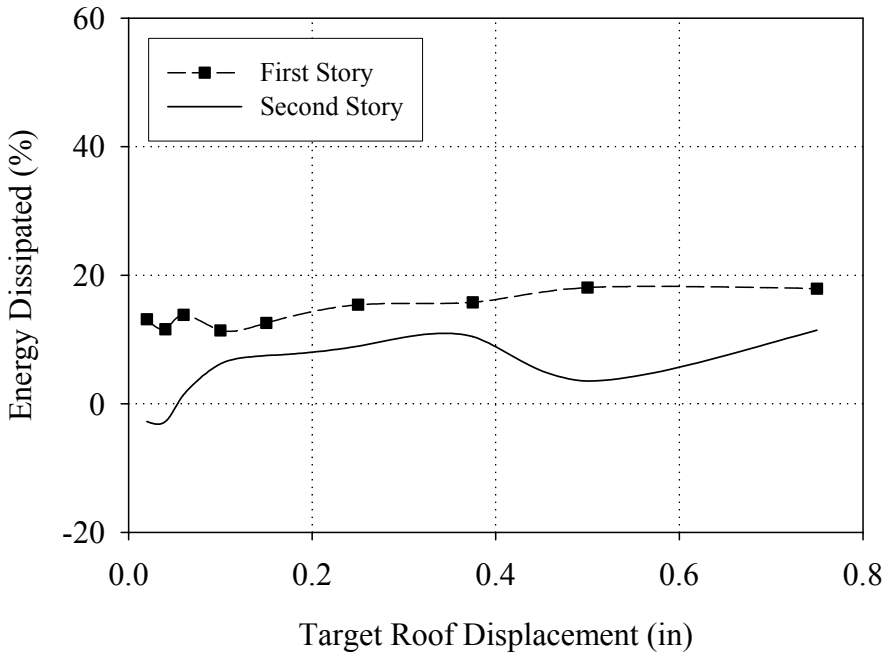

Figure D.11. Percentage of energy dissipated by each story of Wall 2 versus target roof displacement.

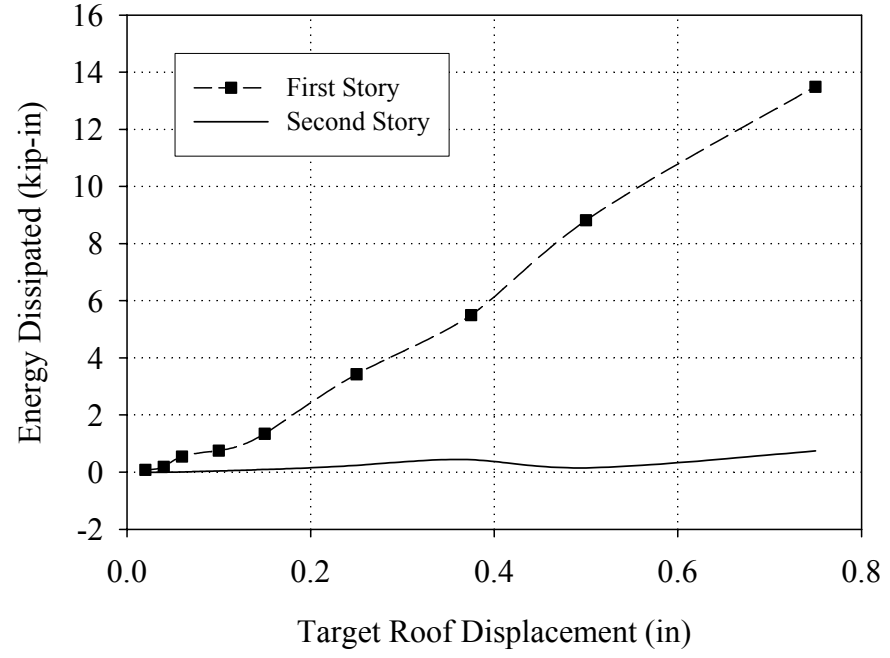

Figure D.12. Energy dissipated by each story of Wall 2 versus target roof displacement.

As apparent from Figure D.12, the percentage of energy dissipated by both the first and second stories remained relatively constant at approximately 15-20% throughout loading. Again, this suggests that the behavior of both stories remained relatively constant throughout loading. From Figure D.12 it is apparent that the first story of Wall 2 dissipated approximately 15 times more energy than the second story. This indicates that majority of the damage in Wall 2 focused on the first story, which is consistent with the imposed displacements.

D.2.3 Residual Displacement

The residual displacement of the first story of Wall 2 was calculated for each test run according to the procedure outlined in Appendix B. Due to the small displacements imposed on the second story the residual displacements measured were negligible and are not discussed. The calculated first story residual displacements are presented in Table D.4 as a percentage of the story drift. In addition, Figure D.13 shows the residual displacement for the first story (as a percentage of the first story drift) versus first story drift.

Table D.4. Residual displacement of Wall 2

Test Run	+ Residual Displacement (% of Story Drift)	- Residual Displacement (% of Story Drift)
11	35	33
12	24	24
13	33	30
14	29	24
15	19	24
16	23	25
17	26	28
18	27	32
19	26	32

From this figure and Table D.4 it is apparent that for small roof displacements (i.e. less than 0.1 in) the residual displacement of the first story was somewhat erratic. This is attributed to the small values of the displacements during these cycles. However, as the roof displacement increased the residual displacements in both directions remained fairly constant at approximately 30% of the first story displacement. This suggests that a moderate amount of sliding deformation occurred in first floor during the larger cycles. In addition, this supports the contention that the behavior of Wall 2 remained relatively constant throughout loading. This is consistent with the discussion of secant fundamental mode shapes and energy dissipation in the previous sections.

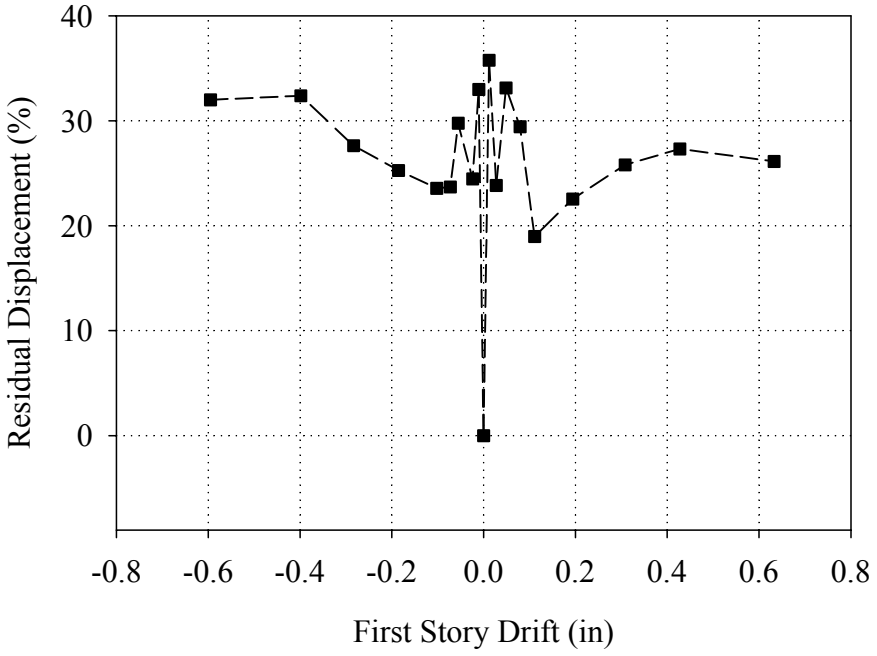

Figure D.13. Residual displacement as a percentage of story drift for the first story of Wall 2 versus story drift.

D.3 Damage Progression and Wall Behavior

The following sections describe the behavior of Wall 2 during each of the three groups of cycles defined in Section D.1. For each group of cycles the general behavior of the wall is first described in terms of crack pattern, visually observed behavior, and representative instrumentation. Next, a description of the external reinforcement behavior is presented including strain gage readings. Finally, the specific behavior of the in-plane piers are described and representative plots of the instrumentation attached to the piers are presented.

D.3.1 Group 1 Cycles (Test Run 11-Test Run 14)

D.3.1.1 Overall Wall Behavior

During the Group 1 cycles no new cracks were observed in Wall 2 or out-of-plane Walls A and B. Figures D.14 through D.16 illustrate the crack pattern in these walls following the Group 1 cycles. The cracks shown in these figures were observed during the in-plane testing of Walls 1 and 2 prior to strengthening. For a complete discussion of the behavior of Wall 2 during the initial testing the reader in directed to Tianyi (2003).

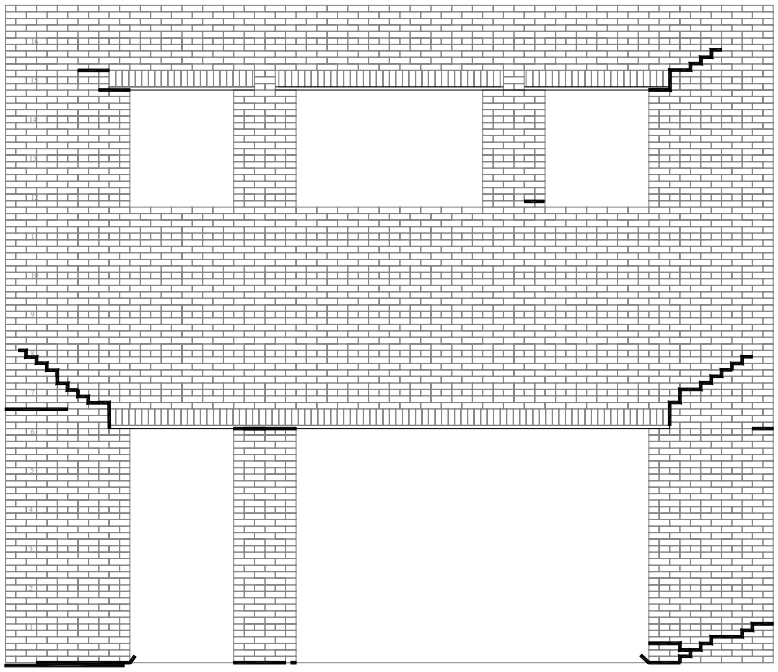

Figure D.14. Crack pattern of Wall 2 following the Group 1 cycles.

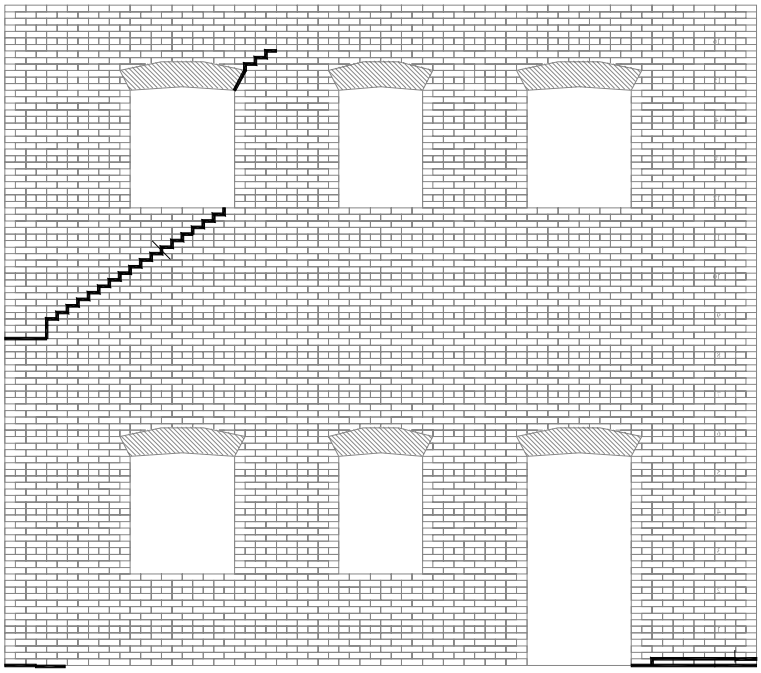

Figure D.15. Crack pattern of Wall A following the Group 1 cycles.

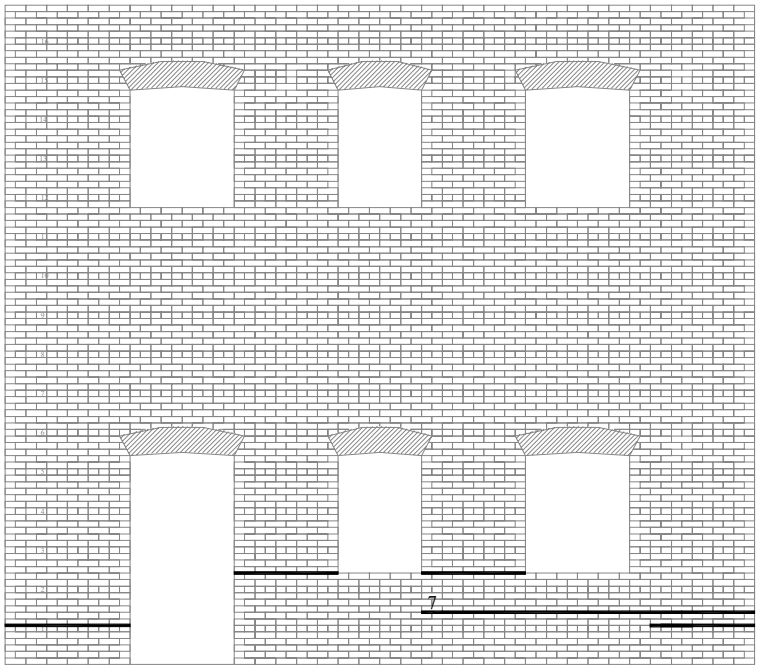

Figure D.16. Crack Pattern of Wall B following the Group 1 cycles.

Figure D.17 shows a schematic illustrating the behavior of Wall 2 and out-of-plane Walls A and B in the positive direction during the Group 1 cycles (note that the location of the LVDT reference points are also shown). As apparent from this figure the deformation of Wall 2 was essentially focused on the first story piers. Based on visual observations, these piers displayed low-level rocking deformation during these cycles. In addition, based on Figure D.17 it is apparent that piers P2-7 and P2-9 displayed different effective heights. That is, the active rocking crack at the top of pier P2-7 extended diagonally upwards from the adjacent door opening where as the active rocking crack at the top of pier P2-9 was essentially horizontal. This is consistent with the behavior of the test structure prior to strengthening.

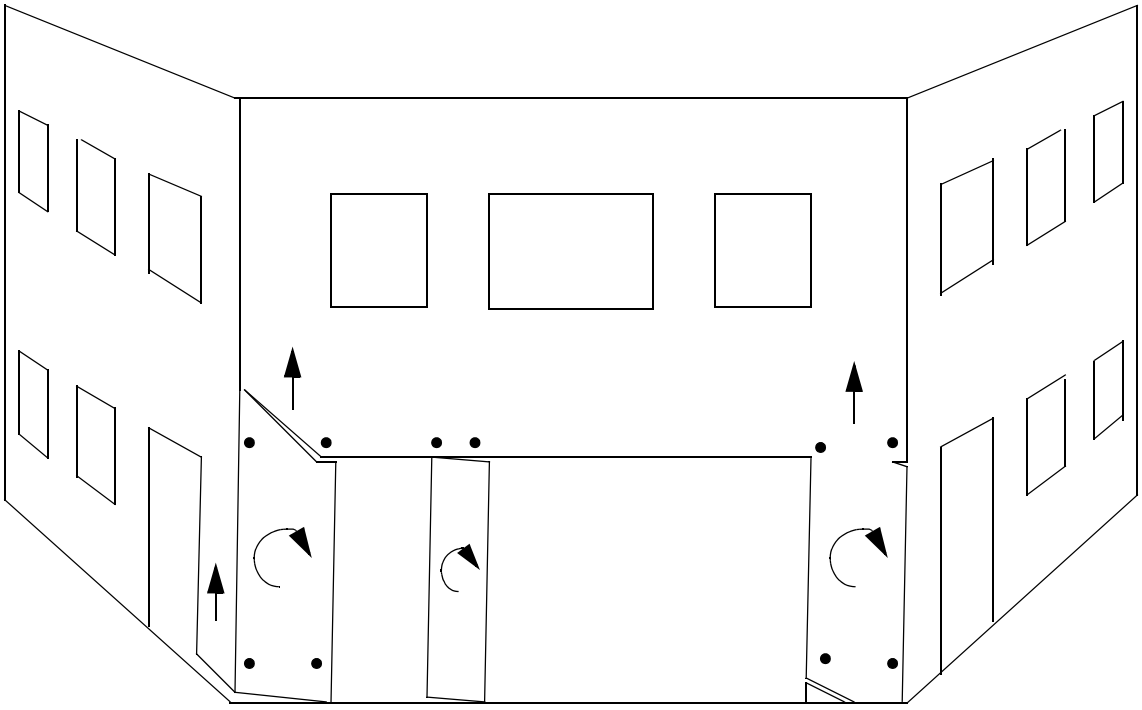

Figure D.17. Exaggerated schematic of the observed behavior of Wall 2 and out-of-plane Walls A and B in the positive loading direction during the Group 1 cycles.

Figure D.18 shows the base strains recorded at peak positive displacement during Cycle 14e. In general, the recorded strain profiles of piers P2-7 and P2-9 are consistent with the observed rocking deformation. In addition, the strain profiles of out-of-plane piers PA-10 and PB-7 indicate that these piers participated to a large degree in the in-plane response of Wall 2. Specifically, the tensile strains measured in pier PA-10 suggest that this pier was being lifted up due to the rocking of adjacent pier P2-7 (see Figure D.17). The compressive strains measured in pier PB-7 suggest that this pier was participating by resisting compressive strains induced by the low-level rocking of adjacent pier P2-9. However, the reader is cautioned that due to large variations in material properties, numerous cracks, and uncertainties inherent in strain gage readings obtained from masonry, only a qualitative discussion of this strain data is appropriate.

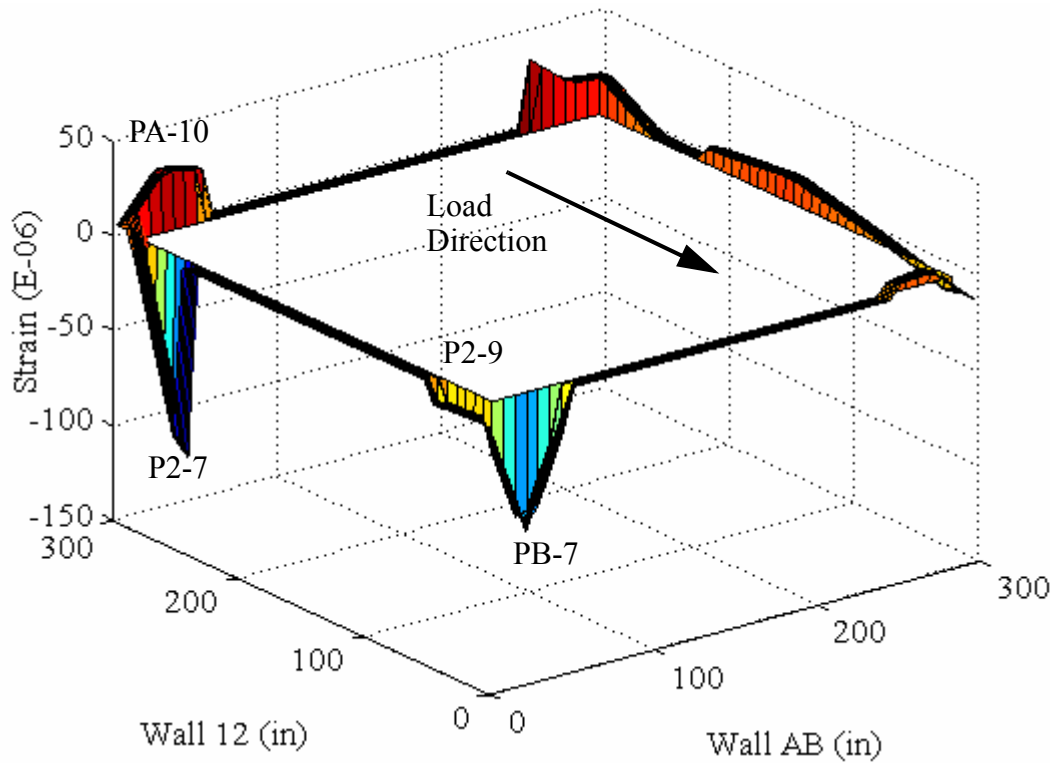

Figure D.18. Base strains recorded at peak positive displacement (Cycle 14e).

Figure D.19 shows a schematic illustrating the observed behavior of Wall 2 and out-of-plane Walls A and B during the Group 1 cycles in the negative direction (note that the location of the LVDT reference points are also shown). From this figure it is clear that the response of Wall 2 in the negative direction was essentially identical to the observed response in the positive direction. That is, the majority of the deformation of Wall 2 was due to the low-level rocking deformation of the first story piers. In addition, the unsymmetrical nature of the active cracks along the top of piers P2-7 and P2-9 were identical to the active crack pattern in the positive direction (see Figure D.17).

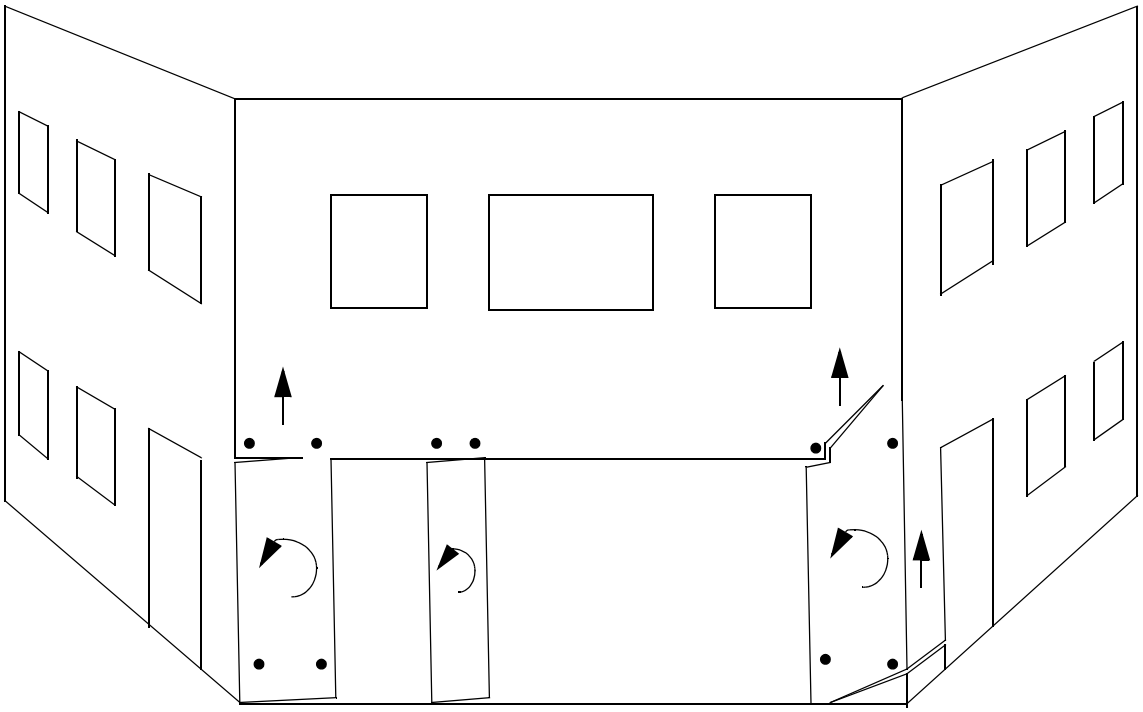

Figure D.19. Exaggerated schematic of the observed behavior of Wall 2 and out-of-plane Walls A and B in the negative loading direction during the Group 1 cycles.

Figure D.20 shows the base strains recorded at peak negative displacement during Cycle 14e. The strain profiles illustrated by this figure are consistent with the observed low-level rocking of piers P2-7 and P2-9. Similar to the positive loading direction, the strain profiles measured in out-of-plane piers PA-10 and PB-7 suggest that the behavior of these piers was similar to the positive direction.

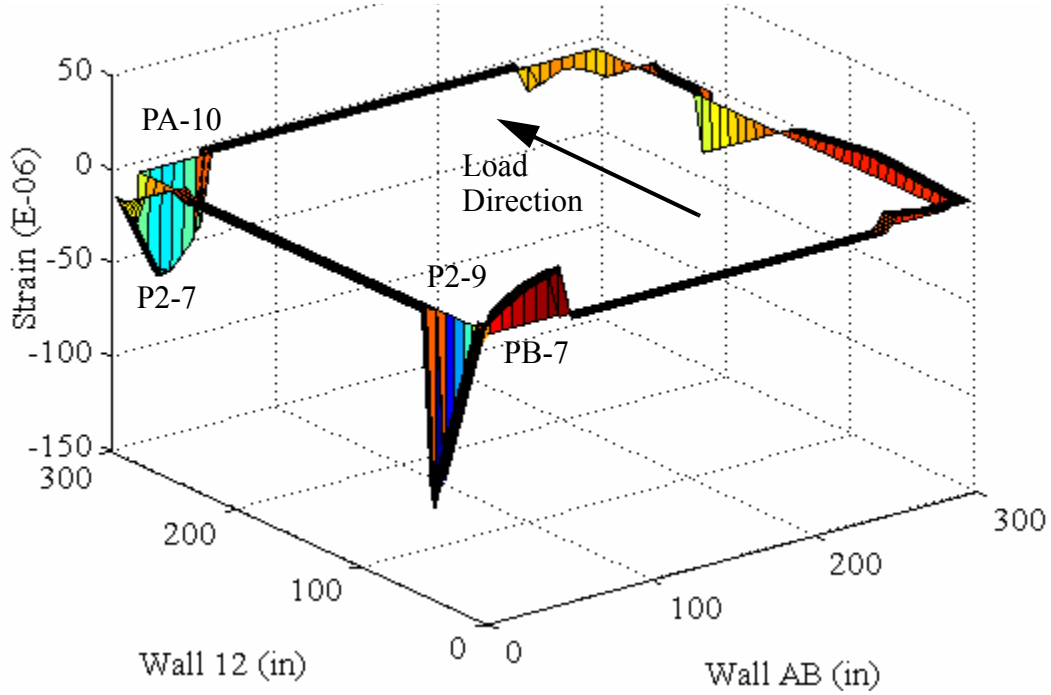

Figure D.20. Base strains recorded at peak negative displacement (Cycle 14e).

D.3.1.2 Behavior of External Reinforcement

During this level of testing several hairline cracks were observed in the external reinforcement along the top of the first story piers. Figure D.21 shows a schematic illustrating the crack pattern in the external reinforcement following the Group 1 cycles. As apparent from the figure, the observed cracks in the reinforcement formed directly adjacent to existing cracks in the masonry substrate (see Figures D.14 through D.16). In particular, during Test Run 13, horizontal hairline cracks appeared in the reinforcement at

the top of pier P2-8 and diagonal cracks appeared in the reinforcement at the top of piers P2-7 (in the positive direction) and pier P2-9 (in the negative direction). The diagonal cracks in the reinforcement on piers P2-7 and P2-9 propagated to the length shown in Figure D.21 during Test Run 14.

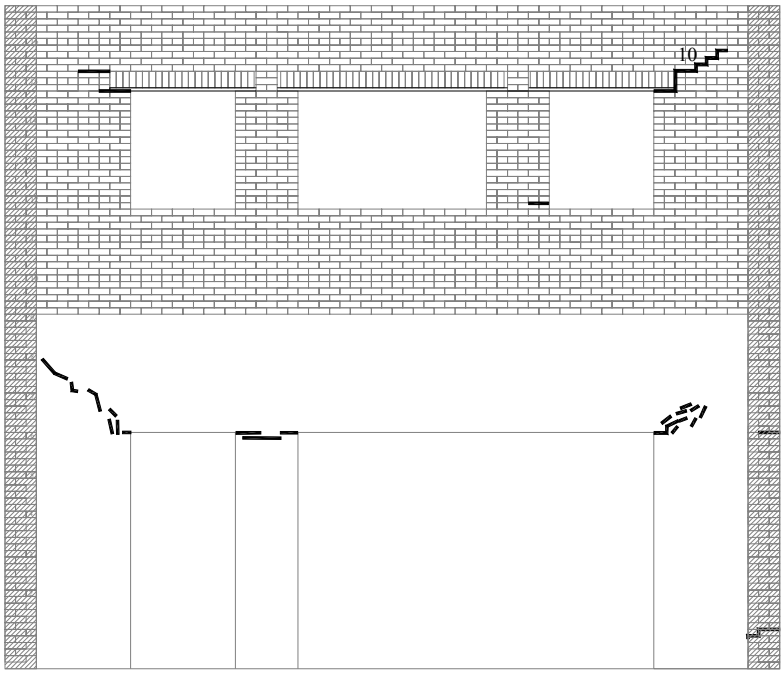

Figure D.21. Crack pattern in the external reinforcement following the Group 1 cycles.

The behavior of the external reinforcement was monitored by several strain gages throughout these cycles. Unfortunately, the cracks that formed in the reinforcement propagated through the gages rendering them useless. As a result, the data obtained from these strains gages during Cycle 12b (the last complete cycle prior to gage damage) was chosen to illustrate the response of the reinforcement. Figures D.22 through D.24 show the strains measured in the reinforcement versus bases shear during Cycle 12b. The strain profiles shown in these figures indicates that the reinforcement was actively resisting the rocking deformation of the adjacent piers.

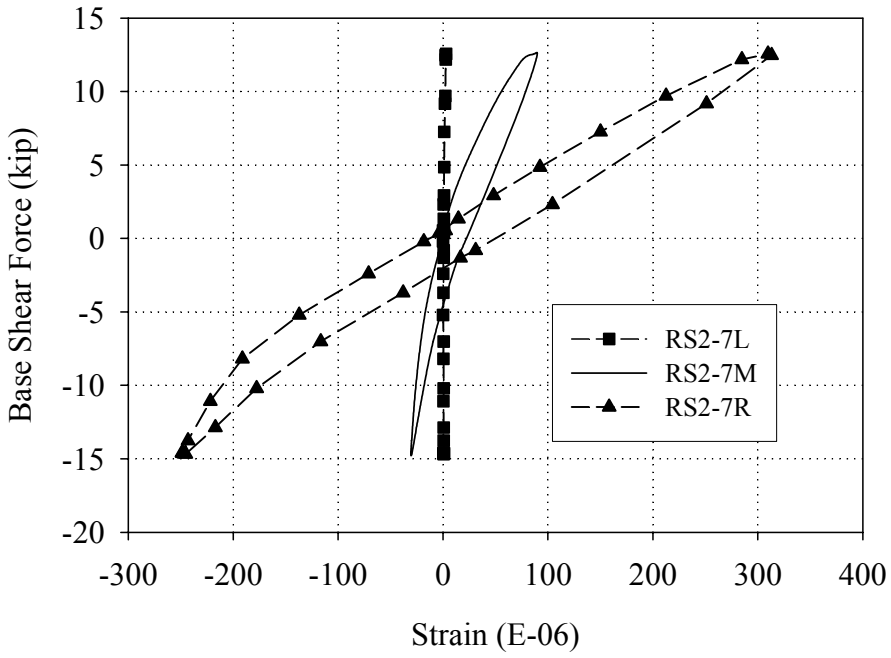

Figure D.22. Strains measured in the external reinforcement applied to the inside of pier P2-7 (Cycle 12b).

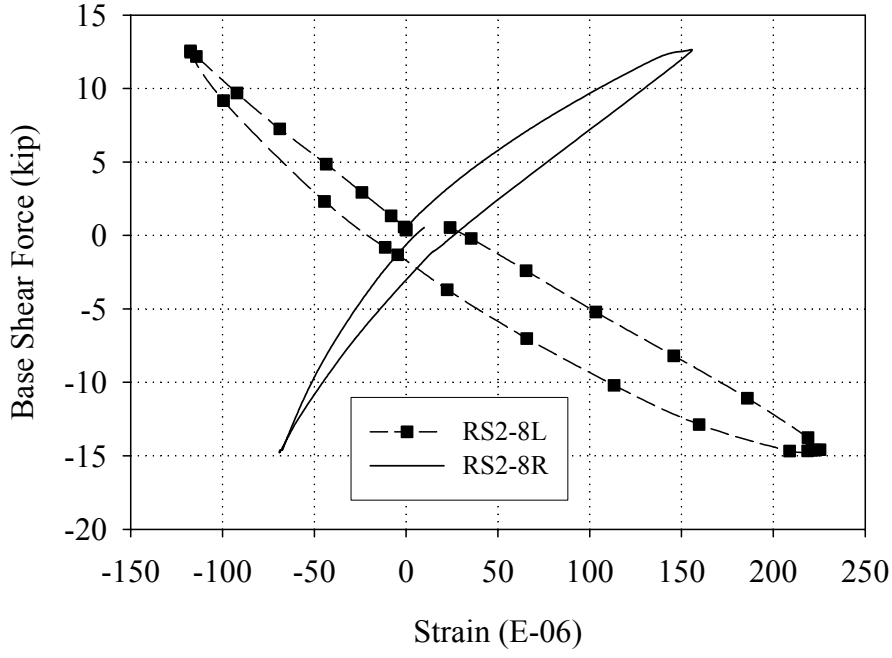

Figure D.23. Strains measured in the external reinforcement applied to the inside of pier P2-8 (Cycle 12b).

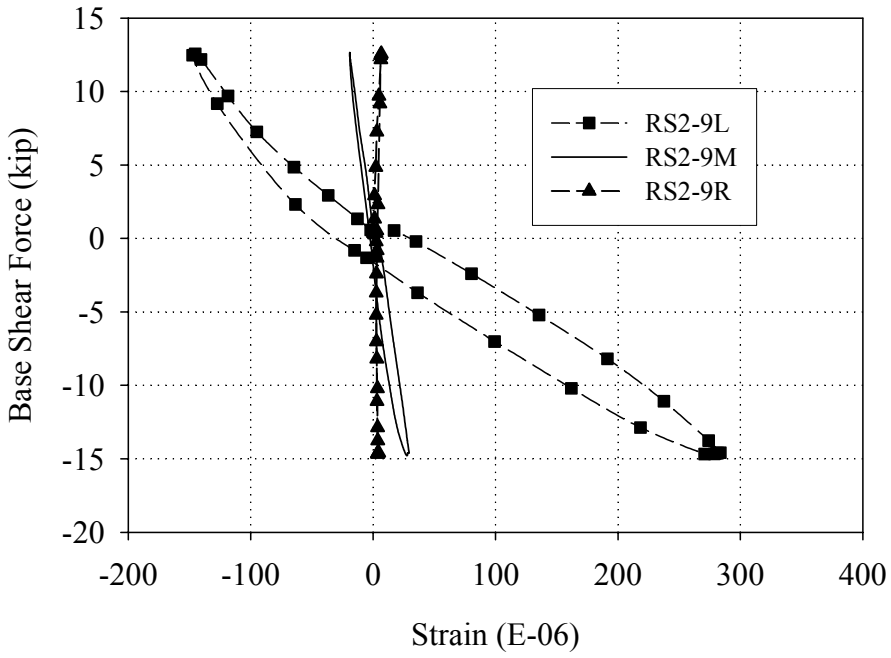

Figure D.24. Strains measured in the external reinforcement applied to the inside of pier P2-9 (Cycle 12b).

D.3.1.3 Local Pier Behavior

Due to the observed crack opening in the first story piers, the location of the LVDT reference points relative to the active cracks is of paramount importance. As a result, the descriptions of pier behavior given in this section will utilize Figures D.17 and D.19, which show the location of the LVDTs attached to the piers in reference to the displaced shape. In addition, since all of the piers displayed similar behavior during the Group 1 cycles, the data obtained during Cycle 14b will be used to illustrate the behavior of each pier.

Figures D.25 and D.26 show the readings obtained from the LVDTs attached to pier P2-7. Figure D.27 shows the readings of the vertical LVDTs attached to pier P2-8. Figures D.28 and D.29 show the readings obtained from the LVDTs attached to pier P2-9.

In many cases the LVDTs attached to the in-plane piers traversed several cracks (see Figures D.17 and D.19), thus a precise determination of each piers rotation and translation cannot be obtained. As a result, only a qualitative discussion will be presented.

In general, the displacements shown in these figures indicate that the deformation of the piers was almost entirely recoverable upon unloading, which is consistent with the observed rocking deformation. In addition, these readings are consistent with the previously described wall behavior. Specifically, the unsymmetrical response measured by gages P2-7RV and P2-9LV was caused by the different active cracks displayed by piers P2-7 and P2-9 in each loading direction. Furthermore, the nearly identical uplift measured by gages P2-8LV and P2-8RV is consistent with rocking deformation. However, this displacement could also have been caused by the upper portion of Wall 2 lifting off of pier P2-8 due to the rocking deformation of the outside piers.

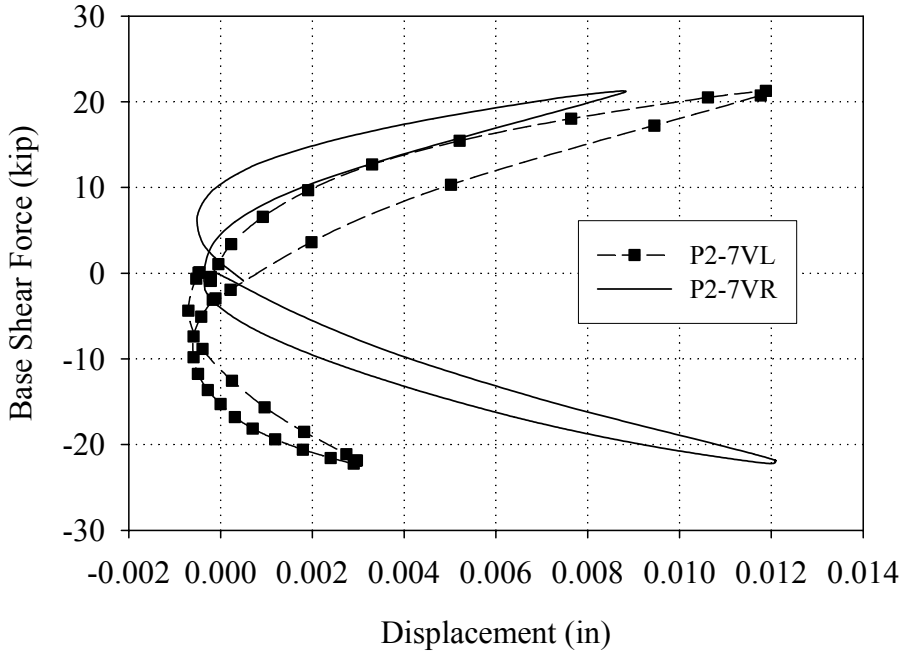

Figure D.25. Readings of the vertical LVDTs attached to pier P2-7 versus base shear force (Cycle 14b).

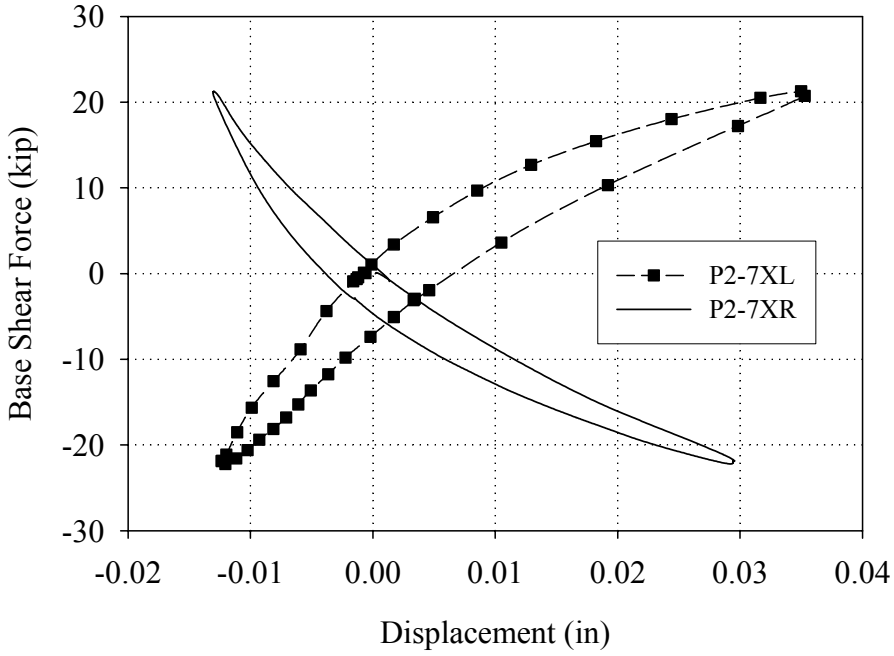

Figure D.26. Readings of the diagonal LVDTs attached to pier P2-7 versus base shear force (Cycle 14b).

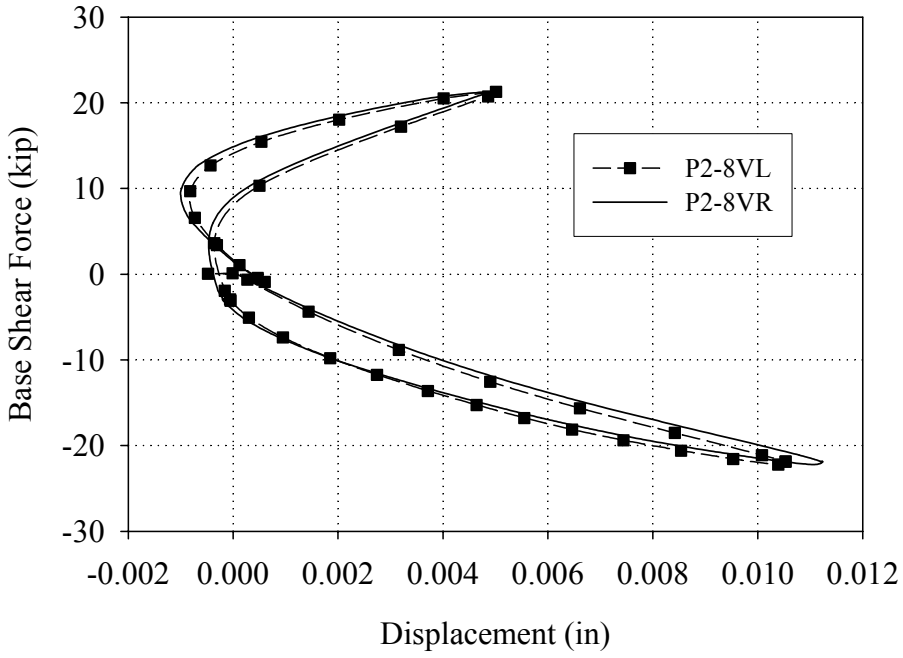

Figure D.27. Readings of the vertical LVDTs attached to pier P2-8 versus base shear force (Cycle 14b).

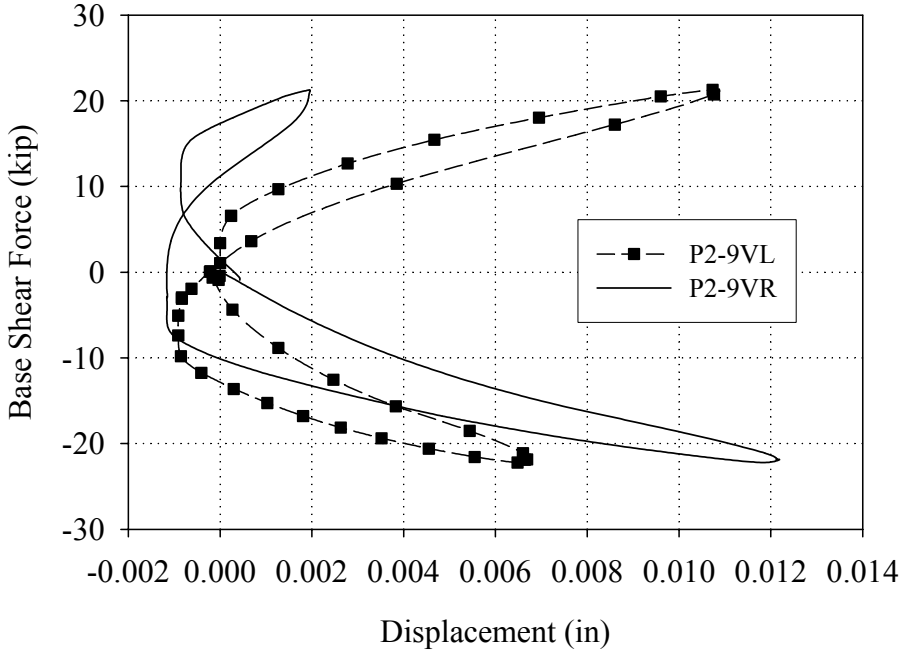

Figure D.28. Readings of the vertical LVDTs attached to pier P2-9 versus base shear force (Cycle 14b).

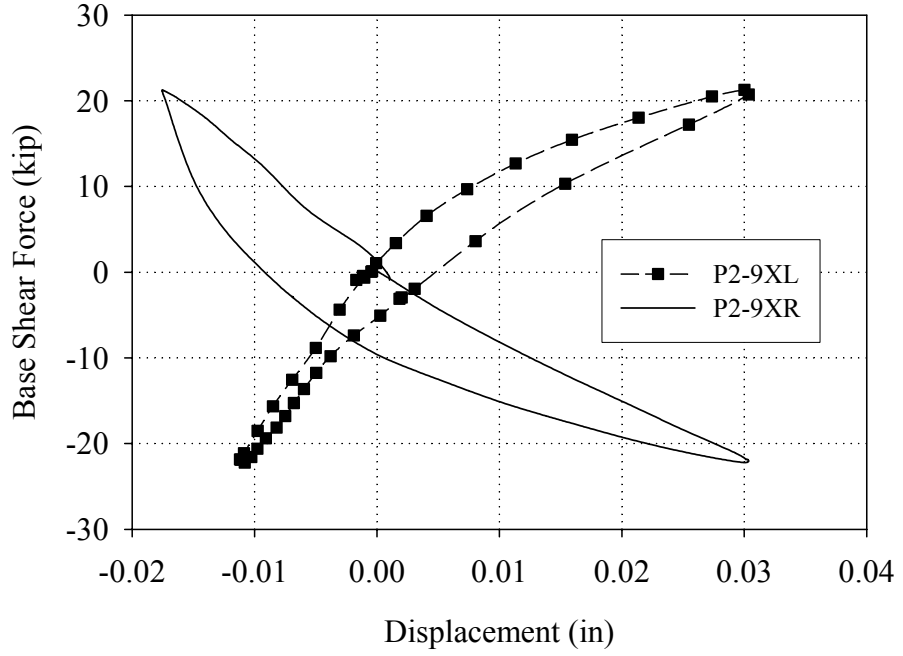

Figure D.29. Readings of the diagonal LVDTs attached to pier P2-9 versus base shear force (Cycle 14b).

D.3.2 Group 2 Cycles (Test Run 15-Test Run 17)

D.3.2.1 Overall Wall Behavior

Figures D.30 through D.32 show the crack pattern in Wall 2 and out-of-plane Walls A and B following the Group 2 cycles (note the cracks that formed during the Group 2 cycles are shown in bold). During Test Run 15 partially developed horizontal cracks were observed at the base of piers P2-3 and P2-4 in the second story of Wall 2. The remainder of the cracks that formed during the Group 2 cycles were observed during Test Run 17.

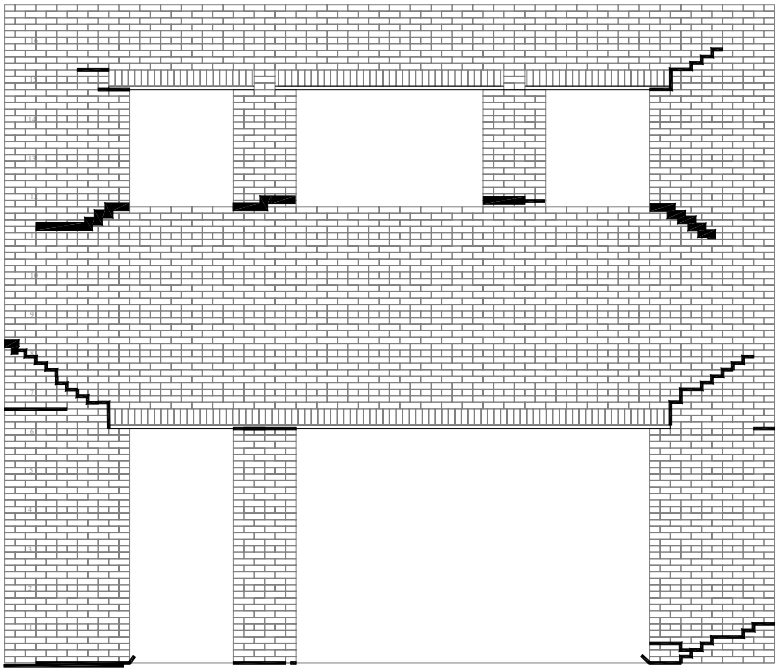

Figure D.30. Crack pattern of Wall 2 following the Group 2 cycles.

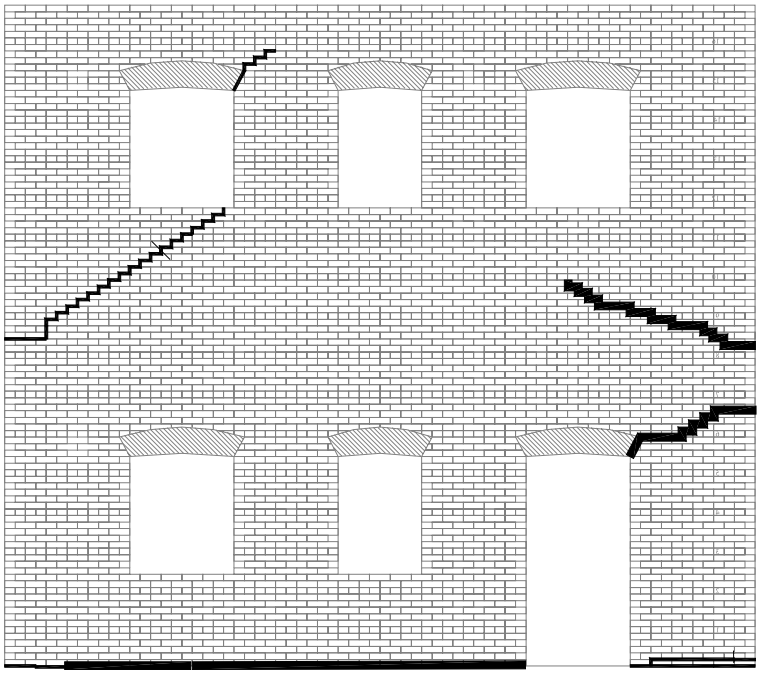

Figure D.31. Crack pattern of Wall A following the Group 2 cycles.

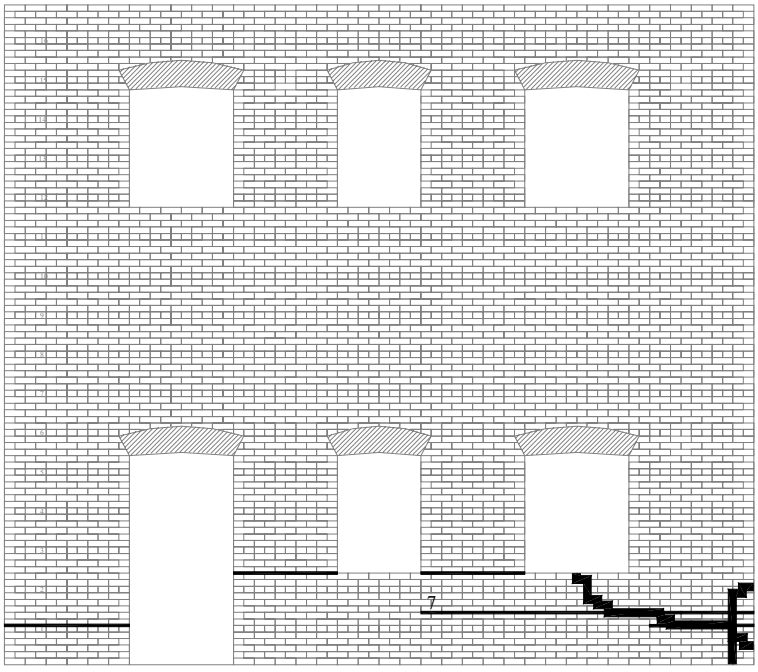

Figure D.32. Crack Pattern of Wall B following the Group 2 cycles.

Figure D.33 shows an exaggerated schematic illustrating the behavior of Wall 2 and out-of-plane Walls A and B during the Group 2 cycles (note that the LVDT reference points are also shown). Based on this figure it is apparent that the response of Wall 2 during the Group 2 cycles was nearly identical to the response observed during the Group 1 cycles (see Section D.3.1.1). That is, the deformation of Wall 2 was focused on the local rocking of the first story piers. The most notable difference in response was the observation that pier P2-7 exhibited a small amount of sliding deformation in addition to rocking. Note that the primary mechanism of pier P2-7 remained rocking, which is supported by the negligible increase in energy dissipation observed during these cycles (see Section D.2.2).

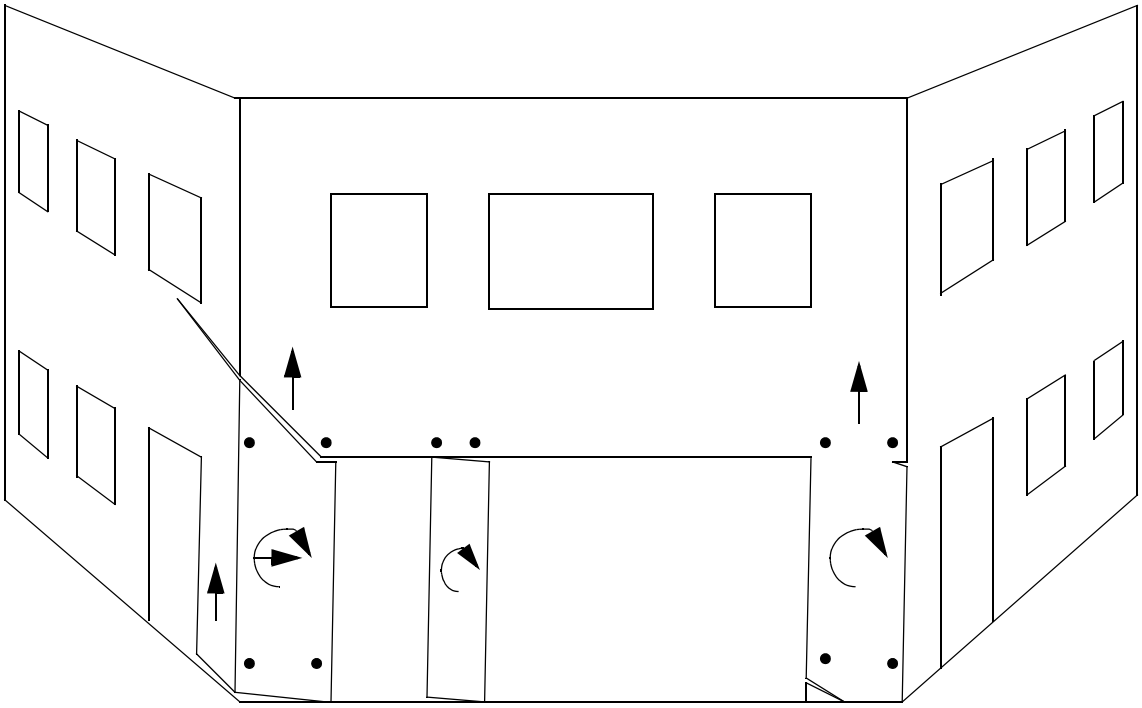

Figure D.33. Exaggerated schematic of the observed behavior of Wall 2 and out-of-plane Walls A and B in the positive loading direction during the Group 2 cycles.

Figure D.34 shows the vertical displacement of each side of Wall 2 versus roof displacement for Cycle 17c. Based on this figure it is apparent that the roof of Wall 2 translated upwards approximately 0.06 in. in the positive direction. Obviously this uplift was a result of the observed rocking of the first story piers. In addition, this observed uplift likely engaged the weight of portions of the out-of-plane Walls A and B.

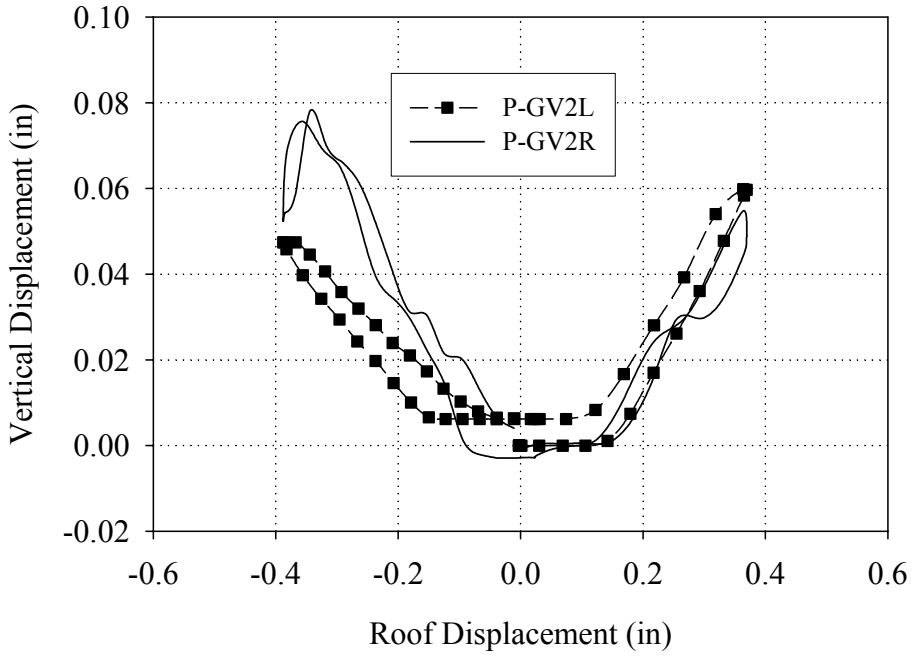

Figure D.34. Vertical displacement of both sides of Wall 2 versus roof displacement (Cycle 17c).

Figure D.35 shows the base strains recorded at peak positive displacement during Cycle 17c. The strain profiles in this figure are clearly consistent with the observed rocking deformation of the in-plane piers. In addition, the strains measured in out-of-plane pier PB-7 suggest that this pier was participating by resisting compressive strain caused by the rocking of adjacent pier P2-9. This conclusion is substantiated by the relative magnitude of compression strains recorded in piers P2-7 and P2-9. That is, the smaller

compressive strains measured in pier P2-9 suggest that the adjacent flange was participating thus reducing the compressive strains measured in this region. Note that the presence of overturing moment would act to increase the compressive strains in this region.

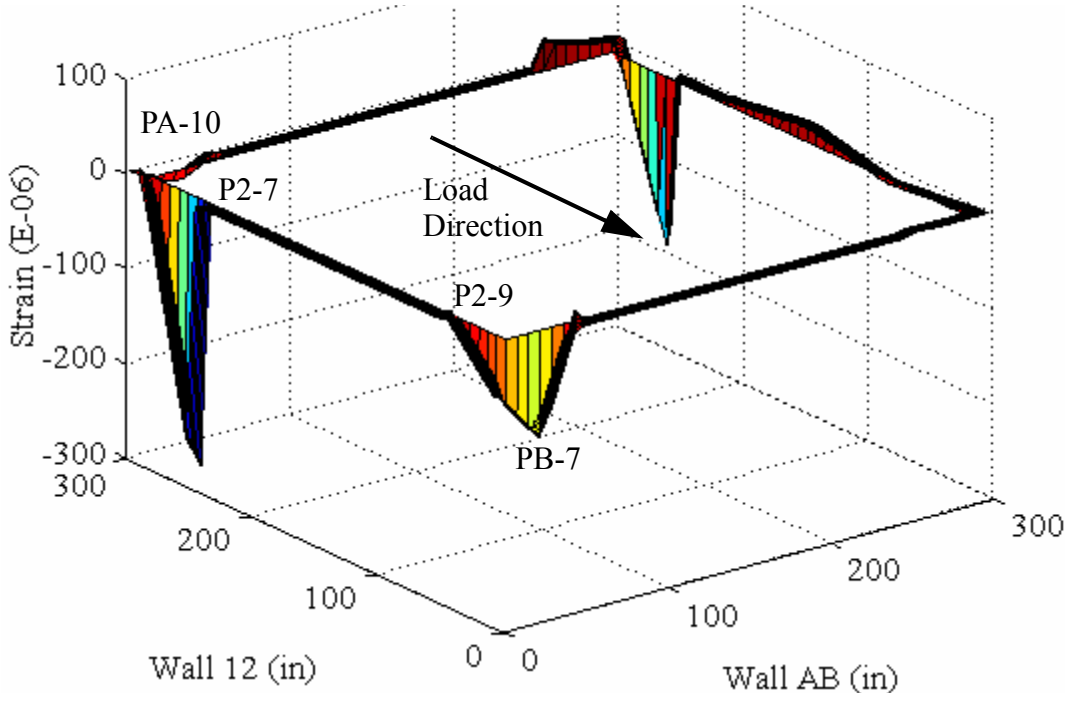

Figure D.35. Base strains recorded at peak positive displacement (Cycle 17c).

Figure D.36 shows a schematic illustrating the observed behavior of Wall 2 and out-of-plane Walls A and B during the Group 2 cycles in the negative direction (note that the location of the LVDT reference points are also shown). From this figure it is clear that the response of Wall 2 in the negative direction was similar to past cycles as well as the response of Wall 2 in the positive direction. That is, the majority of the deformation of Wall 2 was due to the low-level rocking deformation of the first story piers. Similar to the positive direction, pier P2-9 displayed a small degree of sliding along with the observed rocking.

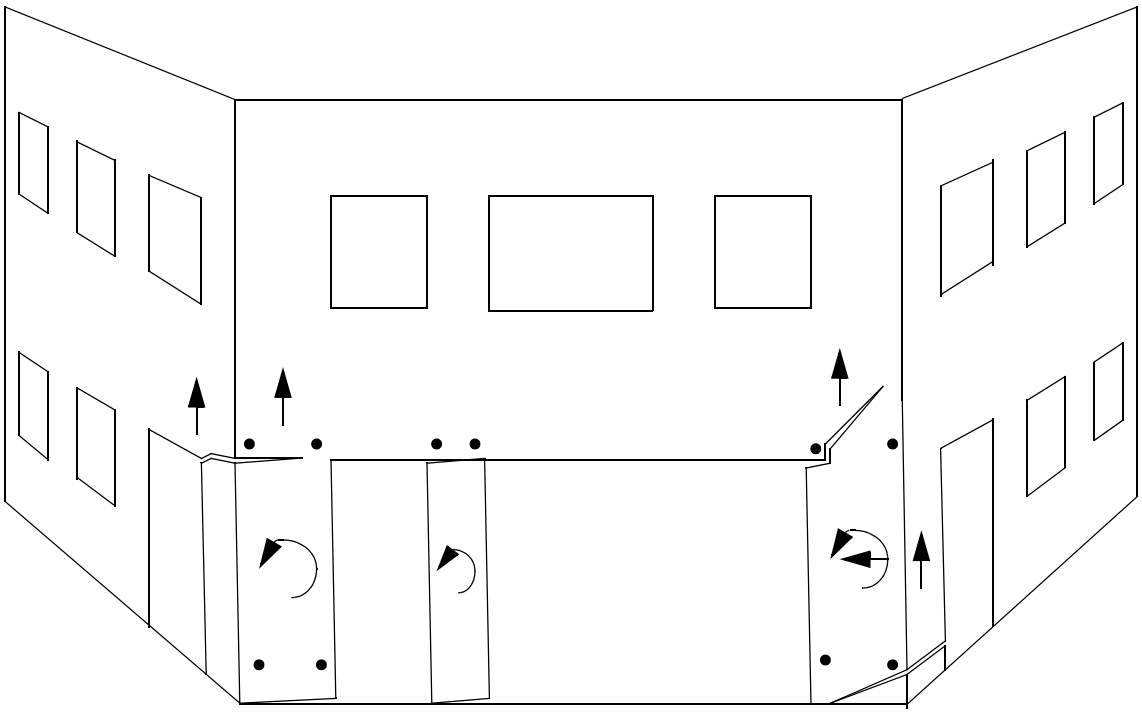

Figure D.36. Exaggerated schematic illustrating the behavior of Wall 2 and out-of-plane Walls A and B in the negative direction during the Group 2cycles.

The most notable difference in the observed response was focused on the behavior of Wall A. The horizontal crack that formed above out-of-plane pier PA-10 highlighted the participation of the out-of-plane walls in the response. In particular, this crack suggests that a portion of the weight of Wall A was engaged by the uplift associated with the rocking deformation of the first story piers. From Figure D.34 it is apparent that the average vertical displacement of the roof was approximately 0.05 in.

Figure D.37 shows the base strains recorded at peak negative displacement during Cycle 17c. From this figure it is apparent that the recorded strains were nearly identical to those discussed in the positive direction, which is consistent with the observed symmetric performance of Wall 2.

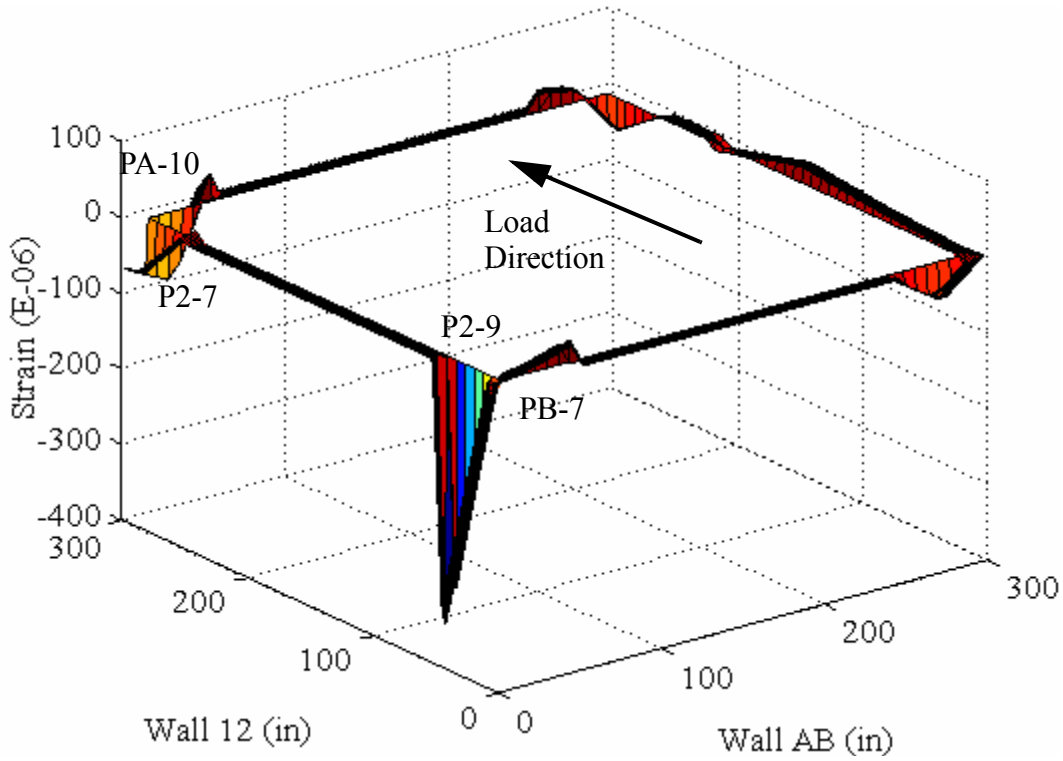

Figure D.37. Base strains recorded at peak negative displacement (Cycle 17c).

D.3.2.2 Behavior of External Reinforcement

During this level of testing additional hairline cracks were observed in the external reinforcement along the top of the first story piers. Figure D.38 shows a schematic illustrating the crack pattern in the external reinforcement following the Group 2 cycles (note that the cracks that formed during the Group 2 cycles are shown in black). Based on the additional cracks observed during these cycles it is clear that the reinforcement was still intact and resisting the rocking deformation of the adjacent piers. As mentioned previously the observed cracks damage the stain gages and thus no strain data is available.

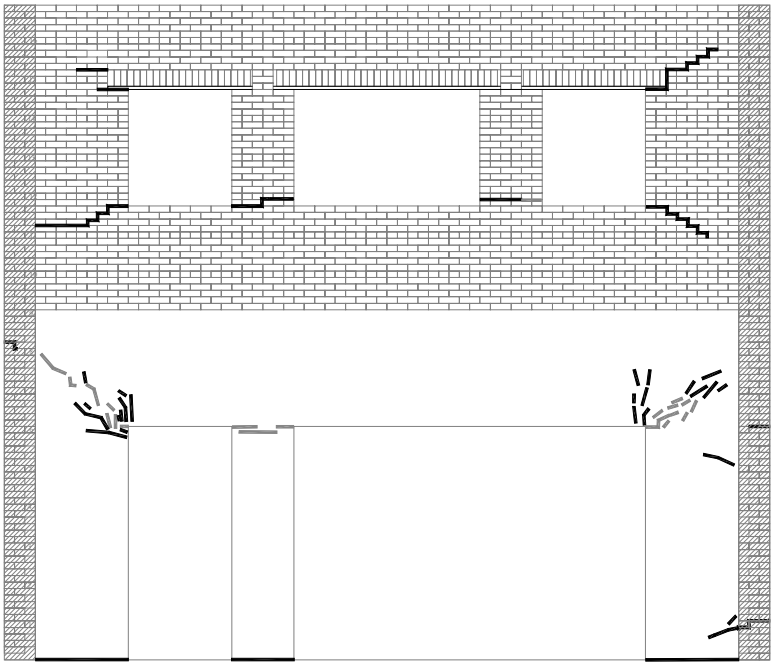

Figure D.38. Crack pattern in the external reinforcement following the Group 2 cycles.

D.3.2.3 Local Pier Behavior

Due to the observed crack opening of the first story piers, the location of the LVDT reference points relative to the active cracks is of paramount importance. As a result, the interpretation of LVDT measurements must utilize Figures D.33 and D.36, which show the location of the LVDTs in reference to the displaced shape. Since all of the piers displayed similar behavior during the Group 2 cycles, the data obtained during Cycle 17c will be used to illustrate the behavior of each pier.

Figures D.39 and D.40 show the readings obtained from the LVDTs attached to pier P2-7. Figure D.41 shows the readings of the vertical LVDTs attached to pier P2-8. Figures D.42 and D.43 show the readings obtained from the LVDTs attached to pier P2-9. In general, the pier response illustrated by these figures is consistent with the observed behavior described previously. Furthermore, this response is consistent with past cycle and the reader is directed to Section D.3.1.3 for further discussion

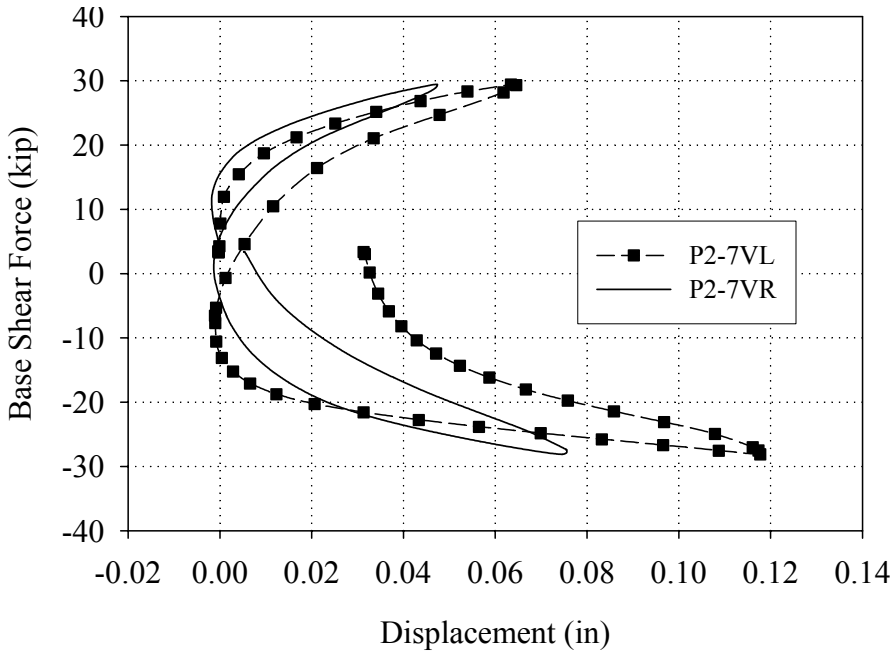

Figure D.39. Readings of the vertical LVDTs attached to pier P2-7 versus base shear force (Cycle 17c).

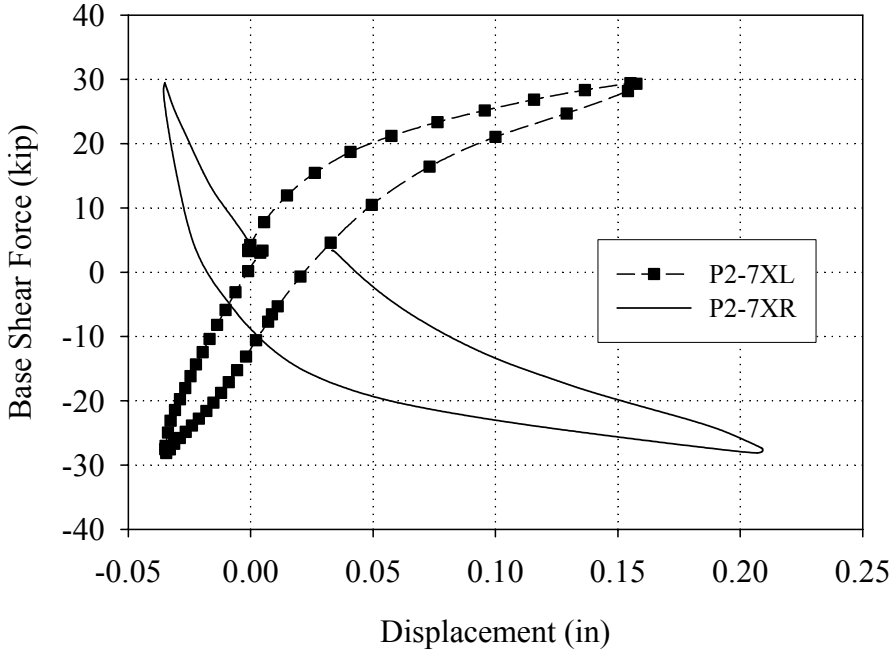

Figure D.40. Readings of the diagonal LVDTs attached to pier P2-7 versus base shear force (Cycle 17c).

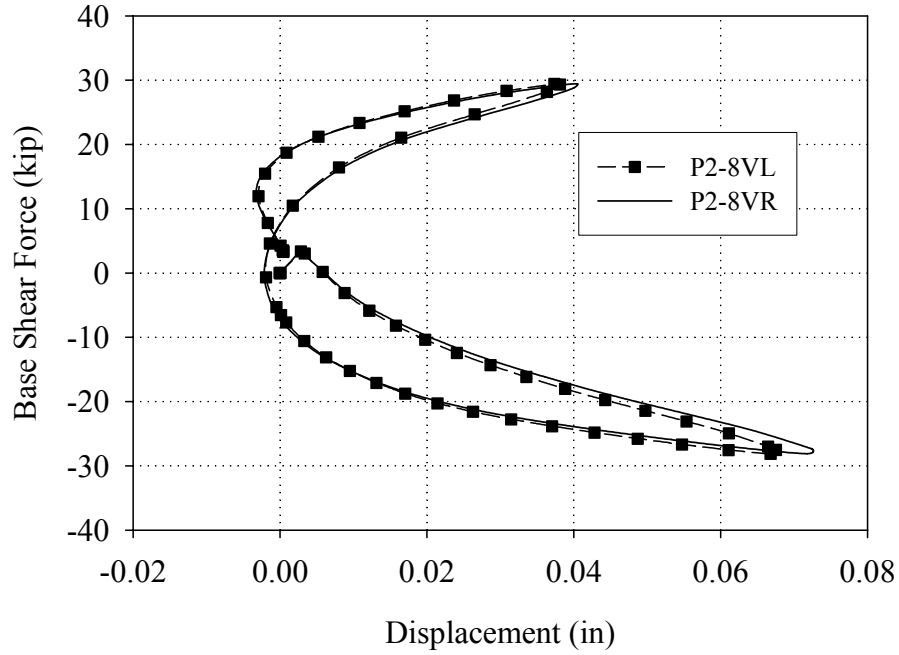

Figure D.41. Readings of the vertical LVDTs attached to pier P2-8 versus base shear force (Cycle 17c).

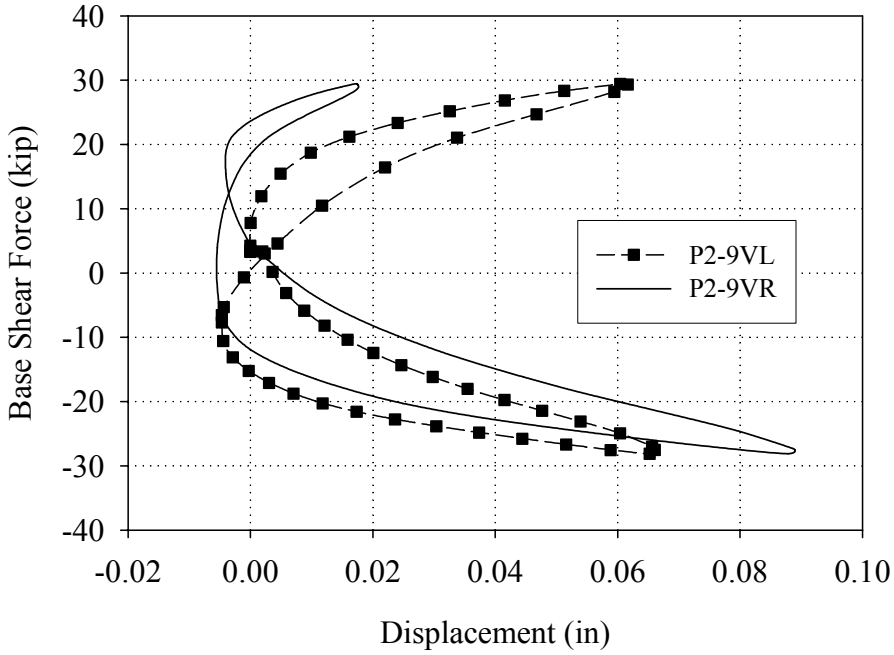

Figure D.42. Readings of the vertical LVDTs attached to pier P2-9 versus base shear force (Cycle 17c).

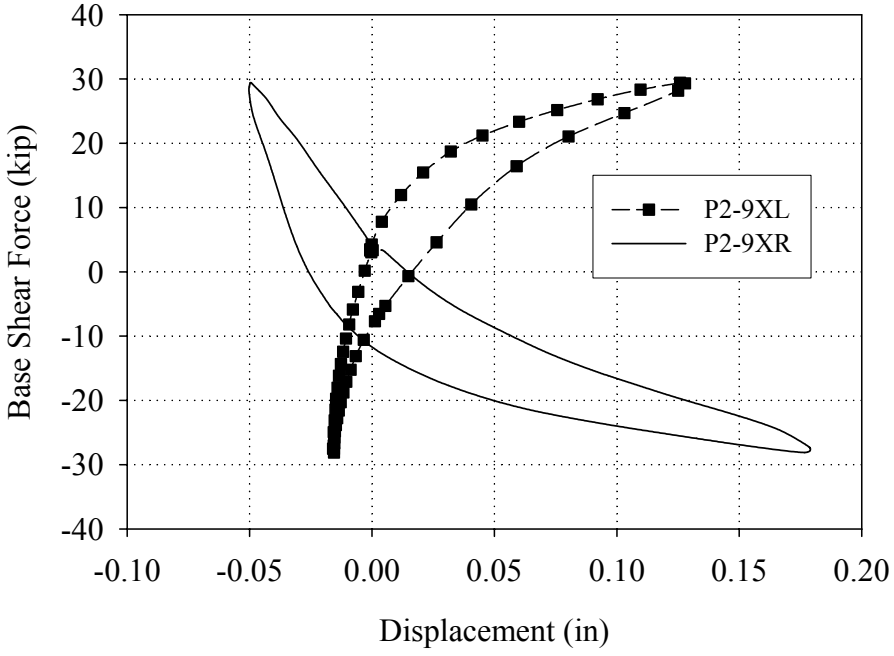

Figure D.43. Readings of the diagonal LVDTs attached to pier P2-9 versus base shear force (Cycle 17c).

D.3.3 Group 3 Cycles (Test Run 18 and Test Run 19)

D.3.3.1 Overall Wall Behavior

Figures D.44 through D.46 show the crack pattern in Wall 2 and out-of-plane Walls A and B following the Group 3 cycles (note the cracks that formed during the Group 3 cycles are shown in bold). All of the cracks that formed during the Group 3 cycles were observed during Test Run 18. The formation of these cracks resulted in a mechanism in both directions and thus no additional cracks were observed during Test Run 19.

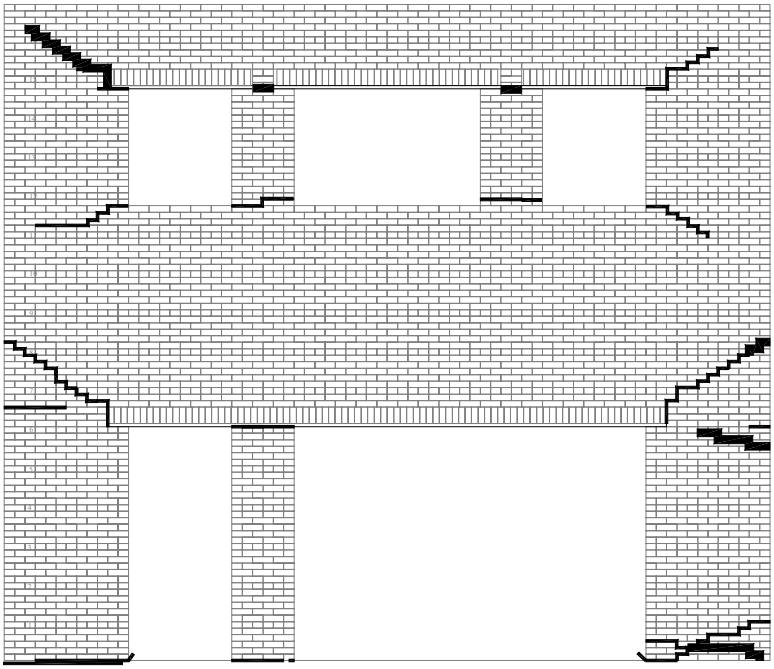

Figure D.44. Crack pattern of Wall 2 following the Group 3 cycles.

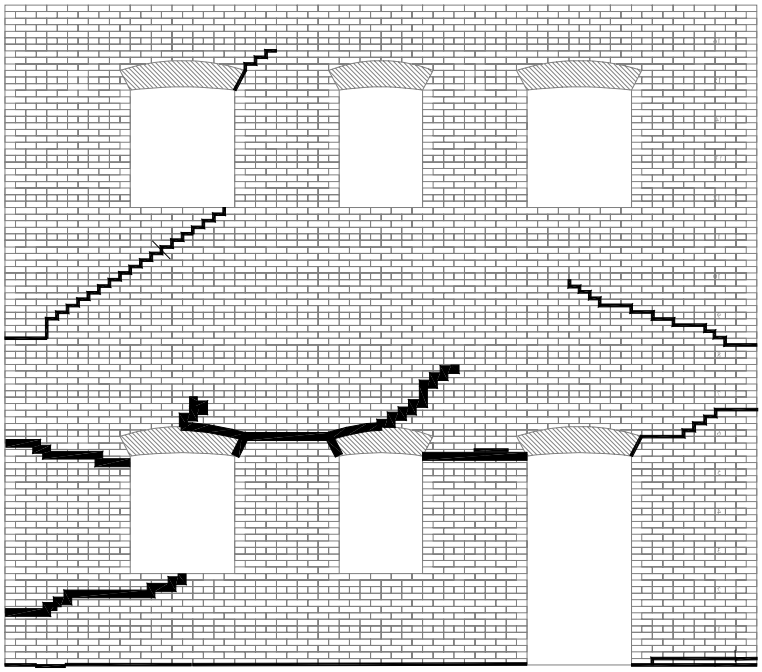

Figure D.45. Crack pattern of Wall A following the Group 3 cycles.

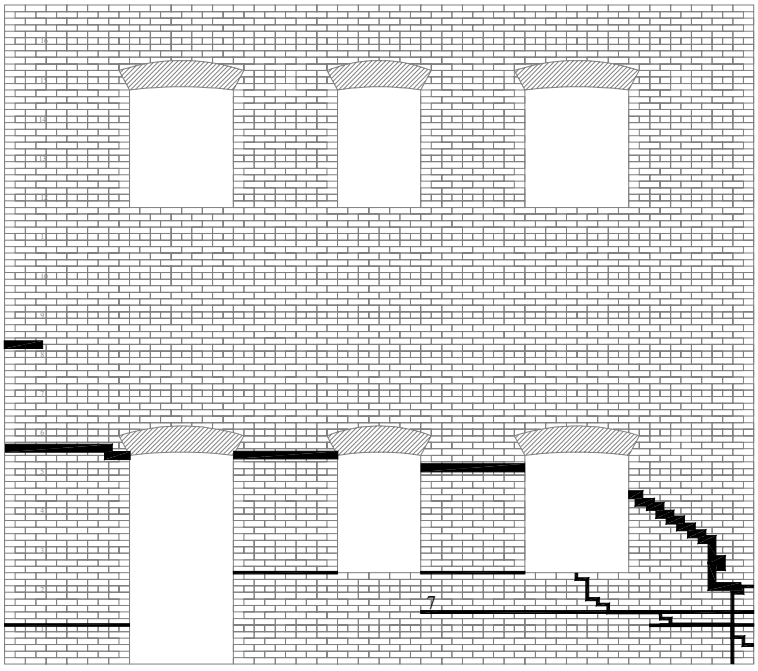

Figure D.46. Crack Pattern of Wall B following the Group 3 cycles.

Figure D.47 shows a schematic illustrating the behavior of Wall 2 and out-of-plane Walls A and B during the Group 3 cycles (note that the location of the LVDT reference point is also shown). As seen from the figure, the behavior of Wall 2 during the Group 3 cycles was consistent with past cycles. The principal difference in behavior was due to the formation of an additional horizontal crack along the top of pier P2-9 and out-of-plane pier PB-7. As illustrated in Figure D.47, this crack was likely caused by the flexural deformation of pier P2-9 and resulted in a fully developed rocking mechanism. In addition this rocking caused an uplift which in turn resulted in a crack along the top of pier PB-7 and lifted up a portion of Wall B.

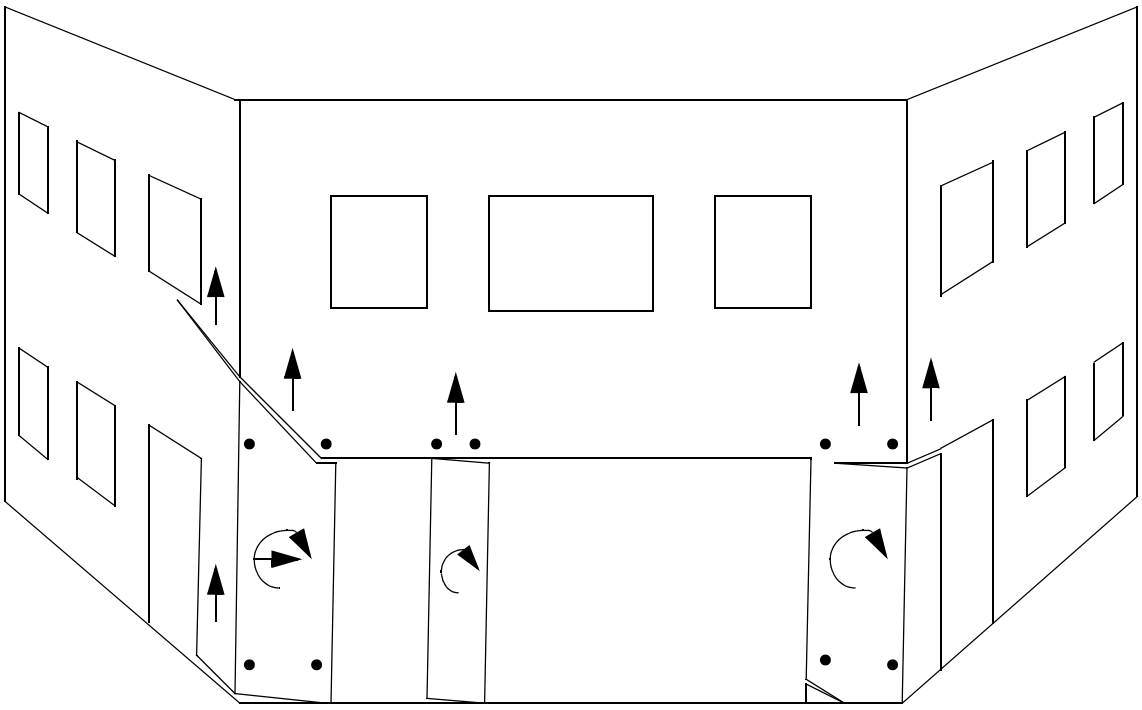

Figure D.47. Exaggerated schematic illustrating the behavior of Wall 2 and out-of-plane Walls A and B in the positive direction during the Group 3 cycles.

Figure D.48 shows a plot of the vertical displacements of both sides of the roof of Wall 2 versus lateral roof displacement for Cycle 19a. Based on this figure, the uplift caused by the rocking deformation of the first story piers is clearly visible. In addition, the differential displacement of each side of the roof suggests that a small amount of rotation was also occurring. This rotation is consistent with the direction of overturning moment and likely represents a global rotation of the entire wall about the base. Since the aspect ratio of Wall 2 is approximately 1.0, the difference between the uplift of either side of the roof is roughly equal to the lateral roof displacement caused by global rocking. Following this assumption the rotation implied by Figure D.48 accounted for approximately 0.06 in. or 8% of the roof displacement during Cycle 19a. While this displacement is fairly modest, it does suggest that the response of Wall 2 did have a global component. This is further substantiated by the diagonal crack below pier PA-5 which is consistent with global overturning.

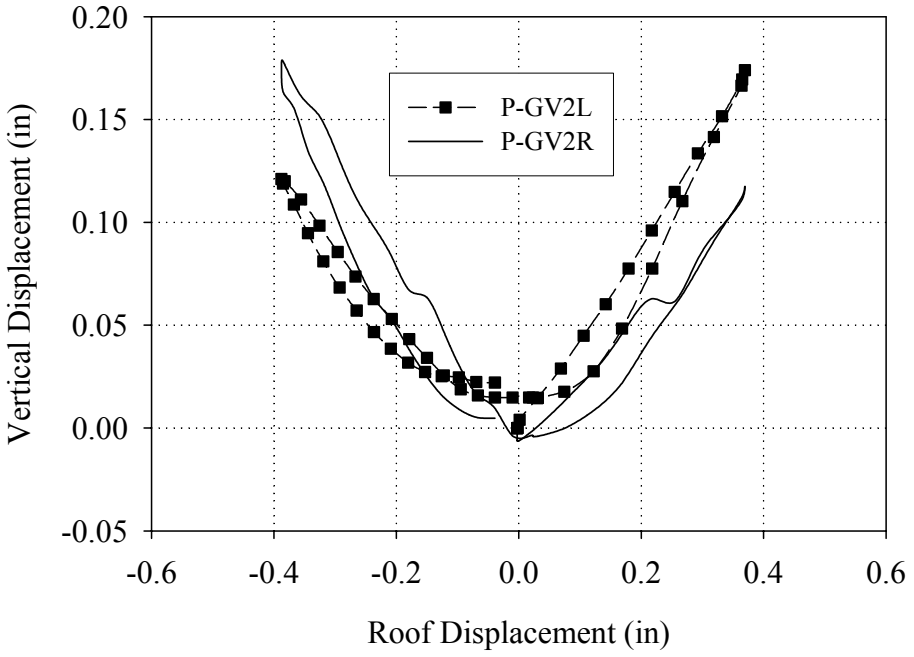

Figure D.48. Vertical displacement of both sides of Wall 2 versus roof displacement (Cycle 19a).

Figure D.49 shows the base strains recorded at peak positive displacement during Cycle 19a. In general, the strain profiles shown in this figure support the previously described response and are consistent with past cycles. The reader is directed to Section D.3.1.1 for further discussion.

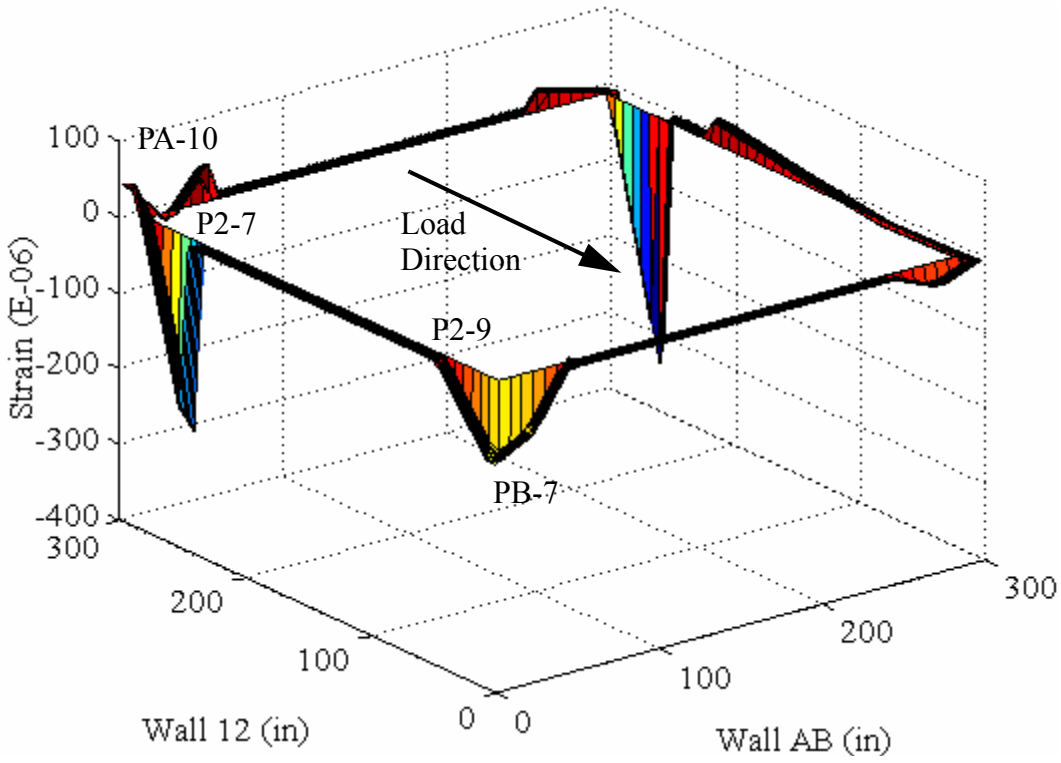

Figure D.49. Base strains recorded at peak positive displacement (Cycle 19a)

Figure D.50 shows a schematic illustrating the observed behavior of Wall 2 and out-of-plane Walls A and B during the Group 3 cycles in the negative direction (note that the location of the LVDT reference points are also shown). From this figure it is clear that the response of Wall 2 in the negative direction was nearly identical to the observed response of Wall 2 in the positive direction. In addition, the response of the first story piers was essentially unchanged from the Group 2 cycles, the reader is directed to Section D.3.2.1 for further discussion.

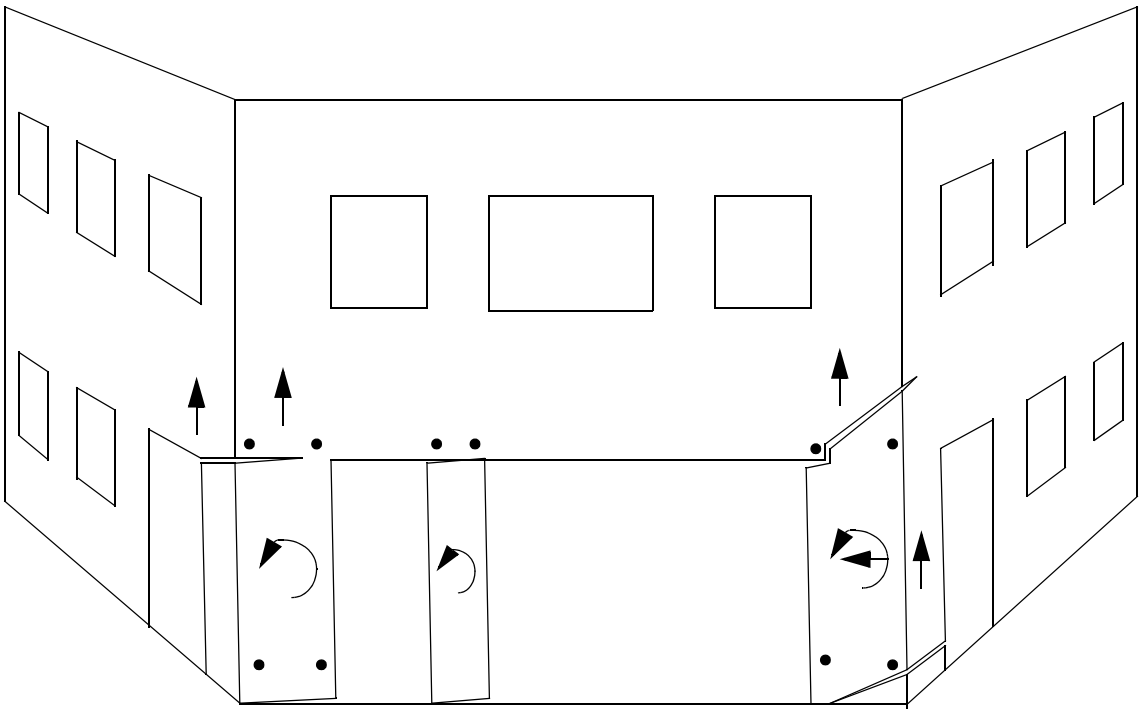

Figure D.50. Exaggerated schematic illustrating the behavior of Wall 2 and out-of-plane Walls A and B in the negative direction during the Group 3 cycles.

Beyond the local response of the first story piers, the deformation of Wall 2 in the negative direction had a small global rocking component. Based on the differential vertical deformation of the roof of Wall 2 shown in Figure D.48 and the previously outlined assumptions, the global rocking of Wall 2 accounted for approximately 0.05 in. or 7% of the imposed roof displacement during Cycle 19a. Recall that a similar level of global rocking displacement was observed in the positive loading direction.

Figure D.51 shows the base strains recorded at peak negative displacement during Cycle 19a. The strain profiles shown in this figure are consistent with the described response of Wall 2 as well as the strain profiles recorded during past cycles. The reader is directed to Section D.3.2.1 for further discussion.

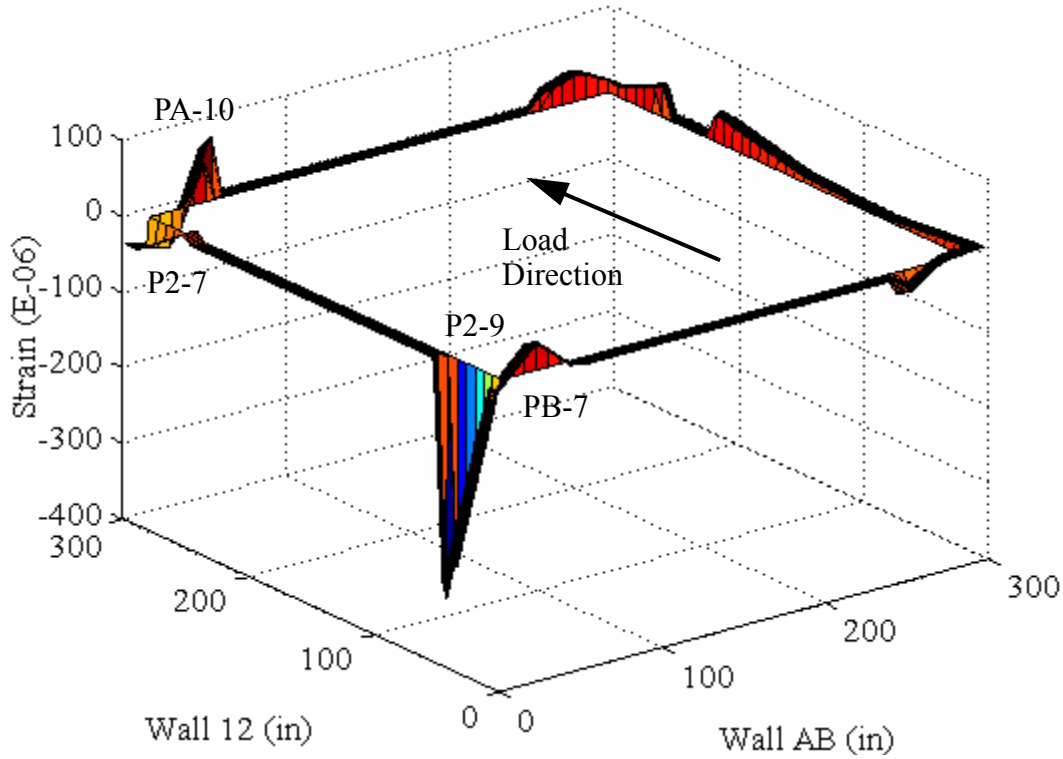

Figure D.51. Base strains recorded at peak negative displacement (Cycle 19a).

D.3.3.2 Behavior of External Reinforcement

During this level of testing additional hairline cracks were observed in the external reinforcement along the top of the first story piers. Figure D.52 shows a schematic illustrating the crack pattern in the external reinforcement following the Group 3 cycles (note that the cracks that formed during the Group 3 cycles are shown in black). Based on the additional cracks observed during these cycles it is clear that the reinforcement was still intact and resisting the rocking deformation of the adjacent piers. As mentioned previously the observed cracks damage the stain gages and thus no strain data is available.

In addition to the formation of cracks, the reinforcement at the upper inside corners (i.e. adjacent to the wall openings) of piers P2-7 and P2-9 was visibly buckling off of the wall when placed into compression during these cycles. Figure D.53 shows a photograph

illustrating the damage and buckling of the external reinforcement at the upper inside corner of pier P2-7. Following this observation the external reinforcement was examined for debonding by tapping it with a small wrench. The results of this evaluation suggested large regions of debonding in the vicinity of the observed cracking (see Figure D.54). This debonding likely grew progressively during each subsequent cycle of increasing magnitude; however, since the debonding of the reinforcement was not monitored no record of the history of this damage is available.

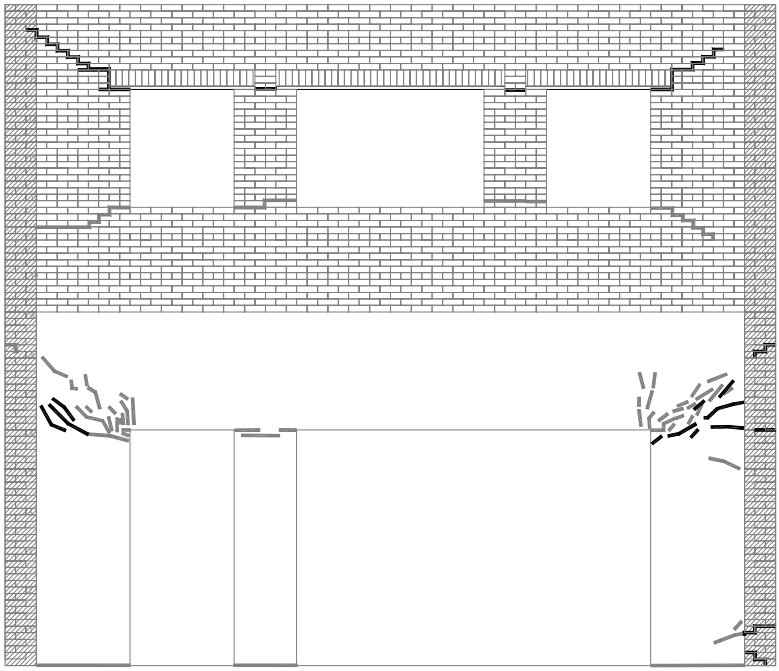

Figure D.52. Crack pattern in the external reinforcement following the Group 3 cycles.

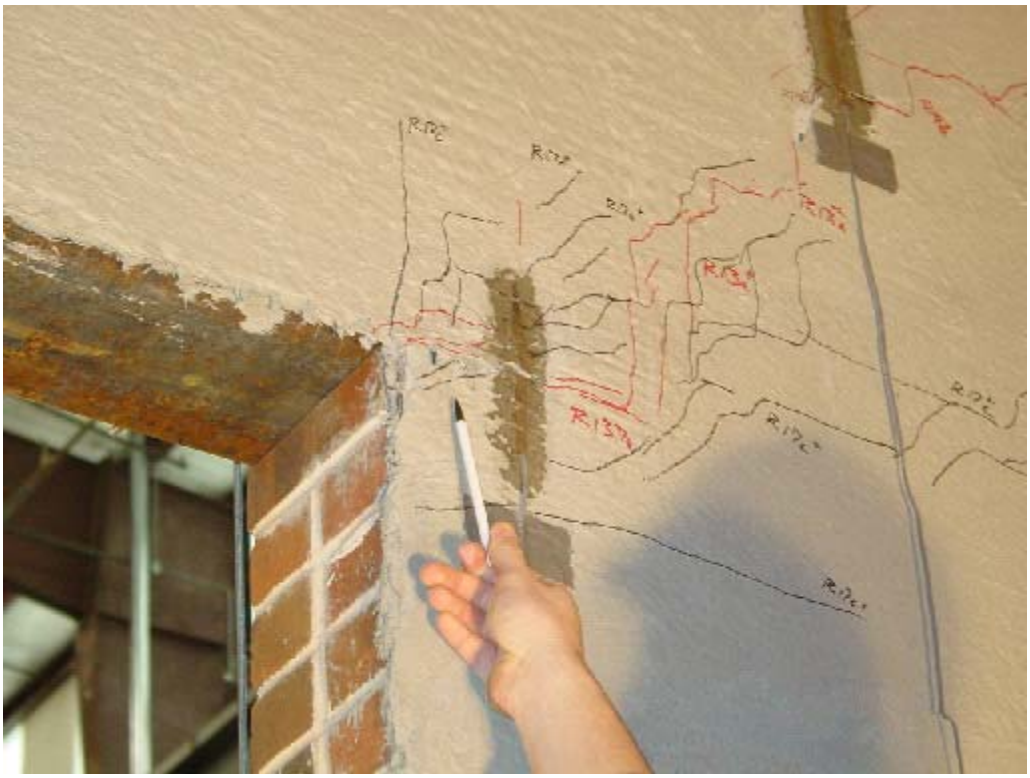

Figure D.53. Photograph illustrating the damage to the external reinforcement and subsequent buckling away from the masonry substrate.

Although no record of this progressive debonding is available, the force-displacement response of Wall 2 described in Section D.2, is consistent with this type of failure. The highly nonlinear response of the wall was likely a result of the apparent softening associated with debonding. That is, as debonding occurred the effective length of the reinforcement increased thus decreasing the effective stiffness. As a result, during each cycle a larger displacement was required to generate a similar level of resistance from the reinforcement. This resulted in the highly nonlinear pseudo-ductile behavior illustrated by the overall force-displacement response.

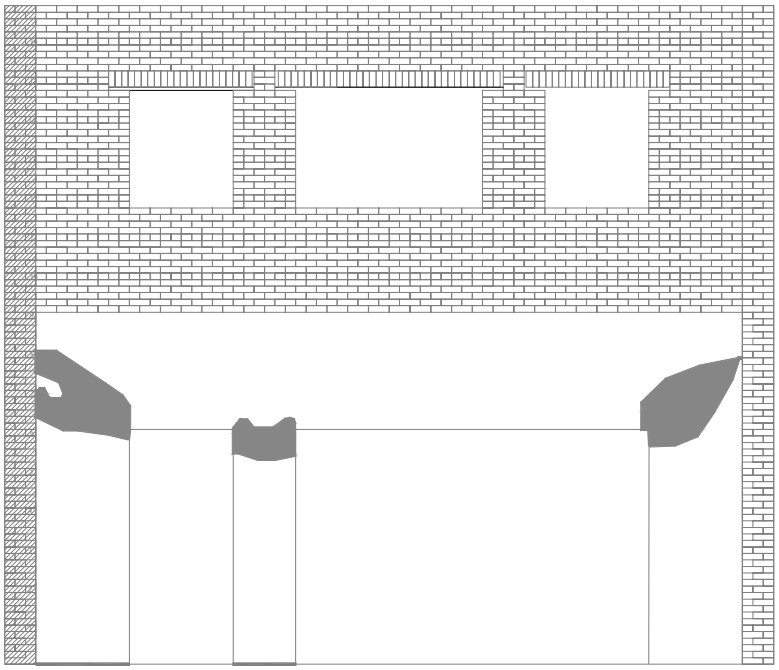

Figure D.54. Schematic illustrating the debonded portions of the external reinforcement following the Group 3 cycles.

D.3.3.3 Local Pier Behavior

Due to the observed crack opening of the first story piers, the location of the LVDT reference points relative to the active cracks is of paramount importance. As a result, the interpretation of LVDT measurements must utilize Figures D.47 and D.50, which show the location of the LVDTs in reference to the displaced shape. Since all of the piers displayed similar behavior during the Group 3 cycles, the data obtained during Cycle 19a will be used to illustrate the behavior of each pier.

Figures D.55 and D.56 show the readings obtained from the LVDTs attached to pier P2-7. Figure D.57 shows the readings of the vertical LVDTs attached to pier P2-8. Figures D.58 and D.59 show the readings obtained from the LVDTs attached to pier P2-9. In general, the pier response illustrated by these figures is consistent with the observed

behavior described previously. Furthermore, this response is consistent with past cycle and the reader is directed to Section D.3.1.3 for further discussion

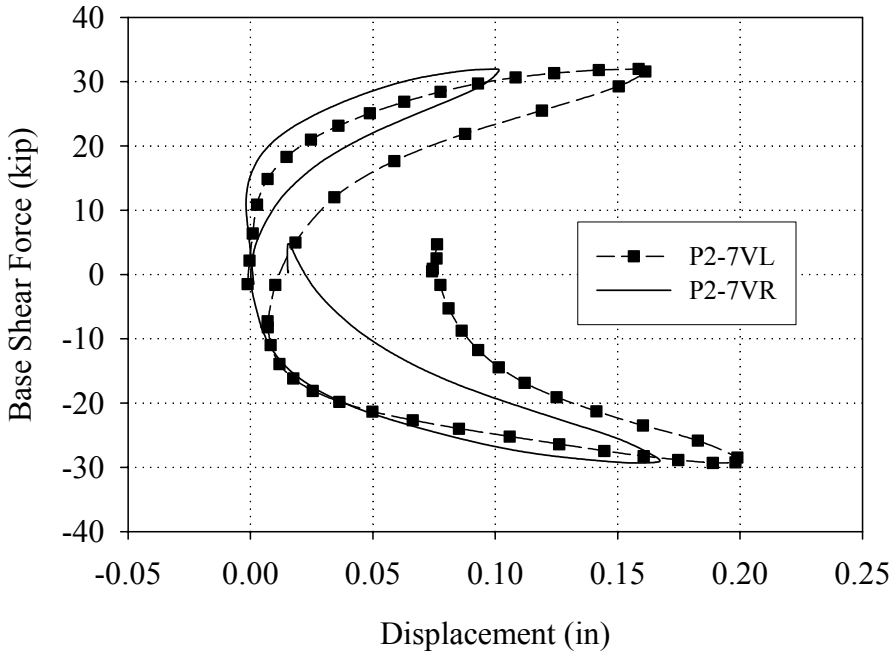

Figure D.55. Readings of the vertical LVDTs attached to pier P2-7 versus base shear force (Cycle 19a).

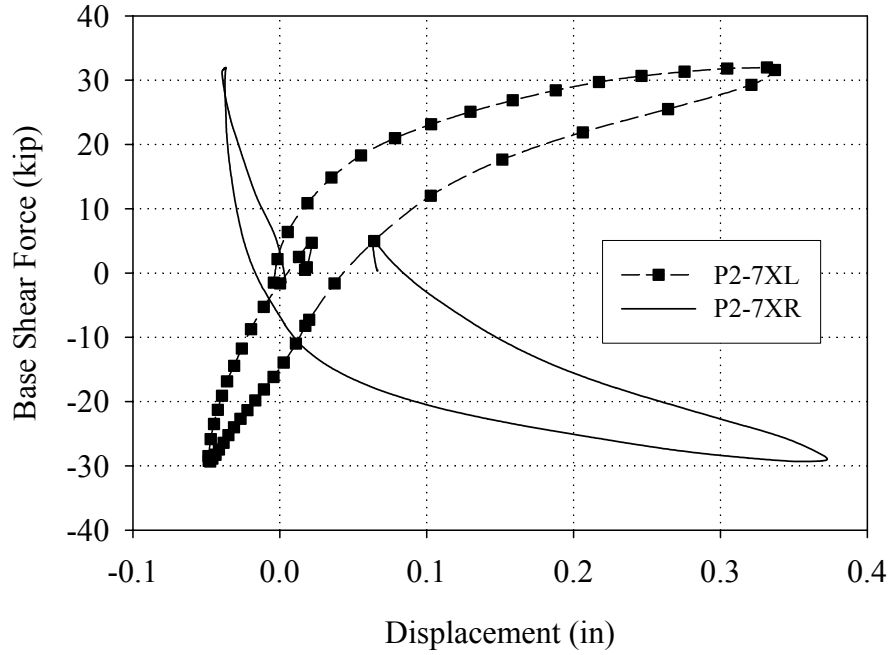

Figure D.56. Readings of the diagonal LVDTs attached to pier P2-7 versus base shear force (Cycle 19a).

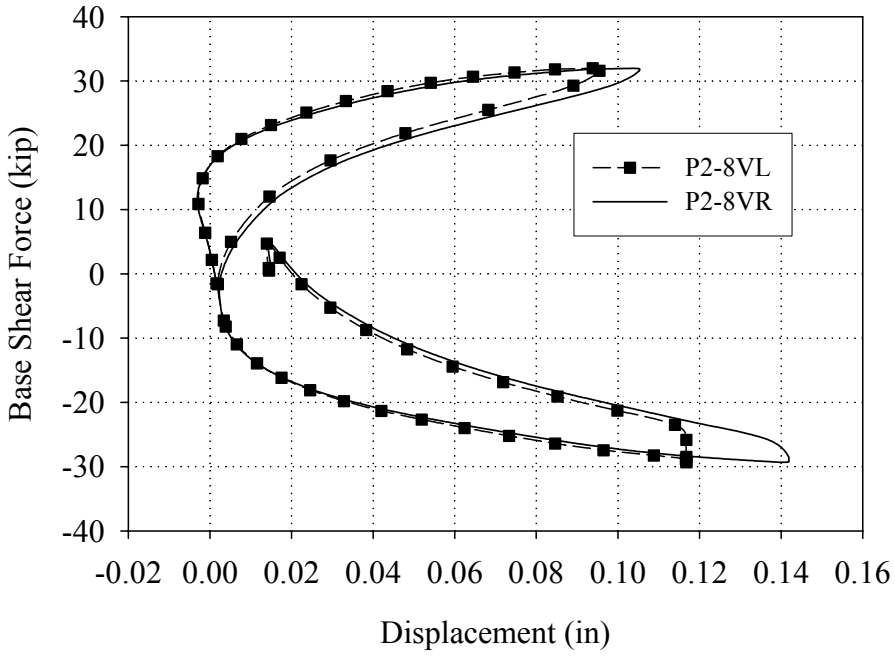

Figure D.57. Readings of the vertical LVDTs attached to pier P2-8 versus base shear force (Cycle 19a).

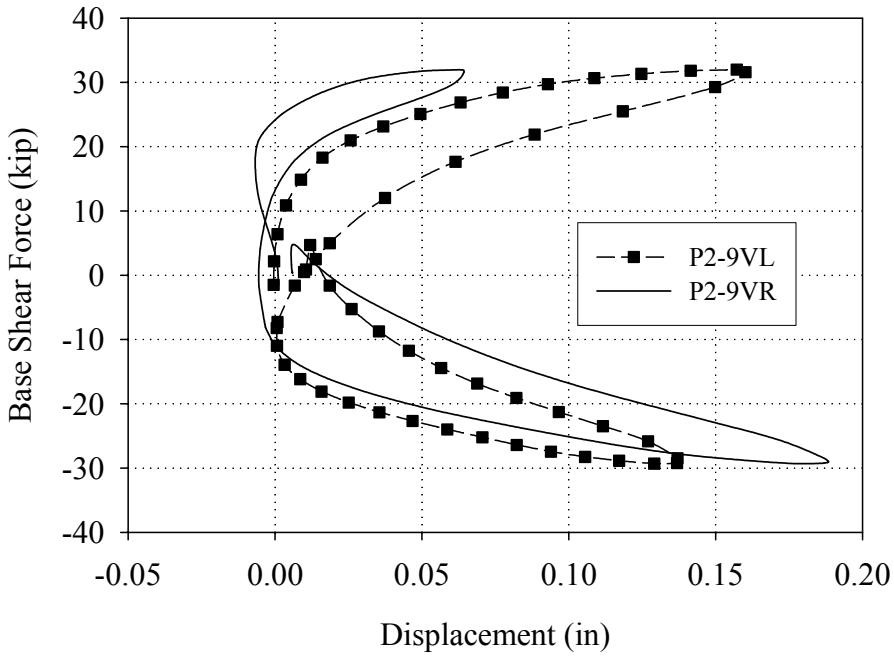

Figure D.58. Readings of the vertical LVDTs attached to pier P2-9 versus base shear force (Cycle 19a).

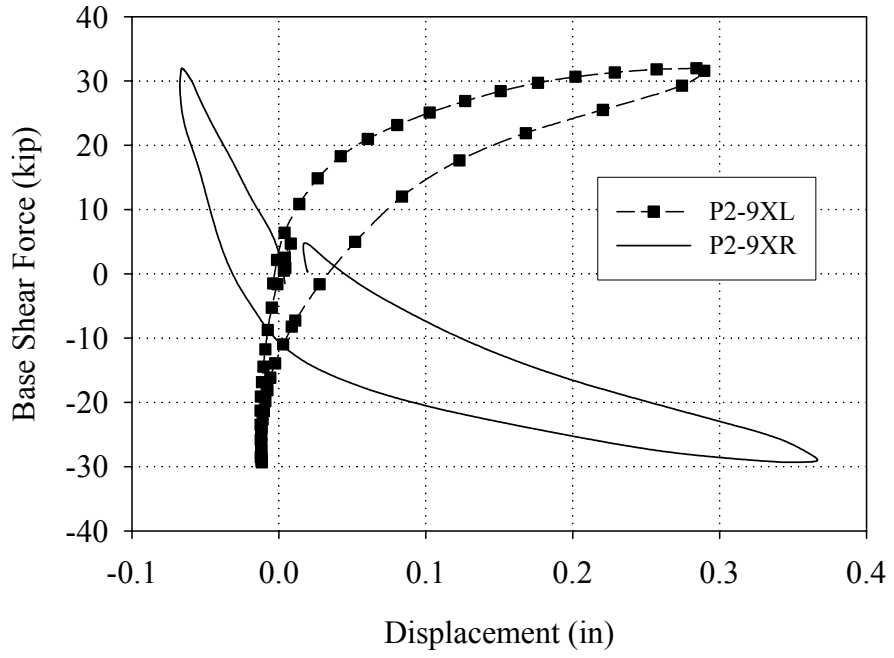

Figure D.59. Readings of the diagonal LVDTs attached to pier P2-9 versus base shear force (Cycle 19a).

APPENDIX E

EXPERIMENTAL RESULTS OF WALL A

E.1 Introduction

The behavior of Wall A after post-tensioning with unbonded tendons is discussed in this appendix. To assess the effect of different levels of prestressing force two different levels were investigated for Wall A. These prestressing levels were 25 kip and 50 kip which correspond to approximately 50% and 100% increase in vertical stress for the first floor piers. Further details on the retrofit, test setup, instrumentation, and loading scheme can be found in Chapter 3.

A summary of the displacements imposed on Wall A are shown in Table E.1 along with the cycle number and prestressing force. As apparent from the table, Wall A was subjected to at least two cycles at each displacement level, which allows degradation and damage accumulation to be assessed. However, for certain comparisons it is necessary to limit the number of cycles considered at each displacement level. In these cases the initial cycle conducted during each test run was used and is shown in italics Table E.1.

Table E.1 Summary of displacements imposed on Wall A

Test Run	PT Force (kip)	Cycles	Target Roof Displacement (in)	Target Second Floor Displacement (in)
27	25	*a*,b	+/-0.04	+/-0.03
28	25	*a*,b	+/-0.06	+/-0.054
29	25	*a*,b,c,d	+/-0.1	+/-0.93
30	25	*a*,b	+/-0.15	+/-0.138
31	25	*a*,b	+/-0.25	+/-0.235
32	25	*a*,b	+/-0.375	0.352, -0.356
33	25	*a*,b	+/-0.5	+/-0.475
34	50	*a*,b	+/-0.05	+/-0.0475
35	50	*a*,b	+/-0.15	+/-0.143
36	50	*a*,b	+/-0.25	+/-0.24
37	50	*a*,b	+/-0.375	0.368, -0.364
38	50	*a*,b	+/-0.5	+/- 0.485
39	50	*a*,b	+/-0.75	0.638, -0.705

The chapter begins by discussing the general force-displacement behavior of Wall A for both the first and second stories. This behavior is quantified for each test run in terms of secant stiffness, secant mode shape, energy dissipation and residual displacement. Next the damage progression and wall behavior are discussed. For this task, the behavior of the wall was divided into four portions: Group 1 cycles (Test Runs 27 through 30), Group 2 cycles (Test Runs 31 through 33), Group 3 cycles (Test Runs 34 through 35), and Group 4 cycles (Test Runs 36 through 39). Finally, the chapter concludes with a brief summary of the behavior of Wall A.

E.2 Force-Displacement Response

The lateral displacement of Wall A was measured through LVDTs referenced to the structure at the second floor and roof levels (see Appendix B). Due to the importance of these measurements, linear potentiometers were also employed for backup. During Test Run 39 the stroke of the second floor LVDT was exhausted and thus the readings of the potentiometer were used. Figures E.1 through E.5 show plots of roof displacement versus base shear response for Test Runs 27 through 30, Test Runs 27 through 33, Test Runs 34 and 35, Test Runs 34 through 39 and all of the cycles conducted on the Wall A, respectively.

From these figures it is apparent that the response of Wall A remained stable throughout all of the cycles. The wall displayed an increased amount of base shear resistance with each increasing level of roof displacement. Furthermore, negligible degradation in stiffness and peak resistance was observed during the redundant cycle at each displacement level. The shape of the force-displacements plots suggests that the wall displayed a combined rocking/sliding behavior. That is, a combination of nonlinear elastic and elastic plastic behavior. In addition from Figure E.5 it is apparent that the behavior of the wall was very similar for both levels of initial prestressing force (i.e. 25 kip and 50 kip). This phenomenon is attributed to an increase of prestressing force during loading and is discussed in detail in Section E.3.

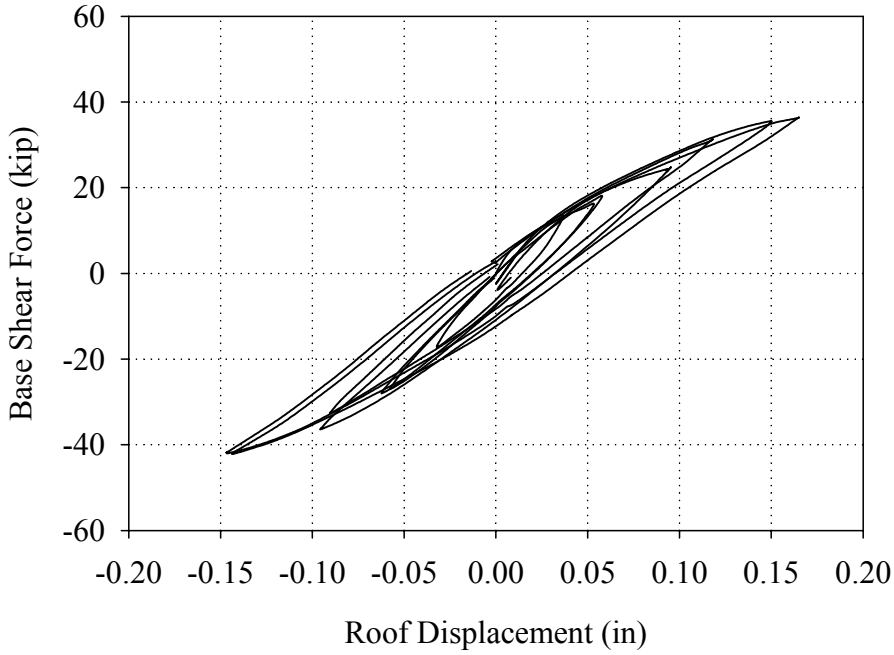

Figure E.1 Base shear versus roof displacement response of Wall A recorded during Test Runs 27 through 30.

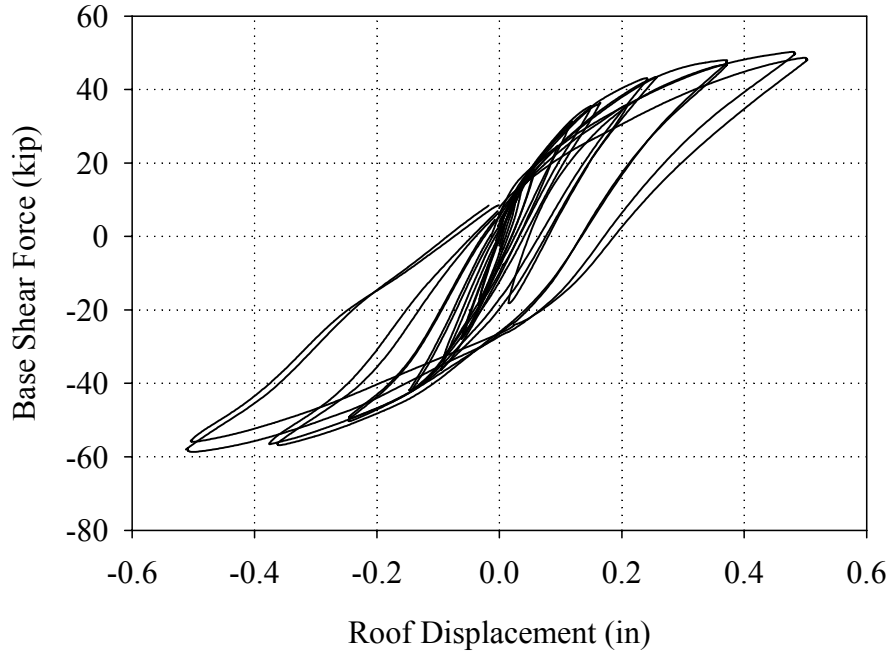

Figure E.2 Base shear versus roof displacement response of Wall A recorded during Test Runs 27 through 33.

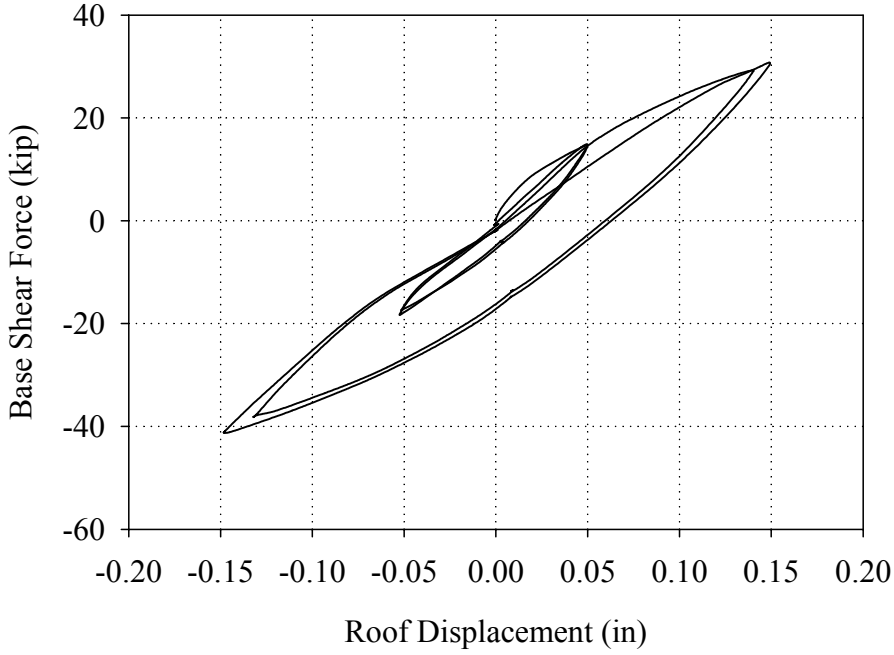

Figure E.3 Base shear versus roof displacement response of Wall A recorded during Test Runs 34 and 35.

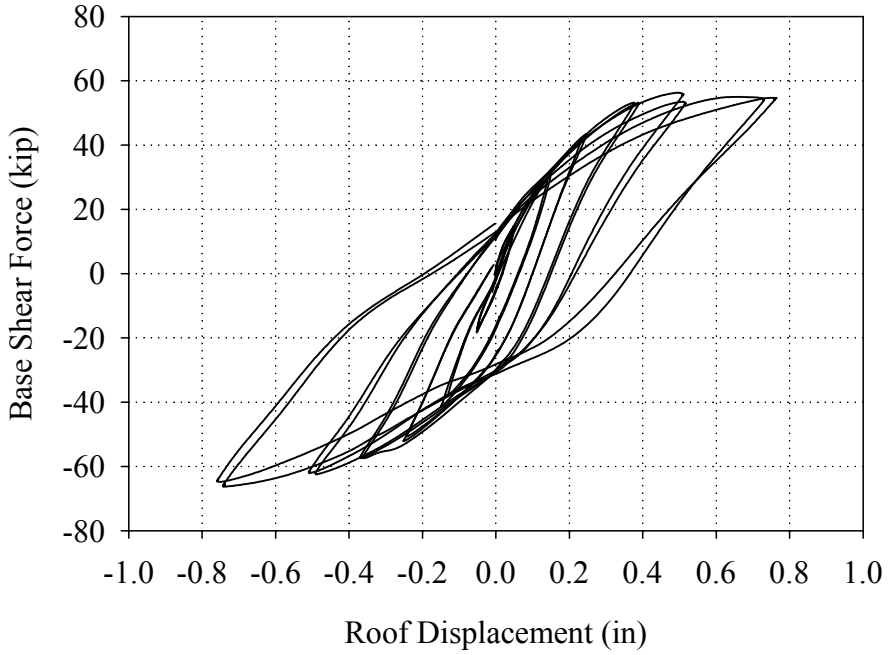

Figure E.4 Base shear versus roof displacement response of Wall A recorded during Test Runs 34 through 39.

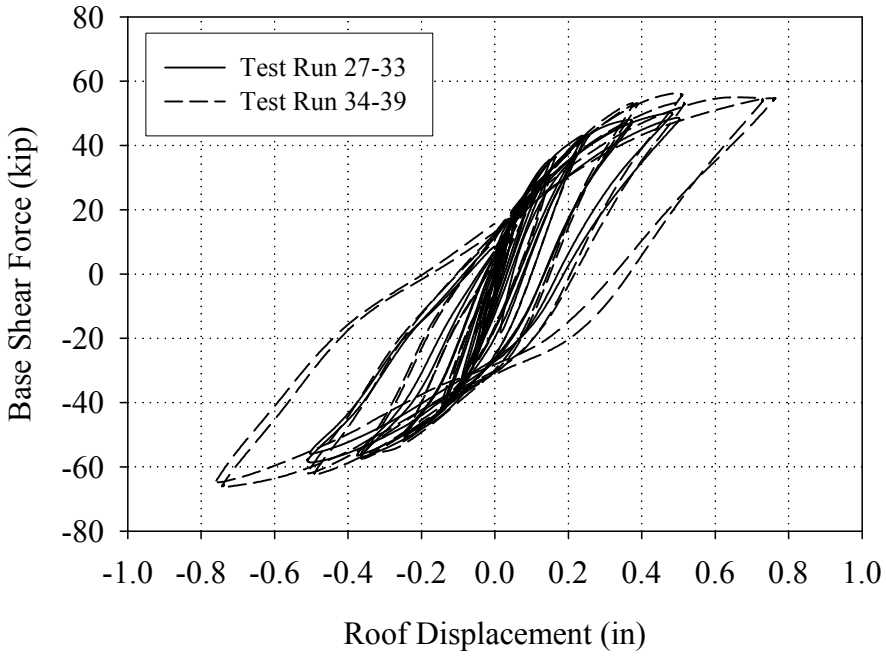

Figure E.5 Complete base shear versus roof displacement response of Wall A.

The force-displacement response of the first story of Wall A is shown in Figures E.6 through E.10 for Test Runs 27 through 30, Test Runs 27 through 33, Test Runs 34 and 35, Test Runs 34 through 39 and all of the cycles conducted on the Wall A, respectively. Figure E.11 through E.13 show the force-displacement response of the second story of Wall A for Test Runs 27 through 33, Test Runs 34 through 39, and all of the cycles conducted on Wall A, respectively.

From Figures E.6 through E.10 it is apparent that the energy dissipation displayed by the base shear versus roof displacement plots was due to the behavior of the first story. In general, the discussion of the base shear versus roof displacement plots applies directly to the behavior of the first story. In contrast, the response of the second story can be classified as nonlinear elastic throughout all of the cycle (see Figures E.11 through E.13). This is attributed to both local rocking of the second story piers as well as global rocking

of the entire structure. Further details on the specific behavior of Wall A can be found in Section E.3.

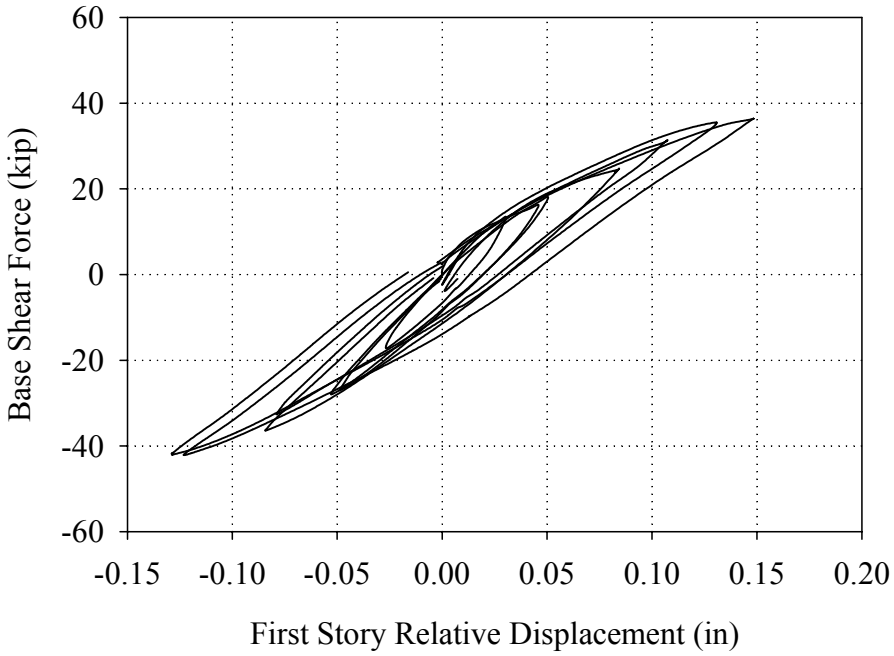

Figure E.6 Force-displacement response of the first story of Wall A recorded during Test Runs 27 through 30)

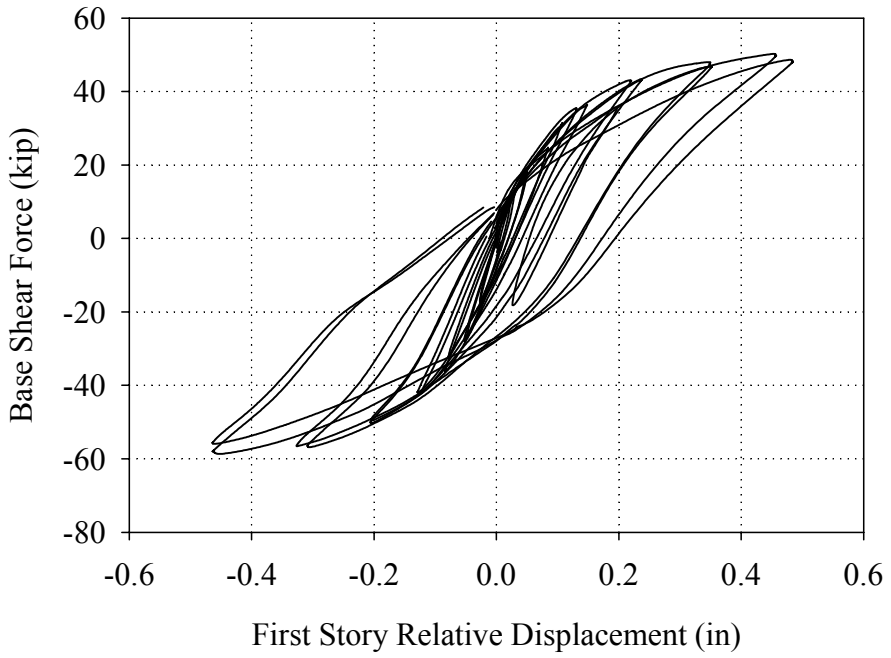

Figure E.7 Force-displacement response of the first story of Wall A recorded during Test Runs 27 through 33.

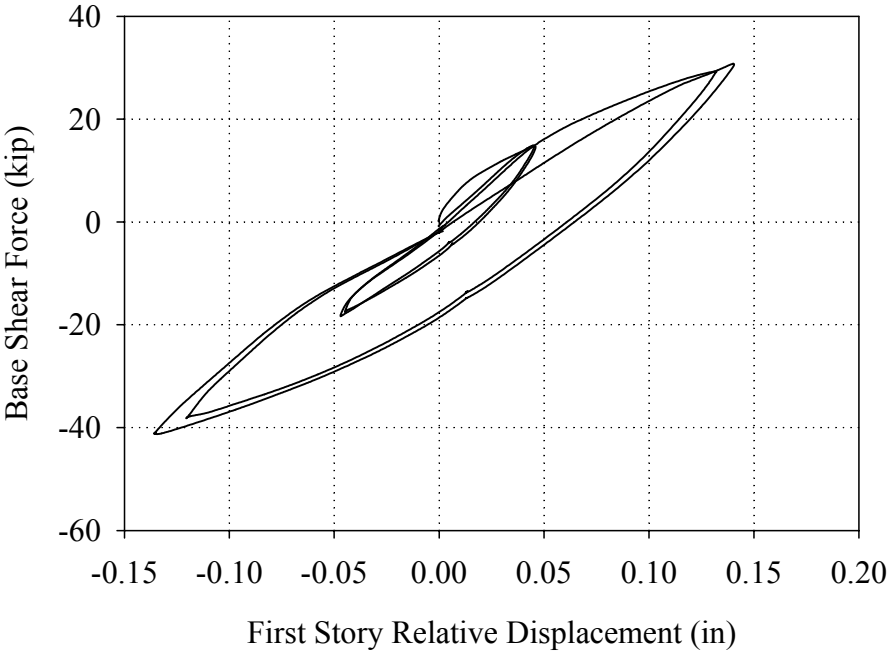

Figure E.8 Force-displacement response of the first story of Wall A recorded during Test Runs 34 and 35.

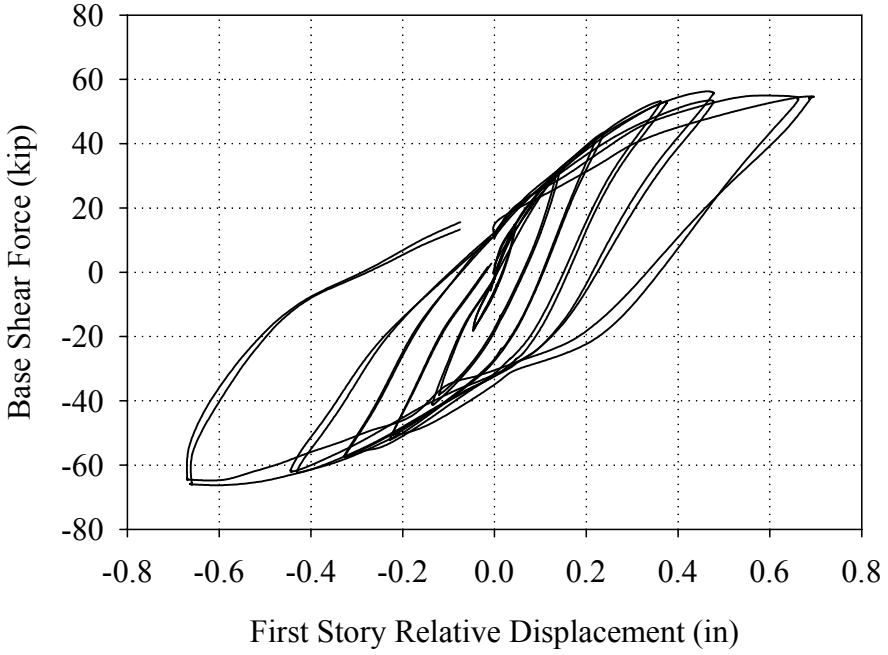

Figure E.9 Force-displacement response of the first story of Wall A recorded during Test Runs 34 through 39.

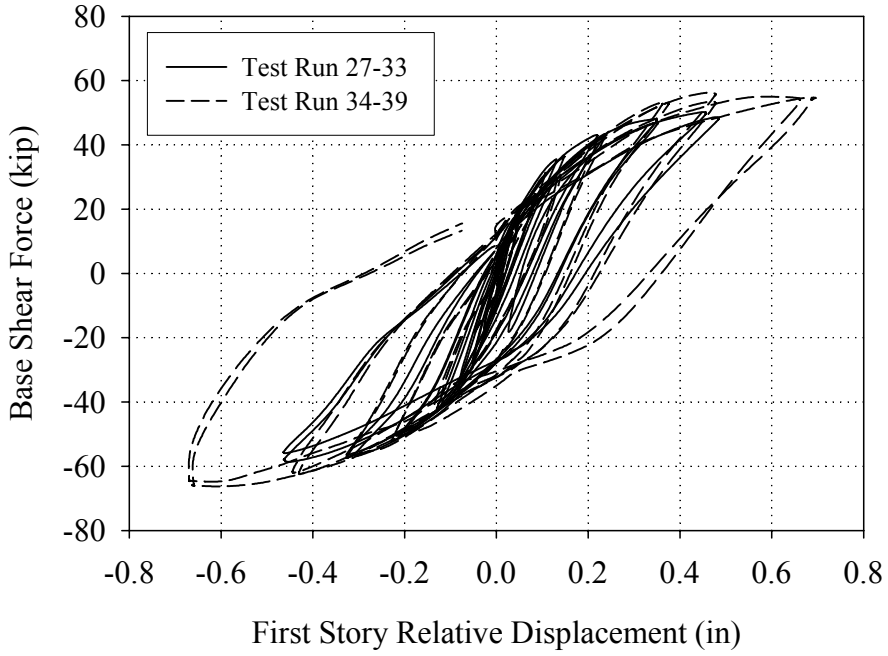

Figure E.10 Complete force-displacement response of the first story of Wall A.

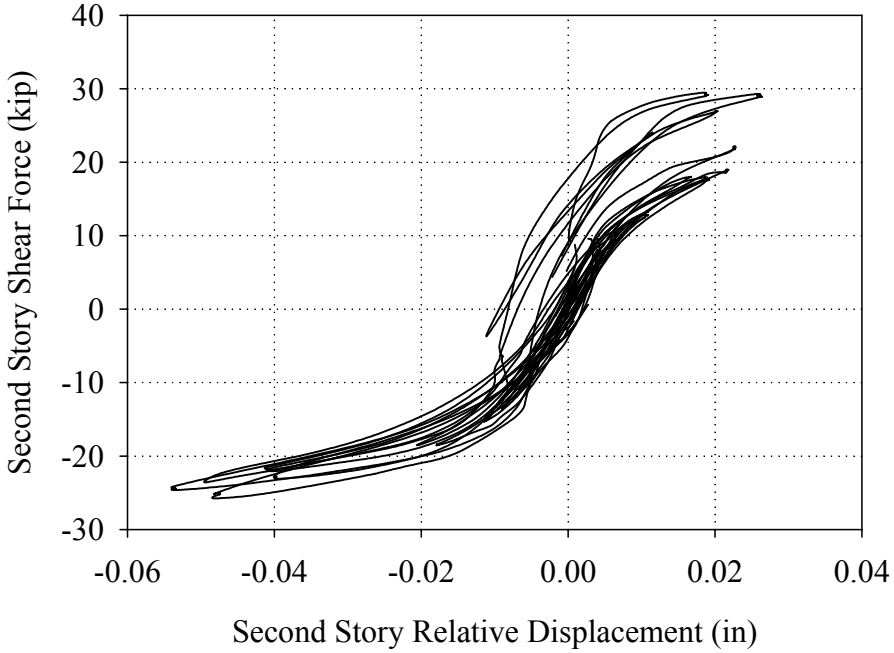

Figure E.11 Force-displacement response of the second story of Wall A recorded during Test Runs 27 through 33.

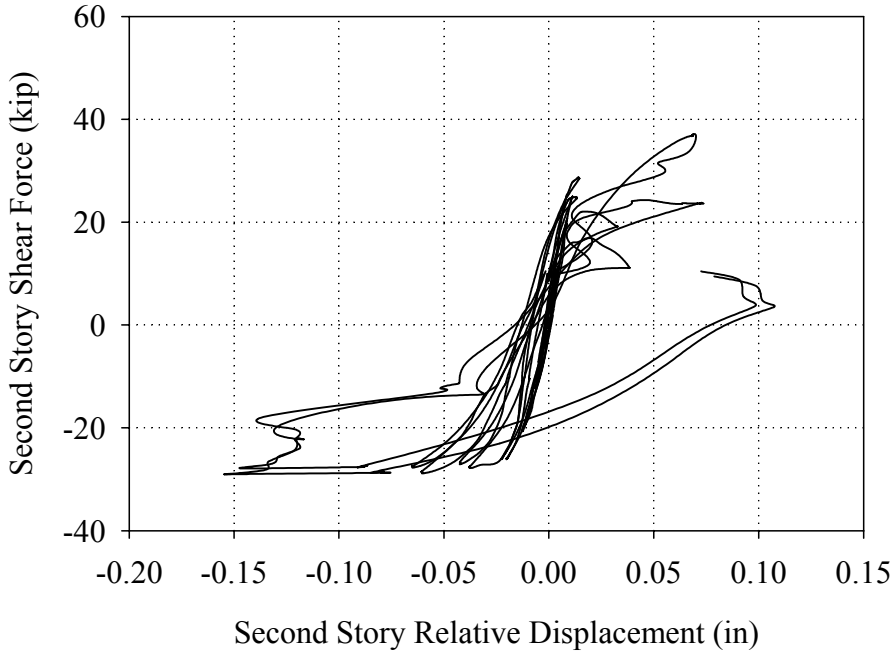

Figure E.12 Force-displacement response of the second story of Wall A recorded during Test Runs 34 through 39.

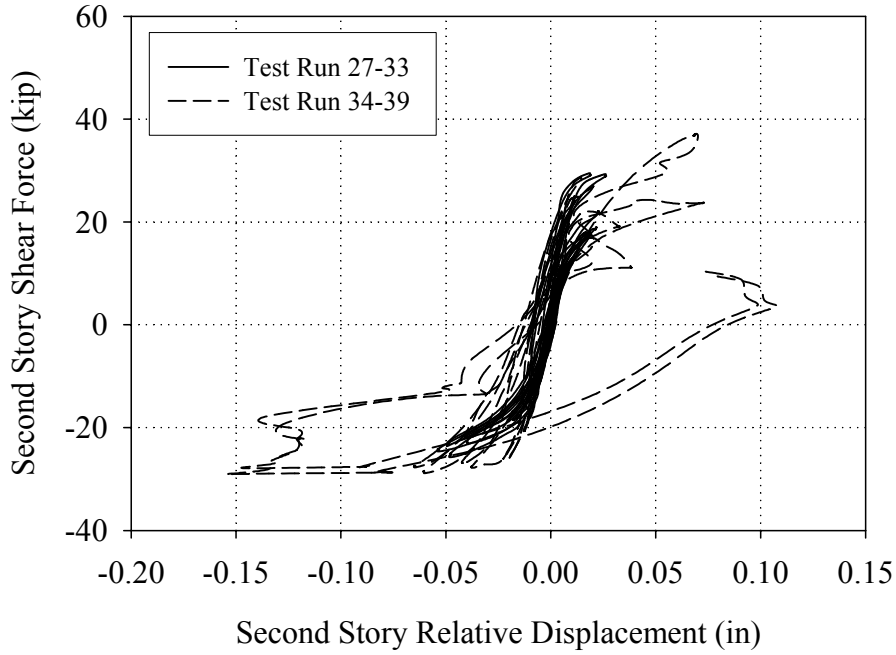

Figure E.13 Complete force-displacement response of the second story of Wall A.

E.2.1 Stiffness and Mode Shapes

For each of the Test Runs conducted on Wall A, the secant stiffness' for both the first story and second story were determined. The secant stiffness of the structure represents an average tangent stiffness, and as such can be used as an indication of damage. The stiffness' were taken as the slope of a line connecting the peak displacement point (both positive and negative) and the point at which the plot crosses the x-axis. This procedure is is discussed in detail in Appendix B. Table E.2 shows the calculated secant stiffnesses for the first and second stories of Wall A for each test run.

Table E.2 Secant Stiffness of Wall A for each test run

Test Run	Story	Positive Secant Stiffness (kip/in)	Negative Secant Stiffness (kip/in)
27	First	429	441
	Second	1598	1274
28	First	354	400
	Second	1509	1448
29	First	318	310
	Second	1496	1187
30	First	287	260
	Second	1019	972
31	First	197	185
	Second	846	581
32	First	120	129
	Second	731	413
33	First	107	94
	Second	876	550
34	First	310	275
	Second	2460	2298
35	First	231	204
	Second	2568	2029
36	First	184	154
	Second	2420	1756
37	First	140	124
	Second	1737	933
38	First	92	101
	Second	328	544
39	First	65	60
	Second	385	208

From this table it is apparent that the secant stiffness of each story decreased during almost every cycle of increasing roof displacement. This is expected since the secant stiffness can also be used as a measured of nonlinear response. Based on the relative decrease between the first and second floor, these stiffness' suggest that the majority of the damage focused on the first floor of Wall A.

That is, particularly for the large level of post-tensioning force, Wall A seemed to form a soft story.

To gain more insight into the seismic behavior of Wall A, the fundamental secant mode shapes were determined for each Test Run and are listed in Table E.3 (see Appendix B for a detail description of this calculation and associated assumptions). In addition, Figures E.14 and E.15 show the calculated secant mode shapes (normalized to roof displacement) for Test Runs 27 through 33 and Test Runs 34 through 39, respectively.

Table E.3 Fundamental secant mode shapes of Wall A normalized to 1.0 for all cycles.

Test Run	Positive Fundamental Secant Mode Shape	Negative Fundamental Secant Mode Shape
27	$\{1.0, 0.92\}^T$	$\{1.0, 0.89\}^T$
28	$\{1.0, 0.93\}^T$	$\{1.0, 0.91\}^T$
29	$\{1.0, 0.93\}^T$	$\{1.0, 0.92\}^T$
30	$\{1.0, 0.91\}^T$	$\{1.0, 0.92\}^T$
31	$\{1.0, 0.93\}^T$	$\{1.0, 0.90\}^T$
32	$\{1.0, 95\}^T$	$\{1.0, 0.90\}^T$
33	$\{1.0, 0.96\}^T$	$\{1.0, 0.95\}^T$
34	$\{1.0, 0.96\}^T$	$\{1.0,0.96\}^T$
35	$\{1.0, 0.97\}^T$	$\{1.0, 0.97\}^T$
36	$\{1.0, 0.98\}^T$	$\{1.0, 0.97\}^T$
37	$\{1.0, 0.97\}^T$	$\{1.0, 0.96\}^T$
38	$\{1.0, 0.91\}^T$	$\{1.0, 0.94\}^T$
39	$\{1.0, 0.95\}^T$	$\{1.0, 0.91\}^T$

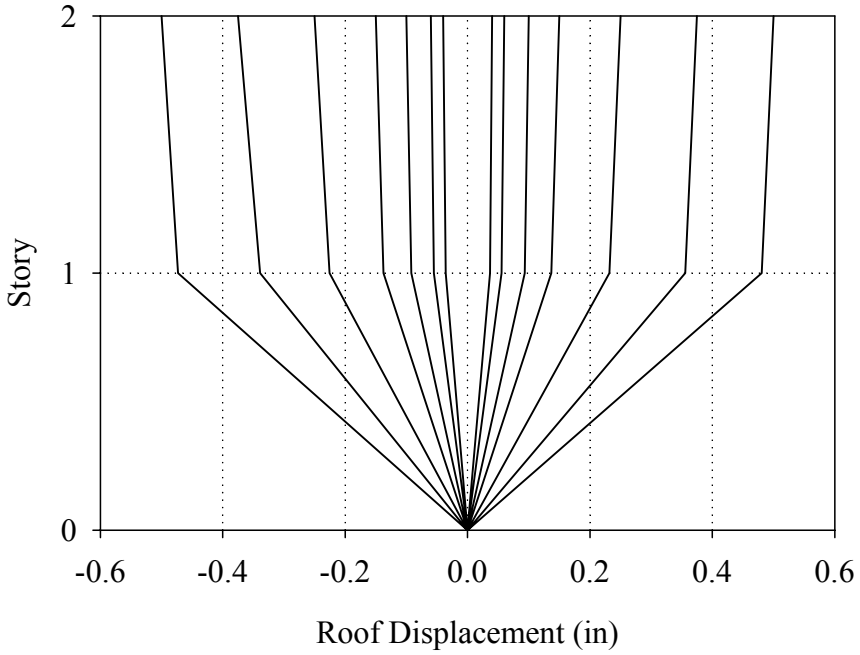

Figure E.14 Fundamental secant mode shapes of Wall A normalized to target roof displacement for Test Runs 27 through 33.

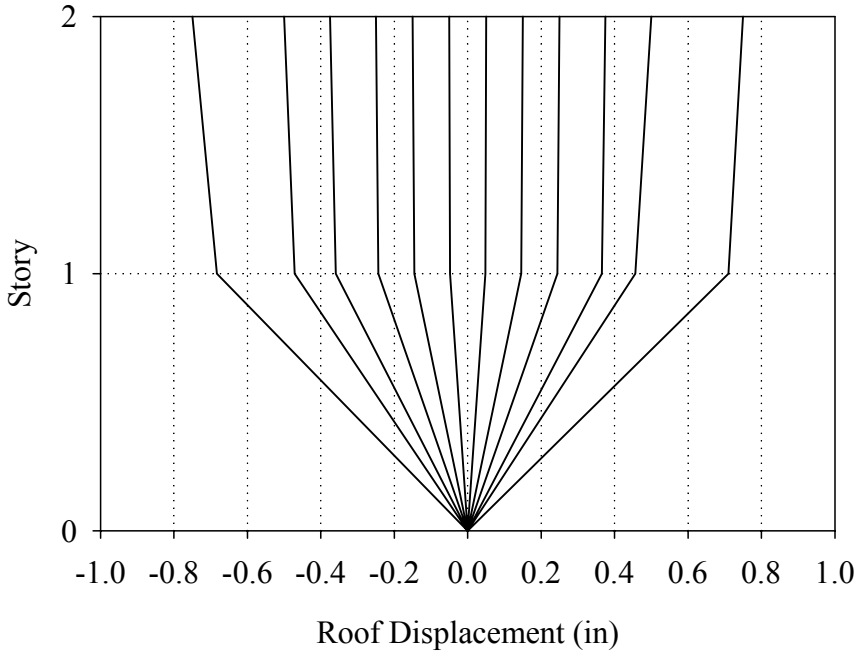

Figure E.15 Fundamental secant mode shapes of Wall A normalized to target roof displacement for Test Runs 34 through 39.

As apparent from this table and figures, the calculated fundamental secant mode shapes changed slightly from cycles to cycle. As the displacement level increased, the percentage of displacement of the first story also increased. This is an indication that the majority of the damage focused on the first floor and may suggest the formation of a soft story. As discussed in relation to the secant stiffness', due to the global rocking behavior of Wall A this trend was not observed during Test Run 38 and 39.

E.2.2 Energy Dissipation

The energy dissipated by each floor of Wall A was calculated for each of the cycles conducted. This was accomplished by numerically integrating the force-displacement plots shown in Figures E.6 through E.13 (see Appendix B). For comparison purposes, the calculated values were divided by the maximum possible energy dissipation capacity, which was defined as the area of a rectangle encompassing the force-displacement plot. Figure E.16 shows the percentage of energy dissipated by each floor versus roof displacement. In addition, Figure E.17 shows the actual energy dissipated by each floor versus roof displacement.

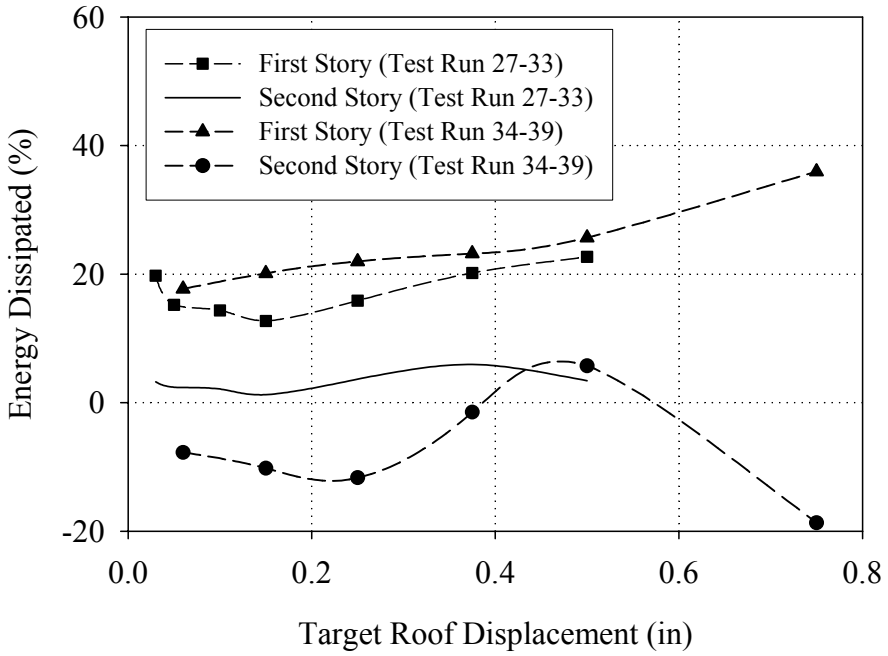

Figure E.16 Percentage of energy dissipated by each story of Wall A versus target roof displacement.

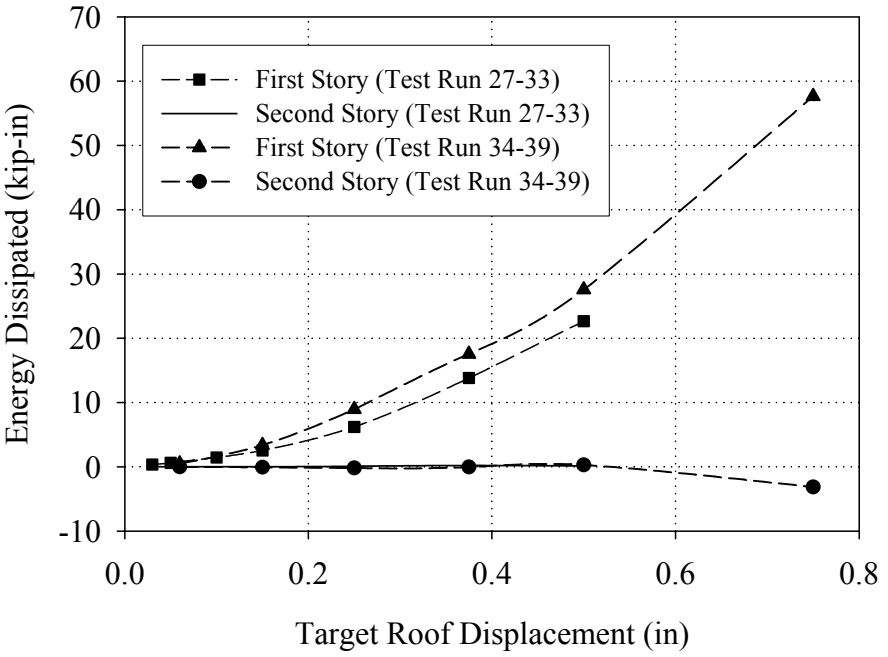

Figure E.17 Energy dissipated by each story of Wall A versus target roof displacement.

From Figure E.16 it is apparent that the percentage of energy dissipated by the first story increased with increasing roof displacement. Furthermore, a slight increase in the percentage of energy dissipated was observed for the larger level of post-tensioning; however, this increase may be a result of additional damage rather than an effect of the level of post-tensioning. Initially, the percentage of energy dissipated for both levels of post-tensioning was approximately 15% to 20%, which is consistent with predominately rocking behavior. As the roof displacement increased this percentage gradually increased up to approximately 40% during Test Run 39. The nature of this increase implies a slow evolution of behavior from primarily rocking to one that incorporated a larger degree of sliding. Also from Figure E.16 it can be seen that the second story dissipated a negative amount of energy during Test Run 34 through 37. This erroneous measurement is likely caused by the low-level global rocking of Wall A as discussed in the previous sections.

As apparent from Figure E.17, the first story of Wall A dissipated far more energy than the second story. This indicates the majority of the damage in Wall A focused on the first story and is expected due to the large relative displacements imposed on the first story. In addition, the extremely small magnitude of energy dissipated by the second story renders the apparent negative percentage of energy dissipated trivial.

E.2.3 Residual Displacement

The residual displacement of each story of Wall A was calculated for each Test Run according to the procedure outlined in Appendix B. However, due to the small displacements imposed on the second story, the residual displacements measured were negligible and are not discussed. The residual displacements for the first story of Wall A

are presented in Table E.4 as a percentage of the story drift. Figures E.18 shows the residual displacement of the first floor of Wall A (as a percentage of story drift) versus story drift for Test Runs 27 through 33 and Test Runs 34 through 39.

Table E.4 Residual Displacement of Wall A

Test Run	+ Residual Displacement (% of Story Drift)	- Residual Displacement (% of Story Drift)
27	5	7
28	38	26
29	38	31
30	25	29
31	36	33
32	41	39
33	44	42
34	46	27
35	44	30
36	44	38
37	44	47
38	51	49
39	58	51

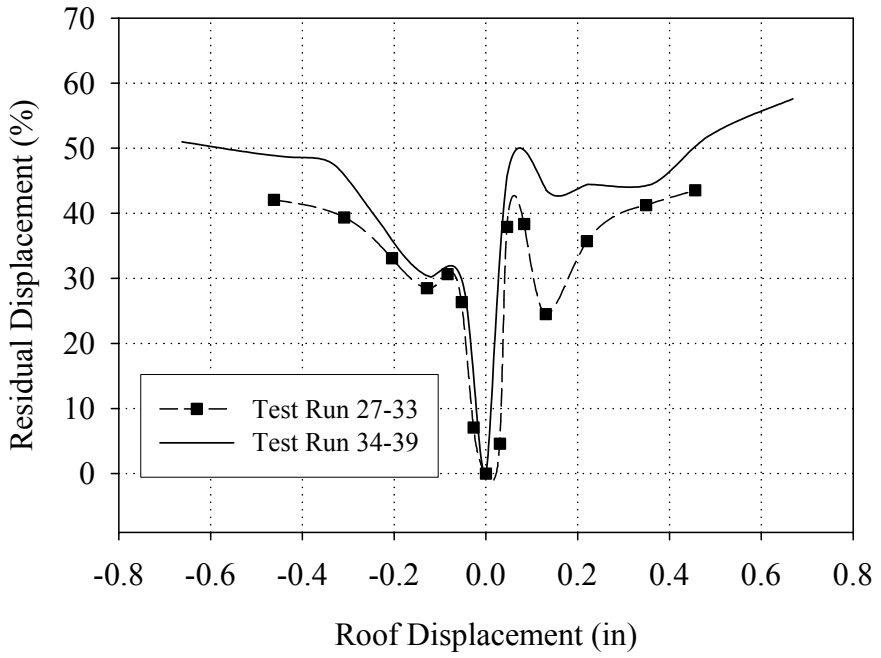

Figure E.18 Residual displacement as a percentage of story drift for the first floor of Wall A versus story drift

From Figure E.18 it is apparent that the residual displacement of the first floor of Wall A recorded during Test Runs 34 through 39 (i.e. post-tensioning force of 50 kip) was slightly greater than the residual displacements measured during the initial cycles. However, the general trend of the behavior was very similar for both levels of post-tensioning. That is, the percentage of residual displacement (as compared to the story drift) increased with increasing displacements. This suggests that as the first story drift increased, the wall displayed an increase in sliding deformation. However, the gradual slope displayed in Figure E.18 (for cycles beyond 0.06 in roof displacement) suggests that this increase in sliding behavior was not a drastic change but rather a slow evolution. This is consistent with the discussion of percentage of energy dissipation in Section E.2.2.

E.3 Damage Progression and Wall Behavior

The following sections describe the behavior of Wall A observed during each of the four groups of cycles defined in Section E.1. For each group of cycles the general behavior of the wall is first described including crack pattern and descriptions of visual observations. Following this description the specific behavior of the in-plane piers are described and representative plots of the instrumentation attached to the piers are presented.

E.3.1 Group 1 Cycles (Test Run 27-Test Run 30)

E.3.1.1 Overall Wall Behavior

Figures E.19 through E.21 show schematics of the crack pattern in Wall A and out-of-plane Walls 1 and 2 following the Group 1 cycles. During these cycles two cracks formed in pier PA-9 and are shown in bold in Figure E.19. The remaining cracks shown in the figure formed during testing of Wall A prior to post-tensioning or during the loading of Walls 1 and 2 in-plane (see Appendix C and D). For a complete discussion of the testing of Wall A prior to post-tensioning the reader is directed to Yi (2004).

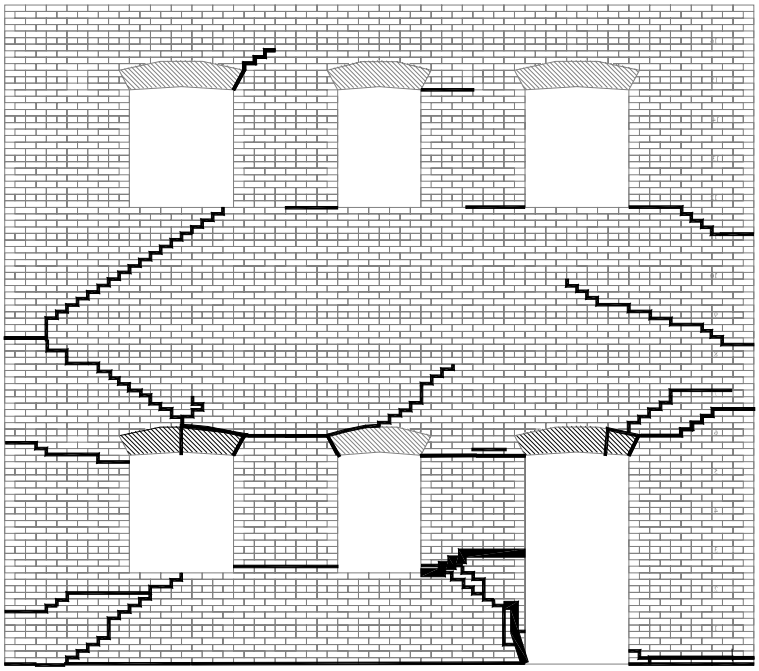

Figure E.19 Crack pattern of Wall A following the Group 1 cycles.

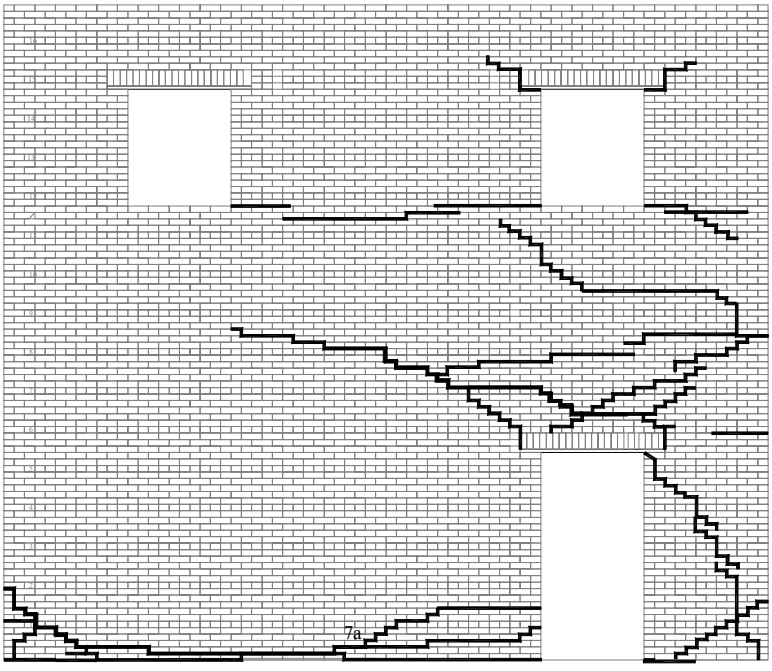

Figure E.20 Crack pattern of out-of-plane Wall 1 following the Group 1 cycles.

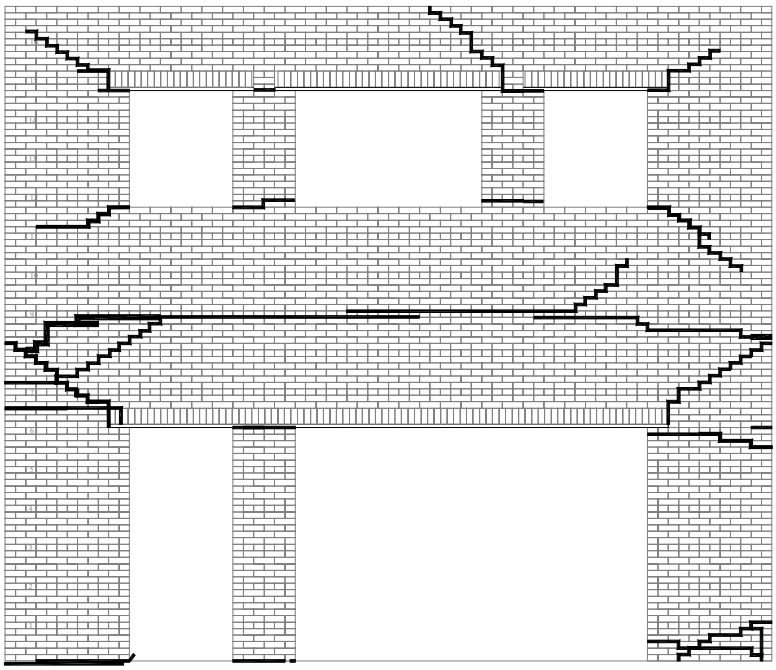

Figure E.21 Crack pattern of out-of-plane Wall 2 following the Group 1 cycles.

Figure E.22 shows a schematic illustrating the behavior of Wall A as well as out-of-plane Walls 1 and 2 in the positive direction. Note that the location of the LVDT reference points are also shown in the figure. In the positive loading direction, Wall A behaved as a culmination of components. That is, the interstory shear force/displacement drove the response of the piers. In general, the behavior of the first floor piers can be classified as a combination of rocking and bed-joint sliding. The observed and measured rigid motion is also shown in Figure E.22 by arrows.

Figure E.23 shows the vertical displacements measured for each side of Wall A versus roof displacement during Cycle 30a. Based on this figure it is apparent that both sides of the Wall A displaced upwards slightly. This uplift is attributed to the local rocking displayed by the first floor piers of Wall A. In addition, this uplift resulted in an increase in

the force in each of the post-tensioning tendons. Figure E.24 shows the force in each of the tendons versus roof displacement for Cycle 30a. Based on this plot it is evident that the total post-tensioning force in Wall A increased by approximately 15% during loading in the positive direction.

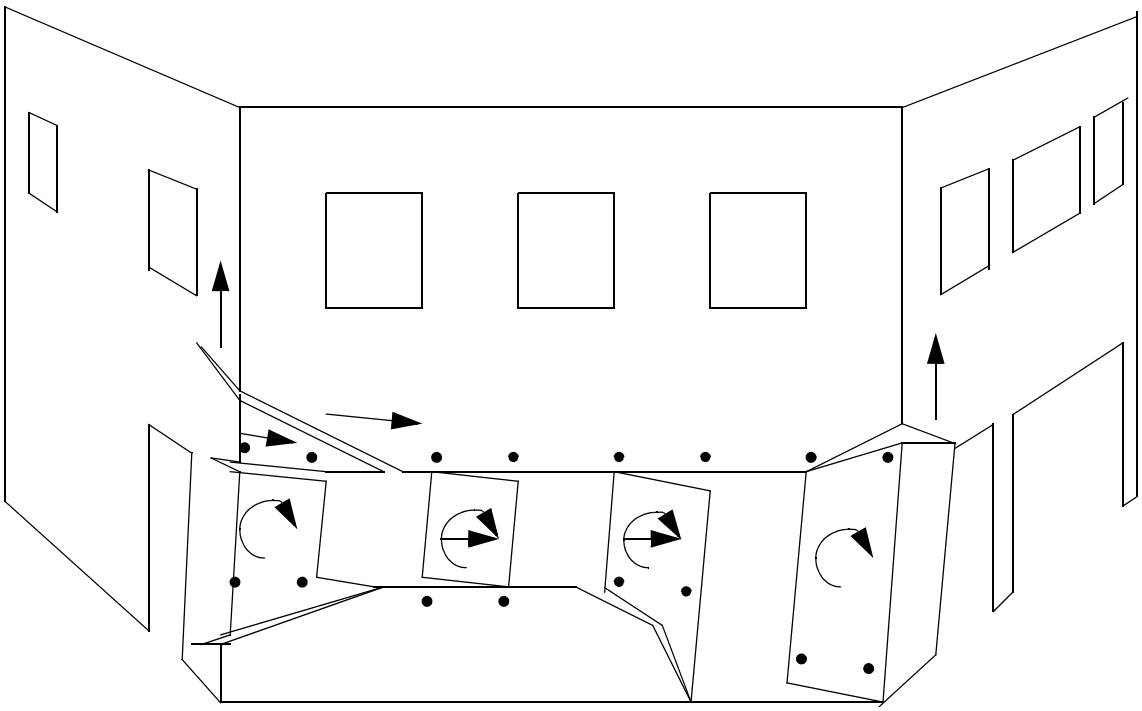

Figure E.22 Exaggerated schematic of the observed behavior of Wall A in the positive loading direction during the Group 1 cycles.

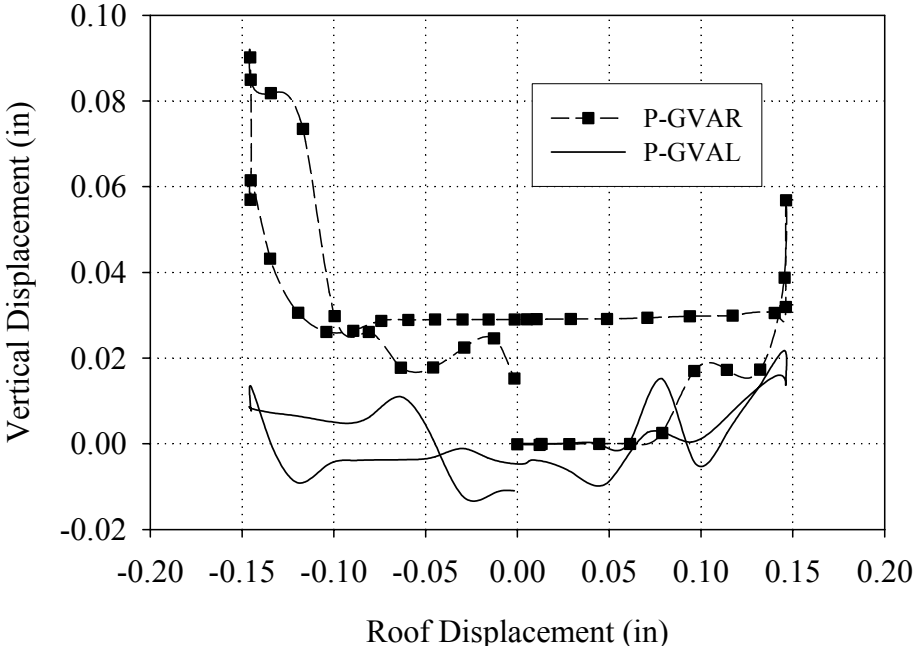

Figure E.23 Vertical displacements of both sides of Wall A versus roof displacement (Cycle 30a)

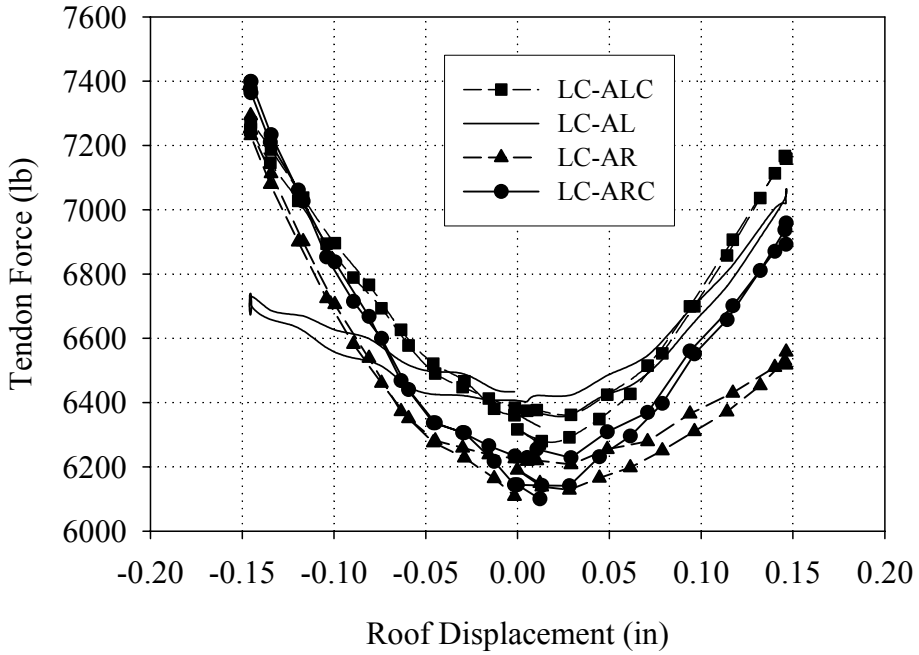

Figure E.24 Post-tensioning force versus roof displacement (Cycle 30a)

In addition to increasing the force in the post-tensioning tendons, the uplift of Wall A engaged portions of out-of-plane Walls 1 and 2 (see Figure E.22). Specifically, the rocking of pier PA-10 caused a vertical displacement and lifted up the portion of Wall 2 above pier P2-7. Based on the small displacements imposed during these low-amplitude cycles, the participation of Wall 1 is unclear; however, the figure illustrates the existing cracks located in Wall 1 that may have been opening.

Figure E.25 shows the base strains recorded at the peak positive displacement during Cycle 30a. As apparent from this figure, the recorded strain profiles of each pier are mostly consistent with the observed rocking deformation. In addition, the recorded strain profiles also support the contention that the out-of-plane walls participated in the response. This is clearly seen by the tensile strains measured in pier P1-7 and the compressive strains measured in pier P2-7. However, the reader is cautioned that due to large variations in material properties, numerous cracks, and uncertainties inherent in strain gage measurements obtained from masonry, only a qualitative discussion of this strain data is appropriate.

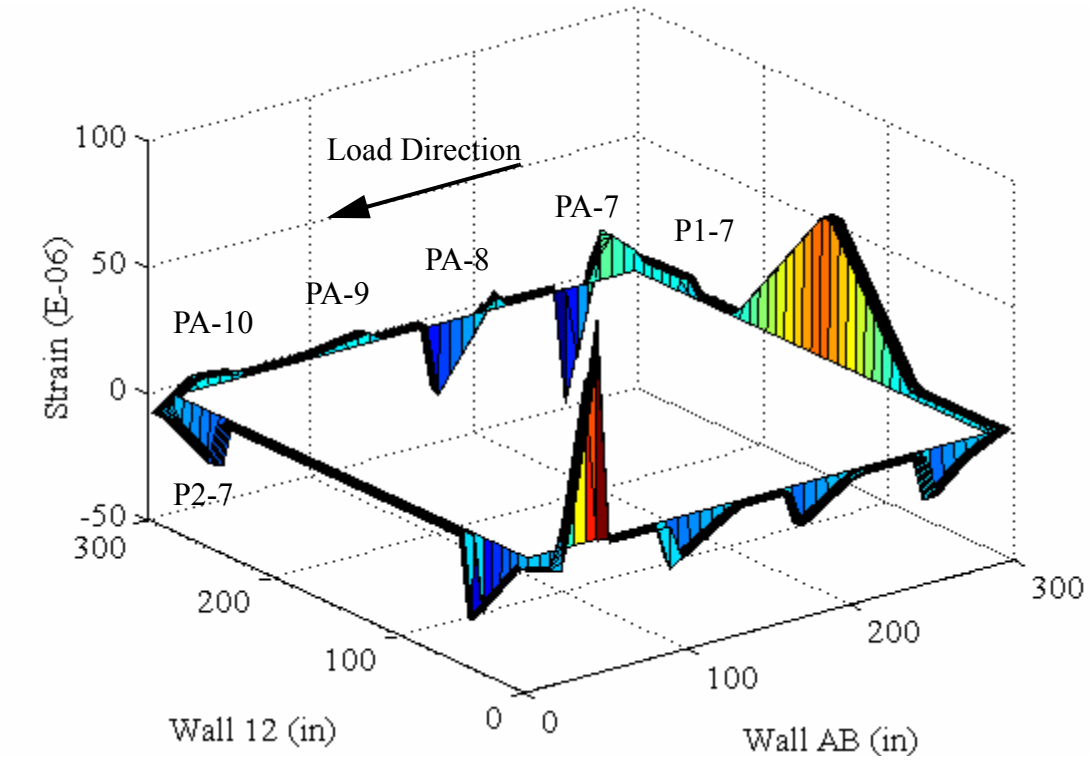

Figure E.25 Base strains recorded at peak positive displacement (Cycle 30a)

Figure E.26 shows a schematic of the behavior of Wall A and out-of-plane Walls 1 and 2 in the negative direction. Note that the location of the LVDT reference points are also shown in the figure. The observed behavior can be classified as a combination of local pier behavior and global rocking behavior. Similar to the behavior in the positive direction, all of the piers displayed some degree of rocking/sliding behavior as shown by arrows in Figure E.26. In addition, visual observations indicated that the low-level global rocking acted to lift the upper portion of Wall A off of pier PA-10, thus effectively leaving this pier behind. However, during this level of testing pier PA-10 was still visibly displaying low-level rocking.

Figure E.23 shows a plot of the vertical displacements of either side of Wall A versus roof displacement recorded during Cycle 30b. From the figure it is apparent that the

measured displacements in the negative loading direction diverged. This implies a rotation of the roof that is consistent with global rocking behavior. Since the aspect ratio of Wall A is nearly 1.0, the difference between the measured vertical displacements is roughly equal to the lateral displacement that resulted from global rocking (assuming rigid body rotation about the base). Following this assumption, the global rocking displacement accounted for approximately 0.08 or roughly 50% of the roof displacement. Conversely this implies that approximately 50% of the roof displacement was due to local pier behavior. In addition, the global rocking implied by Figure E.23 resulted in an increase in post-tensioning force illustrated by Figure E.24. Similar to the behavior in the positive loading direction, the resulting increase in post-tensioning force was approximately 15%.

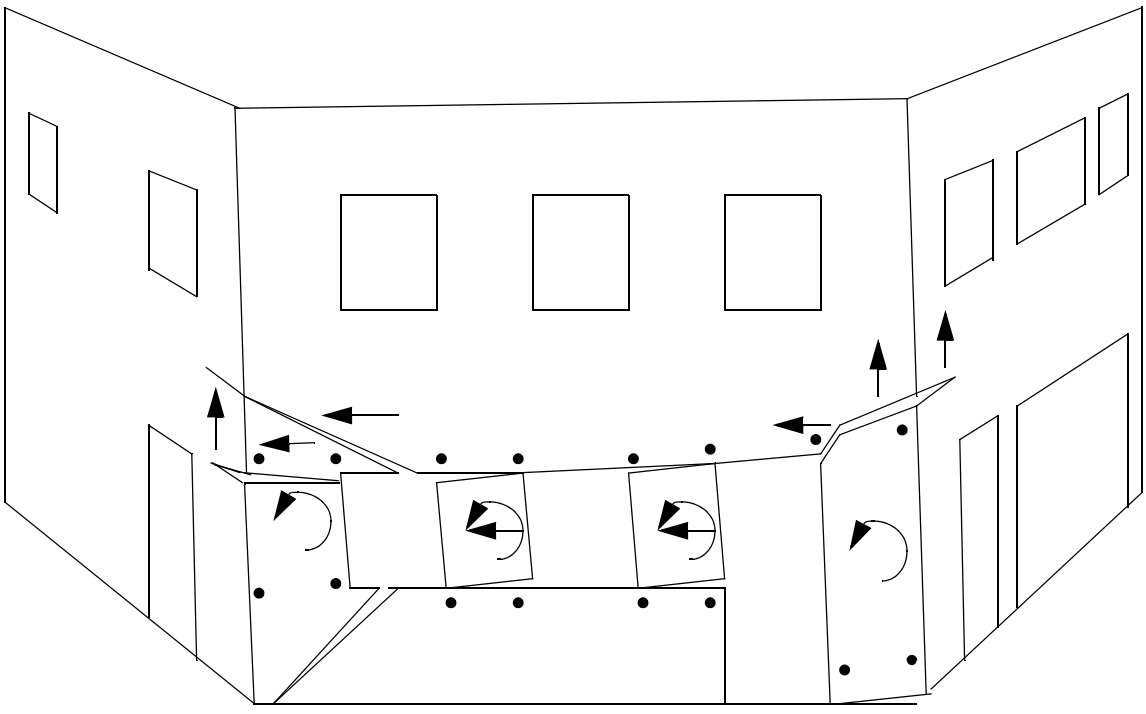

Figure E.26 Exaggerated schematic of the observed behavior of Wall A in the negative loading direction during the Group 1 cycles.

In addition, this uplift engaged portions of Walls 1 and 2 (see Figure E.26). The participation of the out-of-plane walls is also supported by Figure E.27, which shows the base strains recorded at peak displacement in the negative direction during Cycle 30a. As apparent from this figure, the strain profiles in piers PA-9 and PA-10 are consistent with the observed rocking behavior. In addition, the measured strain profile in pier P2-7 is consistent with the observed flange participation illustrated in Figure E.26.

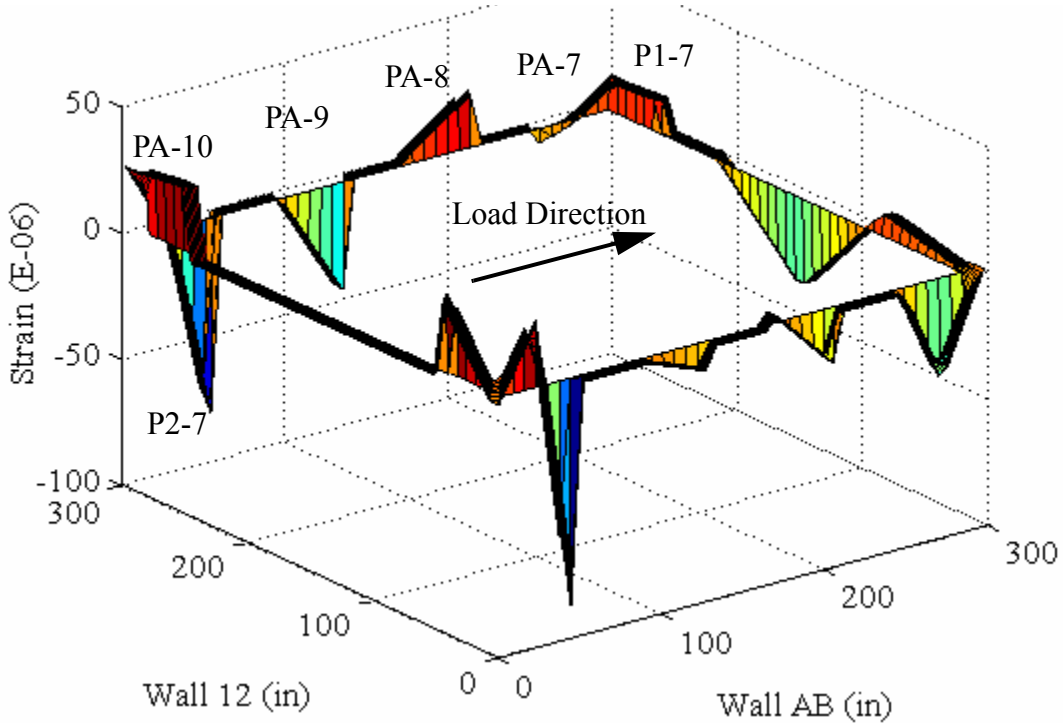

Figure E.27 Base strains recorded at peak negative displacement (Cycle 30a).

E.3.1.2 Local Pier Behavior

Due to the rigid body motion of the first floor piers, the location of the LVDT reference points relative to the active cracks is of paramount importance. As a result, the descriptions of pier behavior given in the following sections utilize Figures E.22 and E.26, which show the location of the LVDTs attached to the piers in reference to the displaced shape. In addition, since all of the piers displayed similar behavior during the Group 1

cycles, the data obtained during Cycle 30a will be used to illustrate the behavior of piers PA-7, PA-9 and PA-10. The behavior of pier PA-8 will be illustrated with data obtained during Cycle 29a since the instrumentation attached to this pier was read improperly during Cycle 30a.

Figures E.28 and E.29 show the readings obtained from the LVDTs attached to pier PA-7; Figure E.30 shows the readings obtained from the LVDTs attached to pier PA-8; Figure E.31 shows the readings obtained from the LVDTs attached to pier PA-9; and Figures E.32 and E.33 show the readings obtained from the LVDTs attached to pier PA-10. In many cases the LVDTs attached to the in-plane piers traversed several cracks (see Figures E.22 and E.26), thus a detailed description of the rotation and translation of each pier is not possible. As a result, only a qualitative discussion will be presented.

In general, Figures E.28 and E.33 indicate that the deformation of piers PA-7 and PA-10 were nearly fully recovered upon unloading, which is consistent with the observed rocking deformation. In contrast, the displacements measured from piers PA-8 and PA-9 showed varying degrees of permanent deformation with pier PA-8 exhibiting the largest permanent set.

Furthermore, the vertical deformation of the outside piers (i.e. PB-7 and PB-10) showed a strong dependence on overturning moment. In contrast, the measured deformation of pier PA-8 seemed to be far more symmetrical in nature. The unsymmetrical response pier PA-9 was likely caused by the change in the location of the active crack as illustrated in the Figures E.22 and E.26. Specifically, in the positive direction, pier PA-9 exhibited a smaller effective aspect ratio than in the negative direction.

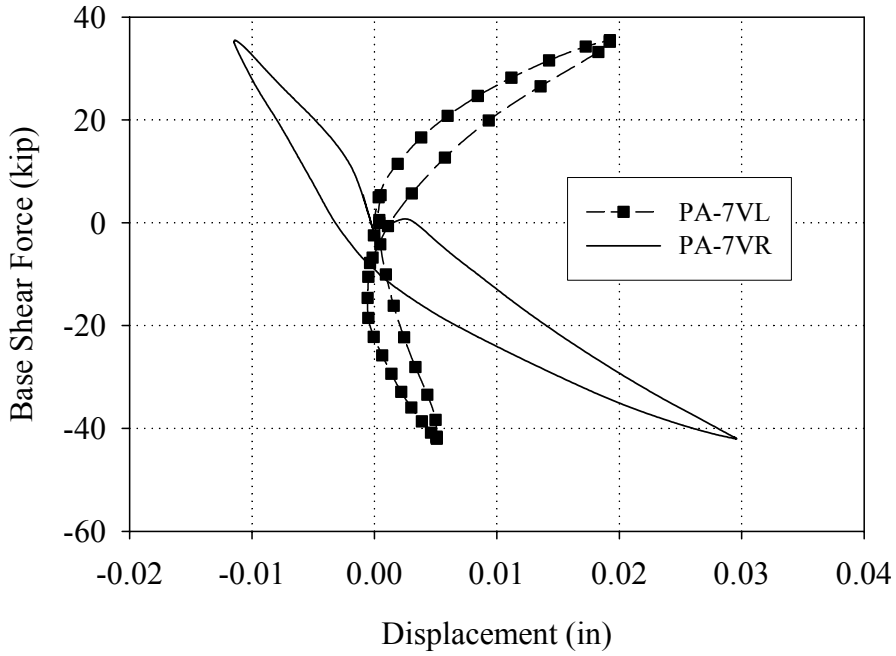

Figure E.28 Readings of the vertical LVDTs attached to pier PA-7 versus base shear force (Cycle 30a)

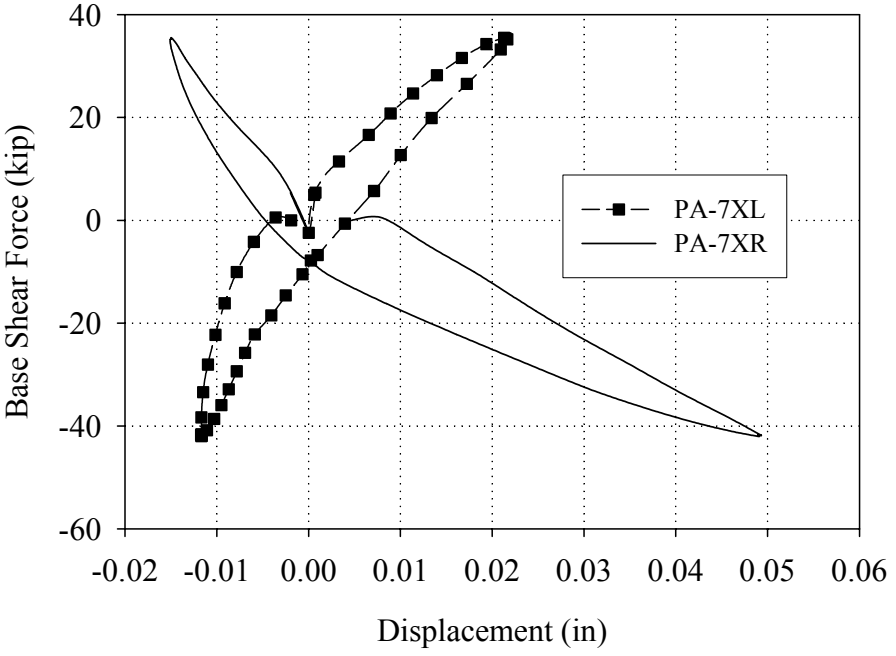

Figure E.29 Readings of the diagonal LVDTs attached to pier PA-7 versus base shear force (Cycle 30a)

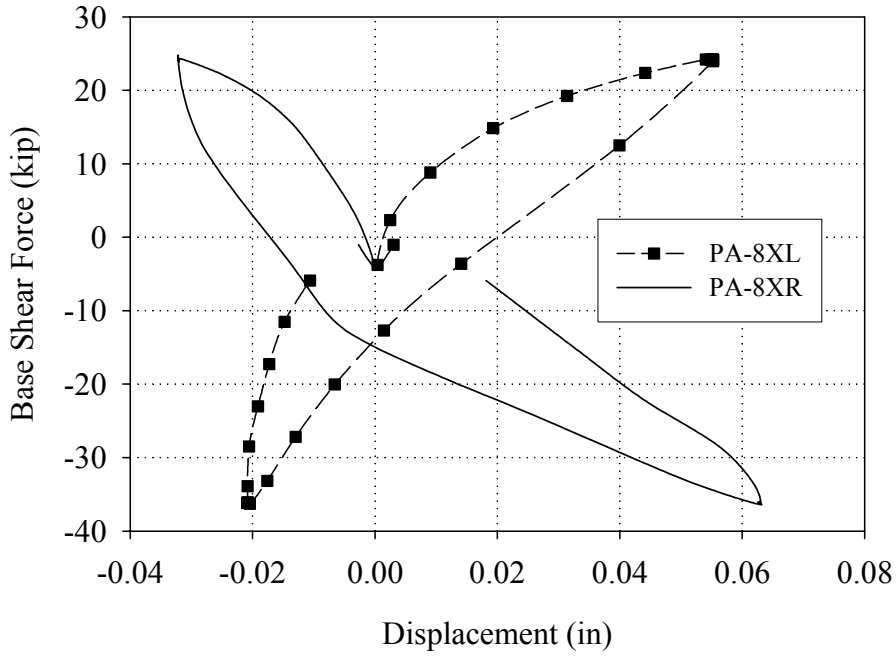

Figure E.30 Readings of the diagonal LVDTs attached to pier PA-8 versus base shear force (Cycle 29a)

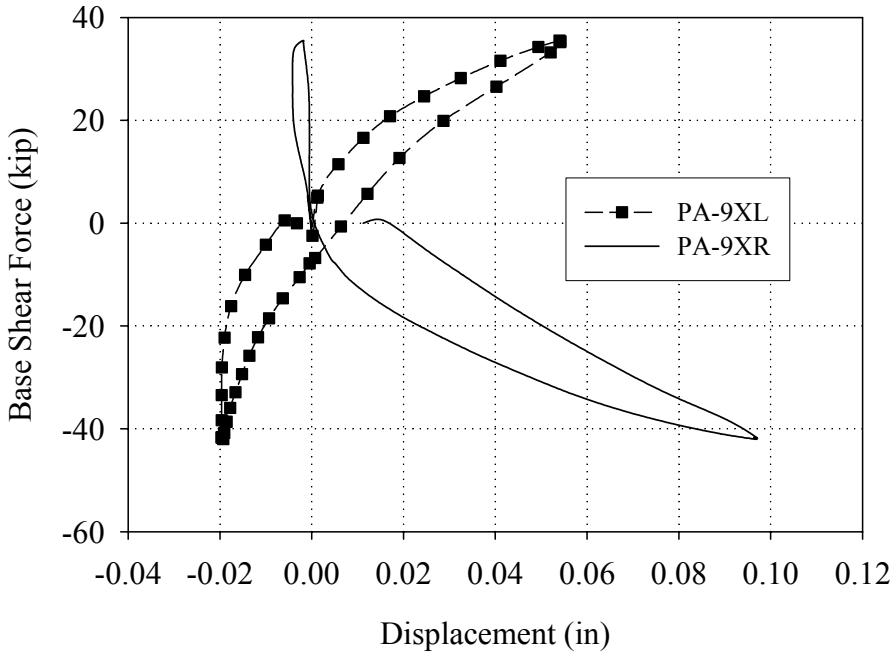

Figure E.31 Readings of the diagonal LVDTs attached to pier PA-9 versus base shear force (Cycle 30a)

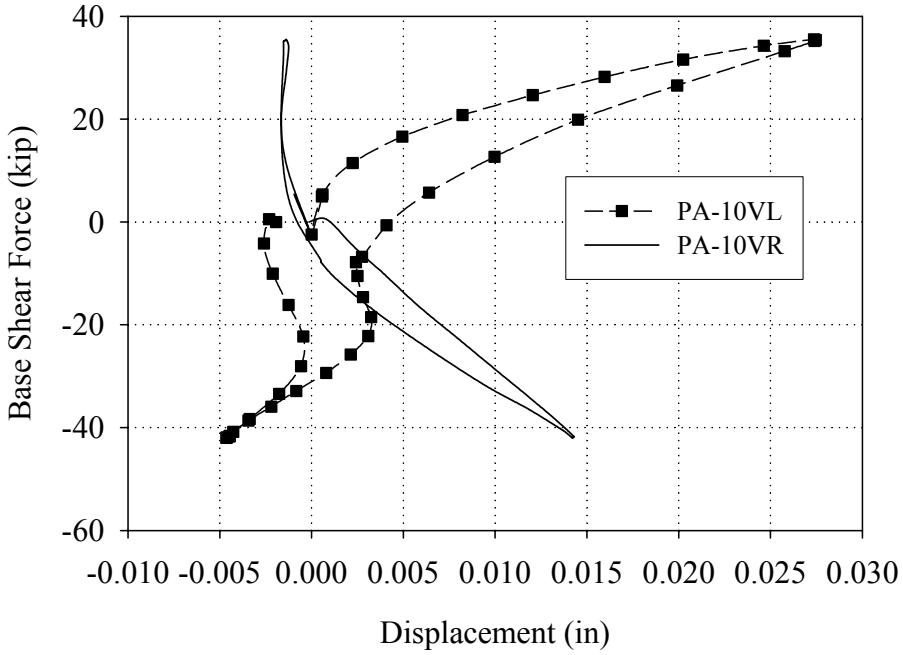

Figure E.32 Readings of the vertical LVDTs attached to pier PA-10 versus base shear force (Cycle 30a)

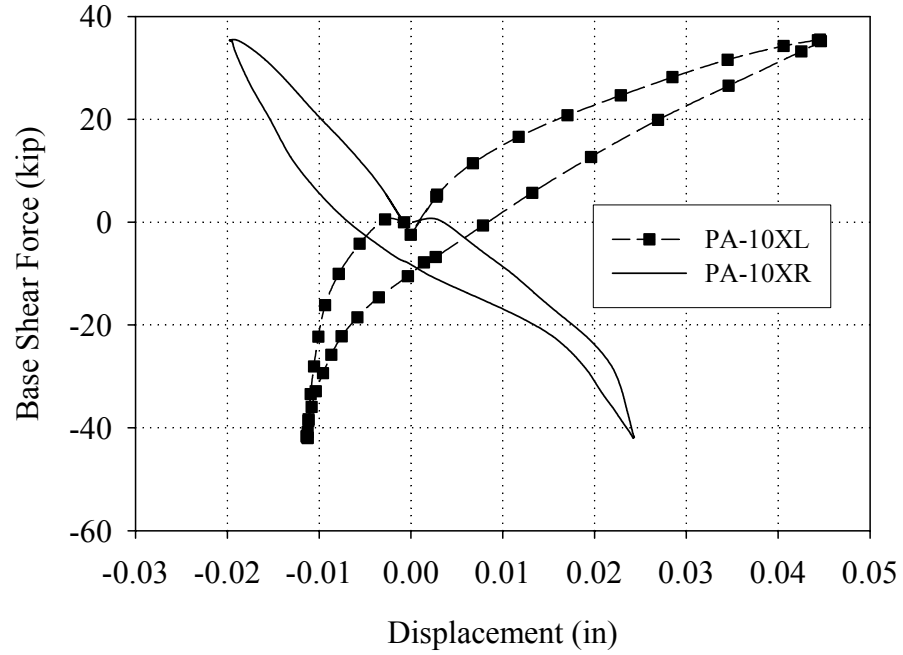

Figure E.33 Readings of the diagonal LVDTs attached to pier PA-10 versus base shear force (Cycle 30a)

E.3.2 Group 2 Cycles (Test Run 31-Test Run 33)

E.3.2.1 Overall Wall Behavior

Figures E.34 through E.36, illustrate the crack pattern in Wall A and out-of-plane Walls 1 and 2 following the Group 2 cycles. In positive loading direction, a crack above pier PA-7 formed and propagated to existing cracks in out-of-plane Wall 2. In the negative loading direction additional cracks formed in pier PA-7 and in out-of-plane pier P1-7. All of these cracks are shown in bold in these figures.

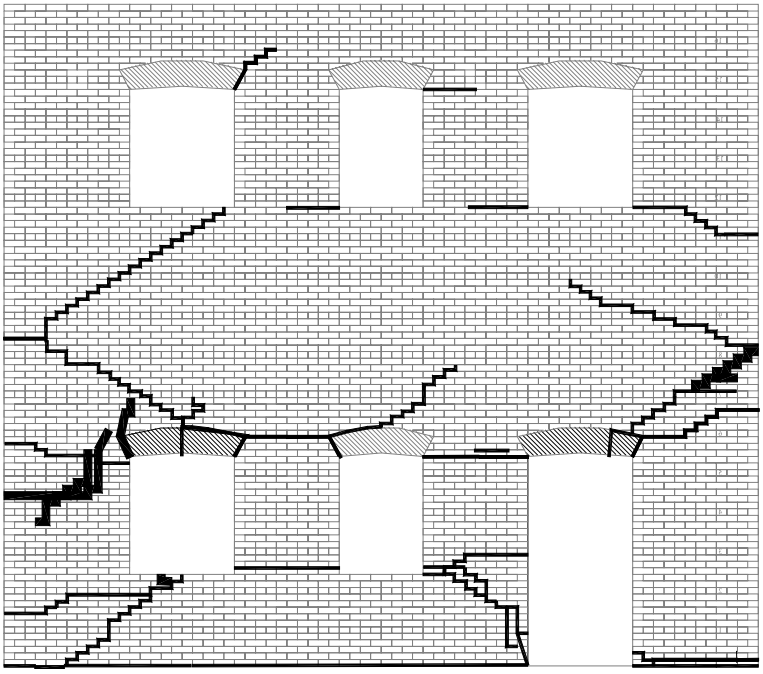

Figure E.34 Crack pattern of Wall A following the Group 2 cycles.

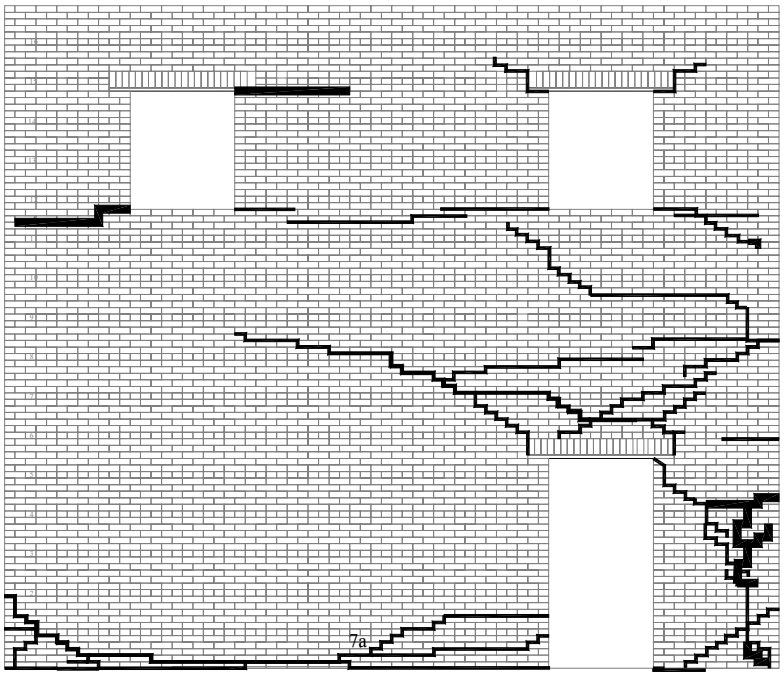

Figure E.35 Crack pattern of out-of-plane Wall 1 following the Group 2 cycles.

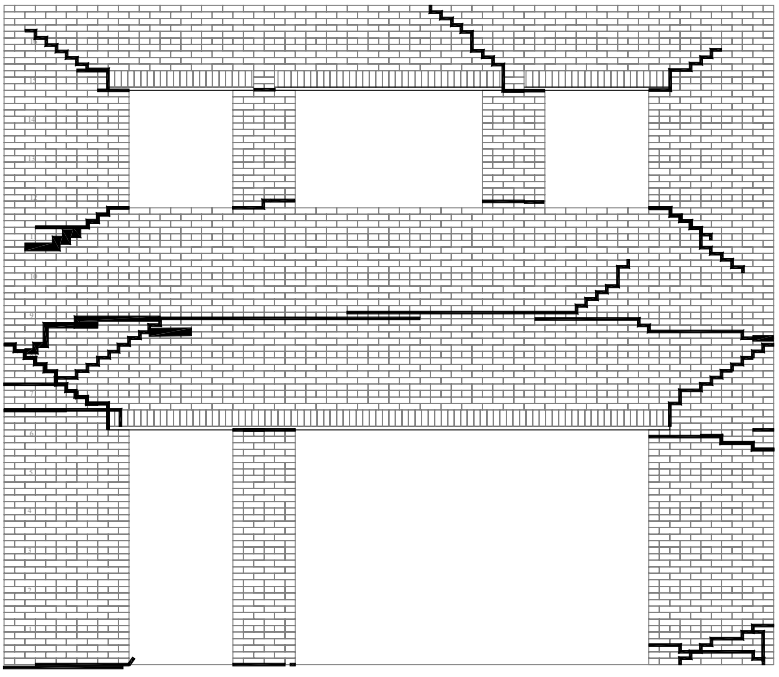

Figure E.36 Crack pattern of out-of-plane Wall 2 following the Group 2 cycles.

Figure E.37 shows a schematic illustrating the behavior of Wall A as well as out-of-plane Walls 1 and 2 in the positive direction. Note that the location of the LVDT reference points are also shown in the figure. In the positive loading direction, Wall A behaved in a similar manner as observed during the Group 1 cycles (see Section E.3.1). The most notable difference in behavior was the large degree of sliding deformation observed in the diagonal crack above pier PA-7. This deformation allowed pier PA-7 to deform only slightly in the positive loading direction. In addition, pier PA-9 displayed a larger amount of sliding deformation than observed during the Group 1 cycles. In general though, the behavior of the first story piers was still mainly a combination of rocking and bed-joint sliding. The observed and measured rigid motion is also shown in Figure E.37 by arrows.

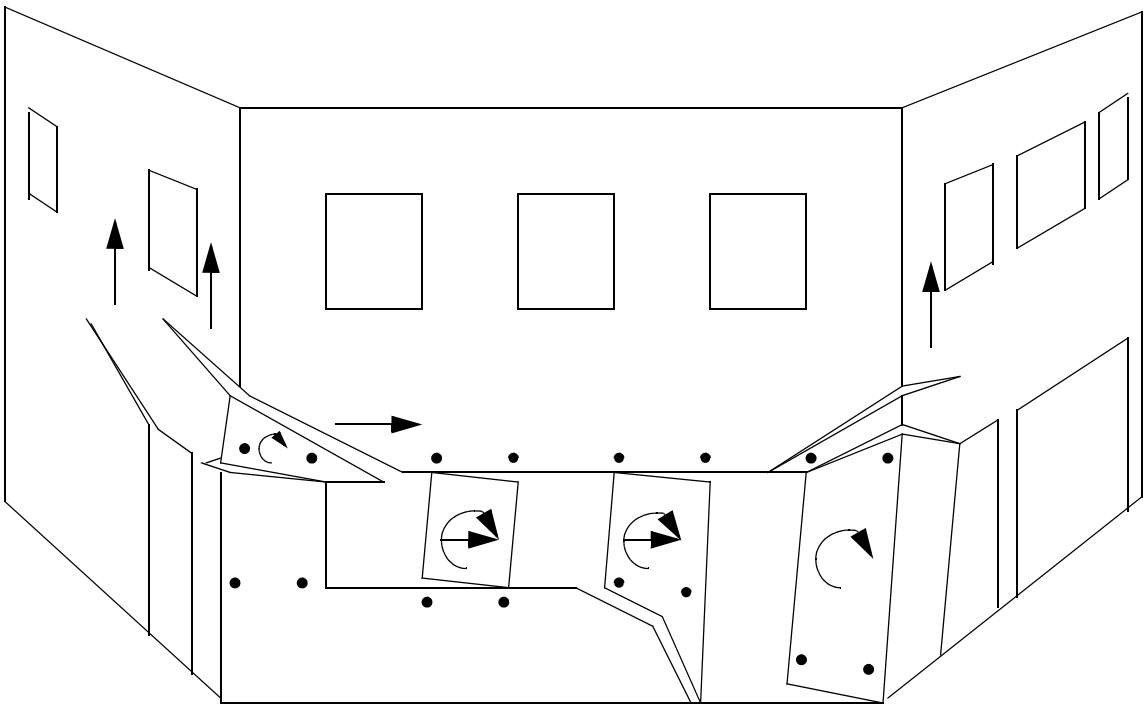

Figure E.37 Exaggerated schematic of the observed behavior of Wall A in the positive loading direction during the Group 2 cycles.

The measured uplift during Cycle 33a of both sides of Wall A is shown in Figure E.38 versus roof displacement. From this figure it is apparent that the vertical uplift of each side of the wall was nearly identical, which implies no rotation or global rocking behavior in the positive loading direction. The vertical translation implied by this figure was likely caused by the observed local pier rocking. In addition, this uplift drastically altered the force in each of the post-tensioning tendons. Figure E.39 shows a plot of the force measured in each of the post-tensioning tendons versus roof displacement for Cycle 33a. From this plot it is apparent that the uplift of Wall A resulted in an increase in post-tensioning force from around 25 kip to 36 kip (an increase of approximately 50%).

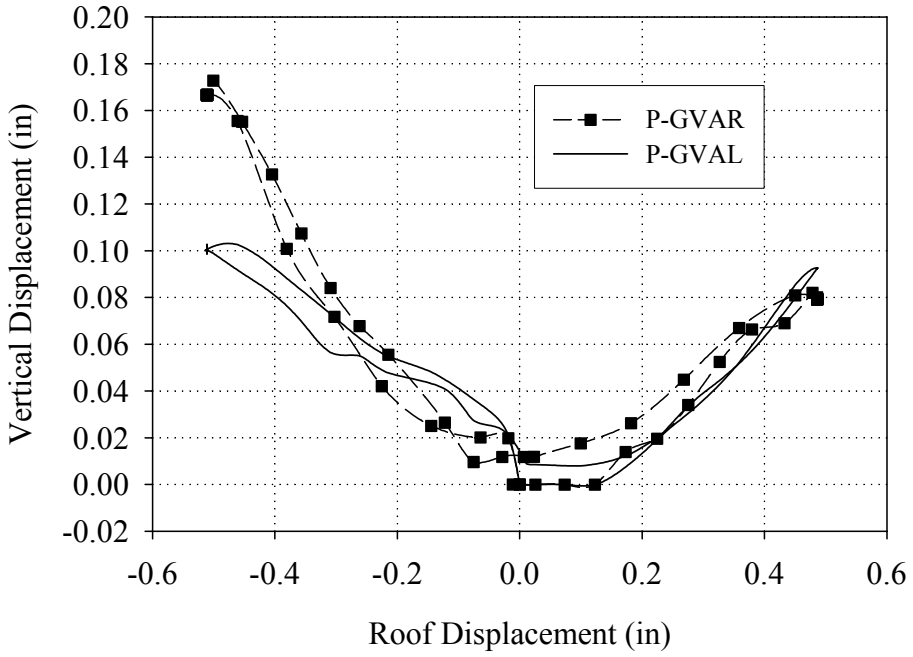

Figure E.38 Vertical displacements of both sides of Wall A versus roof displacement (Cycle 33a)

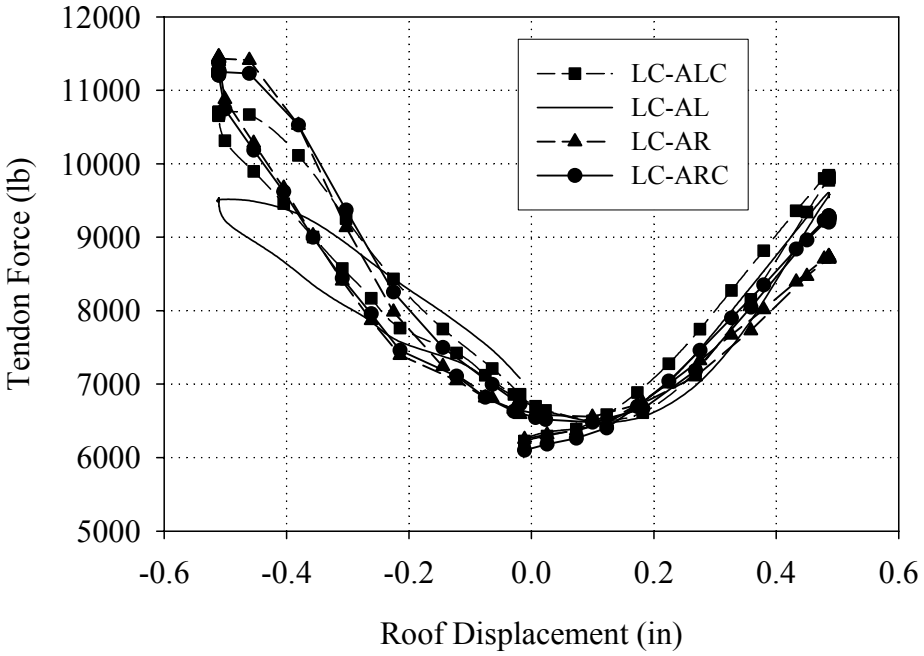

Figure E.39 Post-tensioning force versus roof displacement (Cycle 33a)

In addition to increasing the level of post-tensioning force, the vertical uplift of Wall A engaged portions of out-of-plane Walls 1 and 2 (see Figure E.37). In particular, the uplift caused by the rocking of pier PA-10 lifted up the portion of Wall 2 above pier P2-7. In addition, the global uplift of Wall A engaged a portion of Wall 1 above the active cracks shown in Figure E.37.

Figure E.40 shows the base strains recorded at peak positive displacement during Cycle 33a. As apparent from this figure, the recorded strain profiles of pies PA-7, PA-8, and PA-10 were consistent with the observed rocking deformation. In addition, the recorded strain profiles also support the contention that the out-of-plane walls participated in the response. This is most clearly seen by the compression strains measured in pier P2-7. The lack of tensile strain measured in pier P1-7 was likely cause by the large degree of damage in this area, which resulted in residual crack opening. Recall that these gages were

zeroed at zero roof displacement. Therefore, if the gage was under no strain at zero roof displacement (i.e. due to residual crack opening), then the gage would not record any tensile strain throughout loading.

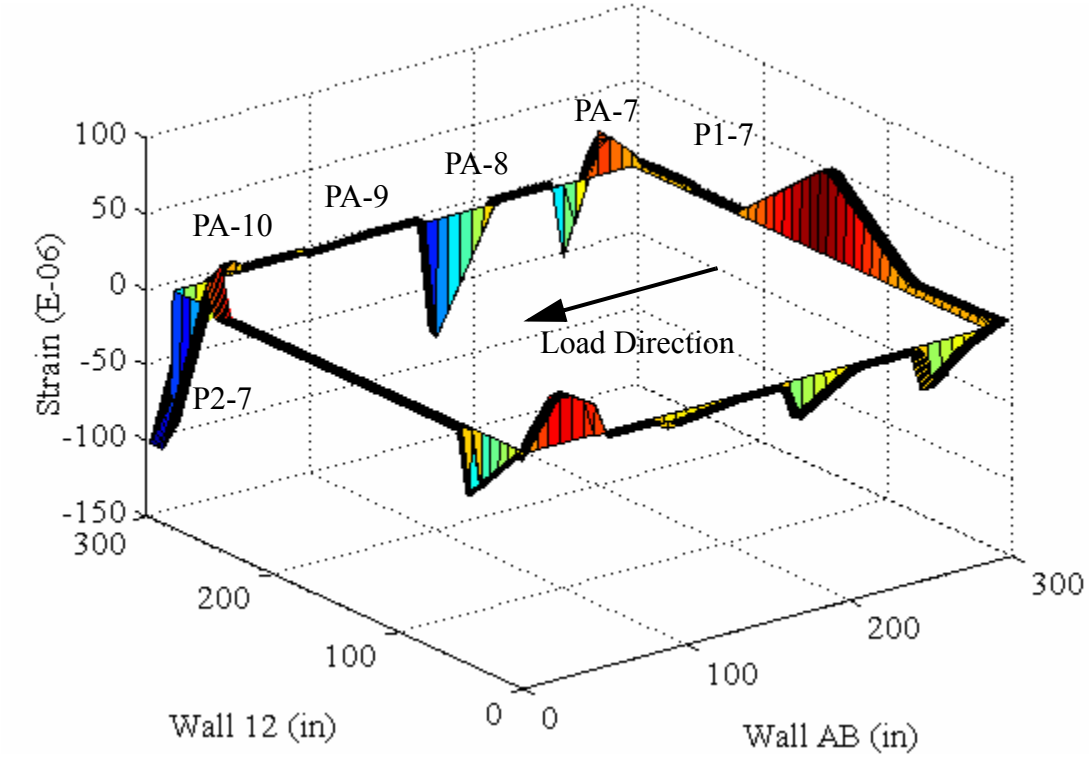

Figure E.40 Base strains recorded at peak positive displacement (Cycle 33a)

Figure E.26 shows a schematic of the behavior of Wall A in the negative direction. As apparent from this figure, the behavior of Wall A during the Group 2 cycles was very similar to the observed behavior during the Group 1 cycles. That is, a combination of local pier behavior and low-level global rocking. Similar to the behavior of Wall A in the positive direction, all of the piers displayed some degree of rocking/sliding behavior as shown by arrows in Figure E.41. In addition, visual observations indicated that the low-level global rocking of Wall A acted to lift the upper portion of the wall off of pier PA-10, thus effectively leaving this pier behind. Similar to the behavior of the upper portion of

pier PA-7 in the positive direction, the upper portion of Wall A slid along the diagonal cracks above pier PA-10.

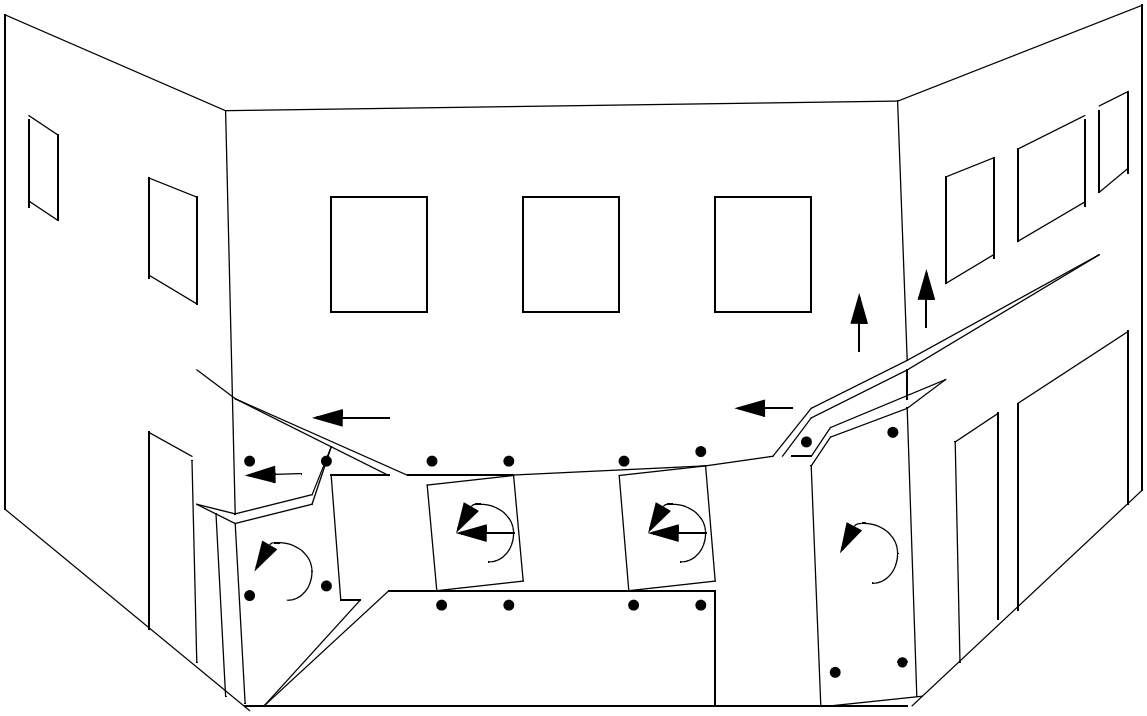

Figure E.41 Exaggerated schematic of the observed behavior of Wall A in the negative loading direction during the Group 2 cycles.

The low-level global rocking measured can be clearly seen in Figure E.38. Based on the simplifying assumptions outlined in Section E.3.1, this global rocking represents approximately 15% of the lateral roof displacement. In addition, this global rocking along with the overall uplift of Wall A (displayed in Figure E.38) caused the force in the post-tensioning tendons to increase substantially during loading in the negative direction. Based on Figure E.39 it is apparent that the total post-tensioning force in Wall A nearly doubled from 25 kip to 44 kip during loading in the negative direction. This increase is larger than was observed for loading in the positive direction and is attributed to the low-

level global rocking deformation, which can be observed in the differential increase in force displayed by the tendons in the negative direction (see Figure E.39)

Also apparent from Figure E.41, portions of Walls 1 and 2 were participating in the response of Wall A. Similar to the behavior in the positive direction, the global rocking and overall uplift of Wall A engaged portions of the out-of-plane walls. In particular, the global rocking engaged a large portion of Wall 2 as shown in Figure E.41. The participation of Wall 1 was more difficult to assess due to the small crack openings possibly caused by this wall being placed into compression due to overturning moment. In addition, pier PA-7 was visibly punching through the lower portion of pier P1-7 during this level of testing.

Figure E.42 shows a plot of the base strains recorded during peak negative displacement during Cycle 33a. Similar to past cycles the strain profiles illustrated by this figure mostly support the flexural response of the in-plane piers as well as the participation of the out-of-plane wall. However, the strain readings obtain from pier PA-8 and P2-7 are somewhat counter intuitive and are considered erroneous.

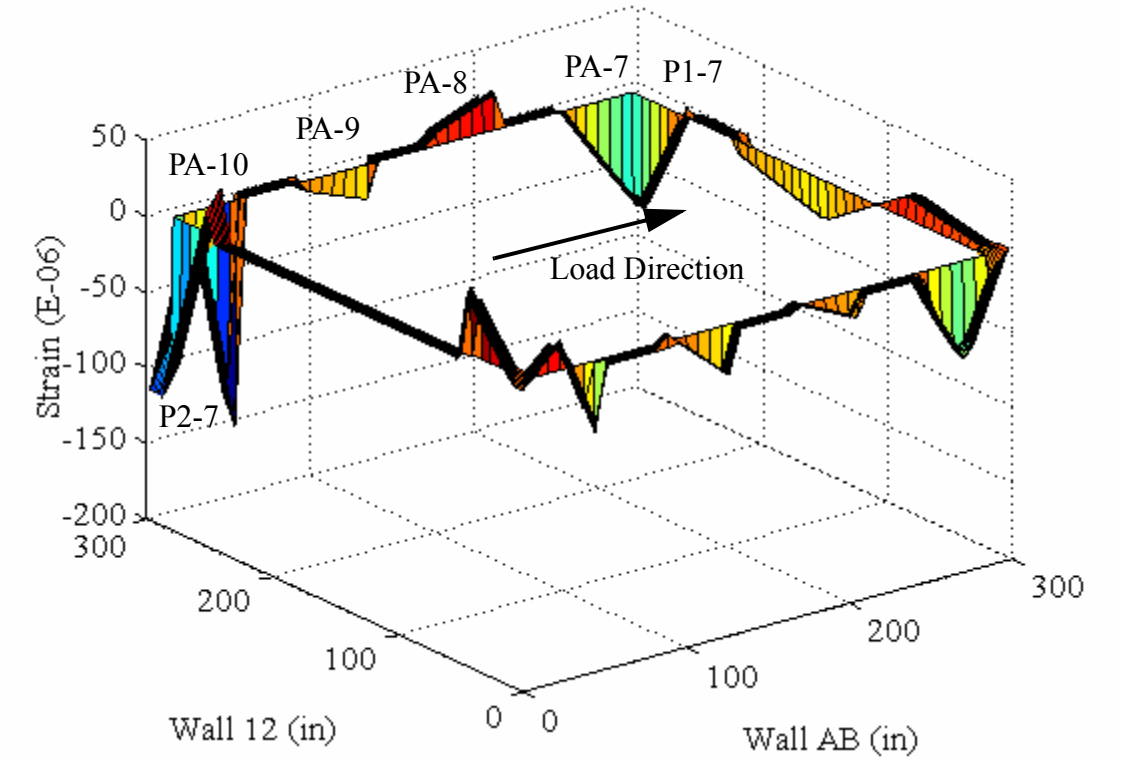

Figure E.42 Base strains recorded at peak negative displacement (Cycle 33a)

Beyond the monotonic behavior of Wall A in each direction, the cyclic nature of loading resulted in the permanent progressive crack opening of several cracks. That is, during each cycle certain cracks displayed an increase in residual opening. This phenomenon was most clearly seen in the diagonal cracks above piers PA-7 and PA-10 as well as the diagonal crack below pier PA-9.

In the case of the cracks above piers PA-7 and PA-10, the root of this phenomenon was likely overturning moment which altered the failure modes in the positive and negative direction. Specifically, when these cracks were placed into tension due to overturning moment they tended to open in a sliding mode; however in the other direction the piers adjacent to these cracks behaved in a rocking mode. The result was a progressive crack growth due to the unrecoverable sliding deformation. In addition, this resulted in a

permanent rotation of piers PA-7 and PA-10. Figure E.43 shows a photograph of the permanent opening of diagonal crack above pier PA-10 following Test Run 33.

In the case of pier PA-9, this phenomenon was due to not only different failure modes but also different active cracks in each direction (see Figures E.37 and E.41). Essentially, the lower portion of pier PA-9 was displaced laterally in the positive direction due to sliding; however, in the negative direction the pier displayed rocking deformation about a different crack. This resulted in a progressive growth of the diagonal crack at the base of pier PA-9.

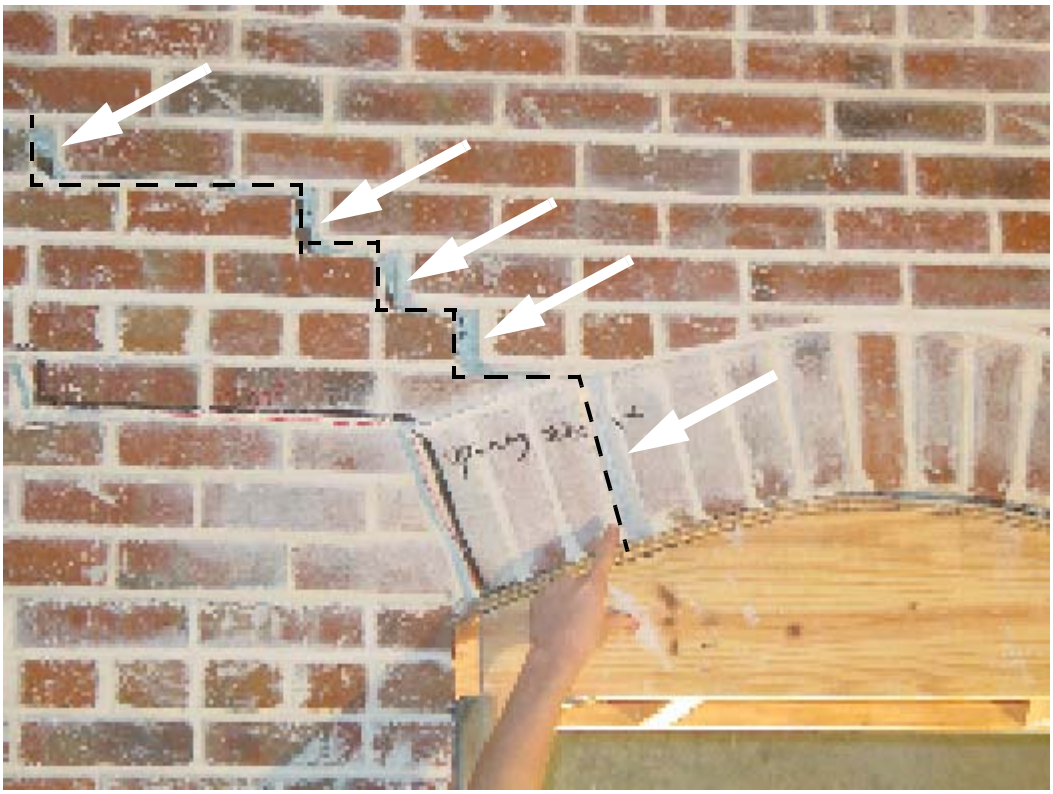

Figure E.43 Photograph of the upper portion of pier PA-10 (from the inside of the structure) illustrating the residual crack opening following Test Run 33.

E.3.2.2 Local Pier Behavior

Due to the rigid body motion of the first floor piers, the location of the LVDT reference points relative to the active cracks is of paramount importance. As a result, the descriptions of pier behavior given in the following sections utilize Figures E.37 and E.41, which shows the location of the LVDTs attached to the piers in reference to the displaced shape. Since the behavior of all of the first floor piers remained relatively unchanged throughout all of the large-amplitude initial cycles, the behavior will be illustrated using the data obtained from Cycle 33a.

Figures E.44 and E.45 show the readings obtained from the LVDTs attached to pier PA-7; Figure E.46 shows the readings obtained from the LVDTs attached to pier PA-8 (note that LVDT PA-8XR was read improperly during Cycle 33a); Figure E.47 shows the readings obtained from the LVDTs attached to pier PA-9; and Figures E.48 and E.49 show the readings obtained from the LVDTs attached to pier PA-10.

In general, the pier responses shown in these figures are consistent with the observed behavior described previously. Similar to past cycles, the effect of overturning moment is clearly apparent from the unsymmetrical response of the outside piers (i.e. PA-7 and PA-10). Specifically, the smaller displacements measured when these piers were located at the heal of the wall supports the contention that the upper portion of Wall A was lifted off of these piers due to overturning moment. In addition, the residual displacements illustrated in Figures E.45 and E.46 are larger than observed during past cycles, which implies an increase in the sliding deformation of piers PA-7 and PA-8.

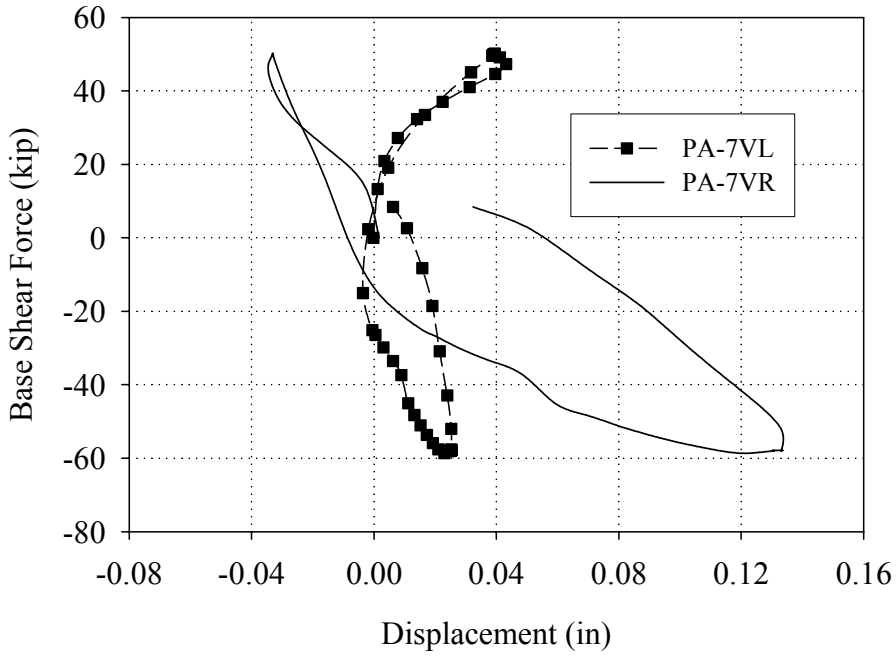

Figure E.44 Readings of the vertical LVDTs attached to pier PA-7 versus base shear force (Cycle 33a)

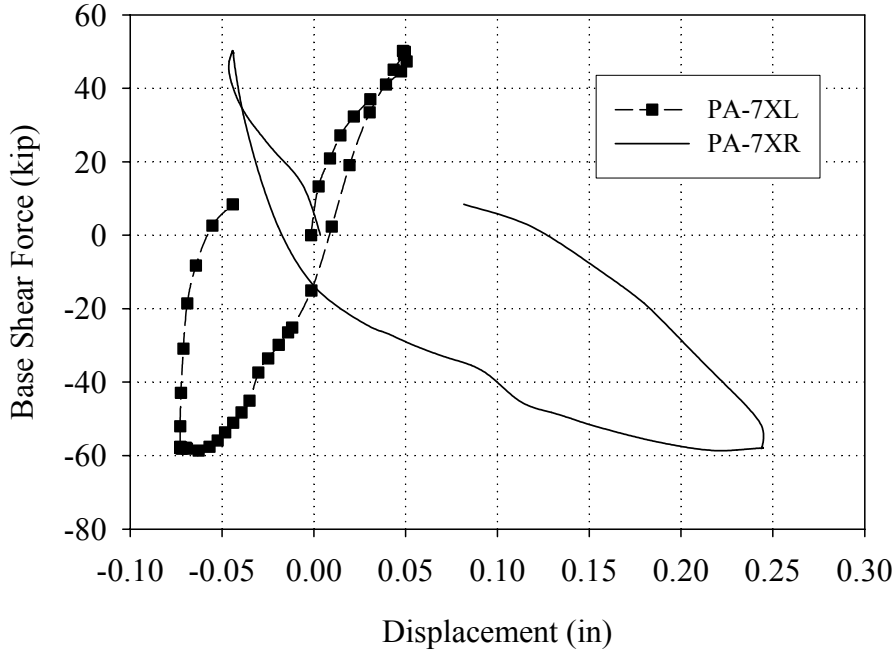

Figure E.45 Readings of the diagonal LVDTs attached to pier PA-7 versus base shear force (Cycle 33a)

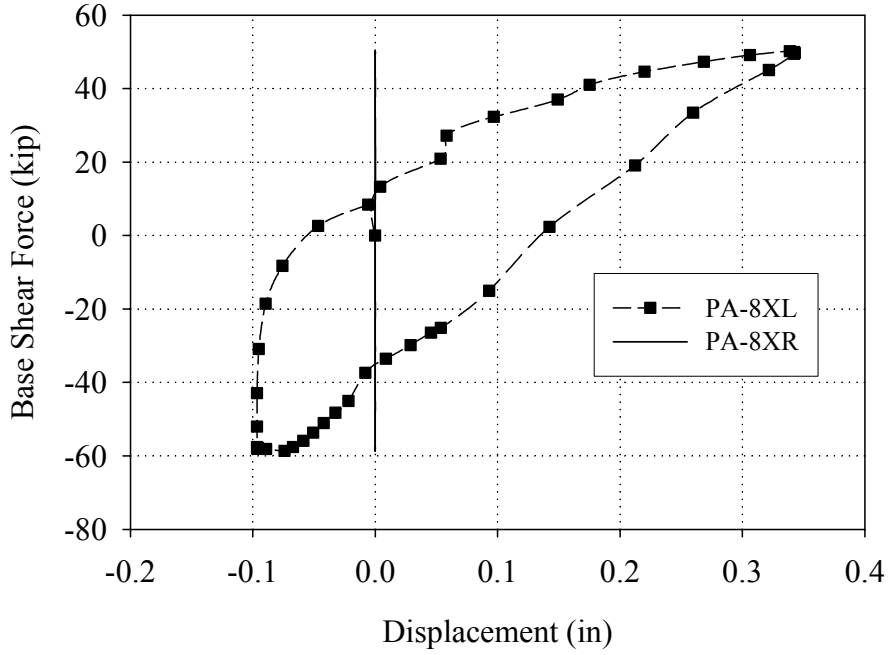

Figure E.46 Readings of the diagonal LVDTs attached to pier PA-8 versus base shear force (Cycle 33a)

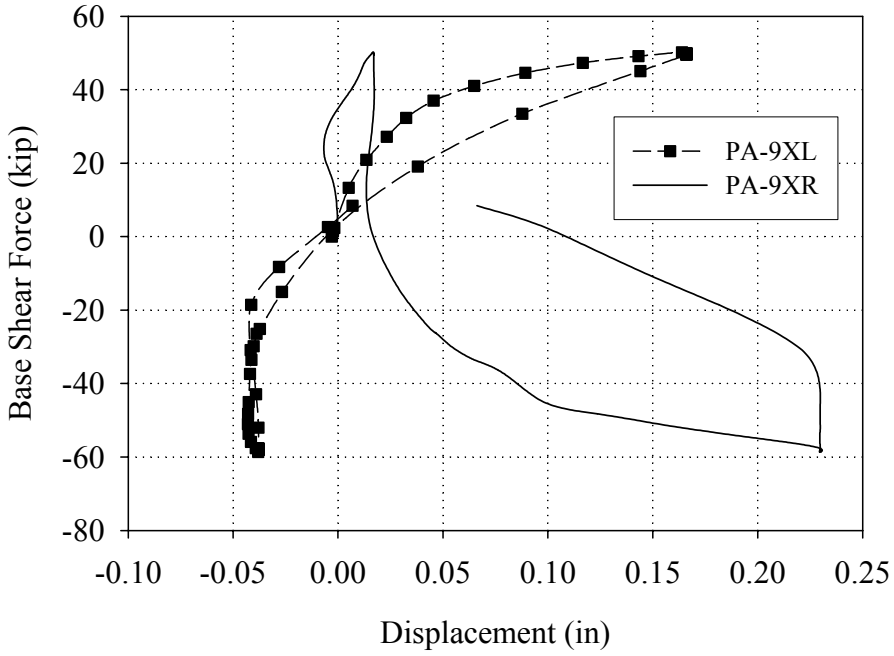

Figure E.47 Readings of the diagonal LVDTs attached to pier PA-9 versus base shear force (Cycle 33a)

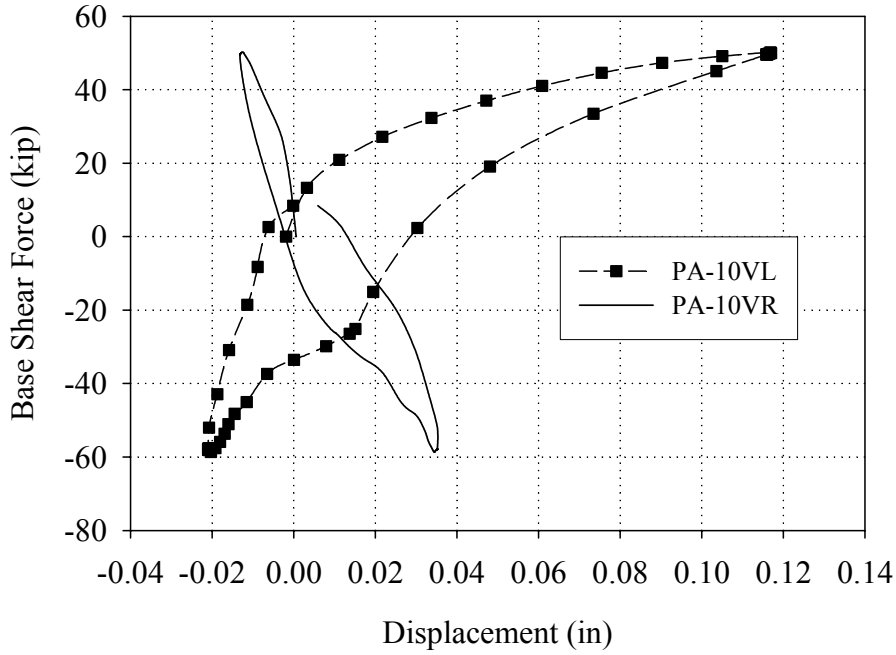

Figure E.48 Readings of the vertical LVDTs attached to pier PA-10 versus base shear force (Cycle 33a)

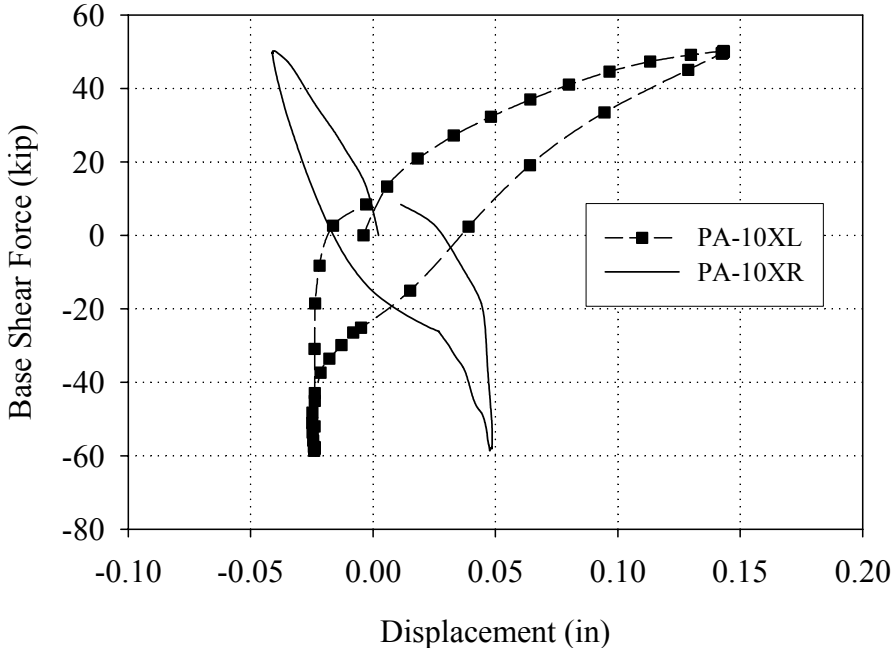

Figure E.49 Readings of the diagonal LVDTs attached to pier PA-10 versus base shear force (Cycle 33a)

E.3.3 Group 3 Cycles (Test Run 34-Test Run 35)

E.3.3.1 Overall Wall Behavior

Figures E.50 through E.52 illustrate the crack pattern in Wall A and out-of-plane Walls 1 and 2 following the Group 3 cycles. The only observed crack was a propagation of the partially formed diagonal crack in the pier PA-7. This crack propagated in the negative loading direction during Cycle 35a and is shown in bold in Figure E.50.

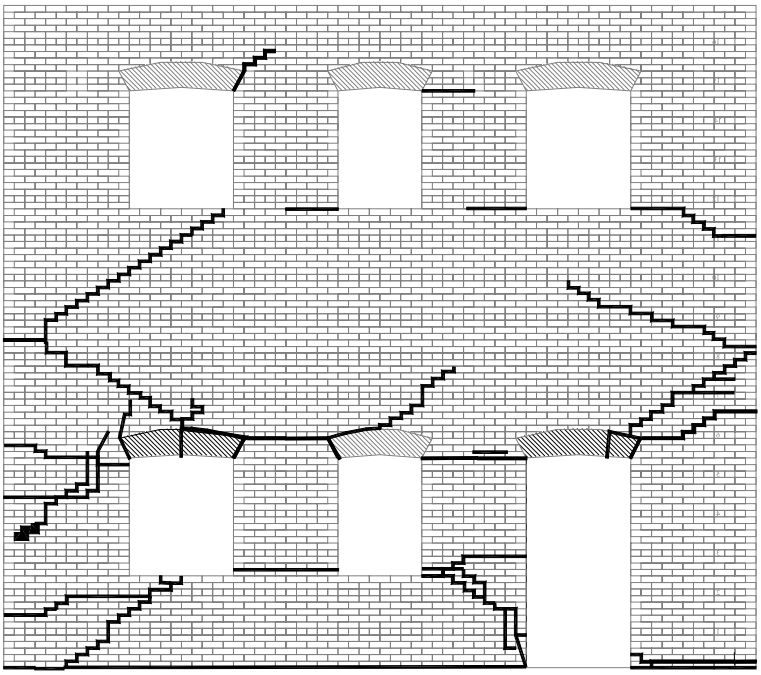

Figure E.50 Crack pattern of Wall A following the Group 3 cycles.

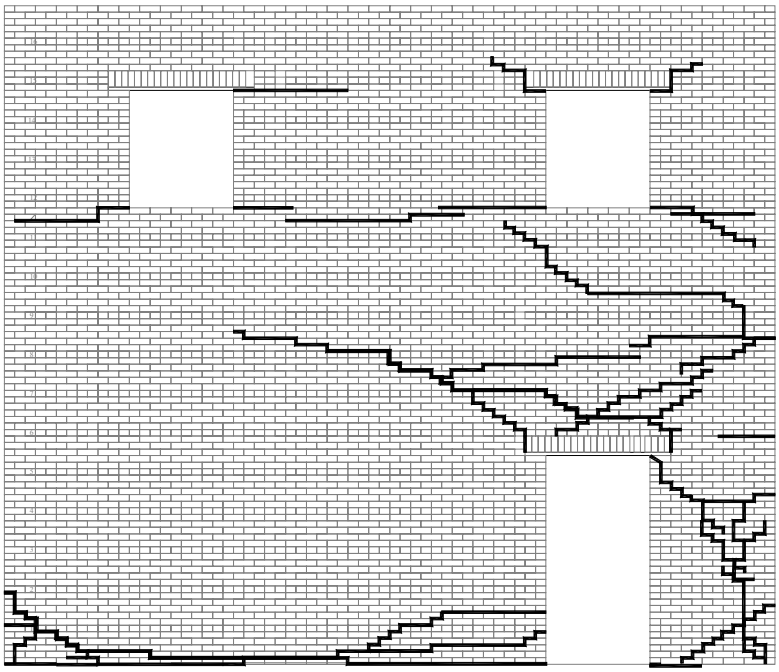

Figure E.51 Crack pattern of out-of-plane Wall 1 following the Group 3 cycles.

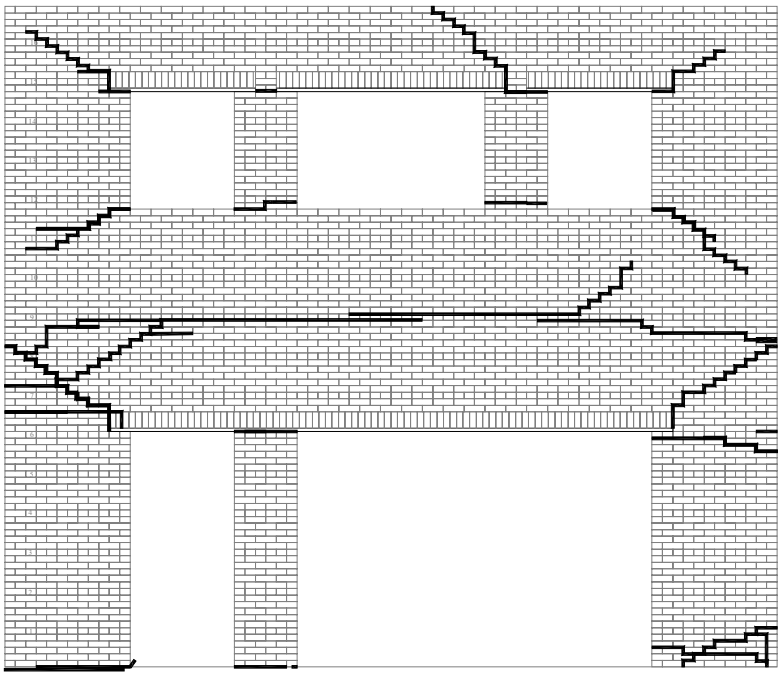

Figure E.52 Crack pattern of out-of-plane Wall 2 following the Group 3 cycles.

The behavior of Wall A in the positive loading direction during the Group 3 cycles was nearly identical to the behavior observed during the Group 1 cycles (see Section E.3.1). The most notable difference in behavior was the diminished uplift of the entire wall. The measured uplift of both sides of Wall A is shown in Figure E.53 versus roof displacement for Cycle 35a. From this figure it is apparent that the vertical uplift of each side of the wall was nearly identical, which implies no rotation or global rocking behavior in the positive loading direction. Furthermore, the average uplift was essentially zero during Cycle 35a compared to approximately 0.03 in or 20% of the roof displacement for Cycle 30a.

Figure E.54 shows a plot of the force measured in each of the post-tensioning tendons versus roof displacement for Cycle 35a. As a result of this decrease in uplift, the force in the post-tensioning tendons underwent negligible change throughout loading. Recall that during Cycle 30a the total post-tensioning force increased by approximately 15%. This may imply that the rocking/sliding behavior observed for the first floor piers consisted of more sliding deformation during the Group 3 cycles than during the Group 1 cycles. This change in behavior was likely caused by the damage induced during the Group 2 cycles as well as the increased level of post-tensioning force investigated during the Group 3 cycles.

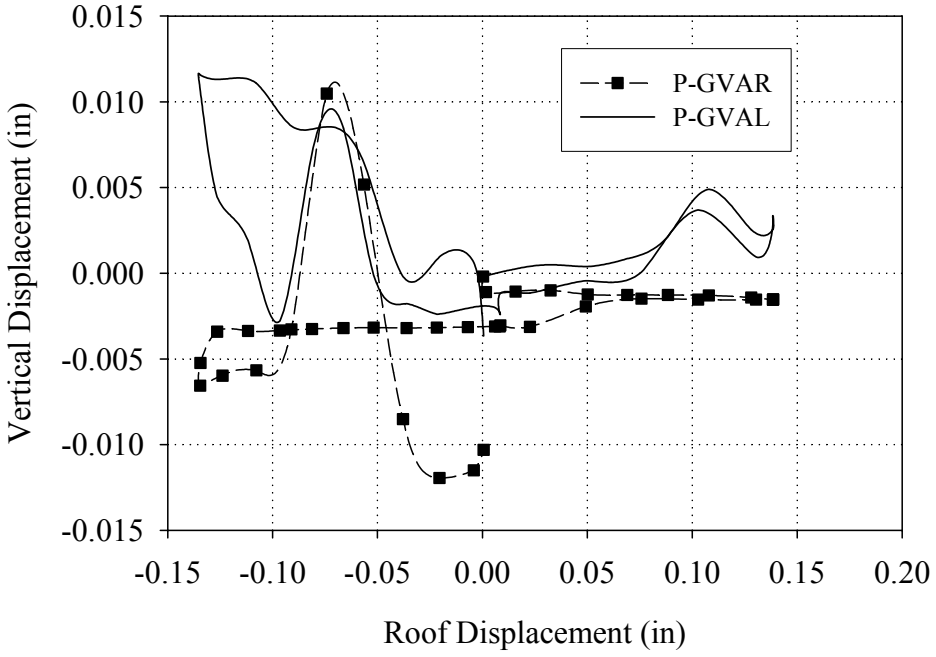

Figure E.53 Vertical displacements of both sides of Wall A versus roof displacement (Cycle 35a)

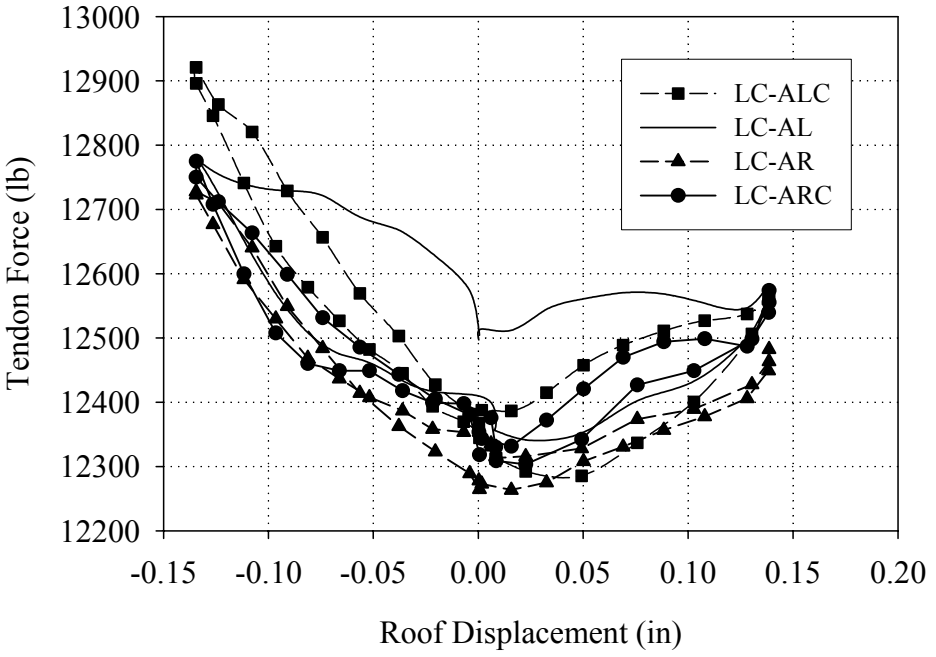

Figure E.54 Post-tensioning force versus roof displacement (Cycle 35a)

In addition, the decrease in overall uplift coupled with the small displacements imposed during these cycles rendered visual observations of flange participation difficult. However, due to the similar behavior of the individual piers and the existing crack patterns, the flange participation was likely similar to past cycles (see Figure E.22).

Figure E.55 shows a schematic of the behavior of Wall A in the negative direction. As apparent from this figure, the behavior of Wall A during the Group 3 cycles was very similar to the observed behavior during the Group 1 cycles (see Section E.3.1). Similar to the positive direction, the most notable difference was the diminished uplift of the entire wall. From Figure E.53 it is apparent that Wall A displayed a small amount of global rocking during Cycle 35a in the negative direction. Based on the assumptions outlined in Section E.3.1, this global rocking displacement accounts for 0.015 in of the overall roof displacement or approximately 10%. Recall that during Cycle 30a, the measured global rocking displacement of Wall A accounted for nearly 45% of the lateral roof displacement (see Figure E.23). Furthermore, this decreased uplift resulted in a nearly constant post-tensioning force throughout these cycles (see Figure E.54).

The observed behavior of the individual piers in Wall A during the Group 3 cycles were nearly identical to the behavior observed during the Group 1 cycles. The principal difference was the behavior of pier PA-7 that deformed due to both a horizontal rocking crack at the top of the pier as well as a partially developed diagonal crack (see Figure E.55). Note that the orientation of this crack is consistent with the effects of overturning moment. That is, the presence of overturning moment likely increased the vertical stress in pier PA-7, thus altering the behavior from rocking to diagonal cracking.

All of the remaining piers displayed some degree of rocking/sliding behavior as

shown by arrows in Figure E.55. In addition, visual observations indicated that the low-level global rocking of Wall A acted to lift the upper portion of the wall off of pier PA-10, thus effectively leaving this pier behind. Similar to the behavior of the upper portion of pier PA-7 in the positive direction, the upper portion of Wall A slid along the diagonal cracks above pier PA-10.

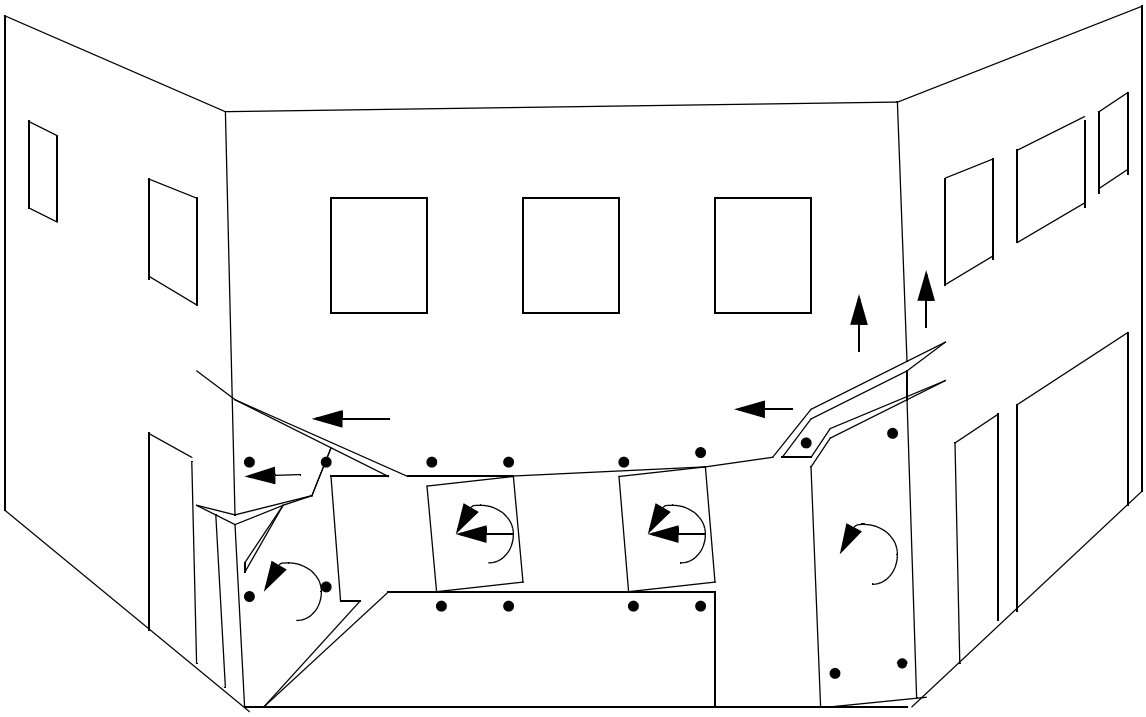

Figure E.55 Exaggerated schematic of the observed behavior of Wall A in the negative loading direction during the Group 3 cycles.

E.3.3.2 Local Pier Behavior

Due to the rigid body motion of the first floor piers, the location of the LVDT reference points relative to the active cracks is of paramount importance. As a result, the descriptions of pier behavior given in the following sections utilize Figures E.22 and E.55, which shows the location of the LVDTs attached to the piers in reference to the displaced

shape. Since the behavior of all of the first floor piers remained relatively unchanged throughout all of the Group 3 cycles, the behavior will be illustrated using the data obtained from Cycle 35a.

Figures E.56 and E.57 show the readings obtained from the LVDTs attached to pier PA-7; Figure E.58 shows the readings obtained from the LVDTs attached to pier PA-8; Figure E.59 shows the readings obtained from the LVDTs attached to pier PA-9; and Figures E.60 and E.61 show the readings obtained from the LVDTs attached to pier PA-10.

In general, the pier responses shown in these figures are consistent with the observed behavior as well as the measured response during past cycles. The reader is direction to Section E.3.1.2 for further discussion.

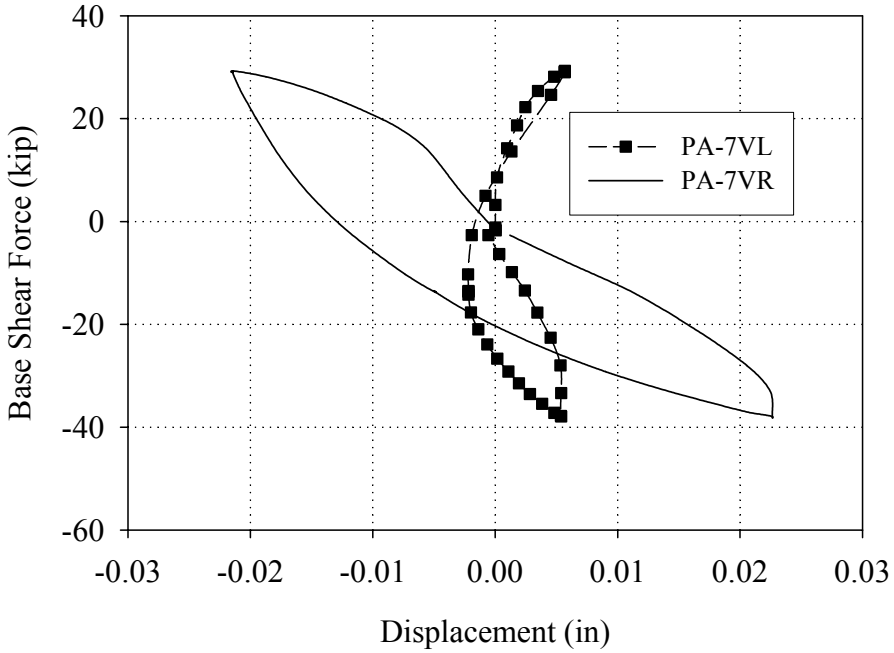

Figure E.56 Readings of the vertical LVDTs attached to pier PA-7 versus base shear force (Cycle 35a)

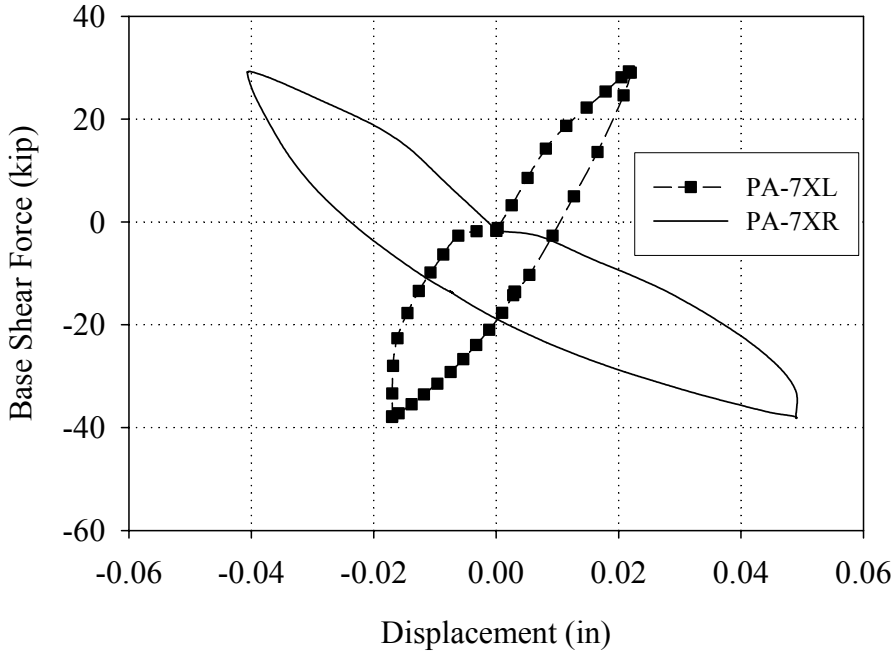

Figure E.57 Readings of the diagonal LVDTs attached to pier PA-7 versus base shear force (Cycle 35a)

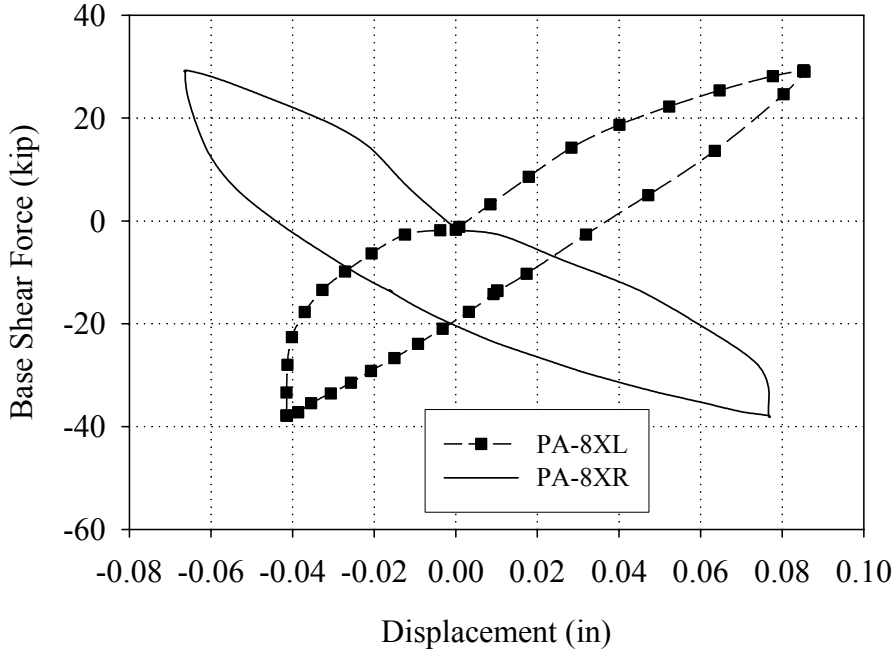

Figure E.58 Readings of the diagonal LVDTs attached to pier PA-8 versus base shear force (Cycle 35a)

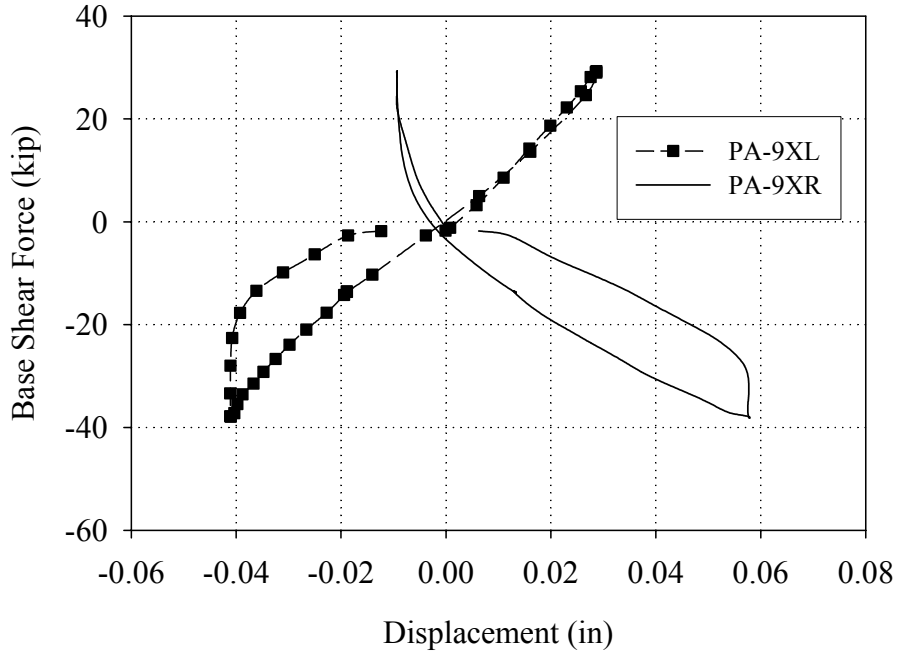

Figure E.59 Readings of the diagonal LVDTs attached to pier PA-9 versus base shear force (Cycle 35a)

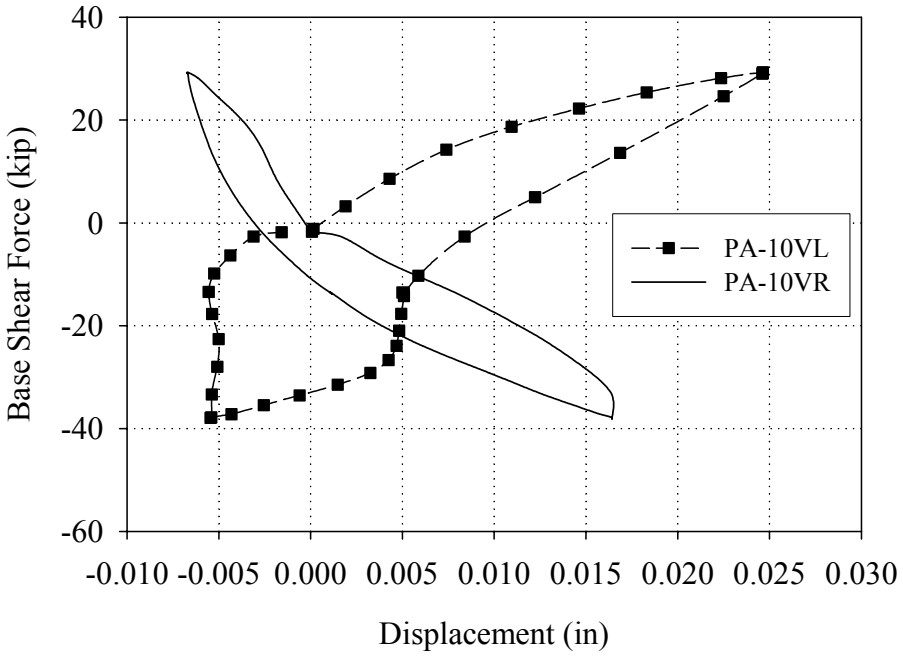

Figure E.60 Readings of the vertical LVDTs attached to pier PA-10 versus base shear force (Cycle 35a)

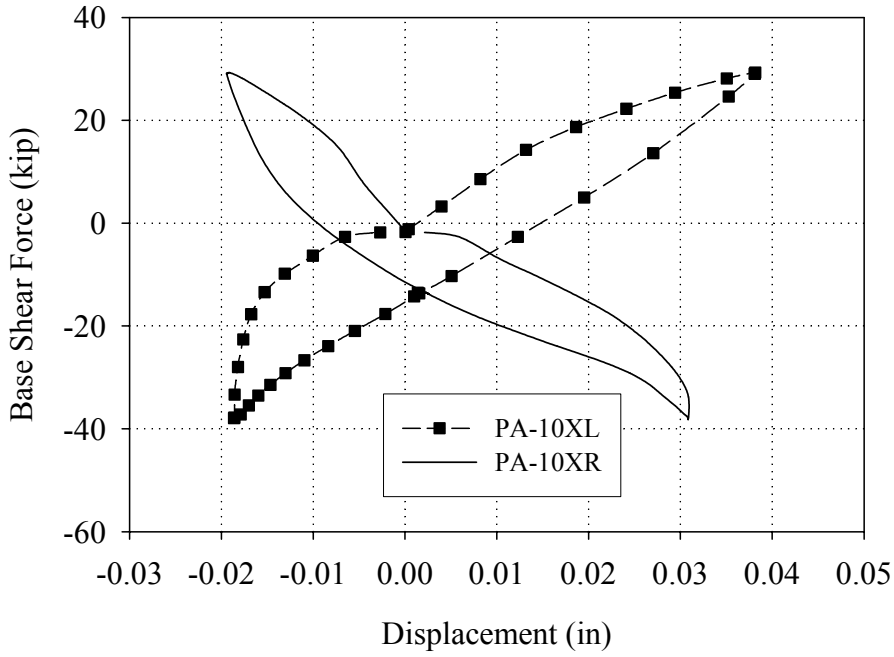

Figure E.61 Readings of the diagonal LVDTs attached to pier PA-10 versus base shear force (Cycle 35a)

E.3.4 Group 4 Cycles (Test Run 36-Test Run 39)

E.3.4.1 Overall Wall Behavior

Figures E.62 through E.63 illustrate the crack pattern in Wall A and out-of-plane Walls 1 and 2 following the Group 4 cycles. In the positive loading direction, an additional horizontal crack formed at the base of pier PA-7 during Cycle 38a. During Cycle 39a, additional diagonal cracks were observed at the top of pier PA-7 as well as in pier PA-10. In the negative direction, the existing diagonal crack in pier PA-7 became fully developed. Furthermore, during these test runs additional vertical cracks were observed at the intersection of Wall A and Wall 1. Based on the location (i.e. three wythes from the corner) these cracks suggest that Wall A was punching through Wall 1 in negative loading direction. All of these crack are shown in bold in Figures E.62 through E.64.

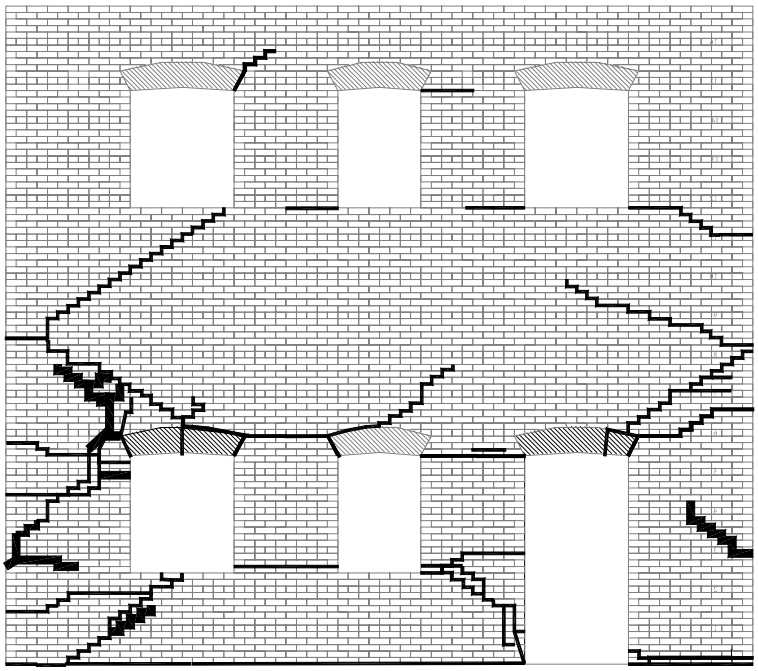

Figure E.62 Crack pattern of Wall A following the Group 4 cycles.

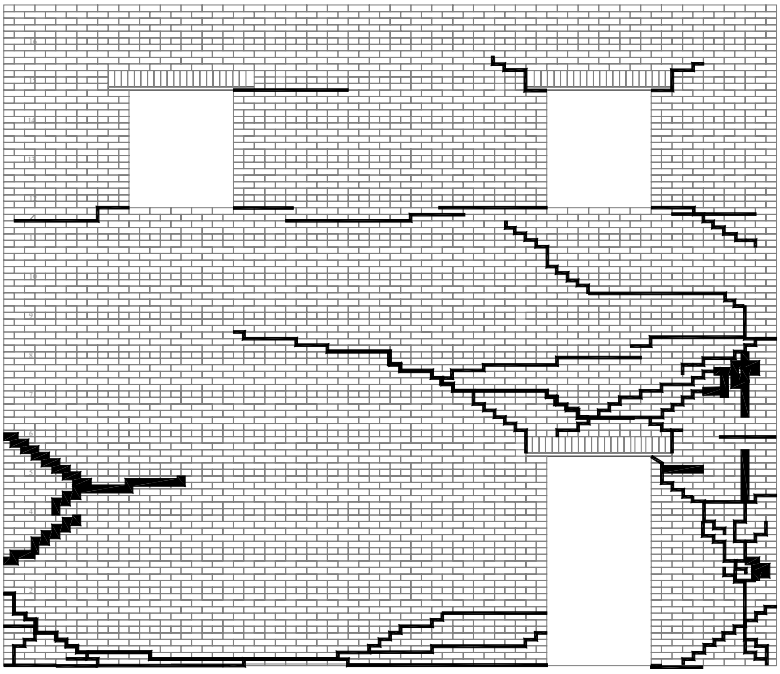

Figure E.63 Crack pattern of out-of-plane Wall 1 following the Group 4 cycles.

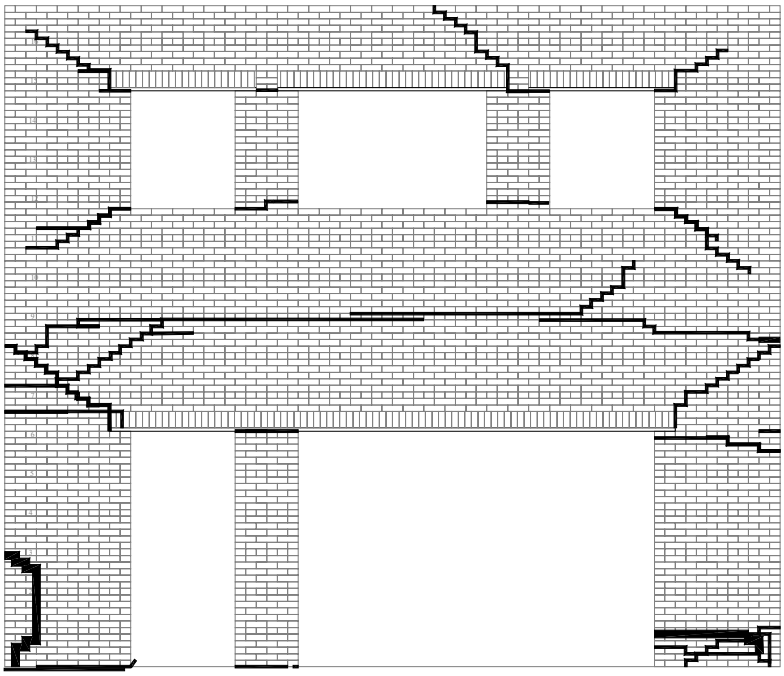

Figure E.64 Crack pattern of out-of-plane Wall 2 following the Group 4 cycles.

Figure E.65 shows a schematic illustrating the behavior of Wall A as well as out-of-plane Walls 1 and 2 in the positive direction. Note that the location of the LVDT reference points are also shown in the figure. In the positive loading direction, the behavior of Wall A deviated from past cycles in two ways. First, the behavior during the Group 4 cycles was a combination of global rocking and component behavior. The measured uplift of both sides of Wall A obtained during Cycle 39a is shown in Figure E.66 versus roof displacement. Based on the simplifying assumptions outlined in Section E.3.1, this measured global rocking behavior accounts for approximately 0.15 in or 20% of the imposed roof displacement. Recall that during all other loading series, negligible global rocking was observed in the positive loading direction. As seen in past cycles, the global uplift of the wall alters the force in the post-tensioning tendons. Figure E.67 shows a plot

of the force measured in each of the post-tensioning tendons versus roof displacement for Cycle 39a. From this plot it is apparent that the uplift of Wall A resulted in an increase in post-tensioning force from around 50 kip to 60 kip (an increase of approximately 20%). In addition, the differential increase in tendon force displayed in Figure E.67 is consistent with the observed global rocking behavior.

The second major difference in wall behavior observed during the Group 4 cycles focused on the behavior of pier PA-10. Recall that during past cycles, the principal mode of pier PA-10 in the positive loading direction was mainly rocking. As apparent from the crack pattern shown in Figure E.62, the behavior of pier PA-10 switched from a rocking mode to a diagonal tension mode during Test Run 39. The orientation of the diagonal crack suggests that a primary cause may be attributed to overturning moment. That is, overturning moment placed pier PA-10 into compression thus increasing its vertical stress and effectively switching the failure mode from rocking to diagonal tension.

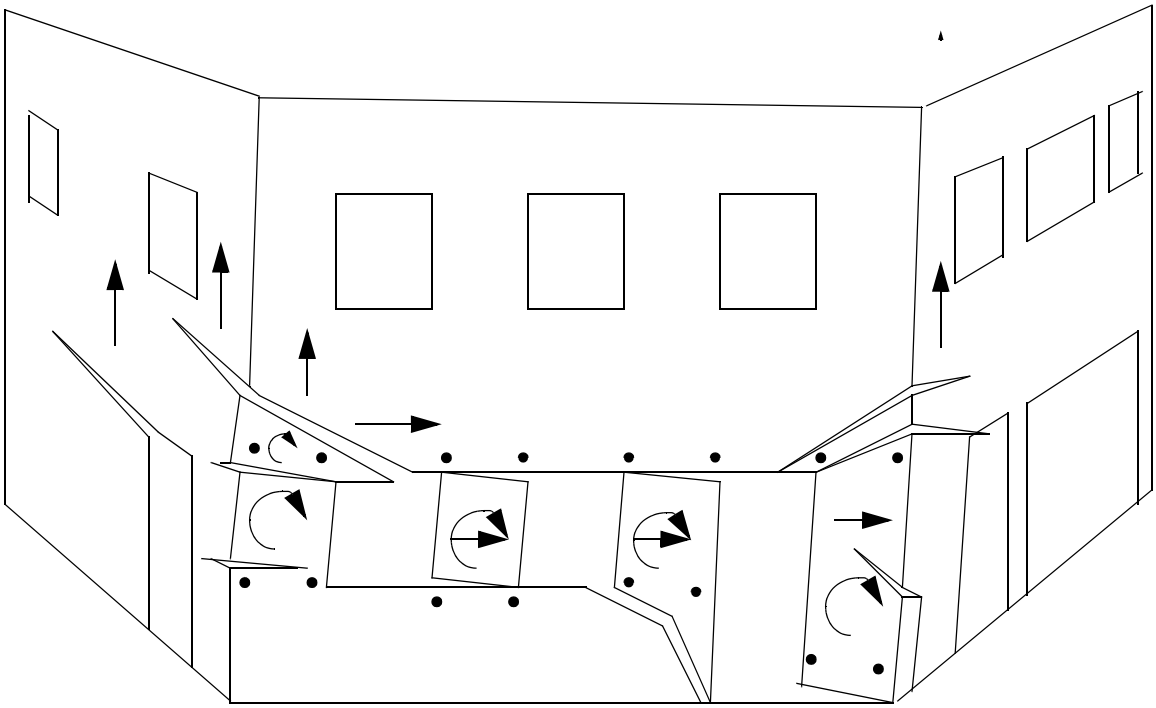

Figure E.65 Exaggerated schematic of the observed behavior of Wall A in the positive loading direction during the Group 4 cycles.

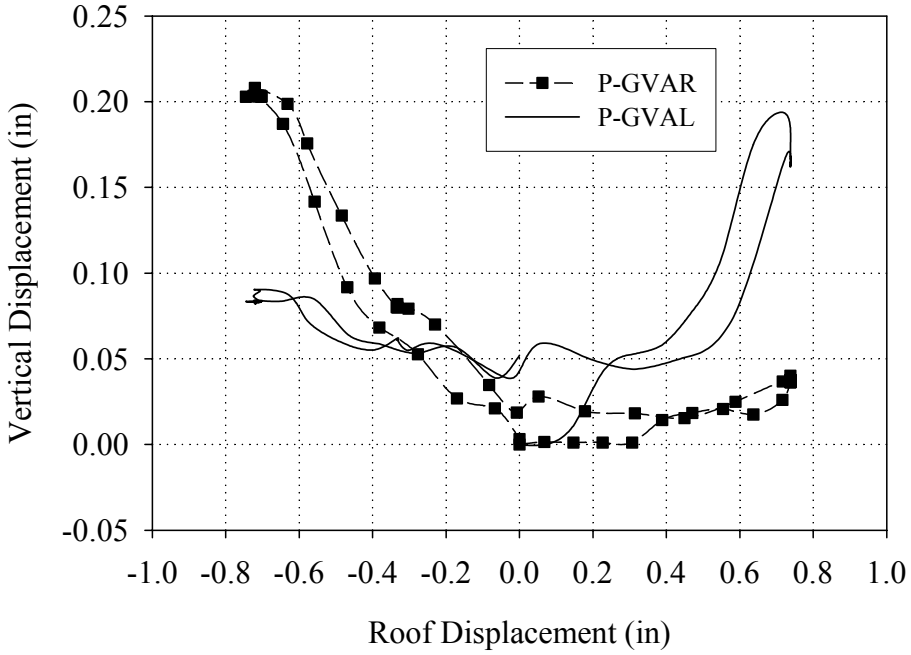

Figure E.66 Vertical displacements of both sides of Wall A versus roof displacement (Cycle 39a)

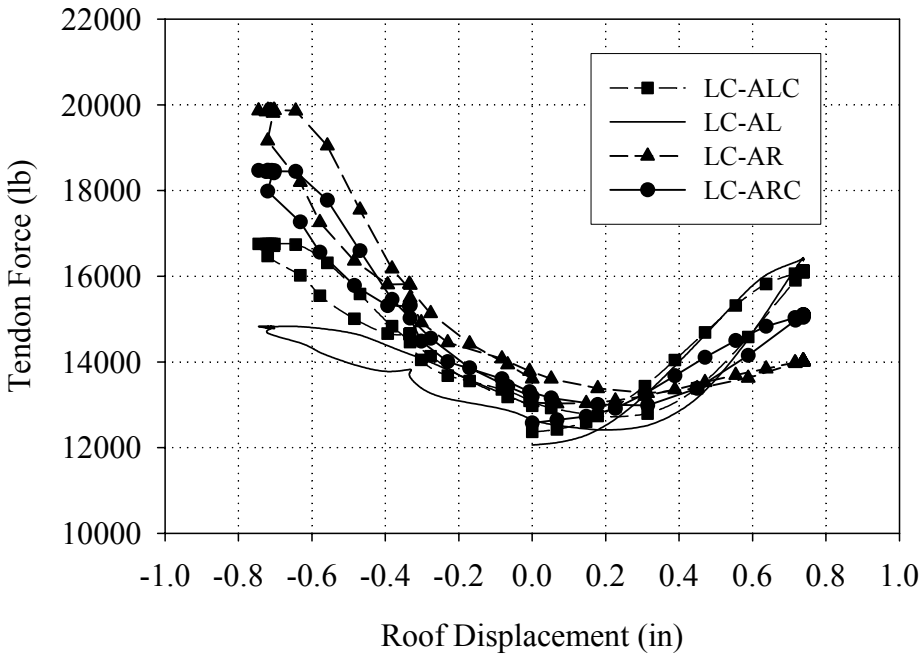

Figure E.67 Post-tensioning force versus roof displacement (Cycle 39a)

As apparent from Figure E.65, the behavior of the remainder of the piers was consistent with the behavior described in Figure E.3.2. However, due to the global rocking in the positive direction, the tendency for pier PA-7 to be left behind was more pronounced during the Group 4 cycles. The observed and measured rigid motion is also shown in Figure E.65 by arrows. Furthermore, the participation of the out-of-plane walls as assessed by uplift was consistent with observations made during past cycles in the positive direction.

Figure E.68 shows the base strains recorded at peak positive displacement during Cycle 39a. As apparent from this figure, the recorded strain profiles of piers PA-7 and PA-8 were consistent with the observed rocking deformation. In addition, the recorded strain profiles also support the contention that the out-of-plane walls participated in the response. This is most clearly seen by the compression strains measured in pier P2-7. The

small tensile strain measured in pier P1-7 was likely cause by the large degree of damage in this area (see Section E.3.2.1 for further explanation).

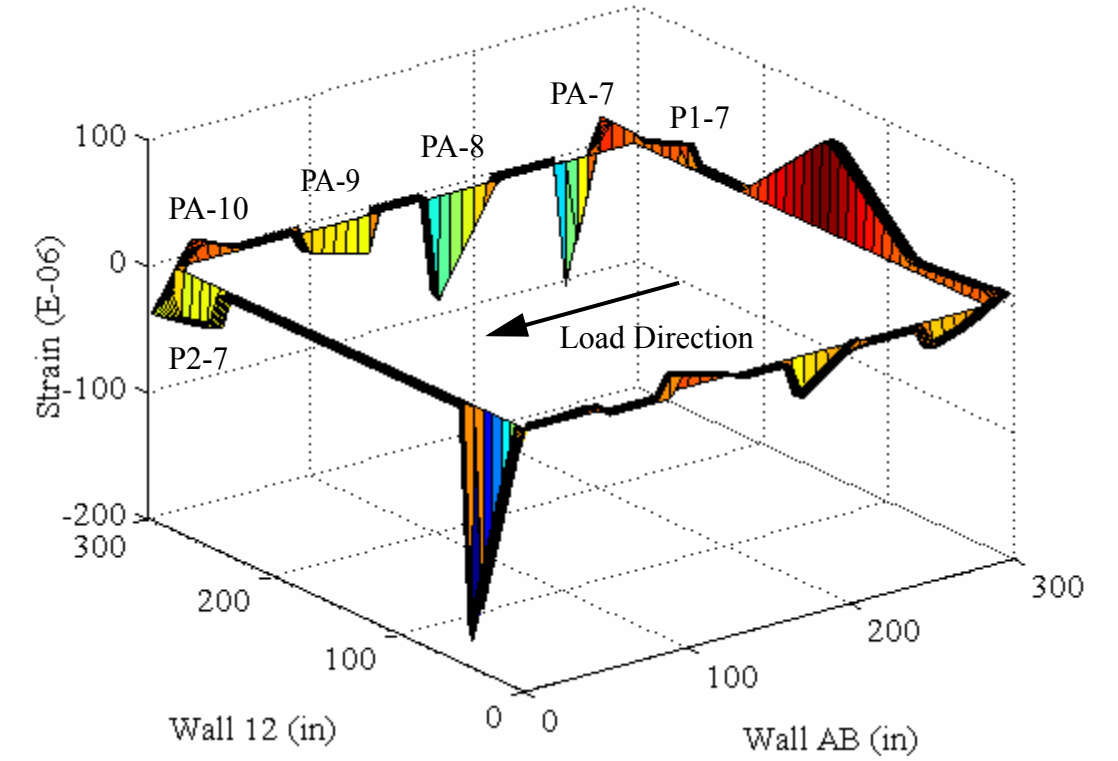

Figure E.68 Base strains recorded at peak positive displacement (Cycle 39a).

Figure E.69 shows a schematic of the behavior of Wall A in the negative direction. As apparent from this figure, the behavior of Wall A during the Group 4 cycles was very similar to the observed behavior during the Group 2 cycles (see Section E.3.2). That is, the behavior of Wall A can be classified as a combination of local pier behavior and low-level global rocking. The low-level global rocking measured can be clearly seen in Figure E.66. Based on the simplifying assumptions outlined in Section E.3.1, this global rocking represents approximately 15% of the lateral roof displacement. As seen previously, this global rocking along with the overall uplift of Wall A caused the force in the post-tensioning tendons to increase during loading in the negative direction. Based on

Figure E.67 it is apparent that the total post-tensioning force in Wall A increased by approximately 40% from 50 kip to 70 kip during loading in the negative direction. In addition, the global rocking can be clearly observed in the differential increase in force displayed by the tendons in the negative direction.

The primary difference between the behavior of Wall A during the Group 4 cycles and past cycles is focused on the behavior of pier PA-7. As apparent from the crack pattern shown in Figure E.62, the diagonal crack in this pier fully developed during these cycles. As mentioned with respect to pier PA-10 in the positive loading direction, this crack strongly suggests the presence of overturning moment. That is, the change in behavior of this pier is likely caused by overturning moment increasing the vertical stress in the pier and thus switching the failure mode from rocking/sliding to diagonal tension.

All of the other piers displayed some degree of rocking/sliding behavior as shown by arrows in Figure E.69. In addition, visual observations indicated that the low-level global rocking of Wall A acted to lift the upper portion of the wall off of pier PA-10, thus effectively leaving this pier behind. Similar to the behavior of the upper portion of pier PA-7 in the positive direction, the upper portion of Wall A slid along the diagonal cracks above pier PA-10.

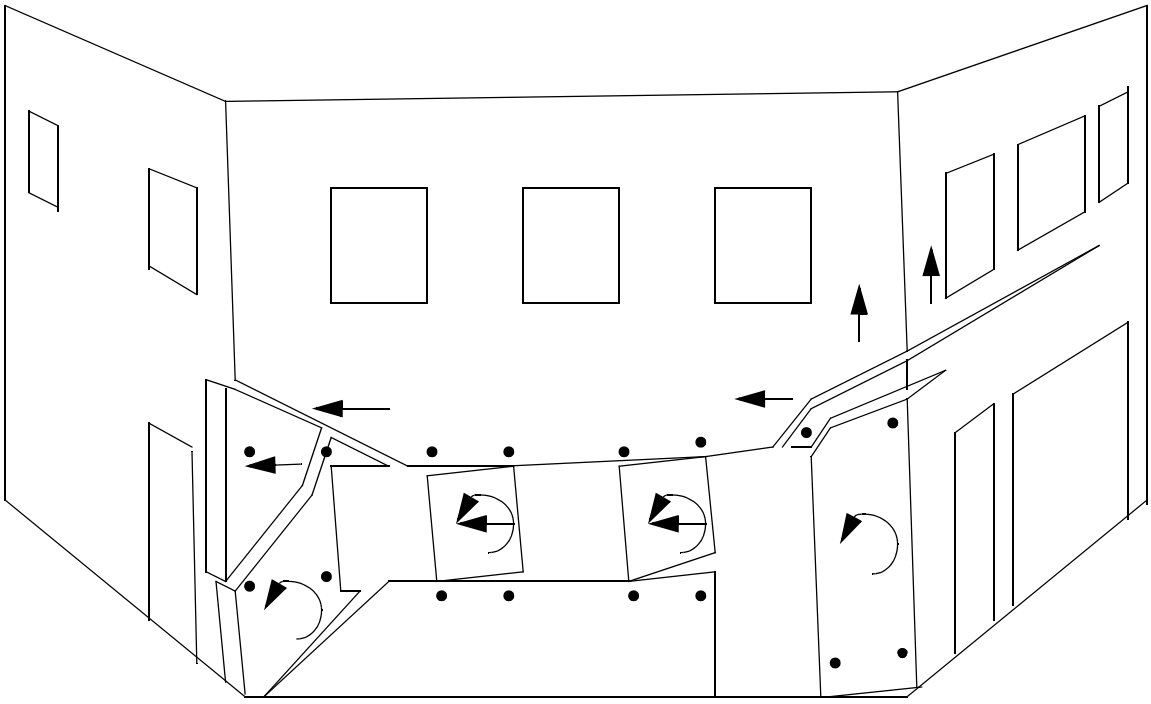

Figure E.69 Exaggerated schematic of the observed behavior of Wall A in the negative loading direction during the Group 4 cycles.

Also apparent from Figure E.69, portions of Walls 1 and 2 were participating in the response of Wall A. Similar to the behavior in the positive direction, the global rocking and overall uplift of Wall A engaged portions of the out-of-plane walls. In particular, the global rocking engaged a large portion of Wall 2 as shown in Figure E.69. The participation of Wall 1 was more difficult to assess due to the small crack openings possibly caused by this wall being placed into compression due to overturning moment. However, pier PA-7 was clearly observed punching through the lower portion of out-of-plane pier P1-7.

Figure E.70 shows the base strains recorded at peak positive displacement during Cycle 39a. As apparent from this figure, the recorded strain profiles of piers PA-7 and PA-

8 were consistent with the observed rocking deformation. However, the strain profiles of piers PA-9 and PA-10 as well as out-of-plane piers P2-7 and P1-7 are in conflict with observed behavior. This inconsistency is attributed to the large degree of damage induced in Wall A as well as the inherent error associated with these measurements (see Section E.3.1.1).

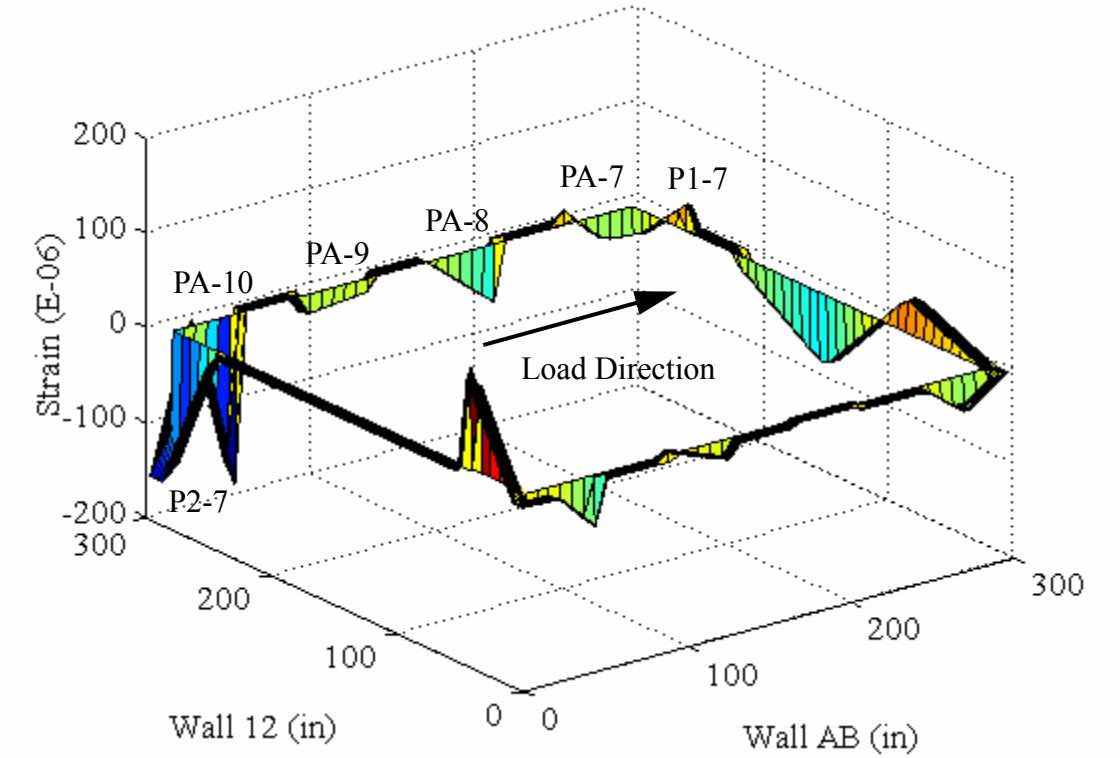

Figure E.70 Base strains recorded at peak negative displacement (Cycle 39a).

In addition to the in-plane behavior of the piers in Wall A, during the Group 4 cycles moderate levels of out-of-plane displacements were also observed. Figure E.71 illustrates the out-of-plane displacement observed in piers PA-7 and PA-10 during these cycles. Based on the figure it is apparent that the cause of the out-of-plane rotation was likely the presence of the flange. Due to the unsymmetrical response illustrated in this

figure, the out-of-plane rotation of the piers was permanent. Following Test Run 39, the out-of-plane rotation of pier PA-10 caused a permanent offset of approximately 1 in at the inside of the door opening. Figure E.72 shows a photograph of this displacement.

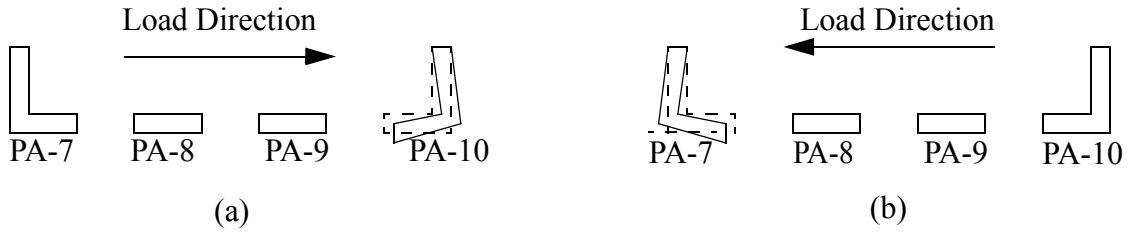

Figure E.71 Plan view illustrating the out-of-plane behavior of piers PA-7 and PA-10 in the (a) positive and (b) negative loading directions.

Figure E.72 Photograph illustrating the residual out-of-plane rotation of pier PA-10 following Test Run 39 (taken from inside the structure).

As described briefly in Section E.3.2, the cyclic nature of the loading resulted in the permanent progressive opening of several cracks. That is, during each cycle certain

cracks displayed an increase in residual opening. Figure E.73 shows a schematic of the residual deformation of Wall A following all of the test runs. Based on visual observations this phenomenon was caused primarily by two factors: overturning moment and unsymmetrical pier behavior modes.

The progressive crack opening in the diagonal cracks above piers PA-7 and PA-10 are attributed to overturning moment. In the case of pier PA-7, overturning moment (in the positive direction) decreased the level of vertical stress, thus causing sliding deformation to occur in the diagonal crack above the pier. In the negative direction, overturning moment acted to increase the vertical stress in this area, which reduced the degree of sliding deformation. As a result, the sliding deformation observed in the positive direction was not recovered. The residual displacement in the diagonal crack above pier PA-10 likely formed in a similar manner.

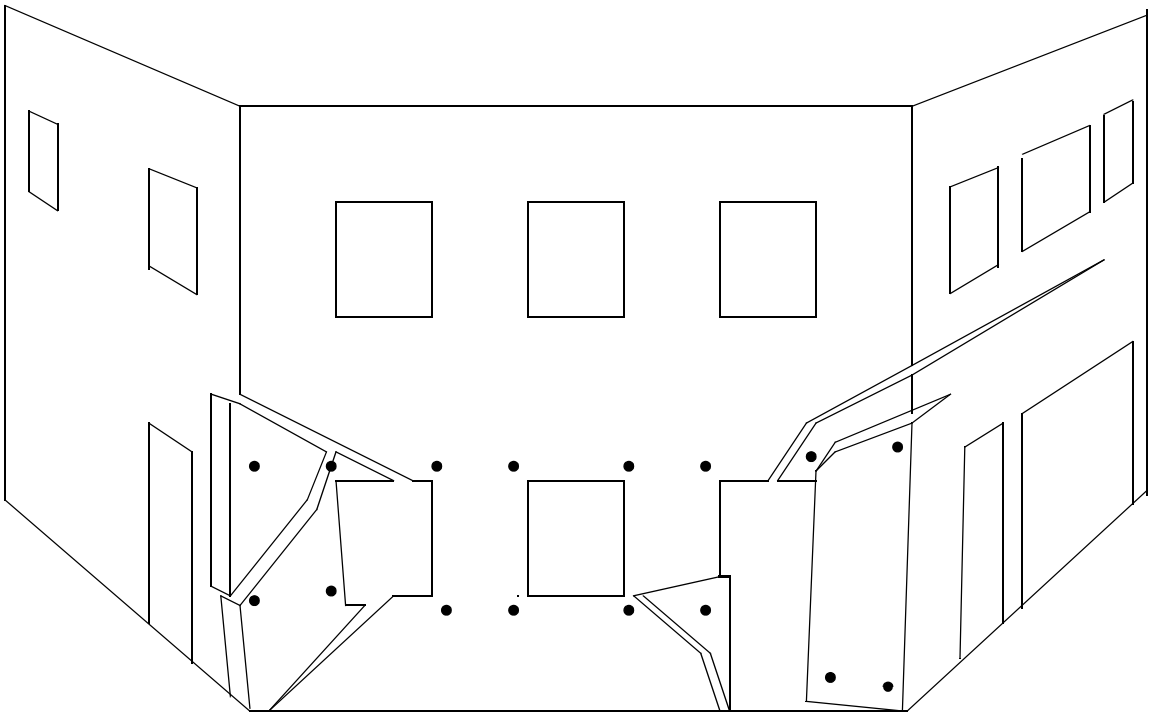

Figure E.73 Schematic illustrating the final residual deformation of Wall A.

In addition, unsymmetrical pier behavior also caused progressive crack opening in two locations. Specifically, the center of pier PA-7 and the lower portion of pier PA-9. In these cases overturing moment may have played a role; however, the unsymmetrical pier failure mode was the primary cause. For example, pier PA-9 displayed varying degrees of rocking and sliding behavior in both directions; however, the active cracks were different in each direction (see Figures E.65 and E.69). Essentially, the lower portion of pier PA-9 was displaced laterally in the positive direction due to sliding and in the negative direction the pier displayed rocking/sliding deformation about a different crack. This resulted in a progressive growth of the diagonal crack at the base of pier PA-9 (see Figure E.74). The diagonal crack in pier PA-7 opened in a similar manner and is shown in Figure E.75.

The actual residual crack openings observed following Test Run 39 ranged up to 1.5 in. This magnitude clearly indicates the progressive nature of this phenomenon since the maximum roof displacement imposed was 0.75 in. As seen in Figure E.73, this progressive crack opening also resulted in the permanent rotation of pier PA-7 and PA-10. Following Test Run 39 the length of Wall A was measured at approximately 36 in above the foundations (i.e. at the bottom of the window openings), and it was determined that the residual displacement of the cracks had caused the length of the wall to increase approximately 2 in.

Figure E.74 Photograph illustrating the permanent displacement of pier PA-9 following Test Run 39 (photo taken from inside the structure).

Figure E.75 Photograph showing the residual crack opening of the diagonal crack in pier PA-7 following Test Run 39.

E.3.4.2 Local Pier Behavior

Due to the rigid body motion of the first floor piers, the location of the LVDT reference points relative to the active cracks is of paramount importance. As a result, the descriptions of pier behavior given in the following sections utilize Figures E.65 and E.69, which shows the location of the LVDTs attached to the piers in reference to the displaced shape. Since the behavior of all of the first floor piers remained relatively unchanged throughout all of the large-amplitude secondary cycles, the behavior will be illustrated using the data obtained from Cycle 39a.

Figures E.76 and E.77 show the readings obtained from the LVDTs attached to pier PA-7; Figure E.78 shows the readings obtained from the LVDTs attached to pier PA-8; Figure E.79 shows the readings obtained from the LVDTs attached to pier PA-9; and Figures E.80 and E.81 show the readings obtained from the LVDTs attached to pier PA-10.

In general, the pier responses shown in these figures are consistent with the observed behavior as well as measured responses during past cycles. The most notable difference in these measurements is the increase in residual displacement illustrated by the diagonal LVDTs attached to each pier. This indicates that each pier was displaying a larger degree of sliding/diagonal tension deformation. The seemingly bizarre readings provided by gages PA-7XR, PA-8XR, and PA-9XR in the negative direction indicate that these LVDTs had exceeded their stroke and should not be construed to indicate pier behavior.

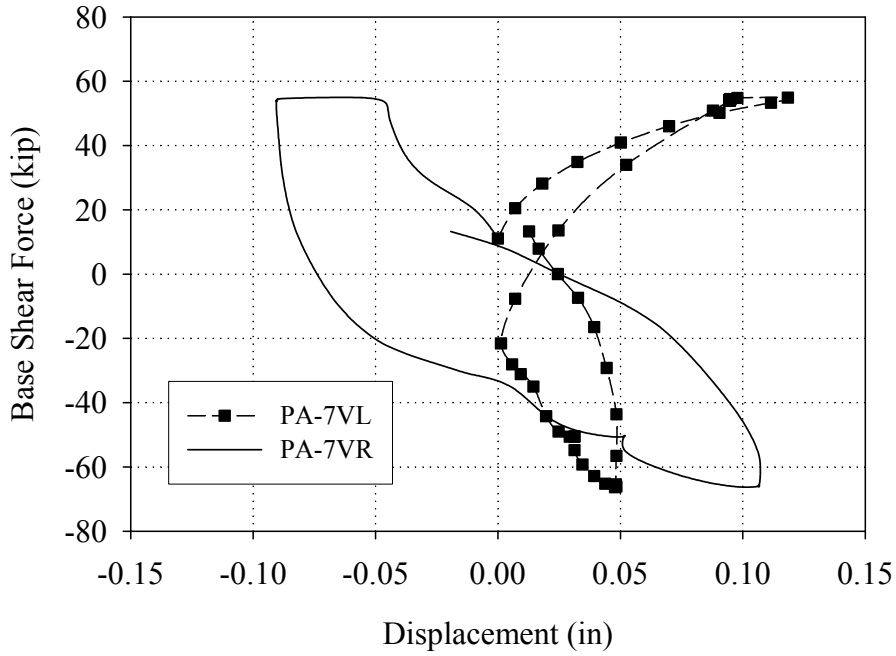

Figure E.76 Readings of the vertical LVDTs attached to pier PA-7 versus base shear force (Cycle 39a)

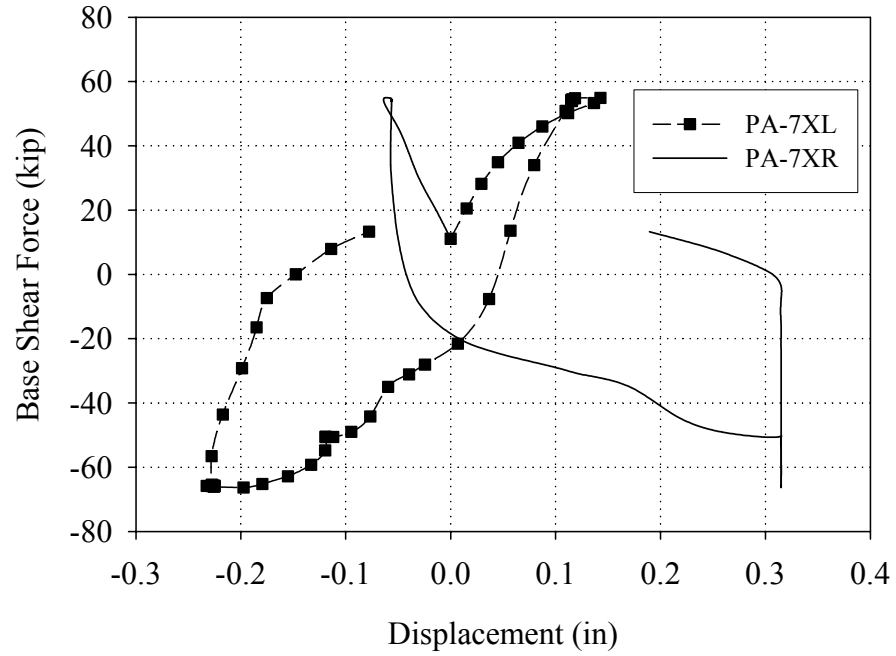

Figure E.77 Readings of the diagonal LVDTs attached to pier PA-7 versus base shear force (Cycle 39a)

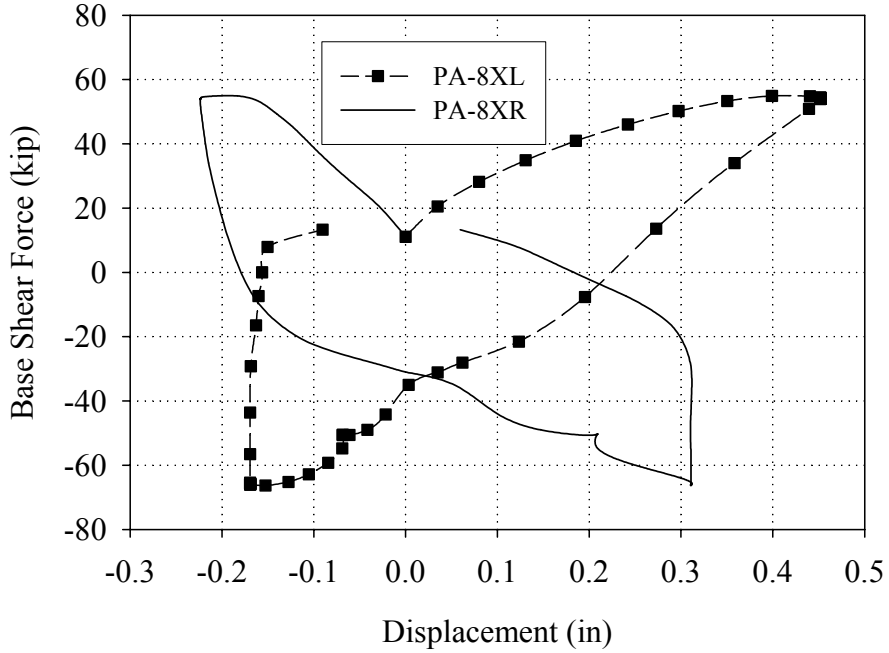

Figure E.78 Readings of the diagonal LVDTs attached to pier PA-8 versus base shear force (Cycle 39a)

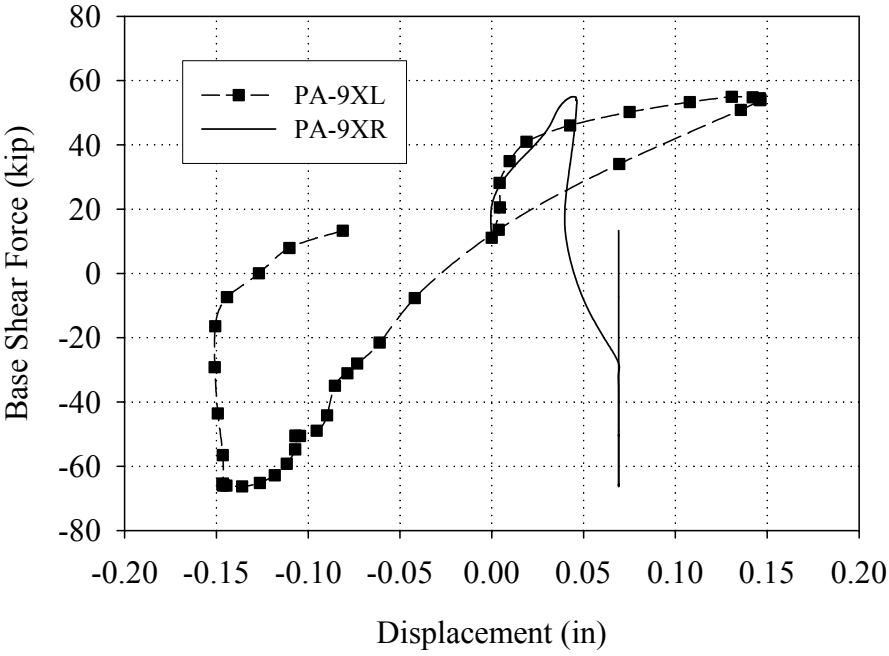

Figure E.79 Readings of the diagonal LVDTs attached to pier PA-9 versus base shear force (Cycle 39a)

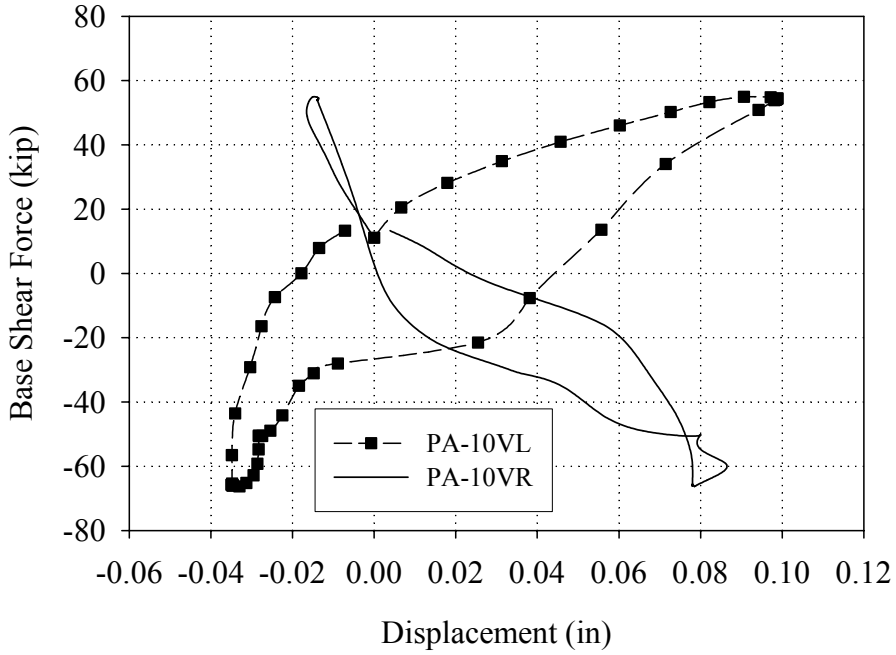

Figure E.80 Readings of the vertical LVDTs attached to pier PA-10 versus base shear force (Cycle 39a).

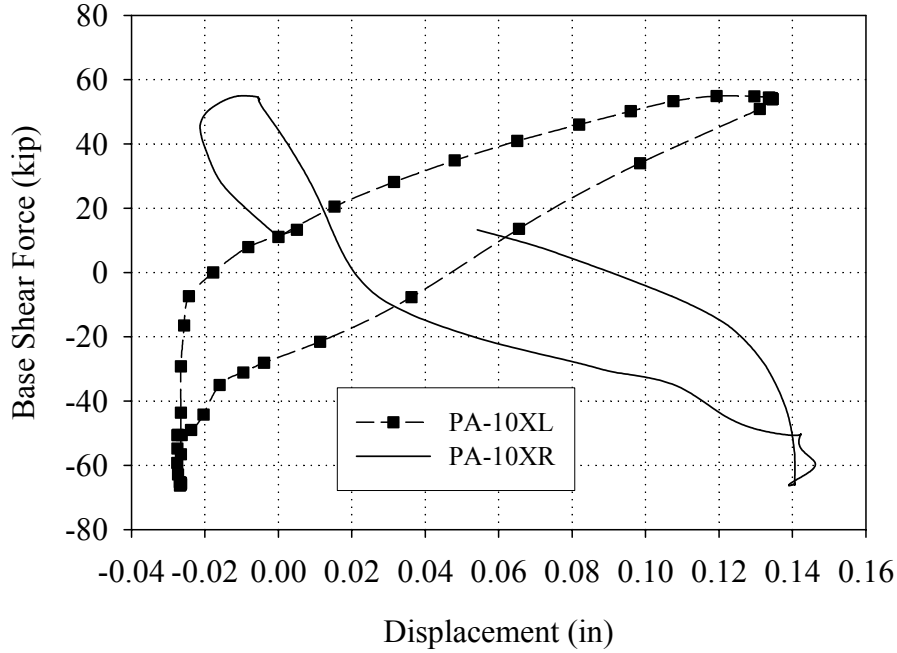

Figure E.81 Readings of the diagonal LVDTs attached to pier PA-10 versus base shear force (Cycle 39a).

APPENDIX F

EXPERIMENTAL RESULTS OF WALL B

F.1 Introduction

The behavior of Wall B following the application of unidirectional glass overlays and glass NSM rods is discussed in this appendix. Further details on the retrofit, test setup, instrumentation, and loading scheme can be found in Chapter 3. A summary of the displacements imposed on Wall B are shown in Table F.1 along with the test run and cycle designation. As apparent from this table, cycles imposing increasing levels of displacement were conducted on Wall B through Test Run 33 (i.e. 0.5 in roof displacement). Following this cycle, Wall B was subjected to a second series of cycles that imposed increasing levels of roof displacement up to 1.5 in. This loading history was chosen to allow the damage caused by the initial set of cycles to be investigated more thoroughly. In addition, during Test Run 40 and 41, Wall A was held at zero displacement. This was done to allow the coupling between in-plane URM walls to be investigated (as well as to avoid excessive damage in Wall A, see Appendix E). For certain comparisons it is necessary to limit the number of cycles considered. In these cases the initial cycle conducted during each test run was used and is shown in italics Table F.1.

Table F.1 Summary of displacements imposed on Wall B

Test Run	Cycle	Target Roof Displacement (in)	Target Second Floor Displacement (in)
27	*a*,b	+/-0.04	+/-0.03
28	*a*,b	+/-0.06	+/-0.043
29	*a*,b,c,d	+/-0.1	0.073, -0.076
30	*a*,b	+/-0.15	0.111, -0.123
31	*a*,b	+/-0.25	0.188, -0.2
32	*a*,b	+/-0.375	0.289, -0.30
33	*a*,b	+/-0.5	0.375, -0.385
34	*a*,b	+/-0.05	+/-0.04
35	*a*,b	+/-0.15	0.115, -0.125
36	*a*,b	+/-0.25	0.205, -0.21
37	*a*,b	+/-0.375	0.30, -0.311
38	*a*,b	+/-0.5	0.405, -0.415
39	*a*,b	+/-0.75	+/-0.623
40*	*a*,b	+/-1.0	0.8, -0.7
41*	*a*,b,c	+/-1.5	1.2, -1.13

* Wall A was held at zero displacement during these cycles

The appendix begins by discussing the general force-displacement behavior of Wall B for both the first and second stories. This behavior is quantified for each Test Run in terms of secant stiffness, secant mode shape, energy dissipation and residual displacement. Next the damage progression and wall behavior are discussed including a discussion of the reinforcement behavior and observed damage. For this task, the cycles imposed on the test structure are divided into five sections: Group 1 (Test Run 27 through

30), Group 2 (Test Run 31 through 33), Group 3 (Test Run 34 through 35), Group 4 (Test Run 36 through Test Run 39), and Group 5 (Test Run 40 and 41). Finally, the appendix concludes with a brief summary of the behavior of Wall B.

F.2 Force-Displacement Response

The lateral displacement of Wall B was measured through LVDTs referenced to the structure at the second floor and roof levels (see Appendix B). Due to the importance of these measurements, linear potentiometers were also employed for redundancy. During Test Run 39 through 41, the stroke of the second floor LVDT was exhausted and thus the readings of the potentiometer were used. Figures F.1 through F.6 show plots of the measured roof displacement versus base shear response for Test Run 27 through 30, Test Run 27 through 33, Test Run 34 and 35, Test Run 34 through 39, Test Run 34 through 41, and all of the cycles conducted on the Wall B, respectively.

From Figure F.2 it is apparent that the response of Wall B was very stable through Test Run 32, and showed very little degradation in terms of peak resistance during the redundant cycles conducted at each displacement level. Although, the force-displacement plots for the redundant cycles do show a slight decrease in stiffness thus indicating that some minor damage had occurred. Furthermore, the resistance displayed by the wall during these cycles increased with increasing roof displacement. In contrast, the peak resistance recorded in the positive direction during the redundant cycle of Test Run 33 was approximately 20% lower than the peak resistance recorded during the primary cycle. This degradation is attributed to the substantial debonding of the FRP overlays and NSM rods that was observed during Cycle 33a (see Section F.3 for a complete discussion of this

damage).

During Test Runs 34 through 37, the behavior of Wall B essentially remained unchanged (see Figures F.3 through F.5). That is, the force-displacement response of Wall B essentially followed the behavior recorded during Cycle 33b. As the displacements increased past those imposed during Test Run 33, a decrease in peak resistance and stiffness was observed for the redundant cycles (see Figures F.4 and F.5). Again, this damage was attributed to the debonding of the FRP overlays and NSM rods that was observed during Test Run 38 through 41 and is discussed in Section F.3.

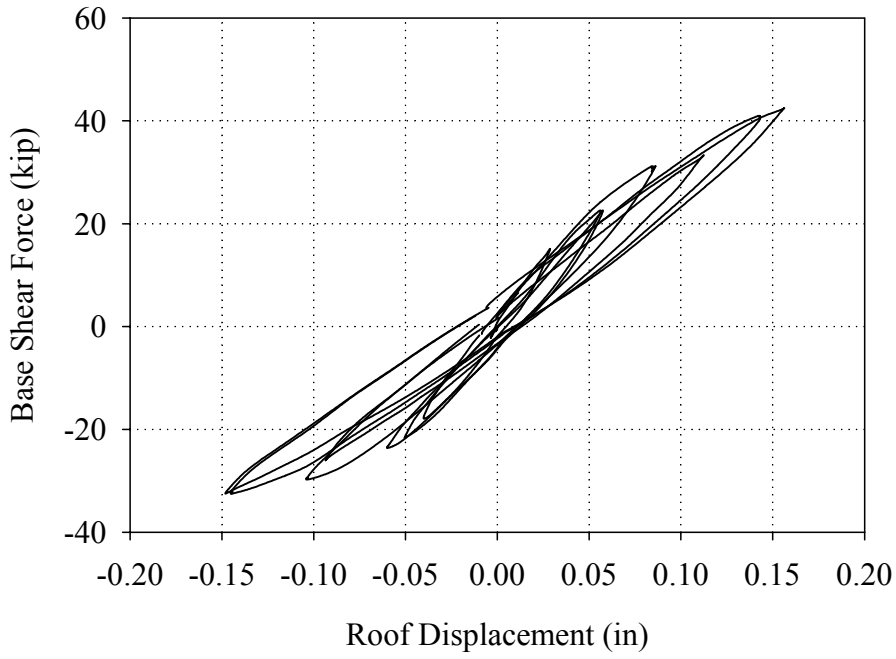

Figure F.1 Base shear versus roof displacement response of Wall B recorded during Test Runs 27 through 30.

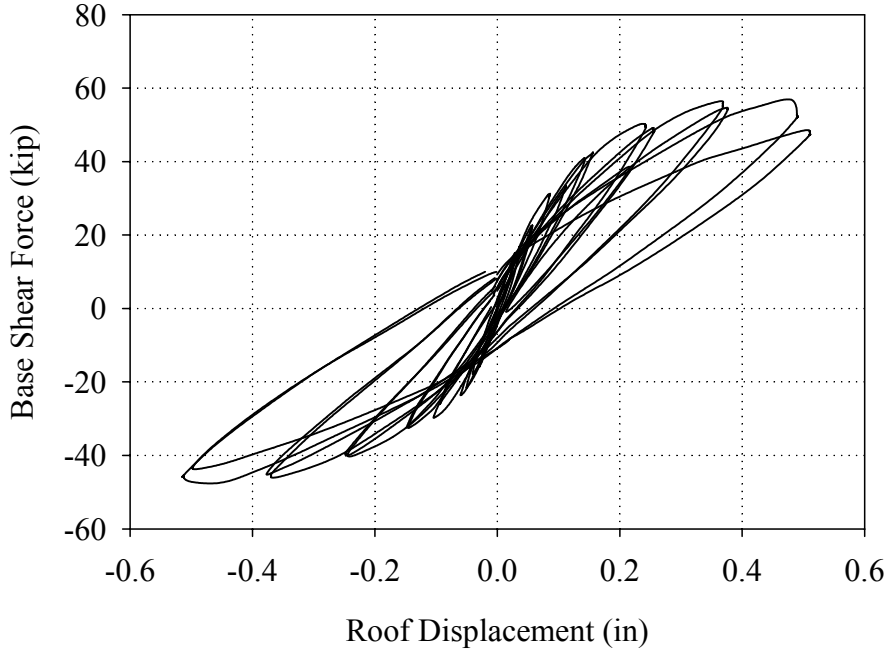

Figure F.2 Base shear versus roof displacement response of Wall B recorded during Test Runs 27 through 33.

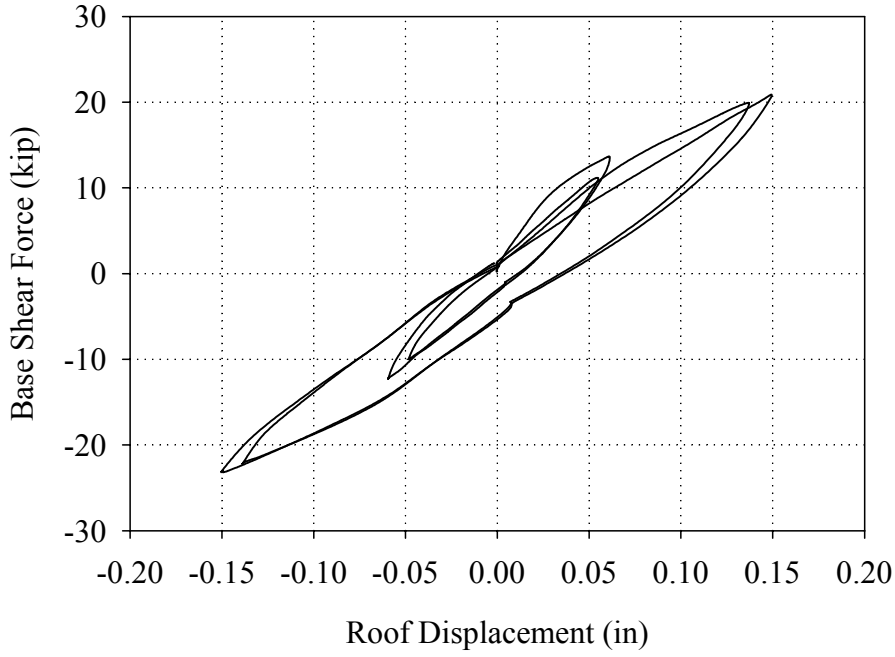

Figure F.3 Base shear versus roof displacement response of Wall B recorded during Test Runs 34 through 35.

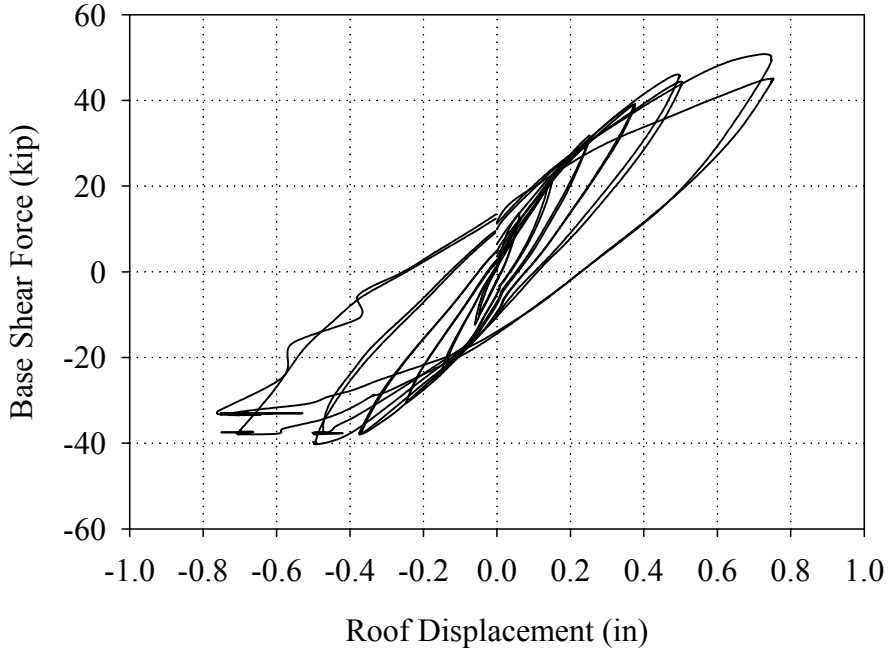

Figure F.4 Base shear versus roof displacement response of Wall B recorded during Test Runs 34 through 39.

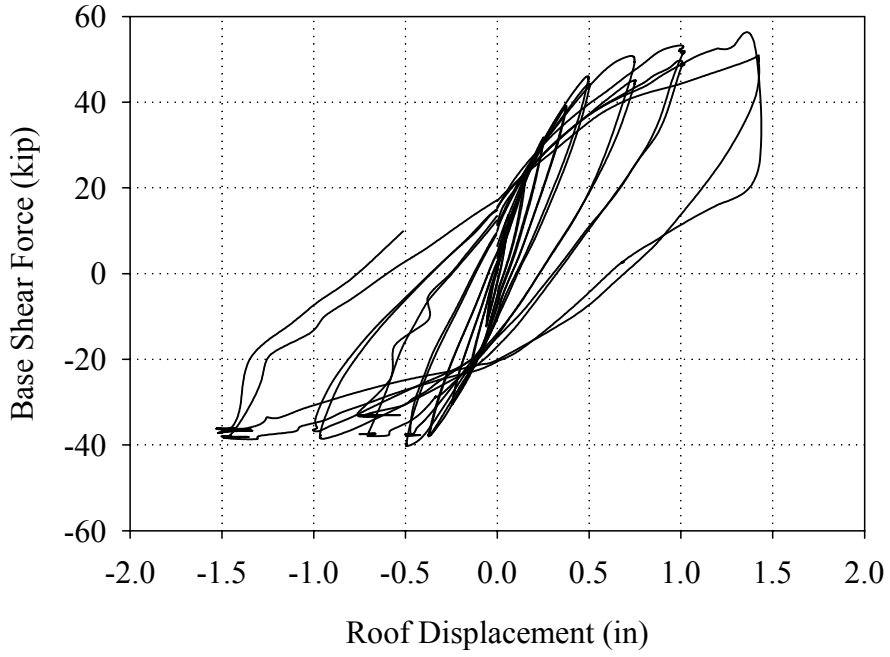

Figure F.5 Base shear versus roof displacement response of Wall B recorded during Test Runs 34 through 41.

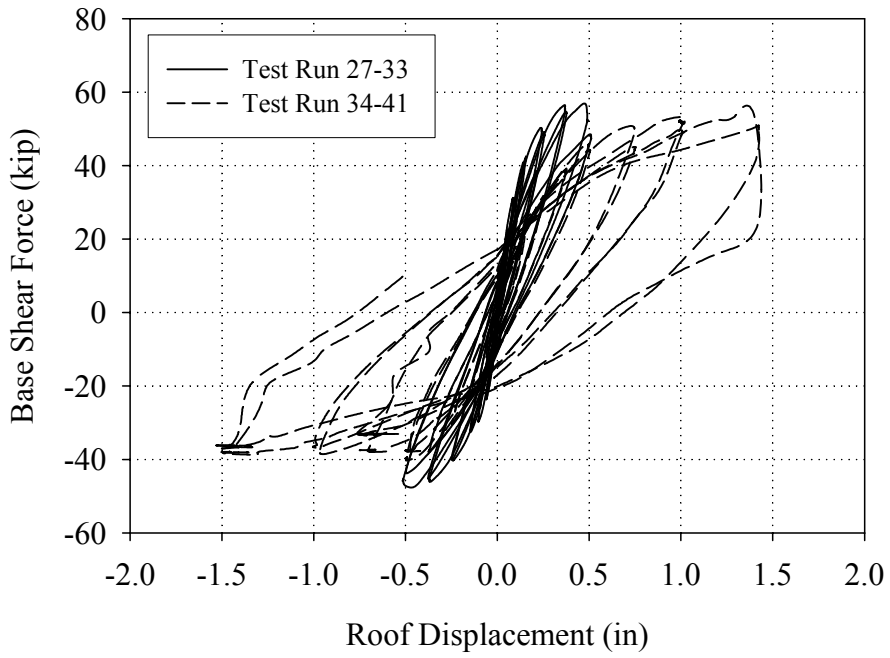

Figure F.6 Complete base shear versus roof displacement response of Wall B.

The force-displacement response of the first story of Wall B is shown in Figures F.7 through F.12 for Test Runs 27 through 30, Test Runs 27 through 33, Test Runs 34 and 35, Test Runs 34 through 39, Test Runs 34 through 41, and all of the cycles conducted on the Wall B, respectively. Figures F.13 through F.15 show the force-displacement response of the second story of Wall B for the Test Runs 27 through 33, Test Runs 34 through 41, and all of the cycles conducted on Wall B, respectively.

From Figures F.7 through F.12 it is apparent that the energy dissipation displayed by the base shear versus roof displacement plots was due to the behavior of the first story. In general, the discussion provided with regards to the the base shear versus roof displacement plots apply directly to the behavior of the first story. In contrast, the behavior of the second story can be classified as nonlinear elastic throughout all of the cycles (see

Figures F.13 through F.15). This behavior is attributed to local rocking of the second story piers as well as the global rocking of the entire wall. This phenomenon is discussed in more detail in Section F.3.

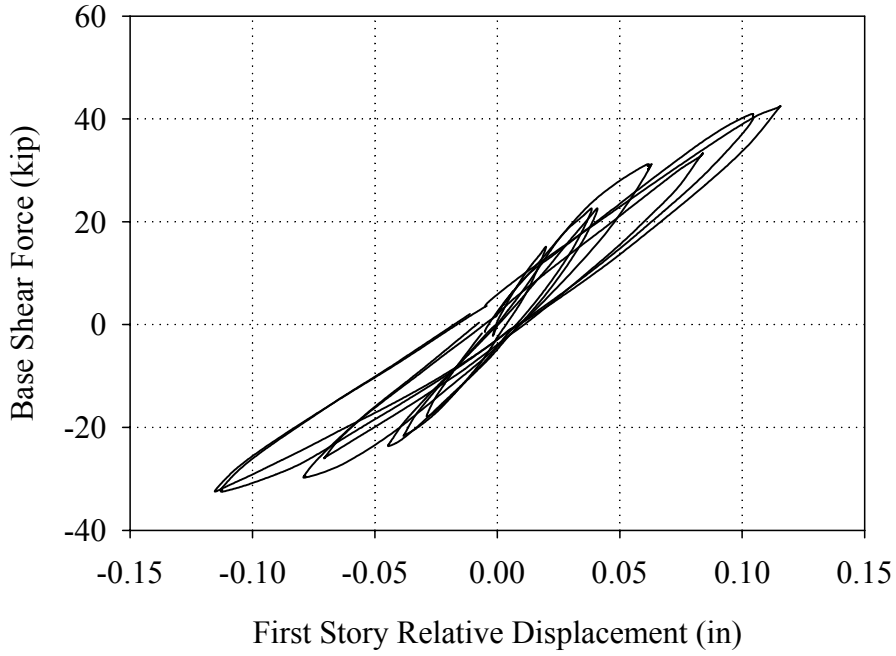

Figure F.7 Force-displacement response of the first story of Wall B recorded during Test Runs 27 through Test Run 30.

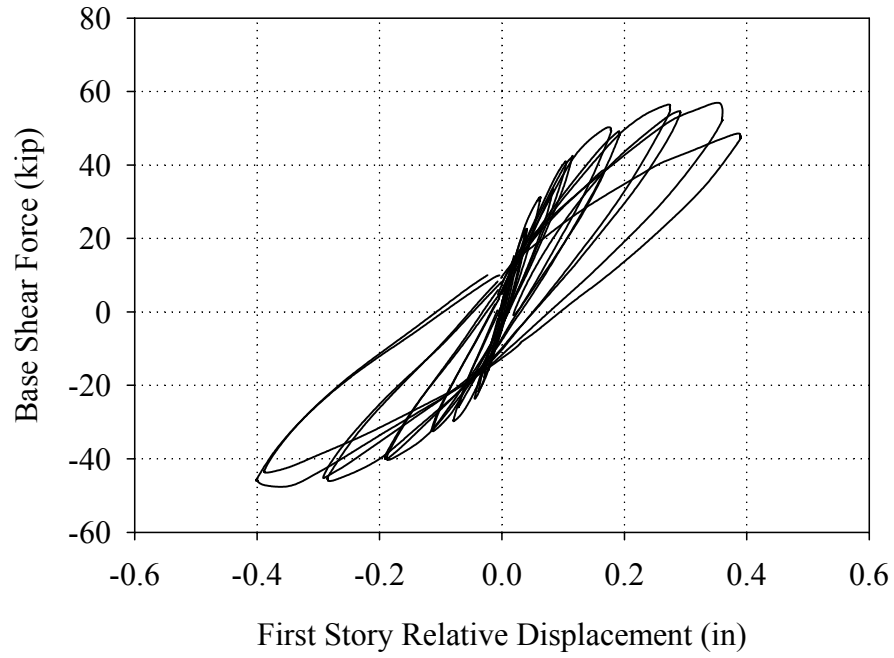

Figure F.8 Force-displacement response of the first story of Wall B recorded during Test Runs 27 through Test Run 33.

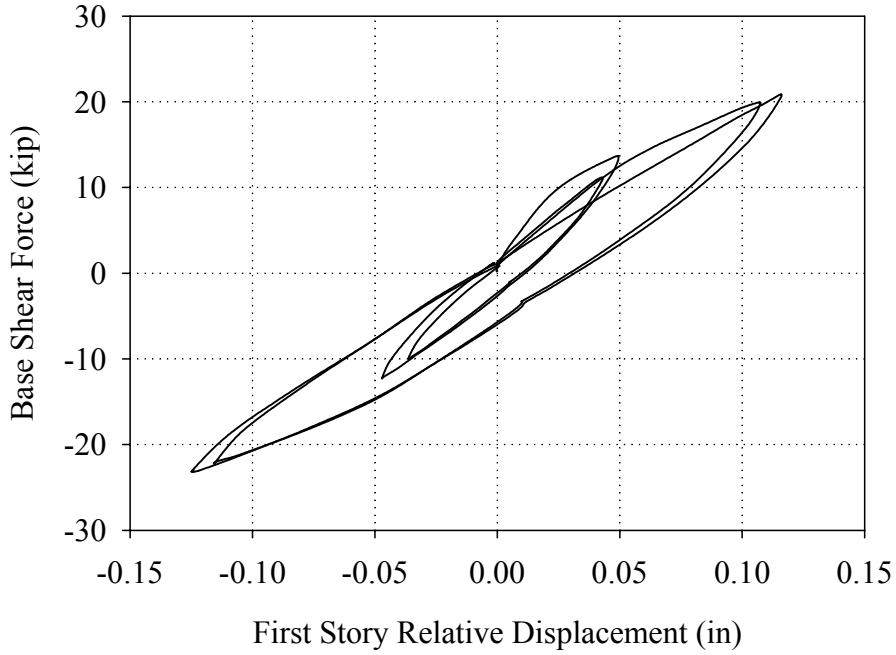

Figure F.9 Force-displacement response of the first story of Wall B recorded during Test Runs 34 and Test Run 35.

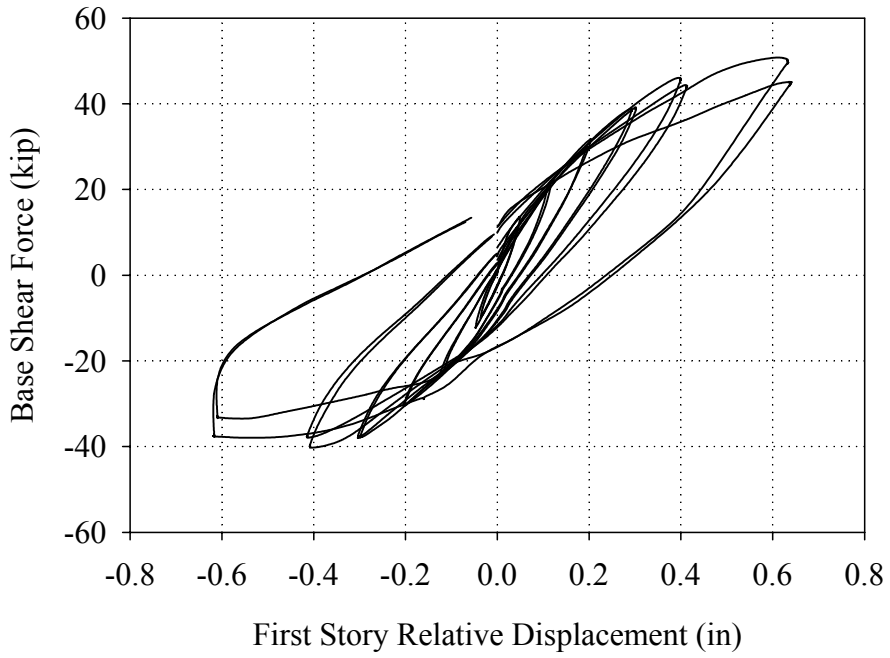

Figure F.10 Force-displacement response of the first story of Wall B recorded during Test Runs 34 through Test Run 39.

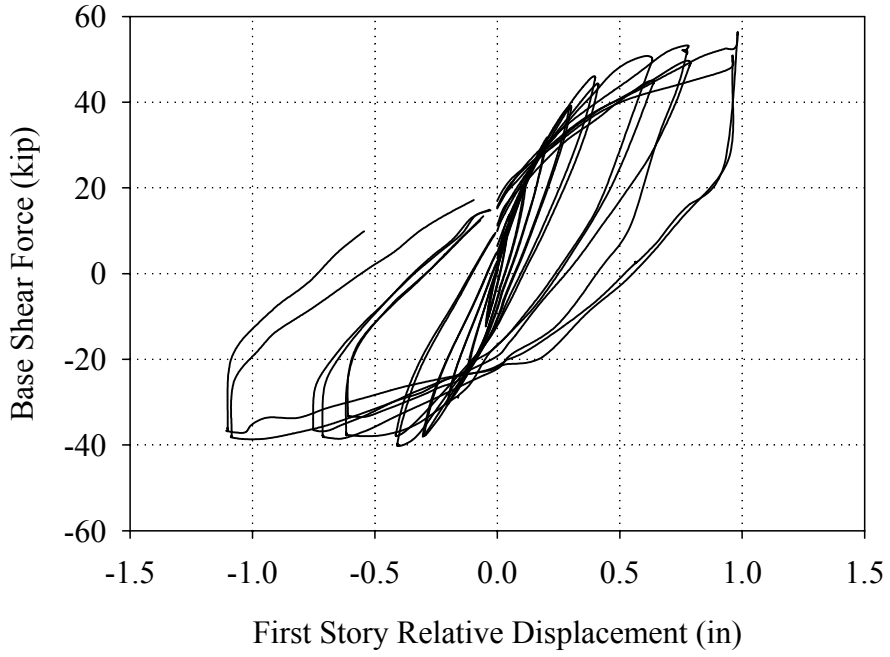

Figure F.11 Force-displacement response of the first story of Wall B recorded during Test Runs 34 through Test Run 41.

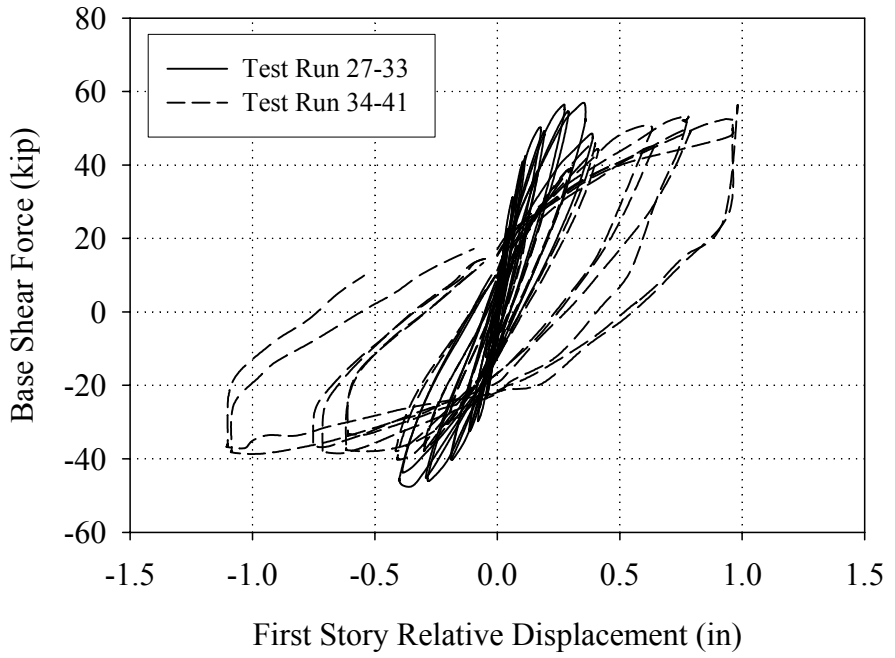

Figure F.12 Complete force-displacement response of the first story of Wall B.

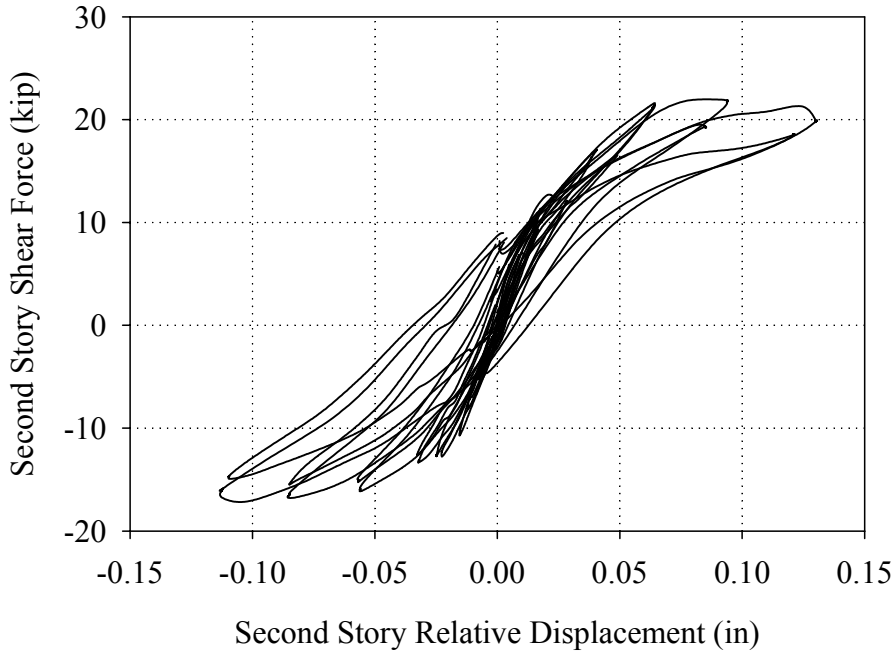

Figure F.13 Force-displacement response of the second story of Wall B recorded during Test Runs 27 through Test Run 33.

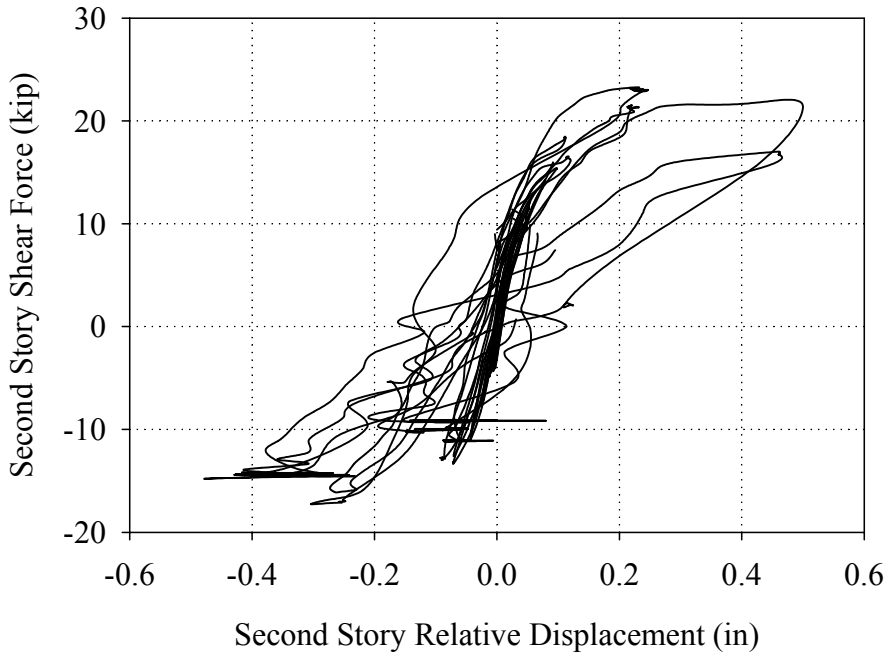

Figure F.14 Force-displacement response of the second story of Wall B recorded during Test Runs 34 through Test Run 41

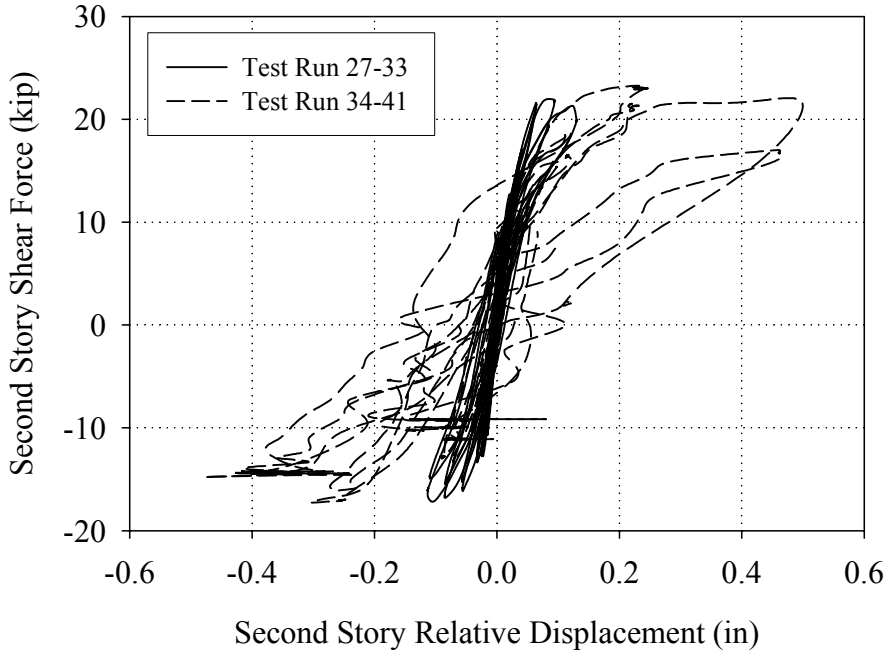

Figure F.15 Complete force-displacement response of the second story of Wall B.

F.2.1 Stiffness and Mode Shapes

For each of the Test Runs conducted on Wall B, the secant stiffness' the both the first story and second story were determined. The secant stiffness of the structure represents an average tangent stiffness, and as such can be used as an indication of damage. The stiffness' were taken as the slope of a line connecting the peak displacement point (both positive and negative) and the point at which the plot crosses the x-axis. This procedure is is discussed in detail in Appendix B. Table F.2 shows the calculated secant stiffnesses for the first and second stories of Wall B in the positive and negative direction for each Test Run.

Table F.2 Secant stiffness of Wall B for each Test Run

Test Run	Story	Positive Secant Stiffness (kip/in)	Negative Secant Stiffness (kip/in)
27	First	743	560
	Second	745	592
28	First	575	471
	Second	649	546
29	First	465	337
	Second	504	492
30	First	361	346
	Second	421	392
31	First	250	229
	Second	299	251
32	First	180	138
	Second	177	163
33	First	132	88
	Second	132	133

Table E.2 Continued

34	First	268	209
	Second	249	227
35	First	177	151
	Second	267	264
36	First	147	120
	Second	222	218
37	First	123	101
	Second	180	155
38	First	99	81
	Second	157	122
39	First	65	25
	Second	141	68
40	First	48	36
	Second	100	141
41	First	39	25
	Second	52	34

From this table it is apparent that the secant stiffness of each story decreased during almost every cycle of increasing roof displacement. This is expected since the secant stiffness can also be used as a measured of nonlinear response. Based on the relative decrease between the first and second floor, these stiffness' suggest that the majority of the damage focused on the first floor of Wall B. The apparent decreased in secant stiffness displayed by the second story is attributed to the global rotation of the entire wall (see Section F.3). That is, the global rotation of Wall B leads to an apparent interstory drift of the second story thus causing a decrease in the calculated secant stiffness.

To gain more insight into the seismic behavior of Wall B, the fundamental secant

mode shapes were determined for each Test Run and are listed in Table F.3 (see Appendix B for a detail description of this calculation and associated assumptions). In addition, Figures F.16 and F.17 show the calculated secant mode shapes (normalized to roof displacement) for Test Runs 27 through 33 and Test Runs 34 through 41, respectively.

Table F.3 Fundamental secant mode shapes of Wall B normalized to 1.0 for all cycles.

Test Run	Positive Fundamental Secant Mode Shape	Negative Fundamental Secant Mode Shape
27	$\{1.0, 0.72\}^T$	$\{1.0, 0.73\}^T$
28	$\{1.0, 0.74\}^T$	$\{1.0, 0.75\}^T$
29	$\{1.0, 0.74\}^T$	$\{1.0, 0.80\}^T$
30	$\{1.0, 0.75\}^T$	$\{1.0, 0.75\}^T$
31	$\{1.0, 0.76\}^T$	$\{1.0, 0.74\}^T$
32	$\{1.0, 0.71\}^T$	$\{1.0, 0.75\}^T$
33	$\{1.0, 0.72\}^T$	$\{1.0, 0.80\}^T$
34	$\{1.0, 0.70\}^T$	$\{1.0,0.73\}^T$
35	$\{1.0, 0.80\}^T$	$\{1.0, 0.83\}^T$
36	$\{1.0, 0.80\}^T$	$\{1.0, 0.83\}^T$
37	$\{1.0, 0.80\}^T$	$\{1.0, 0.81\}^T$
38	$\{1.0, 0.81\}^T$	$\{1.0, 0.80\}^T$
39	$\{1.0, 0.86\}^T$	$\{1.0, 0.89\}^T$
40	$\{1.0, 0.85\}^T$	$\{1.0, 0.92\}^T$
41	$\{1.0, 0.78\}^T$	$\{1.0, 0.78\}^T$

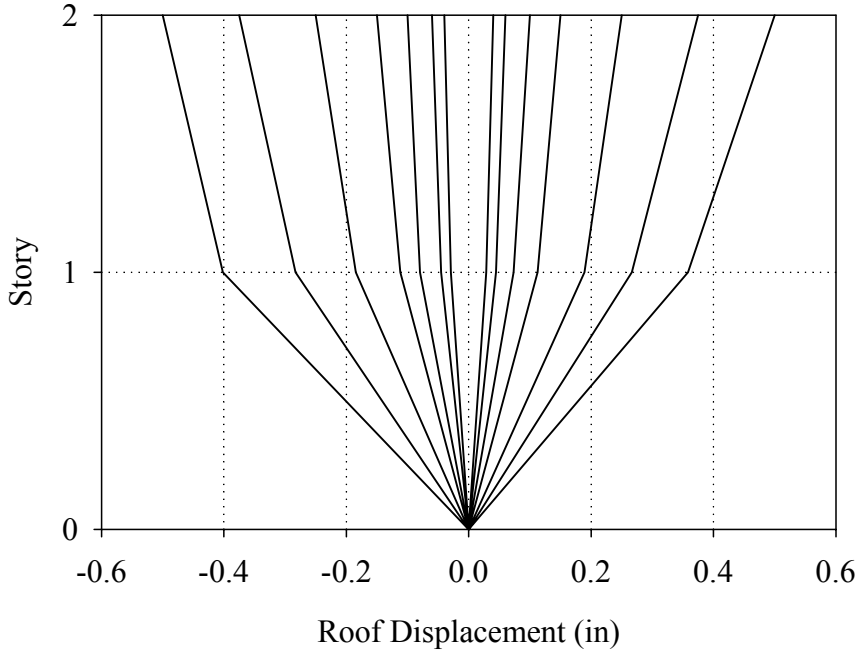

Figure F.16 Fundamental secant mode shapes of Wall B normalized to target roof displacement for Test Runs 27 through 33.

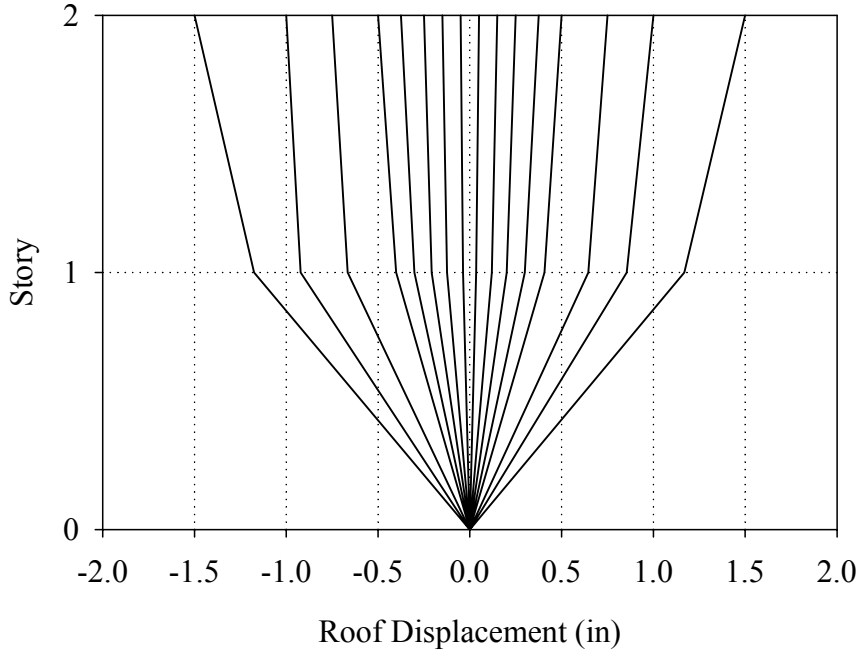

Figure F.17 Fundamental secant mode shapes of Wall B normalized to target roof displacement for Test Runs 34 through 41.

As apparent from this table and figures, the calculated fundamental secant mode shapes were somewhat erratic. This is attributed to the assumptions used to calculate these values, specifically the assumption that all of the measured displacements were a result of interstory shear deformation (see Appendix B). As is discussed in Section F.3, Wall B displayed a global rotation as well as interstory shear displacement thus rendering this assumption erroneous. However, since limited instrumentation was used to capture this global rotation it is difficult to incorporate this degree of freedom into the model.

With this admittedly erroneous calculation, some insight can still be gained into the seismic performance of Wall B. While the calculated mode shapes are somewhat erratic, a general trend of increasing first story displacement can be seen. This increase in first story displacement suggests that a soft story was forming. In addition, it is important to note that this apparent subtle evolution in behavior is masked by global rotation. That is, a global rotation of the wall results in an apparent decrease in stiffness of the second story thus concealing the soft story effect.

F.2.2 Energy Dissipation

The energy dissipated by each floor of Wall B was calculated for each of the cycles conducted. This was accomplished by numerically integrating the force-displacement plots shown in Figures F.7 through F.15 (see Appendix B). For comparison purposes, the calculated values were divided by the maximum possible energy dissipated, which was defined as the area of a rectangle encompassing the force-displacement plot. Figure F.18 shows the percentage of energy dissipated by each floor versus roof displacement. Figure F.19 shows the actual energy dissipated by each floor versus roof displacement.

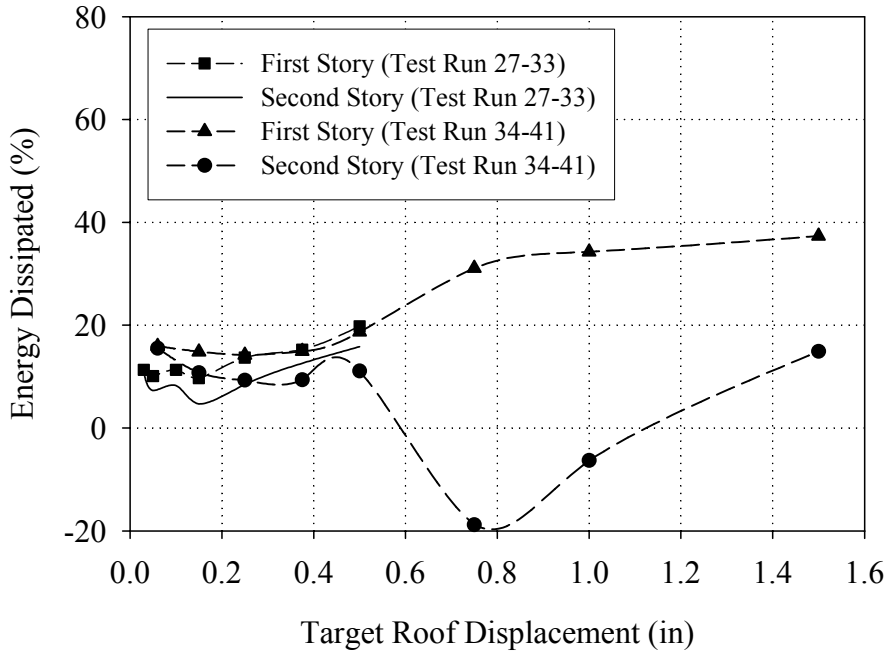

Figure F.18 Percentage of energy dissipated by each story of Wall B versus target roof displacement.

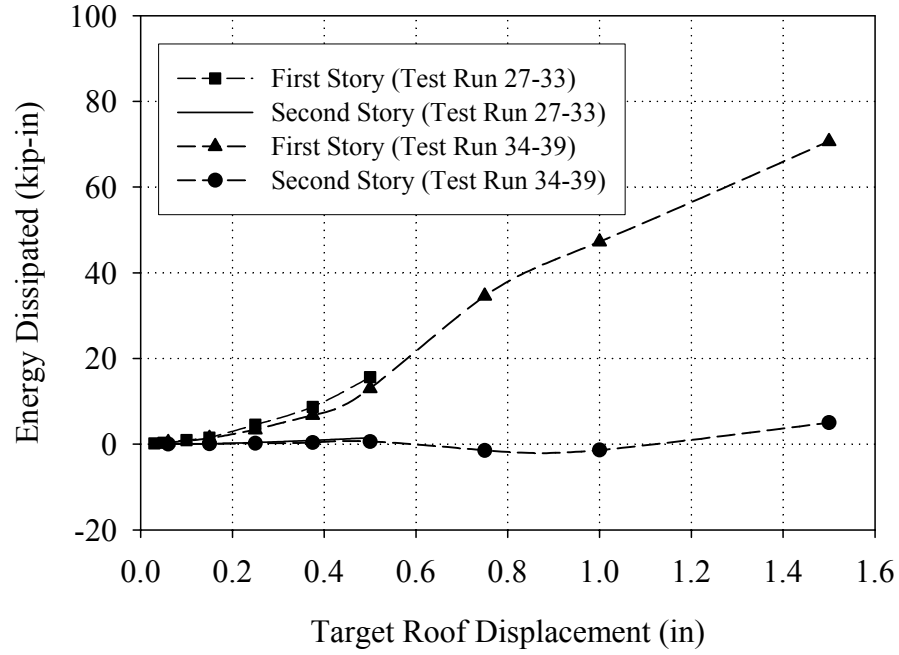

Figure F.19 Energy dissipated by each story of Wall B versus target roof displacement.

From Figure F.18 it is apparent that the percentage of energy dissipated by both stories was relatively constant through Test Run 38 at approximately 15%, which is consistent with rocking dominated behavior. During Test Runs 39 through 41 however, the energy dissipated by the first floor increased substantially to approximately 35%. This level of energy dissipation is more consistent with sliding deformation and likely represents a change in the response of the first story. In addition, during these cycles of the percentage of energy dissipated by the second floor became negative. This erroneous measurement is attributed to the low-level global rocking for reasons outlined in the previous two sections.

As apparent from Figure F.19, the first story of Wall B dissipated orders of magnitude more energy than the second story. As a result, the negative percentage of energy dissipated by the second story is trivial (see Figure F.18).

F.2.3 Residual Displacement

The residual displacement of each story of Wall B was calculated for Test Run according to the procedure outlined in Appendix B. However, due to the small displacements imposed on the second story, the residual displacements measured were negligible and are not discussed. The residual displacements for the first story of Wall B are presented in Table F.4 as a percentage of the story drift. Figures F.20 and F.21 show the residual displacement of the first floor of Wall B (as a percentage of story drift) versus story drift for Test Runs 27 through 33 and Test Runs 34 through 41, respectively.

Table F.4 Residual Displacement of Wall B

Test Run	+ Residual Displacement (% of Story Drift)	- Residual Displacement (% of Story Drift)
27	16	10
28	19	18
29	19	21
30	14	20
31	19	23
32	23	29
33	33	39
34	24	33
35	33	24
36	28	28
37	29	28
38	30	41
39	48	65
40	66	69
41	67	59

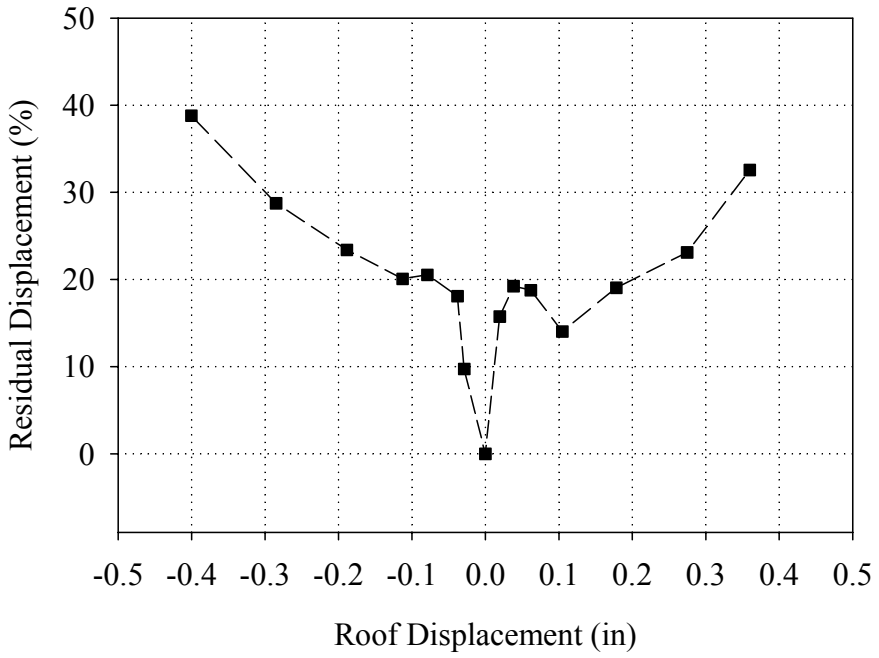

Figure F.20 Residual displacement as a percentage of story drift for the first floor of Wall B versus story drift (Test Runs 27 through 33).

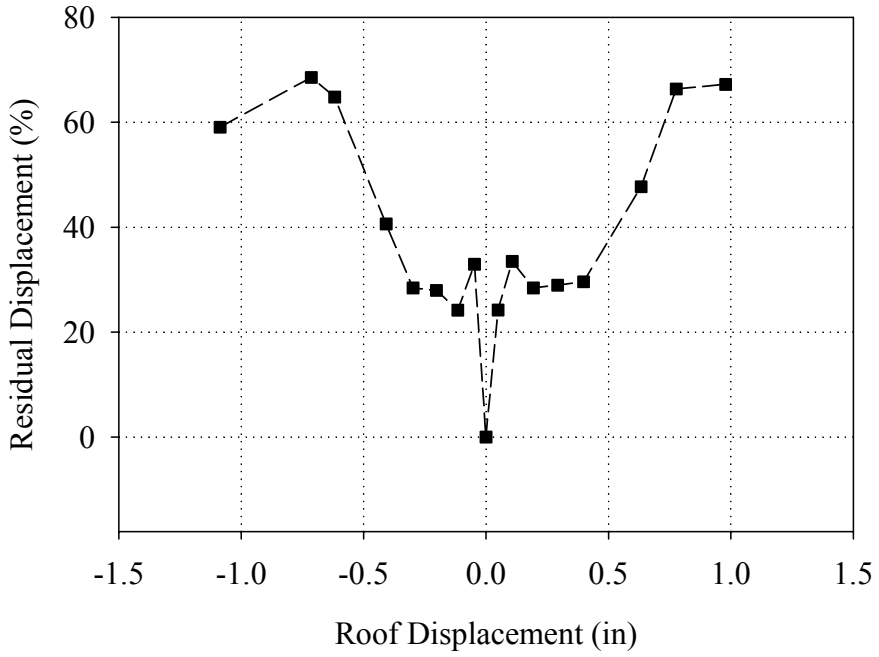

Figure F.21 Residual displacement as a percentage of story drift for the first floor of Wall B versus story drift (Test Runs 34 through 39).

From Figures F.20 and F.21 it is apparent that the residual displacement of the first story increased from 20% to 40% during cycles that imposed roof displacements up to 0.5 in. During Test Run 39 (i.e. 0.75 in roof displacement), a large jump in residual displacement from around 40% to 60% occurred (see Figure F.21). This jump suggests that the amount of sliding deformation in Wall B increased substantially during this displacement level. In addition, Figure F.21 shows that the percentage of residual displacement remained fairly constant during Test Runs 40 and 41. This is consistent with the discussion of energy dissipation (see Section F.2.2), which also suggested an increase in sliding deformation during Test Run 39 and a fairly constant level during the final two displacement levels.

F.3 Damage Progression and Wall Behavior

The following sections describe the behavior of Wall B during each of the five groups of cycles defined in Section F.1. For each group of cycles the general behavior of the wall is first described in terms of crack pattern, visually observed behavior, and representative instrumentation. Next, a description of the external reinforcement behavior (both the FRP overlays as well as the NSM rods) is presented including strain gage readings and photographs of damage. Finally, the specific behavior of the in-plane piers are described and representative plots of the instrumentation attached to the piers are presented.

F.3.1 Group 1 Cycles (Test Run 27-Test Run 30)

F.3.1.1 Overall Wall Behavior

During the Group 1 cycles no new cracks were observed in Wall B or out-of-plane Walls 1 and 2. Figures F.22 through F.24 show schematics of the crack pattern in Wall B and out-of-plane Walls 1 and 2 following these cycles. The cracks shown in these figures formed during testing of Wall B prior to the application of FRP or during the loading of Walls 1 and 2 in-plane (see Appendix C and D). For a complete discussion of the testing of Wall B prior to retrofit the reader is directed to Yi (2004).

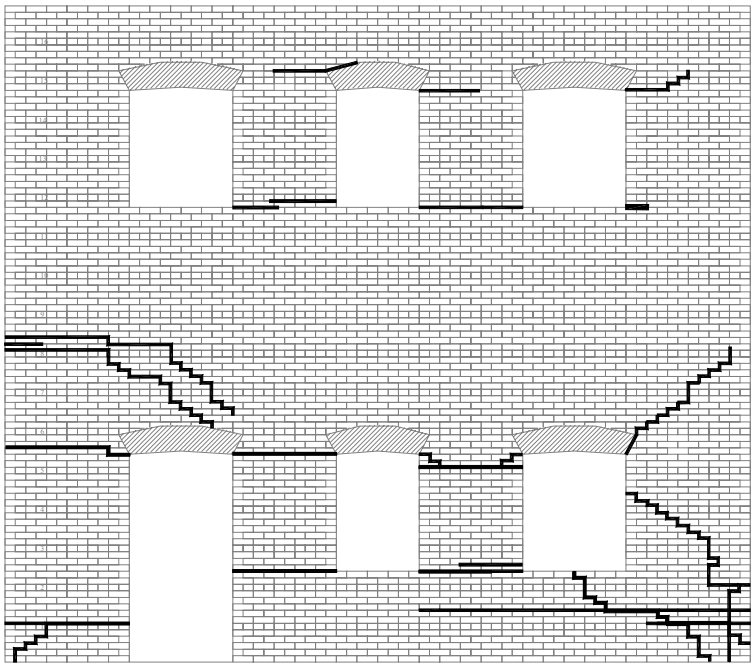

Figure F.22 Crack pattern of Wall B following the Group 1 cycles

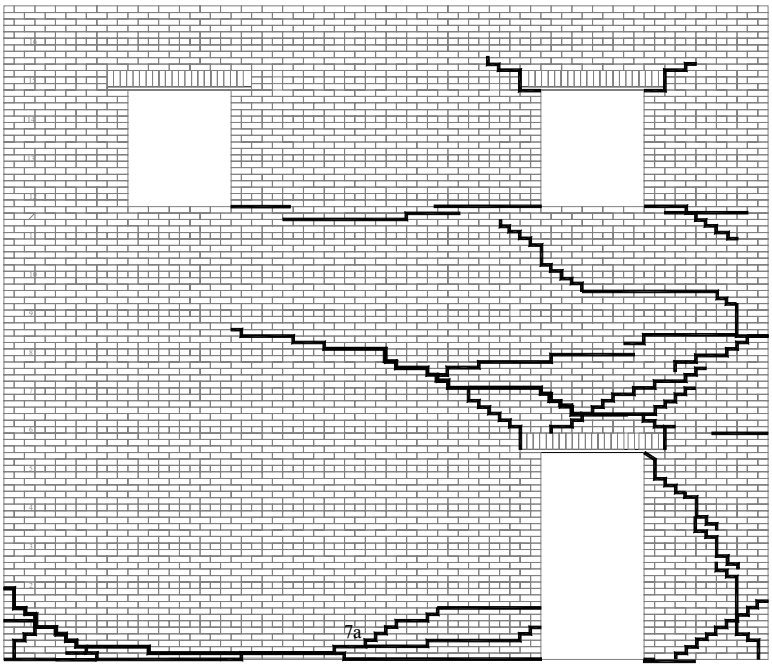

Figure F.23 Crack pattern of out-of-plane Wall 1 following the Group 1 cycles

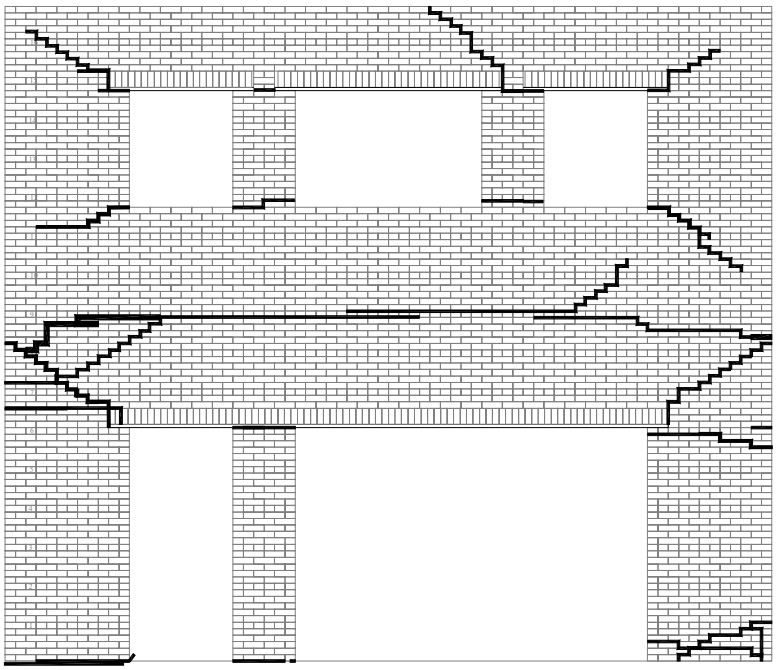

Figure F.24 Crack pattern of out-of-plane Wall 2 following the Group 1 cycles

Figure F.25 shows a schematic illustrating the behavior of Wall B as well as out-of-plane Walls 1 and 2 in the positive direction. Note that the location of the LVDT reference points are also shown in the figure. In the positive loading direction, the behavior of Wall B was a combination of global rocking behavior and component behavior. That is, the roof displacement was caused by both a rotation of the entire wall as well as the shear deformation of the individual piers. In general, the behavior of the first floor piers can be classified mainly as rocking. The observed and measured rigid motion is shown in Figure F.25 by arrows.

Figure F.26 shows a plot of the vertical displacements of each side of Wall B versus roof displacement for Cycle 30b. From this plot it is apparent that the roof of Wall B translated upwards approximately 0.01 in. This vertical translation was likely caused by the local rocking deformation of each individual pier. In addition, the differential displacements of each side of Wall B shown in Figure F.26 suggests that the entire wall was rotating. Since the aspect ratio of Wall B is approximately 1.0, the difference in vertical displacement of each side of the wall is roughly equal to the lateral roof displacement caused by global rocking (assuming rigid body rotation about the base of the wall). Following this assumption, the global rocking displacement shown in Figure F.26 represented approximately 0.02 in or 13% of the lateral roof displacement. Conversely, this indicates that the majority of the displacement (approximately 87%) was due to interstory displacement or pier behavior.

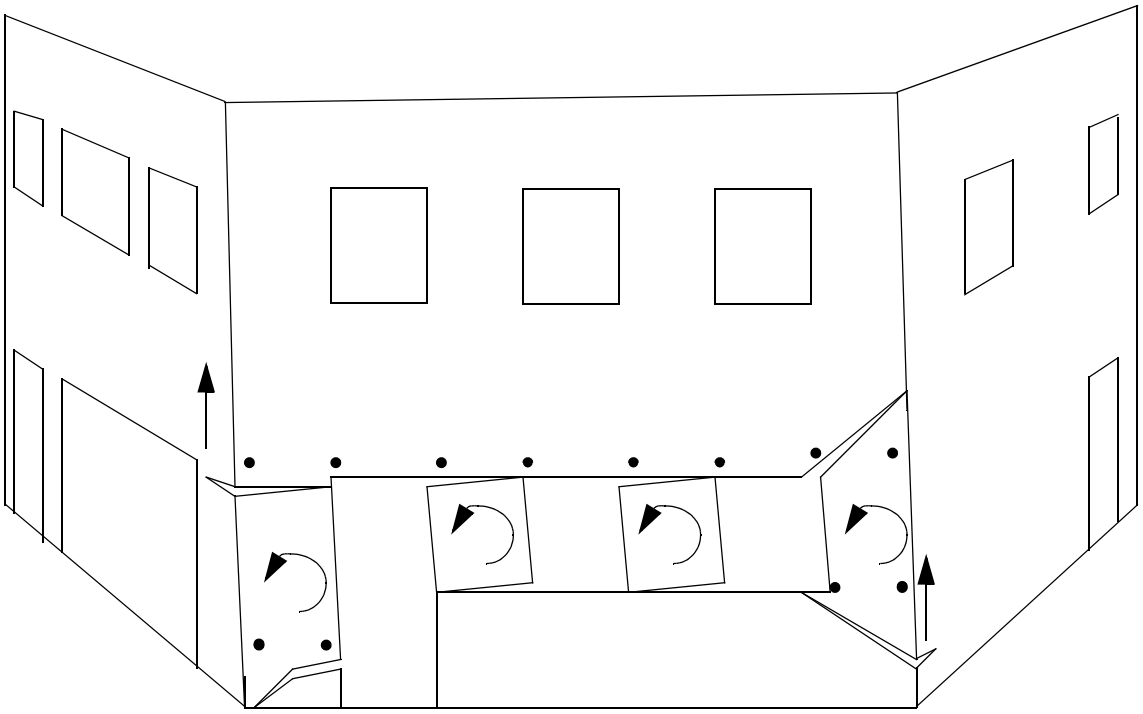

Figure F.25 Exaggerated schematic of the observed behavior of Wall B in the positive loading direction during the Group 1 cycles.

In addition, the observed uplift and rotation of Wall B engaged portions of out-of-plane Walls 1 and 2 (see Figure F.25). Specifically, the rocking of pier PB-7 caused a vertical displacement and lifted up the portion of Wall 2 above pier P2-9. In addition, the rocking of pier PB-10 lifted up a portion of pier P1-6 above the crack at the base. Since the identification of out-of-plane wall participation is based primarily on visual observations, the exact weight of Walls 1 and 2 that participated in the response of Wall B is somewhat unclear. This short coming is addressed in Chapter 5 and a method for approximating the weight is presented.

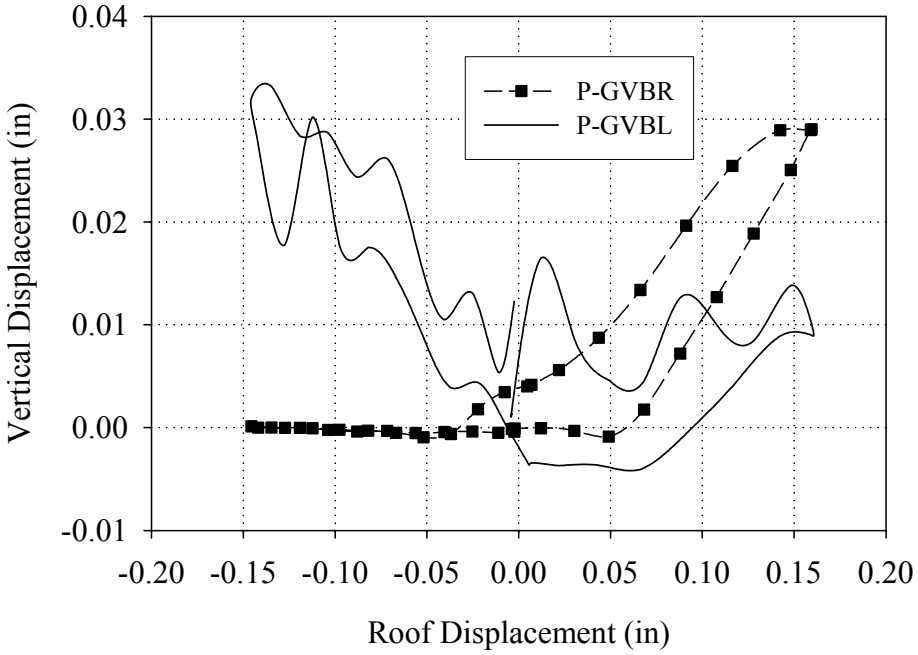

Figure F.26 Vertical displacements of both sides of Wall B versus roof displacement (Cycle 30b)

Figure F.27 shows the base strains recorded at the peak positive displacement during Cycle 30a. As apparent from this figure, the recorded strain profiles of each pier are consistent with the observed rocking deformation. In addition, the recorded strains profiles also support the contention that the out-of-plane walls participated in the response. This is clearly seen by the tensile strains measured in pier P1-6 and the compressive strains measured in pier P2-9. Furthermore, the strains recorded in the out-of-plane walls were similar in magnitude to those recorded in the in-plane walls, which may give some insight into the degree to which the out-of-plane walls were participating. However, the reader is cautioned that due to large variations in material properties, numerous cracks, and uncertainties inherent in strain gage measurements obtained from masonry, only a qualitative discussion of this strain data is appropriate.

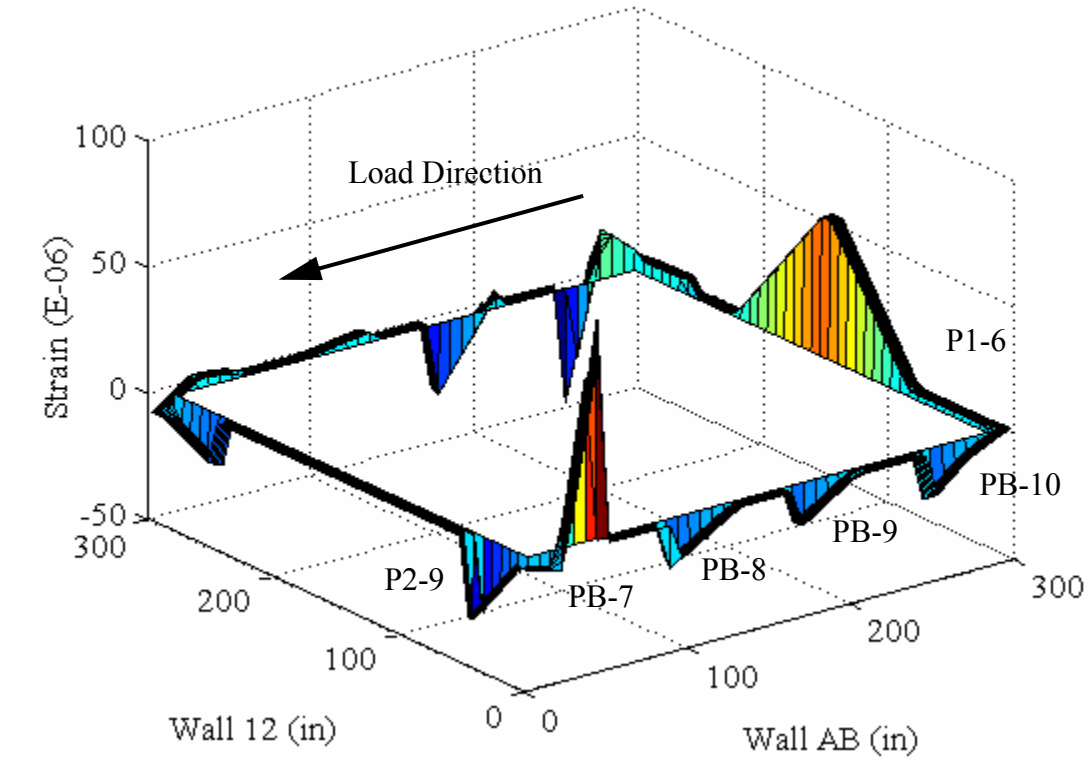

Figure F.27 Base strains recorded at peak positive displacement (Cycle 30a).

Figure F.28 shows a schematic of the behavior of Wall B in the negative direction. Similar to the positive direction, the observed behavior can be characterized as a combination of local pier behavior and global rocking behavior. However, based on Figure F.26 it is apparent that a larger degree of global rocking displacement was observed in the negative loading direction. Based on the assumptions outlined previously, the observed global rocking accounted for approximately 0.03 in or 20% of the imposed roof displacement.

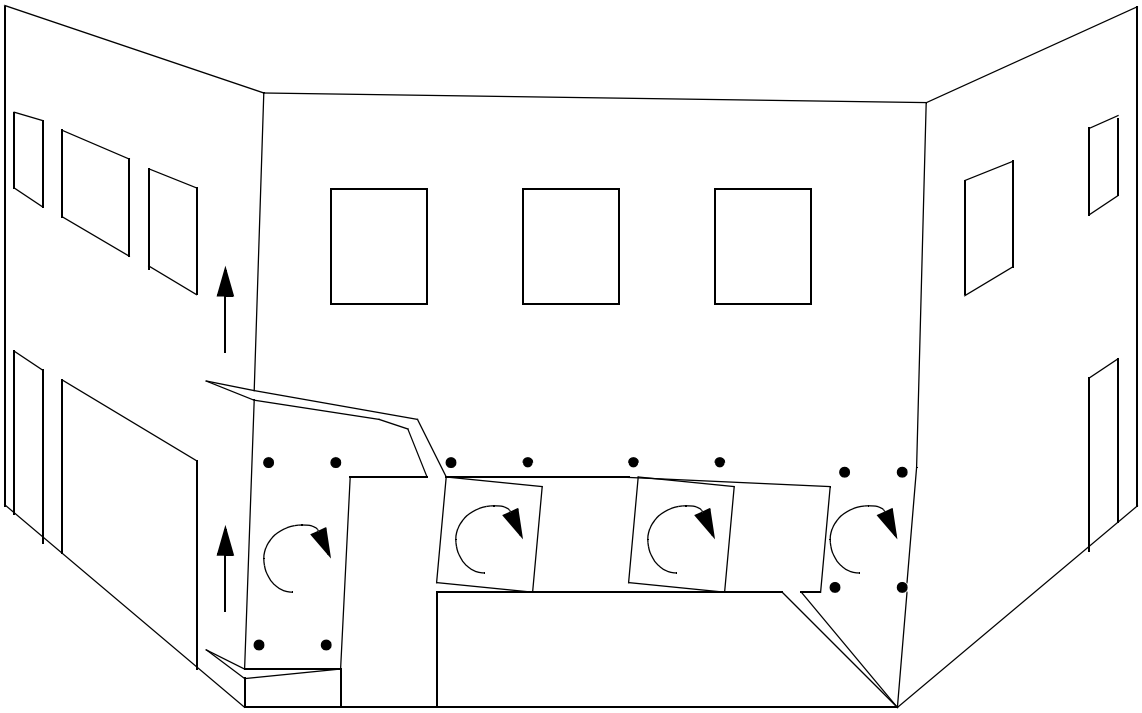

Figure F.28 Exaggerated schematic of the observed behavior of Wall A in the negative loading direction during the Group 1 cycles.

In the negative direction, all of the piers displayed some degree of rocking deformation as shown by arrows in Figure F.28. In addition, visual observations indicated that the low-level global rocking acted to lift the upper portion of Wall B off of pier PB-7. However, the NSM rods applied to the structure above the door opening were effective in tying the spandrel together thus forcing pier PB-7 to participate in the response. No visual observations of rocking deformation of pier PB-10 could be made during this level of testing. As illustrated in Figure F.28, pier PB-10 was essentially rocking with the entire upper portion of Wall B. Obviously other deformation was occurring since the global rocking deformation only accounted for approximately 20% of the roof displacement. However, the small level of displacements coupled with the FRP reinforcement rendered

visual observations of crack openings difficult.

Similar to the behavior in the positive direction, the global rocking shown in Figure F.26 engaged portions of out-of-plane Walls 1 and 2. Based on visual observations the participation of Wall 2 was caused by a combination of global rocking and component behavior (see Figure F.28). The participation of the out-of-plane walls is also supported by Figure F.29, which shows the base strains recorded at peak displacement in the negative direction during Cycle 30a. Similar to the positive direction, the strain profiles illustrated by this plot are consistent with the observed behavior. The small strains recorded at the intersection of Walls 1 and B were likely due to the substantial damage sustained by this region during past cycles (see Yi, 2004).

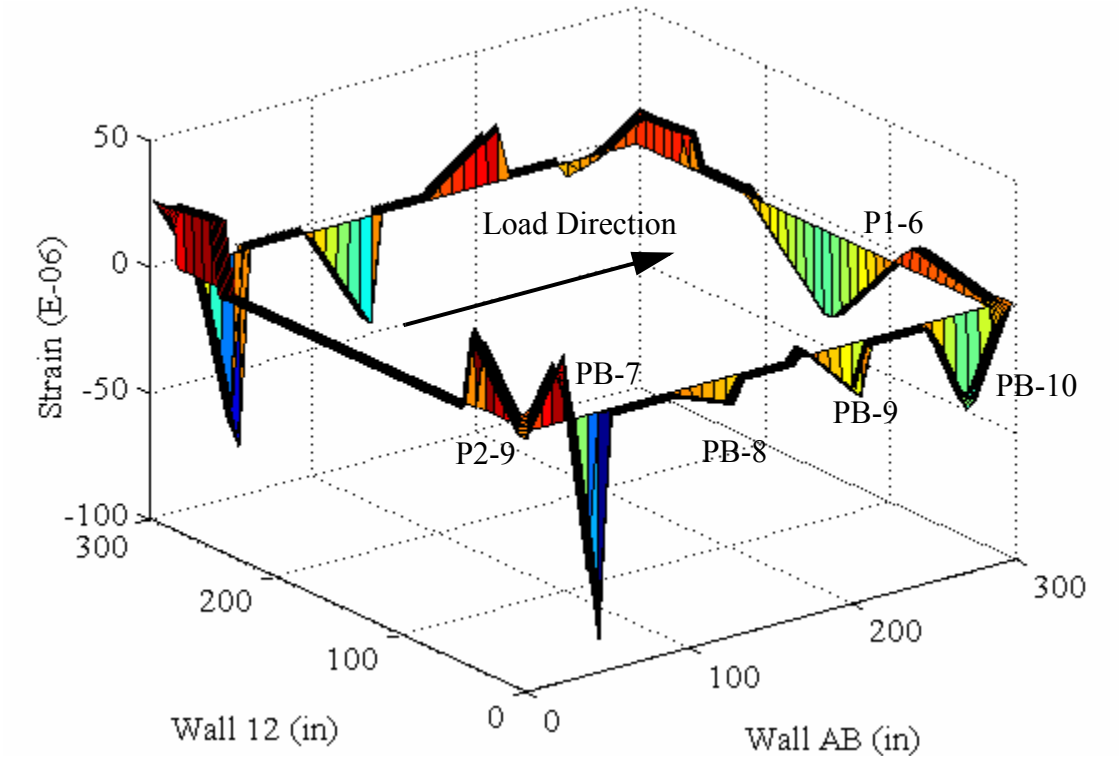

Figure F.29 Base strains recorded at peak negative displacement (Cycle 30a).

F.3.1.2 Behavior of External Reinforcement

During this level of testing no visual damage was observed in either of the external reinforcement systems applied to Wall B. However, popping noises were heard coming from the NSM rods above piers PB-7 and PB-10 during Test Runs 29 and 30. Specifically, these noises seemed to originate in the vicinity of the diagonal cracks above these piers. Based on the behavior of Wall B illustrated by Figures F.25 and F.28, it is likely that the opening of these existing cracks created strain concentrations in the NSM rods thus resulting in damage. However, extensive visual inspection of these areas was conducted and no cracks in the epoxy could be identified and no indication of FRP failure was observed.

The behavior of the FRP overlays applied to the inside of Wall B were monitored by strain gages throughout these cycles. Figures F.30 through F.33 show the recorded strains in the vertical FRP overlays versus base shear force for Cycle 30a. Based on Figures F.30 and F.33 (i.e. strains in the vertical overlays on piers PB-7 and PB-10), it is apparent that the FRP overlays were resisting the global rocking behavior of Wall B. That is, the recorded strains in the reinforcement were consistent with overturning moment and showed little evidence of local pier rocking.

In contrast, the strains recorded from the reinforcement applied on the inside of piers PB-8 and PB-9 suggested local pier rocking (see Figures F.31 and F.32). These plots show that the recorded strains were fairly symmetric and showed little dependence on the direction of overturning moment. This observed behavior is consistent with Euler beam bending theory since the interior piers are closer to the neutral axis and thus experience a diminished overturning effect (assuming elastic behavior).

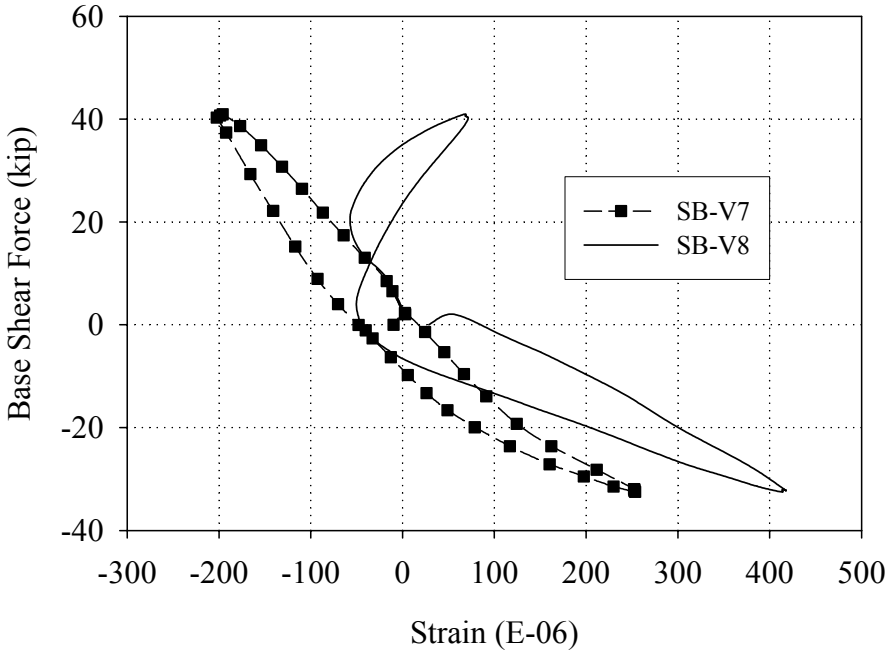

Figure F.30 Strains measured in the vertical FRP overlays applied to the inside of pier PB-7 versus base shear force (Cycle 30a).

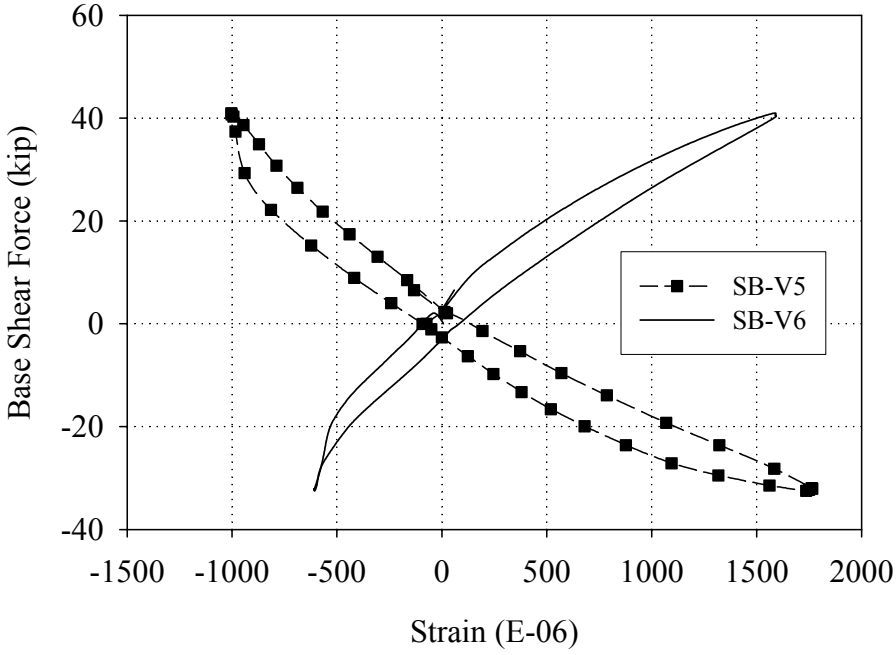

Figure F.31 Strains measured in the vertical FRP overlays applied to the inside of pier PB-8 versus base shear force (Cycle 30a).

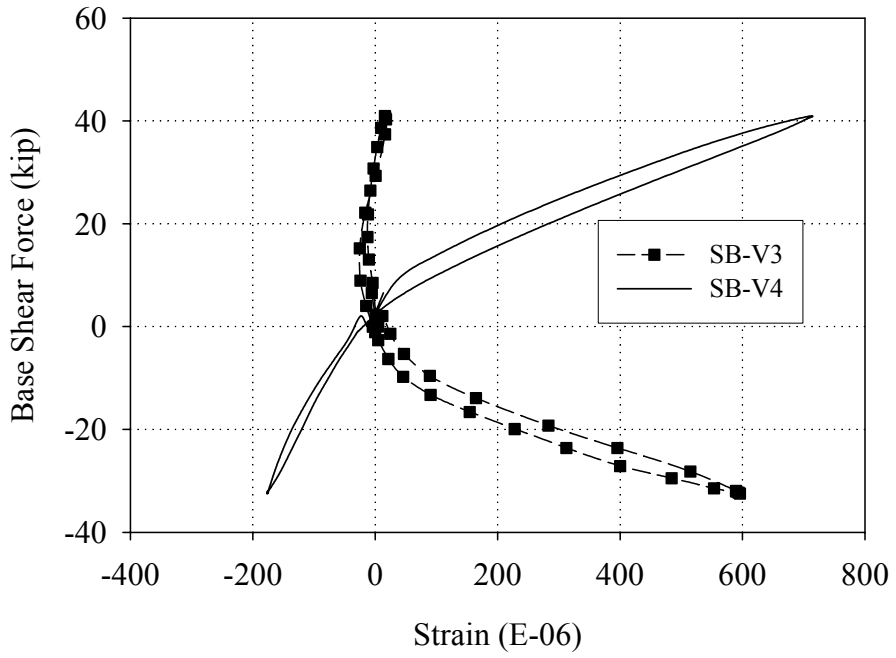

Figure F.32 Strains measured in the vertical FRP overlays applied to the inside of pier PB-9 versus base shear force (Cycle 30a)

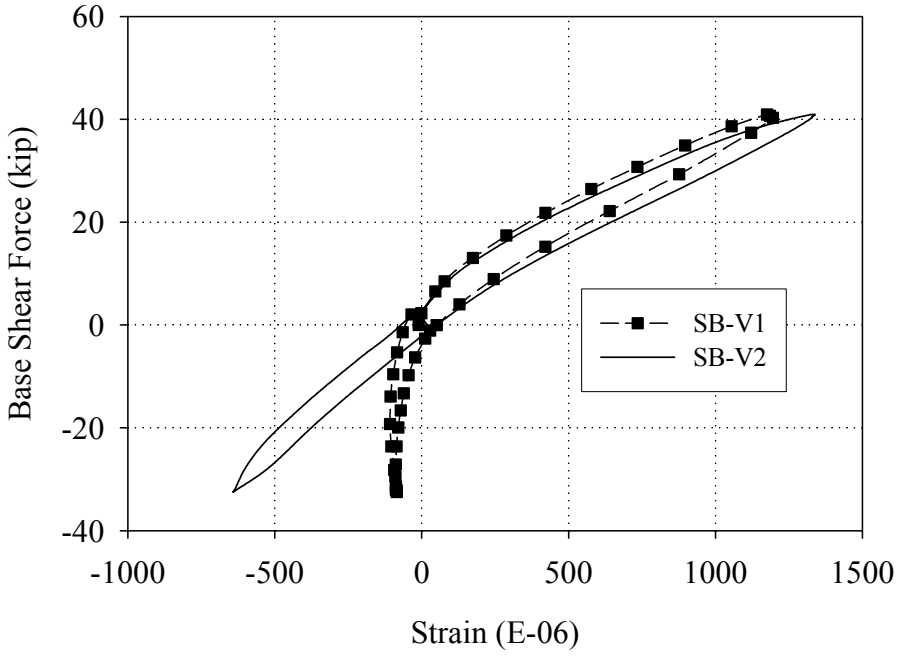

Figure F.33 Strains measured in the vertical FRP overlays applied to the inside of pier PB-10 versus base shear force (Cycle 30a)

F.3.1.3 Local Pier Behavior

Due to the observed crack opening in the first floor piers, the location of the LVDT reference points relative to the active cracks is of paramount importance. As a result, the interpretation of LVDT measurements must utilize Figures F.25 and F.28, which show the location of the LVDTs attached to the piers in reference to the displaced shape. In addition, since all of the piers displayed similar behavior during the Group 1 cycles, the data obtained during Cycle 30a will be used to illustrate the behavior of each pier.

Figures F.34 and F.35 show the readings obtained from the LVDTs attached to pier PB-7; Figure F.36 shows the readings obtained from the LVDTs attached to pier PB-8; Figure F.37 shows the readings obtained from the LVDTs attached to pier PB-9; and Figures F.38 and F.39 show the readings obtained from the LVDTs attached to pier PB-10. In many cases the LVDTs attached to the in-plane piers traversed several cracks (see Figures F.25 and F.28) thus a detailed description of each piers rotation and translation cannot be ascertained. As a result, only a qualitative discussion will be presented.

In general, Figures F.34 and F.39 indicate that the deformation of each pier was nearly entirely recovered upon unloading, which is consistent with the observed rocking deformation. Furthermore, the vertical deformation of the outside piers (i.e. PB-7 and PB-10) showed a strong dependence on overturning moment. In contrast, the measured deformation of the interior piers seemed to be far more symmetrical in nature and consistent with local rocking. This phenomenon was also observed in regards to the strain readings obtained from the external reinforcement and is discussed in the previous section.

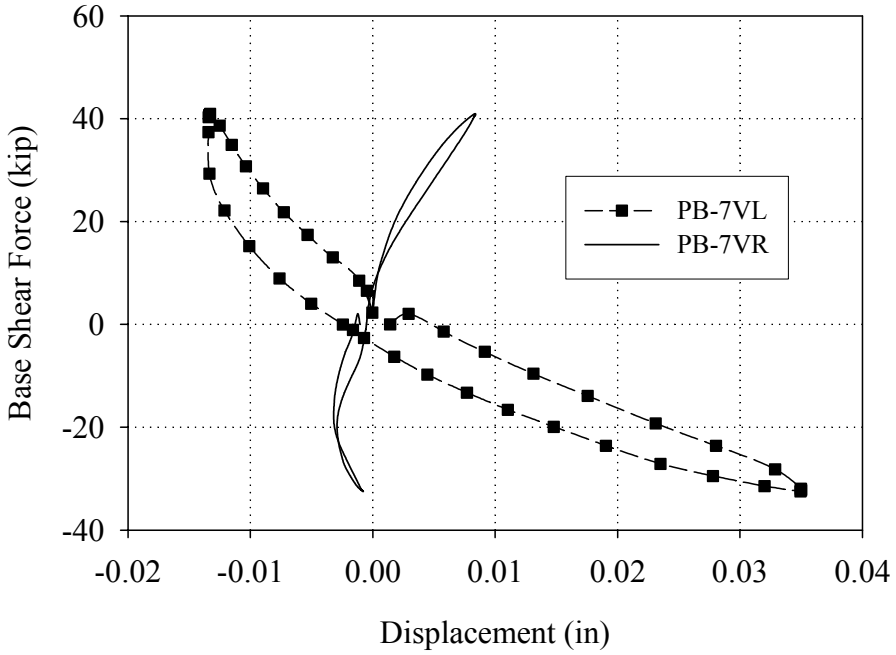

Figure F.34 Readings of the vertical LVDTs attached to pier PB-7 versus base shear force (Cycle 30a)

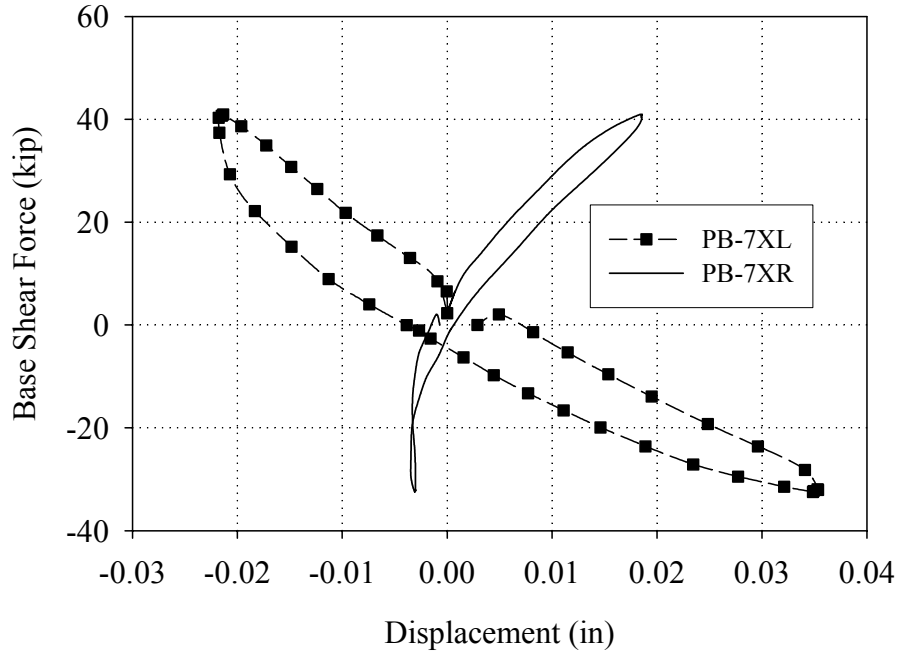

Figure F.35 Readings of the diagonal LVDTs attached to pier PB-7 versus base shear force (Cycle 30a)

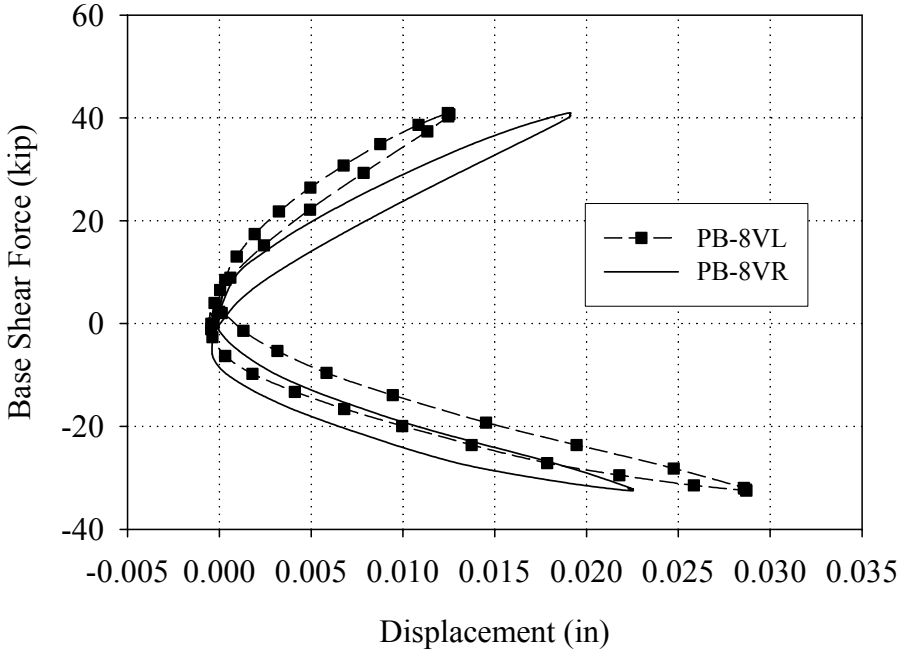

Figure F.36 Readings of the vertical LVDTs attached to pier PB-8 versus base shear force (Cycle 30a)

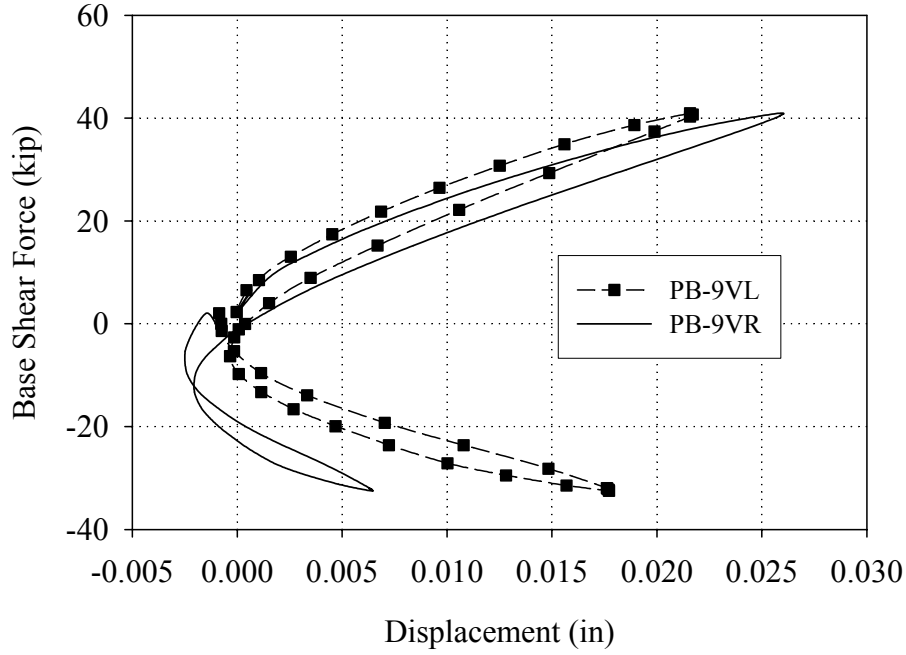

Figure F.37 Readings of the vertical LVDTs attached to pier PB-9 versus base shear force (Cycle 30a)

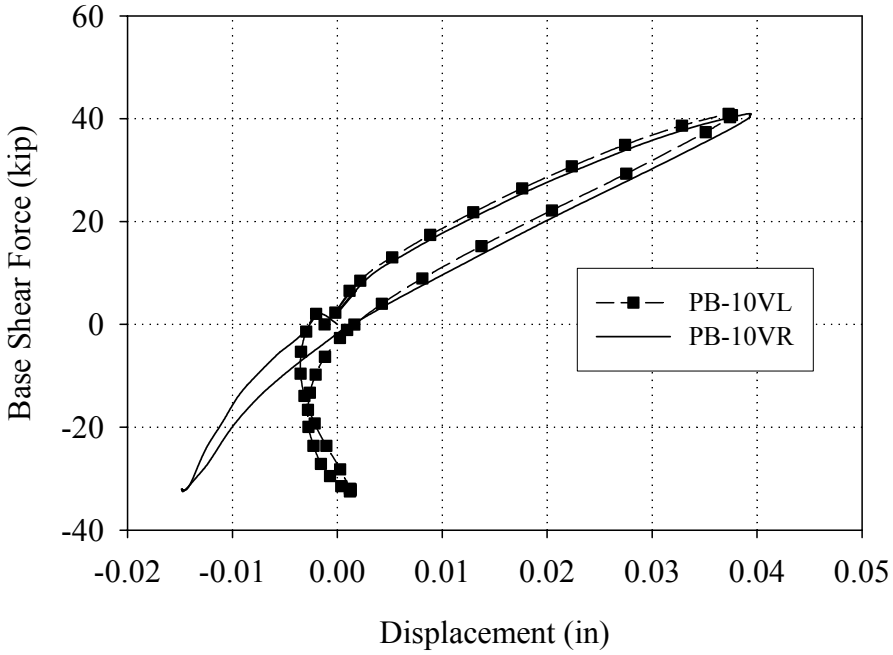

Figure F.38 Readings of the vertical LVDTs attached to pier PB-10 versus base shear force (Cycle 30a)

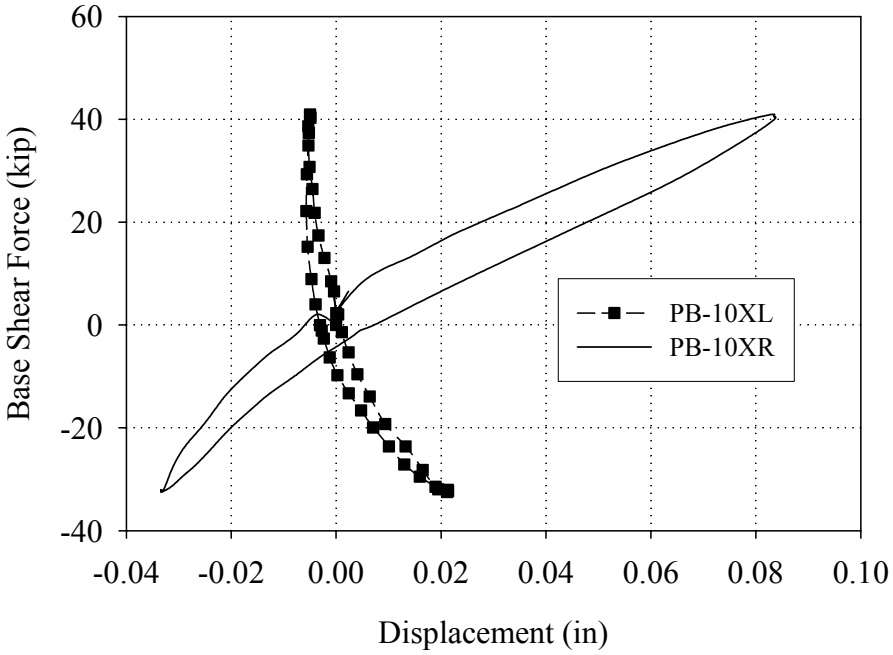

Figure F.39 Readings of the diagonal LVDTs attached to pier PB-10 versus base shear force (Cycle 30a)

F.3.2 Group 2 Cycles (Test Run 31-Test Run 33)

F.3.2.1 Overall Wall Behavior

Figures F.40 through F.42 illustrate the crack pattern in Wall B and out-of-plane Walls 1 and 2 following the Group 2 cycles. In the negative loading direction, the existing diagonal crack in pier PB-10 propagated slightly during Cycle 31b. In addition, several cracks were observed in the second floor. During Cycle 32a in the positive loading direction, cracks were observed at the base of pier PB-5, at the top of pier PB-3 and in out-of-plane Wall 1. During Cycle 33a a crack was observed above pier PB-5 in the positive direction. These cracks are shown in bold in Figures F.40 through F.42.

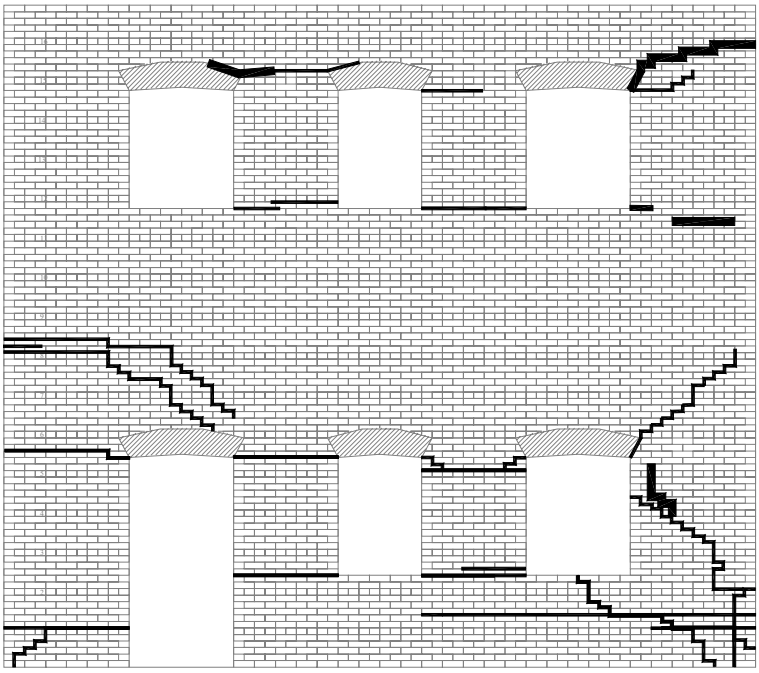

Figure F.40 Crack pattern of Wall B following the Group 2 cycles

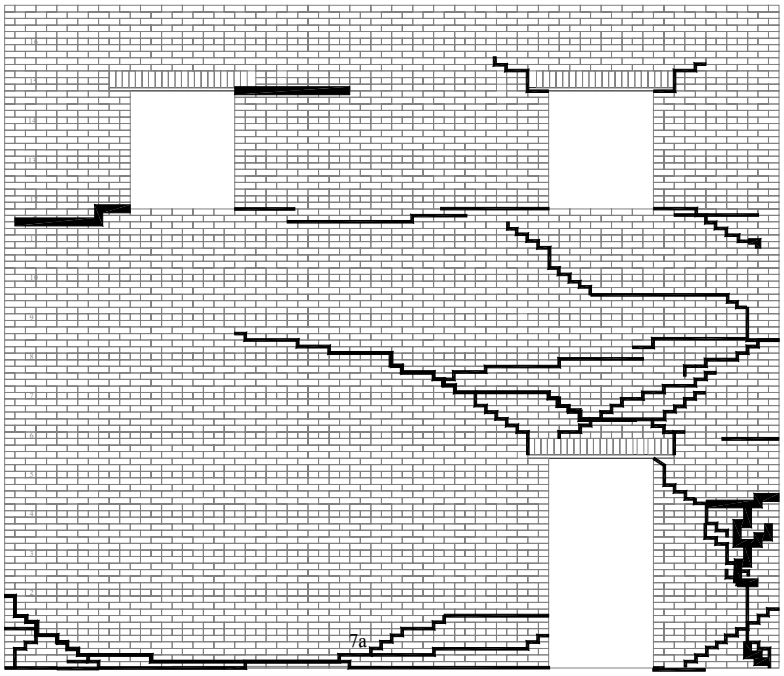

Figure F.41 Crack pattern of out-of-plane Wall 1 following the Group 2 cycles

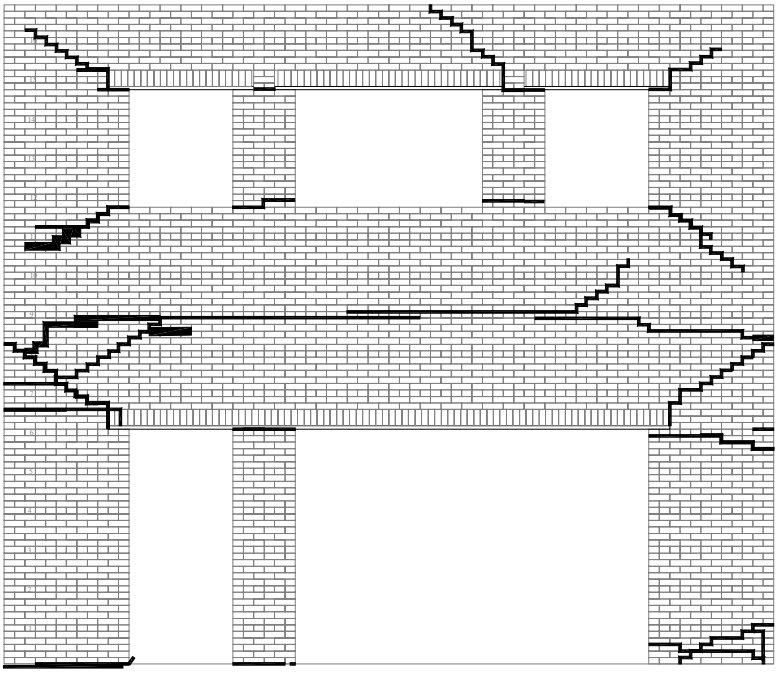

Figure F.42 Crack pattern of out-of-plane Wall 2 following the Group 2 cycles

Figure F.43 shows a schematic illustrating the behavior of Wall B as well as out-of-plane Walls 1 and 2 in the positive direction. Note that the location of the LVDT reference points are also shown in the figure. During the Group 2 cycles the behavior of Wall B in the positive loading direction was very similar to the behavior observed during the Group 1 cycles. In general, the wall behavior can be classified as a combination of global rocking behavior and component behavior. The most notable difference is the observed rigid body rocking of the second floor piers (see Figure F.43). Note that the deformation of the second floor piers in Figure F.43 is exaggerated. The actual deformation of the second floor piers was relatively small compared with the deformation of the first floor piers (see Section F.1 for imposed story displacements). In general, the behavior of the first floor piers can be classified mainly as rocking. The observed and measured rigid motion is also shown in Figure F.43 by arrows.

Figure F.44 shows the vertical displacements measured for each side of Wall B during Cycle 33a versus roof displacement. As mentioned previously, the differential vertical displacement of each side of Wall B suggests that the entire wall was rotating. Based on the assumptions outlined in Section F.3.1, this rotation accounts for approximately 0.18 in or 36% of the roof displacement of Wall B. This represents an increase in global rocking compared with past cycles. Recall that during the Cycle 30a, approximately 13% of the roof displacement was attributed to global rocking.

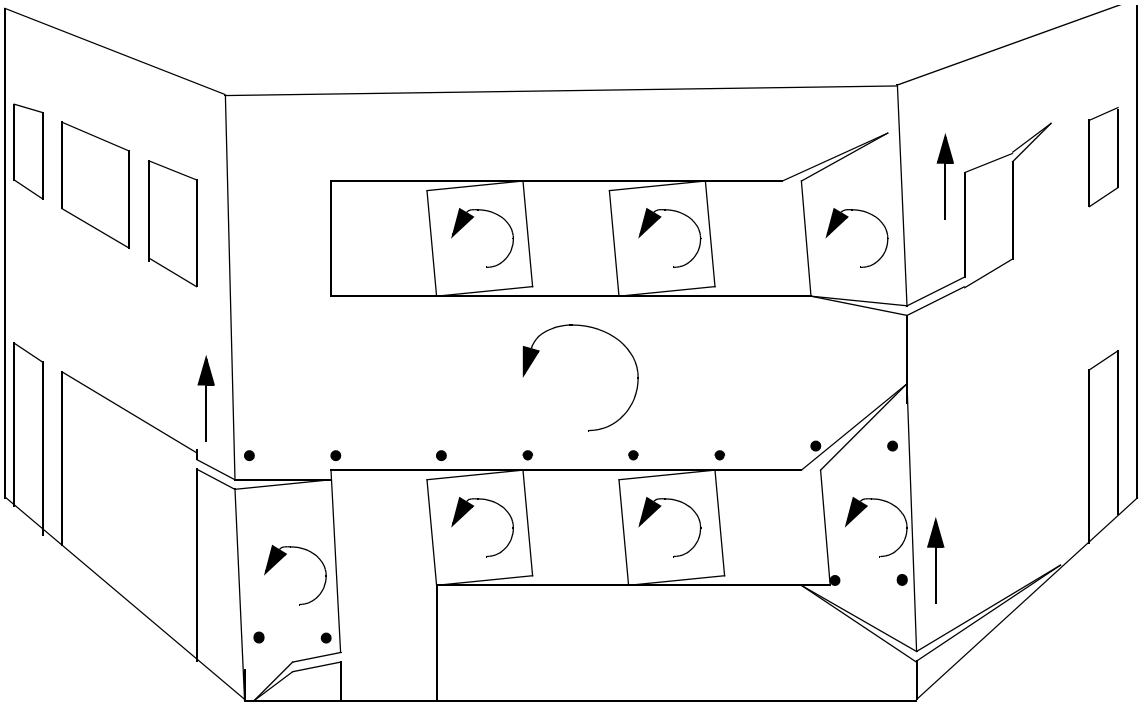

Figure F.43 Exaggerated schematic of the observed behavior of Wall A in the positive loading direction during the Group 2 cycles.

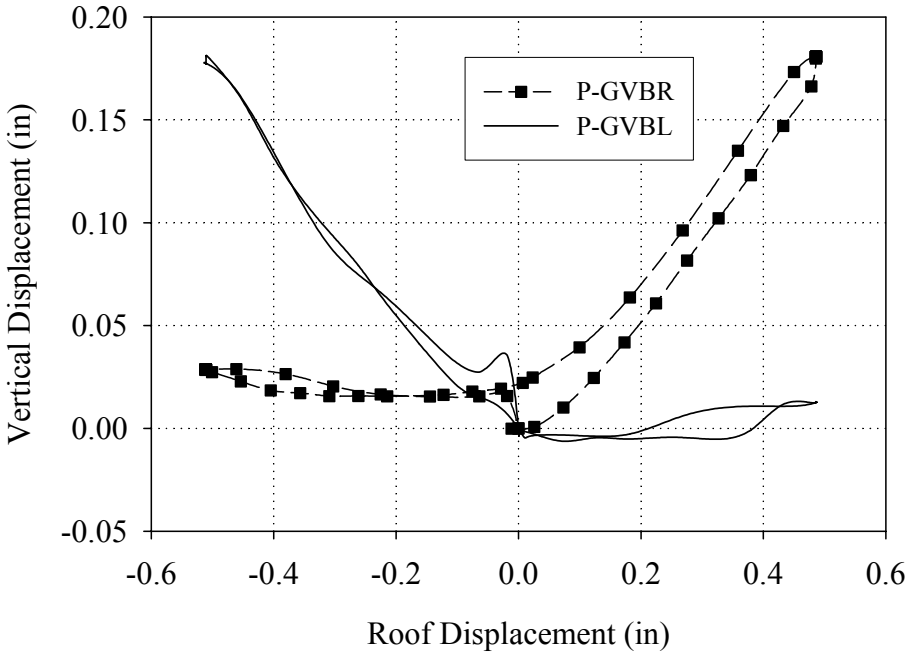

Figure F.44 Vertical displacements of both sides of Wall B versus roof displacement (Cycle 33a)

This observed uplift and rotation of Wall B engaged portions of out-of-plane Walls 1 and 2 (see Figure F.43). Specifically, the rocking of pier PB-7 caused a vertical displacement and lifted up the portion of Wall 2 above pier P2-9. In addition, the rocking of piers PB-5 and PB-10 lifted up portions of piers P1-2 and P1-6, respectively. This contention is also supported by Figure F.45, which shows a plot of the base strains recorded during peak displacement in the positive direction. Clearly, this strain profile indicates that both pier P2-9 and P1-7 were participating in the response. Furthermore, the recorded strain profiles of each of the in-plane piers is consistent with the observed rocking displacement.

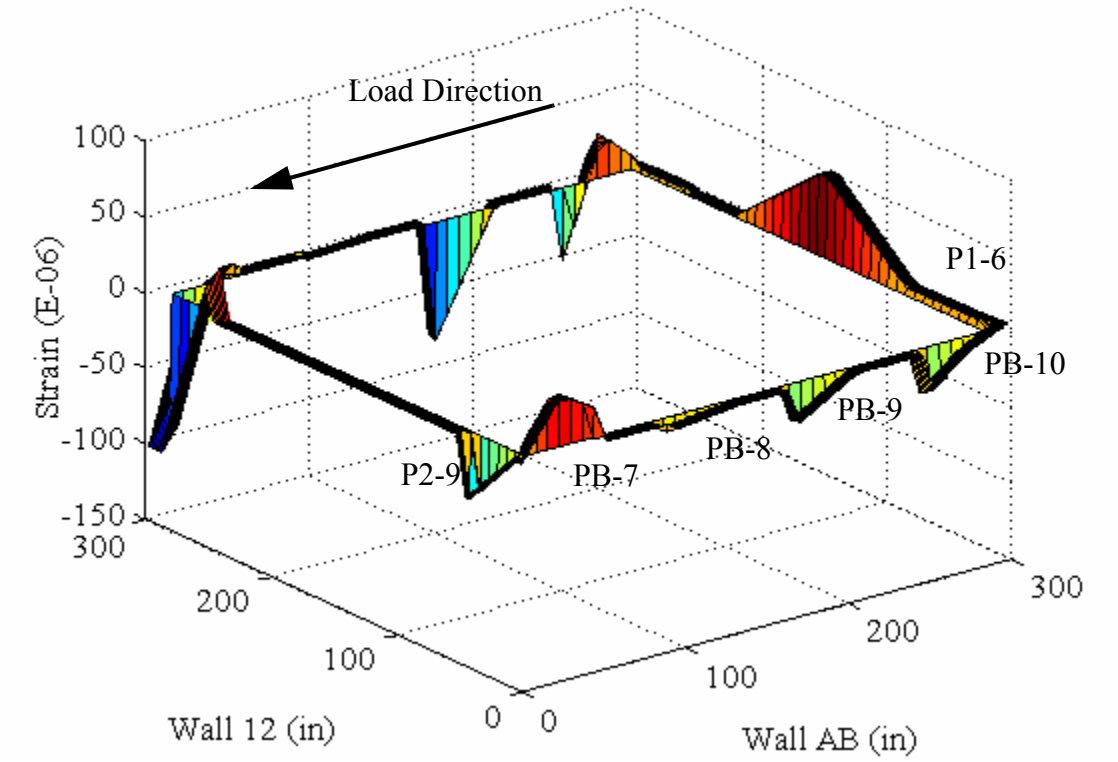

Figure F.45 Base strains recorded at peak positive displacement (Cycle 33a).

Figure F.46 shows a schematic of the behavior of Wall B in the negative direction. As illustrated by this figure, the observed behavior was nearly identical the behavior of Wall B during the Group 1 cycles. Overall, the behavior can be characterized as a combination of local pier behavior and global rocking behavior. However, similar to the behavior in the positive direction, the amount of global rocking displacement increased during this level of testing. Based on Figure F.44, and the assumptions outlined in Section F.3.1, the observed global rocking displacement accounted for approximately 0.15 in or 30% of the roof displacement during Cycle 33a. Recall that during Cycle 30a, the global rocking displacement was estimated to account for approximately 20% of the roof displacement.

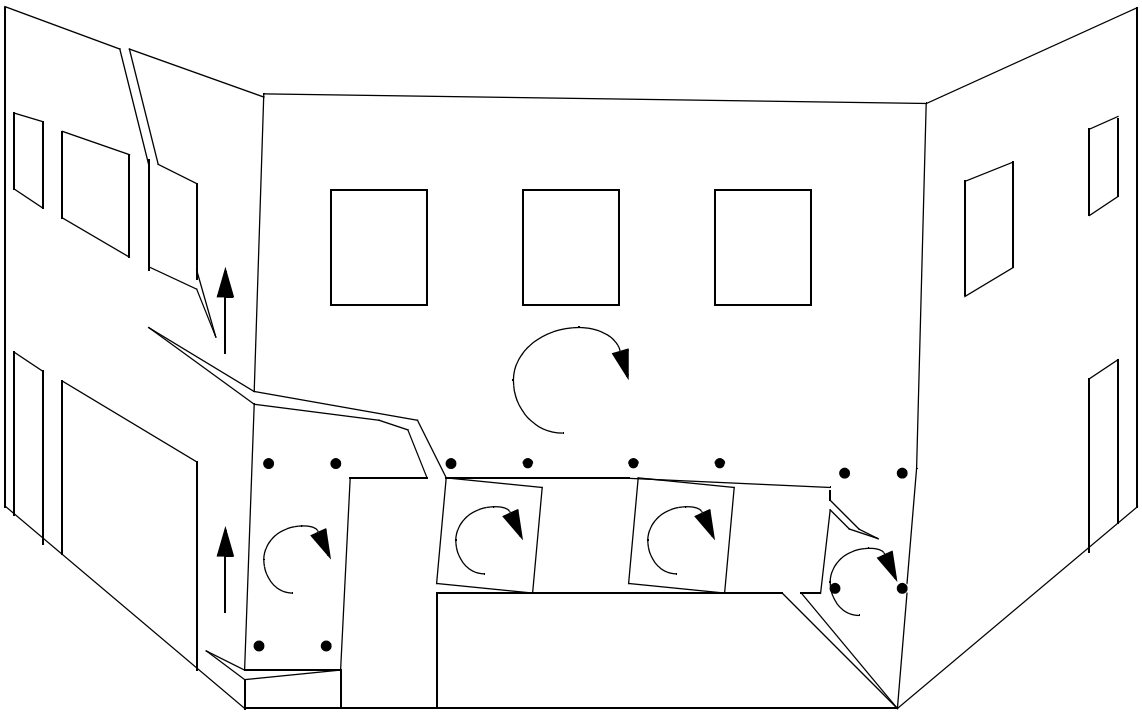

Figure F.46 Exaggerated schematic of the observed behavior of Wall A in the negative loading direction during the Group 2 cycles.

Similar to the behavior in the positive direction, the global rocking shown in Figure F.46 engaged portions of out-of-plane Walls 1 and 2. Based on visual observations the participation of Wall 2 was caused by a combination of global rocking and component behavior. Specifically, the portion of Wall 2 above the second floor level that participated in the response was likely engaged by the global rocking deformation of the entire wall. In contrast, the portion of pier P2-9 that participated in the response was engaged by the local rocking of pier PB-7 (see Figure F.46).

Figure F.47 shows the base strains recorded at peak roof displacement in the negative loading direction. The strain profiles illustrated by this figure support not only the observed rocking deformation of the in-plane piers but also the participation of pier P2-9 in the response. In addition, this plot shows that pier P1-6 was subjected to compression strains. These strains are consistent with both the observed global rocking of Wall B and the local rocking of pier PB-10.

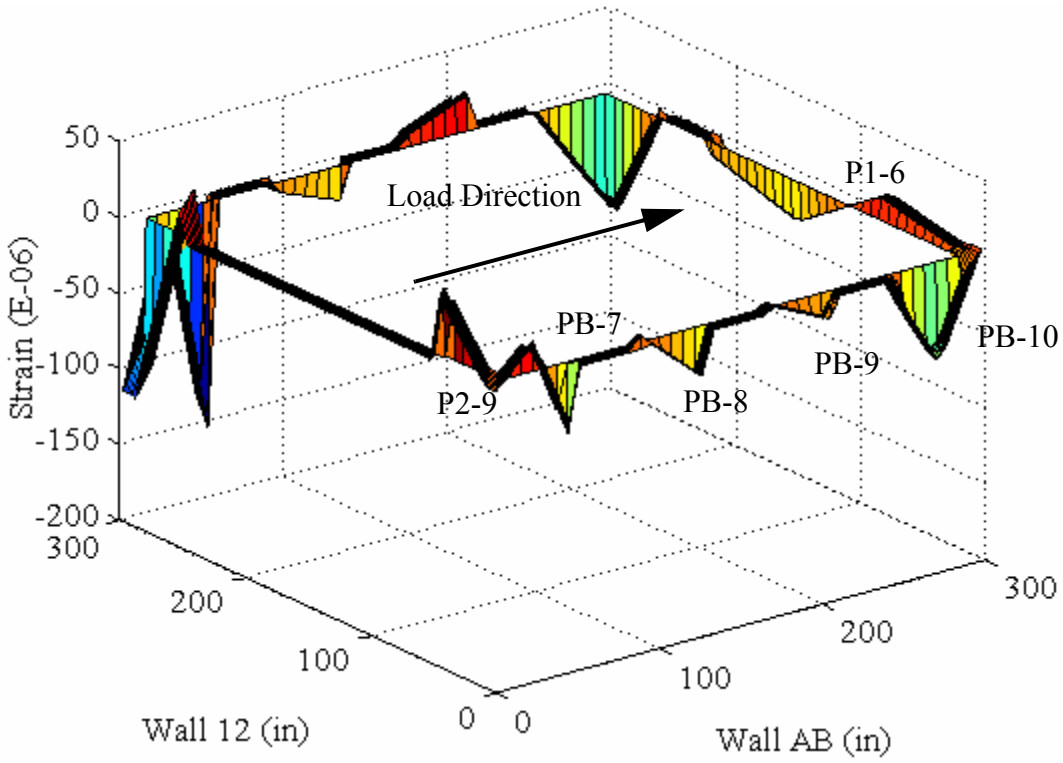

Figure F.47 Base strains recorded at peak negative displacement (Cycle 33a).

F.3.2.2 Behavior of External Reinforcement

During this level of testing, visual damage was observed in both the FRP overlays applied to the inside of the wall and the NSM rods applied to the outside of the wall. In the case of the NSM rods, the damage consisted of hairline cracks in the matrix aligned perpendicular to the axis of the reinforcement (see Figure F.48). This damage was observed along the active diagonal cracks above piers PB-7 and PB-10 (see Figures F.43 and F.46). In many cases, several hairline cracks were visible in the epoxy suggesting that the NSM rods had debonded from the adjacent masonry (see Figure F.48). The distance between the observed cracks in the epoxy was approximately 1 in in nearly all cases.

Figure F.48 Photograph illustrating the observed damage in the NSM rods following Test Run 33.

Similarly, the observed damage in the FRP overlay system can also be characterized as a debonding of the reinforcement. Figure F.49 shows a photograph of a debonded region following Test Run 33. Based on visual observations, this debonding failure can be classified as a cohesive failure of the masonry substrate. This failure was likely caused by local strain concentrations in the reinforcement directly adjacent to the active cracks illustrated by Figures F.43 and F.46. These strain concentrations resulted in large tensile stresses in the overlays, which in turn caused large shear stresses in the adjacent masonry substrate. As the displacement of the wall was increased, these shear stresses exceeded the surface shear strength of the masonry and resulted in the failure illustrated by Figure F.49.

Figure F.49 Photograph illustrating the observed damage in the FRP overlays following Test Run 33

In addition, the extent of the debonding was further identifying by tapping on the external reinforcement with a small wrench. In areas of damage, the resulting sound was hollow indicating that the reinforcement was detached from the substrate. Figure F.50 shows a schematic illustrating the locations of debonded regions following the Group 2 cycles. In all cases the damage was located adjacent to existing cracks (see Figures F.40 and F.50).

The damage observed in both reinforcement systems (i.e. NSM rods and FRP overlays) resulted in larger effective lengths, thus lowering the apparent stiffness of the adjacent reinforcement. This decrease in the apparent stiffness of the reinforcement

resulted in the highly nonlinear force-displacement response of the first story shown in Figure F.8. While this damage certainly altered the effectiveness of the reinforcement, the load carrying capacity of both the NSM rods and the FRP overlays was preserved throughout loading.

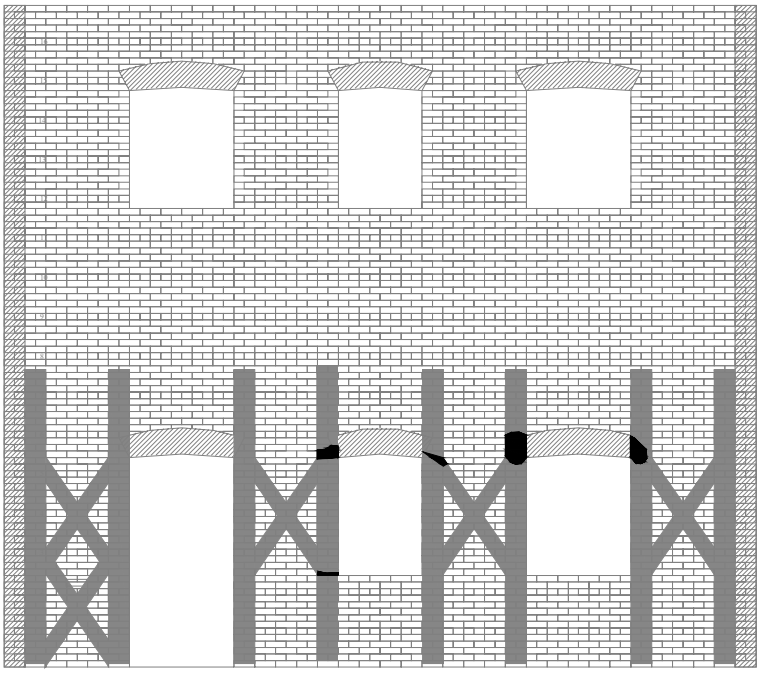

Figure F.50 Schematic showing the areas of debonding observed through Test Run 33.

The behavior of the FRP overlays applied to the inside of Wall B were monitored by strain gages throughout these cycles. Figures F.51 through F.54 show the recorded strains in the vertical FRP overlays during Cycle 33a versus base shear force. Based on these figures, it is apparent that the measured behavior of the FRP overlays during the Group 2 cycles were very similar to the behavior of the FRP overlays recorded Group 1. The reader is directed to Section F.3.1.2 for further explanation.

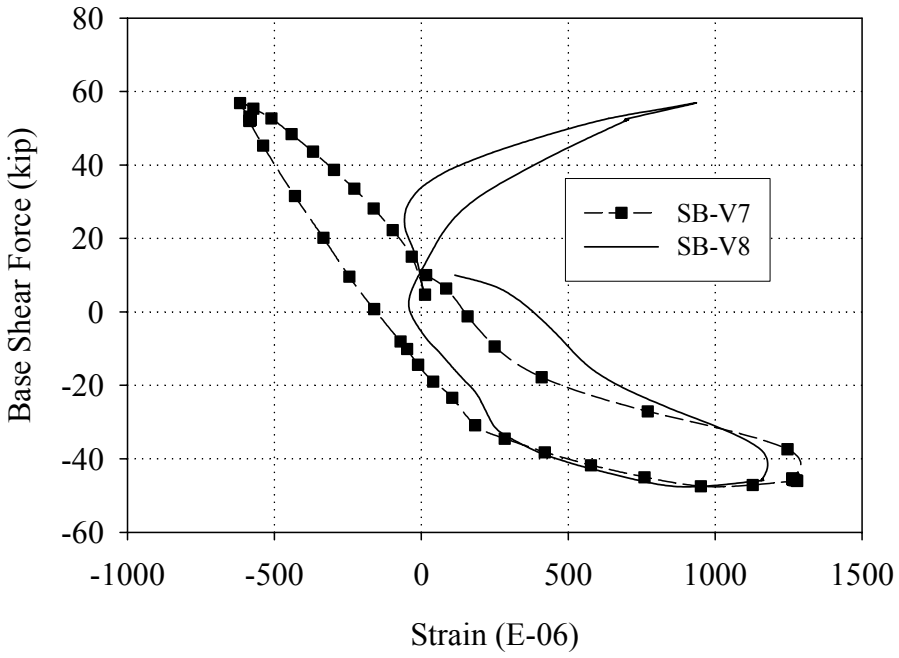

Figure F.51 Strains measured in the vertical FRP overlays applied to the inside of pier PB-7 versus base shear force (Cycle 33a).

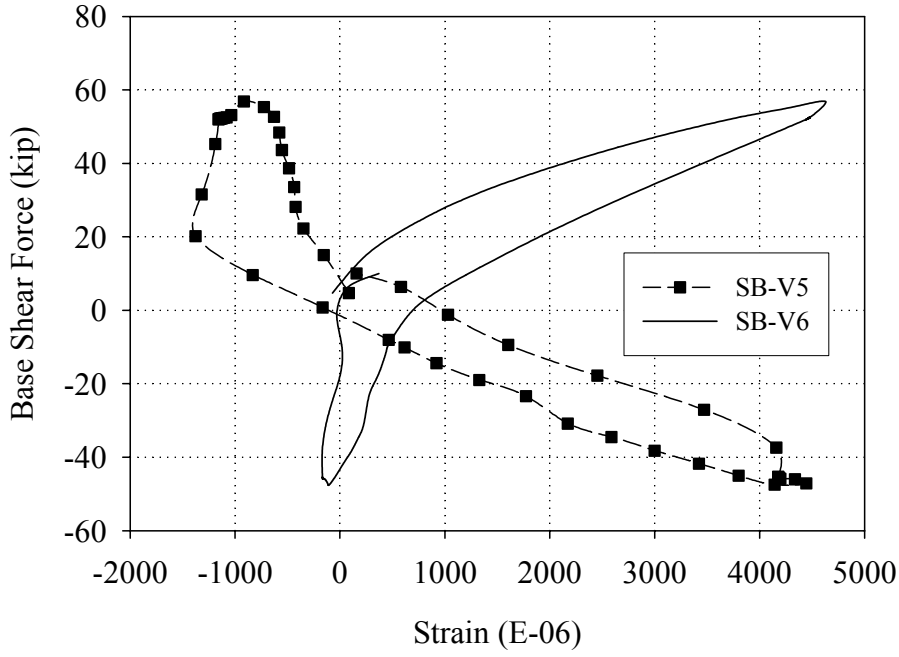

Figure F.52 Strains measured in the vertical FRP overlays applied to the inside of pier PB-8 versus base shear force (Cycle 33a).

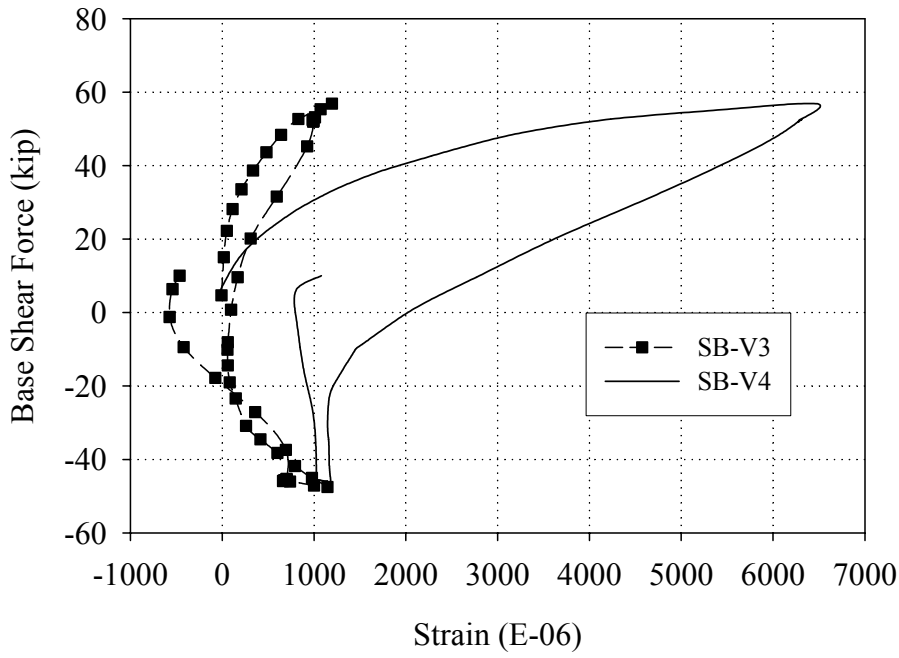

Figure F.53 Strains measured in the vertical FRP overlays applied to the inside of pier PB-9 (Cycle 33a)

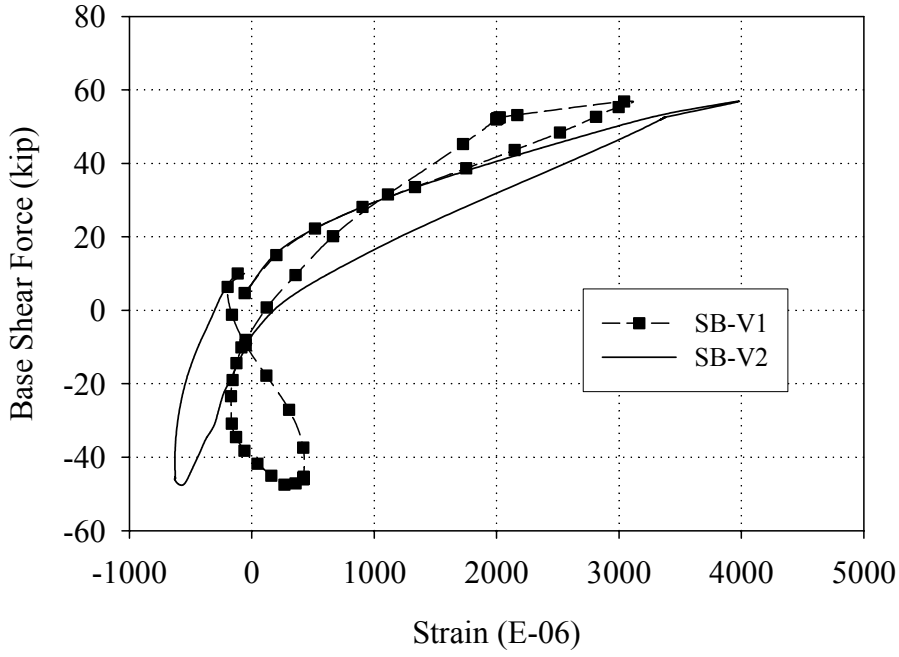

Figure F.54 Strains measured in the vertical FRP overlays applied to the inside of pier PB-10 (Cycle 33a)

F.3.2.3 Local Pier Behavior

Due to the observed crack opening in the first floor piers, the location of the LVDT reference points relative to the active cracks is of paramount importance. As a result, the descriptions of pier behavior given in the following sections utilize Figures F.43 and F.46, which show the location of the LVDTs attached to the piers in reference to the displaced shape. In addition, since all of the piers displayed similar behavior during the Group 2 cycles, the data obtained during Cycle 33a will be used to illustrate the behavior of each pier.

Figures F.55 and F.56 show the readings obtained from the LVDTs attached to pier PB-7; Figure F.57 shows the readings obtained from the LVDTs attached to pier PB-8; Figure F.58 shows the readings obtained from the LVDTs attached to pier PB-9; and Figures F.59 and F.60 show the readings obtained from the LVDTs attached to pier PB-10. In general, Figures F.55 through F.60 are consistent with the observed behavior described in the previous sections as well as the recorded response during the Group 1 cycles. The reader is directed to Section F.3.1.3 for further discussion.

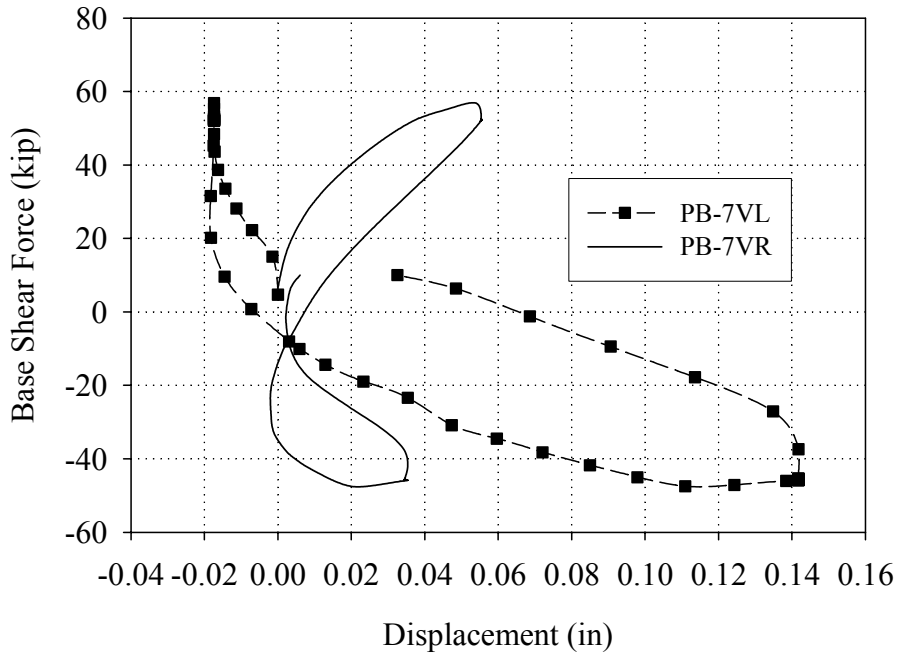

Figure F.55 Readings of the vertical LVDTs attached to pier PB-7 versus base shear force (Cycle 33a)

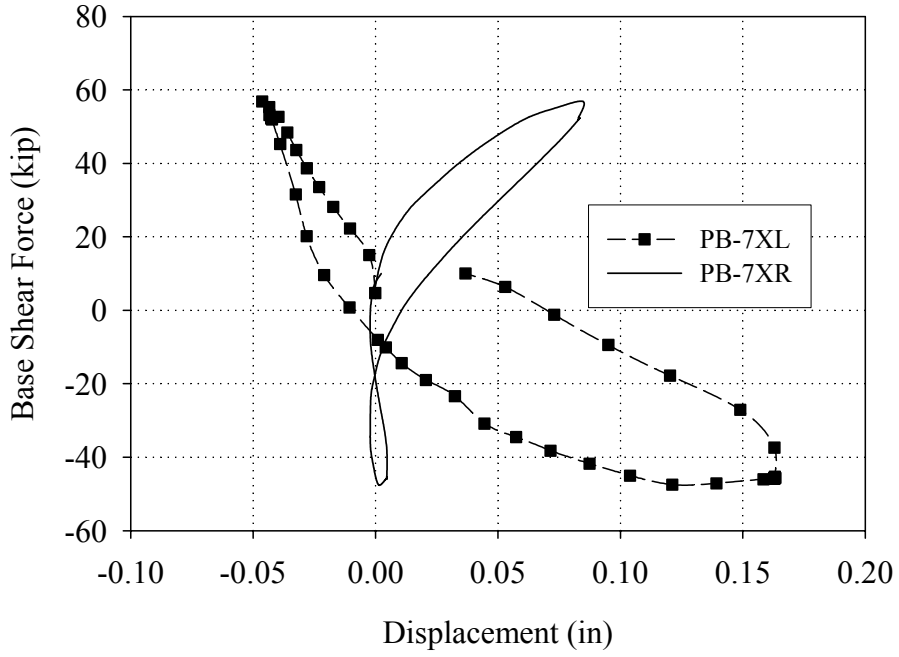

Figure F.56 Readings of the diagonal LVDTs attached to pier PB-7 versus base shear force (Cycle 33a)

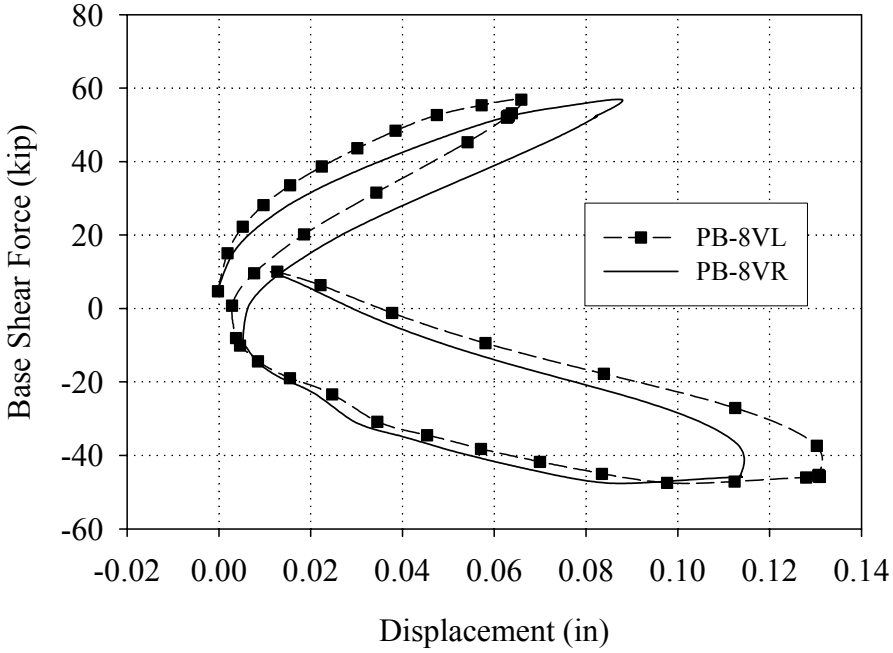

Figure F.57 Readings of the vertical LVDTs attached to pier PB-8 versus base shear force (Cycle 33a)

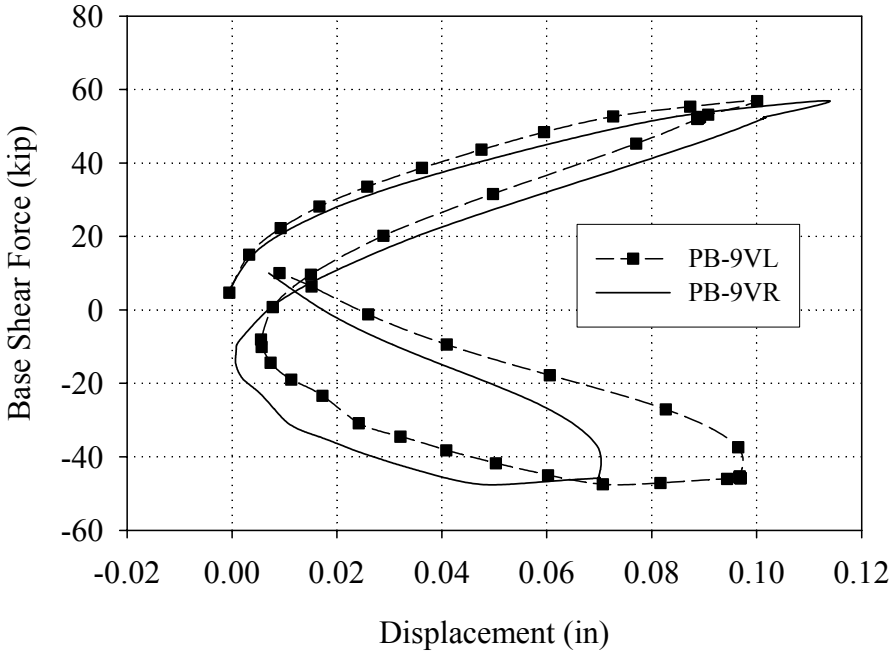

Figure F.58 Readings of the vertical LVDTs attached to pier PB-9 versus base shear force (Cycle 33a)

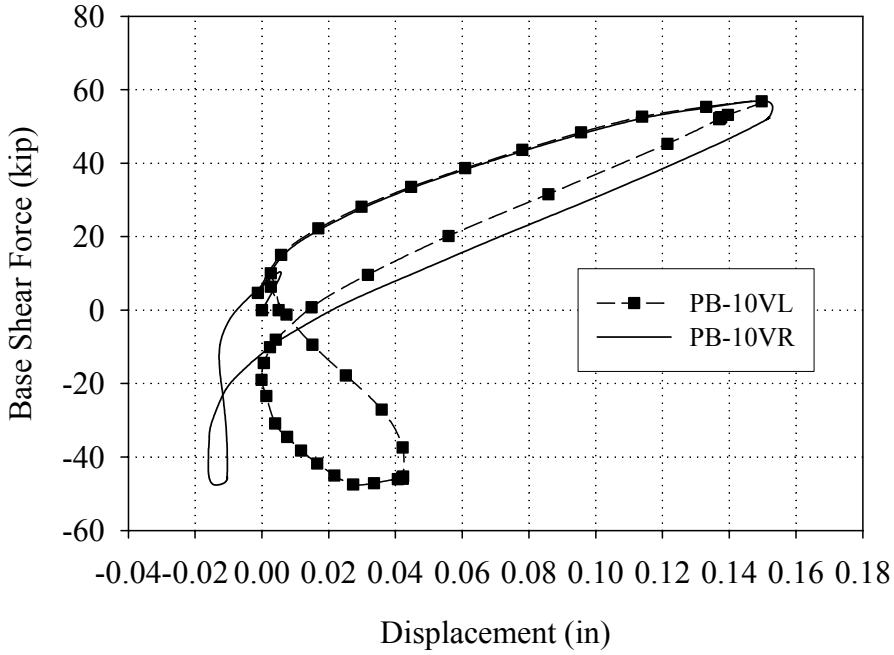

Figure F.59 Readings of the vertical LVDTs attached to pier PB-10 versus base shear force (Cycle 33a)

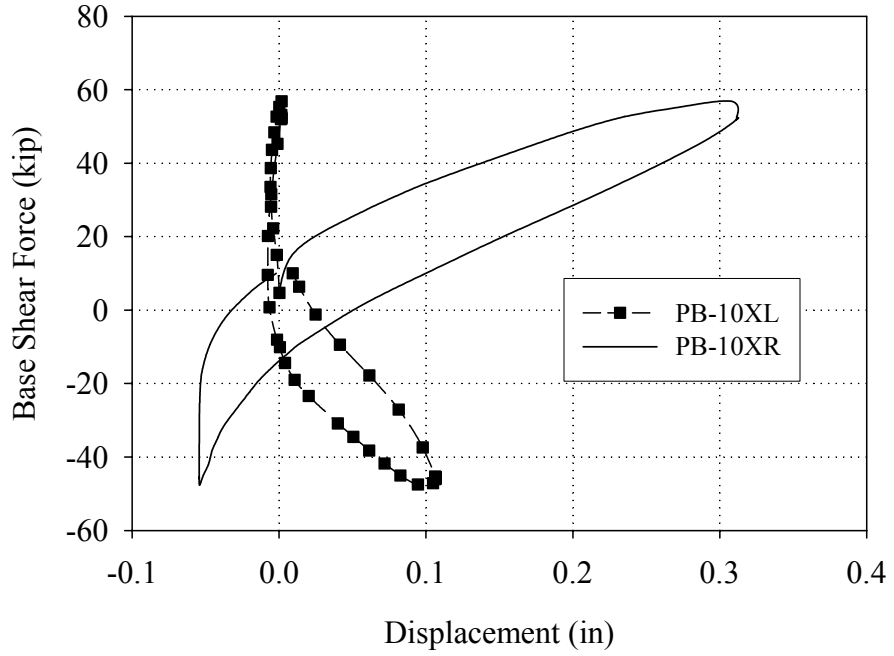

Figure F.60 Readings of the diagonal LVDTs attached to pier PB-10 versus base shear force (Cycle 33a)

F.3.3 Group 3 Cycles (Test Run 34-Test Run 35)

During the Group 3 cycles no new cracks were observed in Wall B or out-of-plane Walls 1 and 2. In general, the observed wall behavior during these cycles was nearly identical to the behavior observed during the Group 1 cycles as described in Section F.3.1. That is, the overall behavior was a combination of global rocking and local pier rocking.

The most notable difference in wall response was most clearly seen by the force-displacement behavior. Figure F.61 shows the force-displacement response of the first story recorded during Test Runs 27 through 30 and 33 through 35. From this plots it is apparent that the overall stiffness of the wall during the Group 3 cycles was lower than observed during the Group 1 cycles. This is attributed to the debonding of the FRP overlays and NSM rods described in Section F.3.2.2 (which lower the effective stiffness of the reinforcement) as well as additional damage induced in the masonry walls. In addition, Figure F.61 also shows that the observed stiffness during these cycles was nearly identical to the stiffness measured during Cycle 33b (recall that the majority of the debonding occurred during Cycle 33a).

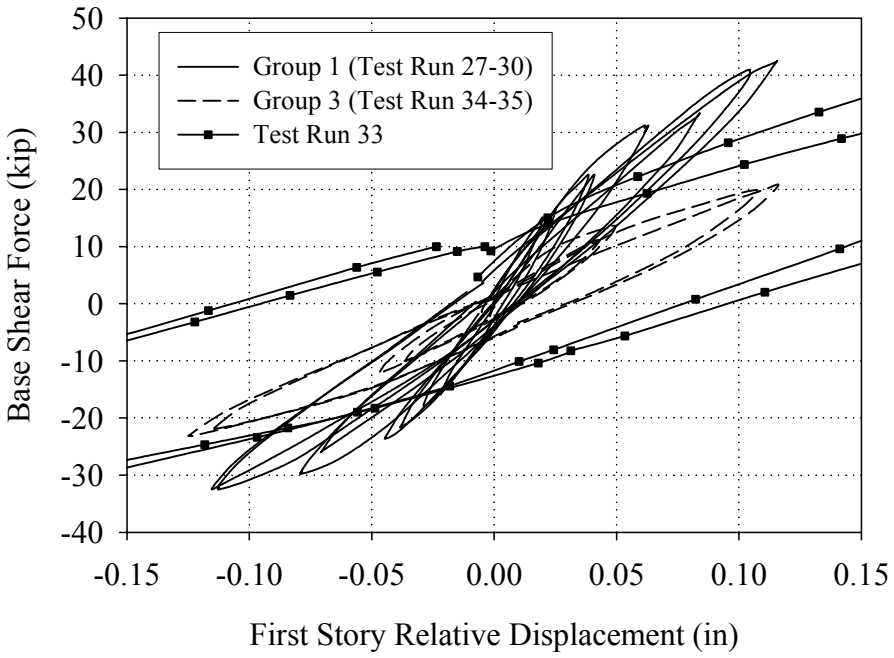

Figure F.61 Force-displacement response of the first floor recorded during Test Runs 27 through 30 and 33 through 35.

The contention that the effective softening of the reinforcement due to debonding caused the lower stiffness displayed during the Group 3 cycles is also supported by strain measurements obtained from the external reinforcement. Figures F.62, through F.65 show the recorded strains in the vertical FRP overlays versus base shear force for Cycle 35a. Comparing these plots with those shown in Figures F.30 through F.33 (Cycle 30a) it is apparent that, while the behavior of the reinforcement was similar during both cycles, the recorded strains were smaller during Cycle 35a. Recall that the imposed displacements during these cycles were identical. As a result, the decrease in measured stains is consistent with the progressive debonding observed during the Group 2 cycles and supports the contention of this debonding resulting in a lower wall stiffness. That is, for the same displacement level, the reinforcement was subjected to lower strains thus

resulting in lower resistance to deformation.

Due to the similarity in wall behavior observed during the Group 1 and Group 3 cycles, and for the sake of brevity, the reader is directed to Section F.3.1 for a more complete description of behavior.

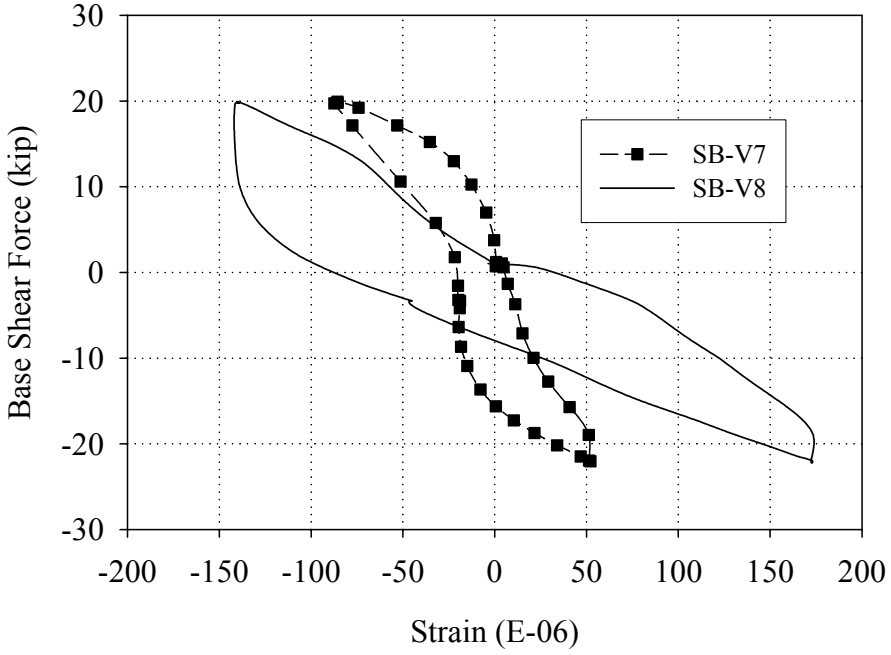

Figure F.62 Strains measured in the vertical FRP overlays applied to the inside of pier PB-7 versus base shear force (Cycle 35a).

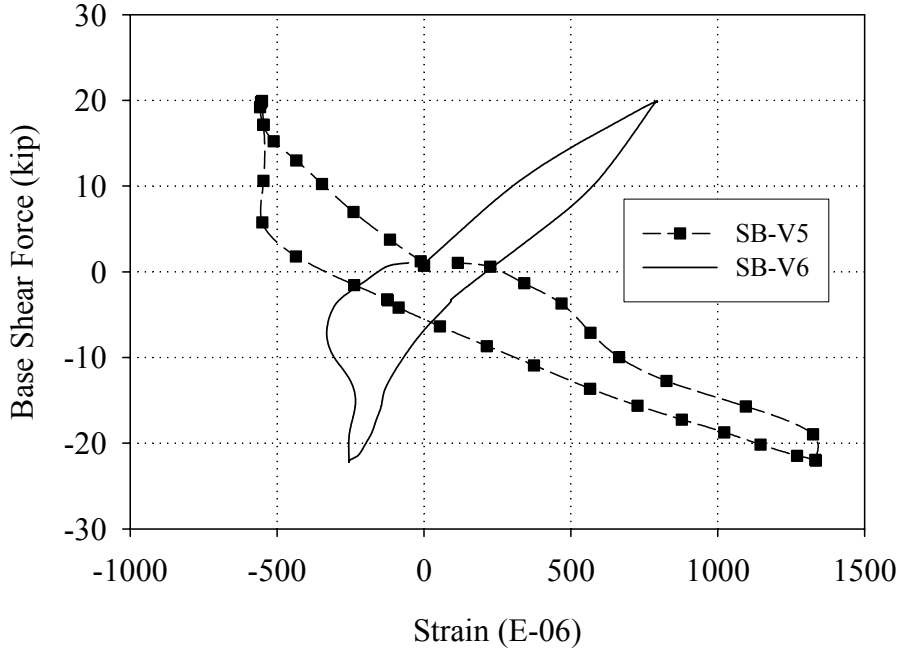

Figure F.63 Strains measured in the vertical FRP overlays applied to the inside of pier PB-8 versus base shear force (Cycle 35a).

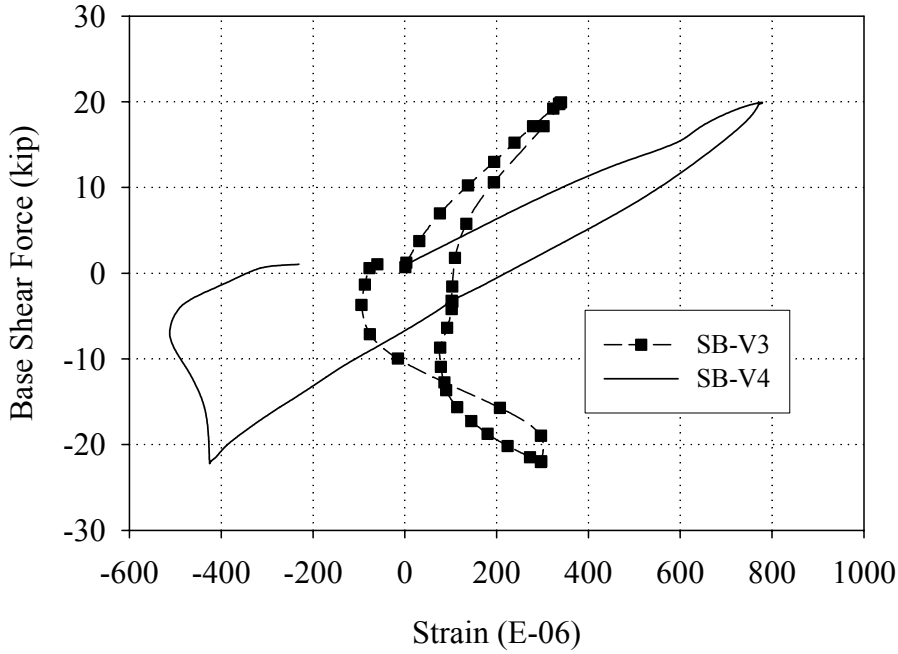

Figure F.64 Strains measured in the vertical FRP overlays applied to the inside of pier PB-9 (Cycle 35a)

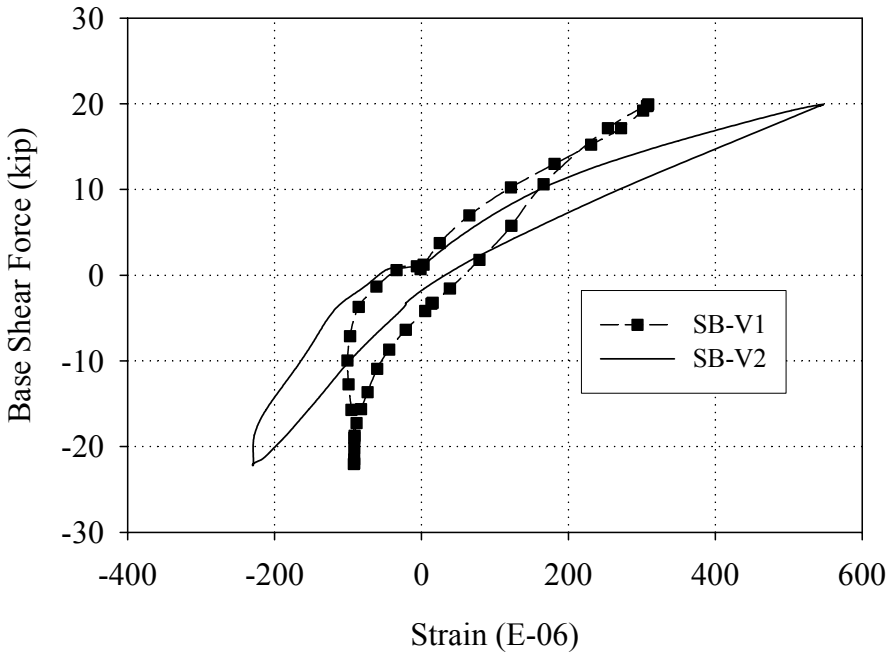

Figure F.65 Strains measured in the vertical FRP overlays applied to the inside of pier PB-10 (Cycle 35a)

F.3.4 Group 4 Cycles (Test Run 36-Test Run 39)

F.3.4.1 Overall Wall Behavior

Figures F.66 through F.68 illustrate the crack pattern in Wall B and out-of-plane Walls 1 and 2 following the Group 4 cycles. In the positive loading direction, the existing diagonal crack in pier PB-10 propagated into out-of-plane Wall 1 diagonally upwards approximately 5 ft. In addition, a diagonal crack in the spandrel above the door opening formed. In the negative direction, a horizontal crack was observed at the base of pier P2-9. All of these cracks are shown in bold in Figures F.66 through F.68.

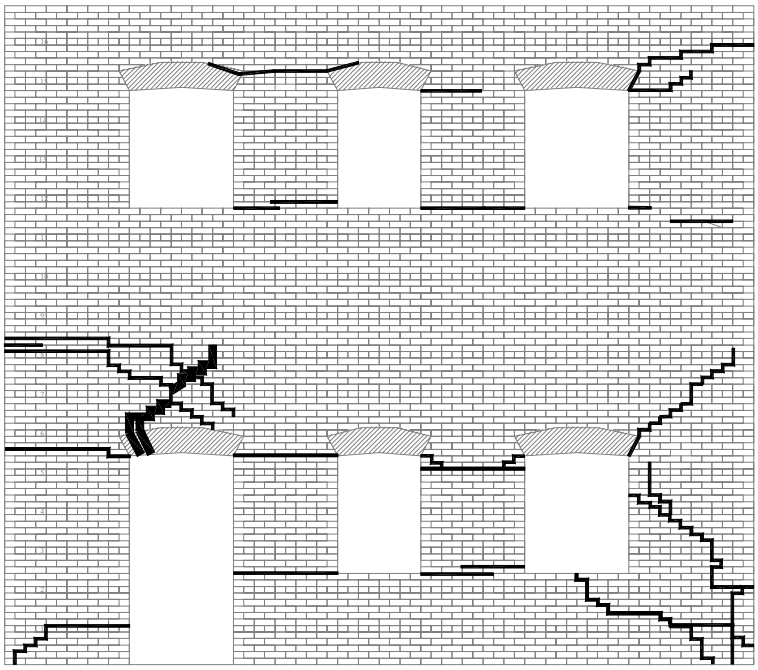

Figure F.66 Crack pattern of Wall B following the Group 4 cycles

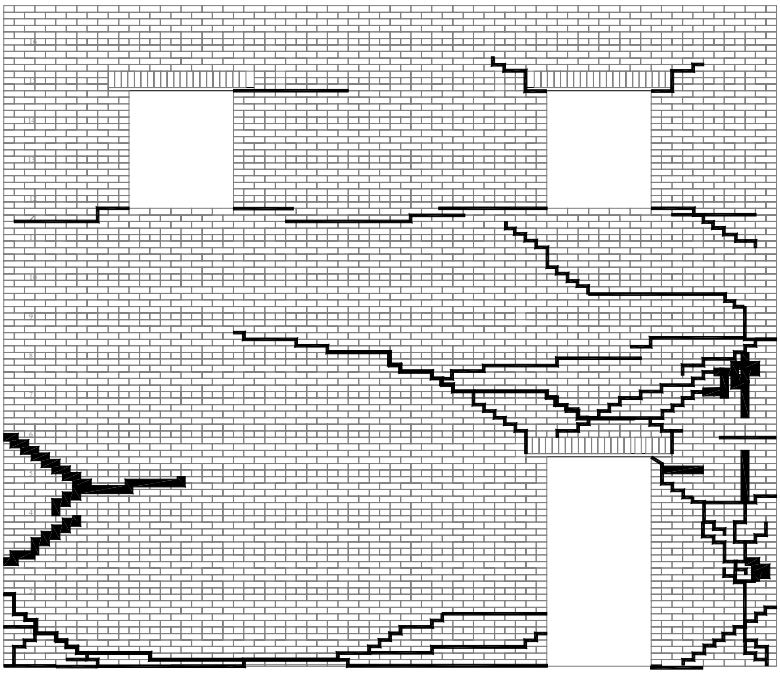

Figure F.67 Crack pattern of out-of-plane Wall 1 following the Group 4 cycles

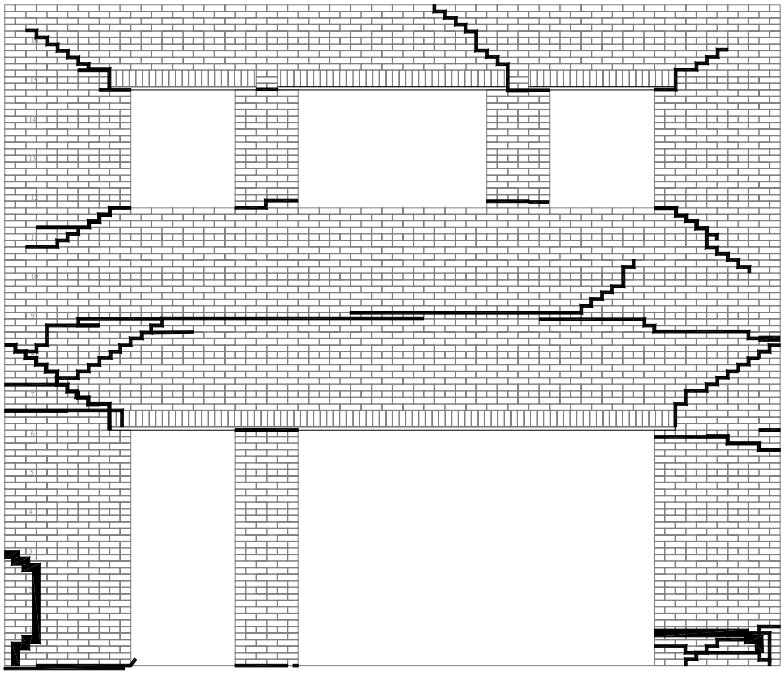

Figure F.68 Crack pattern of out-of-plane Wall 2 following the Group 4 cycles

Figure F.69 shows a schematic illustrating the behavior of Wall B as well as out-of-plane Walls 1 and 2 in the positive direction. Note that the location of the LVDT reference points are also shown in the figure. During the Group 4 cycles the behavior of Wall B in the positive loading direction was very similar to the behavior observed during past cycles. That is, the wall displayed a combination of global rocking and component rocking behavior. The observed and measured rigid body motion is shown in Figure F.69 by arrows.

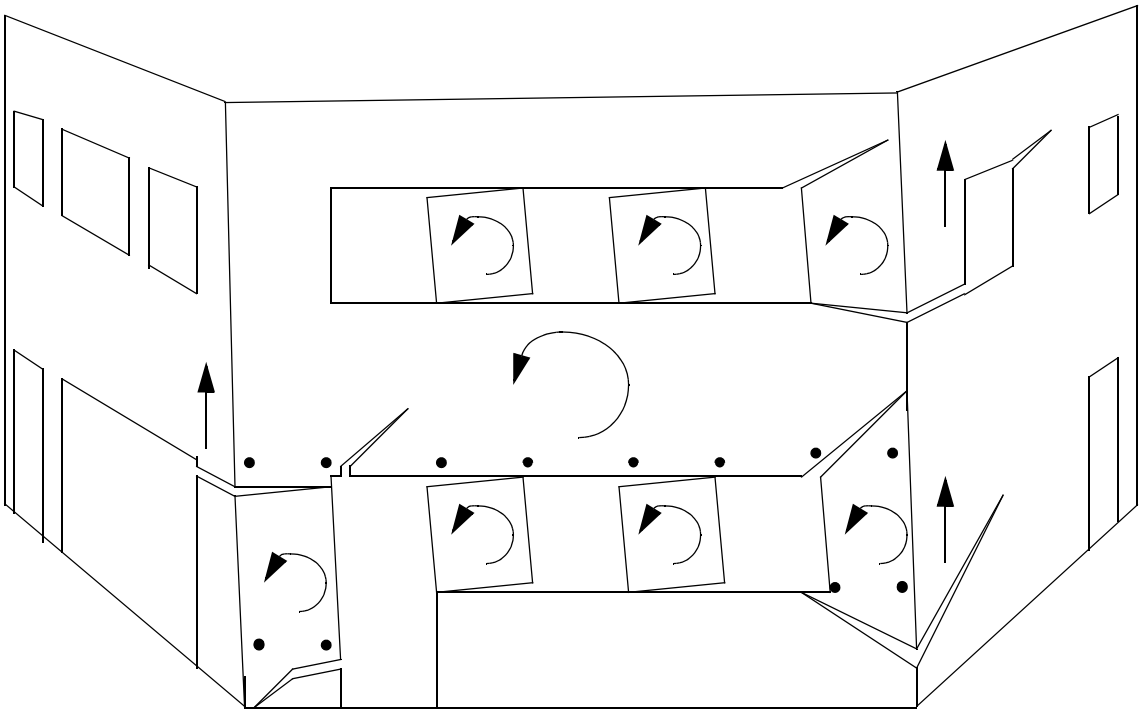

Figure F.69 Exaggerated schematic of the observed behavior of Wall A in the positive loading direction during the Group 4 cycles.

Figure F.70 shows the vertical displacements measured for each side of Wall B during Cycle 39a versus roof displacement. Based on the assumptions outlined in Section F.3.1, the rotation implied by this figure accounts for approximately 0.2 in or 26% of the roof displacement in the positive direction. This implies a slight decrease in global rocking displacement. Recall that during Cycle 33a approximately 36% of the imposed roof displacement was attributed to global rocking deformation.

Similar to past cycles, the observed uplift and rotation of Wall B engaged portions of out-of-plane Walls 1 and 2 (see Figure F.69). The most notable change in response was the diagonal crack that formed in pier P1-6 during loading in the positive direction. Prior to the formation of this crack, the in-plane deformation of Wall B lifted up a portion of pier P1-6 above the crack at the base of the wall. The remaining out-of-plane wall

participation was consistent with past cycles.

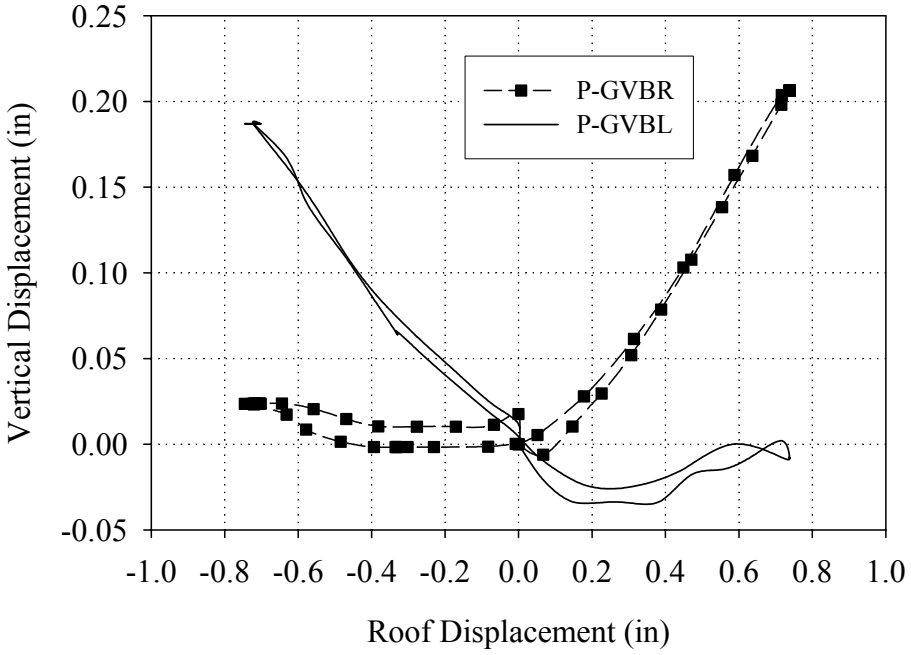

Figure F.70 Vertical displacements of both sides of Wall B versus roof displacement (Cycle 39a)

Figure F.71 shows the base strains recorded at peak positive displacement during Cycle 39a. Unlike past cycles, some of the strain profiles of the in-plane piers do not support the observed rocking behavior (namely pier PB-8). This is attributed to the large amount of damage induced directly adjacent to the gage and underscores the caution that must be exercised when interpreting the results. In general, these reading do support the contention of flange participation, in fact this plot indicates that the flanges were subjected to larger strains than the in-plane piers during loading. This observation also supports the presence of global overturning effects.

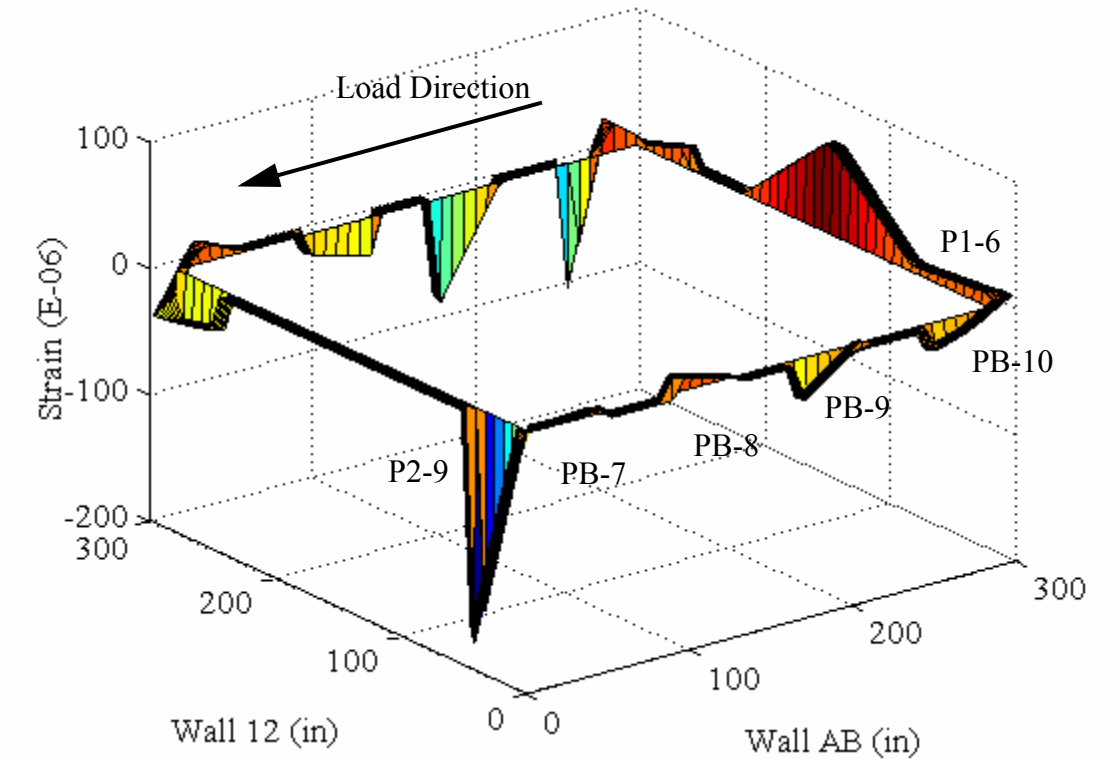

Figure F.71 Base strains recorded at peak positive displacement (Cycle 39a)

Figure F.72 shows a schematic of the behavior of Wall B in the negative direction. As apparent from the figure, the observed behavior was nearly identical to past cycles. Again the reader is directed to Section F.3.2 for a more complete description of the observed behavior. Based on Figure F.70, and the assumptions outlined in Section F.3.1, the observed global rocking displacement accounted for approximately 0.16 in or 21% of the roof displacement during Cycle 39a. Considering that during Cycle 33a the global rocking displacement accounted for approximately 30% of the roof displacement, this implies a decrease in global rocking deformation.

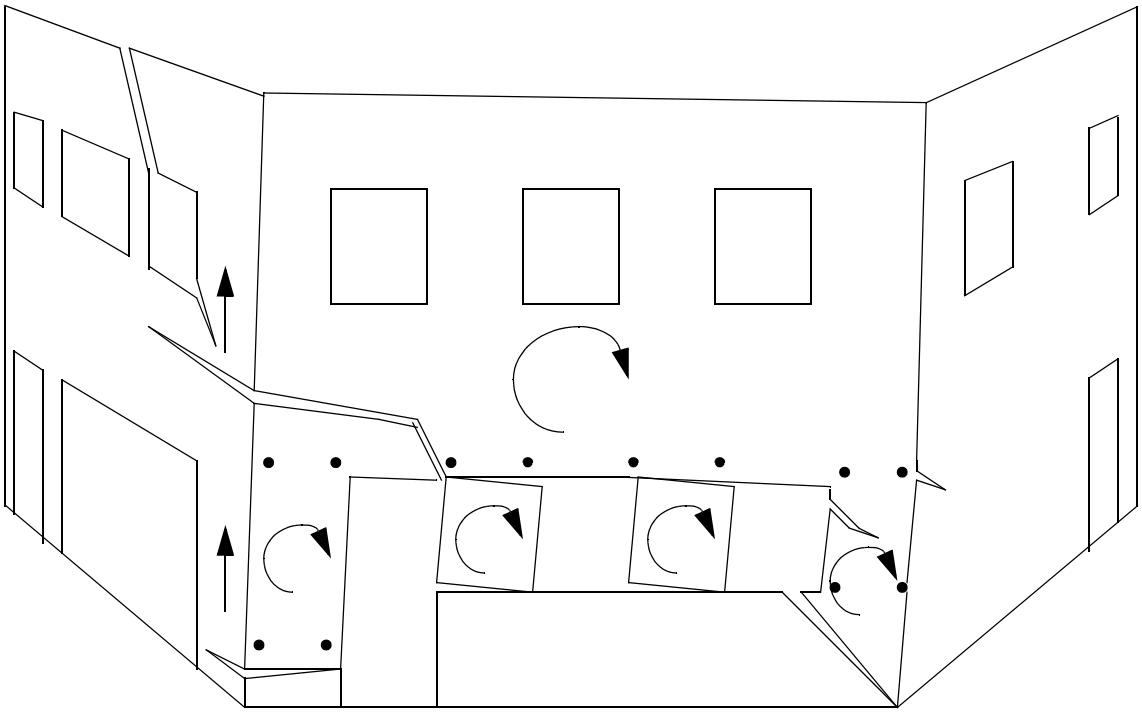

Figure F.72 Exaggerated schematic of the observed behavior of Wall A in the negative loading direction during the Group 4 cycles.

Similar to the behavior in the positive direction, the global rocking shown in Figure F.72 engaged portions of out-of-plane Walls 1 and 2. Figure F.73 shows a plot of the base strains recorded at peak negative displacement during Cycle 39a. Similar to the positive loading direction, this plot supports the contention of flange participation. Note that the magnitude of the strains in the out-of-plane walls are larger than the strains recorded in the in-plane piers. Again, this is consistent with a global overturning of the entire wall.

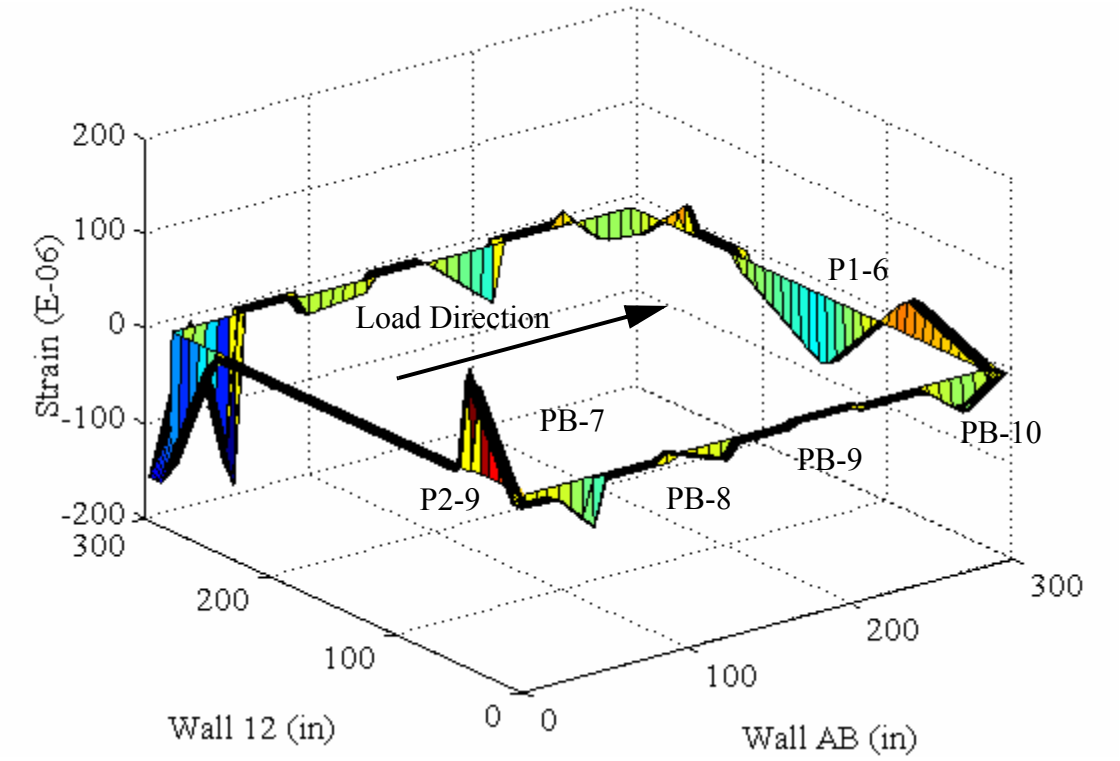

Figure F.73 Base strains recorded at peak negative displacement (Cycle 39a)

F.3.4.2 Behavior of External Reinforcement

During this level of testing, further damage was observed in both the FRP overlays and the NSM rods. For both types of reinforcement the damage can be classified as a debonding. The reader is directed to Section F.3.2.2 for a more complete description of this damage type including photographs. Figure F.74 shows a schematic illustrating the locations of the observed damage (Note that the debonding that occurred during the Group 4 cycles is shown in black).

The additional debonding shown in this figure was observed only during Test Runs 38 and 39, with the majority of the damage being observed during Test Run 39. Recall that during Test Run 33 this wall was displaced approximately the same amount as during Test

Run 38. The reason for the lack of damage during Test Runs 36 and 37 is likely due to the fact that the debonded FRP was more flexible thus did not attain the required stress to fail the adjacent masonry substrate. This is also consistent with the observed decrease in overall wall stiffness discussed in Section F.3.3.

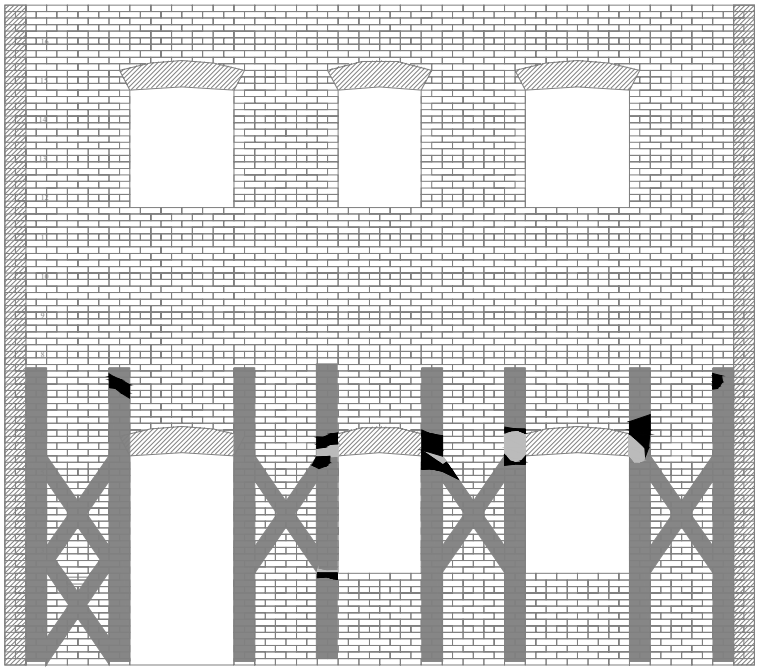

Figure F.74 Schematic showing the areas of debonding following Test Run 39

The behavior of the FRP overlays applied to the inside of Wall B were monitored by strain gages throughout these cycles. Figures F.75 through F.78 show the recorded strains in the vertical FRP overlays during Cycle 39a versus base shear force. Based on these figures, it is apparent that the measured behavior of the FRP overlays during the Group 4 cycles was very similar to the behavior of the FRP overlays during past cycles. The reader is directed to Section F.3.1.2 for further explanation.

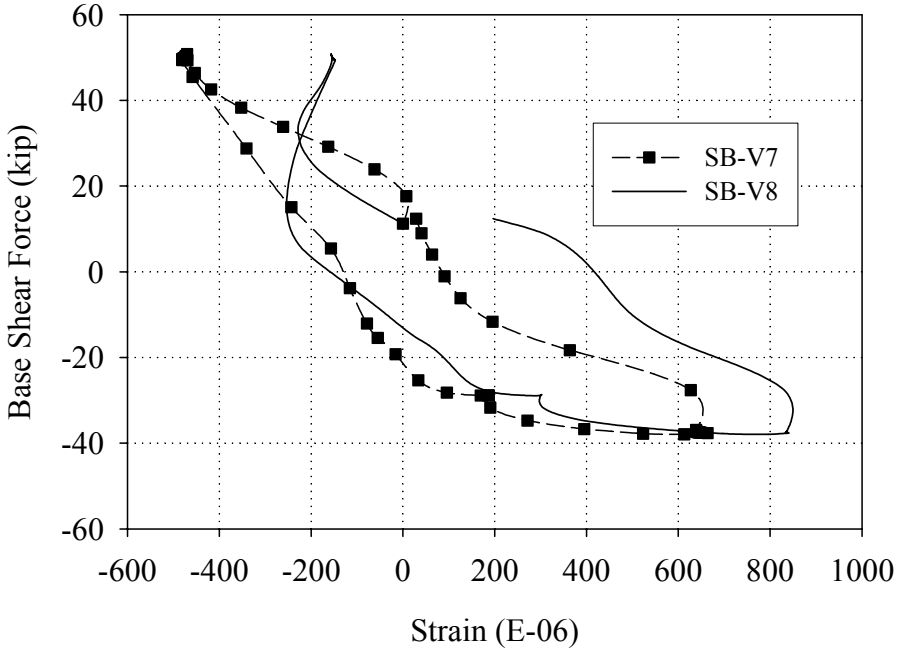

Figure F.75 Strains measured in the vertical FRP overlays applied to the inside of pier PB-7 versus base shear force (Cycle 39a).

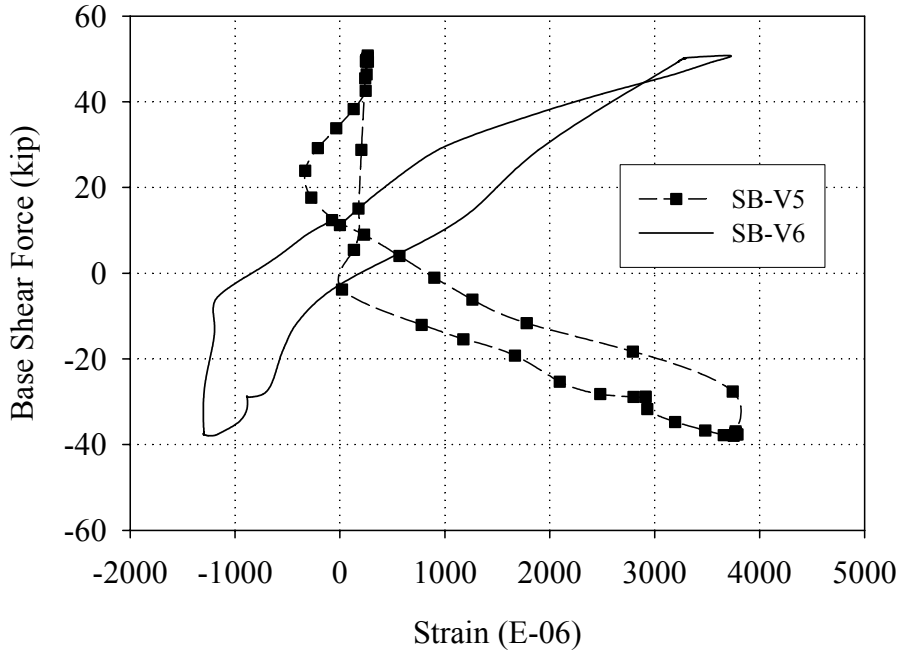

Figure F.76 Strains measured in the vertical FRP overlays applied to the inside of pier PB-8 versus base shear force (Cycle 39a).

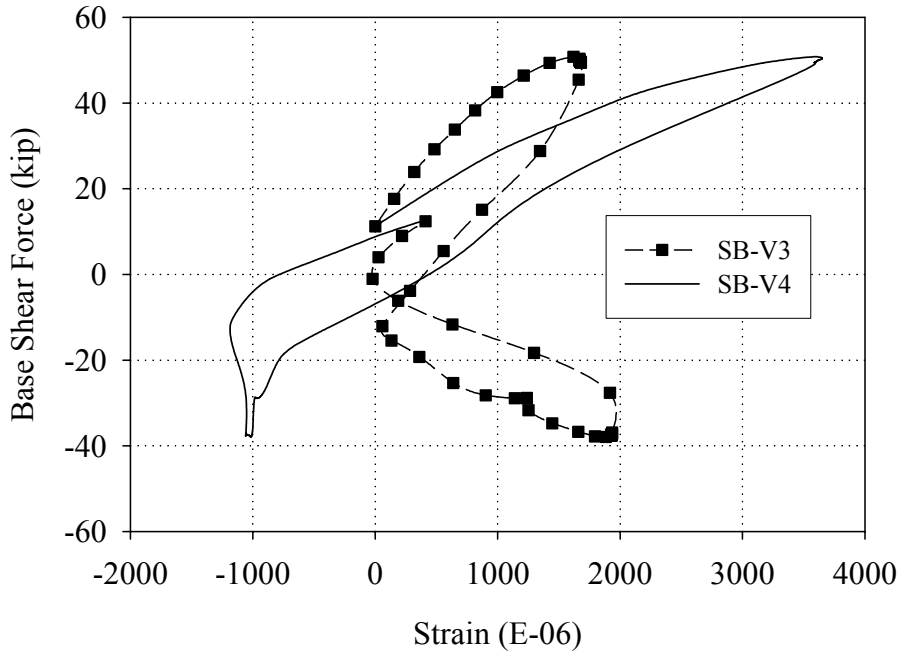

Figure F.77 Strains measured in the vertical FRP overlays applied to the inside of pier PB-9 (Cycle 39a)

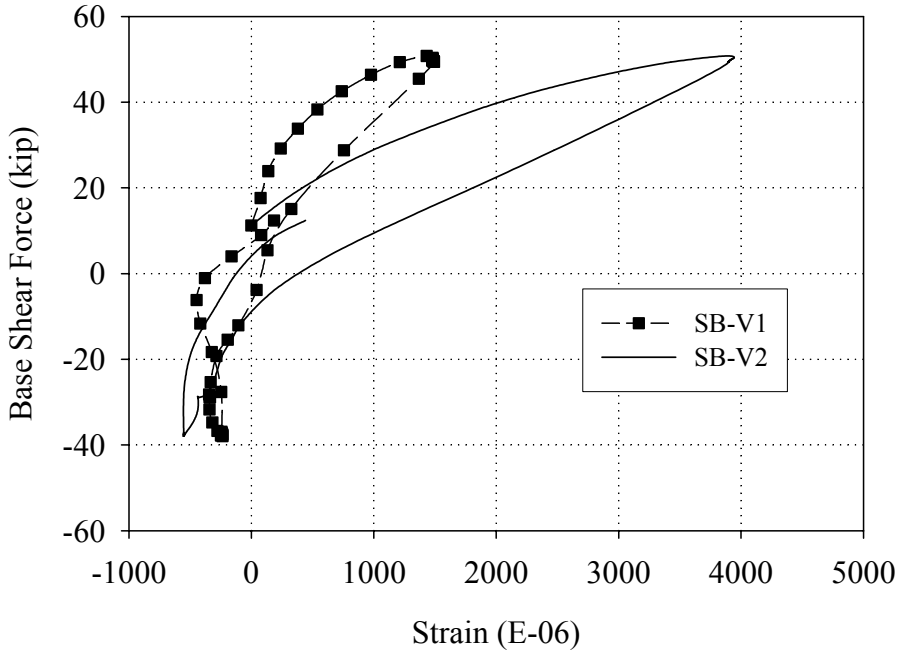

Figure F.78 Strains measured in the vertical FRP overlays applied to the inside of pier PB-10 (Cycle 39a)

F.3.4.3 Local Pier Behavior

Due to the observed crack opening in the first floor piers, the location of the LVDT reference points relative to the active cracks is of paramount importance. As a result, the descriptions of pier behavior given in the following sections utilize Figures F.69 and F.72, which show the location of the LVDTs attached to the piers in reference to the displaced shape. In addition, since all of the piers displayed similar behavior during the Group 4 cycles, the data obtained during Cycle 39a will be used to illustrate the behavior of each pier.

Figures F.79 and F.80 show the readings obtained from the LVDTs attached to pier PB-7; Figure F.81 shows the readings obtained from the LVDTs attached to pier PB-8; Figure F.82 shows the readings obtained from the LVDTs attached to pier PB-9; and Figures F.83 and F.84 show the readings obtained from the LVDTs attached to pier PB-10. In general, Figures F.79 through F.84 are consistent with the observed behavior described in the previous sections as well as the recorded response during the Group 1 cycles. The reader is directed to Section F.3.1.3 for further discussion.

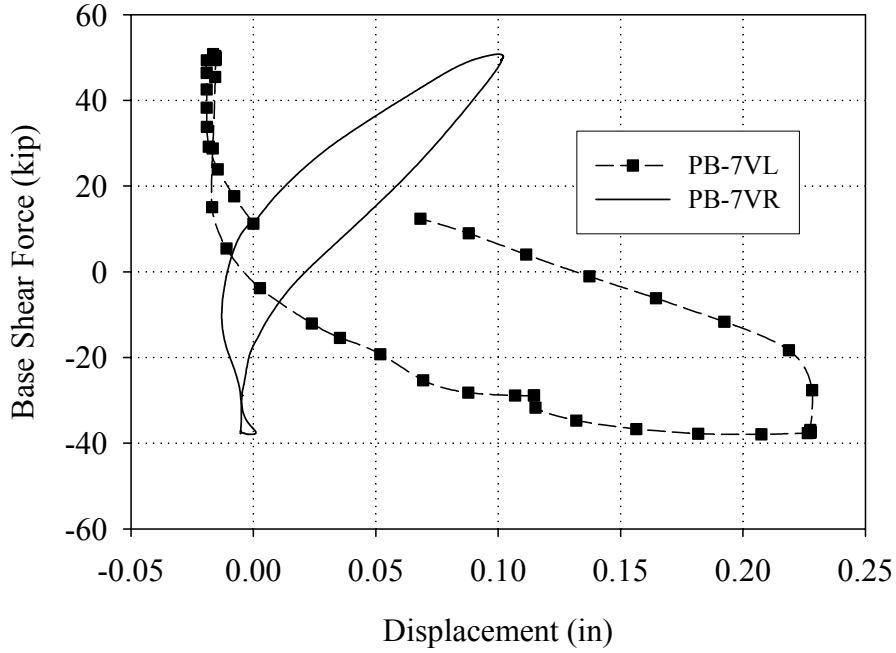

Figure F.79 Readings of the vertical LVDTs attached to pier PB-7 versus base shear force (Cycle 39a)

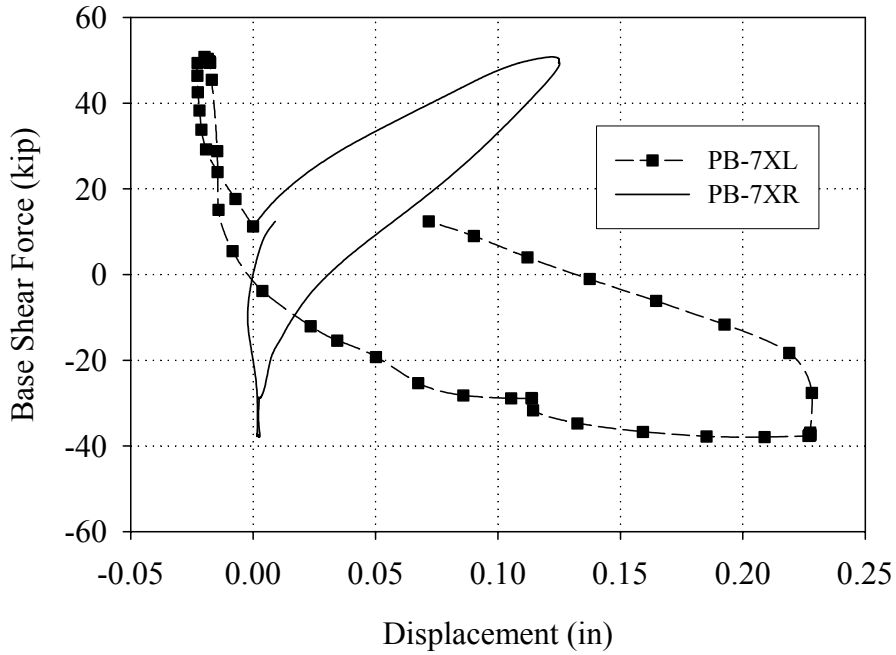

Figure F.80 Readings of the diagonal LVDTs attached to pier PB-7 versus base shear force (Cycle 39a)

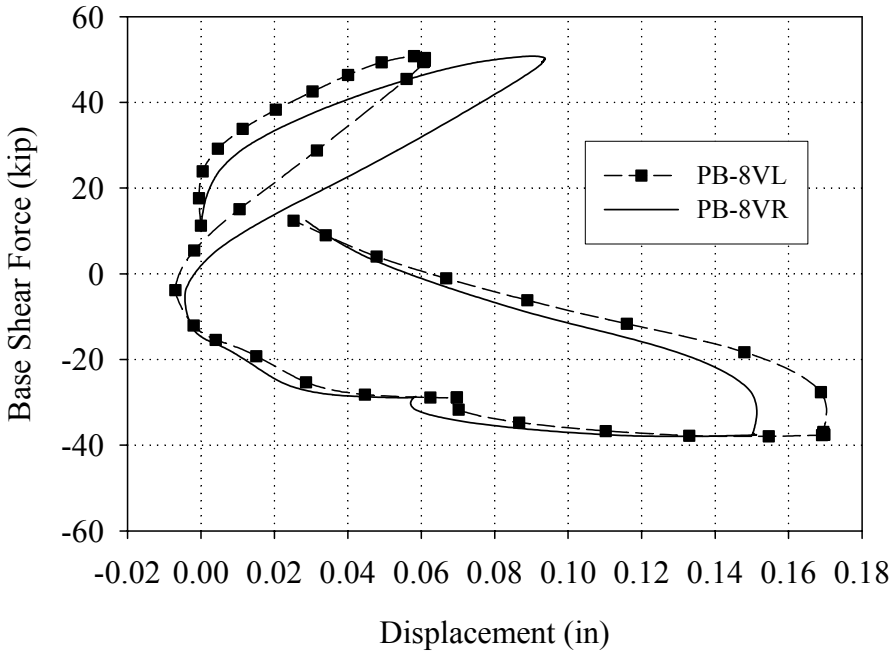

Figure F.81 Readings of the vertical LVDTs attached to pier PB-8 versus base shear force (Cycle 39a)

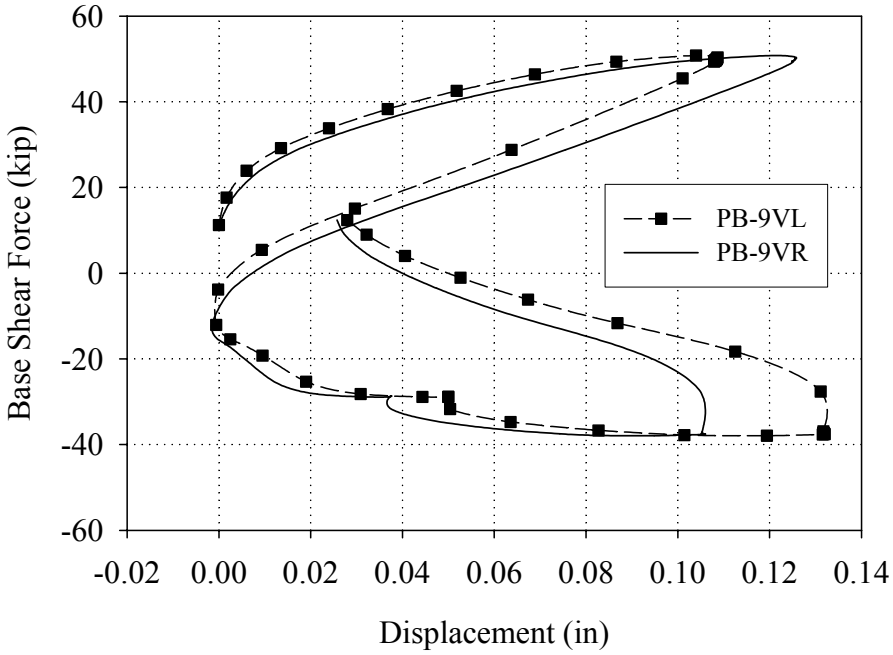

Figure F.82 Readings of the vertical LVDTs attached to pier PB-9 versus base shear force (Cycle 39a)

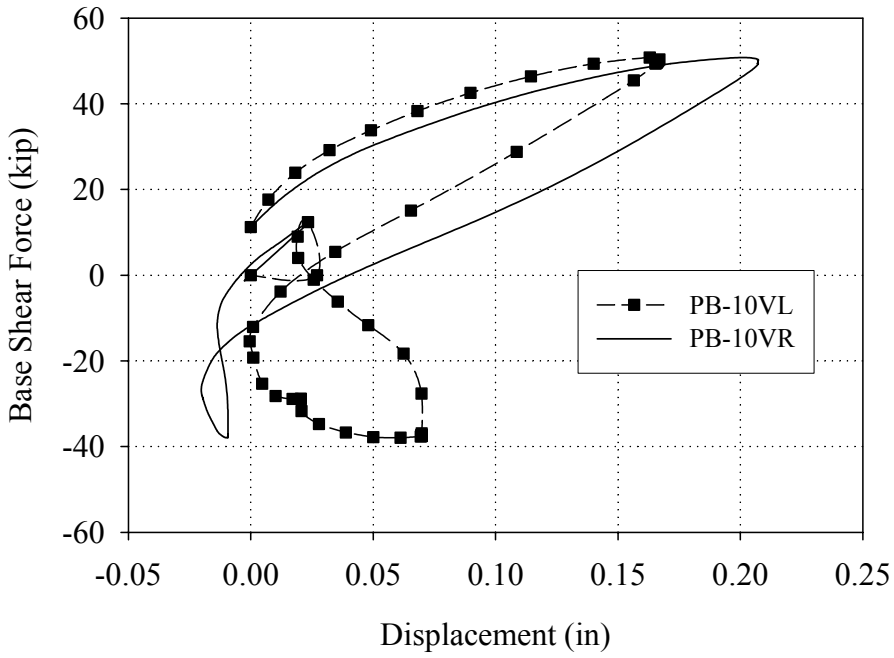

Figure F.83 Readings of the vertical LVDTs attached to pier PB-10 versus base shear force (Cycle 39a)

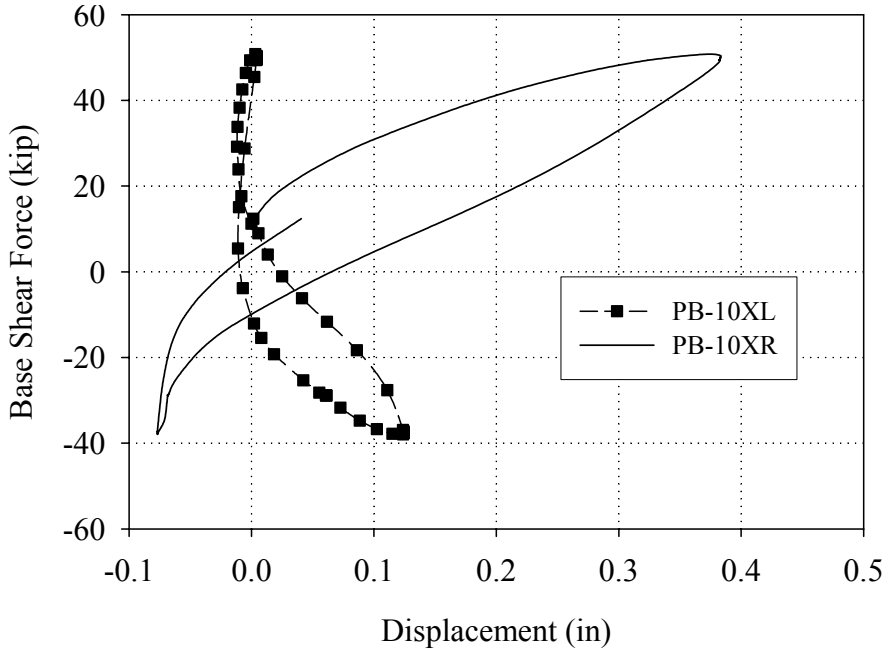

Figure F.84 Readings of the diagonal LVDTs attached to pier PB-10 versus base shear force (Cycle 39a)

F.3.5 Group 5 Cycles (Test Run 40-Test Run 41)

F.3.5.1 Overall Wall Behavior

Figures F.85 through F.87 illustrate the crack pattern in Wall B and out-of-plane Walls 1 and 2 following the Group 5 cycles. As apparent from the figure, substantial cracking was observed in the spandrel above the first floor piers in both loading directions. In the positive loading direction, diagonal cracks were observed below piers PB-8 and PB-9 as well as in pier P1-6 (during both Test Runs 40 and 41). In the negative loading direction, additional cracks formed below pier PB-10 as well as above pier P2-9. In addition, during Test Run 40 a horizontal crack at the base of Wall B below piers PB-8 through PB-10 was observed. All of these cracks are shown in bold in Figures F.85 through F.87.

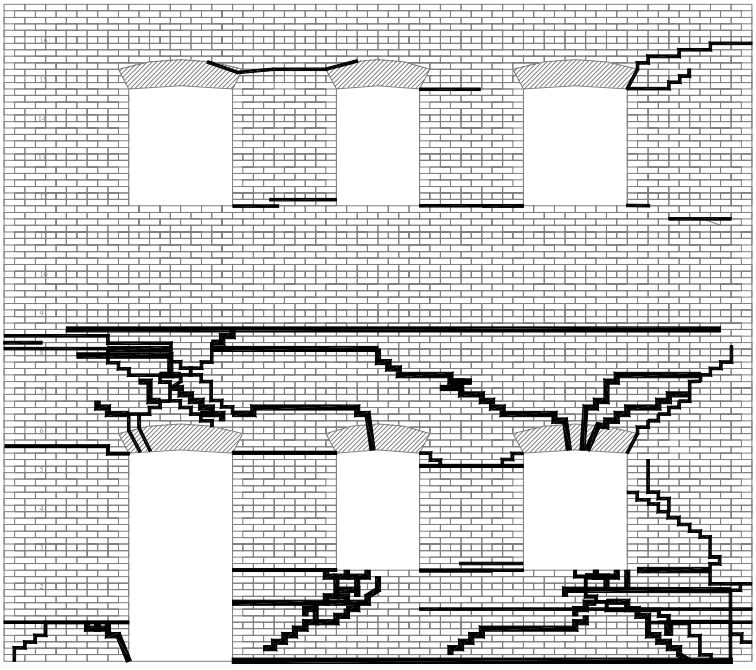

Figure F.85 Crack pattern of Wall B following the Group 5 cycles

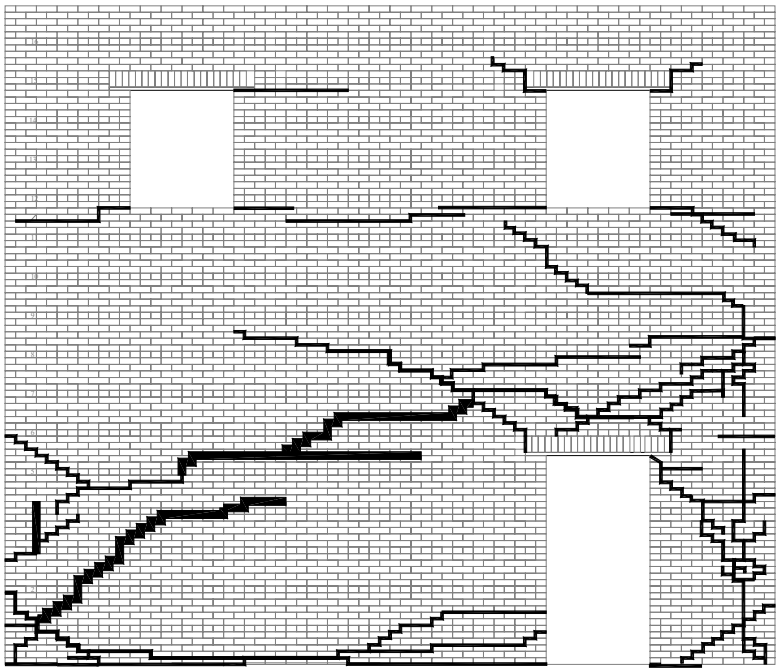

Figure F.86 Crack pattern of out-of-plane Wall 1 following the Group 5 cycles

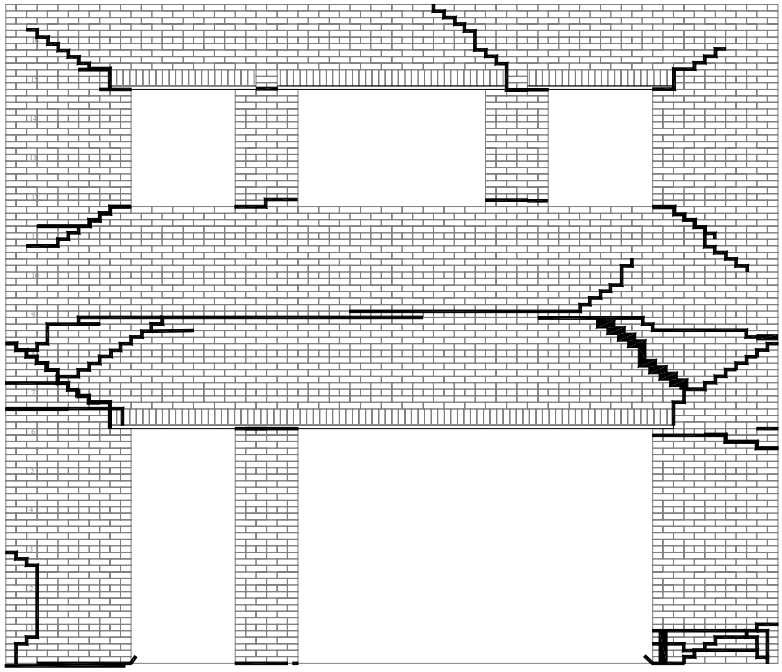

Figure F.87 Crack pattern of out-of-plane Wall 2 following the Group 5 cycles

Figure F.88 shows a schematic illustrating the behavior of Wall B as well as out-of-plane Walls 1 and 2 in the positive direction. Note that the location of the LVDT reference points are also shown in the figure. During the Group 5 cycles the behavior of Wall B was similar to past cycles in that both global rocking and local pier rocking were observed. However, following the formation of the horizontal crack at the base of the wall during Cycle 40a (see Figure F.85), the portion of the wall below piers PB-8 through PB-10 began to slide along the foundation (see Figure F.88). Figure F.89 shows a photograph taken below pier PB-8 that illustrates this observed sliding deformation. In general, this deformation increased with increasing roof displacement up to approximately 0.5 in during Test Run 41 (i.e. roof displacement of 1.5 in). This observed behavior is consistent with the previously discussed increases in energy dissipation and residual displacement during these cycles (see Sections F.2.2 and F.2.3). The observed and measured rigid body motion is shown in Figure F.88 by arrows.

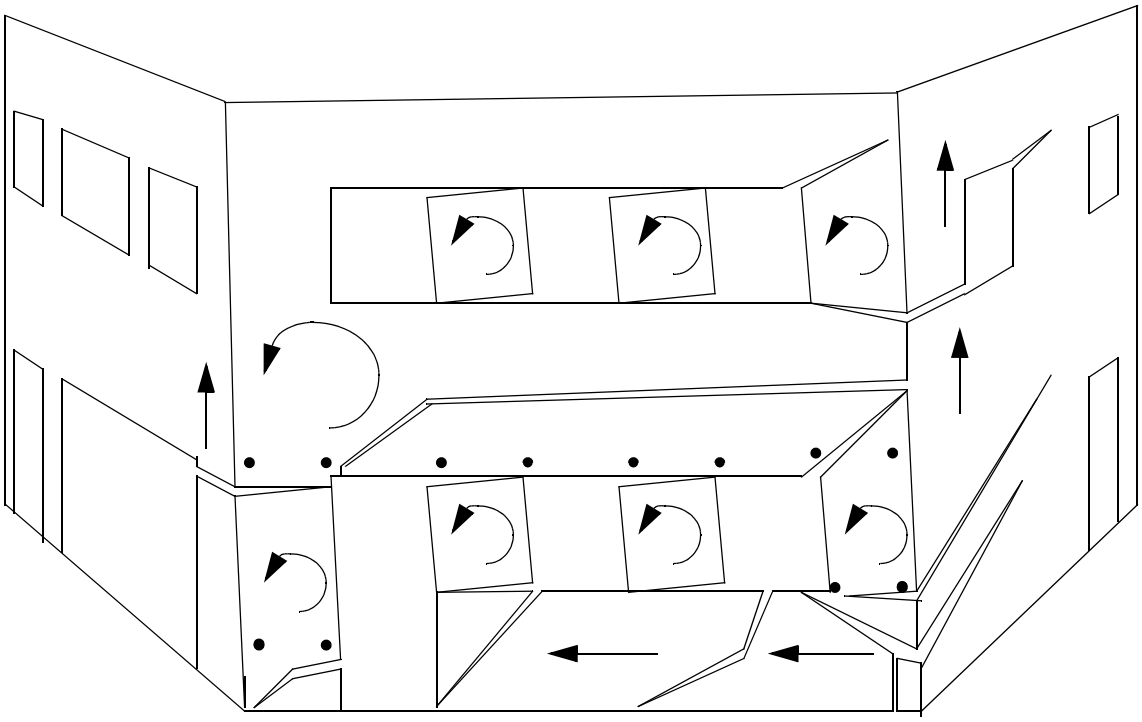

Figure F.88 Exaggerated schematic of the observed behavior of Wall A in the positive loading direction during the Group 5 cycles.

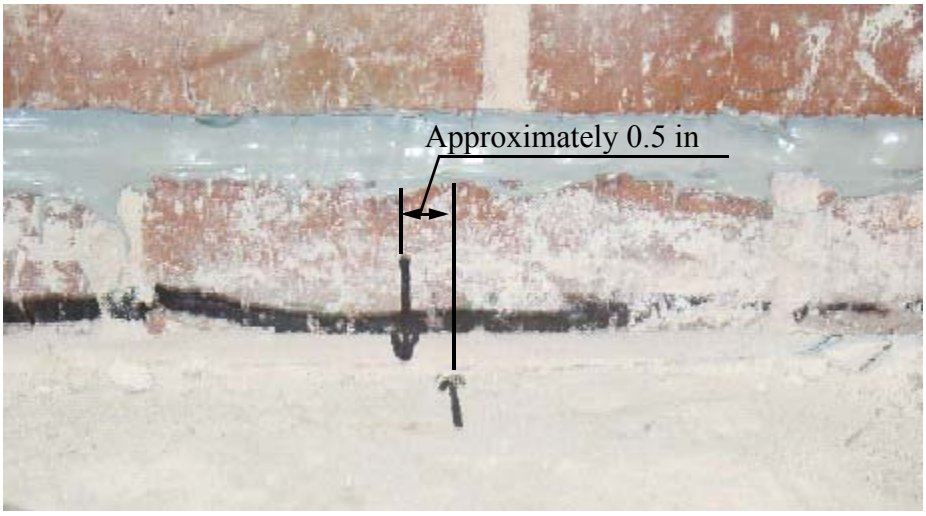

Figure F.89 Photograph showing the sliding at the base of Wall B (Cycle 41a)

Figure F.90 shows the vertical displacements measured for each side of Wall B during Cycle 41a versus roof displacement. Based on the assumptions outlined in Section F.3.1, the rotation implied by this figure accounts for approximately 0.1 in or 7% of the roof displacement in the positive direction. This implies a substantial decrease in global rocking displacement. Recall that during Cycle 39a approximately 26% of the imposed roof displacement was attributed to global rocking deformation. This decrease in global rocking was likely due to the sliding deformation that occurred at the base of the wall.

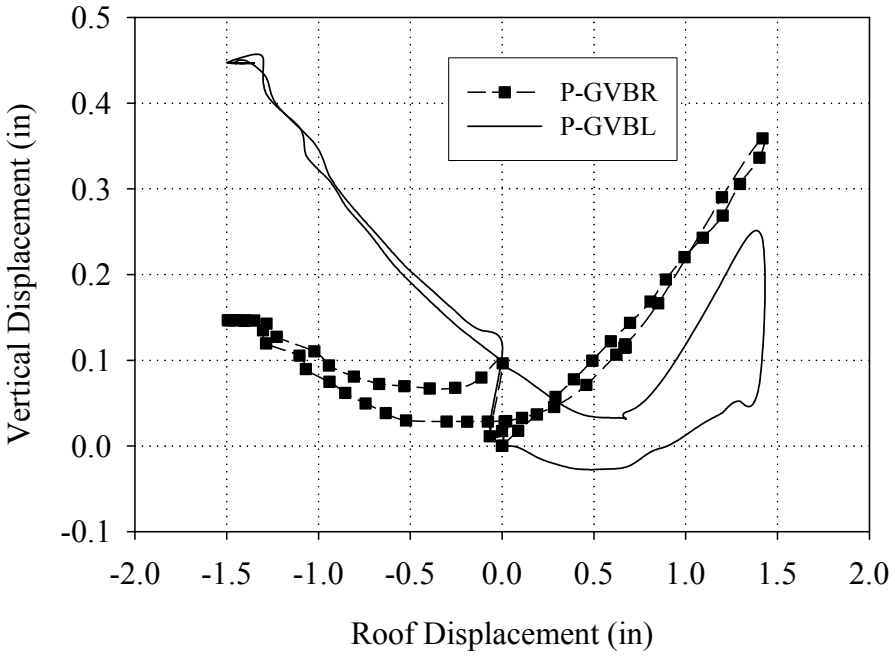

Figure F.90 Vertical displacements of both sides of Wall B versus roof displacement (Cycle 41a)

Similar to past cycles, the observed uplift and rotation of Wall B engaged portions of out-of-plane Walls 1 and 2 (see Figure F.88). Figure F.91 shows a plot of the base strains recorded at peak positive displacement during Cycle 41a. The most notable

difference between this plot and plots generated from past cycles is the relatively small strains recorded in pier P1-6. This decrease in strain is likely due to the evolution from global rocking deformation to sliding deformation at the base of the wall observed during these cycles. In contrast, Figure F.91 shows that pier P2-9 was still participating to a large degree in the response.

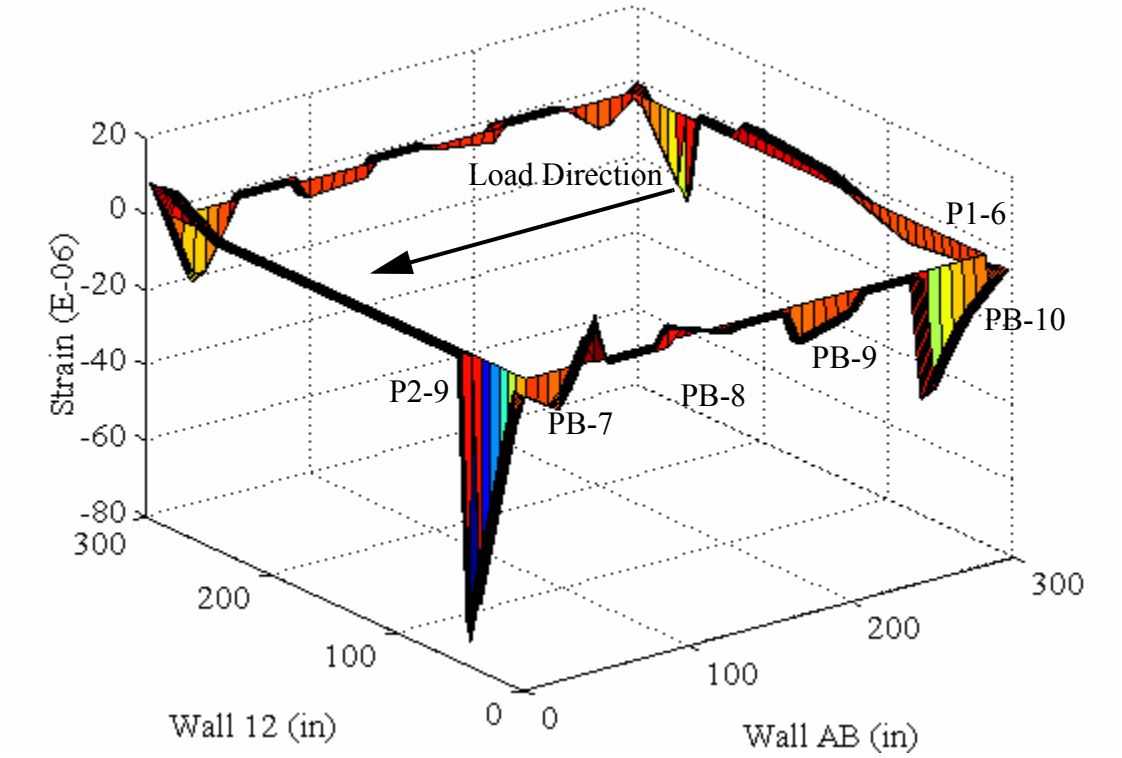

Figure F.91 Base strains recorded at peak positive displacement (Cycle 41a)

Figure F.72 shows a schematic of the behavior of Wall B in the negative direction. Similar to the observed behavior in the positive direction, significant sliding deformation was observed along the foundation below pier PB-8 through PB-10. In general, the sliding deformation in the negative loading direction was approximately equal to the sliding deformation in the positive direction, thus resulting in very small residual displacements.

Again, this observed sliding is consistent with the discussions of energy dissipation and residual displacements presented in Sections F.2.2 and F.2.3.

Aside from this sliding deformation, the response was similar to past cycles in that both global rocking and local pier rocking were observed. Based on Figure F.70, and the assumptions outlined in Section F.3.1, the observed global rocking displacement accounted for approximately 0.3 in or 20% of the roof displacement during Cycle 41a. Recall that during Cycle 39a the global rocking displacement accounted for approximately 21% of the roof displacement.

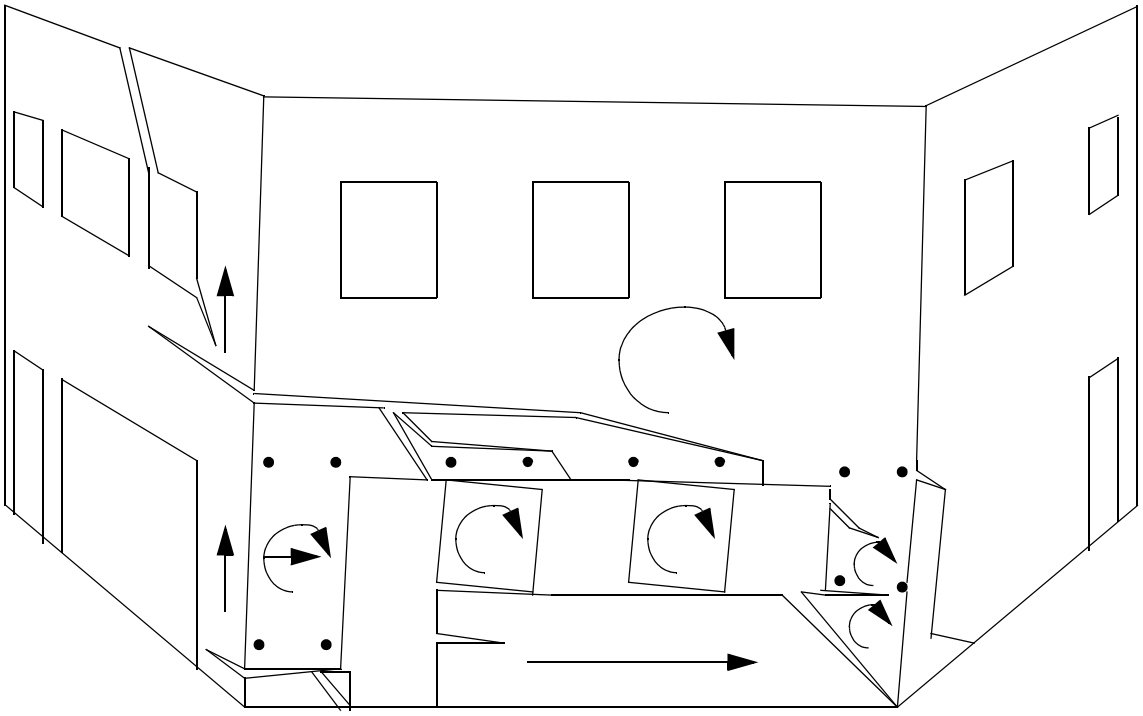

Figure F.92 Exaggerated schematic of the observed behavior of Wall A in the negative loading direction during the Group 5.

In addition, during Cycle 41c pier PB-7 underwent a fairly dramatic change in behavior. At a roof displacement of approximately 1.3 in, the lower corner of pier PB-7

separated from the remainder of the pier causing the pier to rotate downward and slide along the base (see Figures F.92 and F.93). Essentially, the rotation of the pier was recovered and translated into sliding deformation. This evolution of behavior occurred suddenly and was accompanied by a loud deep bang.

Figure F.93 Photograph showing the damage observed in the lower corner of pier PB-7 during Cycle 41c.

Similar to the behavior in the positive direction, the global rocking shown in Figure F.90 engaged portions of out-of-plane Walls 1 and 2. Figure F.91 shows a plot of the base strains recorded at peak negative displacement during Cycle 41a. Similar to past cycles, this figure supports the contention that pier P1-6 was participating in the response. In addition, this figure indicates that the toe of pier PB-7 was experiencing relatively large strains during Cycle 41a. Recall that during the following cycle (Cycle 41c), the damage illustrated Figure F.93 in was observed in this region.

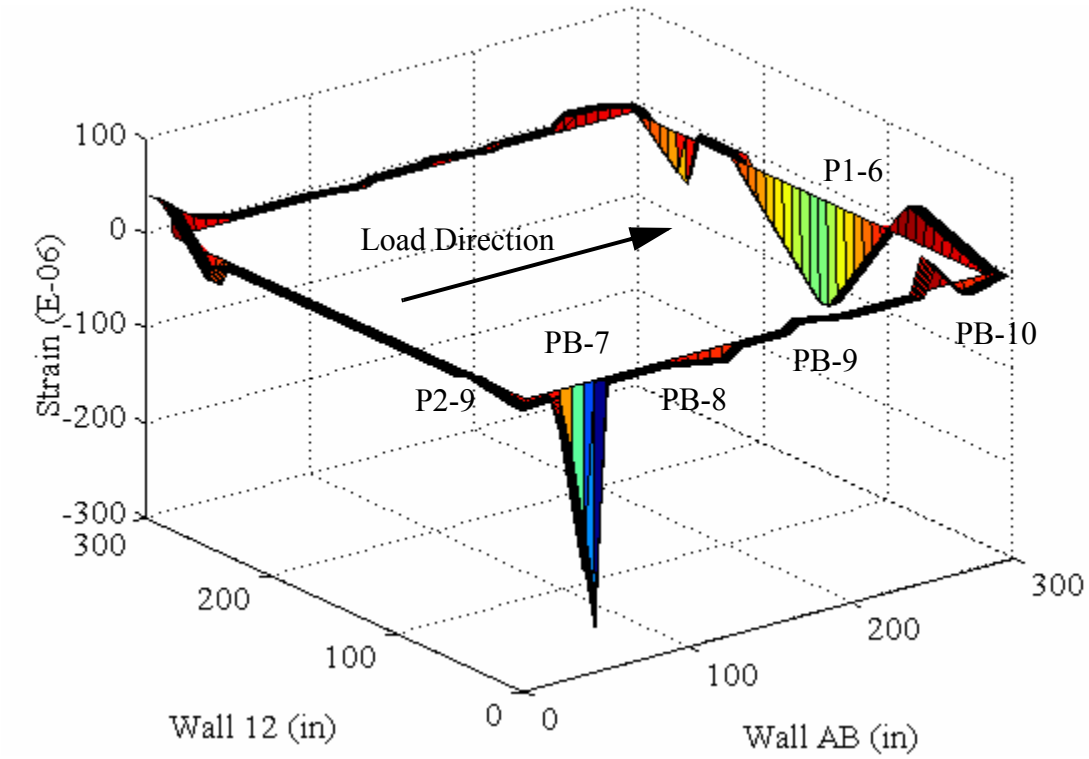

Figure F.94 Base strains recorded at peak negative displacement (Cycle 41a)

F.3.5.2 Behavior of External Reinforcement

During this level of testing, further debonding was observed in both the FRP overlays and the NSM rods. This damage was consistent with past descriptions given in Section F.3.2.2. In general, the observed sliding deformation at the base of Wall B in both directions was the intended response of the wall and indicates that the retrofit was somewhat successful.

In the case of the NSM rods, the observed damage occurred in the vicinity of the active cracks in the spandrel above the first floor piers as well as in the region below piers PB-8 through PB-10 (see Figures F.88 and F.92). The distributed nature of the cracks in these regions suggest that the NSM rods were effectively reinforcing the wall and that their structural integrity remained intact throughout loading (see Figure F.85).

Figure F.74 shows a schematic illustrating the locations of the observed debonding in the FRP overlays (Note that the debonding that occurred during the Group 5 cycles is shown in black). From this figure it is apparent that limited debonding was observed during the Group 5 cycles. This is attributed to the increased sliding deformation observed along the foundation, which likely diminished the drift of the piers relative to the roof displacement.

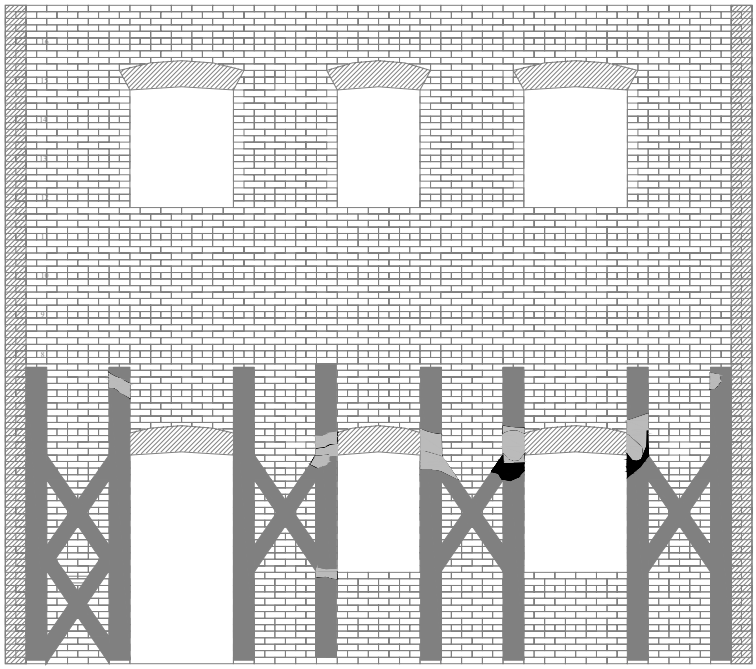

Figure F.95 Schematic showing the areas of debonding observed through Test Run 41

The behavior of the FRP overlays applied to the inside of Wall B were monitored by strain gages throughout these cycles. Figures F.96 through F.99 show the recorded strains in the vertical FRP overlays during Cycle 41a versus base shear force. Based on these figures, it is apparent that the measured behavior of the FRP overlays during the Group 5 cycles was very similar to the behavior of the FRP overlays during past cycles. The reader is directed to Section F.3.1.2 for further explanation.

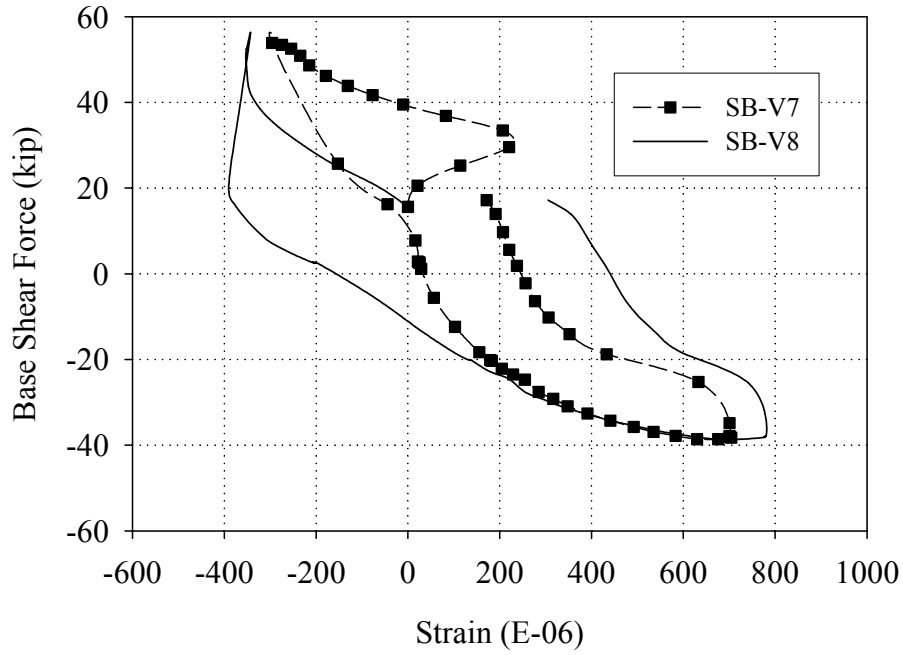

Figure F.96 Strains measured in the vertical FRP overlays applied to the inside of pier PB-7 versus base shear force (Cycle 41a).

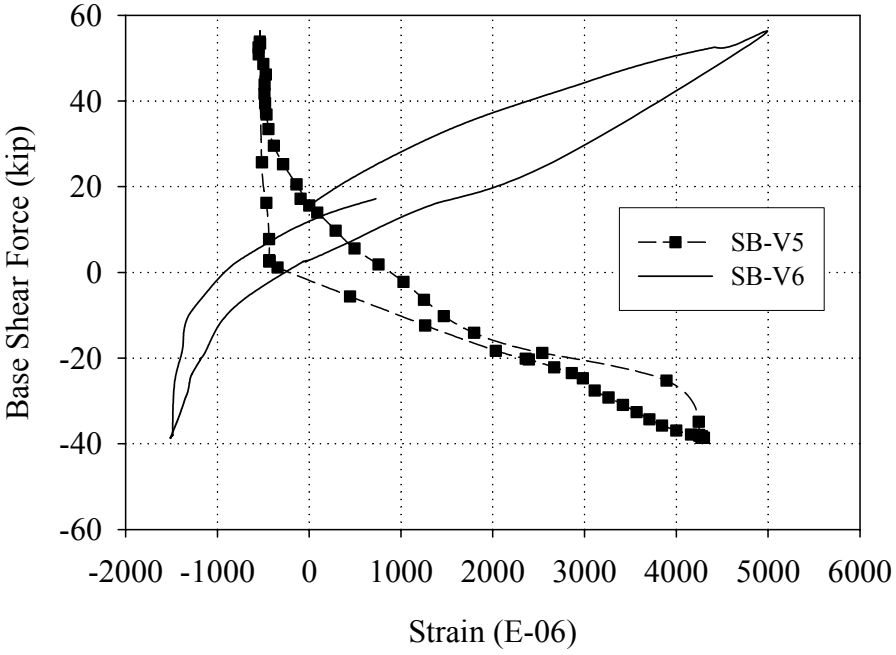

Figure F.97 Strains measured in the vertical FRP overlays applied to the inside of pier PB-8 versus base shear force (Cycle 41a).

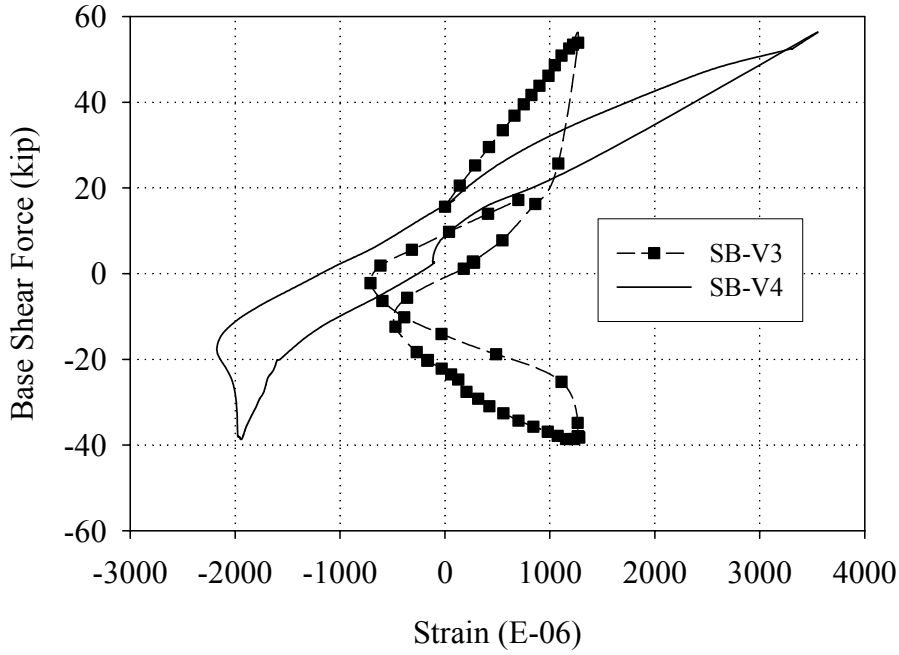

Figure F.98 Strains measured in the vertical FRP overlays applied to the inside of pier PB-9 (Cycle 41a)

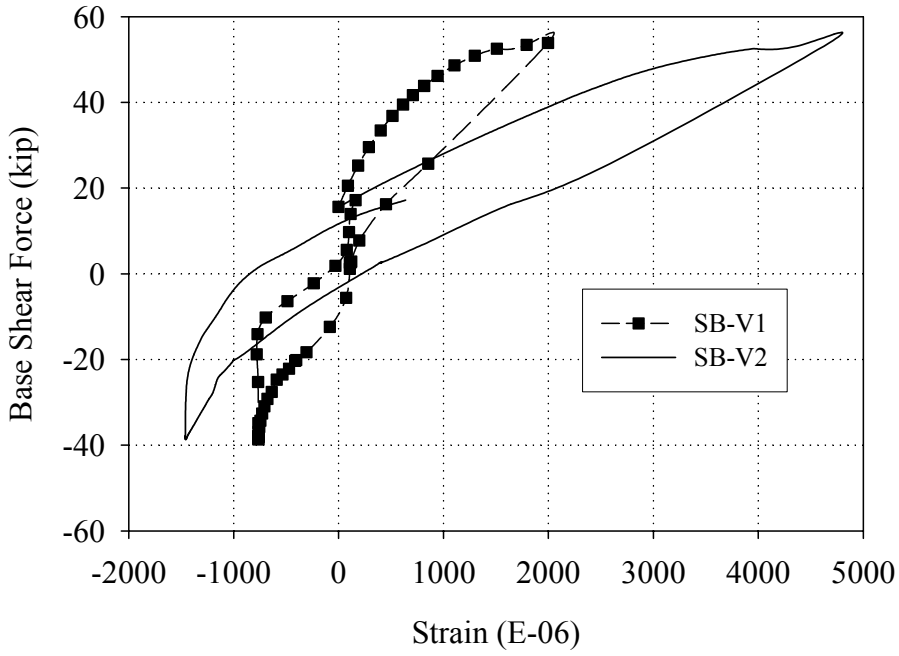

Figure F.99 Strains measured in the vertical FRP overlays applied to the inside of pier PB-10 (Cycle 41a)

F.3.5.3 Local Pier Behavior

Due to the observed crack opening in the first floor piers, the location of the LVDT reference points relative to the active cracks is of paramount importance. As a result, the descriptions of pier behavior given in the following sections utilize Figures F.88 and F.92, which show the location of the LVDTs attached to the piers in reference to the displaced shape. In addition, since all of the piers displayed similar behavior during the Group 5 cycles, the data obtained during Cycle 41a will be used to illustrate the behavior of each pier.

Figures F.100 and F.101 show the readings obtained from the LVDTs attached to pier PB-7; Figure F.102 shows the readings obtained from the LVDTs attached to pier PB-8; Figure F.103 shows the readings obtained from the LVDTs attached to pier PB-9; and Figures F.104 and F.105 show the readings obtained from the LVDTs attached to pier PB-10. In general, Figures F.100 through F.105 are consistent with the observed behavior described in the previous sections as well as the recorded response during the Group 1 cycles. The reader is directed to Section F.3.1.3 for further discussion.

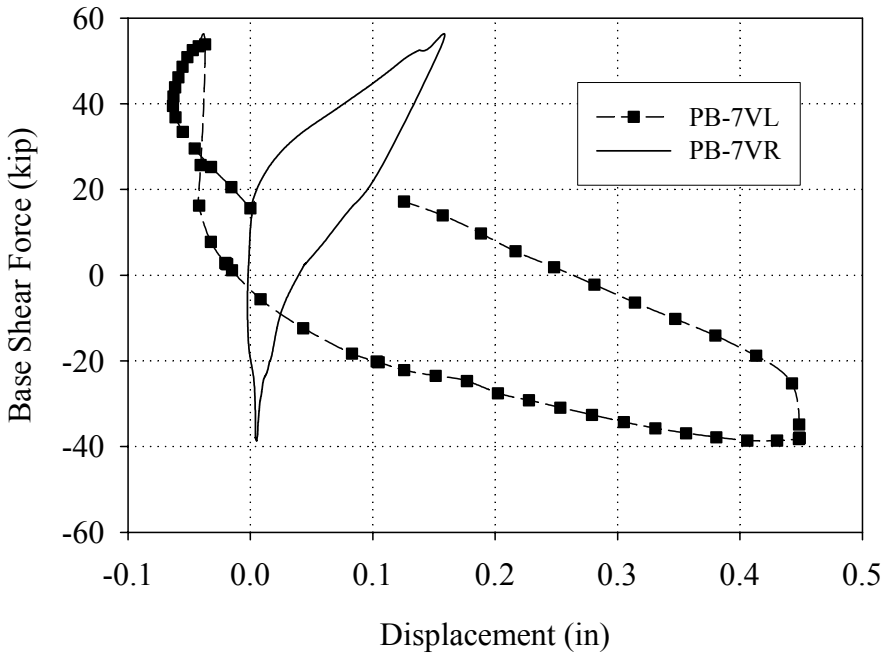

Figure F.100 Readings of the vertical LVDTs attached to pier PB-7 versus base shear force (Cycle 41a)

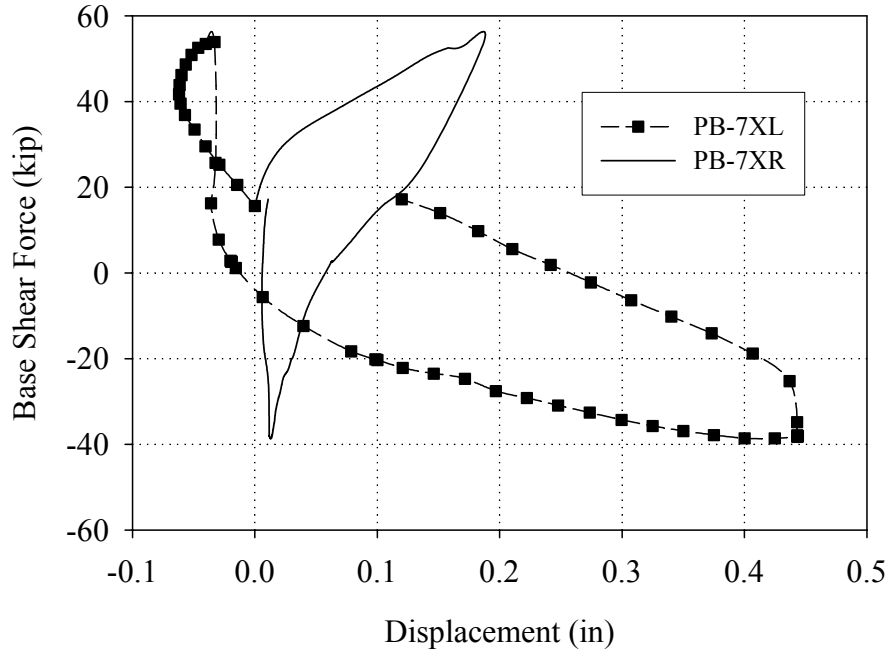

Figure F.101 Readings of the diagonal LVDTs attached to pier PB-7 versus base shear force (Cycle 41a)

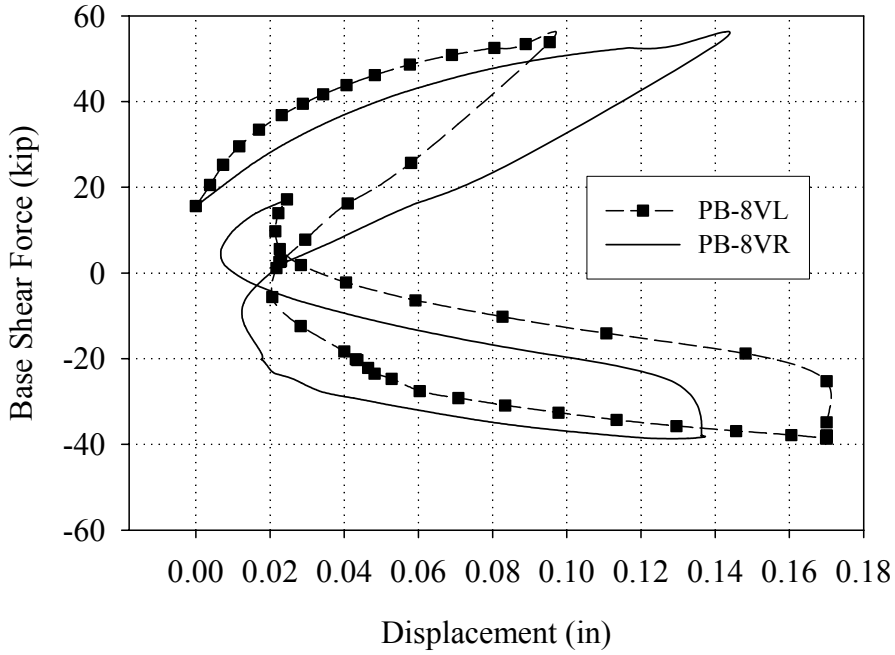

Figure F.102 Readings of the vertical LVDTs attached to pier PB-8 versus base shear force (Cycle 41a)

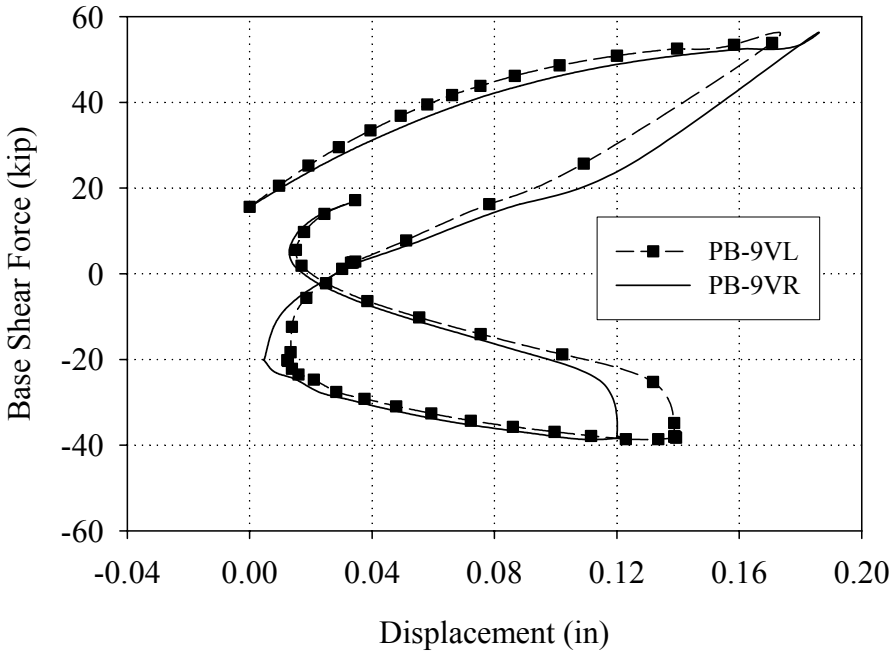

Figure F.103 Readings of the vertical LVDTs attached to pier PB-9 versus base shear force (Cycle 41a).

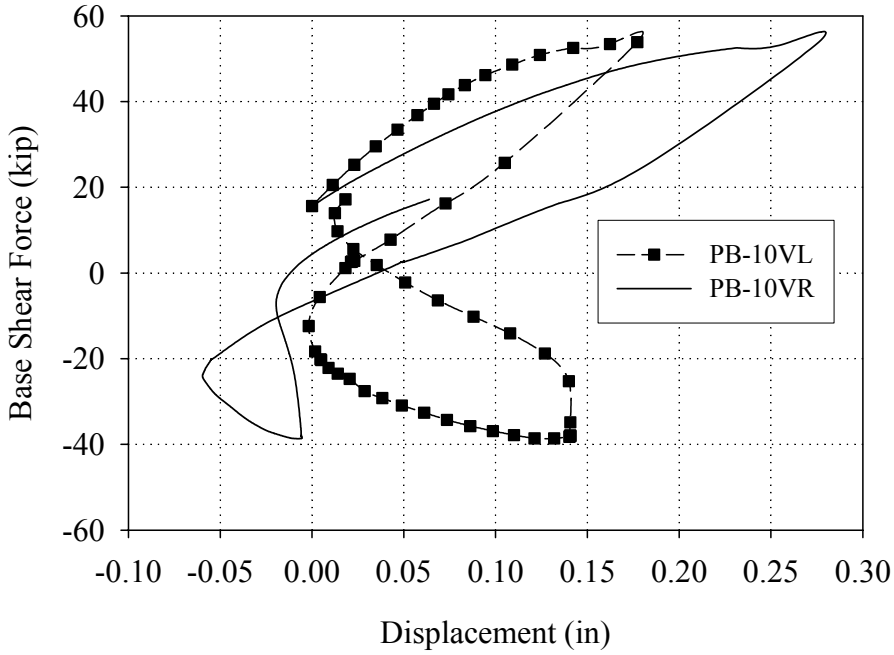

Figure F.104 Readings of the vertical LVDTs attached to pier PB-10 versus base shear force (Cycle 41a)

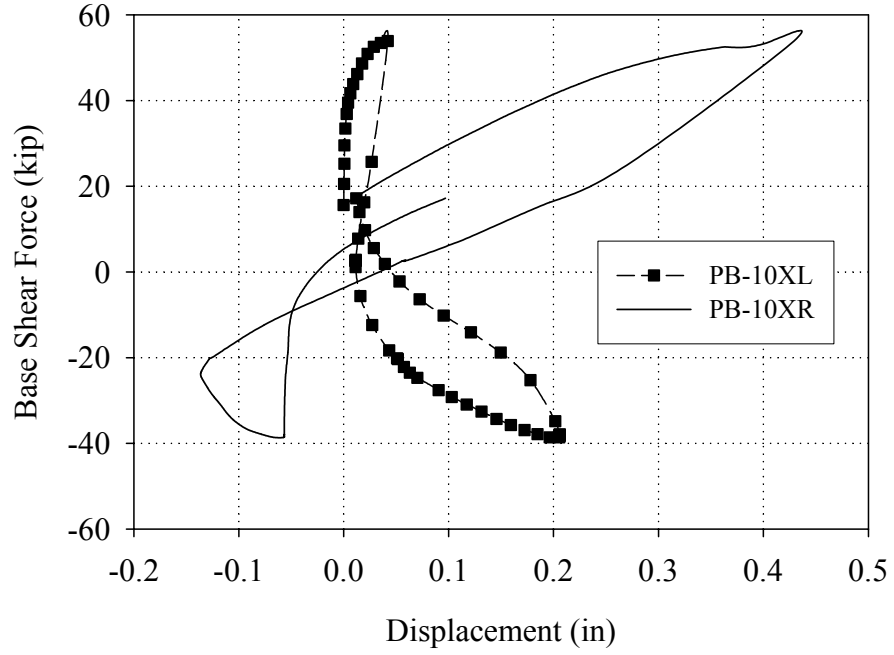

Figure F.105 Readings of the diagonal LVDTs attached to pier PB-10 versus base shear force (Cycle 41a)

F.4 Summary

The behavior of Wall B during the Group 1 through Group 4 cycles was similar in both the positive and negative loading directions. In general, the behavior was a combination of global rocking and local pier rocking. During these cycles both the FRP overlays and the NSM rods progressively debonded (see Section F.3); although no damage that would decrease the capacity of the reinforcement was observed. The debonding caused an effective softening of the reinforcement and contributed to the highly nonlinear force-displacement response of the wall discussed in Section F.2.

In addition, to the resistance offered by Wall B, out-of-plane Walls 1 and 2 also participated in the response. The participation of the out-of-plane walls occurred in two ways. First, the deformation of the in-plane wall resulted in a vertical displacement that lifted up a portion of the out-of-plane wall, thus exploiting its weight to increase resistance to lateral displacement. Second, the out-of-plane walls also resisted compressive stresses thus reducing the compressive stresses of the in-plane wall. In many cases the largest strains in the structure were measured from theta-of-plane walls.

During the Group 5 cycles the response of the Wall B underwent a major change. Specifically, a crack formed at the base of the structure and significant sliding (approximately 0.5 in in each direction) was observed at the base. This sliding likely occurred due to the resistance to local pier rocking offered by the FRP systems. In addition, following the onset of sliding deformation little damage was observed in the external reinforcement. Similar to the lower level cycles, the out-of-plane Walls 1 and 2 also participated; however, the increase sliding deformation resulted in a decrease of global rocking deformation.

This onset of sliding deformation was also observed from the force-displacement response of the wall. Specifically, this sliding deformation resulted in an increase in the percentage of energy dissipated during each cycle as well as an increase in residual displacement.

APPENDIX G

NUMERICAL EXAMPLE

This appendix contains a numerical example illustrating the proposed method to calculate the response of in-plane URM walls. For simplicity, a URM wall prior to retrofit was chosen.

Problem statement

Calculate the base shear capacity of the URM wall shown in Figure G.1. The required material properties are given in Table G.1 (see Section 5.24). For simplicity, assume no live load or superimposed dead load.

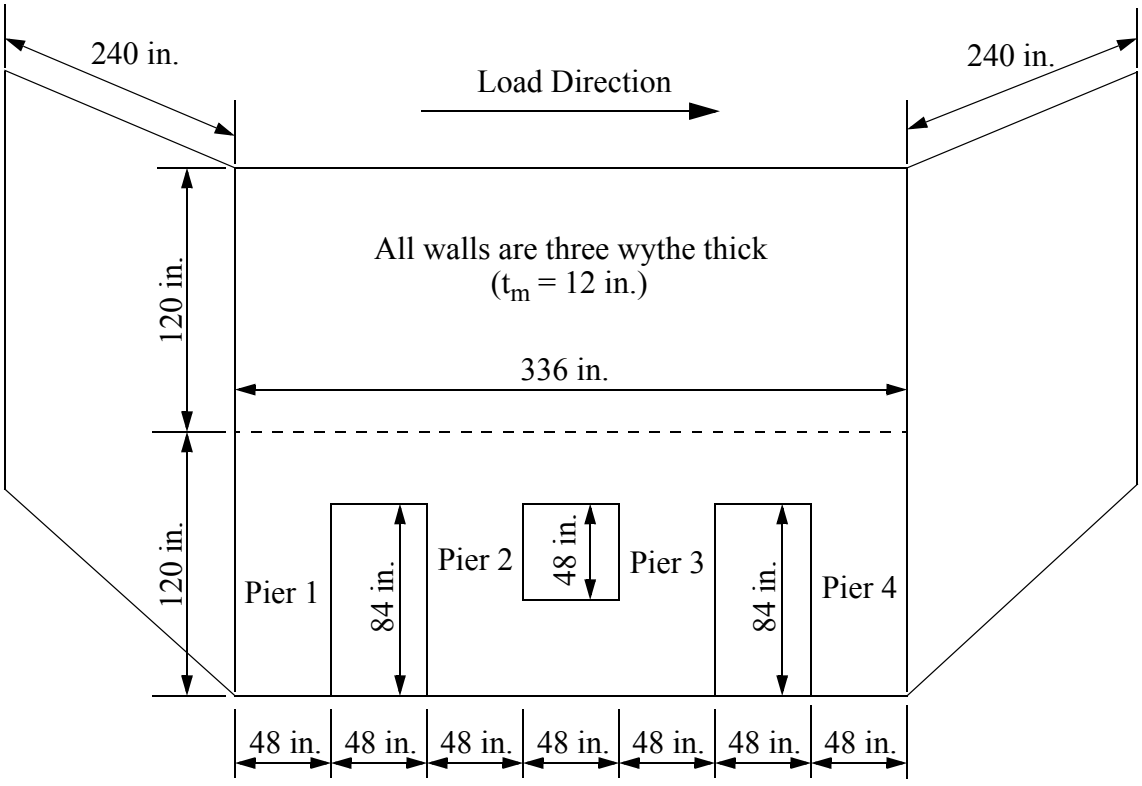

Figure G.1. Example structure.

Table G.1. Masonry material properties.

Property	Mean
Unit weight of masonry (ρ_m)	120 pcf
Masonry compressive strength (f'_m)	1500 psi
Bed-joint shear strength (v_{te})	60 psi
Bed-joint coefficient of friction (μ)	0.75
Expected bed-joint sliding shear strength (v_{me})	$v_{me} = \mu \frac{P}{A_n}$
Elastic modulus of masonry (E_m)	800 ksi
Diagonal tension strength of masonry (f_{dt})	$f_{dt} = \frac{0.75\left(v_{te} + \frac{P}{A_n}\right)}{1.5}$

Step 1: Define piers and flanges

Based on the procedure outlined in Section 5.2.1, the first story piers can be defined as shown in Figure G.2. Note that using this definition allows all piers to be analyzed as fixed-fixed (i.e. $\alpha = 1.0$). The procedure outlined in Section 5.2.4 gives the tension flange definitions shown in Figure G.2.

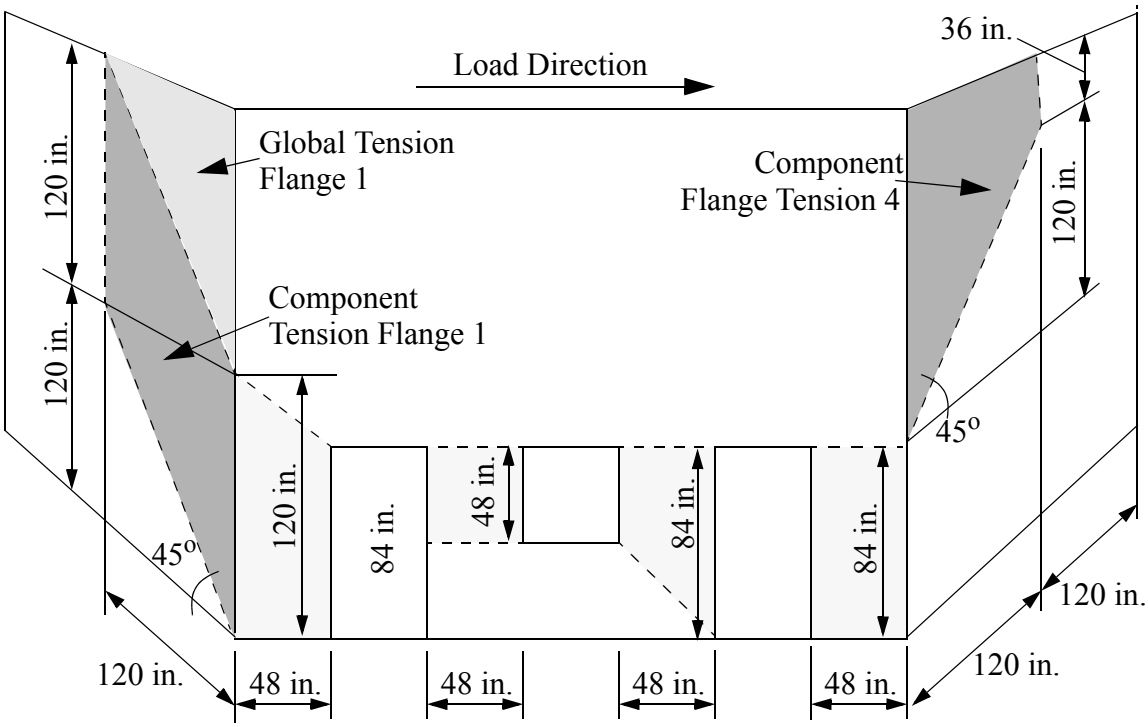

Figure G.2. Schematic illustrating the definition of piers and flanges.

Step 2: Calculate gravity force on piers and weight of tension flanges

For simplicity the gravity force on each of the first floor piers is assumed to be equal, and is calculated as:

$$P_i = \left(\frac{1}{4}\right)(Vol_m)(\rho_m)$$

where

P_i = axial force in Pier *i*

Vol_m = volume of the in-plane wall above the first story piers

$$P_i = \left(\frac{1}{4}\right)(240in - 84in)(336in)(12in)\left(\frac{1ft^3}{1728in^3}\right)(120pcf)$$

$$P_i = 10,920lb = 10.9kip$$

Similarly, the weight of the tension flanges can be calculated as:

Global Tension Flange 1:

$$W_{gf1} = \left(\frac{1}{2}\right)(120\text{in})(120\text{in})(12\text{in})\left(\frac{1\text{ft}^3}{1728\text{in}^3}\right)(120\text{pcf}) = 6,000\text{lb} = 6\text{kip}$$

Component Tension Flange 1:

$$W_{cf1} = (120\text{in})(120\text{in})(12\text{in})\left(\frac{1\text{ft}^3}{1728\text{in}^3}\right)(120\text{pcf}) = 12,000\text{lb} = 12\text{kip}$$

Component Tension Flange 4:

$$W_{cf4} = \left(\left(\frac{1}{2}\right)(120\text{in})(120\text{in}) + (120\text{in})(36\text{in})\right)(12\text{in})\left(\frac{1\text{ft}^3}{1728\text{in}^3}\right)(120\text{pcf})$$

$$W_{cf4} = 9,600\text{lb} = 9.6\text{kip}$$

where

W_{gf1} = weight of Global Tension Flange 1

W_{cfi} = weight of Component Tension Flange *i*

Step 3: Calculate the equivalent global tension flange length

Using Eqn 5.45,

$$L_{gf} = \frac{W_{gf}}{t_{gf} f_{flange}}$$

where

$$f_{flange} = \frac{P_i}{t_i L_i} = \frac{10,900\text{lb}}{(12\text{in})(48\text{in})} = 19\text{psi}$$

Substituting gives:

$$L_{gf} = \frac{6,000\text{lb}}{(12\text{in})(19\text{psi})} = 26.3\text{in}$$

Step 4: Determine the relationship between pier/flange axial force and overturning moment

To develop a relationship between axial force and overturning moment the following simplifying assumptions are made:

- plane sections remain plane
- masonry is linear in compression
- masonry has zero tension strength
- flange weight acts at the edge of the in-plane wall

For simplicity, the overturning moment corresponding to several stress distributions (denoted Cases 1 through 4) is calculated. For values of overturning moment that differ from these cases, the pier and flange axial force is determined by linearly interpolating between values. Figure G.3 shows the first stress distribution considered (Case 1) which represents the gravity stress condition.

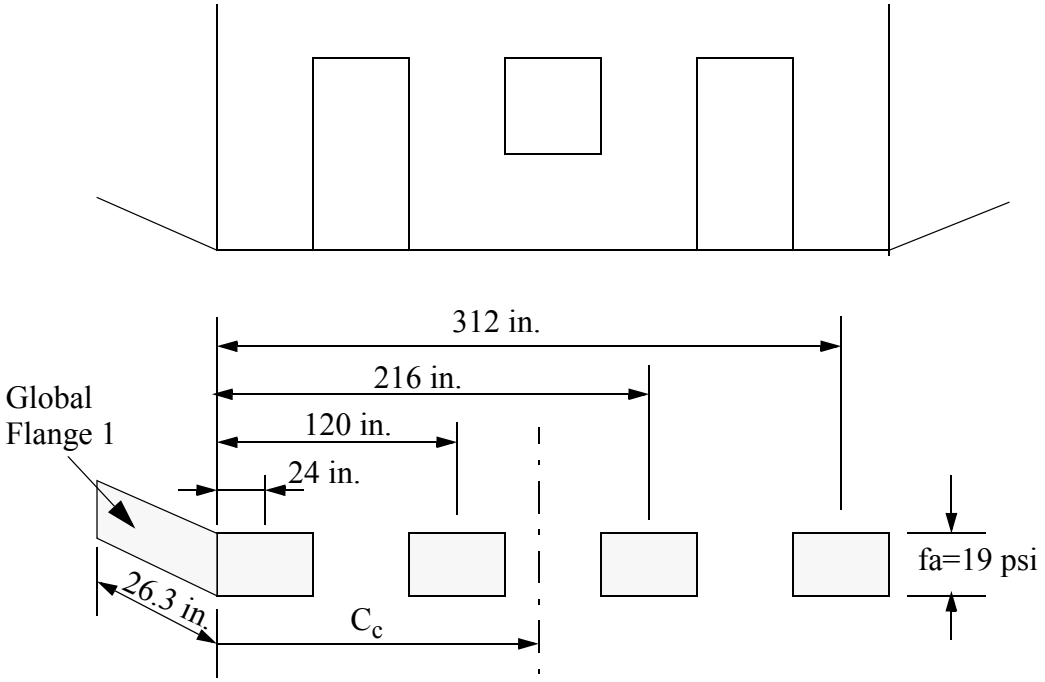

Figure G.3. Axial stress distribution of wall for Case 1 (gravity load).

Using the Case 1 stress condition (i.e. no overturning moment), the center of compressive force, C_c, can be calculated as:

$$C_c = \frac{(W_{gf1})(x_{gf1}) + \sum_{1}^{4}(P_i)(x_i)}{W_{gf1} + \sum_{1}^{4}(P_i)(x_i)}$$

where

x_{gf1}= the distance from the global tension flange to the left edge of the wall

x_i = the distance from the center of Pier *i* to the left edge of the wall

$$C_c = \frac{(6kip)(0in) + (10.9kip)(24in + 120in + 216in + 312in)}{6kip + 4(10.9kip)}$$

$$C_c = 147.6in$$

The second stress condition considered (Case 2) is shown in Figure G.4. This case represents the stress condition at the point where the global tension flange is under no vertical stress.

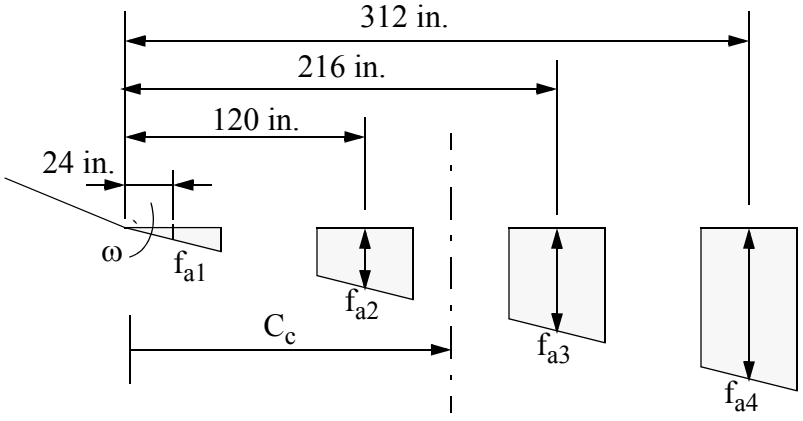

Figure G.4. Case 2 stress distribution.

The average vertical stress in each pier (i.e. f_{ai}) can be related to the stress gradient, ω, as:

$$f_{ai} = \omega(x_i)$$

In addition, the total vertical compressive load can be related to the average vertical stress in each pier as:

$$P_{Total} = \sum_{1}^{4}(A_i)(f_{ai}) \text{ or } P_{Total} = \sum_{1}^{4}(A_i)(\omega(x_i))$$

Substituting:

$$6kip + 4(10.9kip) = (12in)(48in)(\omega(24in) + \omega(120in) + \omega(216in) + \omega(312in))$$

Solving for ω gives:

$$\omega = 0.128psi\left(\frac{1}{in}\right)$$

Solving for f_{ai} gives:

$$f_{a1} = 3.1psi \;;\; f_{a2} = 15.4psi \;;\; f_{a3} = 27.6psi \;;\; f_{a4} = 39.9psi$$

Solving for P_i gives:

$$P_1 = 1.8kip \;;\; P_2 = 8.9kip \;;\; P_3 = 15.9kip \;;\; P_4 = 23.0kip$$

By summing moments about the center of compression, C_c, (as determined from the gravity case), the overturning moment can be approximated as:

$$OM = \sum_{i=1}^{4}(P_i)(x_i)$$

$$OM = (-123in)(1.8kip) + (-27.6in)(8.9kip) + (68.4in)(15.9kip) + (164.4in)(23kip)$$

$$OM = 4400kip \cdot in$$

The stress distribution for Cases 3 and 4 are shown in Figure G.5 and G.6. For the sake of brevity the calculation of vertical stress for these cases is not presented, but the results of all cases are summarized in Table G.2 and plotted in Figure G.7.

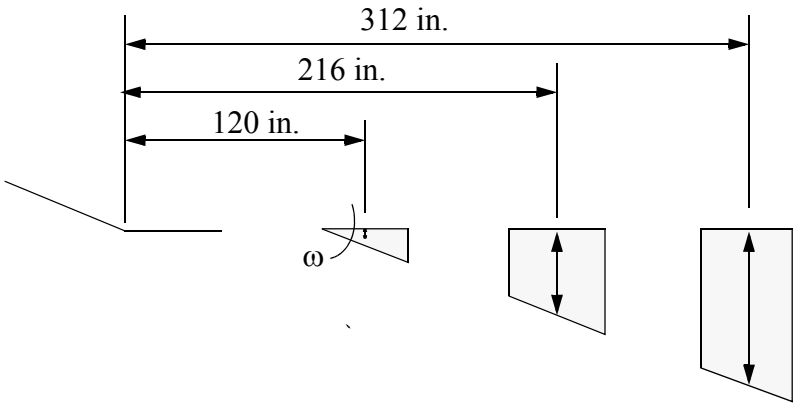

Figure G.5. Stress distribution for Case 3.

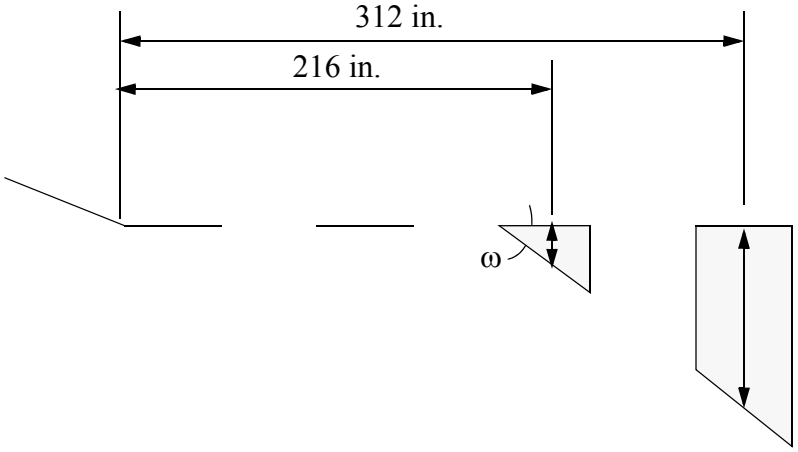

Figure G.6. Stress distribution for Case 4.

Table G.2. Summary of pier compressive force and axial load.

Case	OM (kip-in)	Axial Compressive Force *P* (kip)					P_{Total} (kip)
		Global Flange 1	Pier 1	Pier 2	Pier 3	Pier 4	
1	0	6	10.9	10.9	10.9	10.9	49.6
2	4400	0	1.8	8.9	15.9	23.0	49.6
3	5920	0	0	3.3	16.5	29.7	49.5
4	7370	0	0	0	8.3	41.4	49.7

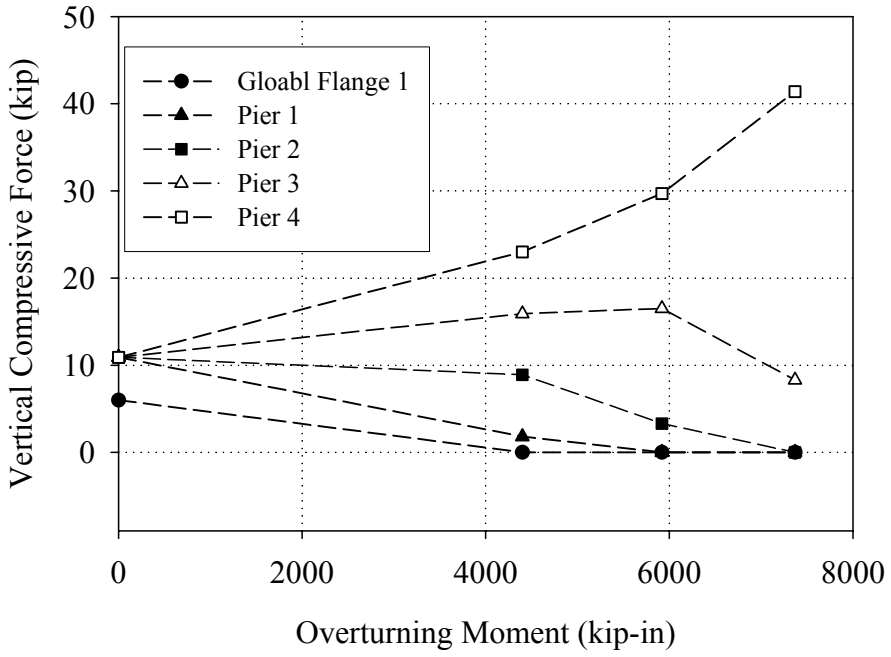

Figure G.7. Vertical compressive force for Piers 1 through 4 and Global Tension Flange 1 versus overturning moment.

Step 5: Calculate Wall Base Shear Capacity

1st Iteration

Due to the dependence of axial force on overturning moment, this process is iterative. The general procedure begins by calculating the shear capacity of each pier

assuming gravity force. Using the modified FEMA 356 (ATC, 2000) pier equations discussed in Section 5.2, this can be done for Pier 1 as follows:

Pier rocking strength:

$$V_r = 0.9(P_1 + W_{cf1} + W_{gf1})\left(\frac{L}{H}\right)$$

$$V_r = 0.9(10.9\text{kip} + 12\text{kip} + 6\text{kip})\left(\frac{48\text{in}}{120\text{in}}\right) = 10.4\text{kip}$$

Pier 1 bed-joint sliding strength:

$$V_{bjs} = \mu(P_1 + W_{gf1})$$

$$V_{bjs} = 0.75(10.9\text{kip} + 6\text{kip}) = 12.7\text{kip}$$

Note that for pier 1, sliding can occur along the top of the pier and thus not engage the weight of the component flange. As a result, the weight of Component Tension Flange 1 is not included in the calculation of bed-joint sliding.

Pier 1 diagonal tension strength:

$$f_{dt} = \frac{0.75\left(v_{te} + \frac{(P_1 + W_{cf1} + W_{gf1})}{A}\right)}{1.5}$$

$$f_{dt} = \frac{0.75\left(0.060\text{ksi} + \frac{(10.9\text{kip} + 12\text{kip} + 6\text{kip})}{(12\text{in})(48\text{in})}\right)}{1.5} = 55\text{psi}$$

$$V_{dt} = \frac{f_{dt}A}{1.5}\sqrt{1 - \frac{\left(\frac{P_1 + W_{cf1} + W_{gf1}}{A}\right)}{f_{dt}}}$$

$$V_{dt} = \frac{0.055\text{ksi}(12\text{in})(48\text{in})}{1.5}\sqrt{1 - \frac{\frac{(10.9\text{kip} + 12\text{kip} + 6\text{kip})}{(12\text{in})(48\text{in})}}{0.055\text{ksi}}} = 29.2\text{kip}$$

Pier 1 toe crushing strength:

$$V_{tc} = (P_1 + W_{cf1} + W_{gf1})\left(\frac{L}{H}\right)\left(1 - \frac{\frac{(P_1 + W_{cf1} + W_{gf1})}{A}}{f'_m}\right)$$

$$V_{tc} = (10.9kip + 12kip + 6kip)\left(\frac{48in}{120in}\right)\left(1 - \frac{\frac{(10.9kip + 12kip + 6kip)}{(12in)(48in)}}{1.5ksi}\right) = 11kip$$

Similarly, the capacity for Piers 2 through 4 can be calculated. The results of these calculations are given in Table G.3. Note that the governing failure mode (i.e. the failure mode of least resistance) is circled in Table G.3.

Table G.3. Capacity of Piers 1 through 4 (1st iteration).

Pier	$V_{rocking}$ (kip)	$V_{bed\text{-}joint\ sliding}$ (kip)	$V_{diagonal\ tension}$ (kip)	$V_{toe\ crushing}$ (kip)
1	(10.4)	12.7	29.2	11
2	9.8	(8.2)	27.6	10.7
3	(5.6)	8.2	18.4	6.1
4	(10.5)	11.3	15.4	24.3

Since all of the governing failure modes are deformation-controlled, the capacity of the wall can be determined by adding the individual pier capacities together as:

$$V_{Total} = (10.4kip + 8.2kip + 5.6kip + 10.5kip)$$

$$V_{Total} = 34.7kip$$

To calculate the overturning moment, the force distribution is assumed to be equal at each floor level (as per FEMA 356 (ATC, 2000)). Figure G.8 shows a schematic of the

structure with the lateral loads as well as the base moments for each of the piers. Note that pier base moments are calculate by multiplying the shear force in each pier by half of the effective height. Since each pier is assumed to be fixed-fixed, half of the height of the pier corresponds to the height of the inflection point.

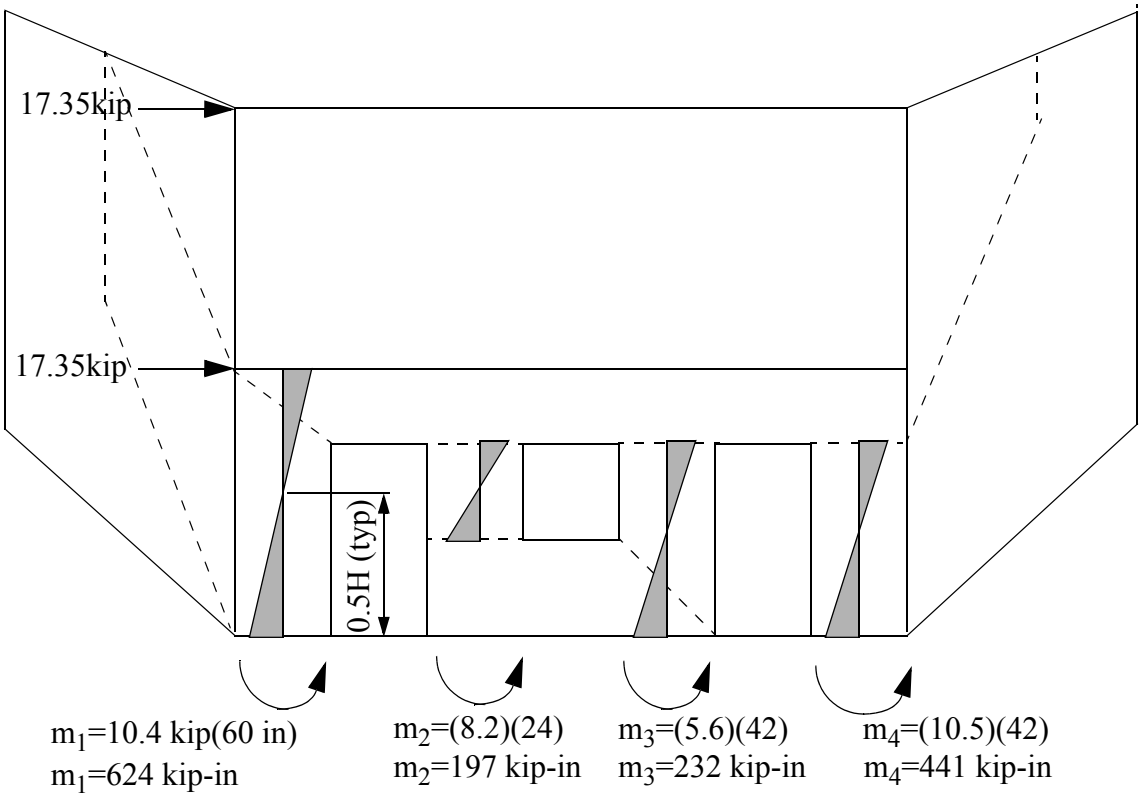

Figure G.8. Schematic illustrating lateral loads and individual pier base moments.

Summing moments about the base of the structures gives:

$$OM = 17.35kip(120in + 240in) - (624k \cdot in + 197k \cdot in + 232k \cdot in + 441k \cdot in)$$

$$OM = 4752k \cdot in$$

Since an overturning moment of 4752 kip-in falls between Cases 2 and 3 in Table G.2, the pier axial forces will be determined by linearly interpolating between these cases.

$$P_1 = (0 - 1.8\text{kip})\left(\frac{4752 - 4400}{5920 - 4400}\right) + 1.8\text{kip} = 1.4\text{kip}$$

$$P_2 = (3.3\text{kip} - 8.9\text{kip})\left(\frac{4752 - 4400}{5920 - 4400}\right) + 8.9\text{kip} = 7.6\text{kip}$$

$$P_3 = (16.5\text{kip} - 15.9\text{kip})\left(\frac{4752 - 4400}{5920 - 4400}\right) + 15.9\text{kip} = 16.0\text{kip}$$

$$P_4 = (29.7\text{kip} - 23.0\text{kip})\left(\frac{4752 - 4400}{5920 - 4400}\right) + 23.0\text{kip} = 24.5\text{kip}$$

2nd Iteration

Using the updated pier axial forces the capacity of each pier can be recalculated. The results of this calculation is given in Table G.4.

Table G.4. Capacity of Piers 1 through 4 (2nd iteration).

Pier	V_r (kip)	V_{bjs} (kip)	V_{dt} (kip)	V_{tc} (kip)
1	4.8	1.1	20	5.3
2	6.8	5.7	24.6	7.5
3	8.2	12.0	21.5	9.0
4	17.5	25.6	32.3	18.7

Summing the individual pier capacities gives a base shear capacity of 32.5 kip. Following the same procedure detailed for the 1st iteration, the overturning moment can be calculated as 4570 kip-in, and the pier axial forces can be calculated as:

$$P_1 = 1.6\text{kip}\,;\;\; P_2 = 8.3\text{kip}\;\;;\; P_3 = 16.0\text{kip}\;;\; P_4 = 23.8\text{kip}$$

3rd Iteration

Using the updated pier axial forces the capacity of each pier can be recalculated. The results of this calculation are given in Table G.5.

Table G.5. Capacity of Piers 1 through 4 (3rd iteration).

Pier	V_r (kip)	V_{bjs} (kip)	V_{dt} (kip)	V_{tc} (kip)
1	4.9	1.2	20.1	5.4
2	7.5	6.2	25.2	8.2
3	8.2	12.0	21.5	9.0
4	17.2	25.0	31.9	18.3

Summing the individual pier capacities gives a base shear capacity of 32.8 kip. Since this capacity is close to the capacity determined during the 2nd iteration, the calculation procedure is stopped and the base shear capacity of the wall is taken as 32.8 kip.

Step 6: Calculate Global Rocking Capacity

To calculate the global rocking capacity of the wall the schematic shown in Figure G.9 is used. Making use of moment equilibrium about point *o* gives:

$$0 = \frac{V_{GR}}{2}(120\text{in} + 240\text{in}) - 10.9\text{kip}(24\text{in} + 120\text{in} + 216\text{in} + 312\text{in}) - 6\text{kip}(336\text{in})$$

Solving for V_{GR} yields:

$$V_{GR} = 51.9\text{kip}$$

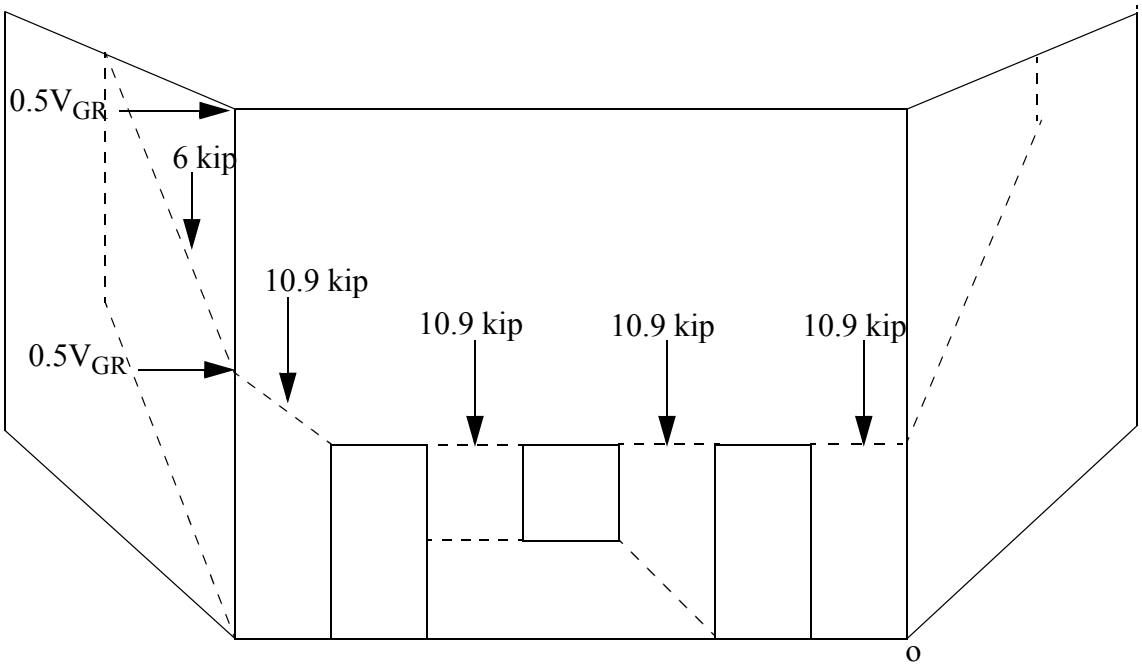

Figure G.9. Schematic used to calculate global rocking capacity.

Step 7: Summarize Results

Since the capacity associated with interstory shear response is less than the capacity associated with global rocking, the base shear capacity is taken as the capacity associated with interstory shear response.

$$\therefore V_{Total} = 32.8 kip$$

Figure G.10 shows a schematic which illustrates the predicted cracks and pier failure modes.

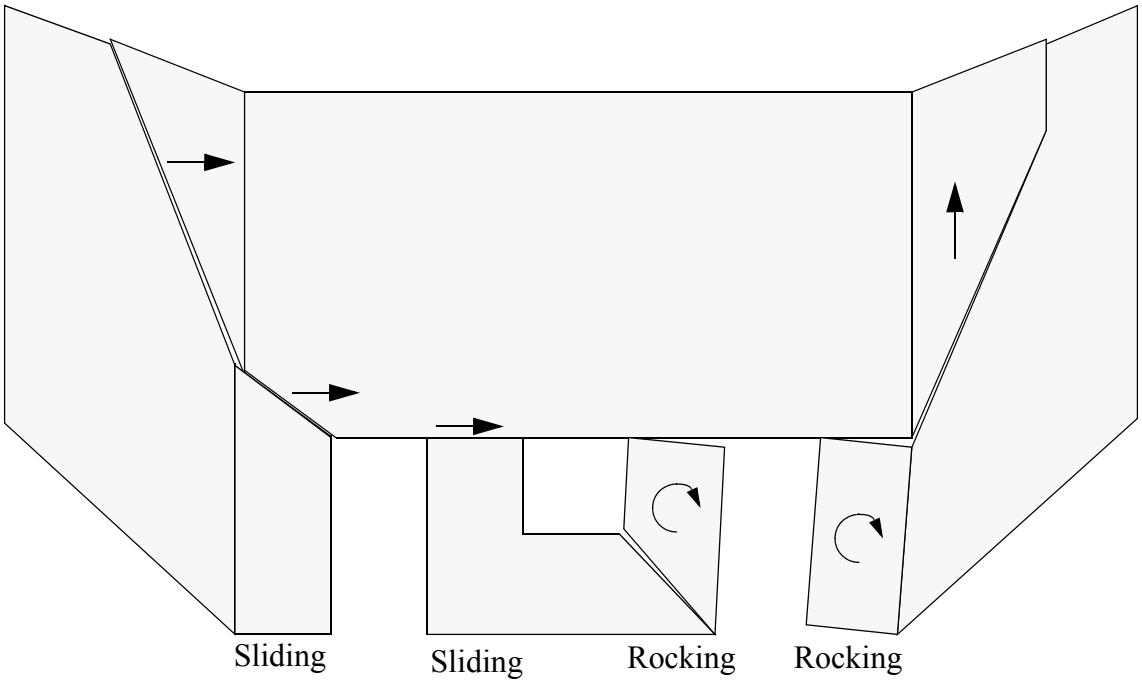

Figure G.10. Schematic illustrating the predicted cracking and pier failure modes.

REFERENCES

ABK (1981b) "Methodology for mitigation of seismic hazards in existing unreinforced masonry buildings: wall testing, out-of-plane". ABK-TR-04, Agbabian & Associates, S.B. Barnes & Associates, and Kariotis & Associates, EI Segundo, Calif.

ABK (1984) "Methodology for mitigation of seismic hazards in existing unreinforced masonry buildings: the methodology". ABK-TR-08, Agbabian & Associates, S.B. Barnes & Associates, and Kariotis & Associates, EI Segundo, Calif

Abrams D. P. (1992) "Strength and behavior of unreinforced masonry elements", 10th World Conference on Earthquake Engineering, Balkema, Rotterdam, pp 3475-3480.

Abrams, D.P. and Shah,N. (1992) "Cyclic load testing of unreinforced masonry walls", College of Engineering, University of Illinois at Urbana, Advanced Construction Technology Center Report #92-26-10.

ACI 530-02/ASCE 5-02/TMS 402-02 (2002) "Building code requirements for masonry structures", The Masonry Standards Joint Committee, ISBN 1-929081-13-8, Boulder, CO.

ACI 440 (2003) "Guide for the design and construction of externally bonded FRP systems for strengthening concrete structures", ACI Committee 440, Technical Committee Document 440.1R-03.

Al-Chaar, G. and H. A. Hasan (1998) "Masonry bearing and shear walls retrofitted with overlay composite material - seismic evaluation and dynamic testing", USACERL Technical Report 98/86, June.

Anthoine, A., Magonette,G., and Magenes,G. (1995), "Shear –compression testing and analysis of brick masonry walls", Proceedings of the 10th European Conference on Earthquake Engineering, Duma.

ASTM International (ASTM) (2000) “Standard test method for compressive strength of masonry prisms”, ASTM C1314-00, West Conshohocken, PA.

ASTM International (ASTM) (2000) “Standard test methods for sampling and testing brick and structural clay tile”, ASTM C67-00, West Conshohocken, PA.

Applied Technology Council (ATC) (1987) “Evaluating the seismic resistance of existing buildings”, Report ATC-14, Redwood City, CA.

Applied Technology Council (ATC) (1989) “A handbook for the seismic evaluation of existing buildings”, Report ATC-22, Redwood City, CA.

Applied Technology Council (ATC) (1992) “NEHRP handbook for the seismic evaluation of existing buildings”, Publication No. 178, Federal Emergency Management Agency, Washington, D.C. (FEMA-178).

Applied Technology Council (ATC) (1997) “NEHRP guidelines for the seismic rehabilitation of buildings”, Publication No. 273, Federal Emergency Management Agency, Washington, D.C. (FEMA-273).

Applied Technology Council (ATC) (1997) “NEHRP commentary on the guidelines for the seismic rehabilitation of buildings”, Publication No. 274, Federal Emergency Management Agency, Washington, D.C. (FEMA-274).

Applied Technology Council (ATC) (1999a) “Evaluation of earthquake damaged concrete and masonry wall buildings, Basic procedures manual”, Publication No. 306, Federal Emergency Management Agency, Washington, D.C. (FEMA-306).

Applied Technology Council (ATC) (1999b) “Evaluation of earthquake damaged concrete and masonry wall buildings, Technical Resources”, Publication No. 307, Federal Emergency Management Agency, Washington, D.C. (FEMA-307).

Applied Technology Council (ATC) (1999c) “Repair of earthquake damaged concrete and masonry wall buildings”, Publication No. 308, Federal Emergency Management Agency, Washington, D.C. (FEMA-308).

Applied Technology Council (ATC) (2000) “Prestandard and commentary for the seismic rehabilitation of buildings”, Publication No. 356, Federal Emergency Management Agency, Washington, D.C. (FEMA-356).

Atkinson, R. H., B. P. Amadei, S. Saeb, and S. Sture (1989) “Repose of masonry bed-joints in direct shear”, Journal of Structural Engineering, Vol. 115, No. 9., ASCE.

Benedetti, D., P. Carydis, and P. Pezzoli (1998) “Shaking table tests on 24 simple masonry buildings” Earthquake Engineering and Structural Dynamics, Vol. 27, pp 67-90.

Boussabah, L. and M. Bruneau (1992) “Review of the seismic performance of unreinforced masonry walls”, 10th World Conference on Earthquake Engineering, Balkema, Rotterdam, pp 4537-4540.

Bruneau, M. (1994) "Seismic evaluation of unreinforced masonry buildings - a state-of-the-art report", Canadian Journal of Civil Engineering. Vol 21, pp512-539

Calvi, G. M., G. R. Kingsley, and G. Magenes (1996) “Testing of masonry structures for seismic assessment”, Earthquake Spectra, Vol. 12, No. 1.

Chen, J. F. and J. G. Teng (2001) “Anchorage strength models for FRP and steel plates bonded to concrete”, Journal of Structural Engineering, Vol. 127, No. 7, ASCE.

Clough, R. H., R. L. Mayes, and P. Gulkan (1979) “Shaking table study of single-story masonry houses, volume 3: summary, conclusions, and recommendations", Report No. UCB/EERC-79/25.

Costley, A.C. and D. P. Abrams (1996) “Dynamic response of unreinforced masonry buildings with flexible diaphragms”, NCEER-96-0001.

Deppe, K. (1988) “The Whittier Narrows, California Earthquake of October 1, 1987 - evaluation of strengthened and unstrengthened unreinforced masonry in Los Angeles City”, Earthquake Spectra, Vol. 4, No. 1.

Ehsani, M.R. (1995) “Strengthening of Earthquake-Damaged Masonry Structures with Composite Material” Non-metallic (FRP) Reinforcement for Concrete Structures.pp680-687.

Ehsani, M.R., H. Saadatmanesh, and A. Al-Saidy (1997) “Shear Behavior of URM Retrofitted with FRP Overlays,” Journal of Composites for Construction, Vol.1, No. 1, ASCE, New York, NY.

Ehsani, M. R. and H. Saadatmanesh (1996) “Seismic retrofit of URM walls with fiber composites”, The Masonry Society Journal, Vol. 14, No. 2,pp 63-72.

Elgwady A. M., P. Lestuzzi and M. Badoux (2002) “Dynamic In-Plane Behavior of URM Wall Upgraded with Composites”, 3 rd ICCII, San Francisco, USA

Epperson, G. S. and D. P. Abrams (1989) “Nondestructive evaluation of masonry buildings”, College of Engineering, University of Illinois at Urbana, Advanced Construction Technology Center Report #89-26-03.

Franklin, S., J. Lynch, and D. P. Abrams (2001) “Performance of rehabilitated URM shear walls: flexural behavior of piers”, Department of Civil Engineering, University of Illinois at Urbana-Champaign.

French, S. and R. Olshansky (2000) “Inventory of essential facilities in Mid-America”, Project SE-1 Final Report, Mid-America Earthquake Center.

Hall, J. D., P. M. Schuman, and H. R. Hamilton III (2002) “Ductile anchorage for connecting FRP of strengthening under-reinforced masonry buildings”, Journal of Composites for Construction, Vol. 6, No. 1, Feb, pp. 3-10.

Hamid, A. and R. C. Drysdale (1980) “Behavior of brick masonry under combined shear and compression loading”, Proc. 2nd Canadian Masonry Symp., Ottawa, Canada, June.

Hamilton, H. R. and C. W. Dolan (2001) “Flexural capacity of glass FRP strengthened concrete masonry walls”, Journal of Composites for Construction, Vol.5, No. 3, pp170-178.

Hegemier, G. A., et al. (1978) “On the behavior of joints in concrete masonry", Proc., North American Masonry Conference, Boulder, CO.

Hinkley, A. T. (1996) “Tests on one-story prestressed brickwork shear walls”, New Zealand Engineering, June, pp245-252.

Holberg, A. M. and H. R. Hamilton III (2002) “Strengthening URM with GFRP composites and ductile connections”, Earthquake Spectra, Vol. 18, No. 1, February, pp 63-84.

Huizer, A. and N. G. Shrive (1986) “Performance of a post-tensioned, single-wythe, clay brick masonry wall tested in shear”, Fourth Canadian Symposium, Fredericton, N.B., Vol. 2, pp 609-619.

ICBO (1991) “Uniform code for building conservation”. International Conference of Building Officials, Whittier, CA.

Jabarov, M., S. V. Kozharinov, and A. A. Lunyov (1980) “Strengthening of damaged masonry by reinforced mortar layers”, Proc. 7th World Conference on Earthquake Engineering, Vol. 4, pp 73-80.

Jai, J. and G. S. Springer (2000a) “Reinforcing masonry walls with composite materials-test results”, Journal of Composite Materials, Vol. 34, No. 16, pp1369-1381.

Jai, J. and G. S. Springer (2000b) “Reinforcing masonry walls with composite materials-model”, Journal of Composite Materials, Vol. 34, No. 18, pp 1548-1581.

Kahn, L. F. (1984) “Shotcrete strengthening of brick masonry walls.” Concrete Inst., Vol. 6, No. 7,pp 34-40.

Kiss, R. M., L. P. Kollar, J. Jai, H. Krawinkler (2002) “FRP strengthened masonry beams. part I - model”, Journal of Composite Materials, Vol. 36, No. 5, pp 521-536.

Konig, G., W. Mann, and A. Otes (1988) “Experimental investigations on the behavior of unreinforced masonry walls under seismically induced loads and lessons derived”, Proceedings of Ninth World Conference on Earthquake Engineering, August 2-9, Tokyo-Kyoto, Japan, Vol VIII, pp 1117-1122.

Kolsch, H. (1998) “Carbon fiber cement matrix (CFCM) overlay system for masonry strengthening”, Journal of Composites for Contruction Vol. 2, No. 2, pp 105-109.

Laursen, P. T., F. Seible, G. A. Hegemier, and D. Innamorato (1995) “Seismic Retrofit and Repair of Masonry Walls with Carbon Overlays”, Non-metallic (FRP) Reinforcement for Concrete Structures, pp 616-623.

Laursen, P. T., and J. M. Ingham (2001a) “Structural testing of single-storey post-tensioned concrete masonry walls”, The Masonry Society Journal, pp 69-82.

Laursen, P., and J. Ingham (2001b) “Seismic resistance of prestressed concrete masonry shear walls”, 2001 Structures Congress and Exposition, Washington, D.C.

Lee, H. H. and S. P. Prawel (1991) “The seismic renovation and repair potential of ferrocement coatings applied to old brick masonry walls.” Proc. 6th Canadian Conference on Earthquake Engineering.

Lissel, S. L., E. Y. Sayed-Ahmed, and N. G. Shrive (1999) “Prestressed masonry-the last ten years”, 8th North American Masonry Conference, Austin, TX, pp 599-610.

Lissel, S. L., D. Tilleman, E. Y. Sayed-Ahmed, and N. G. Shrive (1998) “Carbon fibre reinforced plastic (CFRP) prestressed masonry,” 8th Canadian Masonry Symposium, Jasper, Alberta, pp 610-621.

Magenes, G., and G. M Calvi (1992) “Cyclic behavior of brick masonry walls”, Tenth World Conference on Earthquake Engineering, Balkema, Rotterdam. pp 3517-3522.

Magenes, G., G. R. Kingsley, and G. M Calvi (1995) “Seismic testing of a full-scale, two-story masonry building: test procedure and measured experimental response”.

Marshall, O. S., S. C. Sweeney, and J. C. Trovillion (2000) "Performance Testing of Fiber-Reinforced Polymer Composite Overlays for Seismic Rehabilitation of Unreinforced Masonry Walls", USACERL, ERCE/CERL TR-00-18.

Marshall, O. S. (2001) "Interim wall test report", Memorandum CEERD-CF-M, USACERL, Champaign, IL.

Marshall O. S. and S. C. Sweeney (2002) "Summary of wall tests", USACERL, Champaign, IL.

Marshall, O. S. (2002) "Test report on CMU wall strengthening technology", USACERL, Champaign, IL.

Manzouri, T., M. P. Schuller, P. B. Shing, and B. Amadei (1996) "Repair and retrofit of unreinforced masonry structures." Earthquake Spectra, Vol. 12, No. 4, pp 903-922.

Manzouri, T., P. B. Shing, B. Amadei, M. Schuller, and R. Atkinson (1995) "Repair and retrofit of unreinforced masonry walls: experimental evaluation and finite element analysis", Department of Civil, Environmental and Architectural Engineering, University of Colorado: Boulder, Colorado, Report CU/SR-95/2.

Meli, R. (1973) "Behavior of masonry walls under lateral loads", Proc., 5th World Congress on Earthquake Engineering., pp 853-862.

Moon, F., T. Yi, R. Leon, and L. Kahn (2001) "Retrofit of URM structures with FRP overlays and post-tensioning", Rehabilitation and Repairing the Buildings and Bridges of the America - Hemispheric Workshop on Future Directions, ASCE.

Neubauer, U. and F. S. Rostasy (1997) "Design aspects of concrete structures strengthened with externally bonded CFRP-plates", Proc., 7th International Conference on Structural Faults and Repairs, ECS Publications, Edinburgh, Scotland, 2, pp 109-118.

Page, A. W. and A. Huizer (1988) "Racking Tests on Reinforced and Prestressed Hollow Clay Masonry Walls", 8th International Brick and Block Masonry Conference, Dublin, Ireland, pp 538-547.

Paulson, T. J. and D.P. Abrams (1990) “Correlation between static and dynamic response of model masonry structures”, Earthquake Spectra, Vol. 6, No. 3, pp 573-591.

Paquette, J., and M. Bruneau (2003) “Pseudo-dynamic testing of unreinforced masonry building with flexible diaphragm”, ASCE Journal of Structural Engineering, Vol. 129, No. 6, pp 708-716.

Peralta, D. F., J. M. Bracci, and M. B. Hueste (2000), “Seismic performance of rehabilitated floor and roof diaphragms”, ST-8 Project final report, Mid-America Earthquake Center, Texas A&M University.

Prawl, S. P., A. M. Reinhorn, and S. K. Kunnath (1986) “Seismic strengthening of structural masonry walls with external coatings.” Proc., 3rd U.S. Conference on Earthquake Engineering, Vol. 2, EERI, pp 1323-1333.

Roko, K. E., T. E. Boothby, and C. E. Bakis (2001) “Strain transfer analysis of masonry prisms reinforced with bonded carbon fiber reinforced polymer sheets”,” The Masonry Society Journal, September, pp 57-68.

Sayed-Ahmed, E. Y., S. L. Lissel, G. Tadros, and N. G. Shrive (1999) “Carbon fibre reinforced polymer (CFRP) post-tensioned masonry diaphragm walls: prestressing, behavior, and design recommendations,” Canadian Journal of Civil Engineering, Vol. 226, pp 324-244.

Schultz, A. E. and M. J. Scolforo (1991) “An overview of prestressed masonry”, The Masonry Society Journal, Vol. 10, No. 1, pp 6-15.

Schwegler, G. (1994). “Masonry construction strengthened with fiber composites in seismically endangered zones.” Proc., 10th Eur. Conf. on Earthquake Engrg., A. A. Balkema, Rotterdam, The Netherlands, 454-458.

Sheppard, P. and Terceli. (1980) “The effect of repair and and strengthening methods for masonry walls.” Proc. 7th World Conference on Earthquake Engineering, Vol. 6, pp 255-264.

Teng, J. G., J. F. Chen, S. T. Smith (2001) “Debonding failures in FRP-strengthened RC beams: Failure modes, existing research and future challenges”, Composites in Construction: A reality, 2001, pp 139-148.

Tomazevic, M., M. Lutman, and P. Weiss (1993) “The seismic resistance of historical urban buildings and the interventions in their floor systems: an experimental study", The Masonry Society Journal, August, pp 77-86.

Tomazevic, M. (1999) “Earthquake-Resistant Design of Masonry Buildings”, Imperial College Press.

Triantafillou, T. C. (1998) “Strengthening of masonry structures using epoxy-bonded FRP laminates”, Journal of Composites for Construction, Vol. 2, No. 2, pp 96-103.

Tumialan, J. G., F. Micelli, and A. Nanni (2001) “Strengthening of masonry structures with FRP composites”, 2001 Structures Congress and Exposition, Washington, D.C.

Tumialan J. G., N. Galati, S. M. Namboorimadathil, and A. Nanni (2002) “Strengthening of masonry with FRP bars,” Third International Conference on Composites in Infrastructure (ICCI 2002), San Francisco, CA, June 10-12.

Velazquez-Dimas, J. I., M. R. Ehsani, and H. Saadatmanesh (2000a) “Out-of-plane behavior of brick masonry walls strengthened with fiber composites,” ACI Structural Journal, May-June 2000, pp 377-387.

Velazquez-Dimas, J. I., M. R. Ehsani, and H. Saadatmanesh (2000b) “Seismic retrofit of URM walls with fiber composites”. 12th World Conference on Earthquake Engineering,

Vinson, J. R. and R. L. Sierakowski. (1986) “The behavior of structures composed of composite Materials”, Martinus-Nijhoff Publishers (now Kluwer Academic Publishers) Dordrecht, The Netherlands.

Yi, T. (2004) “Large-scale testing of a two-story URM structure”, Ph.D Thesis, Georgia Institute of Technology, Atlanta, GA.

Zhao, T., Z. Chenjun, X. Jian, and L. Mingguoet (2000) “Study and application of the new technique of repairing and strengthening brick walls with continuous carbon fiber sheets”, Tianjin University, Tianjin, China.